

University of Naples Federico II
Polytechnic and Basic Science School



Doctoral thesis in
Structural, geotechnical and seismic engineering
XXIX CYCLE
PhD Coordinator Prof. Luciano Rosati

**Behaviour of segmental tunnel lining
under static and dynamic loads**

Stefania Fabozzi

May, 2017

Supervisors

Prof. Emilio Bilotta

Department of Civil, Architectural and Environmental Engineering of University of Naples
Federico II

Prof. Aldo Zollo

Department of Physics of University of Naples Federico II

To my mum, my dad and my brother.

Nessuna umana investigazione si può dimandare vera scienza, s'essa non passa per le matematiche dimostrazioni. [...] Nessuna certezza è dove non si può applicare una delle scienze matematiche, over che non sono unite con esse matematiche. [...]

Trattato della pittura, Leonardo da Vinci

Acknowledgements

This research work couldn't have been possible if not under the guidance of professor Emilio Bilotta to whom I want to express my sincere gratitude for his daily presence, for his time, his support in every moment of difficulty and to have waited for me patiently at the start of this 'journey'. His knowledge, experience and devotion to research have been my north star in searching the right way.

I'm very grateful to professor Aldo Zollo and his research group to helping me to develop a part of this work; professor Matteo Picozzi specially supported me in this, with his essential help. Thanks Matteo for your teachings.

I thank all professors of Geotechnical Department of University of Naples Federico II, professor Francesco Silvestri particularly.

All my colleagues, as well as my friends, have been very 'precious' for me, for their scientific, technical and, above all, moral support in these years.

Special thanks to 'Chinese Family' that I've meet in Shanghai at Tongji University where I was been hosted for few months; I want to thank in particular professor Yong Yuan, professor Haitao Yu, professor Xian Liu, Mr. Chong Li and Mr. Zhiming Zhang.

Thanks for the time and the knowledge that professor Haitao Yu has shared with me, giving to me many advices on my work.

Zhiming, my best Chinese friend, has been my support in China and I sincerely thank him for helping me to discover his fascinating culture.

Thanks to Anna, my best friend, but also my best sister, my best confidant, who knows me better than anyone else.

I should to thank my 'first family' that I have found in the University of Campania Luigi Vanvitelli. I like to thank professor Eugenio Ruocco who has been the supervisor of my Master thesis, as well as my reference in these years; I thank him for his capability to listen to me, to understand me and to know how helping me.

Special thanks to professor Alessandro Mandolini to be my 'spiritual guide'. Thank you for conveying to me, with your charismatic personality, the passion for the 'underground', for helping me to take the decision to start this route that probably I would not choose without your support. Thus, the result of this thesis is largely due to you. Hoping that you will be my 'spiritual guide' also in the future.

Finally, I'm endlessly grateful to my family, to my brother Alessio, to the infinite love of my mum and my dad to whom I dedicate this thesis.

Stefania Fabozzi

Contents

Preface	v
<i>Contents and outline of the thesis</i>	vii
FIRST PART	
Behaviour of segmental tunnel lining under static loads	
CHAPTER 1: Segmental tunnel lining	1
Introduction	1
1.1 Technological aspects	1
1.1.1 Segments	2
1.1.2 Connections	2
1.1.3 Sealing and grouting	4
1.2 Effect of segmental layout on lining behaviour	7
1.2.1 Experimental behaviour of joints	7
1.2.2 3D interaction of segments	18
1.3 Design of segmental lining	21
1.3.1 Indirect methods	23
1.3.2 2D calculation methods	26
1.3.3 3D calculation methods	30
CHAPTER 2: Mechanized tunnelling effect on the lining behaviour	41
Introduction	41
2.1 Mechanized tunnelling methods	41
2.1.1 History of mechanized tunnelling	41
2.1.2 Modern mechanized tunnelling	43
2.2 Effects on the lining	47
2.2.1 Effect of jack thrust	47
2.2.2 Effect of grouting	50
2.2.3 Effect of unfavourable conditions during tunnelling	54
2.3 Soil structure interaction	58
2.3.1 Experimental evidence	58
2.3.2 Numerical investigation	61
CHAPTER 3: Case histories	65
Introduction	65
3.1 High speed railway link Bologna-Firenze	65

3.2	<i>Metro Line 6 of Naples</i>	71
3.2.1	<i>Layout and ground conditions</i>	72
3.2.2	<i>Geometry of the tunnel lining and monitoring</i>	75
3.2.3	<i>3D numerical model</i>	79
3.2.4	<i>Details of the EPB-TBM tunnelling</i>	83
3.2.5	<i>Validation of the 3D numerical model</i>	86
3.2.6	<i>Structure and soil behaviour during tunnelling</i>	90

SECOND PART

Behaviour of segmental lining under uniform seismic load

CHAPTER 4: Tunnel - ground interaction during uniform seismic shaking	101
Introduction	101
4.1 <i>Literature review</i>	102
4.2 <i>Approaches of analysis in plane strain</i>	108
4.2.1 <i>Pseudo-static analysis</i>	109
4.2.2 <i>Full dynamic analysis</i>	115
4.2.3 <i>Comparison</i>	117
4.3 <i>Comparison between dynamic behaviour of segmental and continuous lining</i>	118
4.3.1 <i>Experimental benchmark</i>	118
4.3.2 <i>Influence of pre-seismic conditions</i>	125
4.3.3 <i>Influence of the segmental layout</i>	129
CHAPTER 5: Seismic vulnerability of segmental tunnel lining	137
Introduction	137
5.1 <i>Fragility curves</i>	138
5.1.1 <i>Continuous lining</i>	140
5.1.2 <i>Segmental lining</i>	153
5.2 <i>Feasibility of early warning system for segmental tunnel lining</i>	166
5.2.1 <i>Probabilistic seismic hazard approach</i>	170
5.2.2 <i>Real time approach</i>	199

THIRD PART

Behaviour of tunnel under non uniform seismic load

CHAPTER 6: Tunnel - ground interaction during non uniform seismic shaking	207
Introduction	207
6.1 <i>Literature review</i>	208
6.1.1 <i>Analytical solutions</i>	209
6.1.2 <i>Numerical solutions</i>	222

6.2	<i>Numerical analysis</i>	233
6.2.1	<i>3D full dynamic analysis: Free-field condition</i>	233
6.2.2	<i>3D full dynamic analysis: Soil-structure interaction</i>	238
6.2.3	<i>2D multi-masses-beam-springs model: Soil-structure interaction</i>	243
CHAPTER 7: Conclusions		247
Appendix 1.....		251
Appendix 2.....		259
Appendix 3.....		263
References.....		265

Preface

Tunnelling is a branch of civil engineering that has experienced many changes over the time and even today the development of tunnelling technology makes it increasingly powerful. The tunnel construction planning and the study of its behaviour under different load conditions involves many interdisciplinary aspects mainly of geotechnical and structural engineering; it is a complex mechanism of soil-structure interaction strongly influenced by the nature of the soil, lining technology and the excavation process. The soil and the lining suffer a continuous changing of their stress and strain state during tunnelling which plays the main role on the soil and lining behaviour.

Mechanized excavation is a particular tunnel construction technique more competitive with respect to traditional ones since it allows almost contemporary the excavation phases execution and the tunnel lining installation, thanks to the use of Tunnel Boring Machine that, with the aid of sophisticated automation and control systems, advances to tens of meters per day in different geological and hydrogeological conditions.

In urban areas where tunnelling can have a potential impact on the aboveground structures in terms of settlements and deformations, mechanized tunnelling with closed shield is a widespread technique able to ensure front stability and an acceptable range of settlements.

In such construction technique, the structural behaviour of lining is mainly influenced by its installation process and its segmental nature (*Bloom 2001*) which induces a complex three-dimensional interaction mechanism between the single concrete lining segments (*Koizumi 2003*) through the longitudinal joints (between the segments in the same ring) and circumferential joints (between the rings).

The particularity of this technology arises to research many questions about the real structural behaviour of tunnel lining which is not yet completely clear, during tunnel construction, under static and dynamic loads, about the real structural behaviour of longitudinal and transversal joints, about the possibility to optimize lining design obtaining more powerful systems.

Experimental and numerical research produced up to now shows that the joints have an important effect on the tunnel lining behaviour and it can't be neglected in the project of this kind of structure to obtain a realistic modelling.

The knowledge of the behaviour of segmental joints under tunnelling loading is certainly advanced giving a good instrument of interpretation of the global structural behaviour and the main influence parameters which should be taken into account into analytical or numerical approaches for the tunnel lining design. Analytical and two dimensional simplified numerical methods, considering the effect of longitudinal joints on tunnel lining behaviour, are usually applied to pre-dimension the segmental tunnel lining; these approaches can't consider the joint technology and then its three dimensional effect. Only a three dimensional numerical modelling can be used to achieve a very high level of joint detail and definition. This last approach in addition, allows to take into consideration the main forces acting on the lining during the entire tunnel excavation process, influencing the long term state of stress and strain in the lining.

Unlike the static case, the knowledge of dynamic behaviour of segmental tunnel lining is not yet very advanced.

The wave passage along the tunnel can cause 1) bending in the transversal lining section induced by a transversal component of seismic action 2) axial deformation (compression/tension along the tunnel axis) and bending in the longitudinal horizontal plane for the wave passage along the tunnel axis due to the spatial incoherence of the seismic motion.

The first deformation mechanism leads increment of the internal forces acting on the transversal bending plain of the lining and relative displacement/rotation in the longitudinal joints; the second deformation mechanism on the other hand, has an effect on the transversal bending response of the lining, increasing the transversal component of internal forces, and generate also an increment of longitudinal component of lining internal forces and relative displacement/rotation in the circumferential joints.

Such complex soil-structure interaction mechanism under seismic loads are generally studied in the experimental literature with monitored centrifuge or shaking table tests on physical models at reduced scale. These tests allow to monitor the main mechanisms involved in the evolution of observed phenomena to be identified and provide an extensive base of experimental data to calibrate advanced numerical methods of analysis in ideal situations where soil properties, boundary conditions and dynamic loads are clearly defined.

No centrifuge test has been performed up to now considering the presence of the joints in the lining; they usually consider the soil-structure interaction in the case of not jointed lining under uniform load respect the tunnel axis. Multi-points shaking table in a linear array instead allows to simulate the travelling waves passage along the tunnel axis; some experiments have been performed in the technical literature for such immersed tunnel longitudinally jointed, considering the coupled effect of transversal and longitudinal deformation mechanisms due to multi-directional seismic shaking (*Yuan Y. et al 2016, Yu H. et al 2016a*).

Transversal and longitudinal dynamic behaviours of segmental lining are typically approached separately with simplified 1D analytical (pseudo-static) solutions, simplified 2D pseudo-static approach or with 2D full dynamic analysis, without evaluate the real 3D coupled deformation mechanism nor considering the dynamic behaviour of the joints during seismic shaking which excessive rotation could induce a possible damage for the post-earthquake segmental lining functionality.

The three-dimensionality of the problem related to the segmental tunnel lining behaviour is investigate in this work both under static and dynamic loading conditions, including the complex excavation process of mechanized tunnelling in the first case and the asynchronous of the ground motion in the second one.

Such considerations have been carried out on the seismic vulnerability of this tunnel lining technology under plane strain seismic loading.

Contents and outline of the thesis

The aim of the presented dissertation is to provide a three-dimensional numerical model suitable to interpret the static and dynamic behaviour of a kind of segmental tunnel lining in soft soil. The static performance of the structure is investigated during the tunnel construction, involving the main tunnelling loads, obtaining the evolution of the state of stress and strain in the lining.

The dynamic performance of segmental lining has been investigated both under uniform and not uniform seismic loads. In the case of uniform seismic load, pseudo static and full dynamic approaches have been compared, while non-linear coupled analysis have been used to investigate the post-earthquake lining condition.

A study of the seismic vulnerability of such structures has been conducted based on fragility curves for different levels of damage. A procedure for the forecast method of risk assessment has been proposed for the case of segmental tunnel lining assuming as critical damage parameter the longitudinal joints rotation. Furthermore, a study of feasibility of Earthquake Early Warning System, EEWS, based on thresholds has been conducted through a probabilistic and a real-time approach for such tunnel structure.

The coupling effect of multi-directional seismic motion both in transversal and longitudinal direction of the tunnel has also taken into account in the evaluation of dynamic tunnel behaviour. A comparison between the effect of synchronous and not synchronous seismic motion along the tunnel axis has been done in terms of dynamic increment of the components of forces in the lining.

The work has been divided into three main parts.

FIRST PART - Behaviour of segmental tunnel lining under static loads

The first part is strictly related to the behaviour of segmental lining under static loads involved into tunnelling and structured in three chapters.

Chapter 1: A description of longitudinal and circumferential joint mechanical behaviour has been introduced through a literature review of many experimental tests performed up to now on different joint technologies, representing the starting point of the research because it allows to focus the governing factors of the structural response of such structures. The technology effect on the coupling interaction between the segments and different approaches of design have been discussed. Analytical solutions, 2D simplified numerical analysis and more sophisticated 3D numerical analysis are compared to understand the degree of approximation or detail that can be achieved with different approaches

Chapter 2: The behaviour of the segmental tunnel lining is influenced not only by the technology itself but also by the load scheme to which it is subjected and the loads level which undergoes during tunnelling, until to achieve a steady state in long term condition. The chapter discusses the technological aspects of mechanized excavation that mainly influence the tunnel lining loading and its structural behaviour. A literature review of some 3D numerical models of tunnel excavation process is discussed.

Chapter 3: The case history of the segmental lining referred to the connecting railway in Florence, studied by *Do et al. 2013*, is here repurposed. A three dimensional numerical model has been calibrated for the case of study and the comparison with the authors has been proposed in terms of increment of internal forces in the lining in the long term condition. This is a preliminary study for the calibration of the segmental lining numerical model, better investigated and validated for the case history of Metro Line 6 of Naples for which monitoring data of the entire excavation process were available.

The mechanized excavation process of Metro Line 6 of Naples has been implemented in the FE code Plaxis 3D according to the available monitoring data of the Tunnel Boring Machine advancement. The proposed model has been validated against the experimental measurements of the strains of in situ instrumented segmented ring.

SECOND PART: Behaviour of segmental tunnel lining under uniform seismic loads.

Once investigated the static stress and strain condition due to the tunnelling loads, the second part of the work concerns the dynamic behaviour of segmental tunnel lining under seismic uniform load, and is structured in two chapters.

Chapter 4: An overview of the dynamic response of underground structures under transversal earthquake loading is presented with reference to the damages occurred in the underground structures during recent earthquakes. The common analytical solutions, simplified and advanced numerical methods to predict the behaviour of tunnels during seismic shaking are here discussed.

The chapter approaches to the introduced problem investigating from one hand the effect of different literature dynamic methods and from the other hand the effect of segmental lining technology in the following way:

- I. Pseudo-static and full dynamic approaches for the evaluation of the effects of uniform seismic shaking in the tunnel transversal section have been compared in terms of dynamic increment of internal forces. The comparison refers to the plain strain tunnel section of the case study of Metro Line 6 of Naples.
- II. Starting from the interpretation of the results of the centrifuge test model T3 performed by *Lanzano 2009* on a continuous tunnel lining in reduced scale, the study of the soil-structure interaction has been extended to the case of segmental lining. The dynamic behaviour of longitudinal joints has been investigated with a set of non-linear 3D full dynamic analyses on the segmental layout adopted in the Chapter 3. The results have been carried out in terms of joint rotation during the dynamic time for different real recorded earthquakes. The seismic demand of segmental lining has been compared with the continuous lining one, including the effect of the excavation process on the pre-seismic conditions which influence the dynamic response of the lining.

Chapter 5: The numerical results obtained in the Chapter 4 are the starting point for the evaluation of the seismic vulnerability of the segmental tunnel lining studied in this Chapter. The fragility curves have been adopted as forecast method of vulnerability of the structure, constructed for different levels of damage and based on 2D non-linear full dynamic analysis. Longitudinal joint rotation has been assumed as potential damage parameter, in consideration of the higher flexibility of the segmental lining respect the case of continuous one, and the high rotational demand in correspondence of the longitudinal joints. The framework of the problem, procedure of numerical simulations and definition of numerical fragility curves for minor, moderate and extensive damage and for different soil types (B, C and D) are here discussed. The sets of fragility curves carried out have been compared with empirical fragility curves available in literature.

In the structure engineering, fragility curves are commonly used in the application of Earthquake Early Warning Systems (EEWS) based on thresholds which represent a tool for the implementation of protective measures aiming at reducing the vulnerability of structure to seismic risk. In this context, a preliminary study of feasibility of EEWS based on thresholds has been conducted simulating different scenarios of earthquake for some Italian target sites, through the probabilistic hazard disaggregation approach and real-time approach. The PRObabilistic and Evolutionary early warning SysTem (PRESTo; *Satriano et al. 2011*, <http://www.prestoews.org>), for instance, a free and open source software platform for EEW developed by the RISSCLab group of the University Federico II in Naples, Italy, has been used for the real-time simulation.

THIRD PART: Behaviour of tunnel under non uniform seismic loads.

The problem of the underground structures behaviour subjected to asynchronous seismic shaking is here discussed and approached through numerical methods. This part is structured as follows.

Chapter 6: The understanding of soil free field deformation and the interaction with tunnel due to the travelling wave passage is dealt with the literature review of some experimental tests conducted with shaking table on such kind of segmental and immersed tunnels. The chapter itemizes also analytical and numerical solutions developed in the technical literature.

A three dimensional numerical model able to catch the main deformation mechanisms of the soil subjected to multi-directional seismic motion, has been developed in the FE code Plaxis 3D. The free field soil response under travelling waves has been validated against the results obtained on the same model developed in Abaqus 3D. Once validated the free-field numerical model, the soil structure interaction has been investigated with a set of parametrical analysis varying longitudinal time-lag of the travelling wave in terms of dynamic increment of transversal and longitudinal internal forces arising in the lining. A comparison between uniform and not uniform seismic load is shown for different seismic loading cases.

A simplified 2D multi-masses-beam-springs model developed by *Li Chong 2016* has been implemented in Abaqus 2D in order to provide a further validation of the proposed 3D model in terms of soil-structure interaction, comparing the longitudinal component of dynamic increment of internal forces evaluated with 2D and 3D numerical methods.

FIRST PART: Behaviour of segmental tunnel lining under static loads

CHAPTER 1

Segmental tunnel lining

Introduction

Segmental lining is the typical support system of mechanized excavation, realized through the installation of multiple adjacent rings along the tunnel axis, assembled within the TBM tail shield with single precast concrete segments, with defined dimension and shape.

In a such configuration, tunnel lining presents structural discontinuities between the segments of the same ring (longitudinal joint), in a parallel direction to the tunnel axis, and between adjacent rings (transversal or circumferential joint), in the transverse direction.

Each segment is usually in a different angular position of the previous or subsequent ring, giving a 3D staggered lining configuration to the tunnel structure along the longitudinal direction, creating a masonry layout to minimize the sailing problem when four corners of segments coincide (*Bloom 2001*) and avoid the longitudinal joints to be in line.

Joints seem to be the vulnerable locations of tunnel, playing an important rule on the bearing capacity of the lining and, more in general, on its mechanical behaviour. For this reason, technical literature gives particular attention to the joint technology.

Due to the high speed at which the technology has developed within some country, there is a significant variation in the design of such joint connections but also materials, geometry, waterproofing and reinforcement systems of lining can be very different.

1.1 *Technological aspects*

The lining installed with mechanized tunnelling can be one or more layered constructions. The single layer construction, generally realized with segments, has to guarantee itself the support for the excavated cavity and the waterproofing requirements at short and long term. In double layer construction, the outer lining, generally made of shotcrete, has not a long-term structural function, ensured by the inner one very similar to the single layer system, but has to provide an immediate support against the soil pressure without a waterproofing function, usually undertaken by an intermediate membrane.

Segments are designed to provide structural capacity to resist temporary loads, demoulding, storage/stacking, transportation, handling, erection and grouting pressures, permanent loads, external ground loads, external water pressure, TBM thrust, imposed loads (traffic, adjacent foundation/pile loads), external construction (adjacent tunnel construction) and dynamic loads, longitudinal and circumferential joints have to adsorb compressive stresses generated by the TBM thrust during excavation and by the surrounding soil along the segments contact surface.

1.1.1 Segments

In the common practice the single ring is made up of several segments identical in the shape (rectangular, trapezoidal, rhomboidal or hexagonal) unless for the closing segment (the key), the last segment placed in the assembly of the ring to close it.

The rectangular and trapezoidal shapes are the most commonly used in the design practice in particular for largest ring diameters with the tendency to use hexagonal segments for smaller ones. The latter present a significant benefit respect to the other shapes because the TBM can thrust from half of the ring while the other half is being erected. In addition, for the characteristic shape of singular segment, there is no continuous ring joint in this system, as this is offset by a half segment width between adjacent segments, inducing a stiffer structure compared with the rectangular one. Disadvantage of this technology result from the size of the segments with increasing diameter, involving problems in transport and assembly process, therefore preferable for diameters up to 4.50 m.

Segment dimensions are chosen to be as large as possible, resulting in a minimum number of segments per ring, with the aim of optimising the speed at which the tunnel boring machine advances. The segment's width production, transporting and installing needs.

The segment's thickness is function of structural and constructional needs, typically included between 0.20 m to 0.70 m. The minimum thickness has to be such to absorb through the load-bearing area the thrust jacking forces, the maximum one is such to resist bending from external loads. In the case of ordinary tunnel diameter, lining thickness is typically about 1/20 of tunnel diameter (*Bloom 2001*) and the segments are usually precast elements of Ordinary Concrete C35/45 reinforced with steel or steel fibres. Recently the research is investigating other geo-synthetic fibres and innovative solution, such as Glass Fiber Reinforced Polymer, which can be used mainly when a high resistance is required (*Caratelli et al. 2016*).

Reinforced concrete is used to withstand bending moments and splitting forces that occur in the installation process and during the transport. In the case of tunnel with large diameter, lining thickness increases significantly. Typically, for logistic problems related to the construction of such tunnel, the segments are made with steel fibre reinforced high strength concrete C100/115 and ultra high strength concrete C180/210, to reduce the lining thickness up to a value of 1/58 of tunnel diameter.

1.1.2 Connections

Longitudinal connection

Longitudinal connection is the contact surface between two adjacent segments in the same ring. It can be flat, convex or convex-concave contact surfaces (Figure 1.1).

Convex surface contact is usually used in the case of large axial compressive forces demand, and then for high value of joint rotation, unacceptable to ensure the equilibrium in a flat joint. Convex joint system is not very stable during ring installation because there is no ring compressive force and no resistance to rotation, so that it is necessary to add bolting joints to avoid the segment collapse.

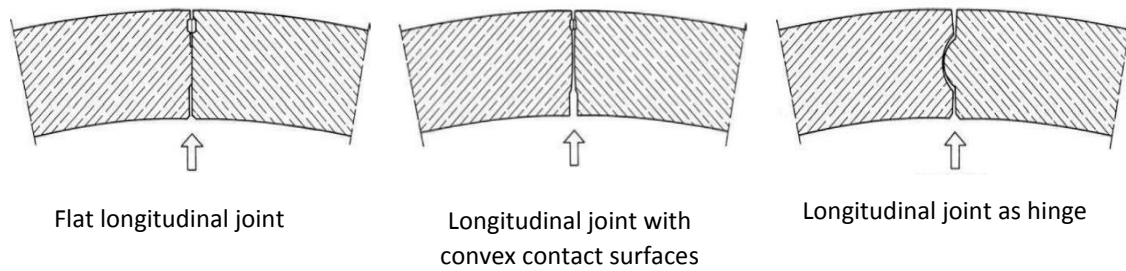


Figure 1.1. Longitudinal contact surfaces (after Maidl B. et al. 2011).

Convex-concave contact surface is preferred for very high rotational demand; in this case the edges of the concave side of the joint are particularly at risk not providing enough reinforcement at this location.

At time, the contact surface between the segments can be just a concrete-concrete surface, can be made of packers material, usually to distribute the loads in the joints neglecting damaging stress concentration, or can be jointed, to increase the node resistance.

The packers material can be made generally of plastic or bituminous, the bolts are generally in steel and they can be straight, curved or inclined (Figure 1.2). For their collocation it is necessary to create “pockets” and “grooves” into which the bolts are inserted, the bolts themselves are metallic while the embedded threads, if present, are generally in plastic.

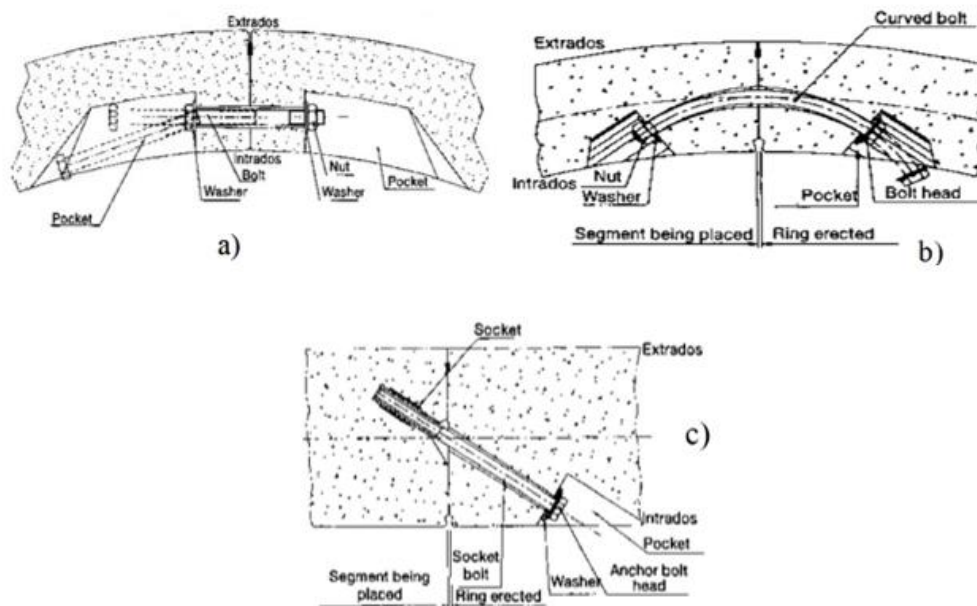


Figure 1.2. Joints with bolts. a) straight bolt, b) curved bolt, c) inclined bolt (AFTES 1999).

Through the contact surfaces and connecting elements if there are, axial ring forces, bending moments from eccentric axial forces and shear forces from external and internal loads are transferred, reducing the forces acting on the adjacent segments.

Circumferential connection

The contact surface between adjacent rings is usually flat or convex-concave and not necessarily perpendicular to the tunnel axis, as in the case of tapered rings (Figure 1.3).

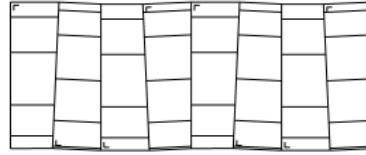


Figure 1.3. Tapered ring.

Circumferential joints are usually a concrete-concrete interface and can be bolted, as for the longitudinal ones, but can be also thickness of packing materials or joints with dowels (Figure 1.4a) which usually doesn't provide a mechanical effort or any coupling transferring mechanism as in the case of permanent bolts, or pin and socket systems (Figure 1.4b) which provides a coupling affect at point location.

In the last years push-fit plastic dowels have replaced steel bolts on the circumferential joint in many parts of the world, and there are projects where guiding rods have been used in place of steel bolts on the longitudinal joint (Harding and Chappell 2014).

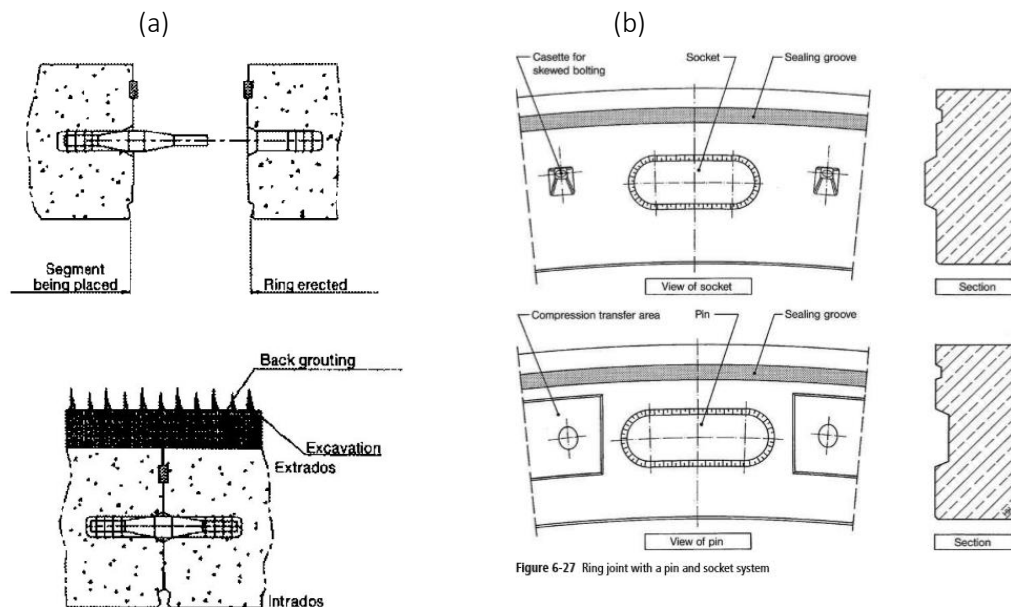


Figure 6-27 Ring joint with a pin and socket system

Figure 1.4. a) Joints with dowels (AFTES 1999); b) Joints with pin and socket system (after Maidl B. et al. 2011).

1.1.3 Sealing and grouting

About the possible infiltration of water in the gallery, the entire tunnel support system has to be waterproof to guarantee the functionality of structure; in multi-layered construction lining, a waterproofing membrane is usually used between inner and outer lining, in the case of single layer

construction this function have to be ensured by the high concrete quality of the segments themselves and a waterproofing joint systems. Usually they are used sealing elements (or gaskets) positioned in special grooves placed on each single side of all segments close to the extrados; these elements are always under compression and their choose is function of the maximum and minimum pressure that they will be subjected to in the presence of the maximum gap and offset vales, with an adequate safety system. In the case of joints rotation, the gaskets can undergoes to pressure or de-compression, if is subjected to sagging or hogging moment, and the de-compression effect on the gasket could influence its water tightness function.

Sealing and gaskets system has little influence on the joint mechanical behaviour, their presence doesn't affect the joint rotation angle and bolt strain more than 4% (*Li et al 2015*)

Another source waterproofing comes from the grout used to fill the annular gap between the segments and the soil, providing an appropriate bedding for the lining. The gap filling is a very sensitive operation playing an important rule on the minimization of the surface settlements and, at the same time, on the evaluation of the loads acting on the lining which are very influenced by the rheological properties of the injected materials, typically classified into three main types, 1) inert mixes, 2) cement mixes and 3) two-component mixes.

All these materials are in an initial fluid state and differ for the time of their consolidation process, which is strictly related also to the soil permeability, faster in the case of high permeable soil like sand and slower in less permeable soil like clay. This phenomenon, which implies a stress release around the tunnel cavity, explains why the grout pressure decreases in the time going into a plastic state and into a final hardened state; the loads derived from the grout, acting on the lining, are clearly time-dependent.

Bezuijen and Talmon 2004 show the grout pressures measurements around two of the lining segments of the Sophia Rail Tunnel.

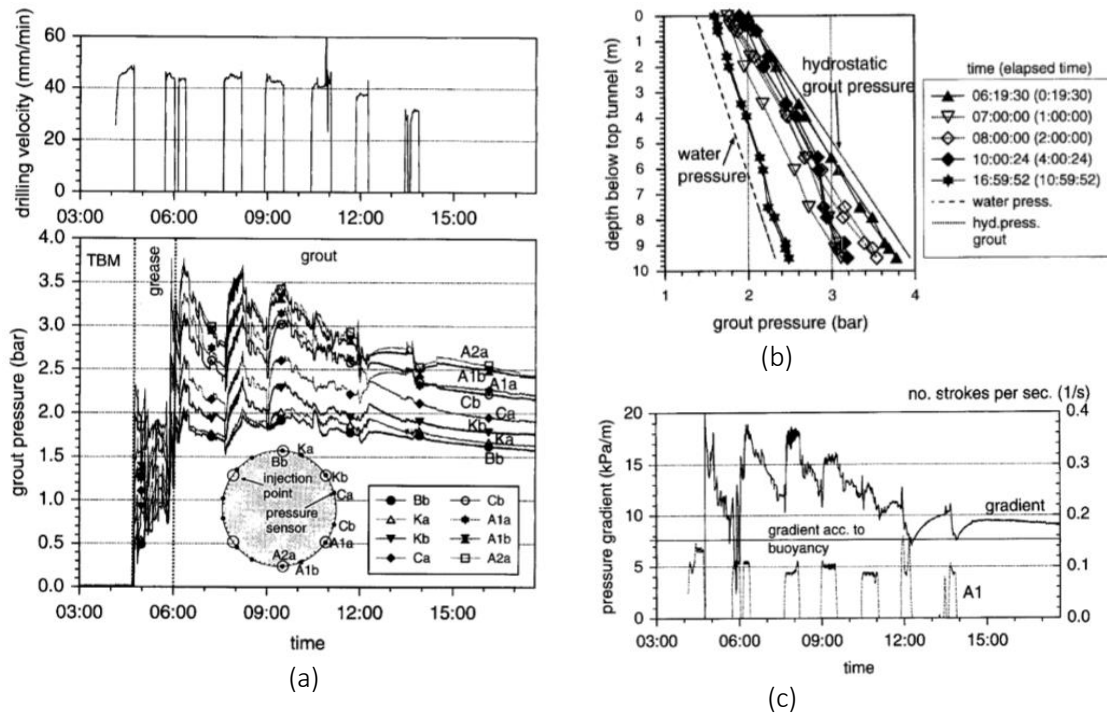


Figure 1.5. (a) Grout pressure in the time in function of drilling velocity; (b) Variation of grout pressure with the depth below the top of the tunnel section; (c) Variation of grout pressure gradient in the time (*Bezuijen and Talmon 2004*).

Figure 1.5(a) plots the grout pressure as function of the time together with the drilling velocity; the pressure starts from zero, increases during drilling when the grout is injected and decreases during the periods of standstill, due to consolidation of the grout (dewatering of the grout into the soil). Figure 1.5(b) shows the distribution of the pressures as function of the height below the top of the tunnel section which increases almost linearly with the height but with a vertical gradient not constant in the time, starting from a lower slope respect the hydrostatic condition and decreasing until to reach a steady state in gradient, as also showed in the Figure 1.5(c) where the pressure gradient is plotted in the time.

The last technologies privilege the back-filling of ultra-fluid two-component mixes, limiting the consolidation time, ensuring a complete filling of the gap and avoiding all negative aspects correlated with the use of traditional cementitious grouts such as the risks of choking pipes and pumps. The two-component grout consists of an A and B components: A-Component is a stabilized grout containing varied combinations of water, binders, bentonite, and admixtures; B-Component is a liquid accelerator that is added to the A-Component when injected into the annulus. The flowability of A-component needed for the pumping requirement is function above all of 1) water to cement ratio, 2) solids content and 3) time since the stabilizer (or retarder) was mixed before the injection with B-component; it is usually measured using a flow cone as indicated in the ASTM C939–10. When the A and B components are mixed, the grout takes a gel consistency and the gel time (5s-10s) has to be sufficient to distribute throughout the annulus to guaranty a homogeneous confinement to the ring and the minimum early stiffness of the grout (ASTM C942-10). The early grout compressive strength is required to ensure the segments to support the loads imposed by the backup gantry as well as to transfer the loads between the segments and the soil. It is between 0.1 to 1 MPa in 1 hour and between 1 to 5 MPa in 28 days and it is function of the amount of the mixed materials. *Peila et al. 2011* show the results of a series of tests related to the behaviour of a two-component injection grout for filling the annular voids behind the segmental lining during mechanized tunnelling with EPB machines. The authors tested the gout in the fresh and hardened state confirming this typical range of the grout strength and observed also how the grout consolidation process has its more effect on the last 1-3 installed rings, in function of the TBM velocity of advancement.

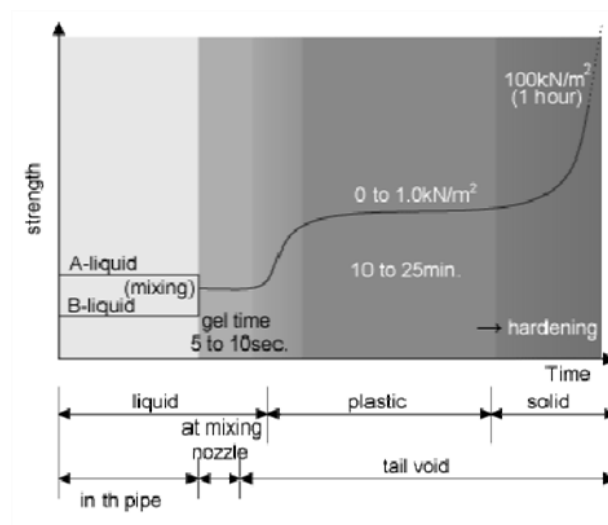


Figure 1.6. Properties of 2 component backfill grout material ETAC (Hashimoto et al. 2000).

Simultaneous backfill grouting in shield tunnelling was introduced for the first time in 1982 in the construction of No. 4 line of the Osaka Subway in Japan and after exported in many regions of the world, such as Asia, Europe and America, for its capability to keep the settlement in the range of 10 - 30 mm (*Hirata 1989*). In Europe the most widespread two component simultaneous backfill grout is the ETAC, developed in the Netherlands using local materials, and used for the first time in the soft-ground EPB excavation of the Botlek rail tunnel (*Feddema et al. 2001*).

Figure 1.6 shows the properties of the ETAC material. After mixing, the A and B materials become gel in 5-10 seconds; in the next 10-25 minutes the material sustain plastic state and, after others 30 minutes, hardens completely.

1.2 Effect of segmental layout on lining behaviour

The joints technology has a double effect on the global structural lining behaviour: 1) the connections make the lining a multi-hinged structure where the nodes behaves as semi-rigid connections (*Do et al. 2014*) with an intermediate behaviour between a ideally fully rigid and a pinned connection, able to transmit axial forces, shearing forces and bending moments through the connections; 2) the presence of the joints in the staggered configuration generates a coupling mechanism of transfer of the forces between the segments subjected to a longitudinally distributed loads and this leads the lining to behave as a 3D structure in a stiffer configuration than an isolated ring (*Arnau and Molins 2012*).

A direct way to understand the structural behaviour of longitudinal and circumferential joints is to follow their evolution of stress and strain states during experimental tests.

1.2.1 Experimental behaviour of joints

Many experimental study have been conducted by different authors considering the effects of such technologies of joint, putting in evidence their strict dependence.

An interesting experimental study carried out by *Cavalero and Aguado 2011* highlights some behaviour aspects of joints with packers under simple (normal) stress and under coupled (normal and tangential) stresses up to failure. Two different test configurations were designed to reproduce the conditions found in some Spanish tunnels (Line 3 in Madrid, Line 9 in Barcelona, M30 in Madrid, Cela Tunnel in Madrid and Pajares tunnel in Asturias) varying the packers' material (bituminous, rubber, plywood).

The first test consists of cycles of loading and unloading to which the packers are submitted through contact with two concrete blocks or two steel plates. The packer's behaviour under simple stress presents, at the first loading stage, the increase of the measured strain for each stress application, at the sustained step an increase of strain for a constant load and at the unloading stage the decrease of measured strain with the decrease of stress (Figure 1.7). This non-linear elastic hysteretic behaviour is function of the packers' material, more evident for bituminous ones, and can be translated into a softening of the material after the first load cycle due to a change in the microstructure of the packers at the maximum normal load.

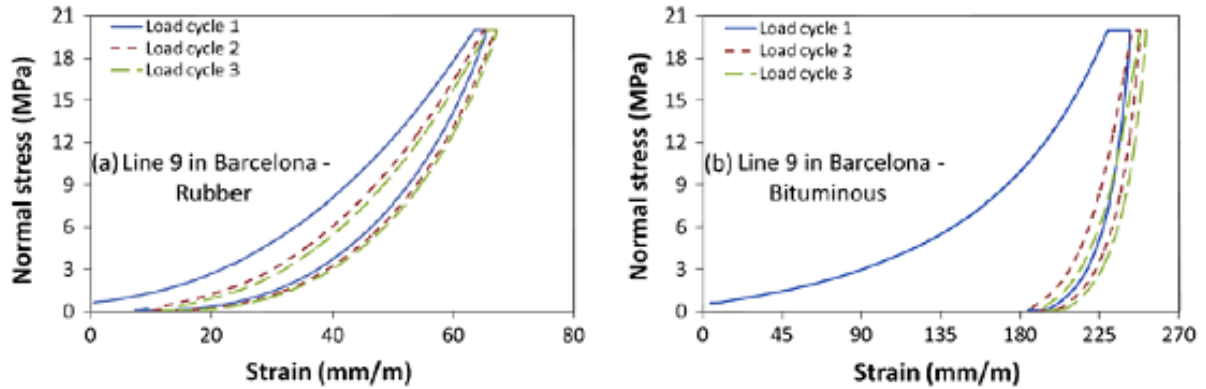


Figure 1.7. Behaviour of elastomeric and bituminous joints under simple compression
(Cavalaro and Aguado 2011)

According with the authors, the presence of plastic range in both materials' behaviour, that is the transition zone between the stiff and yielding zone, shows that the physical mechanism isn't a simple friction between two surfaces but probably there is a second resistant mechanism increasing the tangential resistance of the joint.

The test under normal and tangential stress required two different configuration of load, one horizontal in which three concrete blocks are placed horizontally with the packer in the middle, and one vertical in which three concrete blocks are placed vertically with the packer in the middle; first the normal load is applied, with hydraulic jacks in the first case and with a press in the second case, second the tangential load is applied with a gantry and an hydraulic jack respectively. The relate tangential stress-displacements curves (Figure 1.8) carried out for different level of load (1.5 - 8 -12 MPa), are very different in the case of rubber material (Figure 1.8a), bituminous material (Figure 1.8b) and in the case of direct contact (Figure 1.8c). For the rubber, the tangential stress-displacements curve identifies a first stiff phase in which an increase of tangential load produces a reduced increase of displacements of the middle block until the reach, a second plastic phase characterized by bigger displacements of the middle block and, reached the maximum tangential stress τ_{max} , a yield phase with big displacements and a small reduction of the tangential stress applied τ_2 . The bituminous exhibits a shorter stiff initial stage, under a lower level of tangential stress, a longer plastic stage until to reach the maximum tangential stress at the end of the test, without an evident transition between the plastic and the yielding stage. The direct contact finally shows a very stiff initial stage, with a not significant increment of displacements, reaching a higher value of tangential stress respect the other cases under the same load, with observed cracks and simultaneous movements of middle block.

So the behaviour of these three different packer joints is identified with low friction (bituminous material), intermediate friction (rubber material) and high friction (concrete-concrete).

The work represents a clear identification of the physical mechanisms that occur in the joints with packers and clarifies some aspect to be taken into account in the conceptual model that describes a nonlinear behaviour and a failure mechanism of the joints governed by a 1) *simple friction mechanism*, between the materials in contact and 2) *interlocking effect* (Figure 1.9) due to the superficial porosity of the concrete at the interface, function of the applied normal stress and increases with this, which deforms in the contact area penetrating the irregularities of the concrete generating a certain anchorage effect.

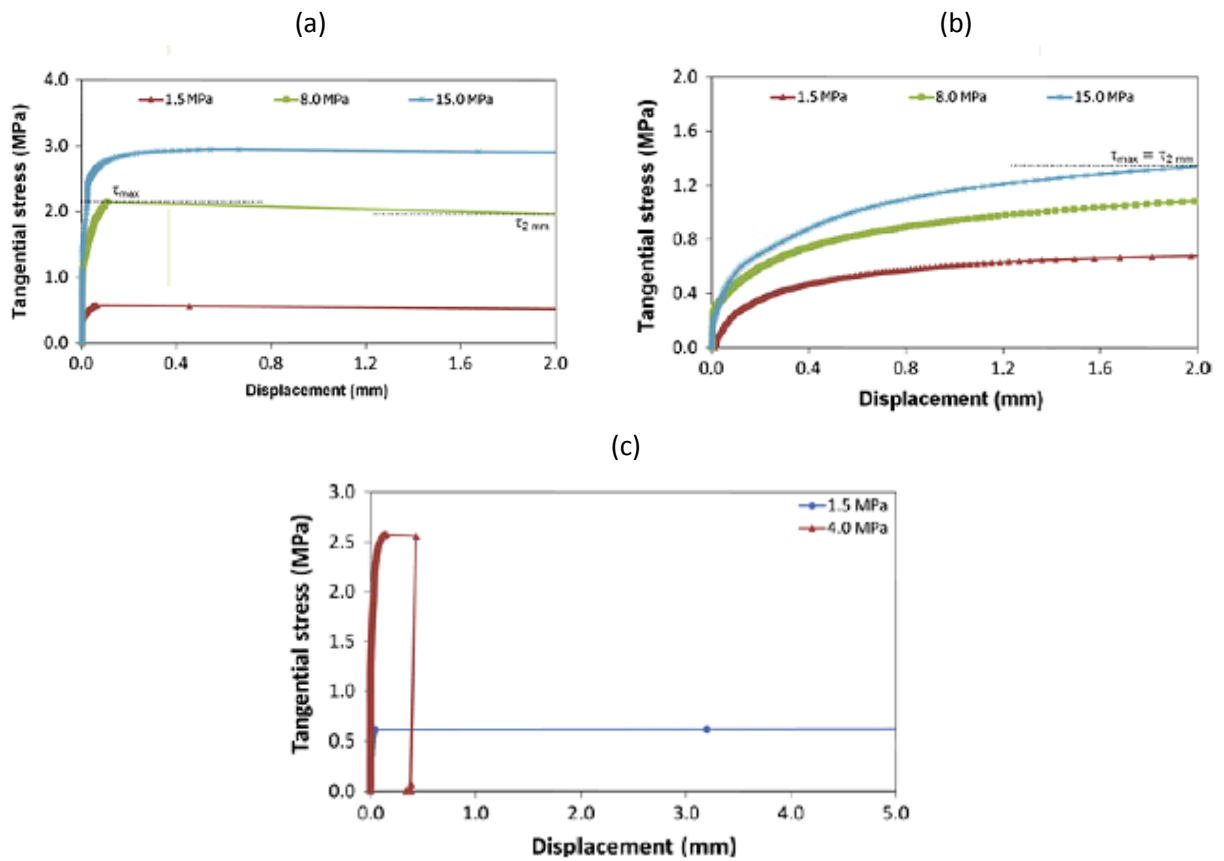


Figure 1.8. Tangential stress-displacement curve for packers in rubber (a), in bituminous (b) and with direct contact (c) (Cavalero and Aguado 2011).

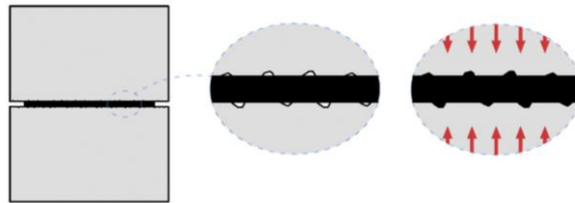


Figure 1.9. Interlocking effect in the packer-concrete interface (Cavalero and Aguado 2011).

If the tangential stress of interface is higher than that resisted by the packer material, the failure occurs in packer material like in the mechanism 1 (Figure 1.10), where the packer material is subjected to very high deformation and displacements.

If the tangential stress of interface is lower than that resisted by the packer material, the failure occurs in the interface like in the mechanism 2 (Figure 1.8), where relative displacements between the concrete and the packer material are observed.

In the case of joints with concrete-concrete interface contact, the failure is governed only by a friction mechanism with the failure of the concrete interface itself which exhibits a more fragile behaviour respect the case of joints with packers.

Because in a lining ring longitudinal joints are located in different points of the section and then subjected to different bending schemes, a realistic overview of the behaviour of the joints in a

segmental ring can be derived from a full scale test on the joint, investigating different joints load configurations.

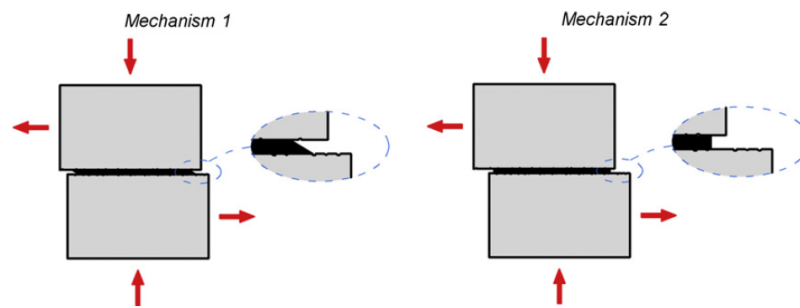


Figure 1.10. Failure mechanisms in joint with packer material (Cavalaro and Aguado 2011).

Li et al 2015 for example, have studied the flat bolted longitudinal joint structural behaviour of Shanghai Metro Line No.13 with a full-scale test conducted continuously loading the joint until it is completely failure. The segments are 0.35m thick, 1.2m of width and 6.2m of external diameter. The high-strength C55 concrete has been used for the segments, connected with two bolts M30. The joint is loaded into four loading stages in both the sagging and hogging moment cases. Figure 1.11 shows the test scheme for the bending case, where horizontal and vertical loads simulate the axial and bending moments; for the hogging case the system is rotated upside down.

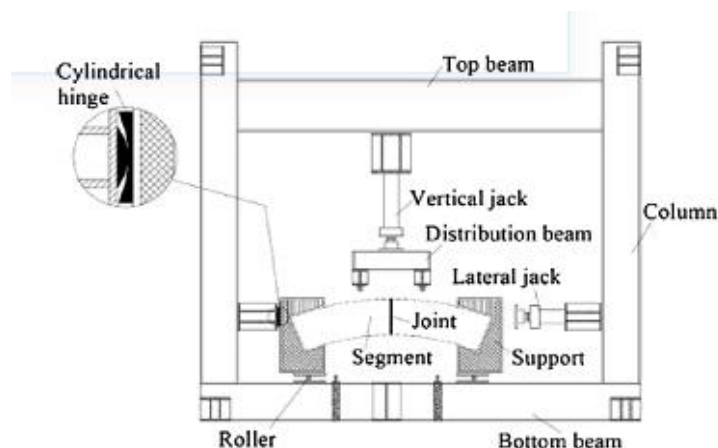


Figure 1.11. Scheme of bending test (Li et al 2015).

During the loading test it can be possible distinguish four different states of stress to which the joint is subjected, both for the sagging -positive- bending (Figure 1.12) then the hogging -negative- bending (Figure 1.13).

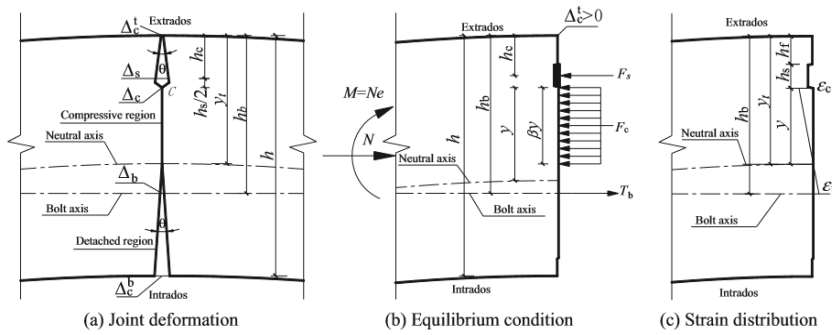
- State 1: The contact surface joint is closed without joint rotation. The bolt strain is close to zero, and the neutral axis of the cross section is above (sagging moment) or below (hogging moment) the position of the bolt.
- State 2: The contact surface joint is gradually opening from the internal (sagging moment) or the external (hogging moment) side, and joint starts to rotate. The bolt tensile strain start to increase and the neutral axis estranges from the intrados (sagging moment) or the extrados (hogging moment).

State 3: Increase of joint opening until to close the gap between the two concrete segments at the external (sagging moment) or internal (hogging moment) edge. This leads an additional concrete contact force F_0 at the external (sagging moment) or internal (hogging moment) edge and the joint opening tend to slow down.

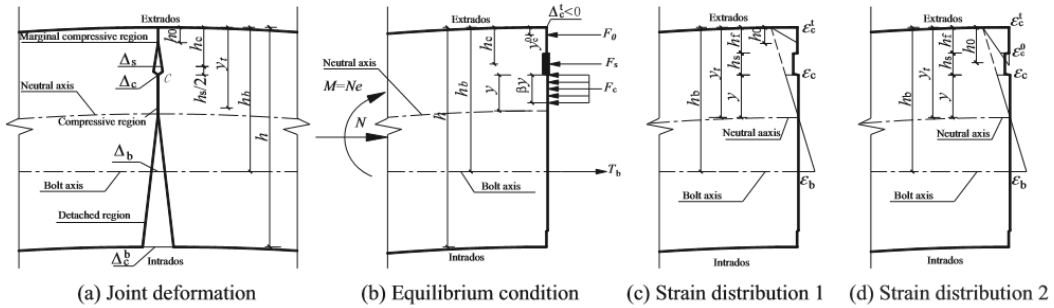
State 4: The bolt strain exceeds its yield strain while the joint opening accelerates. With the increasing of compressive deformation of the concrete at the external (sagging moment) or internal (hogging moment) edge, the concrete undergoes to failure together with the complete opening of the joint.

JOINT SUBJECTED TO SAGGING MOMENT

STATE 2



STATE 3



STATE 4

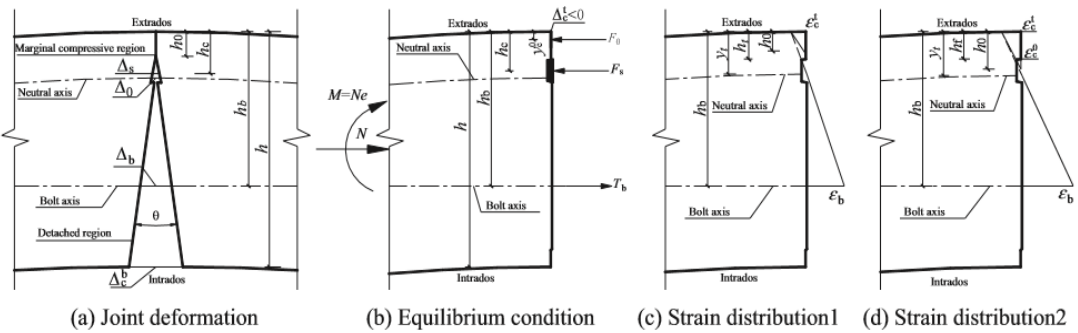
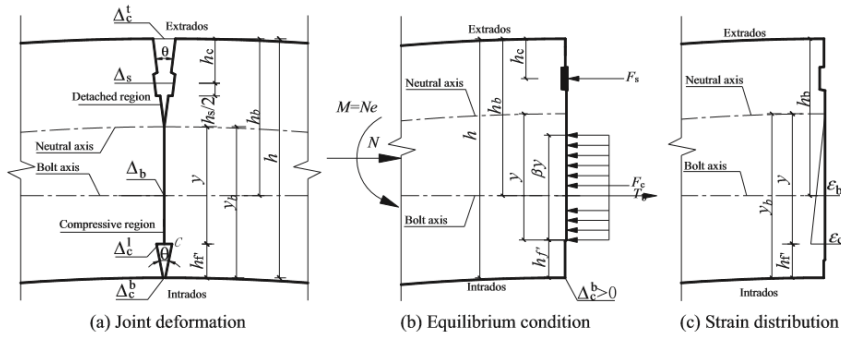


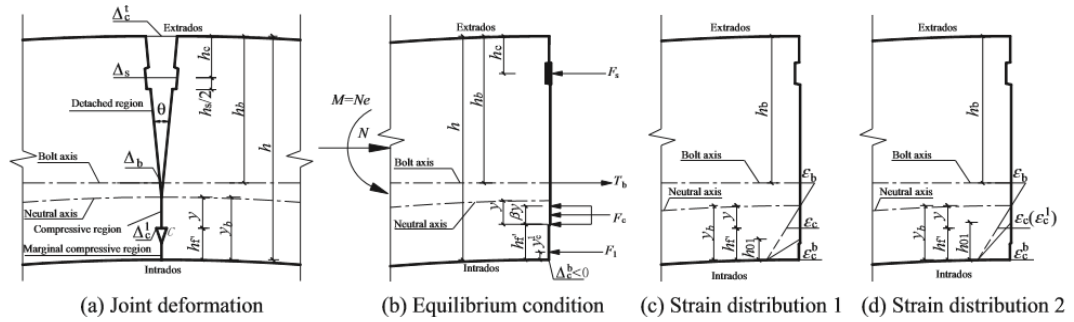
Figure 1.12. Stress state in sagging moment during the loading phases (Li et al 2015).

JOINT SUBJECTED TO HOGGING MOMENT

STATE 2



STATE 3



STATE 4

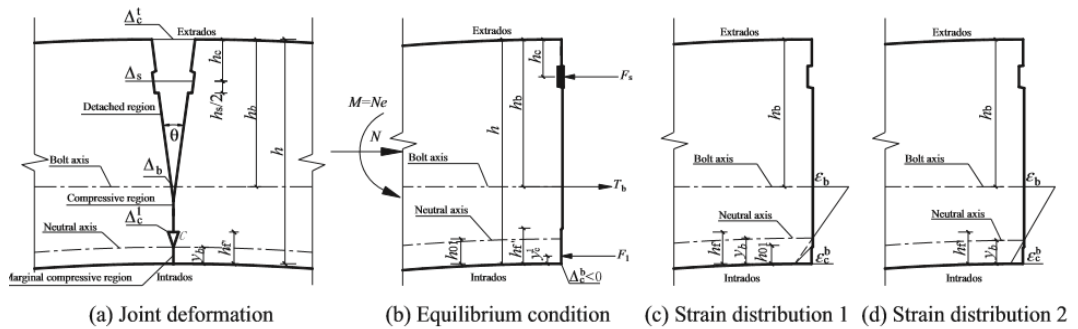


Figure 1.13. Stress state in hogging moment during the loading phases (Li et al. 2015).

The mechanical behaviour of the longitudinal joint subjected to a hogging moment is very similar to that subjected to a sagging moment as Figure 1.10 and Figure 1.11 show. The main difference consists in the value of moment for which they reach the same opening: the joint under negative moments reaches the same value of rotation respect the case of positive moment for lower value of moment (Figure 1.14).

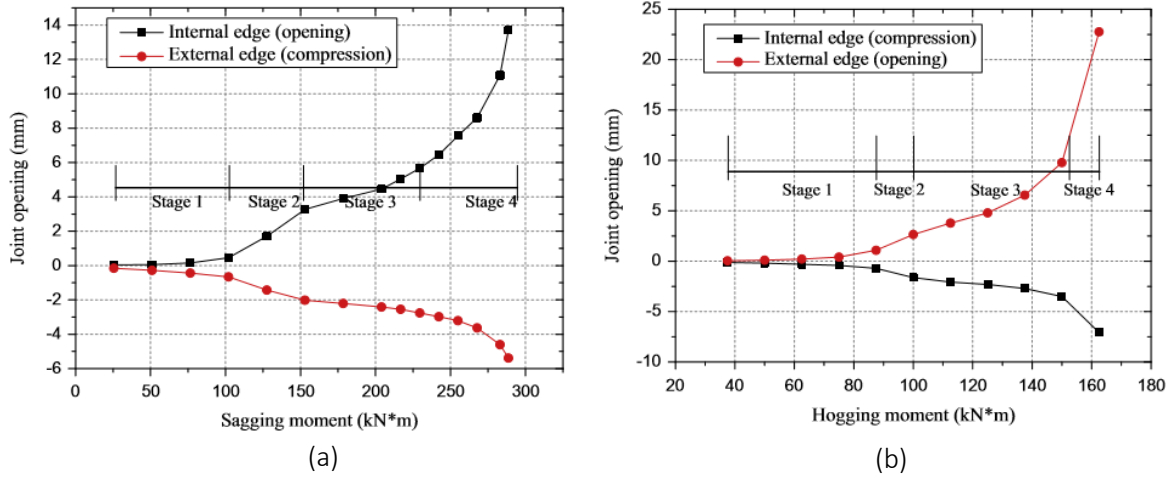


Figure 1.14. Development of the joint opening with (a) sagging moment and (b) hogging moment (Li et al. 2015).

Another important conclusion has been carried out by the authors by means of a series of parametric analysis with their analytical progressive mechanical model, varying the bolt location.

When the bolt is located to the internal edge, the smaller joint opening is read under sagging moment, and the larger joint opening is read under hogging moment (Figure 1.15)

This means that the bolt position along the surface contact influence the joint behaviour but also its behaviour itself; when the bolt is located closer to the internal edge in fact, the bolt strains and the bearing capacity are larger for the joint subjected to a positive moment than in the case of joint subjected to a negative moment.

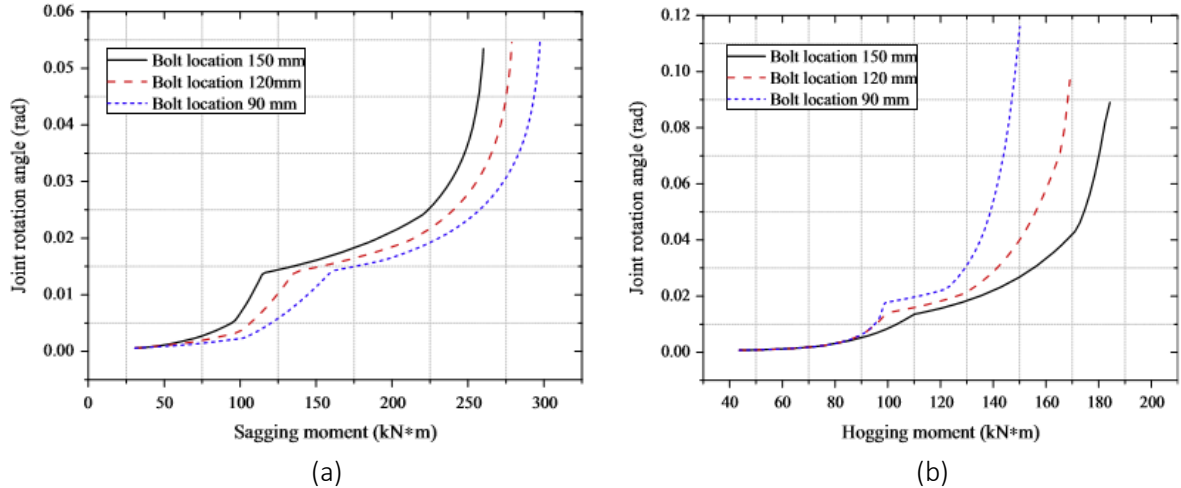


Figure 1.15. Development of the joint opening with (a) sagging moment and (b) hogging moment (Li et al. 2015).

Same conclusions can be done for the axial load influence. For the sagging moment case, the joint rotation angle and bolt strain increase with the increasing of the axial load, for the hogging moment case, the joint rotation angle and bolt strain decrease with the increasing of the axial load. According with this test results, other authors (Do et al. (b) 2013) also have numerically confirmed the influence of joint pattern configuration on the lining forces distribution, for which the joint rotational stiffness under negative bending moment was approximately to be $\frac{1}{2}$ - $\frac{1}{3}$ of the stiffness under a positive moment.

Liu *et al.* 2017a have performed a similar test on the same joint, considering a different load system according to existing full-scale testing results obtained by the same author on the ultimate strength of continuously-jointed segmental tunnel linings (Liu *et al.* 2015b). The authors show the results in terms of segments deflection (Figure 16) and joint rotation (Figure 1.17), in function of the bending moment, for the sagging and hogging case.

Figure 1.16a shows how the segments reach the final deflection value under a higher value of sagging moment respect the case of hogging (Figure 1.16b) with a consequent stiffer behaviour. The joint behaves linear elastically until a bending moment equal to 90 kNm in the case of sagging (Figure 1.17a) and until 127.5 kNm in the case of hogging (Figure 17b) when the full concrete section is under compression. Then the elastic stage is larger for the joint under negative bending which exhibits a lower stiffness. The surface contact starts to open until a limit value of moment equal to 250kNm for positive moment and 200 kN/m for negative moment.

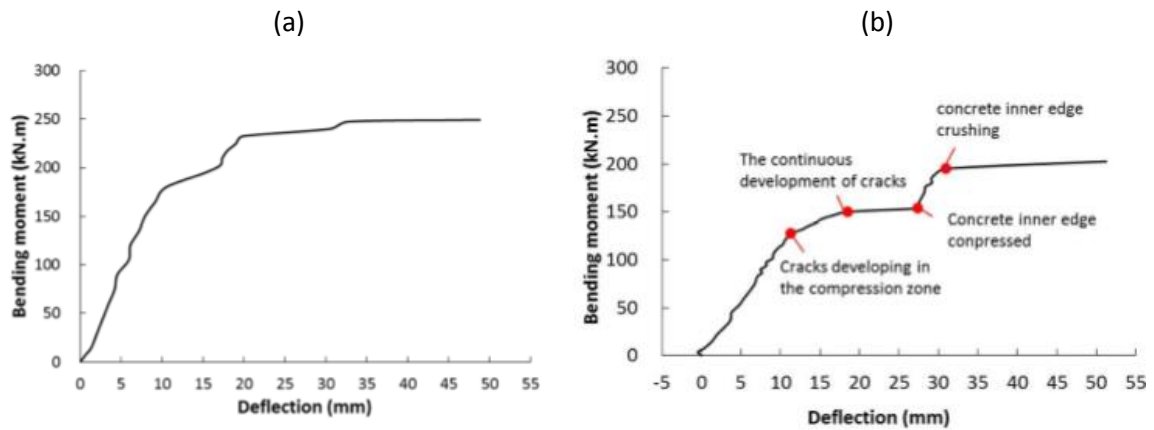


Figure 1. 16. Sample deflection in case of sagging (a) and hogging (b) moment (Liu *et al.* 2017a).

Figure 1.17 shows the results in terms of moment-joint rotation. The initial rotation angle rigidity of the positive bending moment joint is about 11000 kNm/rad, and that of the negative bending moment joint is 6500 kNm/rad. In addition the plot shows how the stresses in the bolts are almost absent when full cross-section or partial cross-section is under compression.

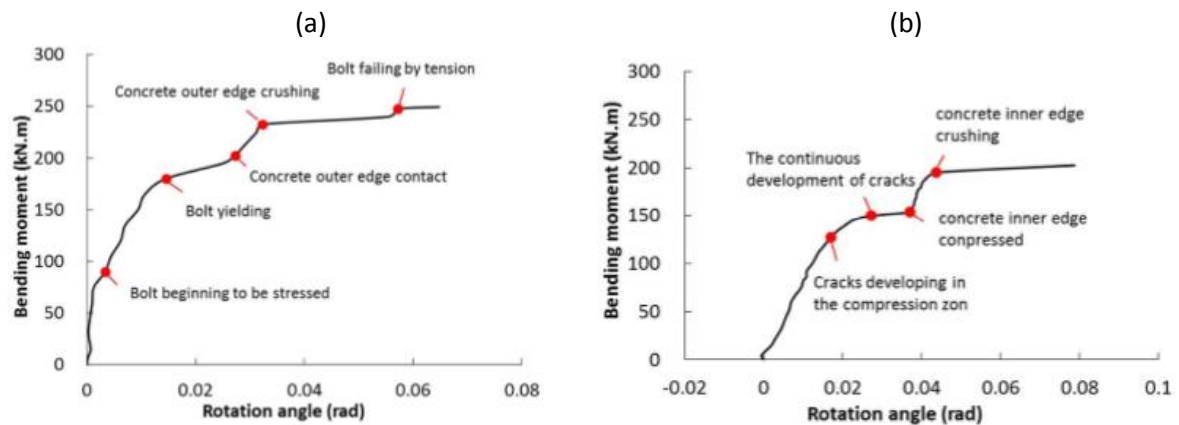


Figure 1.17. Joint rotation in case of sagging (a) and hogging (b) moment (Liu *et al.* 2017a).

This experimental evidence can lead to the conclusion that a not-bolted flat joints behaves as a bolted flat joint in the first stages of loading.

Liu *et al.* 2017b performed an interesting experimental tests on the structural scheme in Figure 18 which reproduce the typical staggered configuration of a segmental lining within two segments in the middle, representative of the middle ring, and other two adjacent on both sides, with the same properties of the previous experimental test, with the add of circumferential joints, equal to the longitudinal ones. On this layout the authors performed three different test:

- 1) Three-ring compression bending test: the three rings are loaded with longitudinal, axial and vertical load (Figure 1.18a). The test allow to monitor the rings deflection, longitudinal joints opening, circumferential dislocation, concrete and bolt strains.
- 2) Single-ring compression-bending test: in the scheme of Figure 1.18a, only the central ring is loaded with axial and vertical loads
- 3) Shear test on circumferential joints: in the scheme of Figure 1.18b, a longitudinal stretch of the lining is loaded in longitudinal and vertical direction.

The combination of the different tests allow to investigate the effect of interaction between the segment both on the segments behaviour than on the longitudinal and circumferential joints behaviour.

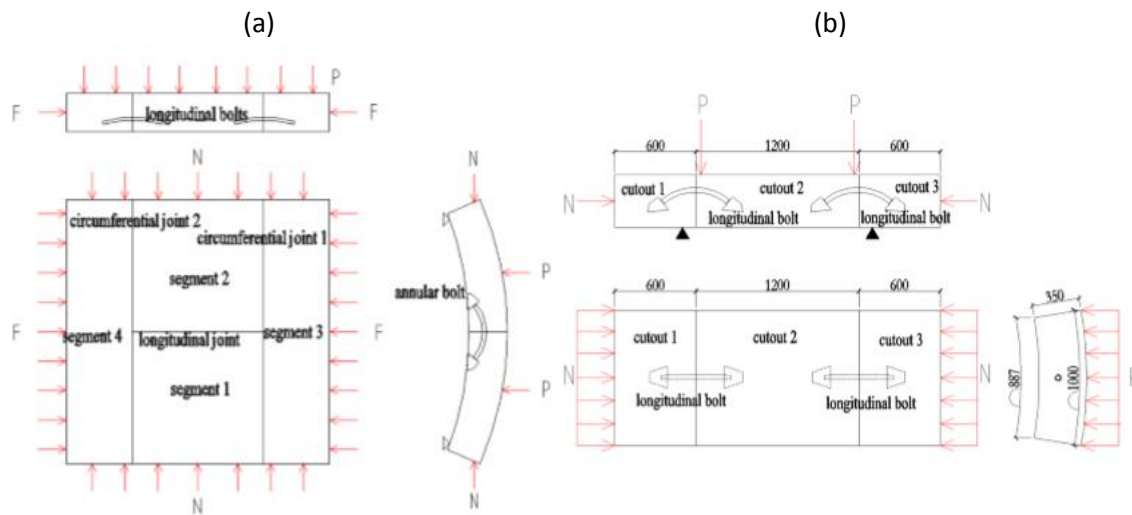


Figure 1.18. Layout of the scheme of (a) three ring compression bending test and (b) shear test (Liu *et al.* 2017b).

The comparison between the results obtained from the first two tests shows a constraining effect on the middle ring. Figure 1.19, for example, plots a lower deflection of the middle ring obtained in the three ring bending test (stiffer behaviour) respect the case of the test on a single ring (lower stiffer).

The failure occurs earlier in the middle ring in the test 2 because it is concentrated only in the longitudinal joints, while during the test 1 the failure is distributed along both joint directions.

Looking at the longitudinal joint rotation, Figure 1.20 shows an increase of rotational stiffness due to the interaction between the three rings where the joint failure appears for higher value of bending moment and lower value of its rotation respect the case of isolated ring.

The comparison between test 1 and test 2 shows how the longitudinal and circumferential bolts start to carry a load later in the case of the test 2, in any case the circumferential bolts start to be stressed before the longitudinal ones.

The rotational stiffness remains constant during all the test 1 while presents a decrease in correspondence of the inflection point in the test 2, as observed also in the previous showed bending tests on single ring (Figures 1.14, 1.15, 1.16, 1.17).

The rotational stiffness of longitudinal joint is function of the longitudinal load level, increasing with the longitudinal load increase (Figure 1.21a, b).

Looking at the behaviour of circumferential joints during the bending test on three ring, Figure 1.22 shows the increasing of joints dislocation in function of the bending load increasing. For the circumferential joint 1, negative values refer to the internal surface of the joint, positive values refer to the external surface of the joint; the opposite convention has been adopted for the circumferential joint 2.

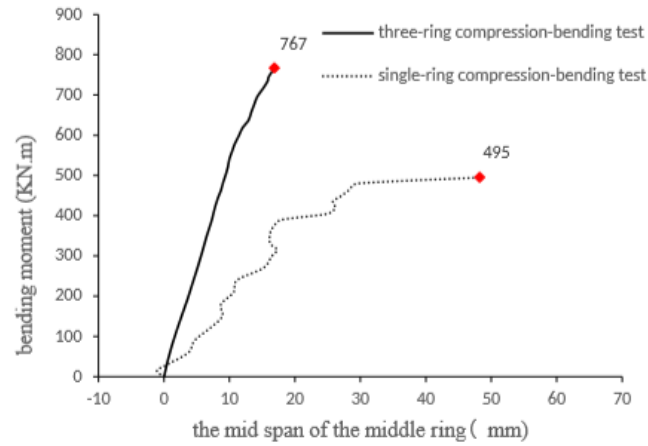


Figure 1.19. Comparison between test 1 and test 2 in terms of deflection of the middle ring (Liu et al. 2017b).

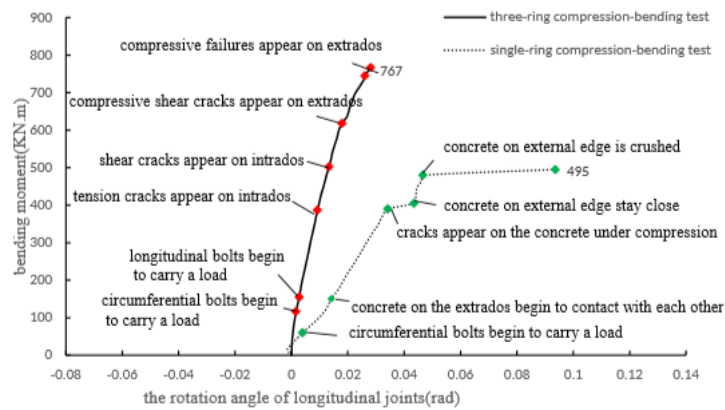


Figure 1.20. Comparison between test 1 and test 2 in terms of longitudinal joint rotation (Liu et al. 2017b).

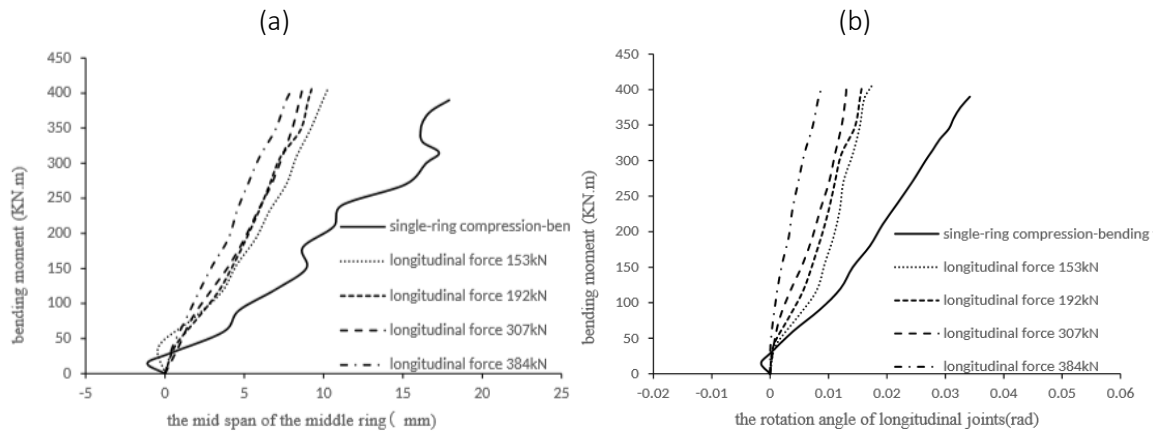


Figure 1.21. Effect of longitudinal force on the (a) middle ring deflection and (b) longitudinal joint rotation (Liu et al. 2017b).

The maximum deflection of circumferential joints is reached in correspondence in the middle of the sections and equal for both of them to 0.004m for the failure bending loads of 767 kNm. In correspondence of the edges instead, circumferential joint 1 reaches the maximum deflection value of 0.002m in the external surface while the circumferential joint 2 reaches the maximum deflection value about of 0.004m in the internal surface.

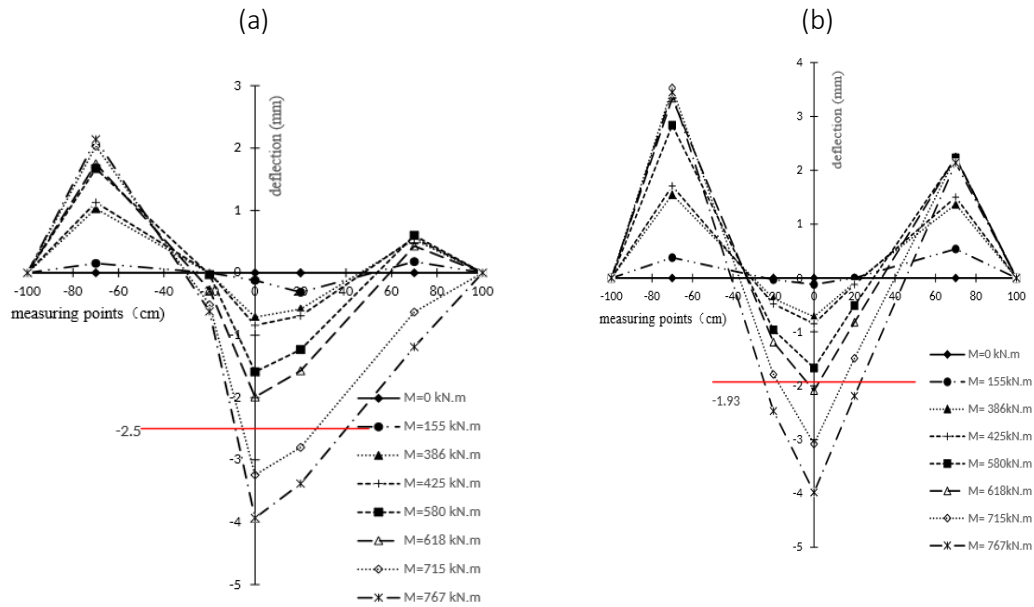


Figure 1.22. Circumferential joint 1(a) and 2(b) behaviour during test 1 (Liu et al. 2017b).

During test 3 circumferential joints are directly tested. Figure 1.23 shows the surface of shear failure in both joints 1 and 2 with the achievement of shear failure in the intrados of joint 2.

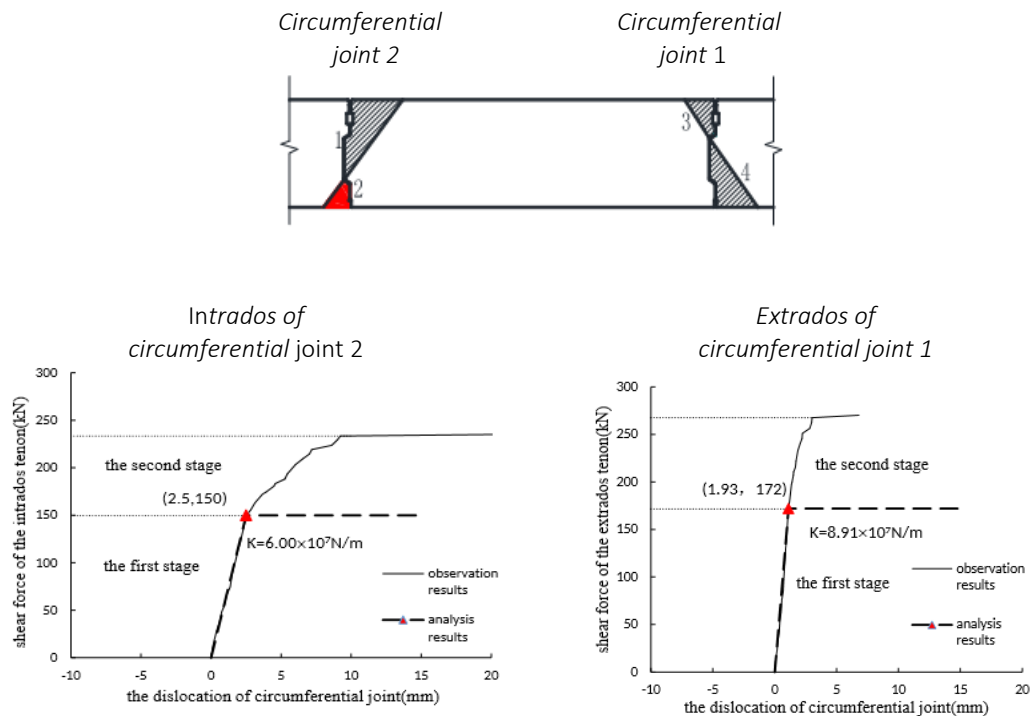


Figure 1.23. Shear failure in the circumferential joints (Liu et al. 2017b).

The relative shear force-dislocation joint plot, shows an initial working stage where the joint is under compression exhibiting a high shear stiffness; in this stage the main interaction mechanism between the two surfaces in contact is the *friction* while the circumferential joint starts to be stressed and dislocated. There is a second working stage in which cracks began to appear and, with the shear load increasing, the joint reduces the own shear stiffness until the failure of the concrete at the intrados (joint 2) and the shear failure of the joint. Circumferential Joint 1 and 2 behaviour is the same, joint 1 reaches the failure after the joint 2 exhibiting a higher shear stiffness.

1.2.2 3D interaction of segments

As seen so far, literature experimental tests on lining joints on single or multiple rings put in evidence the 3D behaviour of segmental tunnel lining.

When an *isolated ring* is loaded by the surrounding ground, it deforms according to its flexibility, and its radial displacements are due to mainly the longitudinal joint rotations in function of its rotational stiffness.

When *multiple rings* are loaded by a distributed load, there is a transferring of longitudinal displacements between the segments through the circumferential joints, which determines the structural interaction between the rings and, at the same time, a transferring of transversal displacements between the segments through the longitudinal joints, which determines the structural interaction between the segments in the same ring.

This double coupling effect generates differences in terms of radial and axial displacements for each ring providing a lower global deformation, or a higher stiffening of the lining with a consequent increasing of internal forces.

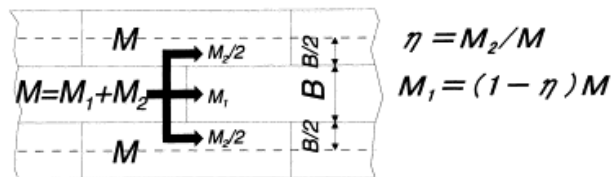


Figure 1.24. 3D interaction mechanism between the segments in the segmental tunnel lining (Koyama 2003)

Koyama 2003 shows the structural scheme of this interaction mechanism (Figure 24). He assumes that each segment transfers part of bending moment M_1 to following segment in the same ring, by means of longitudinal joints, and another part M_2 to adjacent two rings through lateral joints. The author defines the *effective ratio of bending rigidity* η , corresponding to the ratio between the transversal deflection of a continuous ring ΔD_2 and a segmental ring ΔD_1 for the presence of longitudinal joints (Figure 1.25); it is a function of the transversal segment's size and longitudinal joint rotational stiffness.

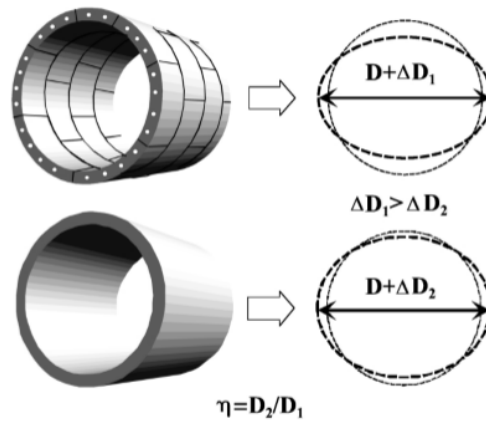


Figure 1.25. Concept of the efficient ratio of bending rigidity (Koizumi 2003).

The bending moment calculated considering the presence of longitudinal joint has to be increased within an additional rate of bending moment ζ , which takes into account the transfer of bending moment through the circumferential joints, and then function of the longitudinal segment size and stiffness of circumferential joint.

It is not so easy to define a clear method to estimate these parameters because they involve many variables and in particular because, thinking to a typical mechanized excavation process where longitudinal load acting on a ring changes during excavation advancement, the ratio ζ can't be constant and, as consequence, also the ratio η which are clearly load-dependent.

Many literature works have studied the possible calibration and influence of these parameters, which seem to be the main parameters for the evaluation of lining loads in their structural project.

Fei *et al.* 2014 have studied the transverse bending rigidity efficiency of segmental lining performing laboratory structural model tests. The authors investigate the η value for three different segmental lining configurations, straight and stagger jointed ring, uniform ring (Figure 26) and consider flat bolted joints both for longitudinal and lateral connections under different pre-tightening forces.

Figure 1.27 shows that under the same loading condition a straight jointed segmental ring has the largest deformation rate followed by the stagger jointed ring and the uniform ring, with the experimental evidence that longitudinal joints reduce the transversal bending rigidity of the ring.

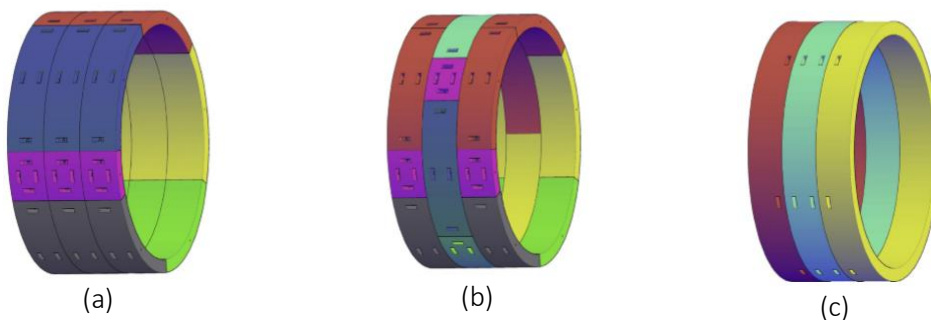


Figure 1.26. Joint segmental ring models (a) straight jointed ring; (b) stagger jointed ring; (c) uniform ring (Fei *et al.* 2014).

The tests show in addition how the effective ratio η of the transverse bending rigidity of stagger configuration is higher than in the case of straight configuration, in particular is between 0.3 and 0.8 in the first case and between 0.09 and 0.23 in the second one.

The tests don't take into account the effect of longitudinal forces on the bending of the middle ring and then its influence on the additional rate ζ .

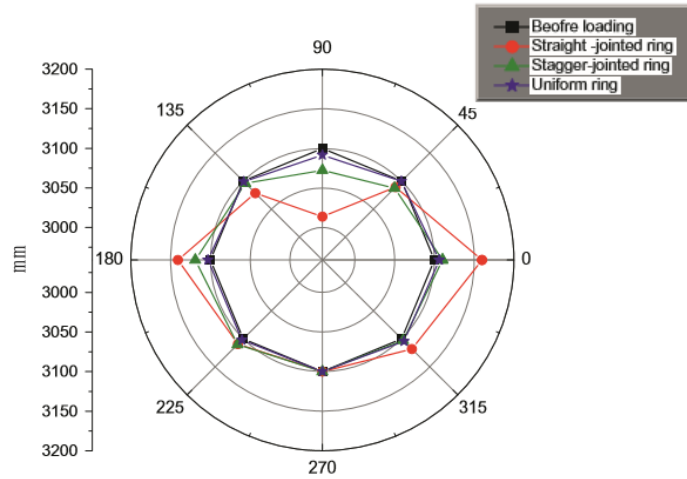


Figure 1.27. Deformations of middle ring (Fei et al. 2014).

Liu et al. 2017b have been evaluate the inter-ring (longitudinal) forces transmission on the compression-bending test performed on the three rings showed before, taking into account both the longitudinal than the transversal load transfer. Comparing the deflection of the middle ring obtained with the test 1 (three ring test) and test 2 (single ring) under different longitudinal load levels, the authors are able to evaluate the coefficient of bending transmission in the transversal bending plane named ξ_1 , taking into account the effect of longitudinal forces and the load level, as in the scheme of Figure 1.28. The bending moments acting in the segments have been back calculated starting from the strains recorders.

Table 1.1 shows the calculated values of transfer bending coefficient ξ_1 with the increasing of the longitudinal force for both cases of positive and negative bending which is constant during the tests, and the redistribution of bending moment between the segments during the tests.

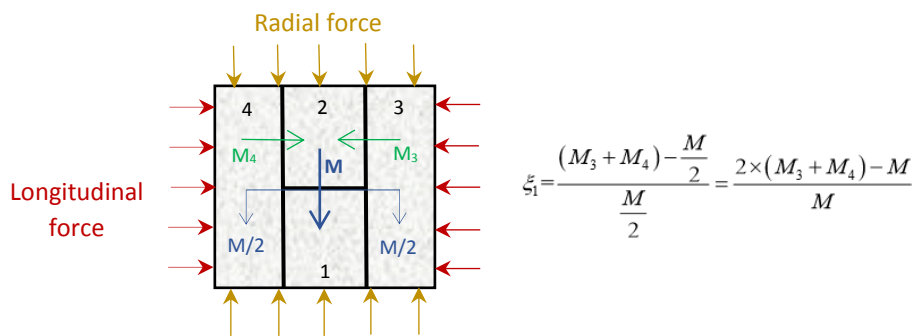


Figure 1.28. Scheme for the evaluation of the transfer bending coefficient in the middle ring.

The coefficient ξ_1 increases with the increasing of longitudinal load and it is higher in the case of hogging. The calculated range is between 0.198 and 0.438, respectively in correspondence of the lower and the higher value of applied longitudinal force.

(a)					(b)				
Longitudinal force (kN)	M _{1,2} (kN·m)	M ₃ (kN·m)	M ₄ (kN·m)	ξ_1	Longitudinal force (kN)	M _{1,2} (kN·m)	M ₃ (kN·m)	M ₄ (kN·m)	ξ_1
153	162.74	131.20	112.06	0.198	77	65.07	58.10	41.83	0.211
192	150.27	91.44	164.29	0.260	96	57.44	56.00	51.56	0.260
307	147.42	152.22	106.36	0.274	307	55.62	67.54	41.84	0.326
384	132.94	177.96	95.10	0.345	384	46.40	67.67	50.93	0.438

Table 1.1. Transfer bending coefficient for positive (a) and negative (b) compression-bending test in function of longitudinal load (Liu et al. 2017b).

The authors investigate also the influence of the bending load on the interaction mechanism between the segments. Table 1.2 shows the calculated values of transfer bending coefficient ξ_1 with the increasing of the bending moment for both cases of positive and negative bending, while the longitudinal force is constant during the tests, and the redistribution of bending moment between the segments during the tests.

The coefficient ξ_1 increases with the increasing of bending moment and it is higher in the case of hogging again. The calculated range is between 0.182 and 0.504, respectively in correspondence of the lower and the higher value of applied bending moment.

The experimental results confirm that, unless the geometrical and mechanical properties of the lining and the joints, the main parameter of influence of the 3D interaction mechanism between the lining segments in transversal and longitudinal direction is load level condition.

Only a three dimensional approach could be able to follow the forces redistribution in the segments together with the evolution of the loads acting in any direction.

(a)					(b)				
M (kN·m)	M _{1,2} (kN·m)	M ₃ (kN·m)	M ₄ (kN·m)	ξ_1	M (kN·m)	M _{1,2} (kN·m)	M ₃ (kN·m)	M ₄ (kN·m)	ξ_1
155	63.40	51.16	40.44	0.182	99	35.3	38.07	25.62	0.287
425	152.16	76.68	191.16	0.261	297	87.20	114.85	92.95	0.399
618	211.67	229.70	176.63	0.315	446	119.47	166.07	160.07	0.463
767	248.50	265.91	252.59	0.352	644	159.65	264.87	219.48	0.504

Table 1.2. Transfer bending coefficient for positive (a) and negative (b) compression-bending test in function of bending load (Liu et al. 2017b).

1.3 Design of segmental lining

Although the knowledge on the tunnel lining behaviour is still not completely well known, literature experimental tests review conducted on such complex structure discussed up to now, gives to us a good instrument of interpretation of the global structural behaviour and the main influence parameters which should be taken into account into analytical or numerical approaches for the tunnel lining design.

It should be said that, as for every problem of civil engineering, the passage from the experimental approach to the analytical or numerical one is something rather difficult which has to consider very often simplified assumptions. It is not possible to analytically or numerically reproduce what exactly happens in the observed mechanism, and probably it is not necessary for the engineering needs. “*Models should always be of only adequate complexity*” (Wood 2004) respect the problem, not more not less.

In this context, a model of adequate complexity which returns a good interpretation of this kind of tunnel lining behaviour, in any design approach, have to consider:

- Presence of longitudinal joints or their effect in the lining;
- Presence of circumferential joints or their effect in the lining;
- Prevision of the real load level acting on the lining.

In technical literature, this issue is dealt in very many different ways, in function of the adopted level of design.

Lee et al. 2001 classified all tunnel lining design methods into four main type:

1. Empirical design methods, based on past tunnelling practices;
2. Design methods, based on in situ measurement and laboratory testing;
3. Circular ring in elastic foundation method;
4. Continuum mechanics models, including analytical methods and numerical methods.

The last two methods are the most commonly adopted for design purposes where the joints influence is taken into account with two different approaches: the indirect method and the direct method (*Do et al. 2014*).

The *indirect method models* simulate the joints effect on the tunnel lining assuming a reduction of lining rigidity, the *direct methods* instead, model the segments and the joints as structural elements. At the same time the loading condition induced by the surrounding soil can be applied by means of active or passive loading mode (*Bloom 2002*). The *active loading mode* assumes that the surrounding ground applies the earth/water pressures to the lining structure actively, calculated with theoretical or empirical formulas; the *passive loading mode* takes into account the soil-structure interaction and the earth/water pressure transferred to the lining are calculated through the displacement compatibility between the soil and the lining.

Koizumi 2003 summarises in the Figure 1.29 the proposed literature structural models for segmental tunnel lining using for analytical and numerical solution.

The uniform rigidity ring model is an indirect method to take into account the joints presence within reduced stiffness of the lining; the multi-hinge ring method models the joints as fully hinges not considering the flexural behaviour of concrete-concrete contact area, ignoring the partial moment transmitting capacity; the beam-spring model is a more realistic method modelling the joint behaviour with rotational spring with a proper stiffness low. The beam-spring I models the circumferential joints with rigid links, the beam-spring II models the circumferential joints shear spring.

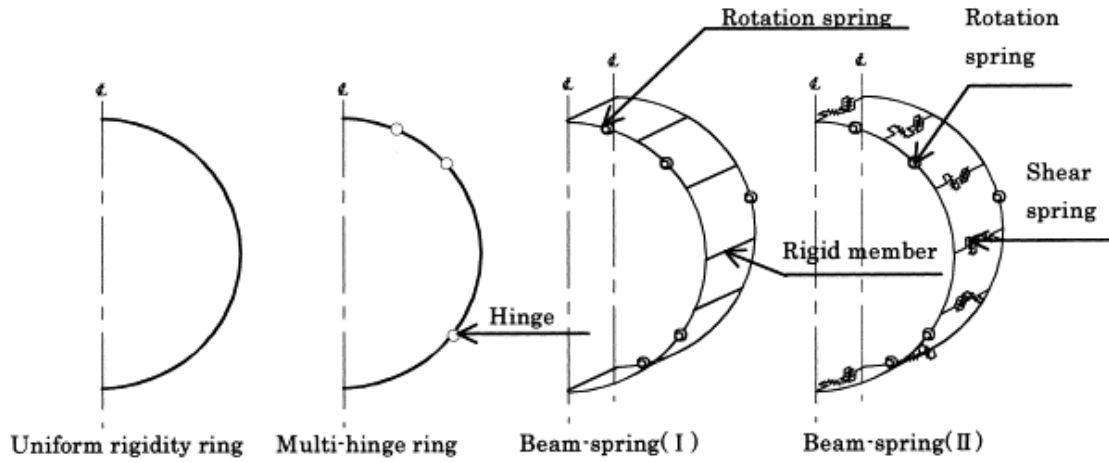


Figure 1.29. Structural models of the segment ring (Koiama 2003)

1.3.1 Indirect methods

Analytical methods and simplified 2D numerical analysis are a preliminary level of lining design, suggesting solutions able to take into account in a simplified way the global longitudinal joint effect on the lining.

Literature review proposes different approaches to take into account the presence of the joints within indirect approach.

The *Reducing liner rigidity model* (RR model) models a continuous ring with a reduced rigidity by applying the reduction factor η (Equation 1.1) to the bending stiffness Ei of continuous lining respect the segmental lining one $(EI)_{eq}$ (Bloom 2001, JSCE 1996, Lee et al 2001, El Nagar et al. 2008) which is the key parameters of this method, with a rather difficult interpretation as discussed before (c.f. 1.2.1).

$$\eta = \frac{(EI)_{eq}}{(EI)} \quad (1.1)$$

Many authors have investigated the η value via analytical methods, as for example Liu et Hou 1991 and Lee et Gee 2001.

Liu & Hou 1991 evaluate η value correlating the moment reduction factor to the maximum horizontal displacement of a continuous ring (Eq. 1.2) within the parameter b (Eq. 1.3):

$$\eta = \frac{1}{1+b} \quad (1.2)$$

$$b = \frac{3EI}{RK_{RO}} \sum_{i=1}^m \cos\varphi_i \cos 2\varphi_i \quad \left(0 < \varphi_i < \frac{\pi}{2}\right) \quad (1.3)$$

Where EI is the bending rigidity of the tunnel lining per unit length; K_{RO} is the rotational spring stiffness of the joints, φ_i is the angle measured from the vertical direction around the tunnel of the i_{th} joint in the range $0 - 90^\circ$; m is the number of joints in the range of $0-90^\circ$; and R is the tunnel radius.

Lee & Gee 2001 proposed an analytical model to determine the internal forces and displacements of jointed segmental tunnels taking into consideration the effect of joint stiffness within an iterative application of the force method.

Table 1.3 resumes the main results obtained by the authors: joint stiffness, joint number and joint geometry are the main factors affecting the effective rigidity ratio η , according to the experimental test performed by Liu *et al.* 2017a, b.

Factor	$(EI)_e / (EI)$
Joint stiffness ratio K_θ / EI (1)	Sensitive (1)
Coefficient of soil resistance K_s (1)	Not sensitive if K_s is less than 30 000 kN/m ³ (1)
Joint distribution (uniform, \rightarrow)	Not sensitive (1)
No. of joints (1)	Sensitive (1)
Geometry	
Thickness (1)	Depends on total number of joints (1 when 3 joints; 1 when 4 joints)
Radius (1)	Sensitive (1)
Joint stiffness reduction	Sensitive (1)

Table 1.3. Main factors affecting the effective rigidity ratio η (Lee & Gee 2001)

The authors provided graphical relations between the reduction factor of the bending rigidity η and soil resistance K_s , relating the η parameter and the joint stiffness, within a dimensionless parameter called the joint stiffness ratio λ (Eq. 1.4) which represents the relative stiffness of the joint over the rigidity of the lining segment.

$$\lambda = \frac{K_\theta l}{EI} \quad (1.4)$$

In the Equation 1.4, the calculation length l is usually assumed equal to 1 m, k_θ is the rotational stiffness of the joint per unit length. Figure 1.30 plot the effective rigidity ratio, η , against stiffness ratio in logarithmic scale, $\log \lambda$, for different soil resistance K_s . The higher slope η - $\log \lambda$ relation is higher for lower value of λ indicating that the effective bending rigidity ratio is more sensitive in the case of more flexible segmental ring, which varies between 0.1 and 0.4, in the typical range of the effective rigidity ratio λ .

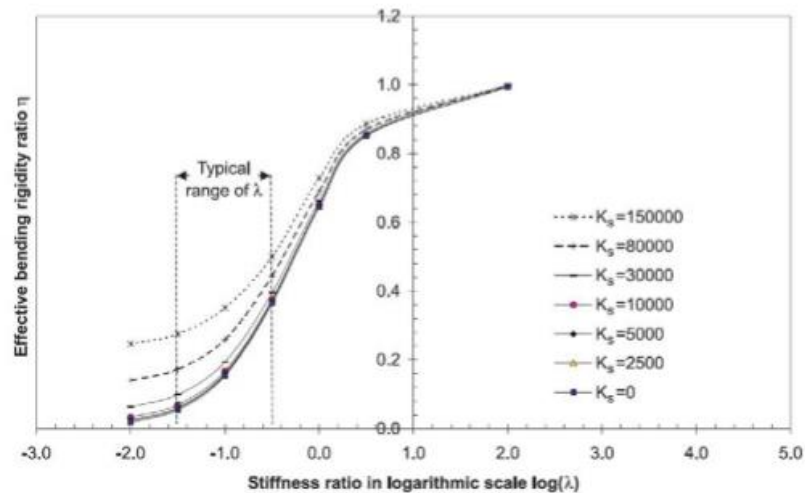


Figure 1.30. Effective bending rigidity ratios η in function of the joint stiffness ratio λ (Lee & Gee 2001).

Different approach is that used in the *Effective moment of inertia of liners model* (EMI model) proposed by Muir Wood 1975 within the following equation 1.5 reducing the moment of inertia of a ring in function of the number of joints.

$$I_e = I_j + \left(\frac{4}{n}\right)^2 I \quad (1.5)$$

The parameter n is the joints number, I_j the joint inertia, I the continuous lining inertia. The approach doesn't consider the joint rotational stiffness neither the influence of their orientation and staggering along the tunnel axis neither the circumferential joints.

The model has been adopted by many authors (Henfry et al. 2004, Henfry et al. 2006, Ding et al. 2004) and, as the RR model, presents a limit due to the fact that the lining stiffness affects itself the lining internal forces and the key parameters η and I_e have a very large range on their application (Koizumi & Nashimura 1998, Zhong et al. 2003, Huang et al. 2006, Feng et al. 2011); because segmental lining behaviour is strictly dependent on joint technology, this approach can return not in every case a good prevision of lining internal forces.

Table 1.4 shown in Lee & Gee 2001 compares the effective rigidity ratios η obtained by the author himself for six tunnel cases with the η values predicted by the approaches of Muir Wood 1975 and Liu & Hou 1991. Muir Wood and Liu & Hou methods were developed for evenly distributed joints around the tunnel ring, thus these approaches are not applicable for case 2 and case 6 tunnels with uneven joint distribution, while the Lee & Gee method is applicable to a six-joint lining system, and therefore not applicable for the case 3 tunnel with an eight-joint lining system. The comparison shows how Lee & Gee 2001 and Liu & Hou 1991 evaluated very similar η value which significantly differ from the results predicted by Muir Wood (1975) which can't take into account any structural effects such as tunnel geometry, joint stiffness, and joint orientation and any dependency of load.

Blom 2001 introduced a reduction factor, named ζ , of a continuous lining bending stiffness, derived from the analytical solution introduced by the author for jointed lining. Equation 1.6 shows the adopted formula where the coefficient C_x^* and C_y^* (Equations 1.7 and 1.8) are function of the angle β_i at the i_{th} joint location (Figure 1.31a).

Figure 1.31b shows the results of the Equation 1.6 for several numbers of segments (and longitudinal joints) in function of the joint contact area I_c , segmental thickness t and the radius R .

$$\zeta = \frac{1}{1 + \frac{3}{4} \frac{t^3}{I_c^2 r} (C_x^* + C_y^*)} \quad (1.6)$$

$$C_x^* = \sum_{\frac{\pi}{2} < \beta_i < \frac{3\pi}{2}} \cos(\beta_i) \cos(2\beta_i) \quad (1.7)$$

$$C_y^* = \sum_{\frac{\pi}{2} < \beta_i < \frac{3\pi}{2}} \sin(\beta_i) \cos(2\beta_i) \quad (1.8)$$

The reducing factor ζ of bending stiffness increases with the joints number and with the decreasing of the ratio $\frac{I_c^2 r}{d^3}$ that refers to the rotation capability of the joint.

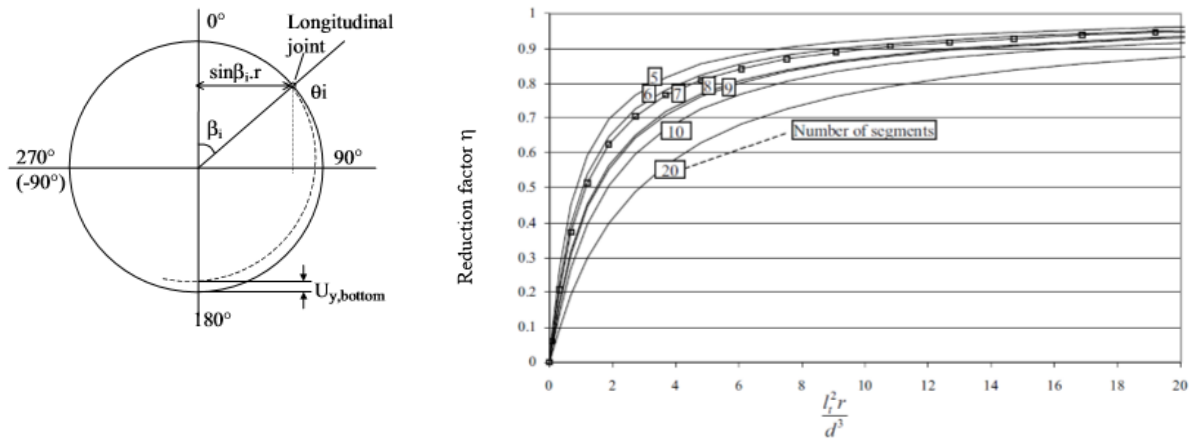


Figure 1.31. (a) Scheme of β_i angle; (b) effective bending rigidity ratio η in function of the joint stiffness ratio λ (Blom 2001).

	Flexibility		Method of Muir Wood 1975 (η_1)	Method of Liu and Hou 1991 (η_2)	Proposed equation		
	λ	$\log \lambda$			η_2 (simplified equation)	η_2 (analytical)	R_{rel}
Case 1: $R = 2.35$ m, 6 evenly distributed joints							
1-1	0.010	-2.0	0.444	0.018	0.038	0.025	0.509
1-2	0.032	-1.5	0.444	0.054	0.061	0.062	0.571
1-3	0.100	-1.0	0.444	0.153	0.164	0.161	0.633
1-4	0.316	-0.5	0.444	0.364	0.370	0.370	0.735
1-5	1.000	0.0	0.444	0.644	0.657	0.648	0.852
Case 2: $R = 2.925$ m, 6 unevenly distributed joints							
2-1	0.016	-1.8	na	na	0.040	0.015	0.608
2-2	0.032	-1.5	na	na	0.077	0.058	0.877
2-3	0.100	-1.0	na	na	0.222	0.206	0.999
2-4	0.316	-0.5	na	na	0.460	0.463	1.034
2-5	1.000	0.0	na	na	0.725	0.731	1.029
Case 3: $R = 5.225$ m, 8 evenly distributed joints							
3-1	0.010	-2.0	0.250	0.044	na	0.024	0.367
3-2	0.032	-1.5	0.250	0.126	na	0.107	0.743
3-3	0.100	-1.0	0.250	0.313	na	0.298	0.910
3-4	0.316	-0.5	0.250	0.590	na	0.581	0.970
3-5	1.000	0.0	0.250	0.820	na	0.816	0.990
Case 4: $R = 2.925$ m, 6 evenly distributed joints							
4-1	0.010	-2.0	0.444	0.022	0.077	0.043	0.444
4-2	0.032	-1.5	0.444	0.066	0.105	0.086	0.558
4-3	0.100	-1.0	0.444	0.184	0.217	0.201	0.640
4-4	0.316	-0.5	0.444	0.416	0.426	0.428	0.752
4-5	1.000	0.0	0.444	0.692	0.695	0.699	0.866
Case 5: $R = 5.225$ m, 6 evenly distributed joints							
5-1	0.010	-2.0	0.444	0.039	0.138	0.120	0.359
5-2	0.032	-1.5	0.444	0.113	0.194	0.188	0.551
5-3	0.100	-1.0	0.444	0.287	0.357	0.348	0.677
5-4	0.316	-0.5	0.444	0.560	0.599	0.597	0.816
5-5	1.000	0.0	0.444	0.801	0.825	0.818	0.917
Case 6: $R = 2.35$ m, 6 unevenly distributed joints							
6-1	0.016	-1.8	na	na	0.050	0.018	0.715
6-2	0.032	-1.5	na	na	0.069	0.053	0.897
6-3	0.100	-1.0	na	na	0.170	0.179	0.998
6-4	0.316	-0.5	na	na	0.375	0.416	1.033
6-5	1.000	0.0	na	na	0.660	0.691	1.032

Note: na, not available.

Table 1.4. Comparison of η values predicted used by the Lee et al. 2001, by Hou et al. 1991 and applying Muir Wood Method (Lee et al. 2001).

1.3.2 2D calculation methods

With reference to the Figure 1.29, the multi-hinge ring model is the least suitable 2D direct method to interpret longitudinal joints which behaves as a semi-rigid connection (Do et al. 2014) and not as a fully rigid or a fully hinged (Figure 1.32).

The beam-spring model (BSM) instead, is a more realistic method respect the previous one, modelling the joint with partial moment transmitting capacity. To this end, the spring is usually modelled as a rotational spring which give a rotational capability to the joint. In this last approach, the key parameter is the joint rotational stiffness low.

In absence of experimental curve for the specific case to be calibrated, the literature proposes many models to simulate and calibrate segmental joint behaviour. *Janßen's joint method 1983* for instance, assumes that the contact area between two lining segments can be represented by a fictitious concrete beam with a depth equal to the joint contact area's width and its height and width equalling the joint's contact height (Figure 1.33a). This concrete beam has an elastic behaviour under compression and doesn't resist any tensile stresses at all.

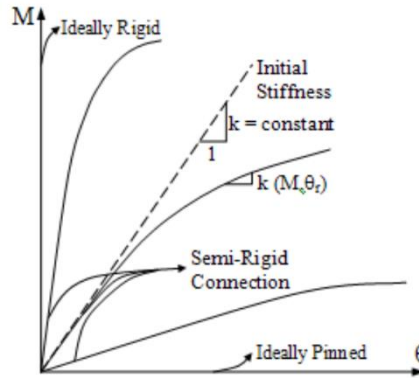


Figure 1.32. Structural behaviour of connections (Kartal et al. 2010).

Figure 1.33b shows the moment-rotation relationship assumed for the joint, where are distinguished three different working stages, function of the eccentricity $e=N/M$ of the resultant of the normal force in the joint section.

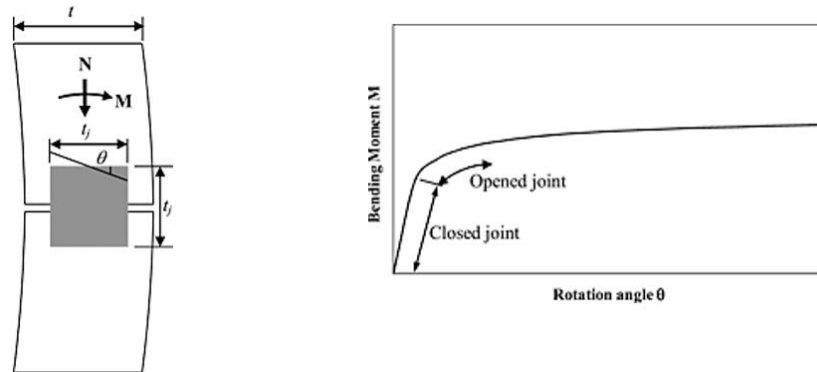


Figure 1.33. a) Cross section of the longitudinal joint; b) $M-\theta$ relationship in Janssen joint.

In the first branch of loading the joint is completely under compression for an eccentricity $e < t_j/6$. This is the case of closed joint when the stresses produced by the bending moment are smaller than normal stresses. In this condition joint will behave linear-elastically with a constant rotational stiffness (linear branch of $M-\theta$ curve). For an eccentricity $e > t_j/6$ the joint starts to open with a not linear elastic behaviour. The rotational stiffness is not constant but decreases with the moment increasing (non-linear elastic branch of $M-\theta$ curve).

The transition between the linear and the non-linear branch occurs theoretically at $M = \frac{1}{6} N t_j$. The equilibrium of the joint section in the non-linear branch of $M-\theta$ relation is guaranteed until the maximum bending moment $M = \frac{1}{2} N t_j$. For high value of rotation, plastic strains occur in the concrete until the joint failure.

Table 1.5 resumes the equation of Janßen's joint model in the different working stages, where b is the width of joint, E_s is the Young's modulus of the lining, t_j is the height of contact, N is the normal force and θ is the rotation.

In correspondence of closed joint condition, the initial stiffness is function only of the Young's modulus of the concrete and the contact height of the joint; for opened joint condition, the rotational stiffness is function also of the bending moment and normal force values.

Closed joint	Exentricity	$e = \frac{M}{N} < \frac{t_j}{6}$
	Rotational stiffness	$k_\theta = \frac{b t_j^2 E_s}{12}$
	Moment transition	$M = \frac{1}{6} N t_j$
Opened joint	Exentricity	$e = \frac{M}{N} > \frac{t_j}{6}$
	Rotational stiffness	$k_\theta = \frac{9 b t_j E_s M \left(\frac{2M}{N t_j} - 1 \right)^2}{8 N}$
	Maximum bending moment	$M = \frac{1}{2} N t_j$
Opened joint with plastic concrete behaviour	Exentricity	$e = \frac{M}{N} \gg \frac{t_j}{6}$

Table 1.5. Janßen's joint model.

How suitable is the Janßen's joint model for the segmental lining joints? *Hordijk and Gijsbers 1996* performed various experimental test on flat joint with concrete-concrete interface, with and without bolts, and compared the M - θ experimental relationship with Janßen analytical one.

Figure 1.34 shows the scheme used for the tests. Tunnel segments are 350 mm thick and 500 mm width with a contact height of the joint is 158 mm. The segments were loaded by increasing bending moments, under different value of normal forces. Figure 1.35 shows the test results in terms of moment-rotation and the results derived from analytical solution.

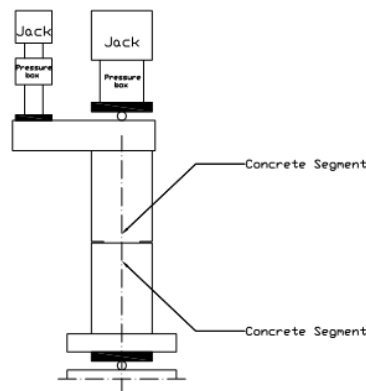


Figure 1.34. Layout of experimental test on flat concrete-concrete joint (*Hordijk and Gijsbers 1996*).

The comparison shows a good agreement between the two results. Janßen's solution is not able to reproduce exactly the initial joint stiffness then, for very low value of rotation, the moment is not fitted very well, and this is true in particular for low value of normal forces.

In addition, according to the authors, the initial rotational stiffness is not affected by the presence of bolts. This interesting conclusion has been carried out also from the experimental test conducted by *Liu et al 1017*, where the bolt start to be stressed not from the start of the test but after a certain load level. The effect of bolt in a concrete-concrete joint is in terms of increasing of ultimate bending moment. In the *Hordijk and Gijssbers* work indeed, the ultimate bending moment of bolted joints is higher than a non-bolted one. This increase in maximum bending moment capacity is in the order of 20 kNm/m and decreases with an increasing normal force.

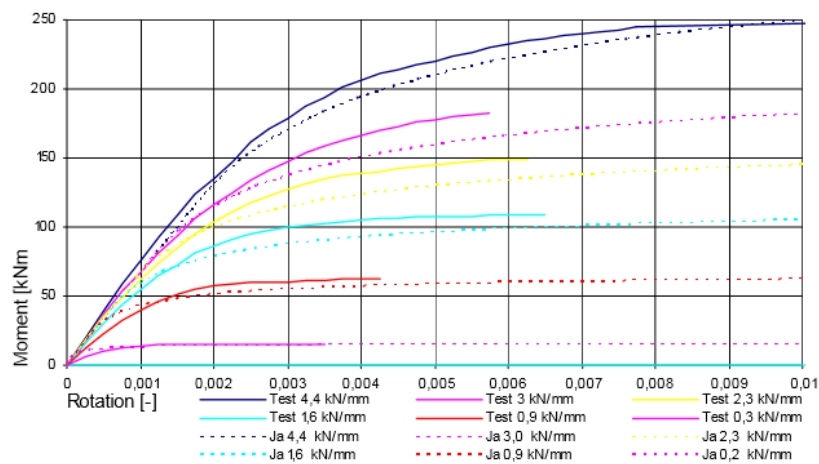


Figure 1.35. Comparison between experimental and analytical solution (Hordijk and Gijssbers 1996).

Klappers et al. 2006 studied the segmental lining behaviour within the beam and spring models (BSM) analysis with coupled and un-coupled spring ring model. The authors consider two different rings configuration as in Figure 1.36a, system I: ring 1 has no hinge at the crown and ring 2 is rotated by half a segment which means that there is a hinge at the crown; system II: all hinges are rotated by 15° compared to system I.

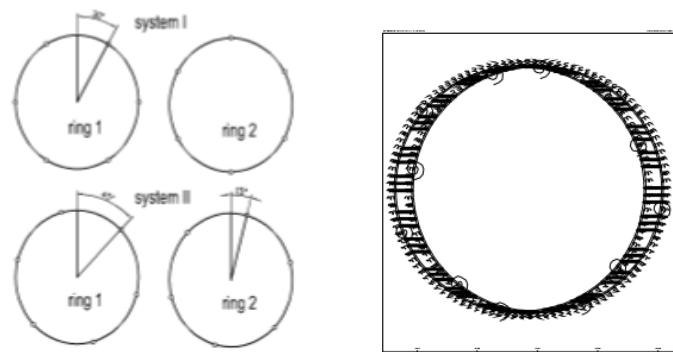


Figure 1.36. (a) Rings configuration; (b) Structural system of coupled spring beam model (Klappers et al. 2006).

Longitudinal joints are modelled with springs with a rotational capability calibrated with the Janßen's $M-\theta$ non-linear relation, while the circumferential joint within radial spring to simulate the coupling between the rings choosing the frictional coefficient $\mu=0.5$.

The following Table 1.6 shows the comparison between the coupled and uncoupled approach for both system I and II, respect the case of rigid ring and Muir Wood ring.

As expected, the bending moments calculated for the coupled rings are always higher than the moment calculated for the uncoupled ring, for both rings configuration.

The coupled calculations show that ring 1 of systems I is stiffer than ring 2 which causes a load transfer from ring 2 to ring 1. The coupling of the rings reduces the deformation, but increases the bending moments especially for the "stiffer" ring.

Muir-Wood ring return similar value of bending moment evaluated with uncoupled calculation of system II and lower value respect the case of rigid ring.

Structural system	rigid ring	Muir-Wood ring	system I				system II			
			uncoupled ring 1	uncoupled ring 2	coupled ring 1	coupled ring 2	uncoupled ring 1	uncoupled ring 2	coupled ring 1	coupled ring 2
max bending moment [kNm/m]	157	132	150	95	206	115	131	122	178	152
percentage	119%	100%	114%	72%	156%	87%	99%	92%	135%	115%
max settlement at crown [mm]	9	9,9	9	11,6	9,5	9,6	9,5	9,6	9,3	9,3
percentage	91%	100%	91%	117%	96%	97%	96%	97%	94%	94%

Table 1.6. Comparison between rigid ring, Muir Wood ring, coupled and uncoupled beam-spring model (Klappers et al. 2006).

1.3.3 3D calculation methods

To predict a realistic segmental tunnel lining three dimensional behaviour, including all aspects that have been introduced so far here, is almost complex and 3D numerical approach is a way to reproduce the three-dimensionality of the problem without introduce too many assumptions as in the aforementioned cases. Here there are shown some literature numerical 3D experiences focusing on the way to model the longitudinal and circumferential joint and their coupling effect in terms of lining structural performance.

Blom et al. 1999 studied the case of the shield-driven "Green Heart" Tunnel of the High Speed Line-South in the Netherlands; the authors proposed a detailed 3D FEM analysis of tunnel structures using Ansys FEM software modelling the longitudinal and the transversal joints, represented by packing material not dealt with in detail, with contact elements behaving as linear spring until the sliding.

Klappers et al. 2006 in the same work discussed before (c.f. 1.3.2) discuss also a 3D FEM model, simulating the longitudinal and circumferential joints behaviour as in the case of beam-spring model. Figure 1.37 shows the numerical 3D model and the effect of coupling (Figure 1.37b) respect the uncoupling (figure 1.37a).

In the uncoupled system only longitudinal joint are activated and each ring deforms independently each other according to their transversal flexibility, in the coupled system the presence of circumferential joints leads to a redistribution of stress along the tunnel axis direction. In the Table 1.7 the authors compare the results carried out with the beam-spring model and FEM analysis.

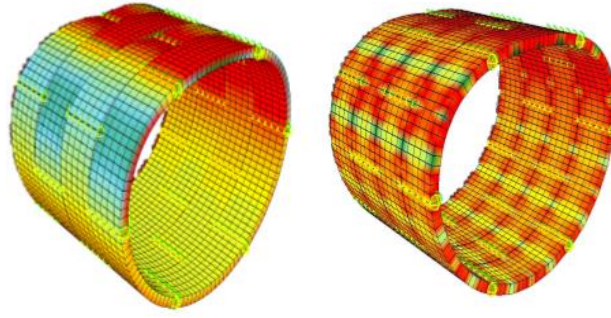


Figure 1.37. Uncoupled (a) and coupled (b) 3D numerical ring model (Klappers et al. 2006).

The comparison shows how the results obtained with the beam-spring model return similar value of those obtained with 3D FEM solution, both for coupled and uncoupled systems. This result demonstrates the reliability of the beam-spring model for transversal bending load. This is true only for this load configuration, any consideration has been evaluated for the 3D effect due to a configuration longitudinal loading.

Structural system	BSM with coupled rings				3D-FEM			
	uncoupled ring 1	uncoupled ring 2	coupled ring 1	coupled ring 2	uncoupled ring 1	uncoupled ring 2	coupled ring 1	coupled ring 2
crown bending moment [kNm/m]	150	95	206	82	155	95	201	82
max settlement at crown [mm]	9	11,6	9,5	9,6	9,1	11,2	9,1	9,3

Table 1.7. Comparison between coupled and uncoupled beam-spring model and FEM analysis (Klappers et al. 2006).

Teachavorasinskun et al. 2010 performed a series of 3D numerical analysis with SAP2000 to investigate the longitudinal joint influence on the segmental lining. The joint are modelled with interface elements, indicated with springs in Figure 1.38a, with a rotational stiffness calibrated numerically against a true scale bending test on a curved bolted flat joint (Figure 1.38b), calculating a range of rotational stiffness between 1000 and 3000 kNm/rad, then a constant elastic rotational stiffness is used to model the joint.

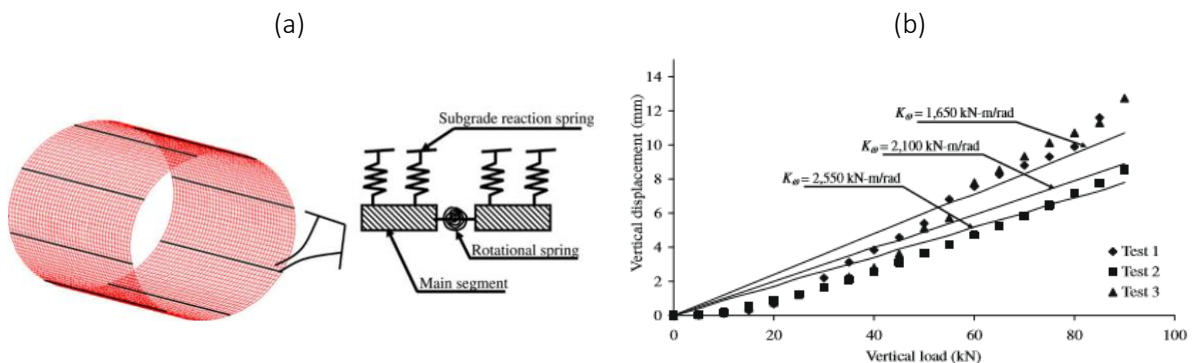


Figure 1.38. (a) Numerical segmental lining model; (b) Calibration of rotational joint stiffness (Teachavorasinskun et al. 2010)

The authors investigate also the influence of longitudinal joints number and position in the transversal lining section. In Figure 1.39a and 1.39b, the upper and lower values of bending in segmental lining, varying the joints number, are plotted respect the maximum bending moment for a not jointed lining, with respect to the variation on rotational stiffness.

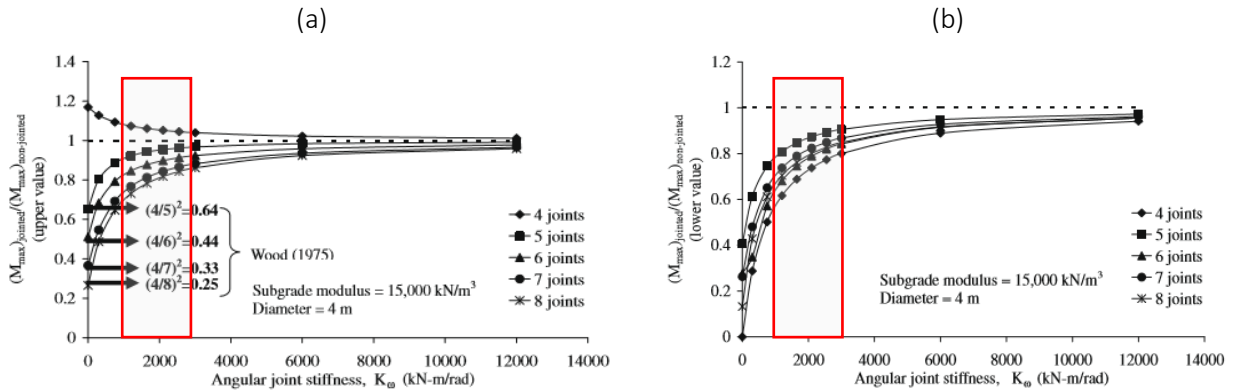


Figure 1.39. (a) Numerical segmental lining model; (b) Calibration of rotational joint stiffness
(Teachavorasinskun et al. 2010)

In the range suggested by the authors, the upper and lower bending moment undergo to a reduction factor η equal respectively about of 0.9-0.85 and 0.3-0.9 respect a not jointed lining. Increasing the joints number the reduction factor η increase, while increasing the joint rotational stiffness jointed lining tend to behave as a not jointed lining. The condition of moment equal to zero correspond to the limit case of perfect hinge, with zero rotational stiffness. The authors don't consider the presence of circumferential joints neither the staggering effect of the longitudinal ones (2D condition).

Arnau and Molins 2012 studied the 3D coupling between adjacent ring for the effect of the uniform longitudinal load induced by the soil weight. The studied case is the Line 9 subway tunnel of Barcelona (excavation diameter equal to 10.9m and lining thickness equal to 0.35m) referring to a section of eleven rings, which presents a concrete-concrete contact surface as longitudinal joint and plastic packers as circumferential joints. The concrete elements are shell elements with linear elastic behaviour, longitudinal and circumferential joints are both non-linear interfaces elements. The frictional packer-concrete behaviour has been reproduced within Mohr Coulomb constitutive model; the Young's modulus has been measured with compression test $E=2 \cdot E^5$ kN/m², while the friction coefficient $\mu=0.2076$ derived from the tangential resistance test conducted by Cavalero 2009. The coupling effect is described respect a reference ring in terms of increment of internal forces respect the case of no coupling effect. Figure 1.40 shows the increment of bending moment with the increasing of longitudinal forces. This increment is also related to the variation of K_0 coefficient and of course decreasing this value, then increasing the bending load, the increment of bending moment is higher.

The authors investigate also the influence of coupling effect with respect of the lining slenderness, defining the coefficient $Sl = \frac{\text{Tunnel diameter}}{\text{lining thickness}}$, equal to 31.1 in their case. Figure 1.41 shows how the increment of lining slenderness, or a the reduction of lining thickness, implies a linear increase of bending moment, then a linear increase of coupling effect, respect the case of uncoupling.

Figure 1.42 instead shows an exponential increase of coupling effect with the reduction of longitudinal joint height in terms of increment of bending moment; increasing the joint height there is a reduction of its rotational stiffness and as consequence a reduction of increment of bending moment. As consequence, minimize the longitudinal joint height implies a direct reduction of the influence of coupling effect.

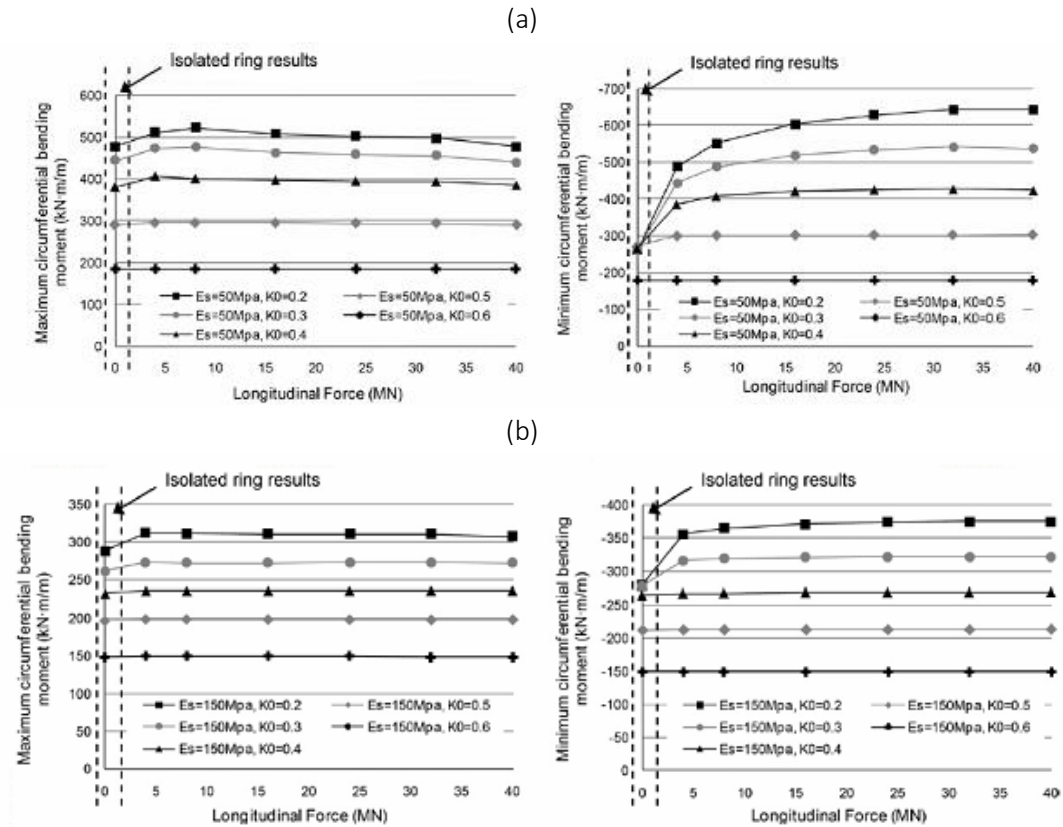


Figure 1.40. Maximum and minimum bending moments for the central ring ring 6 in the case of (a) $E=50\text{MPa}$ and (b) $E=150\text{MPa}$ (Arnau and Molins 2012).

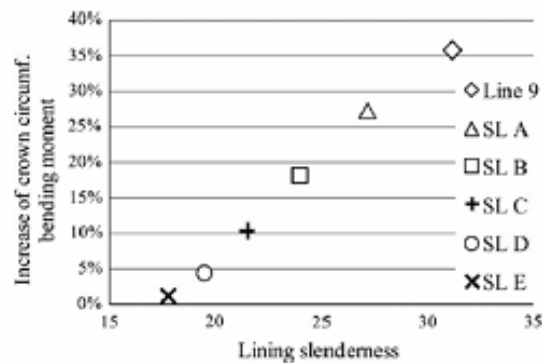


Figure 1.41. Influence of lining stiffness on the coupling rings (Arnau and Molins 2012).

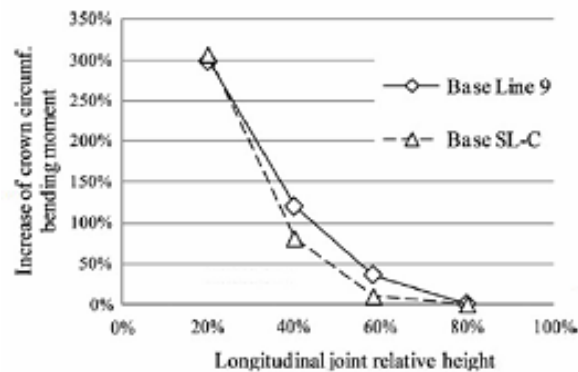


Figure 1.42. Influence joint height on the coupling rings ($E_s=25\text{MPa}$, $K_0=0.5$, $F=40\text{ MN}$) (Arnau and Molins 2012).

Do et al. 2013 studied in Flac 3D the Bologna–Florence railway line project. The authors modelled the joints in both direction with an axial, tangential and rotational springs (Figure 1.43). The axial spring has been represented by a linear relation with a constant coefficient spring, the radial and the rotational spring by means of a bi-linear elastic with a limited bearing capacity using the Janssen joint model.

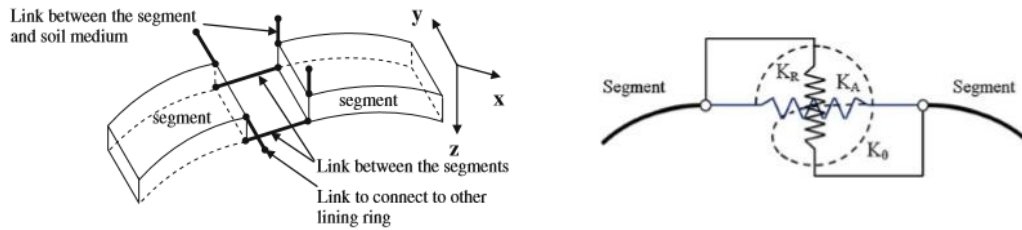


Figure 1.43. Scheme of joints adopted in the 3D numerical model (Do et al. 2014)

Table 1.8 resume the longitudinal and circumferential joints parameters. The rotational stiffness has been calibrated within the *Janßen's joint*, modelling the moment-rotation curve with a bilinear one, not considering the reduced stiffness due to the non-linear joint behaviour (Zhong et al 2006, Van Oorsouw 2010, Thienert and Pulsfort 2011).

Segment joints	Value	Ring joints	Value
Rotational stiffness K_θ (MN m/rad/m)	100	Rotational stiffness $K_{\theta R}$ (MN m/rad/m)	100
Maximum bending moment at segment joint M_{yield} (kN.m/m)	150	Maximum bending moment at ring joint M_{Ryield} (kN.m/m)	150
Axial stiffness K_A (MN/m)	500	Axial stiffness K_{AR} (MN/m)	500
Radial stiffness K_R (MN/m)	1,050	Radial stiffness K_{RR} (MN/m)	1,050
Maximum shear forces at segment joint S_{yield} (MN/m)	0.55	Maximum shear forces at ring joint S_{Ryield} (MN/m)	0.55

Table 1.8. Longitudinal and circumferential joint parameters (Do et al. 2014).

To investigate to coupling effect, the authors compared the result obtained with parametric analysis for the following six joint patterns configuration in terms of bending moment, normal and longitudinal forces (Figure 1.44):

- (a) Model M1: Continuous lining.
- (b) Model M2: straight rings—type 1 joint pattern
- (c) Model M3: staggered rings—type 2 joint pattern
- (d) Model M4: staggered rings—type 3 joint pattern
- (e) Model M5: staggered rings— type 2 joint pattern, rigid link at circumferential joints
- (f) Model M6: staggered rings—type 2 joint pattern, free link at circumferential joints

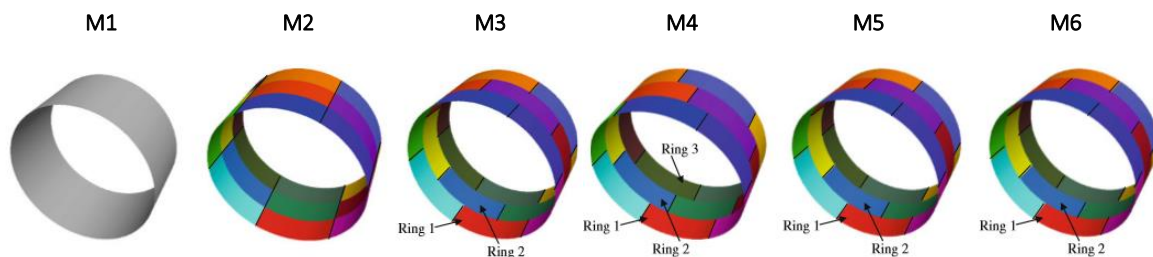


Figure 1.44. Lining models (Do et al. 2014).

The model M1, M2 and M6 don't allow a coupling effect in longitudinal direction. The model M3, M4 and M5 show a different influence in terms on longitudinal coupling due to the fact that the different staggered configuration gives a different global stiffness to the segmental lining with a consequent different redistribution of the forces through the joint. In particular, the minimum differences between the bending moments for these three cases induced in the successive rings are obtained in the case of model M4, the stiffer configuration respect the staggered cases, with a maximum value of bending moment lower than that obtained in the other cases M3 and M5. The authors observed also that the major effect of joint pattern is in terms of bending moment, with a maximum difference between two successive rings of about 26.1 % while the normal force, longitudinal force are in a similar range with a maximum difference between two successive rings of only 1.8 and 3.4 respectively.

In Table 1.9 the authors compare the induced internal forces for the different 6 cases of lining configuration, considering the continuous M1 lining the reference case. The factor R is the ratio between the maximum value of bending moment and normal force in the reference ring for the different staggered configuration respect the model M1.

The maximum positive and negative bending moment of straight joint model M2, is lower than that obtained in the other staggered case, showing the most deformable condition. The normal force in the staggered joint lining cases is always higher than the ones obtained in the case of a continuous lining, unless for the case of straight joint pattern. In terms of longitudinal force, the model M2 calculate the higher value respect the staggered cases.

Parameters	Model M1	Model M2	Model M3	Model M4	Model M5
Maximum positive bending moment (kN.m/m)	92.1	68.2	113	97	104
R_{M+} (%)	100	74.0	122.7	105.3	112.9
Minimum negative bending moment (kN.m/m)	-71.8	-64.3	-109	-98	-117
R_{M-} (%)	100	89.6	151.8	136.5	163.0
Maximum normal force (kN/m)	1,380	1,270	1,640	1,680	1,770
R_N (%)	100	92.0	118.8	121.7	128.3
Maximum longitudinal force (kN/m)	1,860	2,170	1,700	1,900	2,130
R_{LN} (%)	100	116.7	91.4	102.2	114.5

Table 1.9. Comparison of internal forces for the different lining configuration (Do et al. 2014).

An advanced numerical study has been developed by *Majdi et al. 2015* to investigate the moment-rotation behaviour of different segmental joint (Figure 1.45) and its effect on the transversal lining behaviour.

To this end, the authors modelled *Hordijk and Gijsbers 1996* experimental test described before, with 3D ABAQUS finite element software. The numerical calibration (Figure 1.46) has been done modelling the joint with a contact surface which a non-linear stress-strain behaviour. The used constitutive model allows to follow the joint behaviour during all the stage of working until failure, including a failure envelope to define the concrete cracks under tension stress and the crushes that occur under compressive stress and can simulate concrete features after cracking or crushing.

Figure 1.47a shows how increasing the joint height, the initial rotation stiffness and the ultimate bending moment of joints increase. On the contrary, reducing the joint height, there is an increasing of stress joint concentration in a contact area (Figure 1.48) which leads to an increment of joint curvature and then its rotation.

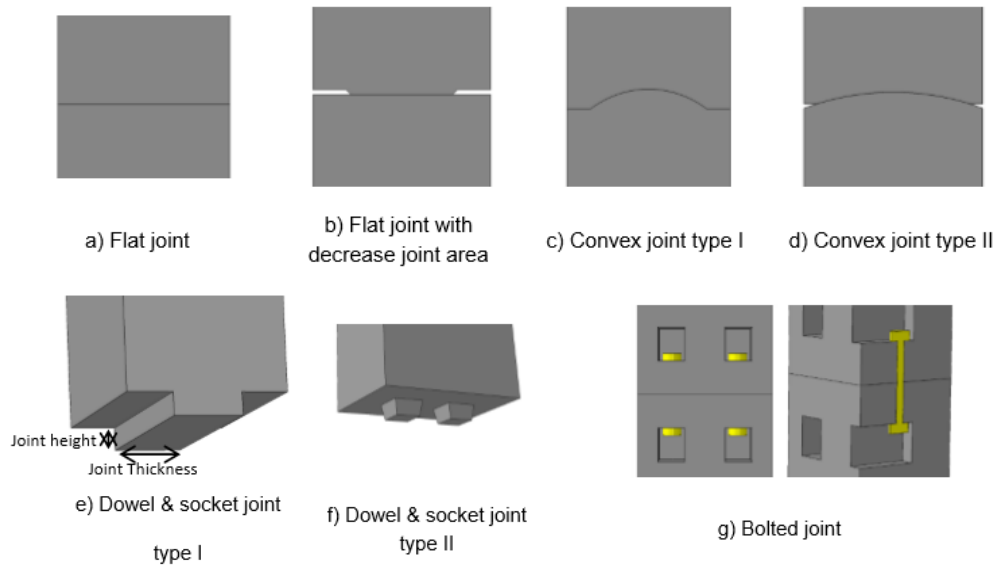


Figure 1.45. Joint models (Majdi et al. 2015).

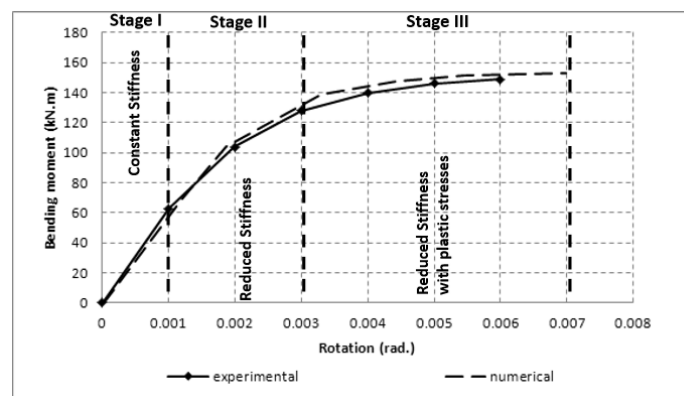
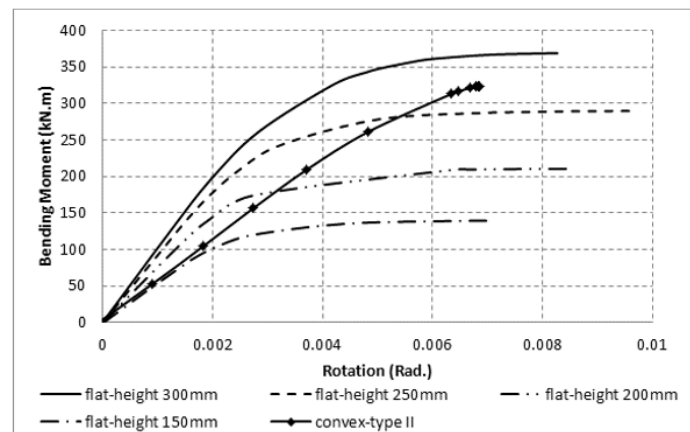


Figure 1.46. Calibration of moment-rotation relation for joint (Majdi et al. 2015).

(a)



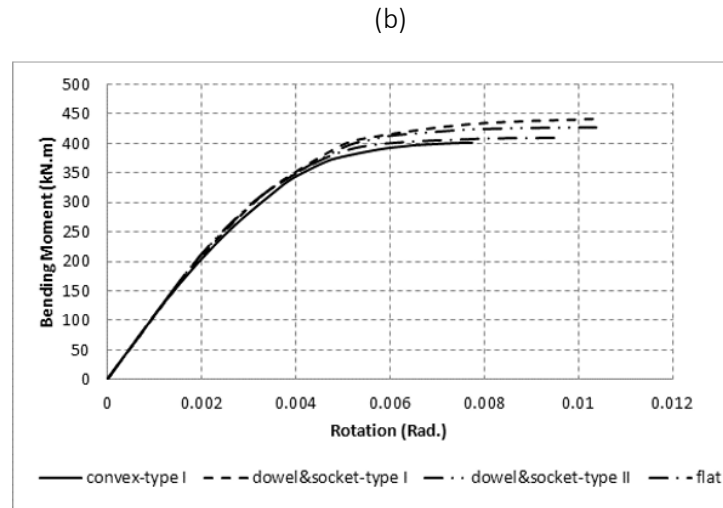


Figure 1.47. Moment-rotation relation for flat and convex II (a) and convex and dowel & socket joints (b) (Majdi et al. 2015).

Convex joint type I, dowel & socket joint type I and II and flat joint shows the same initial rotation stiffness but a light different ultimate bending moment (Figure 1.44b). In particular, the dowel and socket joint (type I) has the highest moment capacity, and the convex joint (type I) the minimum.

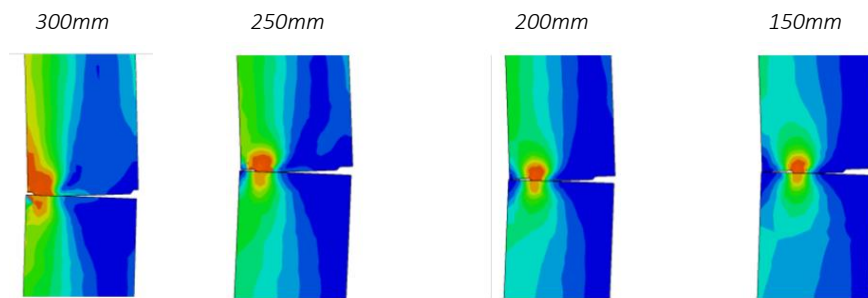


Figure 1.48. Flat joint stresses (Majdi et al. 2015).

Rather different is the convex joint (type I) behaviour (Figure 1.47a). Initial rotational stiffness is similar to that one exhibited by the flat joint with the smaller height but with a very different ability to transfer bending moment. A flat joint is able to transfer bending moments while a such convex geometry no moments will be transferred, and then it behaves like a hinge. For this reason convex joints are usually used for very high rotation (c.f. 1.1.2).

According to experimental results obtained by Liu et al. 2017, Figure 1.49 shows that flat bolted and non-bolted flat joints exhibit the same initial rotational stiffness. The presence of the bolts increments the ultimate bending moment of flat joints.

Guan et al. 2015 studied the segmental lining behaviour of Fuzhou Metro Line 1 within the indirect (uniform ring model) and direct (3D shell-spring model) approaches to investigate the key parameters of both methods, the effective ratio of bending rigidity η and the transfer ratio of bending moment ξ respectively.

Longitudinal and circumferential joint have been modelled in the FE code Flac 3D by means of a rotational and shear springs (Figure 1.50) calibrated against the results of a large scale bending and shearing test for joint-connected segments.

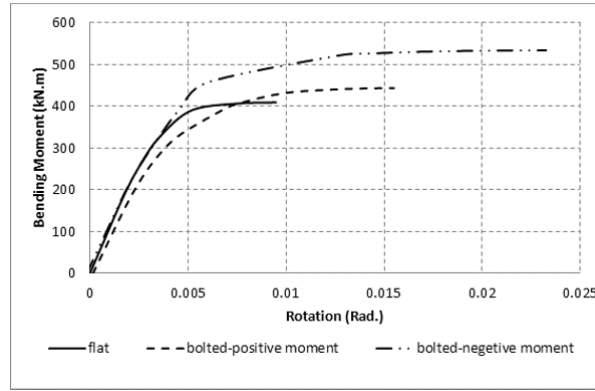


Figure 1.49. Moment-rotation relation for bolted and non-bolted flat joint (Majdi et al. 2015).

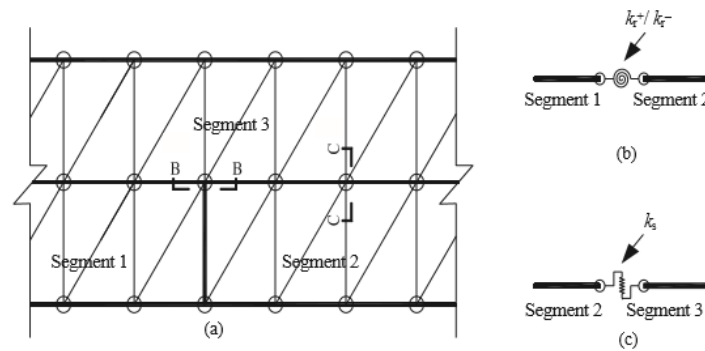


Figure 1.50. Scheme of numerical model of segmented lining of Fuzhou Metro Line 1 (Guan et al. 2015).

Figure 1.51 shows how the rotational stiffness of longitudinal and circumferential joints is described within a bilinear law of moment-rotation. Longitudinal joint behaves differently when subjected to positive or negative bending moment, in accordance with the experimental results showed before (c.f. 1.2.1).

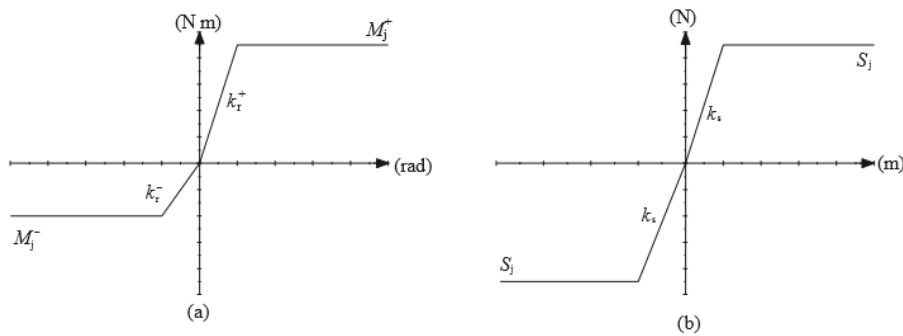


Figure 1.51. Behaviour of (a) longitudinal and (b) circumferential joint of Fuzhou Metro Line 1 (Guan et al. 2015).

In this way the authors calculate a rotational stiffness k_r^+ / k_r^- of 10000/4000 kNm/rad and a shear stiffness 50000 kNm/rad.

To estimate the more suitable value of η and ξ for the studied case, the authors set before the η value a null value of transfer ratio of bending moment, and in a second moment determined the ξ , value which

artificially modifies the bending moment within the Equation 1.9. In this stage the effective ratio of bending rigidity is constant and equal to that one calibrated in the first step.

$$M_S = M_0(1 + \xi); \quad M_J = M_0(1 - \xi) \quad (1.9)$$

where M_0 is the most unfavourable bending moment calculated for the load scheme of Figure 1.52 and M_S and M_J the modified bending moments.

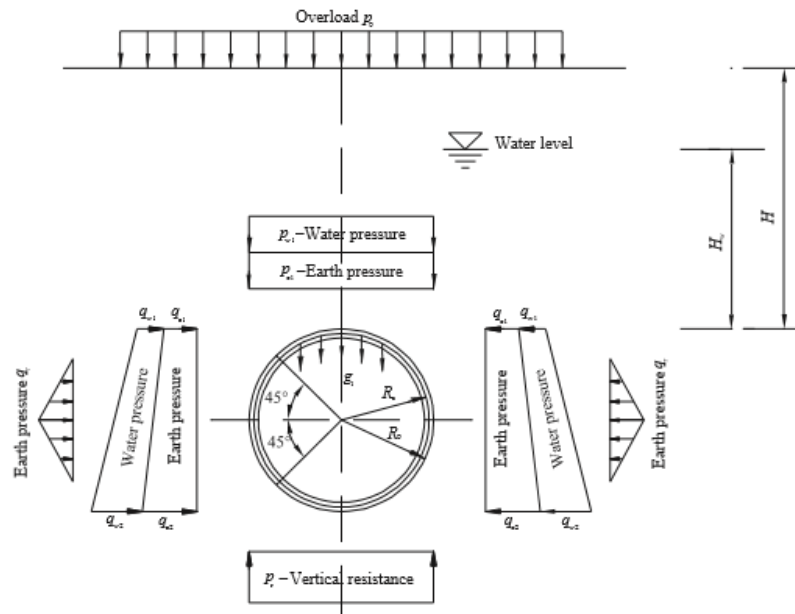


Figure 1.52. Load scheme of uniform ring (Ding et al. 2004).

Table 1.10 shows the results of the two different approaches in terms of bending moment. The values evaluated with the uniform ring method, for a η value set equal to 0.48 and a ξ set equal to 0.45, are slightly higher than those calculated within the shell-spring method.

	Shell-spring model	Uniform ring model
$M^*_S(kNm)$	97	127
$M_S(kNm)$	-99	-102
$M^*_J(kNm)$	33	48
$M_J(kNm)$	-38	-38

Table 1.10. Load scheme of uniform ring (Ding et al. 2004).

Table 1.11 shows the results of η and ξ values for the studied case and the influence of overburden, soil properties and water head.

The effective ratio of bending rigidity increases with the overburden increasing, decreases with the increasing of water head and increases with good soil properties.

The transfer ratio of bending moment is not influenced by the soil parameter but seems to be influenced only by the lining technology itself and load level.

(a)

Selection of η and ξ due to different overburdens and soil properties (water head = 11.5 m).

Overburden (m)	3_1 mud		5_2 silty sand		7_1 residual clay	
	η	ξ	η	ξ	η	ξ
8	0.38	0.44	0.44	0.45	0.63	0.45
14	0.40	0.44	0.48*	0.45*	0.69	0.46
20	0.41	0.45	0.52	0.46	0.72	0.46

Note: "*" denotes standard case.

(b)

Selection of η and ξ due to different water heads and soil properties (overburden = 14 m).

Water head (m)	3_1 mud		5_2 silty sand		7_1 residual clay	
	η	ξ	η	ξ	η	ξ
11.5	0.40	0.44	0.48*	0.45*	0.69	0.46
5.7	0.41	0.45	0.51	0.45	0.71	0.46
0	0.43	0.45	0.55	0.46	0.73	0.46

Note: "*" denotes standard case.

Table 1.11. Selection of η and ξ due to (a) the different overburdens and soil properties (b) and different heads and soil properties (Guan et al. 2015).

CHAPTER 2

Mechanized tunnelling effect on the lining behaviour

Introduction

Tunnelling induces a complex interaction mechanism between the soil, the grout of the filled gap and the concrete of the segments which suffer a continuous changing of stresses and strains during the front advancement until its removal. So that tunnel lining segments must be calculated not only according to the standards of reinforced concrete constructions but “...specific circumstances must be taken in account, which make design much more complicated: the determination of loads during ring erection, advance of the TBM, earth pressure and bedding of the articulated ring, is difficult. The ring model and the design input values must be studied carefully according to the parameters of the surrounding soil (Muir Wood 2012).”

The purpose of this Chapter is to give an overview of different tunnelling technologies developed during years in order to discuss their effects in the lining behaviour.

Many authors have proposed several different tools to predict the internal forces arising in the lining within sophisticated 3D numerical models which are here discussed.

The case history of Bologna-Firenze railway, very well detailed in the work of *Do et al. 2013*, has been adopted as reference benchmark to define a 3D numerical model of segmental tunnel lining developed in Plaxis 3D and compare the results with those obtained by the authors using Flac 3D.

2.1 Mechanized tunnelling methods

2.1.1 History of mechanized tunnelling

Mechanized tunnelling is a type of excavation method which allows almost contemporary the excavation phases execution and the tunnel lining installation directly in the underground space, thanks to the use of Tunnel Boring Machine TBM that, with the aid of sophisticated automation and control systems, advances to tens of meters per day in different geological and hydrogeological conditions. In soft soil, the shield is a protective structure used in the excavation of tunnels to allow the soil to remain stable during the time, serving as temporary support structure for the tunnel during excavation.

In modern urban areas highly populated where soft alluvial deposits are widespread and the demand for tunnels is high (as in Japan particularly), shield tunnelling have contributed greatly to urban infrastructure development, representing the best suitable method of excavation with the less impact on the surrounding.

Shield tunnelling was developed to excavate tunnels through the soft ground below rivers for the first time by Marc Isambard Brunel to build the Thames Tunnel in London in 1825.

Brunel is said to have been inspired in his design by the shell of the shipworm *Teredo navalis* (Figure 2.1), a mollusc whose efficiency at boring through submerged timber he observed while working in a shipyard.

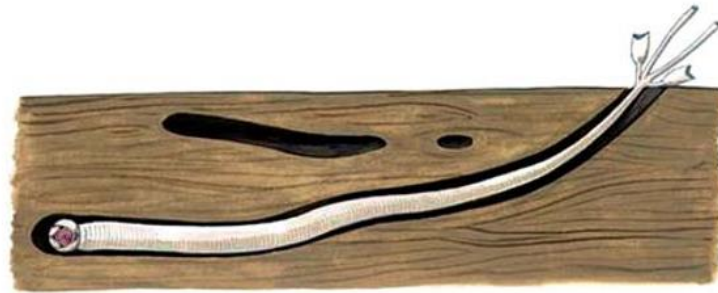


Figure 2.1. The “*Teredo Navalis*” tunnelling (Guglielmetti et al. 2008).

His basic concept was to press a rigid frame (shield) forward through soft ground with jacks, thus preventing the ground from collapsing, and build the tunnel structure within the frames; by repeating the process of jacking then constructing the support structure, the tunnel would move forward (Figure 2.1). The shield use for the Thames Tunnel was rectangular in cross section with 12 adjacent frames divided in 3 chambers.



Figure 2.2. Brunel shield tunnel excavation under River Thames in London (Guglielmetti et al. 2008).

A later redesign with a circular cross section was used by Peter W. Barlow to construct the Tower Subway in 1869, which at once made it simpler in construction and better able to support the weight of the surrounding soil.

The Barlow design was enlarged and further improved by James Henry Greathead for the construction of the City and South London Railway (today part of London Underground's Northern line) in 1884. His system was also used in the driving of the running tunnels for the Waterloo & City Railway which opened in 1898. Cast steel segments, backfilling, and injection were all used by Greathead in his shield work, so his was the prototype of today's shield.

Simultaneously, Alfred Ely Beach of New York City devised a shield, also circular in cross section, which he used to drive the Broadway pneumatic railway tunnel in New York.

The use of compressed air was afterwards studied to control water inrush for work on the Woolwich Tunnel beneath the River Thames in 1876, although it was not actually used until the end of the work. First successful applications of this face support technique were in Antwerp Dock tunnel (1879) and in the Hudson river tunnel, New York 1880.

The failed attempt to drive the Hudson river with caisson and compressed air in 1880 (Figure 2.3) leads Greathead to suggest a combined use of compressed air with the shield technology to support both the face and the tunnel profile (Figure 2.4).

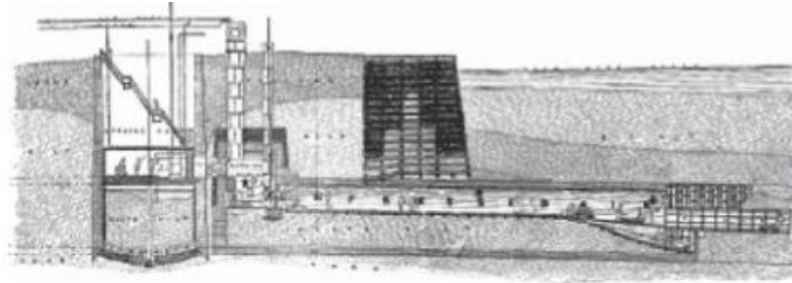


Figure 2.3. Scheme of compressed air technology used for tunnel under Hudson River in New York (Guglielmetti et al. 2008).

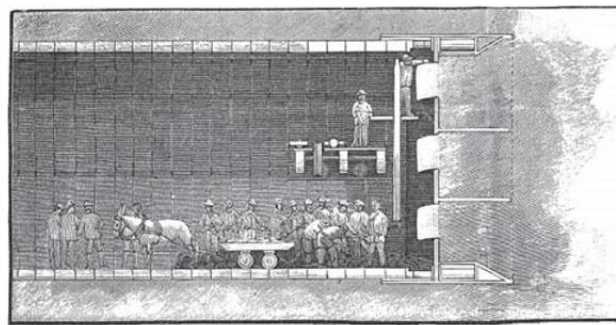


Figure 2.4. Greathead compressed air shield for tunnel under Hudson River in New York (Guglielmetti et al. 2008).

The combination of shield and compressed air represent the design scheme of the first generation shield tunnelling technology developed about 150 years ago. No great advances were developed in the technology until the 1960s when a very fast develop of sophisticated technologies started until the more modern tunnelling shields.

2.1.2 Modern mechanized tunnelling

The modern shielded machines are normally circular tube divided into three main section: front shield, middle shield and tail shield. The front shield consist of the external edge of excavation chamber, where the excavated soil is fed to the transportation system, and the pressure bulkhead. This latter separates the excavation chamber from the rest of the tunnel under atmospheric pressure and transfers the required support to the medium to guarantee the structural stability of possible sliding wedge. Just behind the front shield, there is the main drive with each control device. Under the tail skin the lining rings are assembled.

Shield machines can be classified into three main groups in function of their support to the excavation face: Slurry Shield and Hydro Shield which apply the face pressure hydraulically and Earth Balance pressure (EPB) Shield which applies the face pressure mechanically; in the case of soil with sufficiently high shear strength no active support is needed and the soil is in equilibrium just with the "natural support"

- The Slurry Shield Technology (Figure 2.5a) supports the excavation face by a pressurized bentonite slurry pumped into the excavation chamber, typically composed of a bentonite suspension in water, with some additives if necessary. A pumping system feed the fresh slurry and remove the muck from the excavation chamber through a pipeline; the balance between this in-flow and out-flow controls the pressure to face excavation stability.
- The Hydroshield Technology (Figure 2.5b) is very similar to that one just described, with the add of supplementary chamber with the function of control the slurry pressure within compressed air. In this way, the face pressure is guaranteed in part by the hydrostatic pressure of slurry and in part by air pressure applied on the slurry through the overlying air cushion.

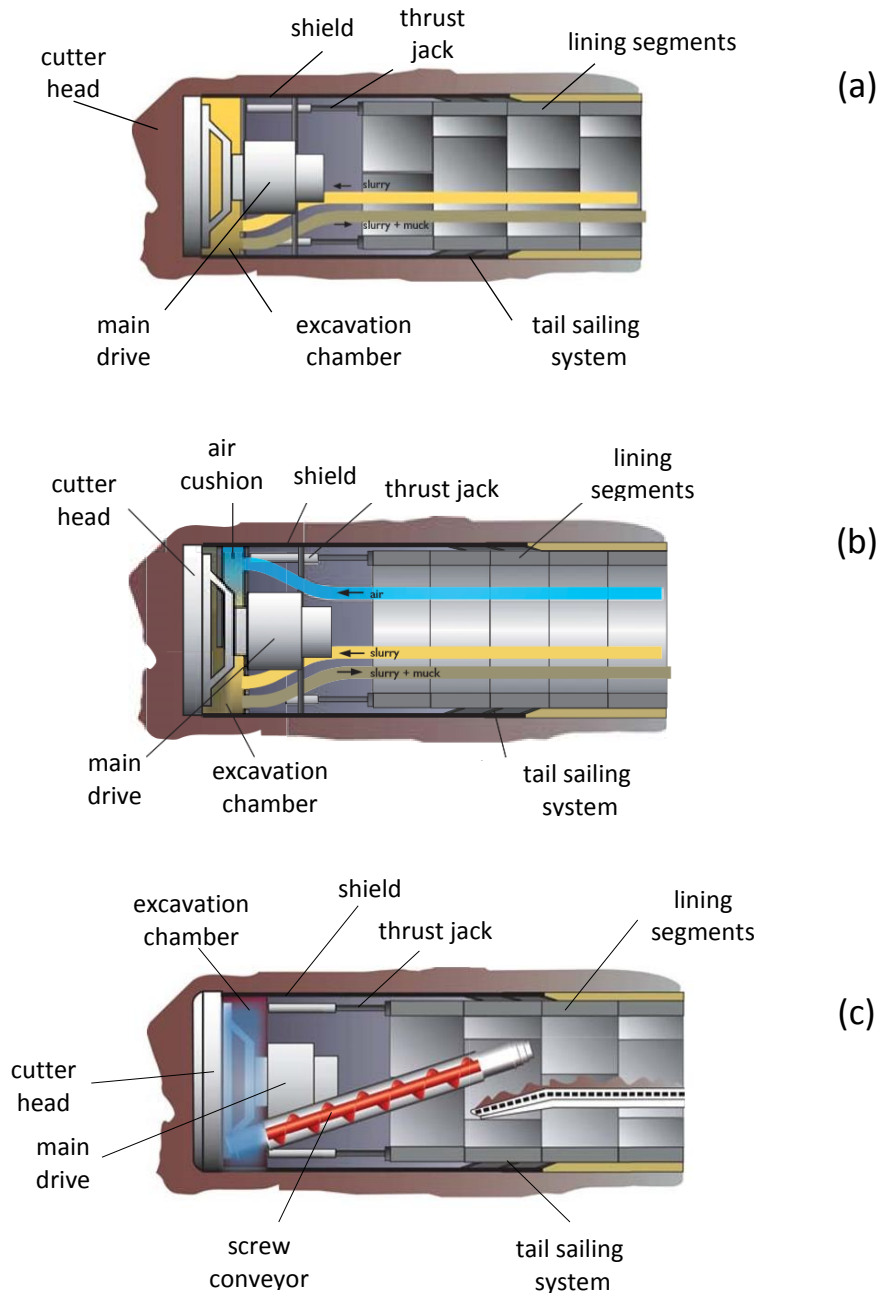


Figure 2.5. Scheme of (a) Slurry Shield SS, (b) Hydro Shield HS and (c) Earth Balance Pressure Shield EPBS (Guglielmetti et al. 2008).

The slurry pressure against the soil creates a film of material (called “cake”), which rheological properties, together with the hydro-geological soil conditions, influence the cake thickness and then the confinement of the soil at the TBM face.

- The EPB Technology (Figure 2.5c) uses the jacks thrust on the last installed lining for the TBM advancement, while the front stability is guaranteed by face pressure applied within the ground just excavated, pressurized in the excavation chamber. The magnitude of the thrust is proportional to the average pressure required at the front, the soil-shield friction and the weight of the machine. The required front pressure is guaranteed by the velocity control of the screw conveyor.

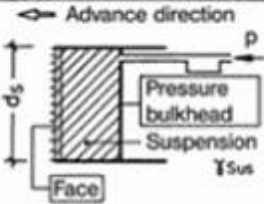
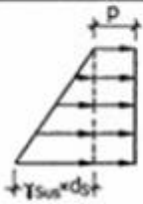

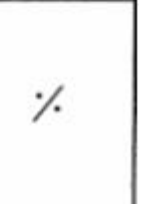
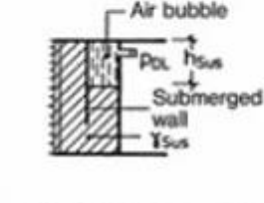



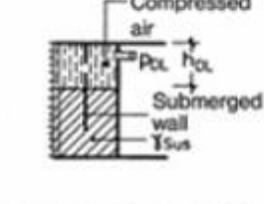


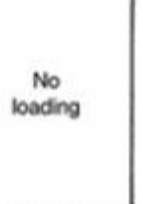
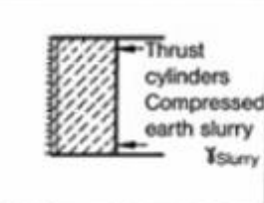
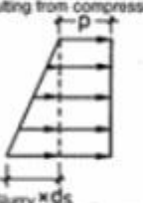

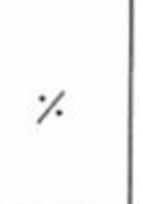
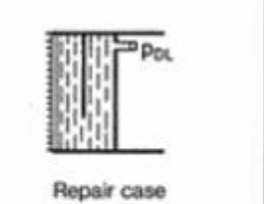
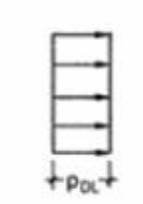

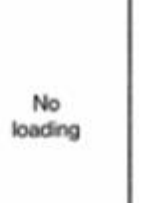
	Shield (working chamber)	Load assumptions resulting from support pressure		
		Pressure bulkhead	Face	Submerged wall
a	Slurry shield 			
b	Hydroshield with compressed air application 			
c	Hydroshield with lowered suspension level 			
d	Earth pressure shield 			
e	Hydroshield with compressed air and without suspension, compressed air shield 			

Figure 2.6. Face loading scheme in function of shield machines technology.

Figure 2.6 shows the face loading scheme in function of shield machines technology. In the case of Hydroshield with partitioned excavation chamber within a submerged wall, the loading pattern of the

pressure bulkhead can vary the load on the face and the balancing load is transferred by the submerged wall itself.

The front excavation is performed, for each shield technology, with a circular cutting head which rotational speed and torque moment calibrated in function of the excavated soil and can be varied for non-homogeneous ground condition. Different technologies are available for the case of Slurry and Hydro shield (Figure 2.7a) and for the case of EPB shield (Figure 2.6b), due to the different functioning principle.

In the first case the ratio between the opening area in the cutter head and the excavation section (opening ratio) is even more of 50% to allow the direct contact of slurry with soil, in the second case instead it is usually less than 35% to support the contrast of the soil.

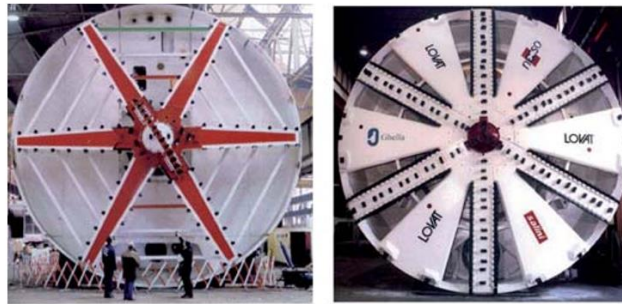


Figure 2.7. Cutter head of a (a) SS and a (b) EPBS (Guglielmetti et al. 2008).

The efficiency of tunnelling machine is very dependent on the soil type, its permeability and the particles size. In the case of SS the key parameter for its efficiency is strictly related to the soil permeability: the formation of the “cake” is difficult in very permeable soil, as in the case of granular material, so there must be an upper limit to the particle size of the ground in the face to be excavated. In the case of EPBS the key parameter for its efficiency is strictly related to the particles size: the soil in the excavation chamber should be a high density mixture which could be not adequate in relatively loose soil and in presence of small fine content percentage (less than 20%).

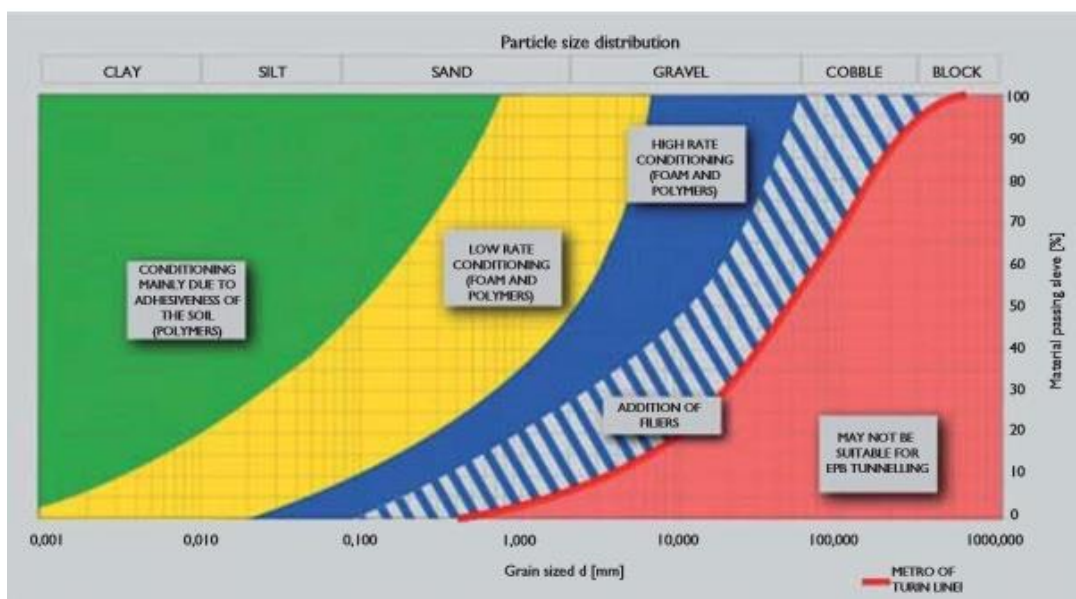


Figure 2.8. Fields of application for SS and EPBS machines and different conditioning techniques (Guglielmetti et al. 2008).

It is possible to extend this theoretically applicable field of EPBS with the use of appropriate additives for ground conditioning (Figure 2.8).

The most common conditioning agents are 1) foams (air dispersed in water), 2) fillers (fine sand or fine crushed limestone) and 3) polymers (usually in combination with foams).

2.2 Effects on the lining

The tunnel support system should to withstand the permanent load of the ground but during tunnel construction different sources of load need to be considered as temporary load.

Lining ring assembly process takes place under protection of the tail shield of the TBM following a prescribed assembling process. The positioning of the first segment is carried out by the erector, hydraulic arm at the back end of the machine, and followed by the others segments, one on the right and one on the left until reaching the counter-crown elements. The first external temporary load acting the lining is the axial force induced by the jack thrust to push the shield forward in the direction of the excavation while the thrust cylinders are placed against the last installed ring which behaves as abutment. While the subsequent ring is installed, the phisic gap between the exstrados of previous ring and the profile of excavation is filled with grout. The grout pressure put the ring under a pre-stressed compression state quite evenly before to support the soil weight. This is a second source of external temporary active load on the lining.

2.2.1 Effect of jack thrust

The thrust on the last installed ring for TBM advancement is completely transferred to the ring through hydraulic jacks system acting on bearing steel pads with a contact area smaller than the lining thickness.

Generally in all the TBMs is possible to apply a constant value of thrust in four different area of transversal lining section as in Figure 2.9a. The possibility to differentiate the applied force simplifies the operation of thrust and measure out in the case of not correct alignment of the machine respect the middle plane of the thrusting lining (Figure 2.9b), often generated by the gravity, especially in the upper part of the shield, or by a curved excavation trajectory.

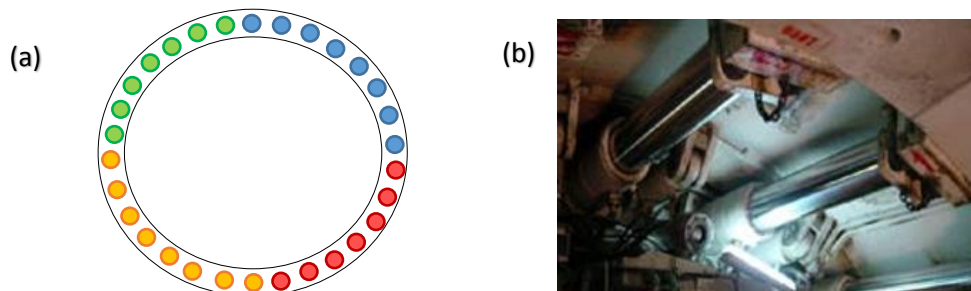


Figure 2.9. (a) Scheme of thrust groups on transversal lining section; (b) Eccentric placement of the thrust jack plate.

Both the different thrust forces and the possible eccentricity of jacks can generate relative displacements between the segments of the ring which can change progressively during the TBM's thrust until the possible cracking of the elements as sometimes is observed in such construction phase due to the induced multi axial state of stress.

Cavallaro 2011 studied numerically the effect of eccentricity of the jack thrust of the group C in Figure 2.10a on the lining behaviour. In the numerical model implemented in Abaqus 3D (Figure 2.10b) a “discrete crack model” has been adopted to simulate the concrete damage plasticity.

Figure 2.11 shows the results in terms of maximum principal tension in absence of eccentricity (case a) and with an eccentricity of 30 mm (case b) and 50 mm (case c). Any cracks develops without eccentricity into any of the elements. While increasing the eccentricity value, cracks start to form with a total maximum length of 20cm in the case b and 68cm in the case c, demonstrating the entity of the cracks increases sensitively with the eccentricity.

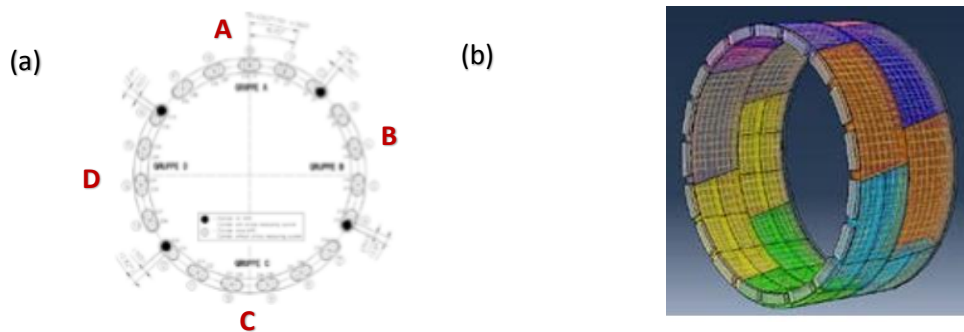


Figure 2.10. (a) Scheme of groups of jacks on the lining; (b) Numerical model in Abaqus 3D (Cavallaro 2011)

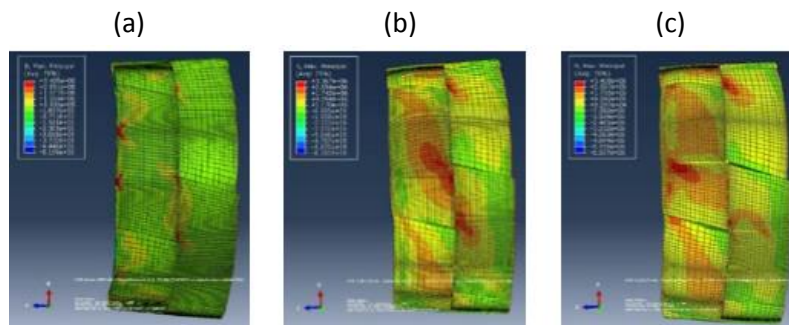


Figure 2.11. Maximum principal tension considering thrusting load (a) without eccentricity (b) with eccentricity of 30mm, (c) with eccentricity of 50mm (Cavallaro 2011)

Also the position of the loaded points in the lining transversal profile influences the segments state of stress and strains. Two jack thrust configurations are commonly used in Europe: 1) in the German configuration (Figure 2.12a) the thrust is applied at both edges and in the middle of each segments, while in the French configuration (Figure 2.12b) the thrust jacks are placed at 1/4 and 3/4 of the segmental length. The first method seems to be more vulnerable to introduce tensile stresses in the pushed segment in the case of errors in the installation of the previous ring.

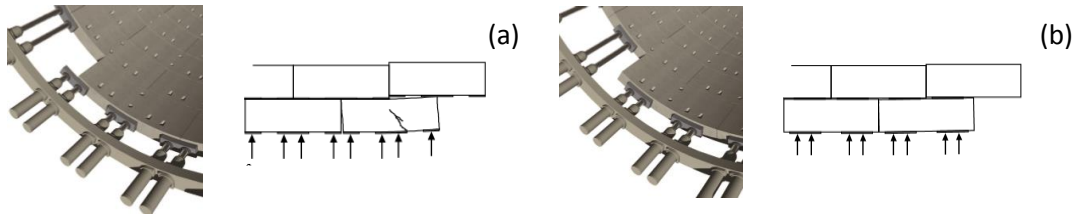


Figure 2.12. (a) German and (b) French jack thrust method (Groenevweg 2007)

The axial force produced by the thrust, induces compressive stresses in the pushed segment with a spread in longitudinal direction as in Figure 2.13; outside the compression trajectory the segment is under tension for equilibrium, both in transversal than in radial direction (along the lining thickness).

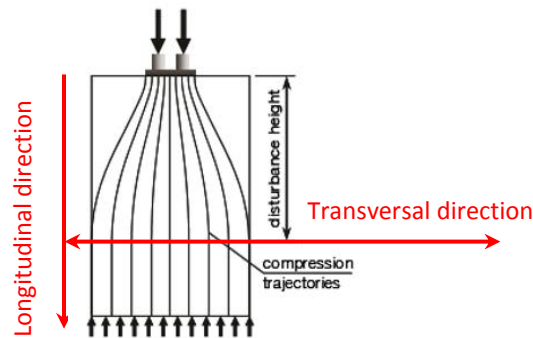


Figure 2.13. Diffusion of compression stresses due to the jack thrust.

This description corresponds to what happens in the French thrust method, where the jacks are located in the middle of the lining section. When jacks is applied on the edge of the two segment, the applied force is not able to spread over the longitudinal compression trajectory symmetrically on both sides of segments but the force will spread over only one side; as a consequence, the compression trajectory is completely different respect the previous one.

To ensure horizontal equilibrium, a tensile spalling force develops in between the compression strut link of jacks forces (Figure 2.14).

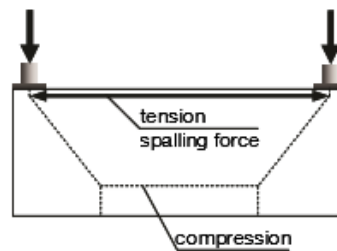


Figure 2.14. Tension spalling force in German jack thrust method (Groenevweg 2007).

Figure 2.15 shows the different stress distribution in the segment under jack thrust in the French and German configuration where this latter is less effective in spreading the introduced thrust jack forces from the TBM.

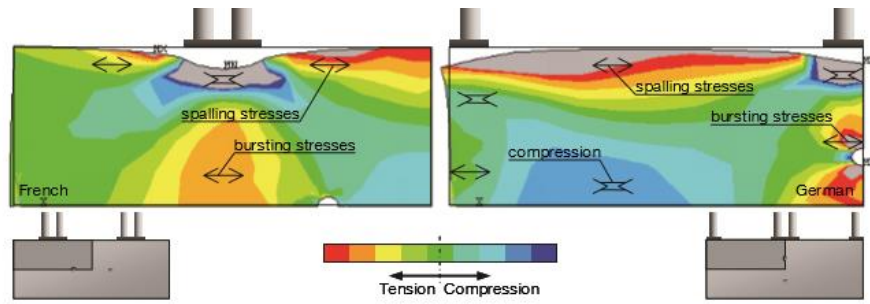


Figure 2.15. Stress distribution in tunnel segments due to introduction of thrust jack forces in the (a) French and (b) German thrust jack configuration (Groenevweg 2007).

Looking at the transmission mechanism of longitudinal thrust between the rings along the tunnel axis conveyed through the circumferential joints, a consequence of the construction sequence is the generation of a permanent longitudinal compression state in the lining. Many authors investigated this aspect with 3D advanced numerical models (Bloom *et al.* 1999, Klappers *et al.* 2006, Mo & Chen 2008, Do *et al.* 2013) where the long term longitudinal stresses remain close to their initial value due to the linear elastic behaviour of the lining, as is generally assumed for such problems. Arnau *et al.* 2012 proposed a numerical model considering the effect of concrete creep during the construction process in order to predict the remaining compression in the lining as a function of the time. The study shows that the longitudinal creep deformations of the lining produces a stress relaxation process involving a gradual loss of the initial longitudinal compressive force until 50% after 10,000 days (Figure 2.16). This aspect, underline the authors, is strictly related to the concrete type and circumferential joints behaviour.

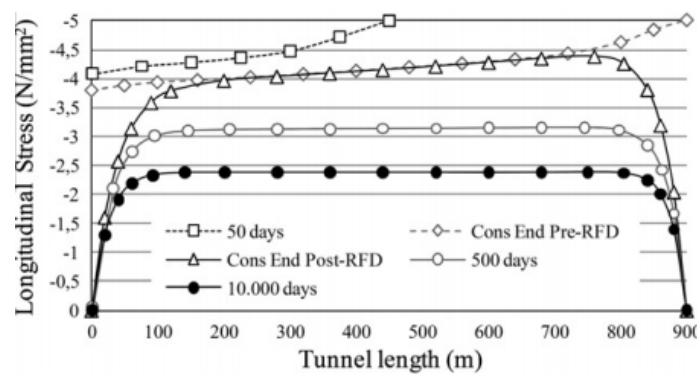


Figure 2.16. Evolution of longitudinal lining compression stress (Arnau *et al.* 2012).

2.2.2 Effect of grouting

The conicity and the thickness of the shield skin, the overcut produced by its cutting wheel and the design of the seal produce an annular gap between the external diameter of the lining and the excavation profile (Figure 2.17) which width range is between 13 and 18 cm (Thewes and Budach 2009).

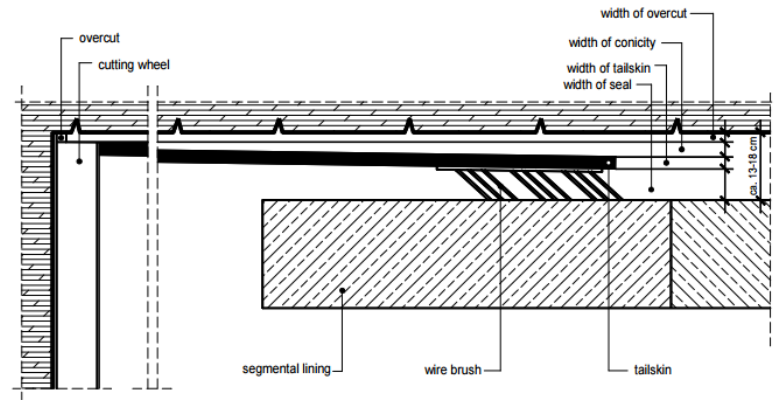


Figure 2.17. Factors of influence of the annular gap (Thewes and Budach 2009).

Grouting of the annular gap has a double effect of loading on the soil and on the lining:

- 1) minimizes and prevents settlements at the ground surface. The reduction of settlements or setting up of lifting can be the result of a good performance of the grouting process, which qualitative description is shown in Figure 2.18;
- 2) ensures embedment of the segmental lining before to support the soil weight.

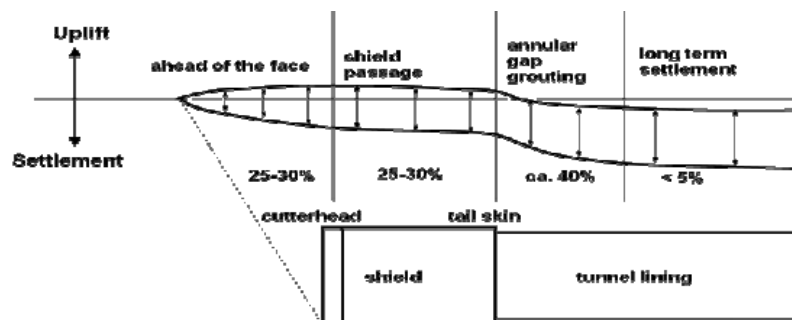


Figure 2.18. Schematic development of settlements and percentage of total settlements (Thewes and Budach 2009).

The hardening grout process, discussed in detail in the previous chapter (c.f.1.1.3), affects directly the induced load from the soil to the lining. Figure 2.19 shows a simplified scheme of what happens in the annular gap around the lining, adopted by *Bezuijen & Talmon 2009* to study the loading on the lining.

There is a length of installed lining loaded by liquid grout and just behind loaded by hardened grout. The step of loading with liquid grout is the most important because determines the bending moment in the lining and; if this length is too long, loading will be too high and tunnelling will not be possible.

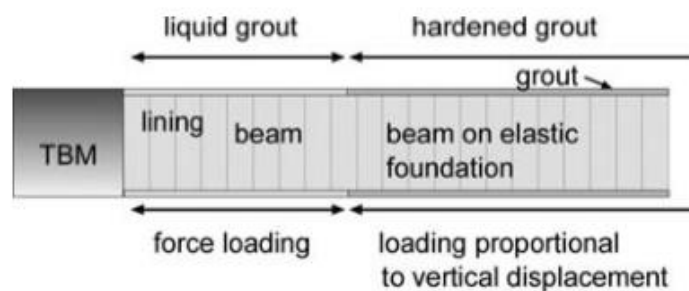


Figure 2.19. Scheme of loading on the lining (Bezuijen & Talmon 2009).

As consequence of this construction mechanism, the rings loaded with liquid grout are pressed upwards by the buoyancy forces; it is necessary to mobilize shear forces from the TBM to achieve a stable tunnel lining which will lead to moments in the lining.

In the case of Groene Hart Tunnel the bending moment in the lining was measured for a large distance behind the TBM using strain gauges installed in the lining segments. Figure 2.20 shows an increase of negative bending moment at some distance from the TBM due to the reaction force to compensate the buoyancy in the fluid grout zone, until to reach positive value when the grout is hardened in a steady state value far from the TBM tail.

The magnitude of the bending moment in the lining is strictly related to the grout composition, and then its stiffness in the fluid (plastic) state, the soil properties (weight, permeability) and of course, the depth of tunnel axis.

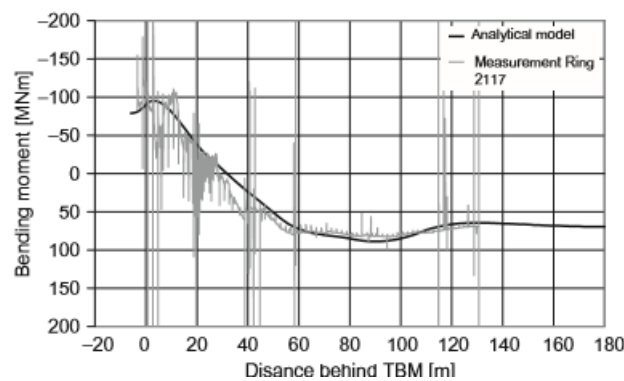


Figure 2.20. Analytical and measured bending moment in ring 2117, Groene Hart Tunnel (Hoefsloot, 2008).

It can happen during grouting phase transverse relative displacements between subsequent rings due to the buoyancy forces developing when the grout is in its fluid state, or relative rotations between the segment due to a not uniform grouting pressure (Figure 2.21).

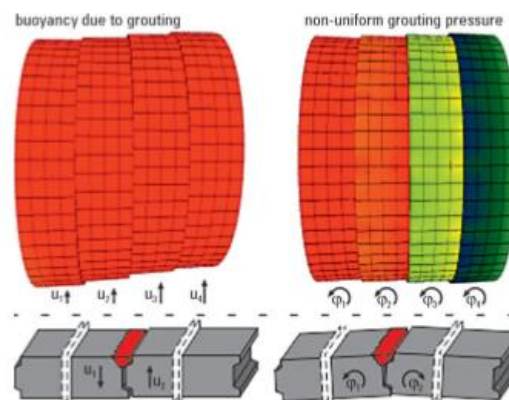


Figure 2.21. Rings behaviour during grouting (Putke et al. 2015).

These two different conditions impact on the structural rings behaviour in terms of internal stresses and, for high values of transversal displacement u_z and relative rotation ϕ can induce shear damage in the circumferential joints.

An optimization concept has been applied by *Putke et al. 2015* to such circumferential joints of concrete segmental lining to investigate their bearing capacity under shear load. The procedure consists of three steps:

1. Numerical analyses using coupled beam or shell models to predict u_z and ϕ for usually stage construction scenarios;
2. The predicted values of u_z and ϕ are used as input parameters or boundary conditions in the mathematical optimization method where concrete material, geometry and reinforcement layout are varied in order to enhance the segment's bearing capacity;
3. Experiments are carried out to assess the designs based on numerical findings.

The criteria has been applied to three different circumferential joint types: S1) cam, S2) pot, S3) dowel; Figure 2.22 provides an overview of all investigated cases including their geometric variations (Figure 2.22a) and the test combination depending on the geometry and type of reinforcement (Figure 2.22b).

(a)						(b)										
sample		geometric variations (dims. in [m])					series		geometry					reinforcement		
series	parameter	variation 1	variation 2	variation 3	variation 4	variation 5	name	symbol	variation 1	variation 2	variation 3	variation 4	variation 5	unreinforced	conventional	fibre cocktail
S1	<i>a</i>	0.15	0.15	0.15	0.12		V1-1	◇	4	–	–	–	–	x	–	–
	<i>b</i>	0.03	0.03	0.06	0.06	–	V1-2	◆	4	–	–	–	–	–	x	–
	<i>c</i>	0.09	0.09	0.03	0.09	–	V2-1	△	–	4	–	–	–	x	–	–
	<i>d</i>	0.03	0.06	0.03	0.06	–	V2-2	▲	–	4	–	–	–	–	x	–
	<i>e</i>	0.55	0.55	0.55	0.55	–	V3-1	□	–	–	2	–	–	x	–	–
	<i>h</i>	0.45	0.45	0.45	0.45	–	V3-2	■	–	–	4	–	–	–	x	–
	α	45°	63°	27°	45°	–	V4-1	○	–	–	–	2	–	x	–	–
	<i>t</i> ¹	0.30	0.30	0.30	0.30	–	V4-2	●	–	–	–	4	–	–	x	–
S2	<i>a</i>	0.15	0.15	–	–	–	V1-1	▲	3	–	–	–	–	–	x	–
	<i>b</i>	0.03	0.03	–	–	–	V1-2	▼	3	–	–	–	–	–	–	x
	<i>c</i>	0.09	0.09	–	–	–	V1-3	♥	3	–	–	–	–	–	–	–
	<i>d</i>	0.03	0.06	–	–	–	V1-4	☉	3	–	–	–	–	–	–	–
	<i>f</i>	0.80	0.86	–	–	–	V2-1	☐	–	3	–	–	–	–	x	–
	<i>h</i>	0.45	0.45	–	–	–	V2-2	▽	–	3	–	–	–	–	–	x
	α	45°	63°	–	–	–	V2-3	♥	–	3	–	–	–	–	–	x
	<i>t</i> ¹	0.20	0.20	–	–	–	V2-4	☉	–	3	–	–	–	–	–	–
S3	<i>i</i>	–	–	–	–	0.20	V5-1	■	–	–	–	–	3	–	x	–
	<i>j</i>	–	–	–	–	0.200/0.185	V5-2	+	–	–	–	–	3	–	x	–
	<i>g</i>	–	–	–	–	0.80	V5-3	#	–	–	–	–	1	–	–	x
	<i>t</i> ¹	–	–	–	–	0.34										

¹ thickness

¹ thickness

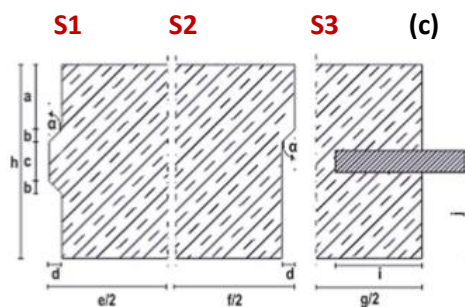


Figure 2.22. (a) Overview of test samples with geometric parameters; (b) Nomenclature of tested samples depending on geometry and reinforcement system; (c) Geometric parameters of the tested samples (*Putke et al. 2015*).

Figure 2.23 resumes the experimental results of all samples tested including statistical, mean values $E(x)$ and standard deviations $\sigma(x)$. The comparisons show that the geometry is the most influencing

parameter on the bearing capacity of the cam-pot joint and, although the extra reinforcement of the pot leads considerable increases in bearing capacity, the pot is the weaker part of this particular joint connection. Joints with dowels exhibit the lower bearing capacities respect all tested joints.

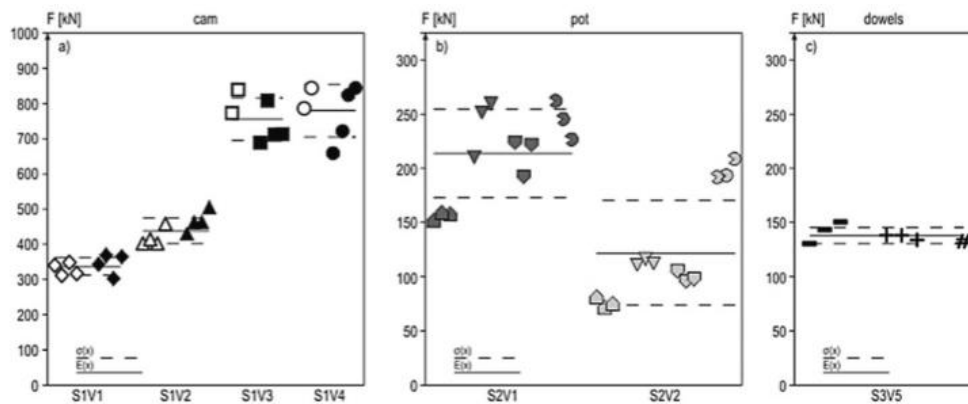


Figure 2.23. Comparison of bearing capacity of S1, S2 and S3 (Putke et al. 2015).

2.2.3 Effect of unfavourable conditions during tunnelling

During mechanized tunnelling, they can be verify particular unfavourable conditions which can lead formation of cracks in the segmental lining. The most common types of cracks are caused by 1) squeezing action due to TBM deflection, 2) uneven contact between segments.

In both cases the lining is not in the commonly adopted load configuration of transversal bending neither the circumferential joints failure happen for the geometrical diffusion of jacks thrust, but multi-directional bending configurations, torsion and eccentricity of jacks force lead the lining deformation mechanisms.

SQUEEZING ACTION DUE TO TBM DEFLECTION

During some shield operation such as turning or adjusting its attitude, TBM can lose the tunnel axis alignment generating squeezing action against the lining and then their possible dislocation of position, which if exceeds certain value could cause cracks in the segment (Sugimoto & Sramoon 2002, Mo & Chen 2007).

When the shield rotates until its tail (Figure 2.24) in fact, because the space between external segments surface and the wire tail brush could be not sufficient after the grout hardening, it contacts the last installed segment generating a reaction force f_{21} from the segment to the shield.

Figure 2.25 shows two extremely condition which could be verified during the TBM driving:

CONDITION 1 when the shield starts to drive forwards and the ring has been just installed, the contact force in the point A is very small, the segment are subjected to the forces induced by the tail brush and the jacks that, when the machine drives with deflection, become eccentric forces respect the middle linings section inducing their dislocation.

CONDITION 2 when after one driving cycle, the jacks draw back, the segment are subjected to contact force in the point C and extrusion force which increase with decreasing of the space between the wire brush and the extrados of the segments.

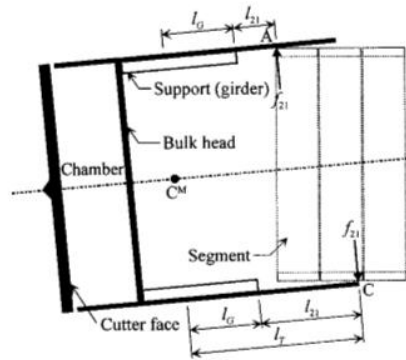


Figure 2.24. Lost of alignment of the shield (Sugimoto & Sramoon 2002).

Mo & Chen 2007 studied this aspects within 3D numerical analysis considering the squeezing action of tail brush in four different driving deflection conditions showed in Figure 2.26 (models 1 and 2 consider shield deflection in horizontal plane, models 3 and 4 consider deflection in the vertical plane) including the effect of jacking forces, grouting pressure and earth pressure.

The numerical results in Figure 2.27 refer to the CONDITION 1 and show for the different angular shield deflections the effect of dislocation which seems to be maximum in terms of relative displacement in the model 2. Dislocation between segment (relative torsion or extrusion) cause cracks in the segments, usually in the key which is the most vulnerable location of the lining, and circumferential joints opening until their shear failure.

CONDITION 1 : Shield starts to drive forwards

CONDITION 2 : After one driving cycle

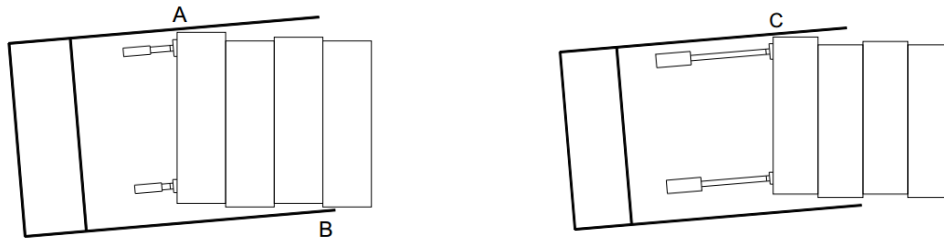


Figure 2.25. Squeezing action on segments during shield driving forwards (Mo & Chen 2007).

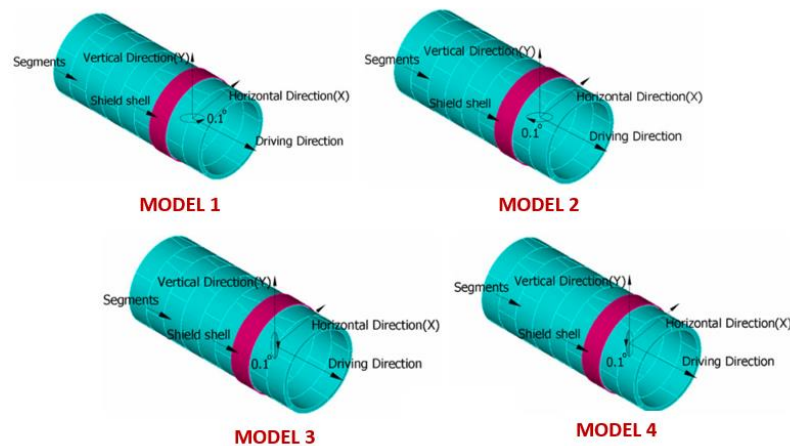


Figure 2.26. Models of driving deflection conditions (Mo & Chen 2007).

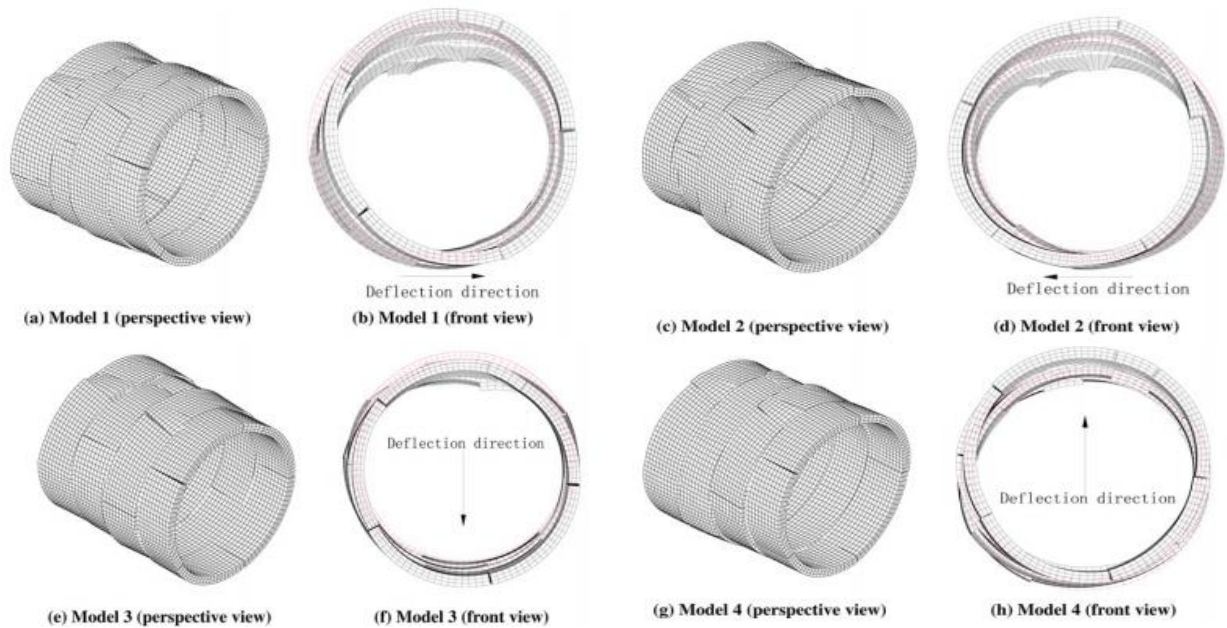


Figure 2.27. Deformed shape of lining subjected to squeezing forces (Mo & Chen 2007).

Toutlemonde *et al.* 2000 conducted experimental tests on concrete lining to study the cracks mechanisms developing under multi-directional load configurations, comparing the performance of steel fibre reinforced concrete (SFRC) and classic precast reinforced concrete (RC) on segments lining.

The results plotted in Figure 2.28 in terms of vertical (a) and horizontal (b) deflection of inner side of the tested segments show that in such critical load configuration the bearing capacity of RC segments is about 2.3 higher than that of SFRC segments which exhibit a rather brittle failure.

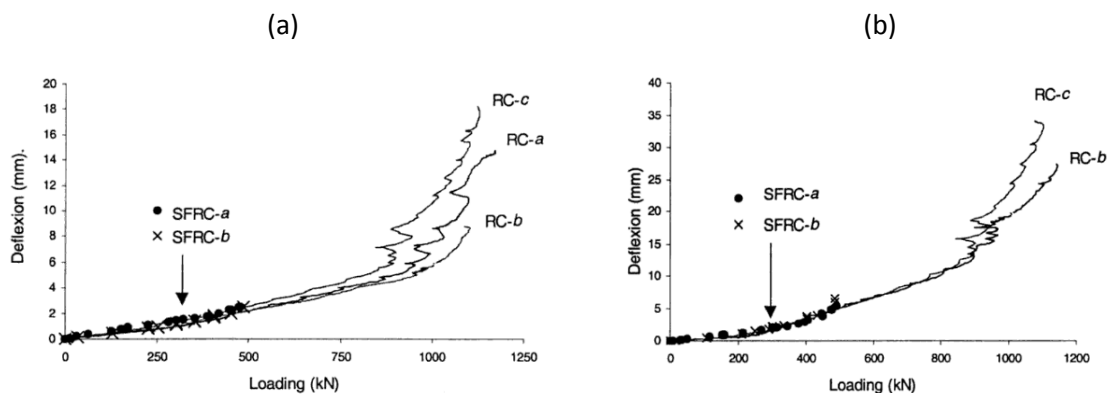


Figure 2.28. Bearing capacity of RC and SFRC under multidirectional flexural load (Toutlemonde *et al.* 2000).

UNEVEN CONTACT BETWEEN SEGMENTS

During lining installation it can be possible that contact deficiencies develop between the segments with the possible consequence of damage in the lining, in particular longitudinal cracks and the chipping of the segments corner are the most common type of damage (Sugimoto 2006).

In the case of longitudinal cracks, the damage usually occurs in the segment that is in contact with other two segments of the previous installed not perfectly aligned. This condition generates a partial contact between circumferential joints and, as the jacks thrusts the segment, a longitudinal crack appears at its centreline (Figure 2.29a).

The chipping of the segments corner instead can be produced by 1) contact deficiencies between longitudinal joints and as consequence a load applied in correspondence of the joint produces localized stress concentration leading cracks formation and the chipping as shown in Figure 2.29b or by 2) a mishandling of the segment during their installation, so the corners of the two segments can collide producing a chipping for the impact.

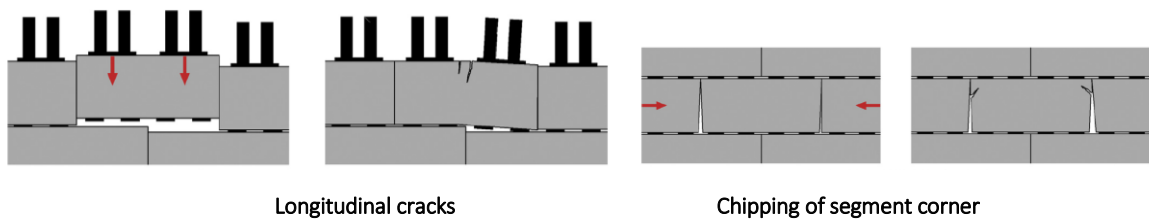


Figure 2.29. Scheme of uneven contact between segments (Cavalaro et al. 2011).

Cavalaro et al. 2011 studied the effect of contact deficiencies along both longitudinal and circumferential joints simulating the uneven contact condition with two types of FE models, validating the results with a simplified iterative analytical solution. The results show that the contact deficiencies affect the maximum load resisted by the segments. The curves that relate the resistance capacity with contact deficiencies are similar in shape for longitudinal (Figure 2.30) and circumferential joints (Figure 2.31), varying the lining thickness.

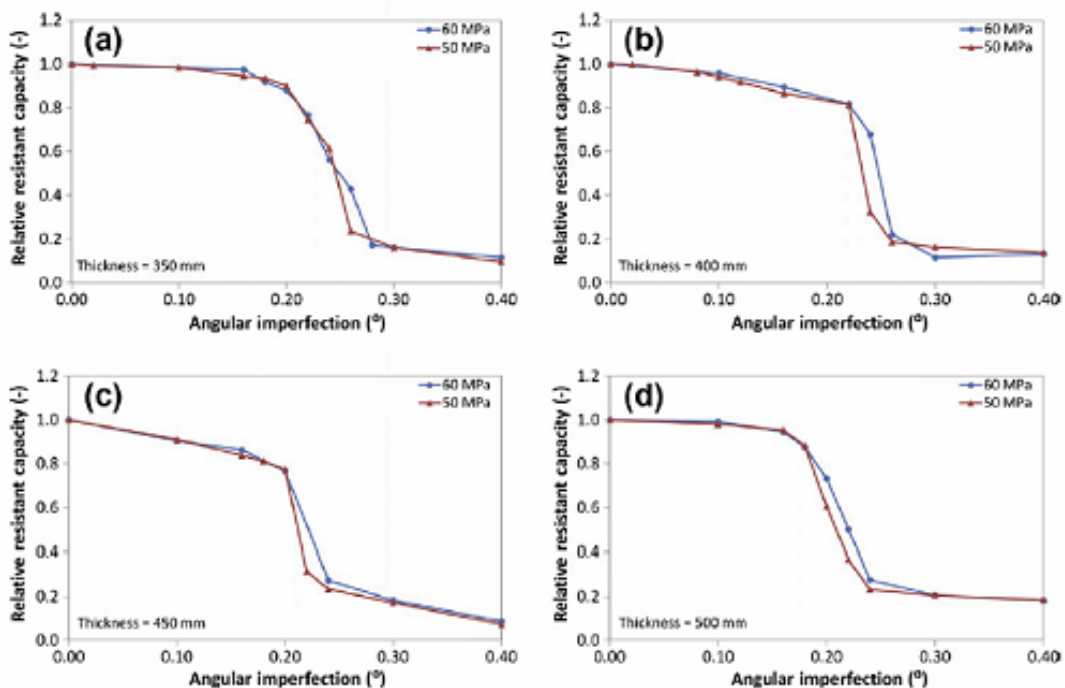


Figure 2.30. Relative resistant capacity in longitudinal joints (Cavalaro et al. 2011).

In figure 2.30 and Figure 2.31 all curves show an initial gradual reduction of the relative resistance capacity until a critical value of contact deficiencies in correspondence of which there is an abrupt drop of the resistance until the final resistant capacity which remain constant in spite of any increase of contact imperfection.

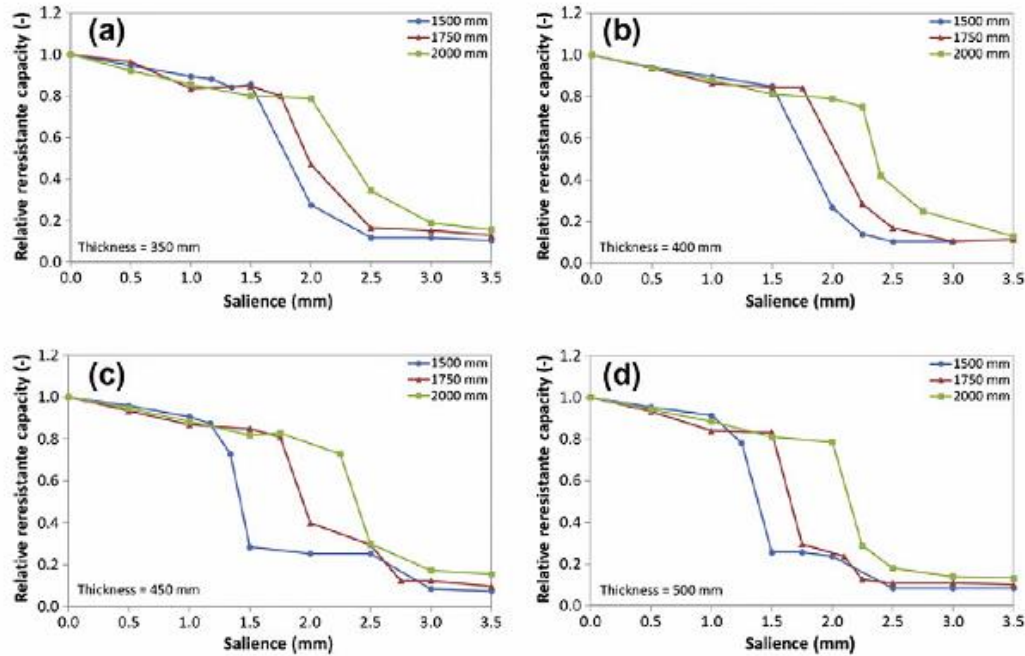


Figure 2.31. Relative resistant capacity in longitudinal joints (Cavalaro et al. 2011).

These mechanisms of failure are very dependent on the lining thickness and stiffness and rotational capability of longitudinal and circumferential joints and they play an important rule to allow the structure to resist additional load reducing the effect of cracking.

2.3 Soil structure interaction

2.3.1 Experimental evidence

The complex excavation process of mechanized tunnelling induce changes in boundaries condition in the tunnel lining continuously during construction, imposing a three dimensional interaction between the lining, the grout and the surrounding soil, which is clearly time- and load-dependent.

Arnau and Molins 2011 have conducted an innovative experimental study able to investigate the real soil-structure interaction and the real 3D interaction mechanism between the segments (c.f. 1.2.1) at the same time.

The study has been done on the structural response of SFRC segmental tunnel lining with an in situ real scale test applied on an experimental section composed by 15 rings of the Line 9 of the Metro of Barcelona in rock formation. The experimental section consisted in universal rings (seven segments plus one key segment), bituminous packers 2mm thick in longitudinal joints, plastic packers 2mm thick in lateral joints. The conceptual definition of the test is based on applying radial loads to the tunnel crown

with hydraulic flat jacks (Figure 2.32a) and measuring the ring displacement and deformation by means of a set of instruments.

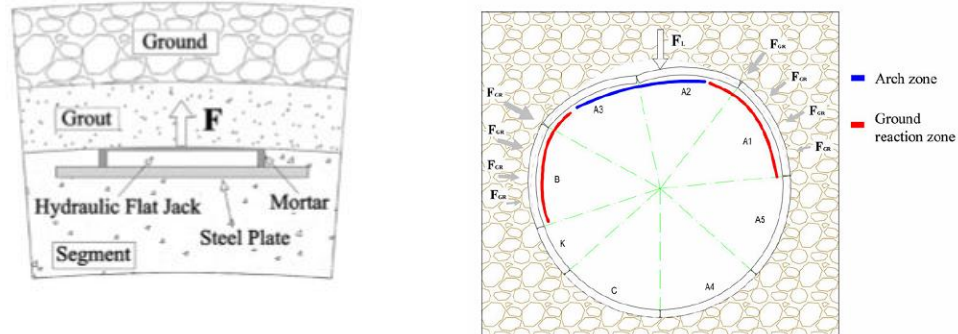
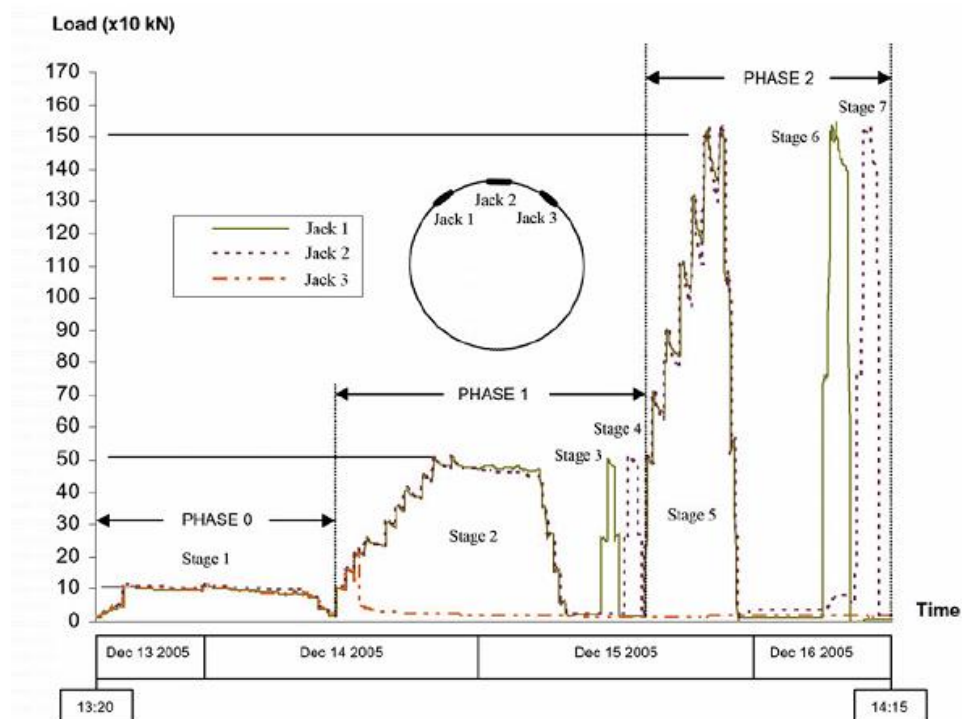


Figure 2.32. (a) Scheme of load on the section crown; (b) Local arch mechanism in the loading stage 5 (Arnau & Molins 2011).

Figure 2.33 shows the scheme of loading during the test: after an initial phase where all the jacks apply the same constant thrust, phase 1 and phase 2 follow applying an increased constant thrust in different combination of jacks working.

A schematic representation of results is shown in Figure 2.34 corresponding to Stage 5 of phase 3 of the test with the maximum load 1500 kN/jack applied by the jacks 1 and 2.

The plot shows 1) the relative displacement of longitudinal joints both in tangential then in radial direction, 2) the pressure distribution of the lining against the soil after loading, with a reduction in the upper part of the loaded ring due to the loose of contact between the lining and the ground for the jack thrust and an increment where there is the soil reaction due to the contact. This particular load condition generates an arch zone with absence of soil-structure contact and a reaction zone due to the contact (Figure 2.32b).



Phase	Stage	Active jacks	Load/jack (kN)
0	1	Jack 1 + Jack 2 + Jack 3	100
1	2	Jack 1 + Jack 2	500
	3	Jack 1	500
	4	Jack 2	500
2	5	Jack 1 + Jack 2	1500
	6	Jack 1	1500
	7	Jack 2	1500

Figure 2.33. Load scheme applied during the in situ test (Arnau & Molins 2011).

The extension of the reaction zone is mainly influenced by the soil stiffness, the lining stiffness and the tangential adherence stresses which develop between the soil and the grout interface (Figure 2.35) due to the different stiffness of the materials in contact. This interaction mechanism between the soil and the grout affect directly the stress distribution and then its structural behaviour in terms of internal forces.

The experimental test provides a significant evidence of the coupled mechanism between the segments associated with the real soil–structure interaction which develops a transfer mechanism of tangential forces on the adherence soil-grout interface and again on the adherence grout-concrete interface.

A realistic prevision of the loading scheme of the lining couldn't neglect the grout effect, neither in its fluid state, because determines the transferred load from the soil to the lining, nor in the hardened state because the transfer of the adherence stresses around the tunnel cavity in tangential direction. Additionally, the presence of longitudinal and circumferential joints allow the continuous redistribution of load in the lining respectively in tangential and longitudinal direction for each deformed configuration during the test.

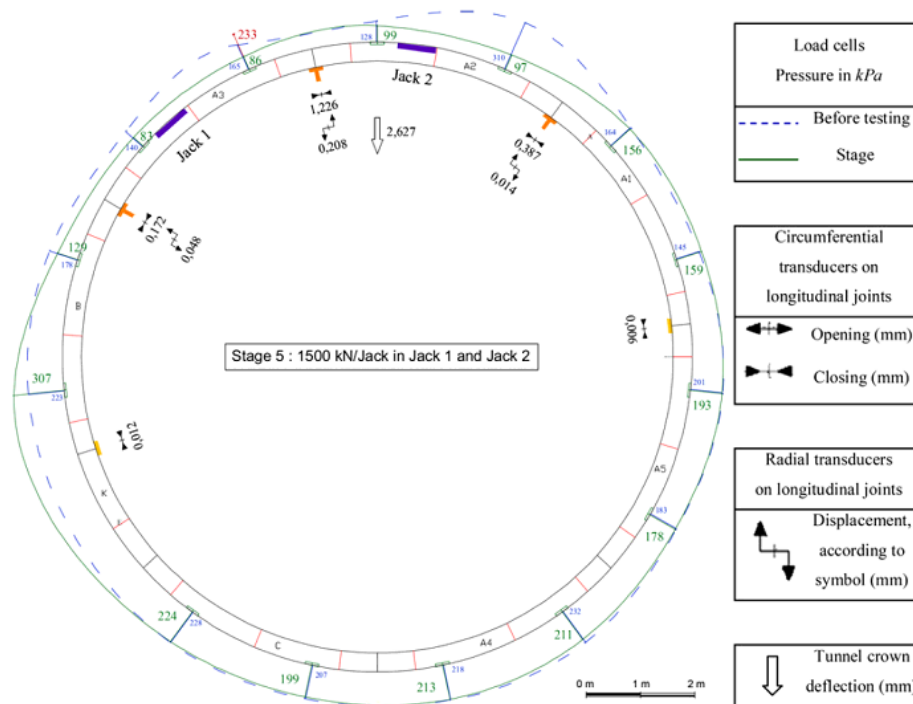


Figure 2.34. Schematic representation of the movements and external pressure at stage 5 (Arnau & Molins 2011).

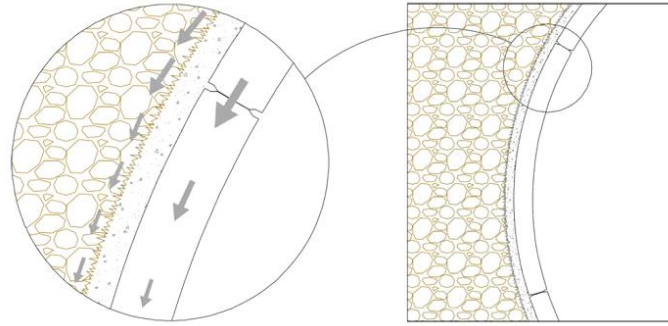


Figure 2.35. Lining-grout-soil tangential force transmission mechanism (Arnau & Molins 2011).

2.3.2 Numerical investigation

Numerical methods are the most common tools adopted to investigate the tunnelling effect on the lining and soil behaviour because able to simulate the coupling mechanism of soil-structure interaction, modelling as realistic as possible the lining structure and using adequate constitutive model for the soil, involving the main influencing factors of the tunnel construction and their evolution in the time.

Finite Element Method (FEM) and Finite Difference Method (FDM) in three dimensional model are the usual tools adopted for the evaluation of soil and lining behaviour during tunnelling until the end of the process, which have seen their first applications in research about twenty years ago and a very high development in the recent years within the following most common software packages:

- *Abaqus 3D* (Ng et al. 2004, Migliazza et al 2009, Ochmanski 2016);
- *Ansys 3D* (Blom 1999);
- *Diana 3D* (Arnau & Molins 2011b);
- *Flac 3D* (Barla et al. 2005, Dias et al. 2000a, Dias et al. 2000b, Mollon 2010, Mollon et al 2010, Lamburghi et al 2012);
- *Plaxis 3D* (Afifipour et al 2011, Fagnoli 2015, Zhao et al. 2015).

Unless the numerical technique to solve boundary problems, the two different methods give the same features to simulate the excavation; what differentiates a model rather than another is the choice of the influence parameters of the studied problem.

In the case of prevision of internal forces arising in the lining during mechanized tunnelling, the most important parameters of influence are:

- Soil properties;
- Geometry of segmental lining and mechanical behaviour of the joints;
- Soil-structures interface properties;
- Grout pressure;
- Effect of consolidation of grout;
- Jack thrust;
- Dimension of mesh and the numerical domain.

One of the most recent and advanced research work involving all the above mentioned parameters is that one developed by *Do et al. 2013*. The work refers to a part of the Italian high speed railway network connecting Bologna and Firenze. The project involves the excavation of two tunnels as in the scheme in Figure 2.36.

The excavation of the first tunnel has been objective of study. The authors provide a 3D numerical model (Figure 2.37a) developed in Flac 3D which allow the evaluation of the segmental tunnel lining behaviour and displacement of the ground surrounding the tunnel.

Three-dimensional simulation of EPB shield tunnelling consists into the three main subsequent steps which scheme is proposed by the authors in Figure 2.37b:

1. Excavating the ground at the tunnel face and simultaneously applying a confinement to ensure tunnel face stability.
2. Installing the tunnel lining, applying the jacking force and injecting the grout behind the segments in order to fill the voids created at the shield tail.
3. The TBM continues to advance, and the ground begins to become stabilized, which is expressed by a consolidation phase.

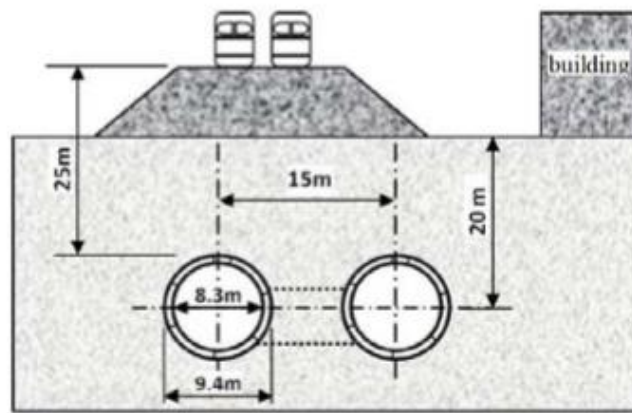
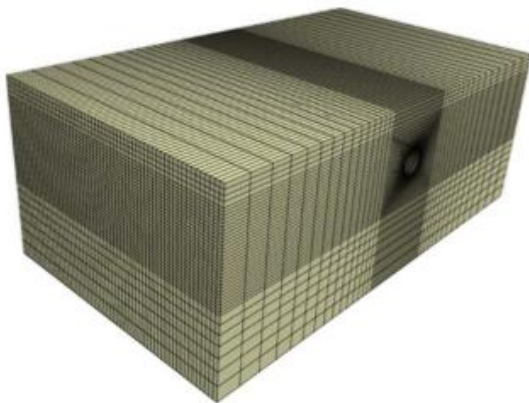


Figure 2.36. Typical cross section of the two tunnels in Bologna-Firenze railway (Do. 2015).

(a)



(b)

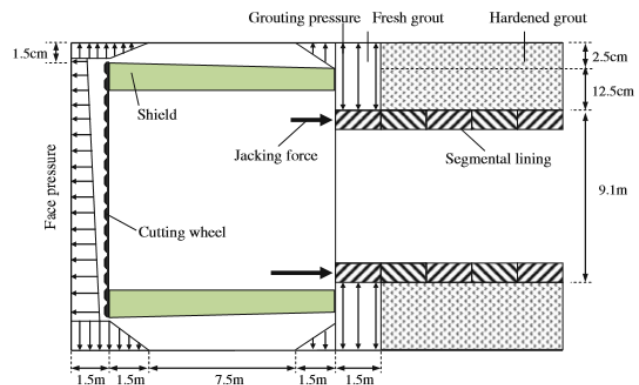


Figure 2.37. (a) 3D numerical model in Flac 3D; (b) Scheme of simulated excavation process (Do et al. 2013).

Figure 2.38 shows some results in terms of surface soil displacements and increment of internal lining forces during TBM advancement respect a reference tunnel section.

The normal and longitudinal forces are in compression forces distribution while the bending mechanism in the transversal section puts under compression the crown and the base of the tunnel and under extension the sides of the lining. The irregular shape of bending moment, normal force and

longitudinal force is due to the presence of longitudinal and circumferential joints generating a local reduction of the forces.

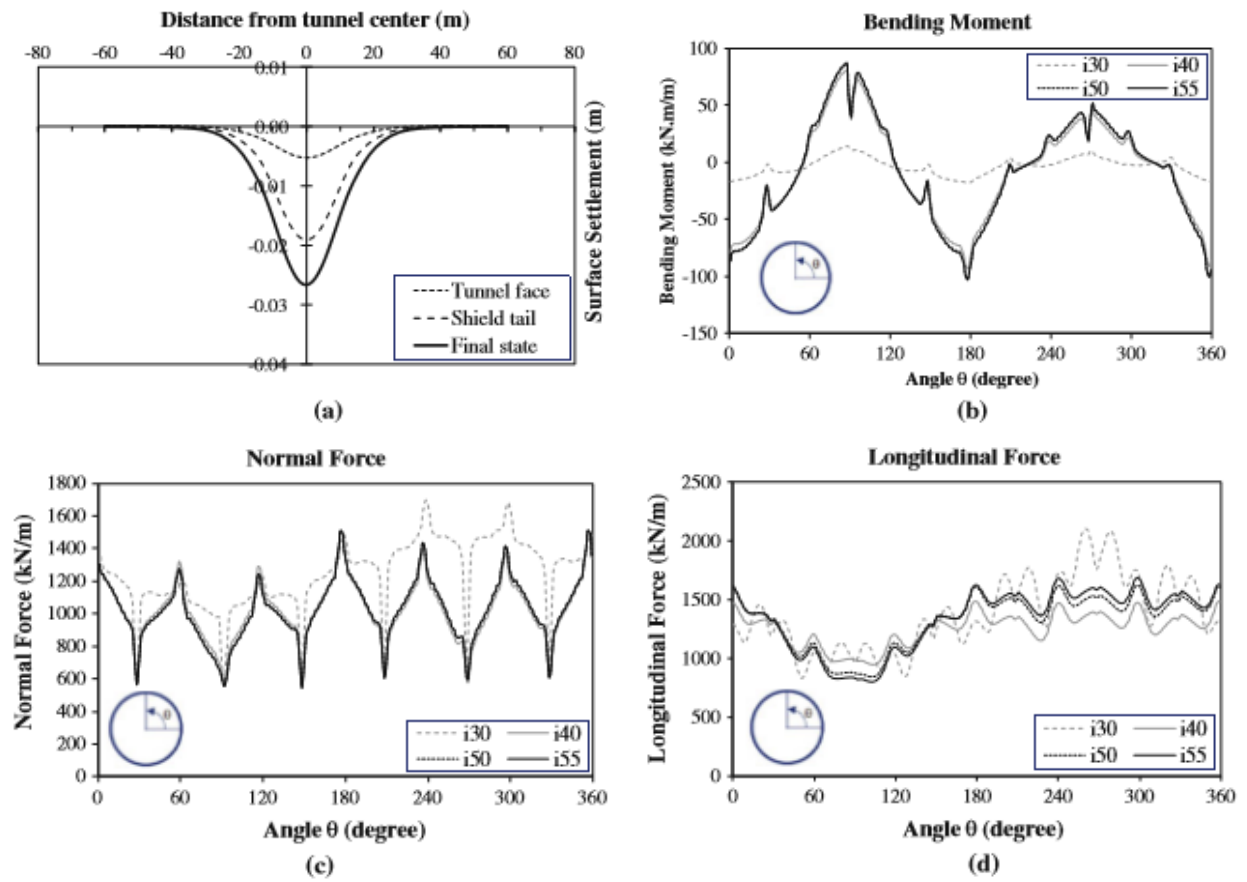


Figure 2.38. Behaviour of the lining and surrounding ground during advancement of the tunnel face (Do et al. 2013).

CHAPTER 3

Case histories

Introduction

Computational model for mechanized tunnel is here dealt with a 3D numerical approach. In the analysis, advanced constitutive law for the soil and a sophisticated numerical model for segmental tunnel structure have been adopted to describe the soil and structure behaviour in order to investigate their influence on the obtained results.

Because the case history of Bologna-Firenze railway has been well detailed in the work of *Do et al. 2013*, already introduced in the Chapter 3, it has been adopted as reference benchmark to calibrate the numerical model of segmental tunnel lining defined in Plaxis 3D and compare the results with those obtained by the authors using Flac 3D. This is a preliminary study for the calibration of the segmental lining numerical model, better investigated and validated in the case history of Metro Line 6 of Naples for which monitoring data of the entire excavation process are available.

The mechanized excavation process of Metro Line 6 of Naples has been implemented in the FE code Plaxis 3D according to the available monitoring data of the Tunnel Boring Machine advancement. The proposed model has been validated against the experimental measurements of the strains of in situ instrumented segmented ring.

3.1 High speed railway link Bologna-Firenze

The project of the high speed railway link Bologna-Firenze, described in details in the PhD thesis of *Do 2015*, involves the excavation of two parallel tunnels with a space distance of 15m in between the two tunnel axes (Figure 2.34). Each tunnel, supported by a segmental lining structure, has an external excavation diameter of 9.4m and an internal diameter of 8.3m, 20m under the ground surface. Two Earth Pressure Balance Shields (EPBs) were used for the excavation, the second tunnel was driven after the first tunnel over a period of 6 months. The author refers to the excavation process of the first tunnel only and, because the segmental tunnel lining numerical model adopted in Flac 3D has not been validated with any experimental-monitoring data, this case history represent a preliminary study to investigate the capability of another commercial code (Plaxis 3D) to reproduce the tunnel lining behaviour in a segmental layout.

Figure 3.1 shows the geometrical model adopted in Plaxis 3D: the width and height of cross section are $B = 120$ m and $H = 60$ m, respectively; the tunnel is 120 m long, its axis is 20 m below the ground surface; the internal diameter of the lining is $d_i = 8.3$ m, while the external excavation is $d_{ex} = 9.4$ m.

Segmental lining consist of six concrete segments 1.5 m wide and 0.4 m thick, staggered along the tunnel axis, while the backfill grout layer is 0.15m thick. Both segments and grout layer have been modelled as material volume with elastic behaviour which parameters are resumed in Table 3.1.

Longitudinal joints, not described in details but assumed by the authors as a non-bolted flat contact, have been modelled as deformable volumes with a width equal to the lining thickness, while circumferential joint has been modelled by an interface between the rings (Figure 3.2).

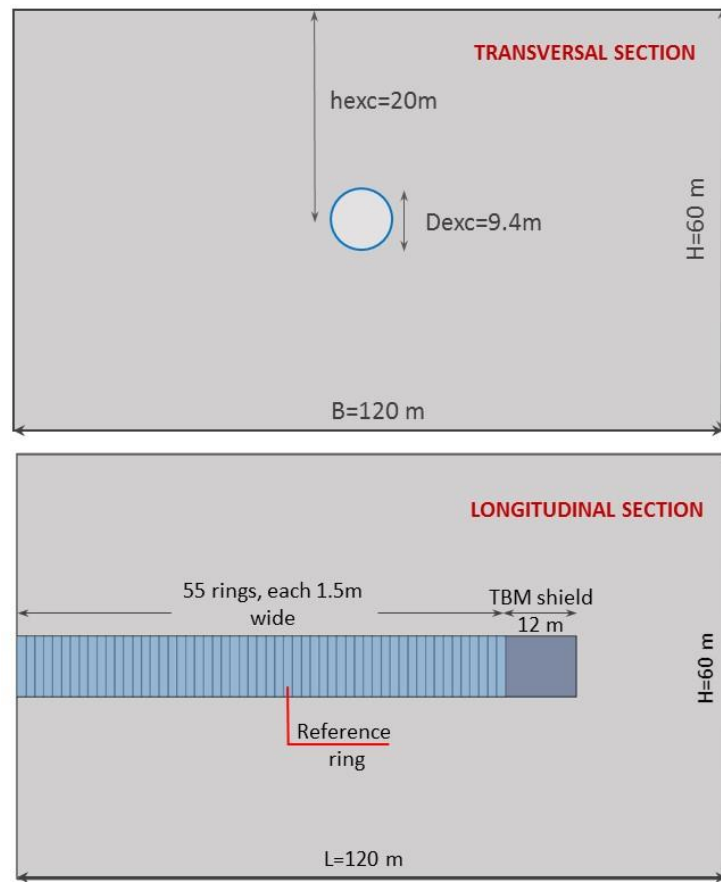


Figure 3.1. Geometrical model adopted for the case of study Bologna-Firenze railway in Plaxis 3D.

The stiffness adopted for the joint volume is lower than that of concrete of the segments and this difference in stiffness between the two materials at contact gives a rotational capability to the lining node.

In particular, the Young's Modulus of the joint volume has been calibrated against the rotational stiffness k_θ set by the authors equal to 100 MNm/rad/m.

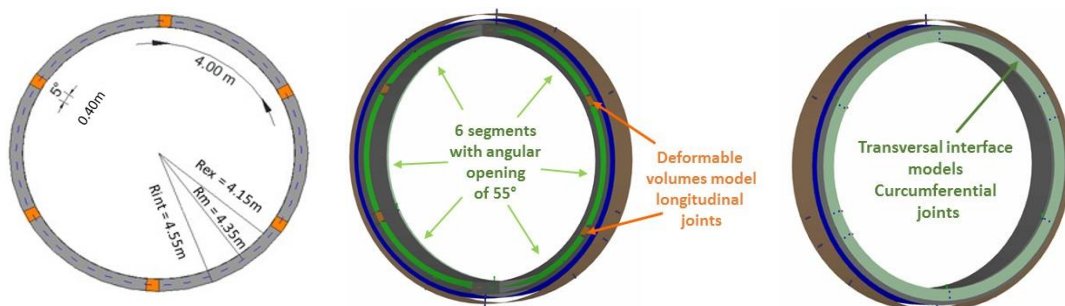
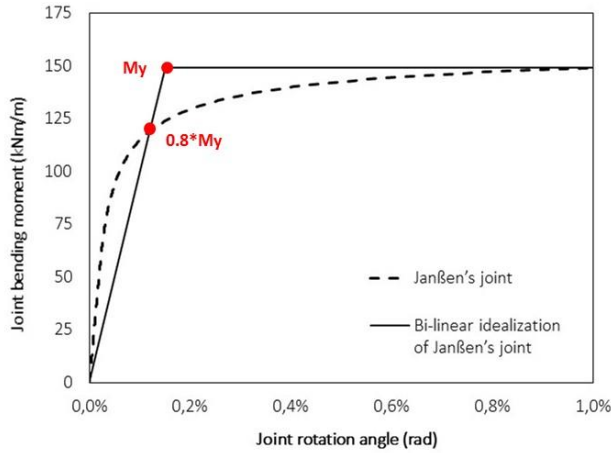


Figure 3.2. Geometrical model adopted for lining of the case of study Bologna-Firenze railway in Plaxis 3D.

As already discussed before (§1.3.3), the rotational stiffness is described by the authors with the analytical *Janßen's* solution, approximating the Moment-Rotation curve as a bi-linear curve, adopting the simplification suggested by *Thienert & Pulsfort 2011*, that is the rotational stiffness is that in correspondence of $0.80 \cdot M_{\text{yield}} / \theta_{0.8}$, where M_{yield} is the yielding moment in correspondence of a rotation angle of 0.01 radians ($\approx 1\%$), for an average value of normal force equal to 1100 kN/m.

Figure 3.3 shows the bi-linear moment-rotation relationship adopted by the authors for the joint.



$$M_{\text{yield}} (N=1100 \text{ kN/m}) = 150 \text{ kNm/m} \quad \text{for } \theta = 1\%$$

$$0.8 \cdot M_{\text{yield}} = 0.8 \cdot 150 = 120 \text{ kNm/m} \quad \text{for } \theta_{0.8} = 0.1212\%$$

$$k_{\theta} = 0.80 \cdot M_{\text{yield}} / \theta_{0.8} = 120 / 0.001212 = 99 \text{ MNm/rad/m}$$

Figure 3.3. Bi-linear moment-rotation curve adopted by Do et al. 2013 for longitudinal joint.

The rotational stiffness evaluated by the authors with Janßen's joint model refers to a joint surface contact equal to 0.3m, lower than the lining thickness.

A principle of dimensional equivalence has been established between the Janßen's joint model (Figure 3.4a) and the adopted model in Plaxis 3D (Figure 3.4b): in order to obtain the same rotational capability, a value of Young's Modulus E^* equal to $7E^6$ kN/m² has been calculated for the adopted model that considers a joint thickness equal to the lining one.

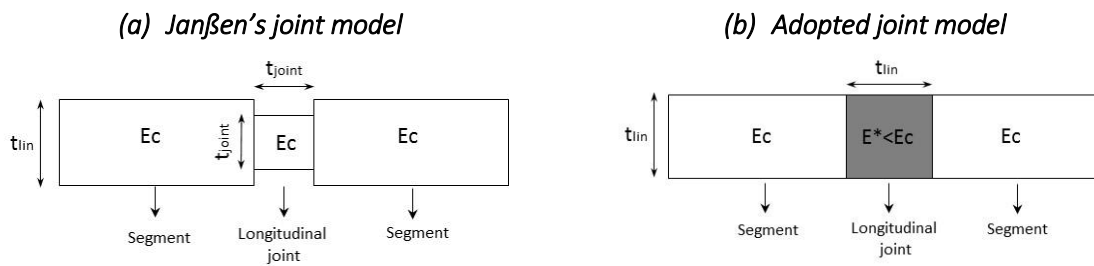


Figure 3.4. Conceptual scheme of (a) Janßen's joint model and (b) adopted longitudinal joint model.

Because the results obtained by the authors show that the joints don't reach in any case the limit value of bending moment equal to 150 kNm/m (Figure 3.3), staying in the elastic branch of the $M-\theta$ curve (Figure 2.36), a linear elastic constitutive model has been adopted for the joints. The same constitutive model has been adopted for the circumferential joints.

Figure 3.5 shows the numerical model adopted for the structure and the entire domain with a total number of nodes equal to 498431 and a number of element equal to 465608, that are 10-nodes tetrahedral elements with four Gaussian integration points (Figure 3.6a).

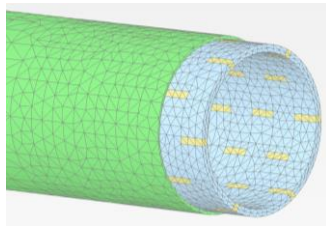
A similar tetrahedral grid is used for the mesh discretization in FLAC 3D. Each quadrangular 8-nodes zone is internally divided in 5 tetrahedra with two different possible overlay configurations (Figure 3.6b).

	Young's modulus kN/m ²	Weight kN/m ³	Poisson's ratio -
Concrete	35 E ⁶	23	0.15
Grout	10 E ⁶	15	0.22
Joint	7 E ⁶	23	0.15

Table 3.1. Lining parameters

The tunnels were excavated through two main formations: alluvial deposits of the late Pleistocene–Pliocene era, which is mostly alluvial deposits from the Savena River with deposits of clay, and sandy soil (clayey sands and Pliocene clays). The authors adopted for this study the section in correspondence of ring 582 of the first tunnel, modelled as an uniform soil layer. The constitutive model used by the authors for the soil is the so-called Cap Yield Model available in Flac 3D, a strain-hardening constitutive model that is characterized by a frictional Mohr–Coulomb shear envelope and an elliptic volumetric cap in the stress (p' , q) plane.

LINING



DOMAIN

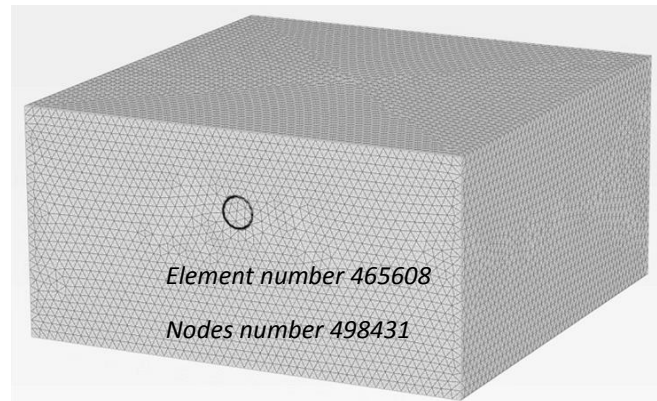


Figure 3.5. Numerical model adopted for the case of study Bologna-Firenze railway in Plaxis 3D

The same behaviour of the soil has been reproduced with the constitutive Hardening Soil Model available in Plaxis 3D. Both constitutive models are based on a hyperbolic relationship between the vertical strain ε_1 and the deviatoric stress q in primary triaxial loading as in the Equation 3.1 where q_a is the asymptotic value of the shear strength and E_i the initial soil stiffness.

$$-\varepsilon_1 = \frac{1}{E_i} \frac{q}{1 - q/q_a} \quad (3.1)$$

In this way, it has been manageable to calibrate the main constitutive parameters of the soil as follows.

Parameters of Cap Yield Soil Constitutive Model in Flac 3D

Poisson ratio	$\nu=0.3$
Reference elastic tangent shear modulus	$G_{\text{ref}}^e = 58 \text{ MPa}$
Elastic tangent shear modulus	$G^e = G_{\text{ref}}^e (\sigma_3/p^{\text{ref}})^m = 98 \text{ MPa}$
Reference effective pressure	$p^{\text{ref}} = 100 \text{ kPa}$

Friction angle	$\phi = 37^\circ$
Dilation angle	$\psi = 0^\circ$
Cohesion	$c = 0 \text{ kPa}$
Lateral earth pressure factor	$k_0 = 0.5$
Failure ratio	$R_f = q_i/q_a = 0.9$

Parameters of Hardening Soil Constitutive Model in Plaxis 3D

Reference elastic Young's modulus	$E_{ref}^e = G_{ref}^e * (2(1+\nu)) = 150 \text{ MPa}$
Elastic shear modulus	$G^e = G_{ref}^e (\sigma_3/p_{ref})^m = 98 \text{ MPa} \rightarrow (\sigma_3/p_{ref})^m = 1.7$
Elastic Young's modulus	$E^e = E_{ref}^e (\sigma_3/p_{ref})^m = 255 \text{ MPa}$
Secant stiffness modulus	$E^e = \frac{2E_{50}}{2-R_f} \rightarrow E_{50} = \frac{E^e (2-R_f)}{2} = 140 \text{ MPa}$
Reference stiffness modulus	$E_{50}^{ref} = E_{50} / (\sigma_3/p_{ref})^m = 82.5 \text{ MPa}$
Un/re-loading reference stiffness modulus	$E_{ur}^{ref} = 2E_{50}^{ref} = 2 * 82.5 = 165 \text{ MPa}$
Tangent stiffness for oedometer loading	$E_{oed}^{ref} = E_{50}^{ref} = 82.5 \text{ MPa}$

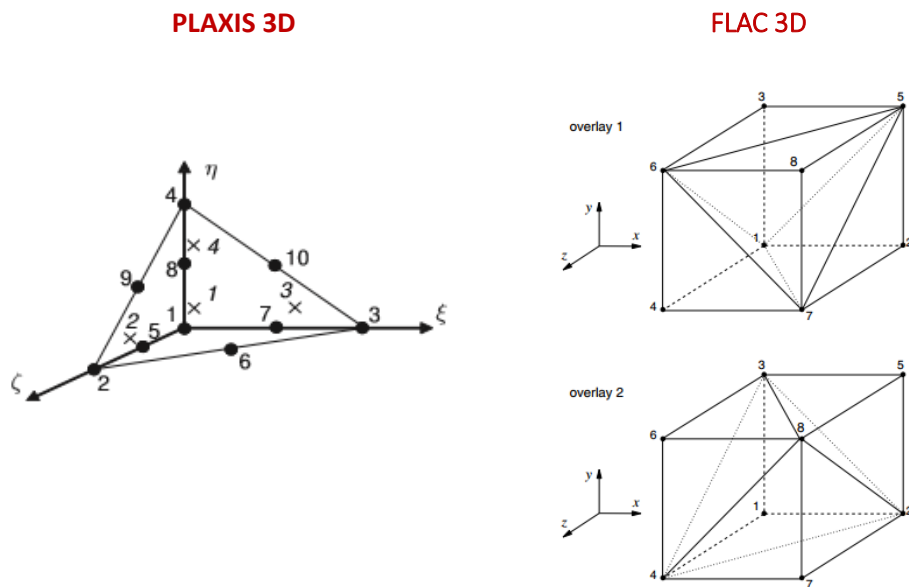


Figure 3.6. (a) Local numbering and positioning on the nodes (•) and integration point (x) of a tetrahedron volume 10-nodes element in Plaxis 3D (Scientific manual, Plaxis 3D); (b) An 8-node zone with 2 overlays of 5 tetrahedra in each overlay (Theoretical background, FLAC 3D).

The excavation process implemented in Plaxis 3D follows the scheme adopted by the authors as in Figure 2.35b. Tunnel construction starts with the entrance of the shield in the tunnel during the first eight steps of the process, corresponding to a 12-m length of the shield machine. These initial phases only

include the excavation of soil at the tunnel front, with the face pressure applied by the authors within a trapezoidal profile, to take into account the weight of the slurry equal to 11 kN/m^3 , and proportional to the horizontal ground pressure through the lateral earth pressure factor k_0 .

After these first eight steps, the tunnel construction continues with the lining installation; to each shield advancement corresponds the installation of a segmental ring at the shield tail thrust by eighteen jacks with a total resultant on the transversal lining section equal to 40 MN. In Plaxis 3D the jacks thrust has been simulated with an uniform pressure acting on the transversal tunnel section.

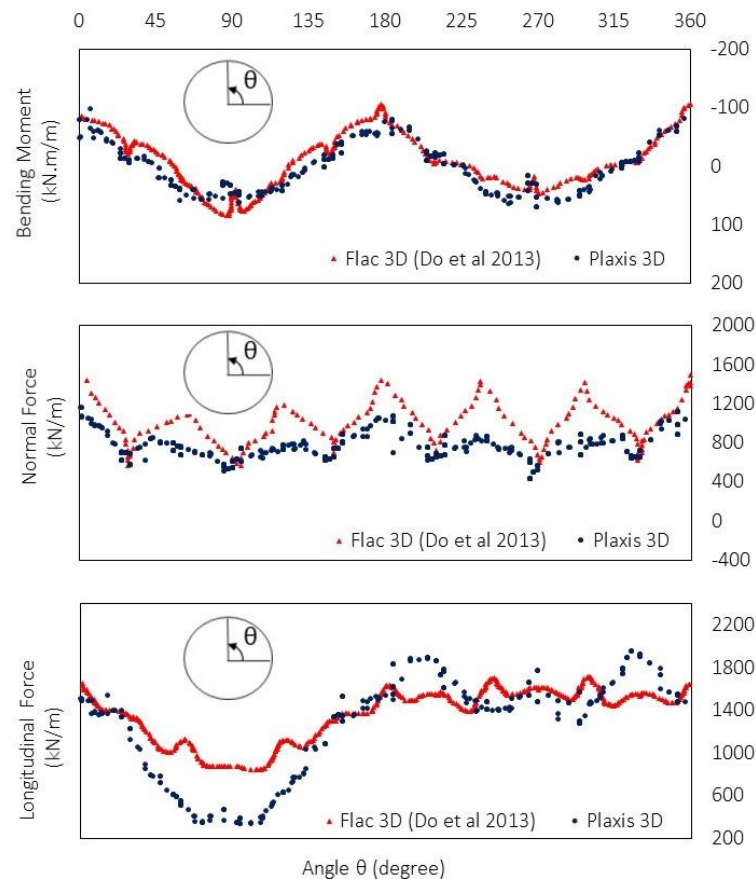


Figure 3.7. Comparison of internal forces of the reference ring at the end of Bologna-Firenze line numerical excavation calculated with Flac 3D by Do et al. 2013 and Plaxis 3D.

At the same time the grout pressure is applied against the soil just behind the tail shield proportionally to the overburden pressure at the tunnel crown multiplied by an amplification set on the value of 1.2. The hardened grout is simulated with the activation of a volume filling the gap between the lining and the tunnel profile.

Figure 3.7 and Figure 3.8 show the comparison between the models implemented in Flac 3D and Plaxis 3D in terms of internal forces in the reference ring (Figure 3.1) and longitudinal and transversal surface settlements respectively, at the end of the excavation process.

The internal forces calculated in Plaxis 3D are in a very good agreement with the same calculated by the authors, in particular in terms of bending moment. The conceptual scheme adopted to model the joints as deformable volumes returns the same response of the authors modelling the joints as springs elements (§1.3.3).

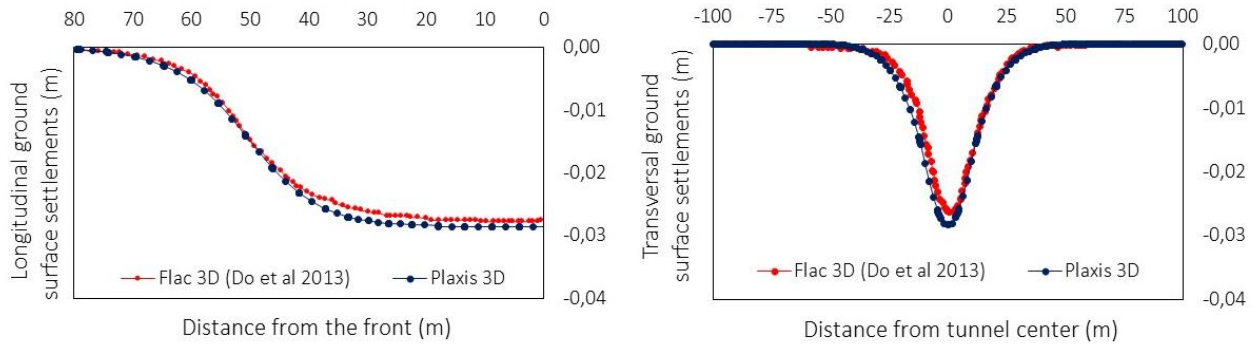


Figure 3.8. Comparison of longitudinal and transversal surface settlements at the end of Bologna-Firenze line numerical excavation calculated with Flac 3D by Do et al. 2013 and Plaxis 3D.

It should be noted how the average value of normal force is slightly lower than that calculated by the authors and the longitudinal force slightly lower in correspondence of the tunnel crown. This is due to the fact that the jacks thrust has been modelled in Plaxis 3D with a uniform distribution of pressure and not as concentrated forces as in Flac 3D and this induces a not equal load distribution along the lining height, affecting the normal and longitudinal forces distribution.

A good matching has been found between the constitutive model adopted for the soil that exhibits the same longitudinal and transversal settlements profile in both models.

This is only a preliminary study of the tunnel lining behaviour, used to calibrated the proposed numerical model of segmental lining against an existing case history. This model is adopted to investigate the case of study proposed in the following paragraph.

3.2 Metro Line 6 of Naples

The Neapolitan Metro Underground system consists of two lines, **Line 1** and **Line 6**, integrated in a wider service network, with different origins and characteristics, which belongs to the historical lines of regional railways: State Railways, Circumvesuviana, Circumflegrea, Cumana, Funiculars (Figure 3.9).

Metro **Line 1** of the Naples was the first metro connecting the city centre with the Vomero hill, the hospital area until Piscinola. Inaugurated in 1993, over the years it has added a number of stations up to eighteen. A part of the line is still under construction and further extensions have been already designed, according with the final design project of railway ring.

Metro **Line 6** of the Naples was inaugurated on 11 January 2007 connecting the districts of Fuorigrotta and Mergellina. This connecting stretch is currently in operation with 2.2 Km of length and four stations including two interchanges at Mostra and Mergellina.

The stretch connecting **Garibaldi Square** with **Dante Square** belonging **Line 1** and the stretch connecting **Mergellina** with **Municipio Square** belonging **Line 6** were excavated with a shield Tunnel Boring Machine.

This section focuses on the case history of **Line 6** of Naples which tunnelling operations and soil conditions have been monitored during the years (Bitetti 2010, Marino 2010, Aversa et al. 2015). A numerical simulation of the tunnelling is presented and discussed in this Chapter, including the technological aspects of the segmental lining introduced in the Chapter 1 and the technological aspects

of the mechanized tunnelling introduced in the Chapter 2. The proposed 3D numerical model has been validated against the experimental measurements of the strains of in situ instrumented segmented ring.

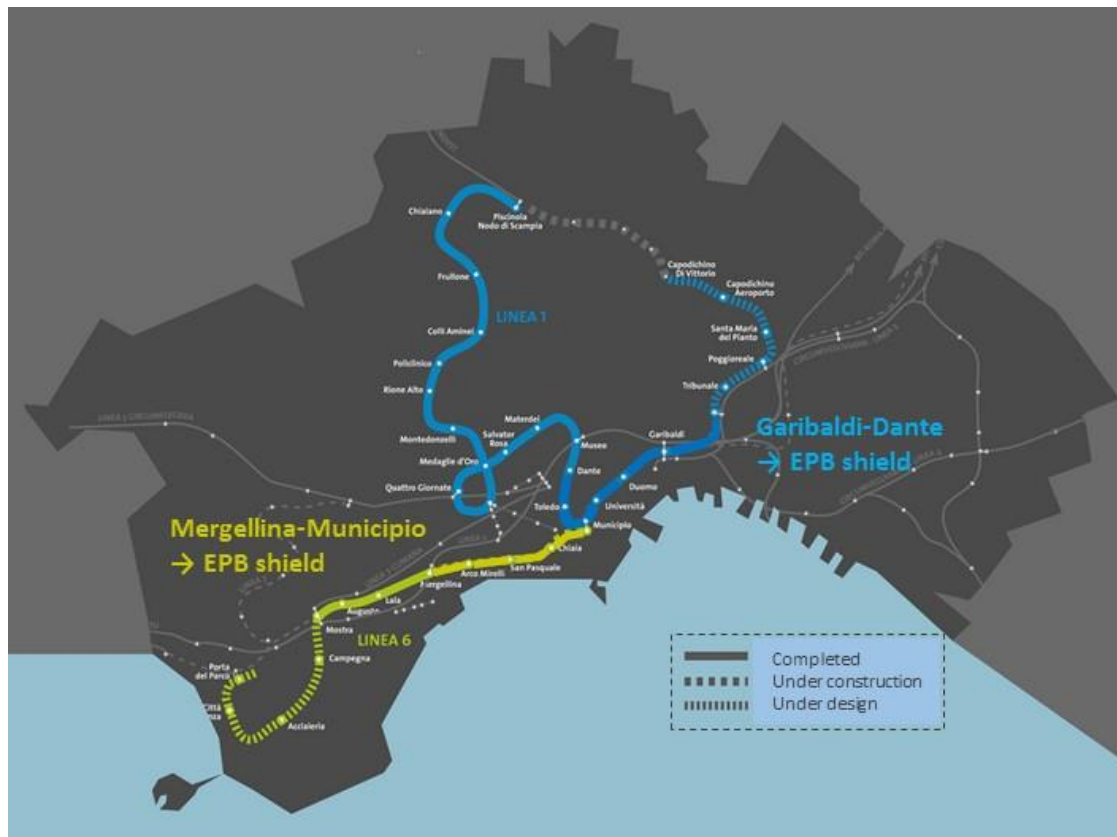


Figure 3.9. Neapolitan Metro Underground system.

3.2.1 Layout and ground conditions

Figure 3.10 shows the layout of the **Line 6** that is made up of four sub-stretches:

FIRST STRETCH: Porta del Parco-Campegna

is under design stage, it is 3.9 Km long, with three stations, including 2 interchanges, one at Acciaieria with the funicular F8 and one at Porta del Parco with line 8.

SECOND STRETCH: Campegna-Mostra

is at a final design stage, it is 1.1 Km long with only a station, Campegna.

THIRD STRETCH: Mostra – Mergellina

is currently in operation, it is 2.2 Km long with four stations, including two interchanges, one at Mostra with the line 2 and line 7, and one at Mergellina with the line 2.

FOURTH STRETCH: Mergellina-Municipio

is currently under construction, it is 3.3 Km long with four stations, including Municipio stations, the major interchange with line 1, funicular F2 and connections routes with the islands.

The stretch of interest Mergellina-Municipio is characterized by four different zones of relatively homogeneous conditions (Figure 3.11).

Overall the tunnel is excavated through a thickness of loose soil (marine, alluvial and volcanic soils) overlying the tuff, and often underwater. Because the roof of the tuff layer is very erratic, probably due to the past erosive action of superficial running water coming from the hills surrounding the bay, some stretches of the tunnel were excavated through the tuff layer.

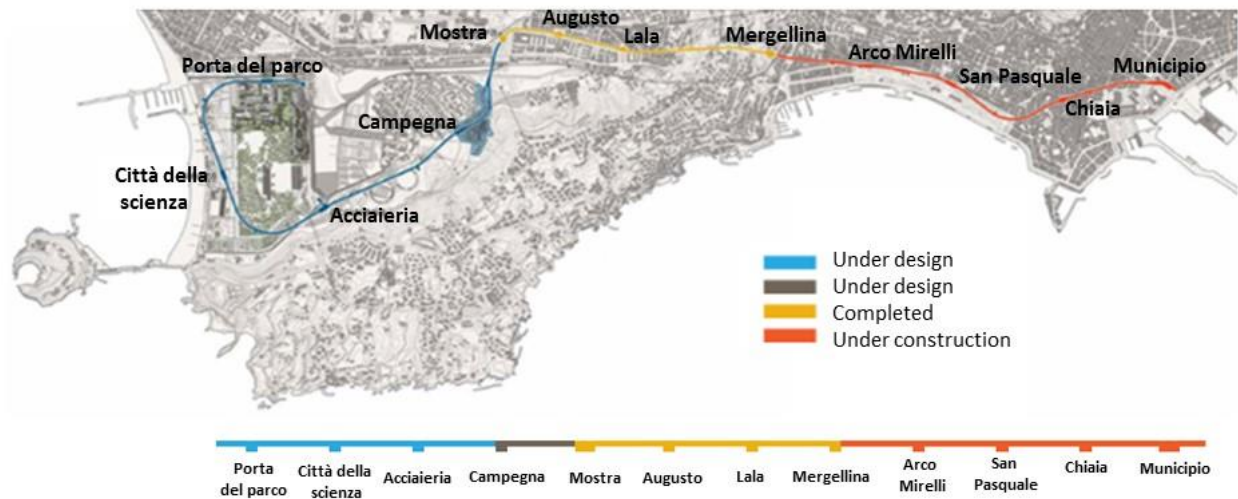


Figure 3.10. Layout of Metro Line 6 of Naples.

ZONE 1

The tunnel is excavated at a depth of about 16m and the stretch is mainly interested by loose soils of pyroclastic origin (pozzolana, pumice, sand). The most superficial layers are processed by the waters and sediments in the marine environment or backshore.

ZONE 2

The tunnel, excavated about at 19m of depth, affects the tuff layer for a certain length. The water table is found at shallow depth, at an altitude of 1 to 1.5 m above sea level and then the tunnel line and the stations are immersed in water.

ZONE 3

The tunnel crosses the subsoil that exhibits the same geotechnical conditions of the ZONE 1, with a deeper tunnel cover about of 20m under the water table.

ZONE 4

The stretch is completely excavated in the tuff layer.

Along the tunnel line, four different segmented rings (sections 1, 2, 3 and 4 in Figure 3.11) have been instrumented to control the strains carried out during tunnelling, starting from the early installation stages until the long term load condition. Section 1 in particular, in between Mergellina and Arco Mirelli that is in green-field condition, has been assumed as the reference experimental section for the studied case.

Figure 3.12 shows the geotechnical model of the subsoil: starting from the ground surface, below a negligible thickness of man-made ground cover, the tunnel is completely excavated in a seashore sandy layer (SS) overlaying a volcanic depth of materials, divided into a layer of pyroclastic silty sand (Pyr) and a layer of the fractured facies of Neapolitan Yellow Tuff, reaching the top of the bedrock at the depth of approximately 40 m. The ground water table is 6m under the ground surface.

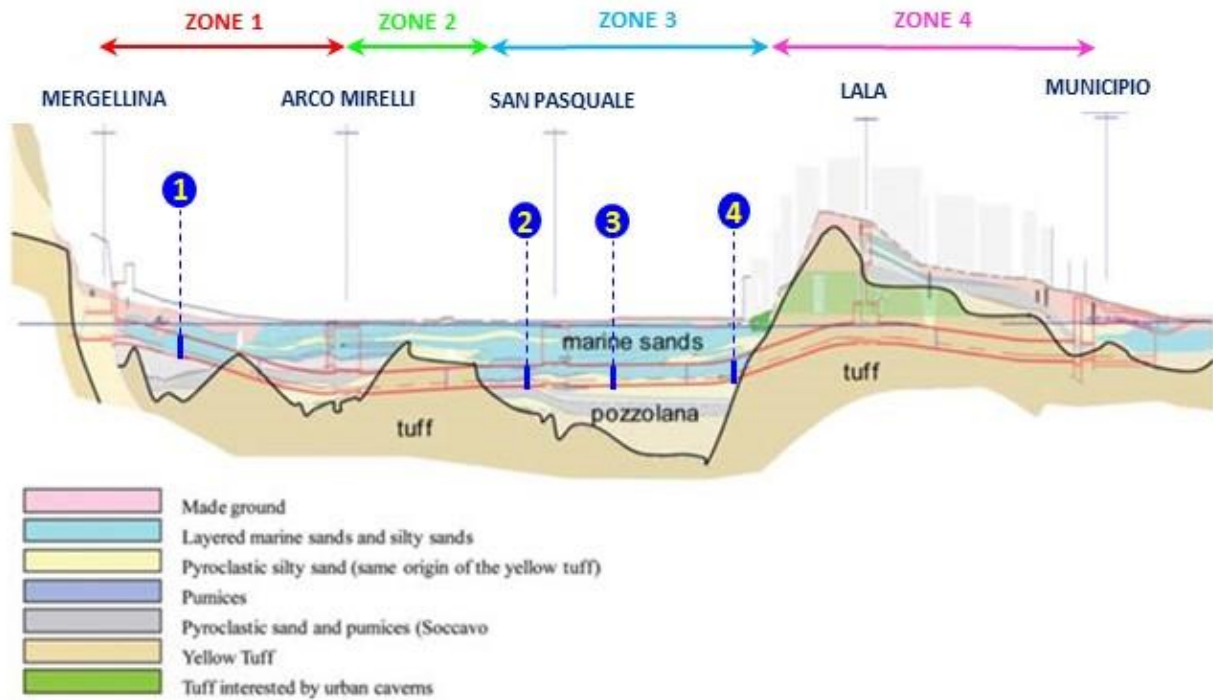


Figure 3.11. Subsoil of Metro Line 6 of Naples across the stretch Mergellina-Municipio.

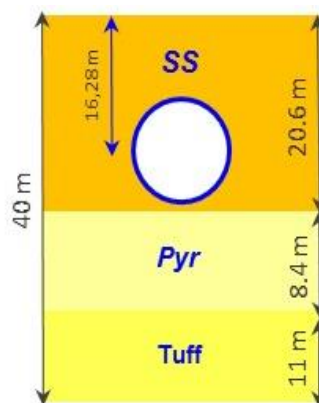


Figure 3.12. Geotechnical model of subsoil of Section Mergellina-Arco Mirelli of Metro Line 6 of Naples.

Table 3.2 resumes the main values of physical and mechanical parameters of the soil layers derived from the extended campaign of geotechnical investigation of 1998-2000, involving both laboratory tests and in situ tests (CPT, SPT and cross-hole tests), and from the scientific literature on the topic (Evangelista & Pellegrino, 1990).

Soil type:	SS	Pyr	Tuff
Depth:	From 0 to 21.6 m	From 21.6 to 29 m	From 29 to 40 m
γ_{sat} (kN/m ³)	18	16	16
Friction angle (°)	37	37	27
Cohesion (MPa)	0	0	0.5
Poisson's ratio	0.3	0.3	0.3
Young Modulus (MPa)	50	40	6,360E ³

Table 3.2. Physical and mechanical parameters for each soil layers of Metro Line 6 of Naples in the Section 1.

3.2.2 Geometry of the tunnel lining and monitoring

The stretch of the line actually in operation (Mostra-Mergellina) was built using the EPB TBM machine (Figure 3.13), installing as system support lining the so called *universal ring*, 1.7m wide, assembled in nine precast concrete elements C34/45, eight larger segments (indicated with the capital letter from **B** to **I** in Figure 3.14), corresponding to a central angle of 41.5 degrees, plus the keystone **A** (Figure 3.14) with angular opening of 33 degrees. The rings are assembled in a staggered configuration along the tunnel axis in such way that the longitudinal joints are not aligned: the links between rings then are realized by connecting a segment belonging to a ring to, at least, two segments of the previous ring and two segments of the following ring. The tunnel has an external excavation diameter of 8.150 m, the lining has an intrados radius of 3.625 m and extrados radius of 3.925 m, for a total thickness of 0.30 m. The annular void between the extrados and the external excavation diameter is backfilled with a bi-component grout 0.15 m thick.



Figure 3.13. TBM produced by WIRTH, model TB816H / GS to excavate the Metro Line 6 of Naples

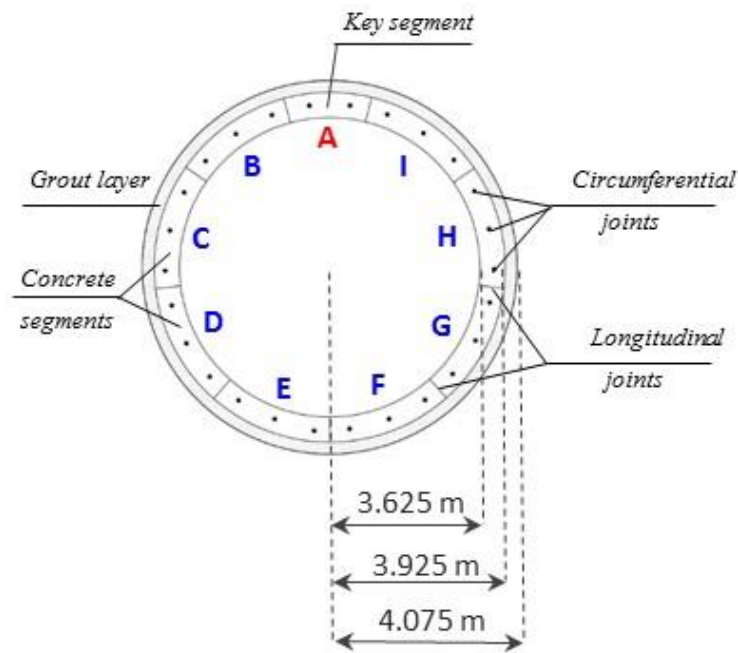


Figure 3.14. Geometry of segmental tunnel lining of Metro Line 6 of Naples.

In order to avoid the possible concentration of stress in correspondence of the extrados and intrados corners between the segments, these latter have a chipping about of 2-5 mm in correspondence of each corner (Figure 3.15).

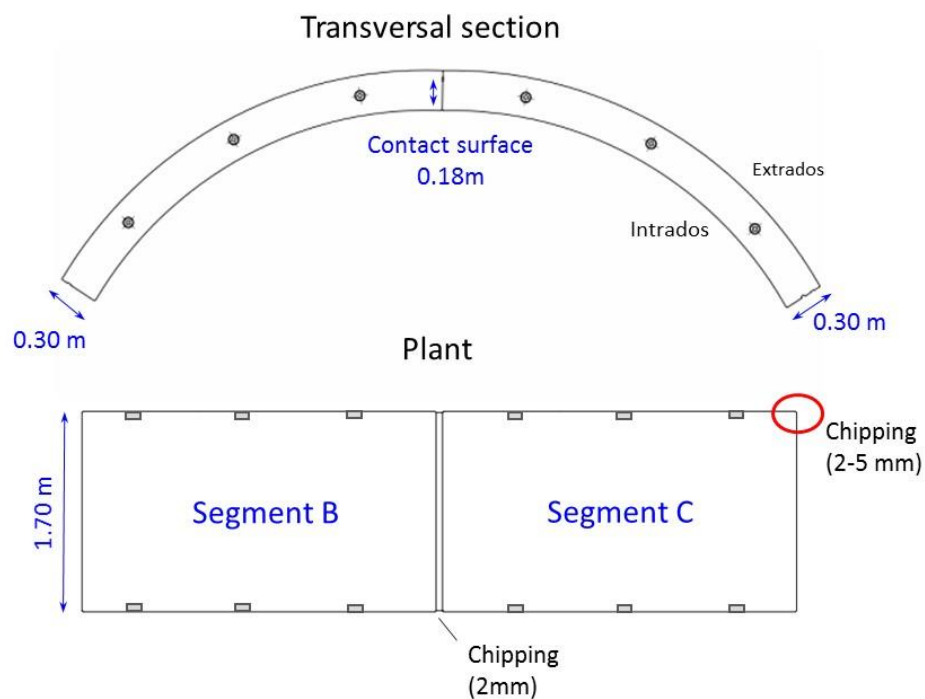


Figure 3.15. Details of design of ring segments of Metro Line 6 of Naples.

Figure 3.16 shows the details of design of the joints. Longitudinal and circumferential joints are direct concrete-to-concrete flat contacts along the height of the lining thickness. The height of the surfaces at contact is about 2/3 of the lining thickness, 0.181m.

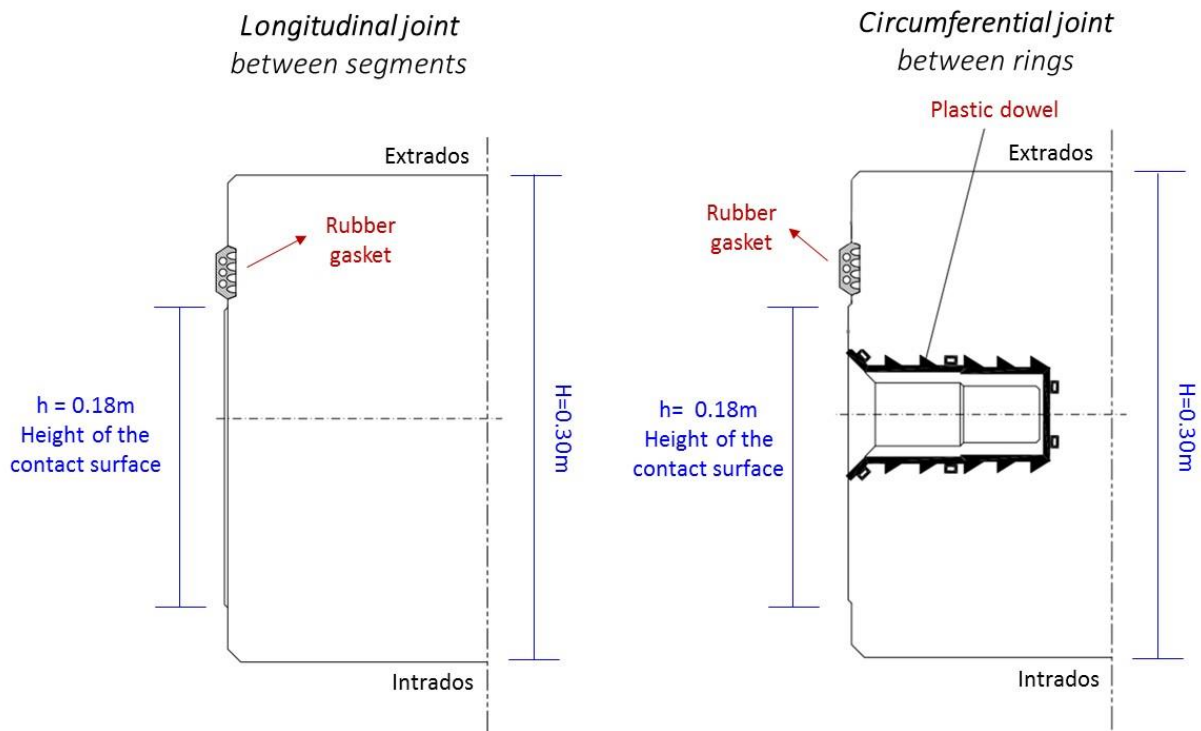


Figure 3.16. Details of design of circumferential and longitudinal joints of Metro Line 6 of Naples.

In correspondence of the circumferential joint there are also dowel connections in plastic with a steel core (Figure 3.16 and 3.17), three for the main segment and two for the key (Figure 3.14). The dowels are completely covered and hidden, are inserted into the segment during the assemblage and are mortise-inserted into the segment of the last assembled ring. The Bi-block system of FIP INDUSTRIALE (pin+sockets), used as longitudinal connectors in circumferential joint of Metro Line 6 of Naples, are design to a minimum resistance to the shear of 95 kN and to the pull out of 60 kN.



Figure 3.17. Bi-block system of FIP INDUSTRIALE type 60/234, used as longitudinal connectors in circumferential joint of Metro Line 6 of Naples.

The waterproofing of the ring is guaranteed by a gasket system in Ethylene-Propylene Diene Monomer (EPDM), placed in special grooves along each side of the segment close to the extrados (Figure 3.16). This system guarantees the water seal for a misalignment until of 12mm of between the segments at contact.

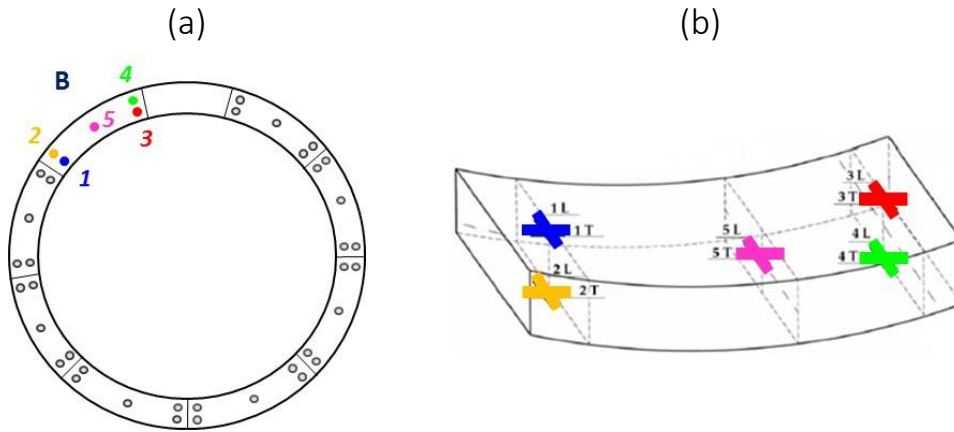


Figure 3.18. Schematic layout of the vibrating wire gauges positioning in the (a) transversal section and (b) in the plan of the segments of the instrumented ring.

The segments of the ring in Section 1 have been instrumented with vibrating wire gauges (Figure 3.19) embedded in the segments during construction at the manufacturer's plant to measure the concrete strains. The measuring instrumentation consists of five pairs of extensometer bars, in transversal and longitudinal direction, arranged as in Figure 3.18a, b: a pair of orthogonal gauges close to the extrados, a pair close to the intrados, the same respect to the axis of symmetry, and a pair of orthogonal gauges in the middle of the section.

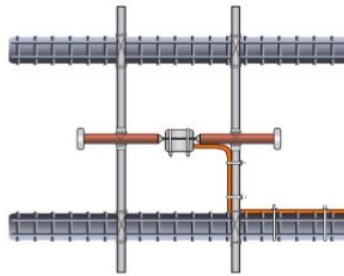


Figure 3.19. Layout of installation of the vibrating wire gauges.

The measurements were recorded using a wireless data logger, which allowed an accurate follow up of the strain changes in the segments since the concreting stage, during installation and for a long time after the tunnel construction. The vibrating wire gauges measure indeed the variation of tensile stress $\Delta\sigma$ of the wire as the variation of its natural frequency of vibration Δf due to the relative displacements at the ends of the strain gage. The deformations $\Delta\varepsilon$ are derived from $\Delta\sigma$ as:

$$\Delta\varepsilon = \frac{\Delta\sigma}{E} = \frac{1}{E} \frac{\rho}{4L^2} \Delta f^2 = k_e \Delta f^2 \quad (3.2)$$

where E is the Young's modulus of the steel wire, L the length of the wire.

The strains records (Figure 3.20) show how the section is mainly under compression; longitudinal strains could be under tension if there is the effect of the jacks eccentricity respect the middle of the ring while the lateral gauges could dilate for Poisson effect.

Overall, it can be noticed also how the strains in the concrete volume of each segment are not uniform, nor in tangential neither in longitudinal direction. This is due to mainly the effect of the installation process that occurs inside the tail skin of the machine: the boundary conditions of each

segment change whenever a new segment is installed, the action and reaction forces transmitted through the joints induce an initial state of strain that is different for each segment (Pepe G. 2008).

The long term monitoring of the strains in each segment of the instrumented ring is included in Appendix 1.

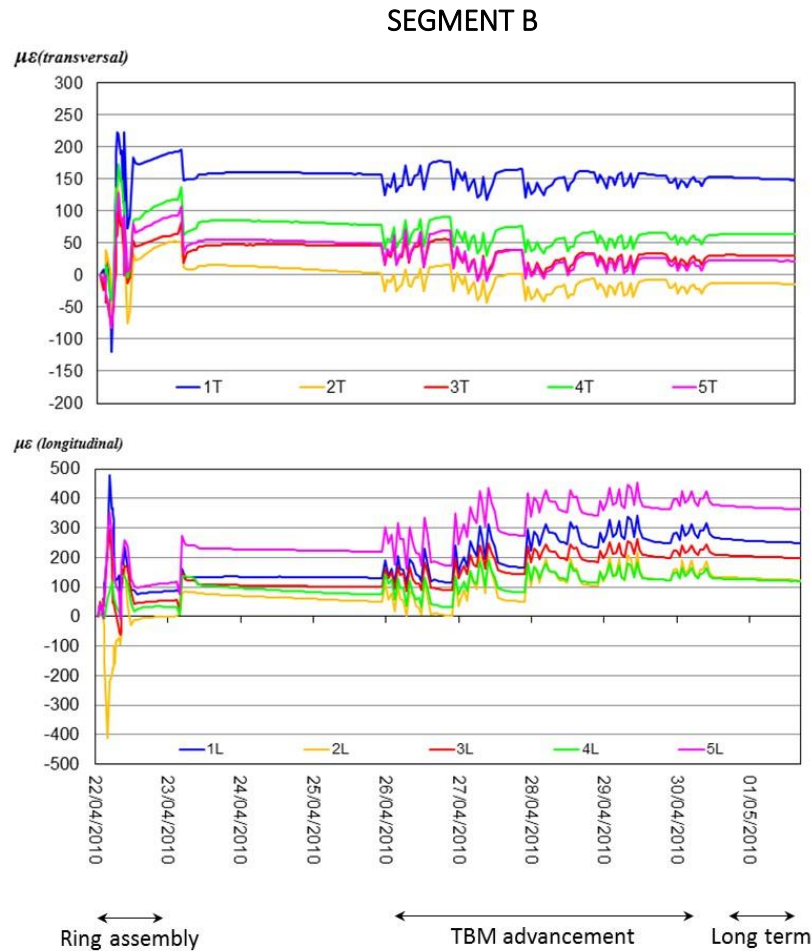


Figure 3.20. Long term monitoring of the longitudinal and circumferential strains in the Segment B of the instrumented ring (Marino 2010).

3.2.3 3D numerical model

The computational model has been developed with the Finite Element Method in Plaxis 3D (Brinkgreve et al. 2013). Figure 3.21 shows the proposed model consisting of 250000 elements. The soil domain, discretised by 10-node tetrahedral elements, has a vertical depth of 40m, width equal to 90m, according with Gunn 1993 in order to minimize the boundaries effect on the structure. The longitudinal dimension of the model, along the tunnel axis direction, has been set equal to 120m after a parametrical analysis to guarantee that plane strain conditions occur in the central reference lining section (Figure 3.21c).

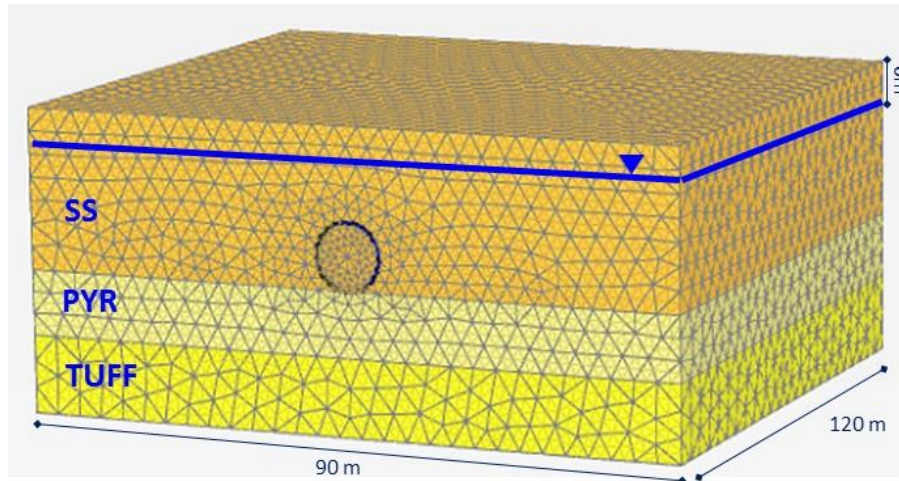
The non-linear soil behaviour has been simulate with an advanced constitutive model, the Hardening Soil Small Strain HSss model (Benz, 2007) available in Plaxis library. This is an elastoplastic model with isotropic hardening that can take into account the stiffness decay with strain level and the plastic deformation in the early stages of loading. Table 3.3 resumes the main HSss constitutive parameters

adopted for the first two layers (Aversa *et al.* 2015, Bilotta *et al.* 2017), and discussed in details in Appendix 2.

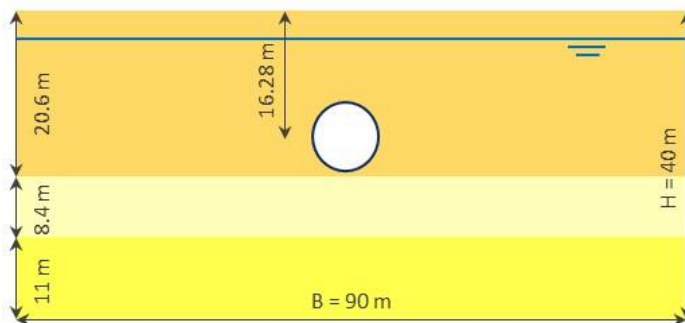
Figure 3.22 reports the curves describing the variation of the equivalent shear stiffness with respect to the small strain value, G_0 . The curves were inferred from previous laboratory tests performed on samples of the same lithotypes taken in other nearby sites (Vinale, 1988). The tuff layer has been modelled with the Mohr Coulomb model (Table 3.2).

Furthermore, the numerical prevision of the adopted constitutive model is included in the figure.

(a) 3D NUMERICAL MODEL



(b) TRANSVERSAL SECTION



(c) LONGITUDINAL SECTION

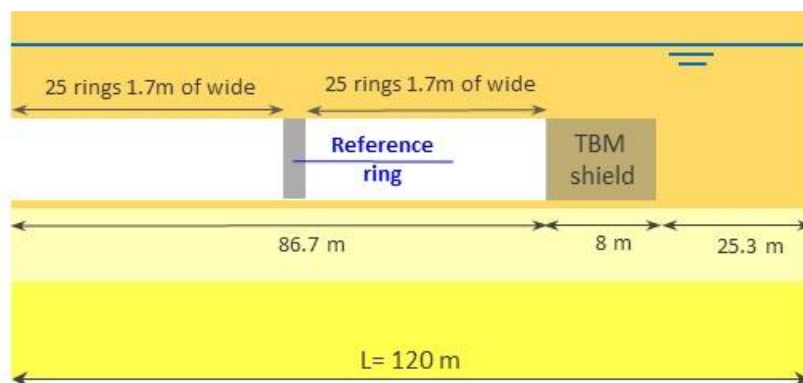


Figure 3.21. Three dimensional numerical model of the Metro Line 6 of Naples.

	E_{ref}^{50}	E_{ref}^{oed}	E_{ref}^{ur}	$\gamma_{0.7}$	G_{ref}^{ef}	ρ_{ref}
	kN/m^2	kN/m^2	kN/m^2		kN/m^2	kN/m^2
SS	40e ³	40e ³	85e ³	0.13e ⁻³	88e ³	115
Pyr	47e ³	47e ³	100e ³	0.19e ⁻³	182e ³	170

Table 3.3. HSs constitutive parameters for SS. and Pyr. layers (Aversa et al 2015, Bilotta et al. 2017).

The literature damping curve, $D(\gamma)$, is also introduced in Figure 3.22, compared with the numerical prevision, and should be used for the dynamic simulation in the next Chapter.

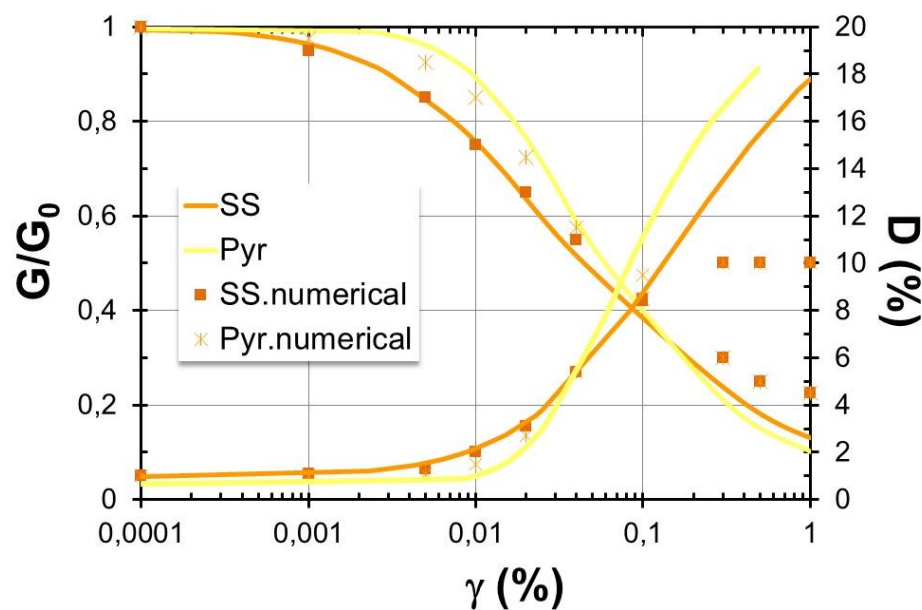


Figure 3.22. Variation with shear strain of normalized stiffness for SS, Pyr layers.

About the tunnel lining structure, the numerical model assumed for the case history of Florence-Bologna railways, back-analyzed in the previous paragraph (§3.1) and used as a preliminar calibration of the numerical model of the lining, has been used also for this case of study, with some modifications. The segments indeed, have been modelled as concrete volume elements with linear elastic behaviour; longitudinal joints, which are non-bolted flat joints, have been modelled as deformable volumes with the height equal to the width, assuming the Mohr-Coulomb elastic-perfectly plastic model; the circumferential joints are modelled as interface elements with elastic-perfectly plastic behaviour, not modelling the bi-block elements which have mainly the function of positioning of the segments along the longitudinal direction and not a real structural function. Figure 3.23a and b shows the numerical 3D model adopted for the lining and the geometry of the longitudinal joint.

In absence of experimental test on the joints, the rotational stiffness of the joints has been calibrated on the base of the analytical solution of *Janßen's* joint model. The rotational stiffness is evaluated in correspondence of $0.80 \cdot M_{yield} / \theta_{0.8}$ (Do et al. 2013, Thienert & Pulsfort 2011, Van Oorsouw 2010, Zhong et al. 2006) where M_{yield} is the yielding moment in correspondence of a rotation angle of 0.01 radians ($\approx 1\%$) equal to 61.5 kNm/m for an average value of normal force of 750 kN/m.

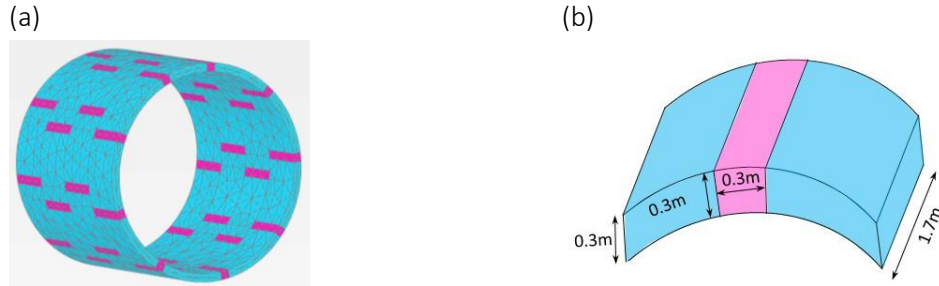
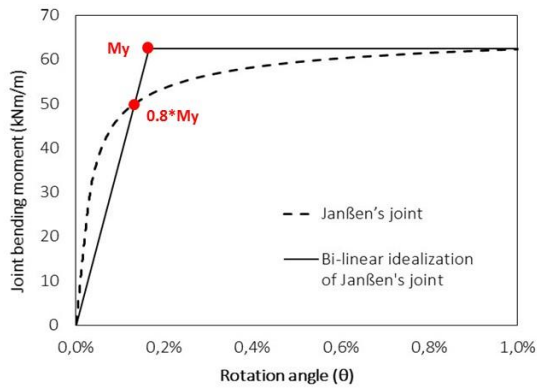


Figure 3.23. (a) Three dimensional numerical model of the segmental lining and (b) particular of the longitudinal joint of the metro Line 6 of Naples.

Figure 3.24 shows the bi-linear moment-rotation relationship adopted for the case of study.



- $M_{yield} (N=750 \text{ kN/m}) = 61.5 \text{ kNm/m}$ for $\theta=1\%$
- $0.8 \cdot M_{yield} = 0.8 \cdot 61.5 = 48.5 \text{ kNm/m}$ for $\theta_{0.8}=0.108\%$
- $k_{\theta} = 0.80 \cdot M_{yield} / \theta_{0.8} = 48.5 / 0.00108 = 45 \text{ kNm/rad/m}$

Figure 3.24. Bi-linear moment-rotation curve adopted for the joints of the metro Line 6 of Naples.

The Young's modulus E^* of the elasto-plastic joint element is set equal to equal to $6E^6 \text{ kN/m}^2$ calculated in function of the joint height (0.811m), observing the equivalence principle established before (§2.4).

For the calibration of Morh Coulomb model of the joint, the cohesion has been back-calculated as:

$$c = \left(-\frac{\sigma_{cy}}{2\sqrt{K_P}} \right) = 9000 \text{ kPa} \quad (3.3)$$

where σ_{cy} is the compressive yielding strength of the concrete C34/45 and K_P is the ratio expressed in Equation 3.4, calculated for $\phi=42^\circ$ (value chosen in the typical range for the concrete).

$$k_P = \frac{(1+\sin\phi)}{(1-\sin\phi)} \quad (3.4)$$

The Equation 3.3 has been obtained as shown in Appendix 3.

Furthermore, The tensile strenght of the joint volume is assumed null, according with Janßen's theory.

Circumferential joint behaves the same as the longitudinal one, assigning directly to the interface that models the circumferential joint, the material properties of the Mohr Coulomb model through the "Custom Option" available in the code.

Interface is modelled in Plaxis 3D with triangular 12-nodes elements, each working in pairs, compatible with the 6-nodes triangular elements of the soil, using 6 Gaussian integration points. The distance between two nodes in pair is zero, each of which has three traslational degrees of freedom to simulate

the possible relative displacement between the nodes.

Table 3.4 shows the parameters adopted for the segments and the joints.

	$E \text{ (kN/m}^2\text{)}$	$\gamma \text{ (kN/m}^3\text{)}$	ν	$c \text{ (kN/m}^2\text{)}$	$\phi \text{ (}^\circ\text{)}$
<i>Segments</i>	35E ⁶	25	0.15	-	-
<i>Joints</i>	6E ⁶	25	0.15	9000	42

Table 3.4. Concrete segments and joints parameters.

The TBM shield has been modelled with a steel plate (Table 3.5) with a linear elastic behaviour. The shield tapering has been simulated with a linearly varying diameter contraction applied along the plate, up to a maximum value of 0.3% of the diameter in correspondence of the front.

<i>TBM shield</i>			
<i>Thickness</i>	t	m	0.35
<i>Weight</i>	γ	kN/m^3	120
<i>Young's Modulus</i>	E	kN/m^2	$2.1 \cdot 10^8$
<i>Poisson ratio</i>	ν	-	0.25

Table 3.5. TBM shield parameters.

The TBM and soil interaction has been simulated via an interface surface characterised by the strength parameters of the adjacent soil reduced by 10%, applying a reducing factor ($R_{\text{interface}}$ available in Plaxis) equal to 0.9.

3.2.4 Details of the EPB-TBM tunnelling

The tunnel excavation process (simplified scheme in Figure 3.25) has been simulated in advancement stages of ground excavation, each including the following steps:

- *TBM advancement.* The TBM advancement is simulated deactivating a slice of soil in correspondence of the front, wide as the lining width (1.7m), and advancing the shield of the same length. The face stability is guaranteed, during tunnelling, applying a horizontal pressure at the front. This value is set equal 170 kN/m² as in the monitoring data available (Figure 3.26) in correspondence of the instrumented ring. A vertical increment of 18 kN/m²/m of the front pressure has been used to take into account the effect of the slurry weight with the depth.
- *Lining installation.* To each step of front advancement corresponds the installation of a ring, simulated with the activation of the concrete lining volume. The ring installation takes place under the TBM tail skin. The jacking thrust on the transversal section of the last installed ring is simulated with concentrate forced in longitudinal direction consisting of 29 point loads, as in the scheme in Figure 3.19. Each jack can achieve a maximum value of thrust of 2215 kN. In the numerical model a

thrust of 2000 kN has been considered for each jack, which resultant on the lining transversal section is that read during the monitoring (Figure 3.27).

- *Grouting.* Just behind the last installed ring, outside the TBM skin, the grout pressure in its early fluid state is applied on the lining and against the soil as radial pressure distribution equal 155 kN/m^2 with a vertical increment of $10 \text{ kN/m}^2/\text{m}$ due to the grout weight. The grout pressure value is that read during the monitoring in correspondence of the instrumented ring (Figure 3.26).
- *Grout hardening.* The annular gap between the lining and the soil is filled with solid element of grout with isotropic elastic behaviour. In a simplified way the effect of the grout hardening was modelled (Figure 3.28): in a first step, a lower stiffness is assigned to the grout to account for the mechanical properties of a plastic grout, in the subsequent step a higher stiffness is assigned to reproduce the hardened grout behaviour. The choice to consider the length of the stretch for which the grout is in the plastic state equal to one ring is compatible with the speed of advancement of the TBM machine and the fast process of hardening of the bi-component grout. The concrete-grout and grout-soil interactions have been modelled with interface elements which behaves elasto-plastically.

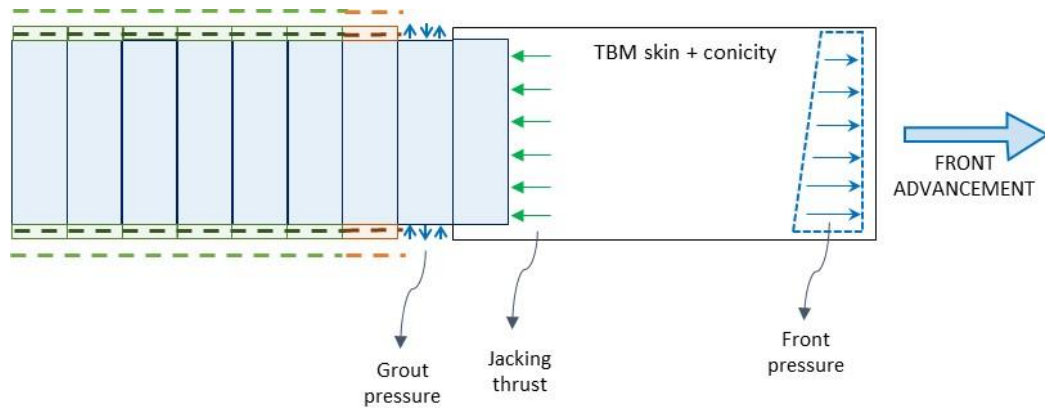


Figure 3.25. Scheme of the TBM EPB tunnelling adopted for the Metro Line 6 of Naples.

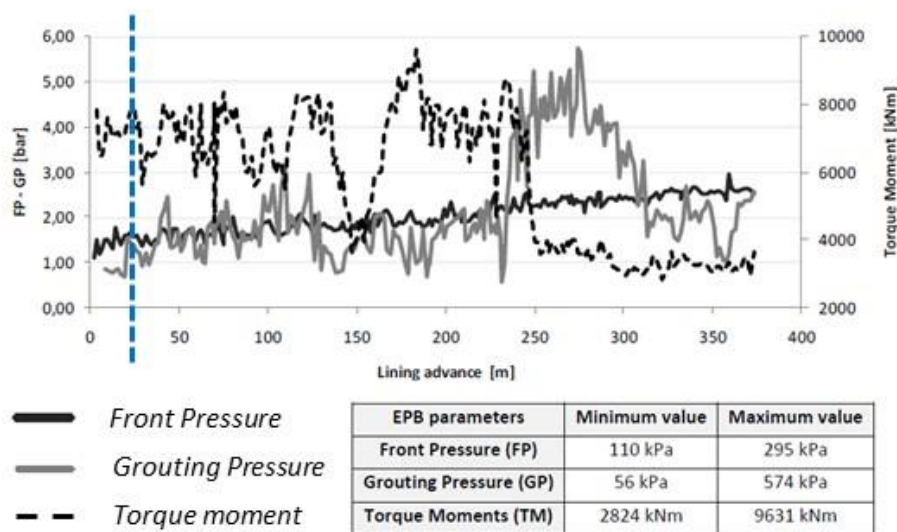


Figure 3.26. TBM performance of Metro Line 6 of Naples (Bitetti B. 2010).

This simplified approach allows to predict and back-calculate the real load transferred from the soil to the lining through the grout. Table 3.6 shows the parameter adopted in the model in terms of Young's Modulus E and reduction factor of the interfaces strength and stiffness R_i .

In the case of hardened grout, the Young's modulus E was known while the reducing factor was fixed. Between the concrete and the grout, in particular, it is set equal to 0.9, simulating a very stiff contact; between the grout and the soil, it is set equal to 0.7, a reasonable value in the case of interaction in sand.

In the case of plastic grout case instead, the Young's modulus of the grout was fixed equal to 0.015 MPa, a reasonable value in correspondence of the early stage of the grout hardening, while the reduction factors R_i of the interfaces have been back-calculated to closely fit the in situ concrete measurements in the circumferential direction.

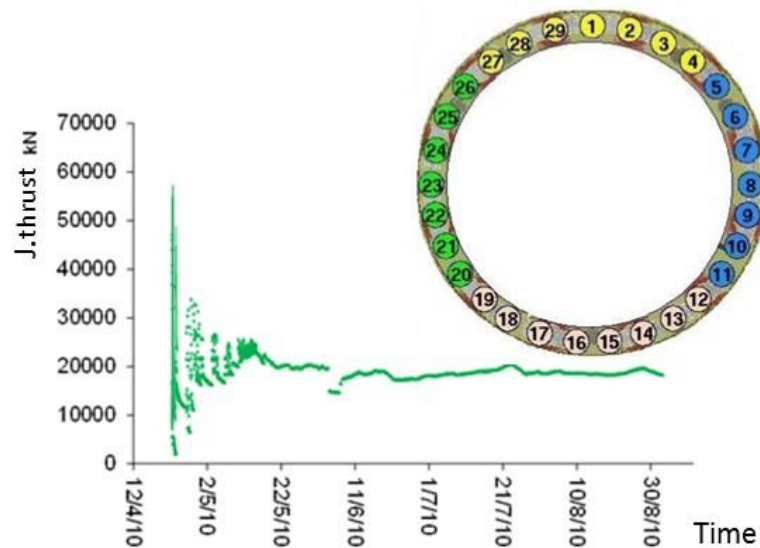


Figure 3.27. Jacking thrust resultant during tunnelling of Metro Line 6 of Naples (Bitetti B. 2010).

The final back-calculated value of R_i is equal to 0.3 in the case of concrete-grout and equal to 0.4 in the case of grout-soil interaction, exhibiting a smoother interface behaviour in the first case than the second one, as expected.

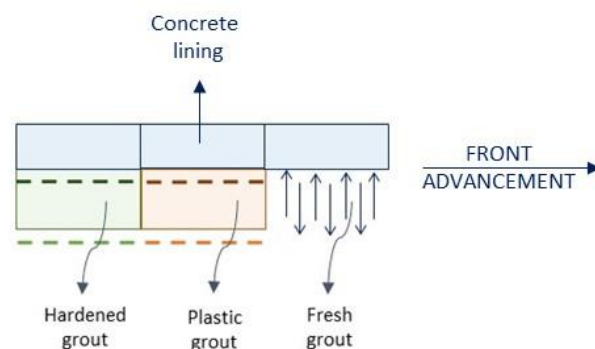


Figure 3.28. Zoom in on the scheme of the interaction mechanism concrete-grout-soil during tunnelling adopted to simulate the effect of the grout hardening.

$E_{\text{plastic grout}}$	GPa	0.015
$\nu_{\text{plastic grout}}$	-	0.45
$R_i \text{ concrete-plastic grout}$	-	0.3
$R_i \text{ plastic grout-soil}$	-	0.4
$E_{\text{hardened grout}}$	GPa	15
$\nu_{\text{hardened grout}}$	-	0.15
$R_i \text{ concrete-hardened grout}$	-	0.9
$R_i \text{ hardened grout-soil}$	-	0.7

Table 3.6. Grout parameters.

3.2.5 Validation of the 3D numerical model

The numerical model has been validated in terms of concrete segments deformations. As the gauges are directed in the transversal section of the lining (Figure 3.18b), the strain gauge readings allow to derive the strains in the specific point in longitudinal direction, parallel to the tunnel axis, and in the tangent direction in the measured point.

For this reason, the comparison between the measured and numerical strains has been done considering the longitudinal component ϵ_{yy} and the tangent (circumferential) component $\epsilon_{\text{circ.}}$ of the strains evaluated, these latter, as the composition of the two orthogonal contributes ϵ_{yz} and ϵ_{yx} as in the Figure 3.29.

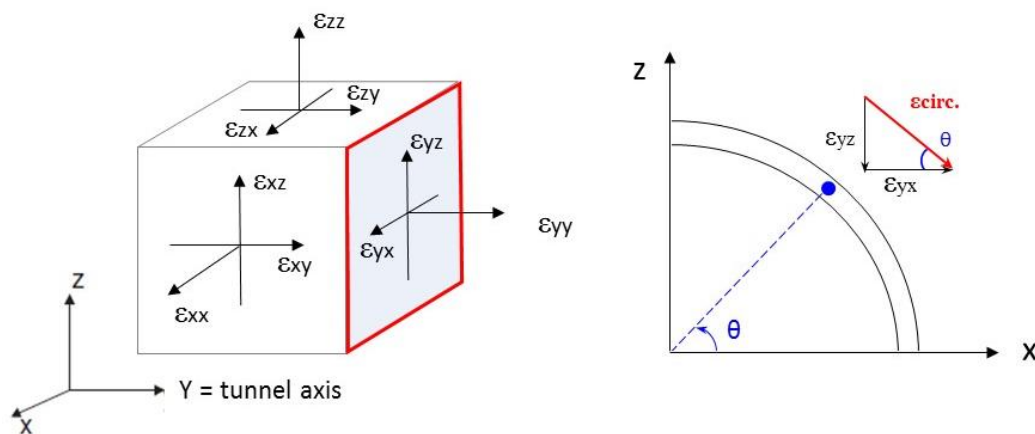
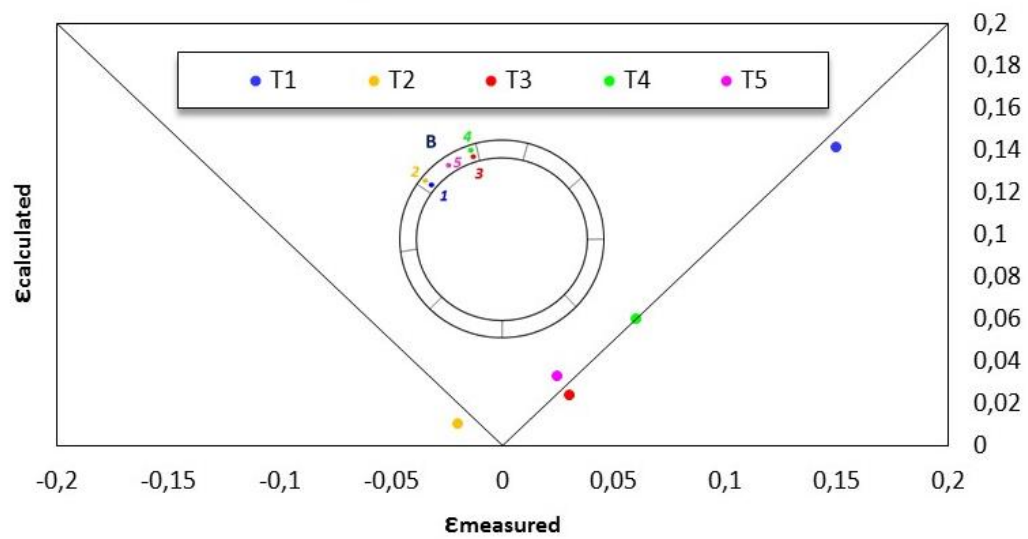


Figure 3.29. Calculation scheme of the circumferential strain in a reference point of the ring.

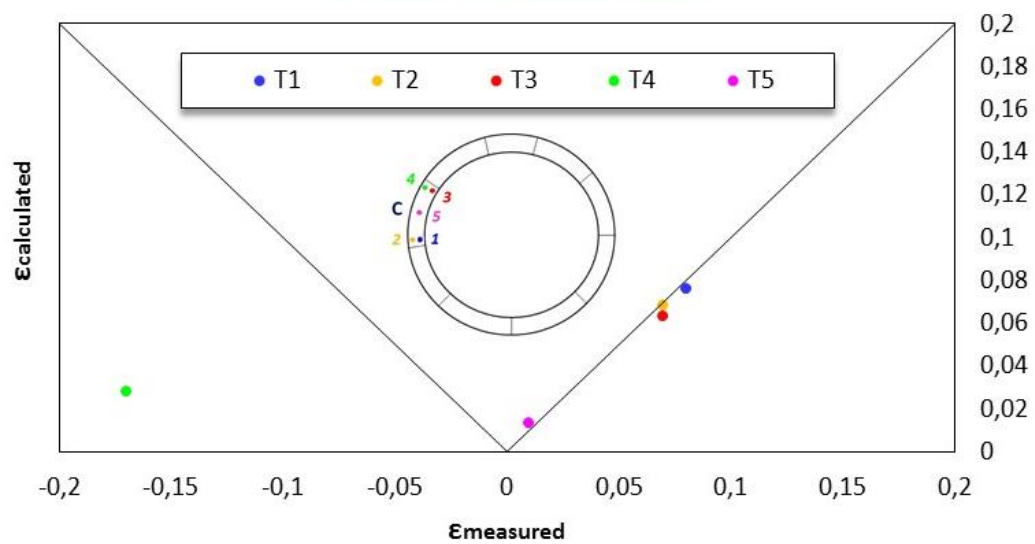
Figure 3.30 and 3.31 show the comparison between the measured and the numerical strains in the case of circumferential and longitudinal strains respectively.

The comparison in terms of longitudinal strains in particular, has been done comparing the average value of calculated strains in each segment with the same obtained from measurements, removing the tensile strains likely caused by the eccentricity of the jack thrust with respect to the middle line of the lining, not considered in the numerical model.

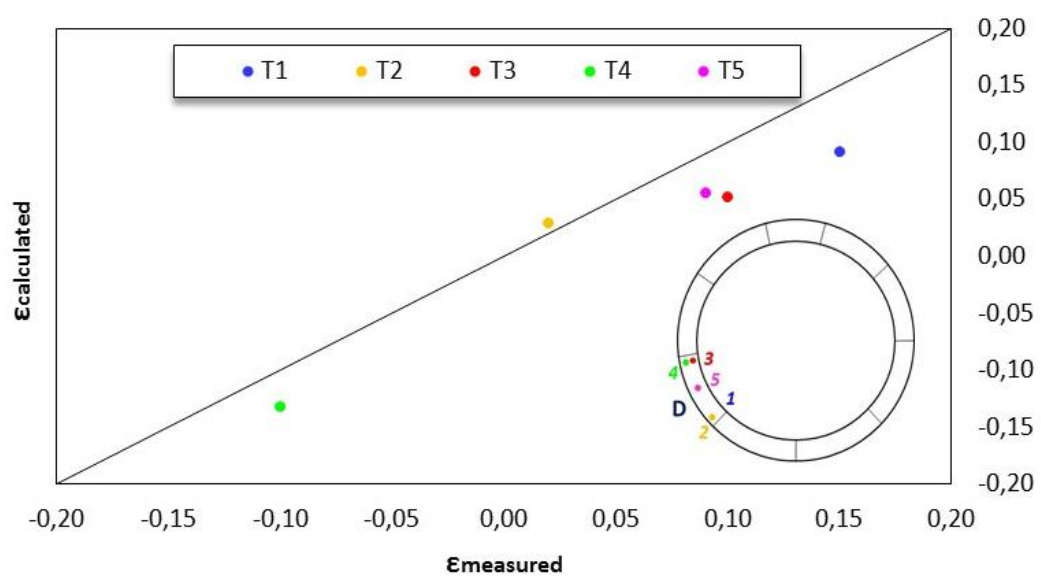
Segment B - Circumferential strains



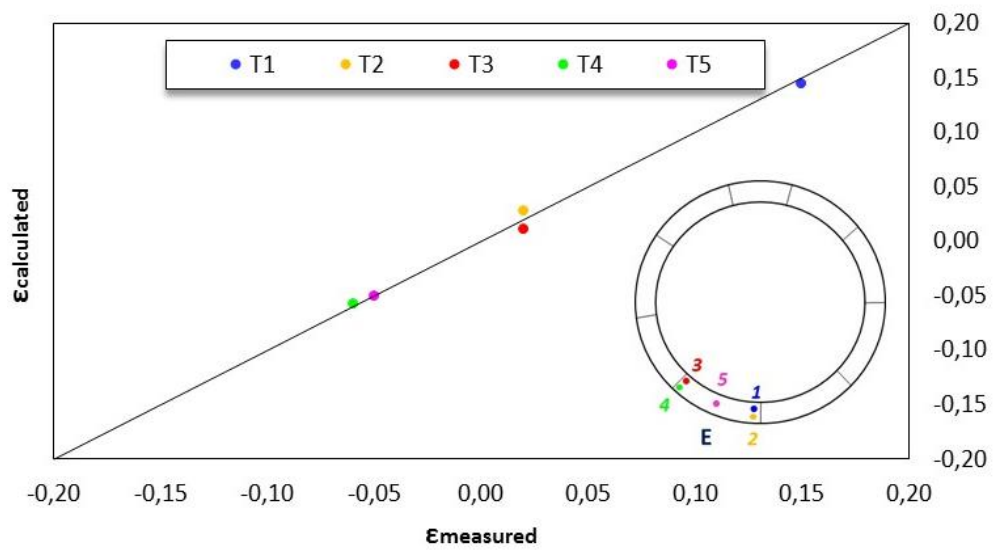
Segment C - Circumferential strains



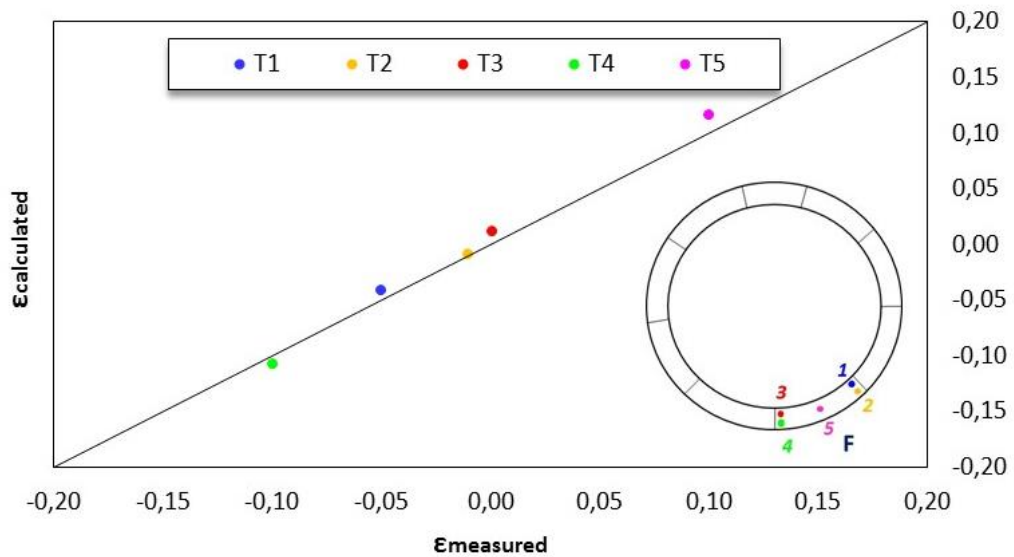
Segment D - Circumferential strains



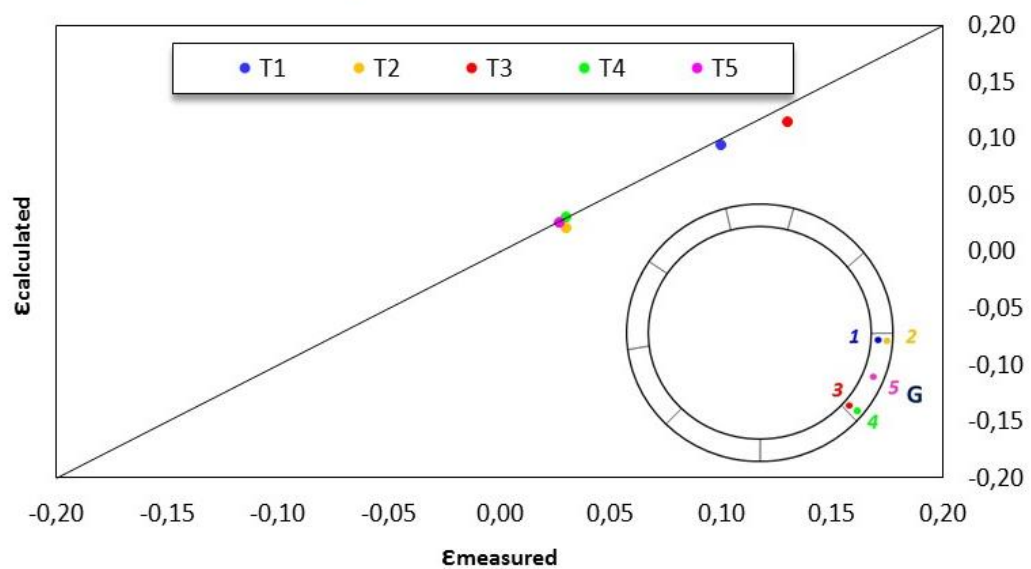
Segment E - Circumferential strains



Segment F - Circumferential strains



Segment G - Circumferential strains



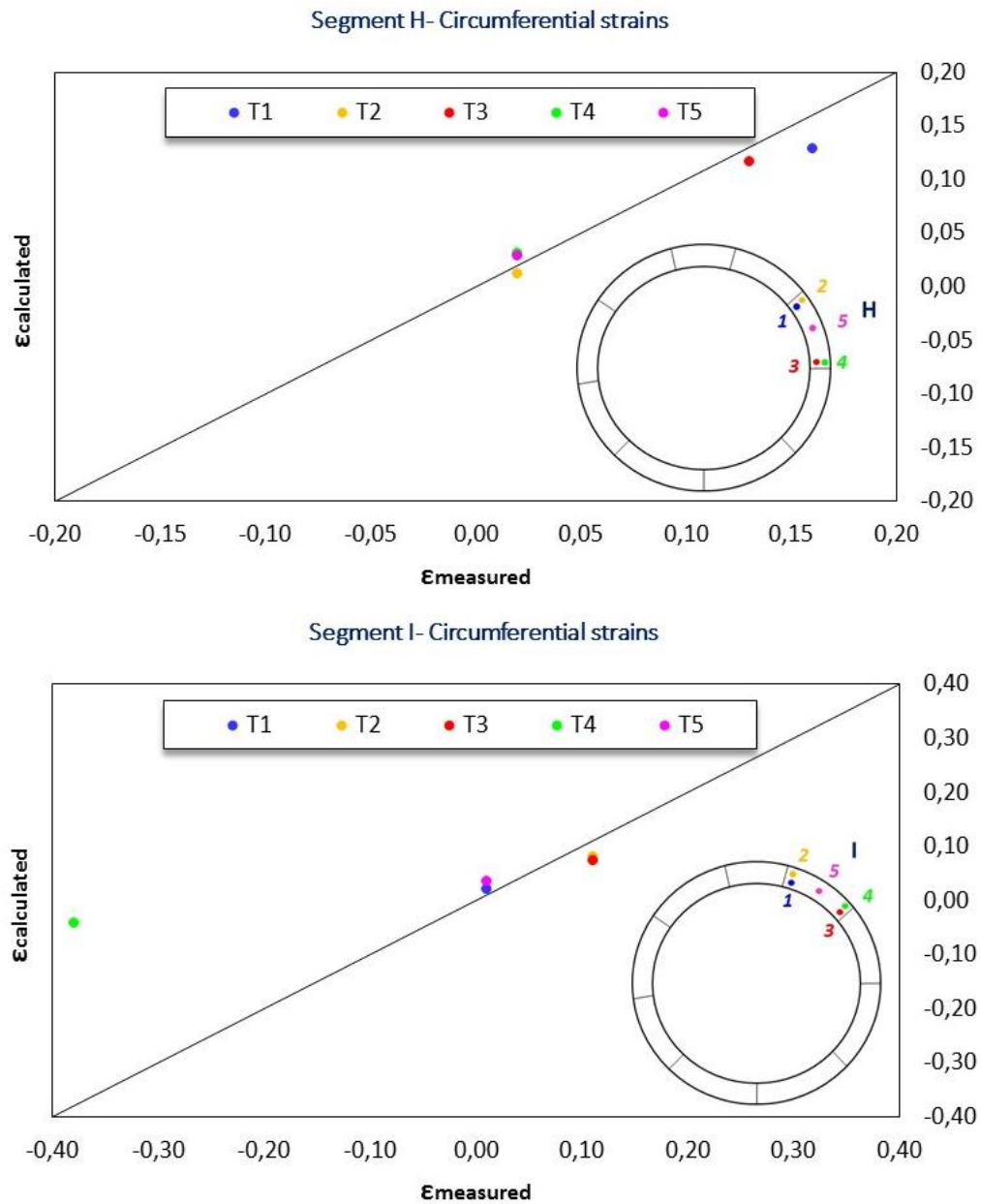


Figure 3.30. Comparison between the measured and calculated circumferential strains.

The comparison in terms of circumferential strains (Figure 2.30) shows a very good agreement between the measures and the calculation both in terms of trend that in terms of magnitude, except for some singular points, where very high strains were measured respect the other points in the relative segments, as in the case of the points T4 of segment C and T4 of the segment I.

Similarly, in terms of longitudinal strains the comparison (Figure 2.31) shows a good matching between the results, although the numerical ones are in average slightly higher than the measured ones due to the fact, not simulating tensile stresses in the numerical model, the ring is subjected only to compressive strains.

Once validated the proposed numerical model comparing the measured and the calculated strains in the instrumented tunnel lining, a series of consideration have been done on the lining and soil behaviour during tunnelling in the following paragraph.

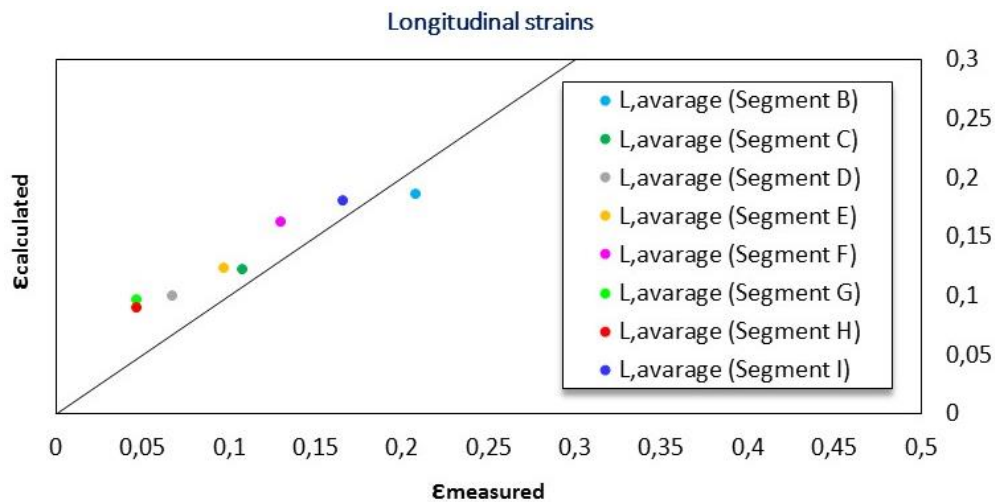


Figure 3.31. Comparison between the measured and calculated longitudinal strains.

3.2.6 Structure and soil behaviour during tunnelling

Tunnelling induces a continuous stresses and strains evolution in the time of excavation both in the lining, as seen before, and in the soil.

The lining behaviour is approached in terms of internal forces distribution in the ring at various stages during constructions, induced by the current state of strain.

The soil behaviour has been analysed in terms of strains and stress paths around the tunnel cavity and in terms of ground movements during the excavation process.

Some considerations on the shear stresses arising at the interface between the soil and the lining through the grout layer surrounding the concrete rings are also discussed

Tunnel structure behaviour

Figure 3.32 shows the distributions of bending moments and normal forces in both directions, along the section of the reference ring, at different stages during tunnel construction: when jack thrusts are applied, when the grout radial pressure is applied and at the end of the entire construction process. The numerical results show how the soil-structure interaction is only in part responsible of the internal forces arising in the tunnel lining, much of which is due to the excavation process itself.

The irregular shape of the bending moment distribution is due to the presence of longitudinal joints while the effect of the jack forces modelled as point loads is more evident in the normal and longitudinal forces distribution, with a local increase in correspondence of the loaded points.

Figure 3.33 puts in evidence the effect of joints on such segmental lining behaviour, comparing the internal forces distribution obtained at the end of excavation process in the case of segmental and continuous lining. In terms of bending moment, the segmental lining exhibits in general a more deformable behaviour, with an average value of the resultant lower than the case of continuous lining.

This difference between the two lining configurations is not really impressive in this case of study due to the fact that the influence of the joints on the reduction of the bending moment decreases with the joint number increasing (*Do et al. 2013b*). In the case of Naples, the segmental lining with a rather high number of longitudinal joints equal to nine, exhibits a quite similar behaviour respect the case of

continuous lining in terms of bending moment.

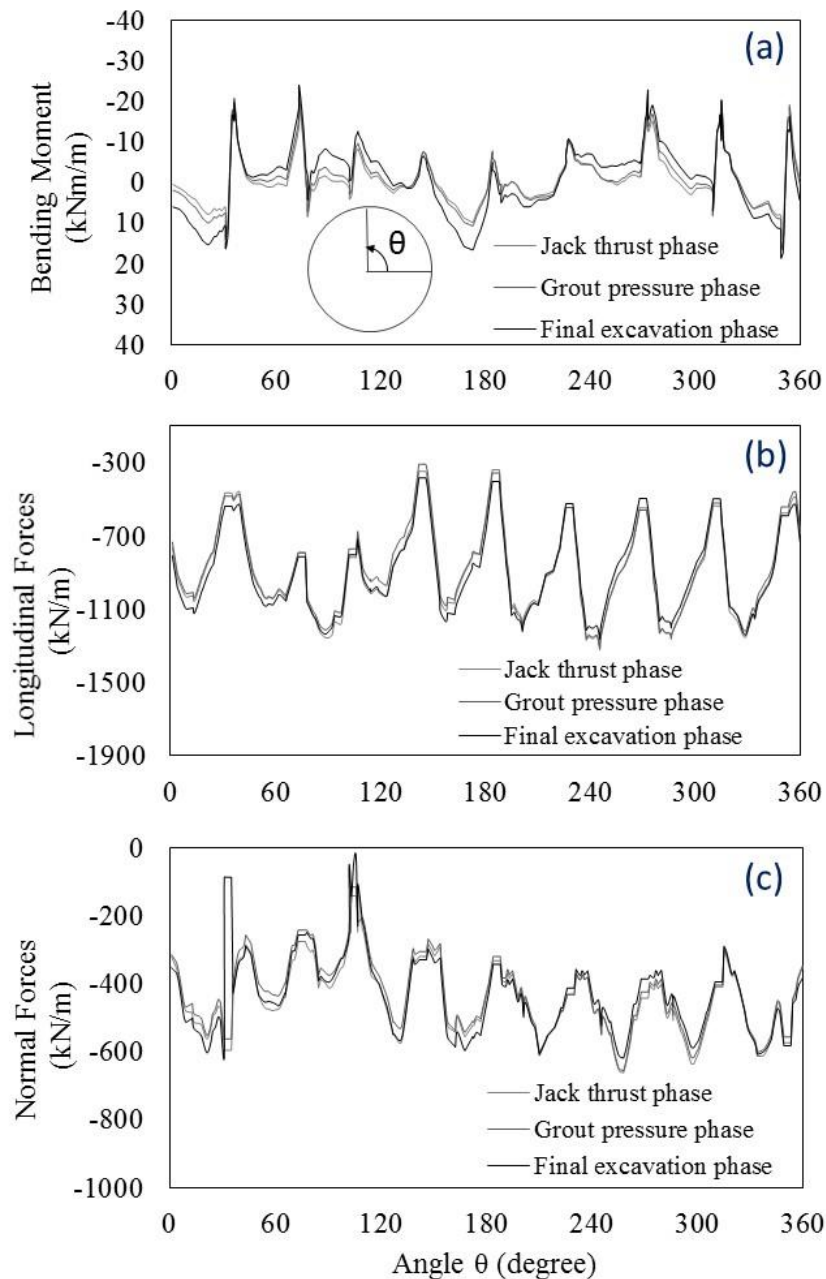


Figure 3.32. Numerical internal forces in transversal section of reference ring in terms of (a) bending moment, (b) longitudinal force and (c) normal force.

Also the normal force is affected by the joints pattern, exhibiting in average a lower value of the resultant in the lining reference section, while the longitudinal force is lower affected by the joints, as observed by other authors (*Do et al. 2013a*), showing the same average value in the section, with a higher oscillation in correspondence of the joints location, respect the case of continuous lining.

Interesting is to understand what happens in the grout annulus during the tunnel excavation. Figure 3.34 for instance shows the evolution of the longitudinal and vertical strains in some points of the grout layer, until to reach a steady state condition when the front is far from the reference section.

There is an increase of the strains during the grout hardening until their stabilization: in the vertical

direction the grout is under compression due to the radial soil stresses; in longitudinal direction instead, the grout undergoes extension for Poisson's effect, both in plastic that in hardened state, since it is neither well confined neither loaded in longitudinal direction.

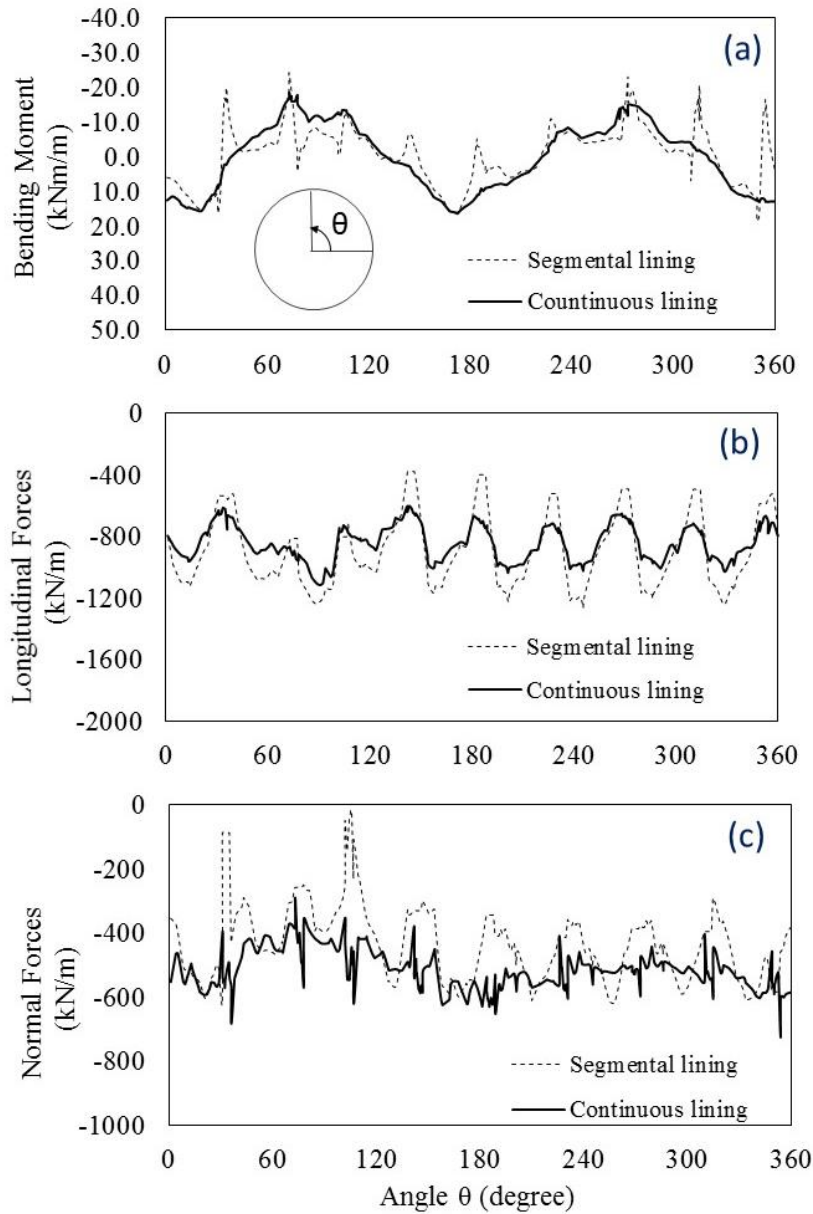


Figure 3.33. Comparison of (a) bending moment, (b) longitudinal force and (c) normal force between continuous and segmental lining.

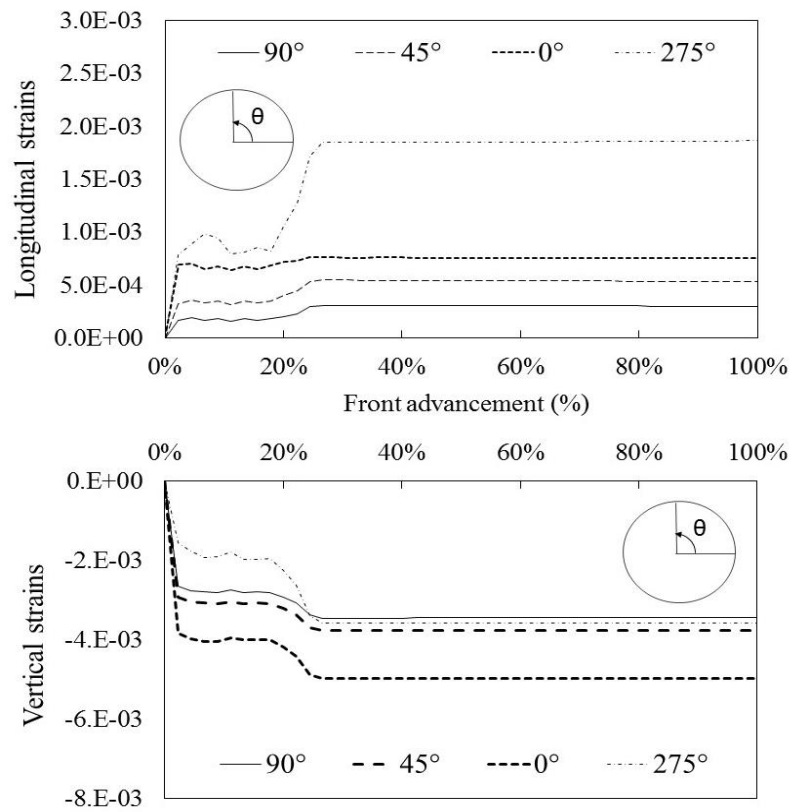


Figure 3.34. Longitudinal and vertical strains on the grout during tunnelling.

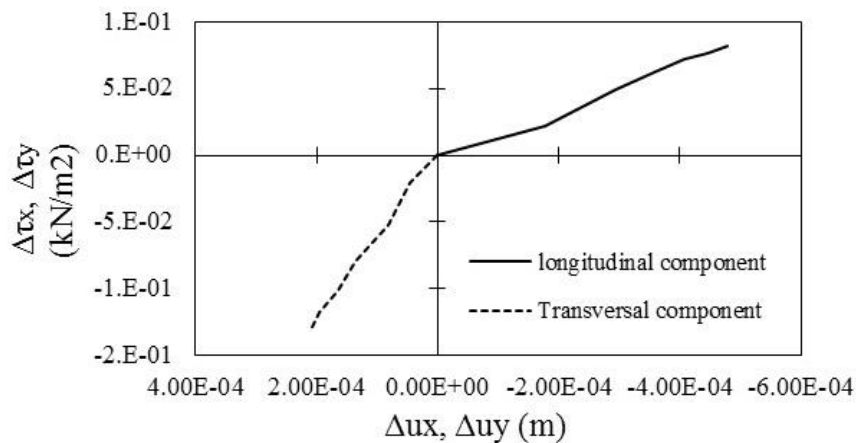


Figure 3.35. Development of the components of shear stresses τ_x and τ_y with displacements in correspondence of the soil-structure interface during tunnelling

During tunneling, frictional forces develop on the surface contact between the surrounding soil and the excavated tunnel. The radial load acting on the lining and the jack thrust acting longitudinally induce normal σ_n and tangential τ stresses on the external lining surface. The surface roughness and hardness of two materials in contact (grout and soil) are the main parameters influencing the interface friction behaviour.

Figure 3.35 shows the development of the two component of shear stress τ_x and τ_y along the transversal and longitudinal directions with, respectively, the transversal and longitudinal component of displacement u_x and u_y , during the front advancement. The results are referred to an interface point on the crown of the reference ring and show the increase of tangential stresses with displacements during front advancement.

The magnitude of the shear stresses arising in this point is such to develop small displacement within the interface which remains elastic during the entire excavation process, as shown in Figure 3.36.

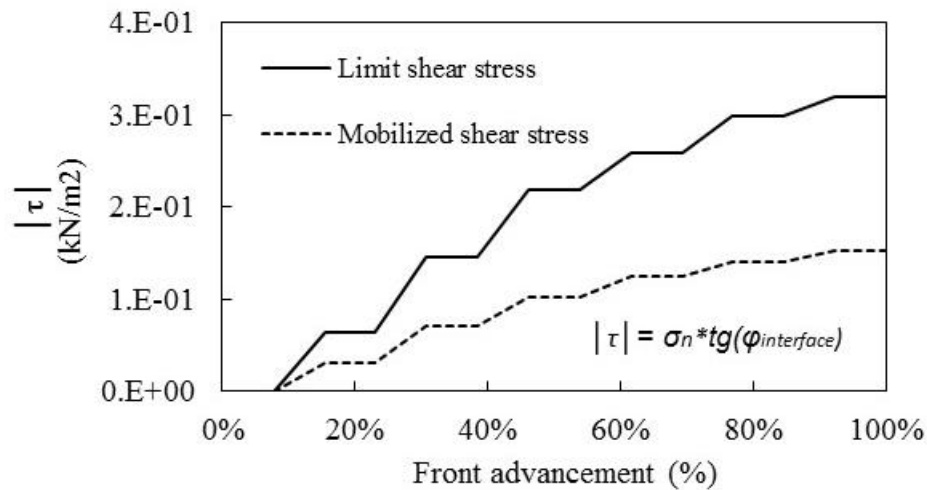


Figure 3.36. Mobilized and limit shear stress at the soil-structure interface.

Soil behaviour

The evolution of soil strains around the tunnel during construction is shown in Figure 3.37. The vertical (a), longitudinal (b) and transversal (c) strain calculated in a number of points around the tunnel cavity, in the middle transversal section of a reference ring ($y=23.35\text{m}$), are shown in the figure. In particular: point K and L are located 2 m and 6 m above the tunnel crown; point M and N are located 2 m and 6 m on the right side of tunnel; point O and P are located 2 m and 6 m below the invert.

The construction stages are also evidenced in the figure. When the excavation starts, the selected points are far from the front and they are subjected to a gradual tendency to compression (negative strains) in longitudinal direction due to the front pressure in advancement, and to extension (positive strains) in vertical direction due to the relaxation around the cavity; transversal strains are not affected very much in this phase.

During the TBM passage, the soil behaves differently depending on the position with respect to the tunnel. For instance, in the case of vertical strains, the points located under and above the tunnel (K-L-O-P) are under compression, the point on the side of tunnel (M-N) are in extension. In particular, in correspondence of grout pressure the strains are subjected to a significant increase after which they keep the same value until long term condition. In longitudinal direction, the points are under compression during the TBM passage, tend to extension for the grout pressure effect and, and then tend again to compression, apart from the points K and O.

The latter are the closest points to the tunnel along the vertical axis, and they remain in extension also in long term condition, although undergoing very low values of strain. In the transverse direction, the points under and above the tunnel are under compression, the points on the right are under tension.

Again an increase of strains is observed in correspondence of the grout pressure.

In any case, the magnitude of strains decreases moving away from the tunnel: higher values of the strains were calculated in the points K, M and O compared to the points L, N and P.

It is also worth looking at the stress paths of the same points around the tunnel cavity, in Figure 3.38. The points labelled as '1' indicate the initial stress conditions, while the two subsequent marked along the stress path indicate the TBM passage and the final state of stress, respectively.

Above the tunnel, the nearest point K starts from a higher deviator stress, q , than the point L and it undergoes a larger decrease. The isotropic stress, p' , is almost constant in L. Beneath the tunnel, both in O and in P an almost similar reduction of both q and p' is calculated. However both above and below the tunnel, the closer is the point to the tunnel, the larger is the stress change.

Points M and N on the right side of tunnel, show a low increase of deviator stress, very similar in the two points and an increase of p' when TBM is passing through the section.

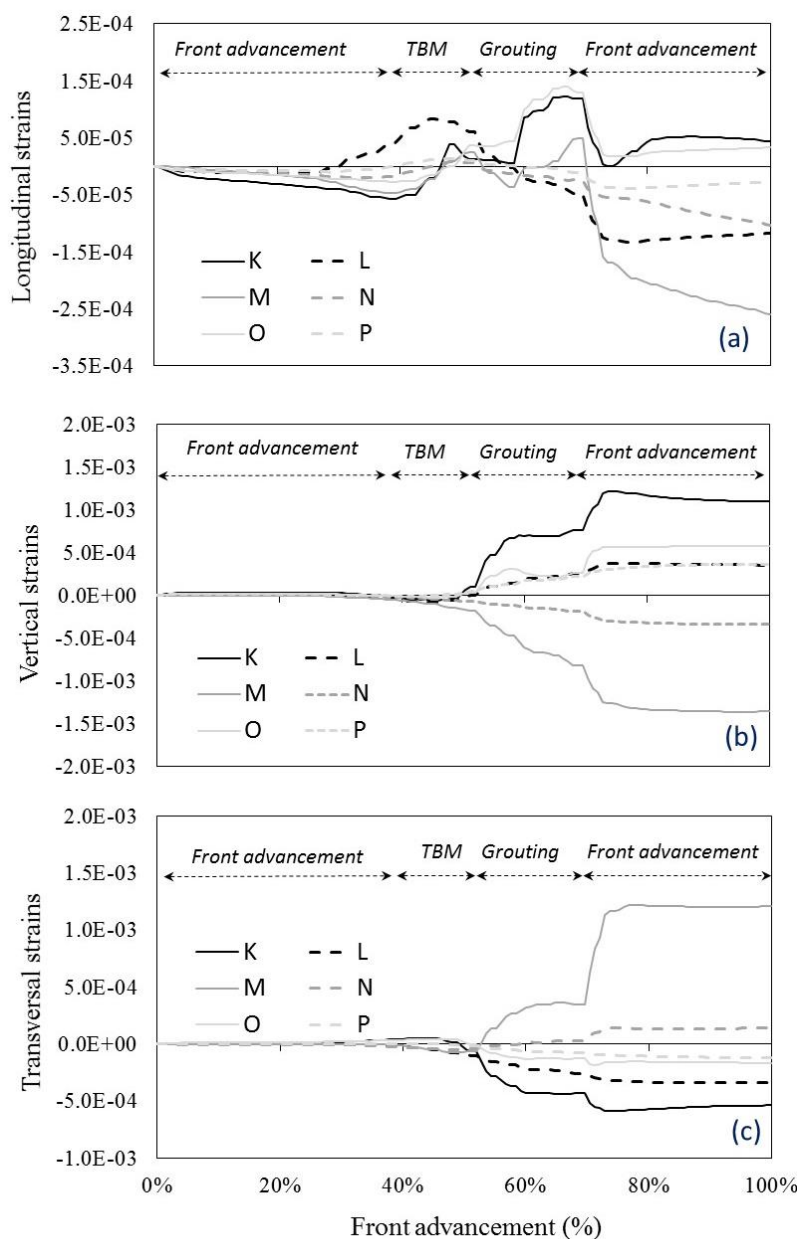


Figure 3.37. Soil strains around tunnel cavity respectively (a) in vertical, (b) longitudinal and (c) transversal direction, during tunnelling.

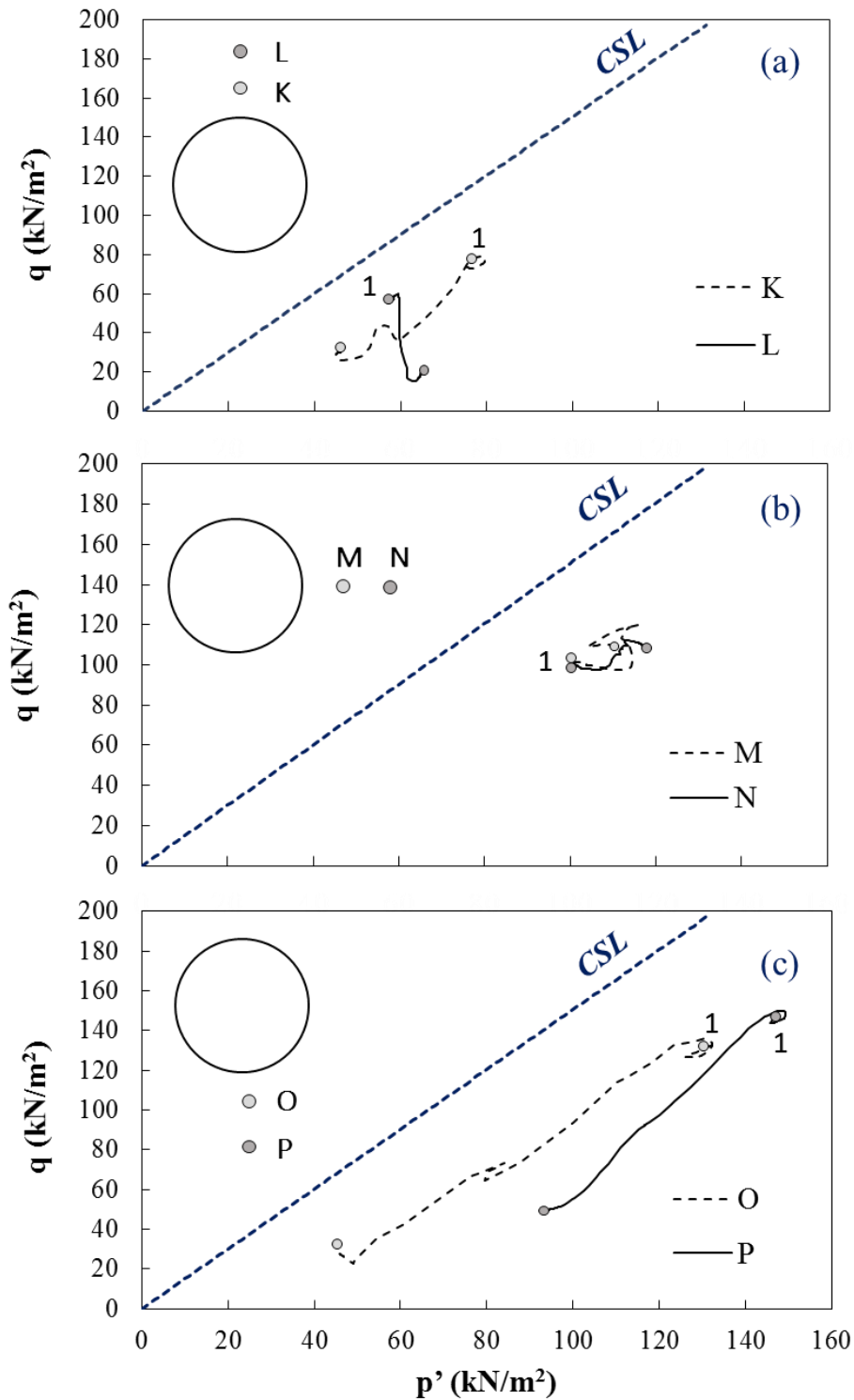


Figure 3.38. Stress paths around tunnel cavity respectively (a) above the crown, (b) on the right side of the tunnel axis; (c) under the bench, during tunnelling.

Looking at the tunnelling effect in terms of induced displacements, the vertical displacements that correspondingly develop at the ground surface in the transverse section while the excavation front advances are shown in Figure 3.39.

The settlement increase with the tunnel excavation up to a value equal to 0.15% of external

excavation diameter while the distance of inflection point “i” from the tunnel axis is about of 1.2D, close to the empirical solution (*Clough and Smith, 1981*).

Figure 3.40 shows the evolution of the surface soil settlements along the longitudinal axis during tunnel construction. It can be observed how the maximum surface settlement increases with the tunnel progression until stabilizing after about 3D of excavation span. The figure also shows that a non-negligible boundary effect develops up to a distance of 2.5-3 D from the lateral boundary, thus confirming the need to create a numerical model longer than 10D.

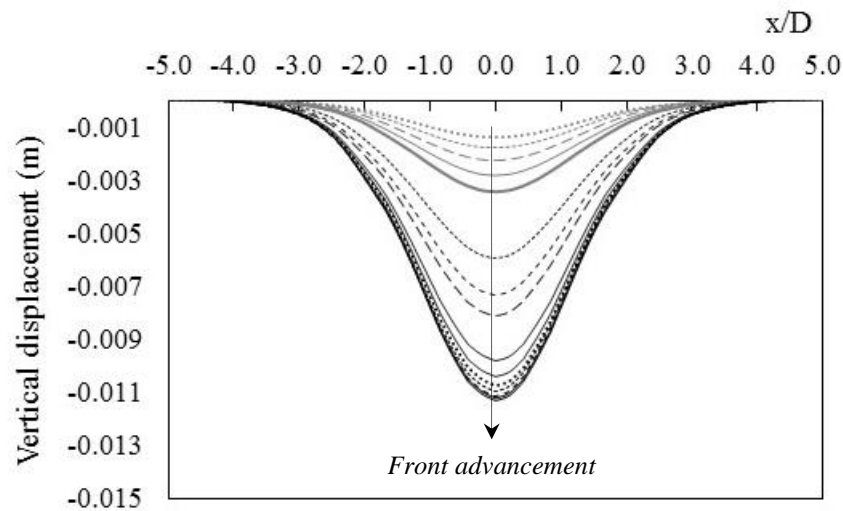


Figure 3.39. Vertical displacements at the ground surface along the transversal section $y=26.35\text{m}$ during tunnelling.

Figure 3.41 shows the vertical settlements along the longitudinal axis at the tunnel crown. The shape of the displacement profile is generally more irregular than at the ground surface, since it is more directly affected by the boundary conditions that model the TBM excavation process

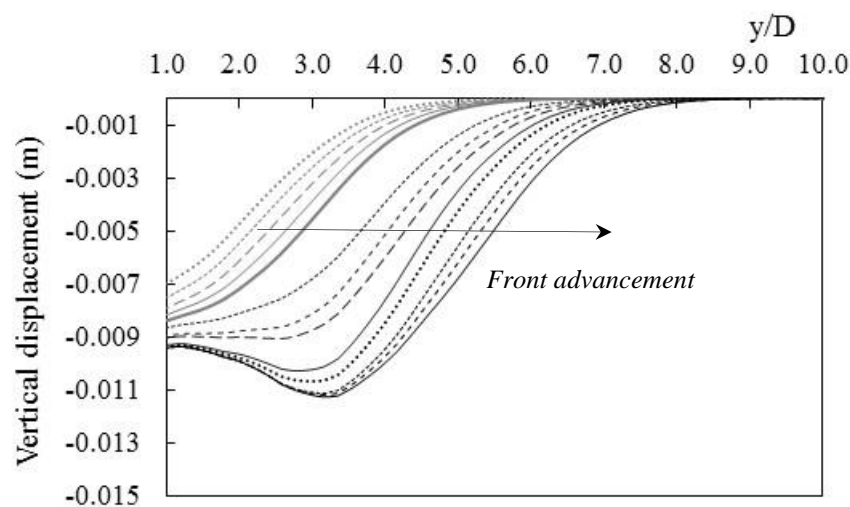


Figure 3.40. Vertical displacements at the ground surface along the longitudinal direction during tunnelling.

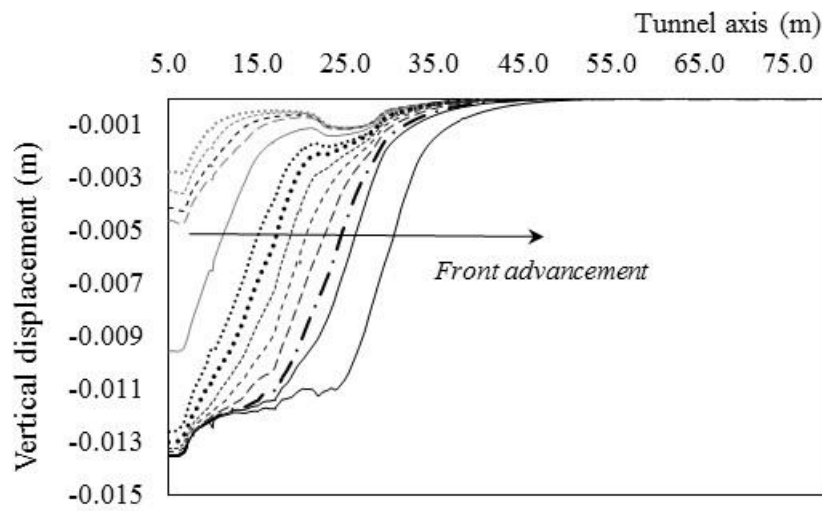


Figure 3.41. Vertical displacements at the tunnel crown along the longitudinal direction during tunnelling.

SECOND PART: Behaviour of segmental lining under uniform seismic load

CHAPTER 4

Tunnel - ground interaction during uniform seismic shaking

Introduction

The behaviour of tunnels under seismic actions is rather complex and until two decades ago it was generally not considered as a major design issue. Only recently, experimental and numerical research has made some significant steps towards the comprehension of the mechanisms governing soil-structure interaction for such a structure under seismic actions.

It is generally assumed that the seismic behaviour of the tunnel in soft ground is governed by the surrounding soil, while the inertial load contribution of the underground structure itself is negligible (*Hashash et al., 2001*). Hence changes of internal forces in the lining due to seismic shaking are generally calculated from the transient response of the ground. During the earthquake, the tunnel lining structure undergoes deformation both in the transverse section (*Hashash et al., 2005*), induced by soil shear strain in the vertical plane, and in longitudinal direction (*St.John & Zahrah, 1987; Kawashima 1999*) due to the asynchronous motion along the tunnel axis; the common design methods approach the two deformation mechanisms separately, not considering the coupled effect.

This Chapter focuses on the response of different design approaches that model in different ways the soil-tunnel interaction (*Hashash et al. 2001, Pitilakis and Tsiniadis, 2014*) subjected to seismic uniform load, with deformation mechanism in the transversal direction only. Pseudo-static and full dynamic approaches for instance, have been compared in terms of dynamic increment of the tunnel internal forces. The comparison refers to the plain strain tunnel section of the case study of Metro Line 6 of Naples.

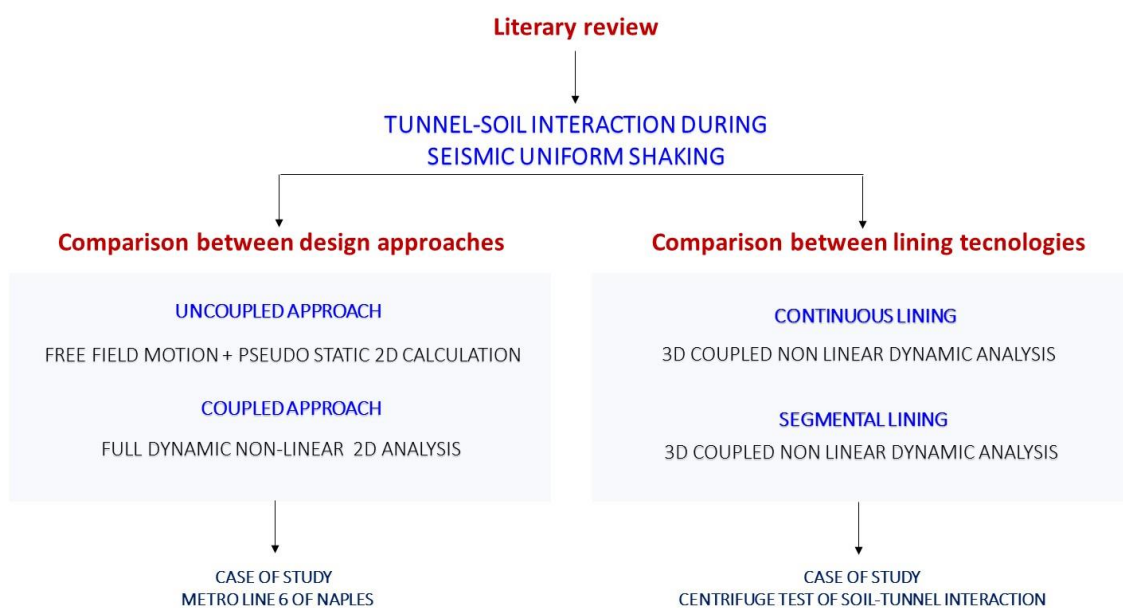


Figure 4.1. Layout of the Chapter 4.

As well as the different seismic design approaches, the Chapter investigates also the effect of the segmental lining technology on the tunnel seismic behaviour. During earthquakes, segmental lining performs better than a continuous ring due to the higher structural flexibility, producing a decrease of deformations in the lining and an increase of the whole structural aseismic capability. However, under high levels of ground shaking, the joints are the most vulnerable points of tunnel structure leading to joints opening, as observed for example during Kobe earthquake (Dean 2006).

Starting from the interpretation of the results of the centrifuge test model T3 performed by Lanzano 2009 on a continuous tunnel lining in reduced scale, the study of the soil-structure interaction has been extended to the case of segmental lining. The dynamic behaviour of longitudinal joints has been investigated with a set of non-linear 3D full dynamic analyses on the segmental layout. The results have been carried out in terms of joint rotation during the dynamic time for different real earthquakes.

Figure 4.1 shows the organization scheme of this Chapter.

4.1 Literature review

Seismic underground structures behaviour is very different, generally better, respect the aboveground ones. In the first case infact the inertial contribution of the tunnel structure is negligible respect the surrounding soil (Wang 1993; Kawashima 2000, Pitilakis & Tsinidis 2010) so that the the soil-structure interaction in mainly due to the kinematic interaction and the response of the embedded structure is then dominated by the soil. Figure 4.2 shows the different response of the two types of structure that, subjected to the same input motion, achieve different level of load and acceleration in the structure.

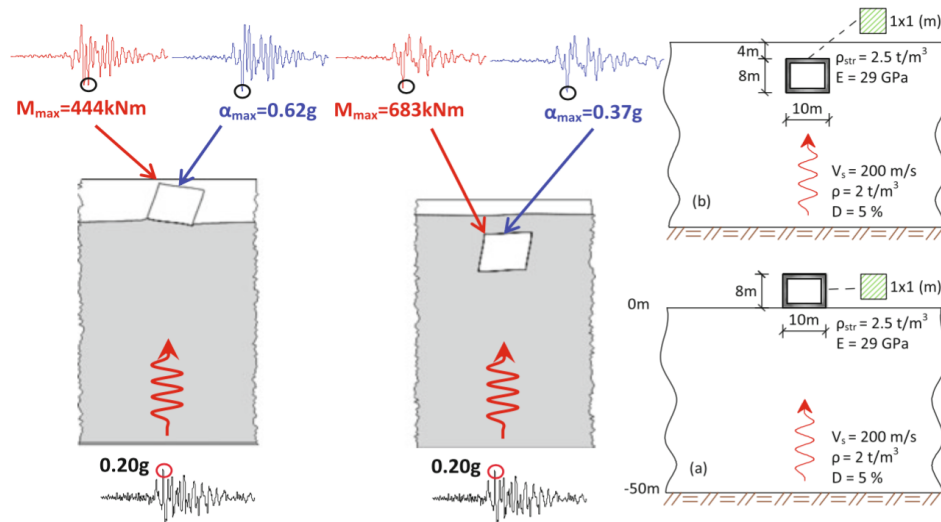


Figure 4.2. Comparison between the seismic behaviour of aboveground and underground structure (Pitilakis & Tsinidis 2010)

The kinematic soil-structure interaction in underground structures is therefore dominated by the relative soil-structure stiffness, that is how flexible is the structure respect the soil. Typically can be verified different situations: 1) when the tunnel is very rigid respect the soil, no deformation arise in the structure; 2) when the structure is stiffer than soil lining deformations are lower than the soil

deformation in absence of the structure (free-field soil condition); 3) when the structure is stiff as the soil, the lining follows free-field deformation; 4) when the structure is less stiff than soil, the lining is subjected to deformation higher than the free-field condition.

Another key parameter in the kinematic interaction is the interface friction of the contact surface between the soil and the tunnel (*Huo et al. 2005, Sederat et al. 2009, Tsinidis et al. 2016*). The two extreme cases of soil-tunnel interface, known in literature as “no slip condition” (rigid contact with a high value of friction coefficient) and “full slip condition” (weak contact with low value of friction coefficient) affect differently the yielding response of the soil at the adjacent area of the tunnel: a no slip interface will lead to reduced deformations and strains in this soil area and thus the soil stiffness and strength will not degrade considerably; a full slip interface will cause increased deformations and strains in the adjacent soil, resulting in a rise of the soil yielding and the soil stiffness degradation (*Tsinidis et al. 2016*).

Also the earthquake loads applied on the structure influence its interaction with the surrounding soil, typically a slip condition is associated to weak earthquakes while no slip condition to strong earthquakes.

Figure 4.3 shows the effect of the two key parameters discussed above in terms of soil plastic strain distributions computed at the end of seismic shaking. The comparisons verify the effect of interface properties on the yielding response of the adjacent soil, with higher values of plastic strains in the case of full slip condition respect the case of no slip. In terms of soil-tunnel relative stiffness, the soil plastic strains are much lower in the case of rigid tunnel than those predicted around the flexible one.

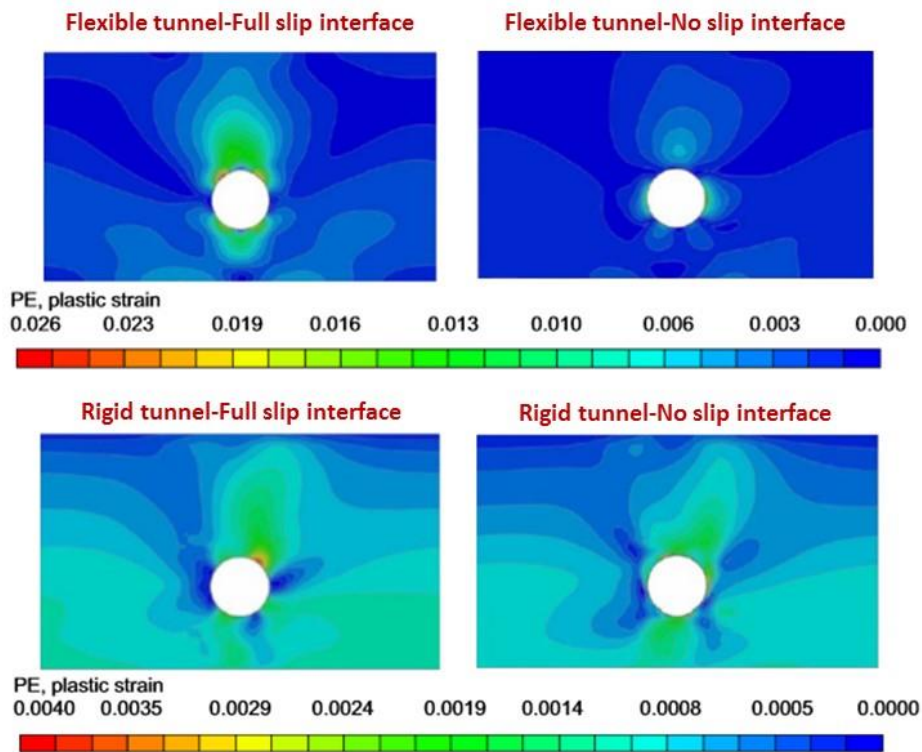


Figure 4.3. Soil plastic strains computed at the end of seismic shaking for flexible and rigid tunnel, in the case of full slip and no slip interface condition (*Tsinidis et al. 2016*).

Similarly, the interface condition and the structure stiffness affect directly the tunnel response in terms of increment of dynamic forces. The effect of the mobilized friction along the interface in particular, is significant for the dynamic axial force, while it becomes almost negligible for the dynamic

bending moment (Huo et al. 2005; Sedarat et al. 2009; Kouretzis et al. 2013, Tsinidis et al. 2016). Soil-tunnel stiffness instead, affect both axial and bending moment and change during seismic shaking both in transversal than in longitudinal tunnel section.

Figure 4.4 how the dynamic increment of normal force ΔN increases with the friction increasing, while this effect is negligible in terms of bending moment ΔM , and how the rigid tunnel suffer higher value of ΔN and ΔM respect the flexible one.

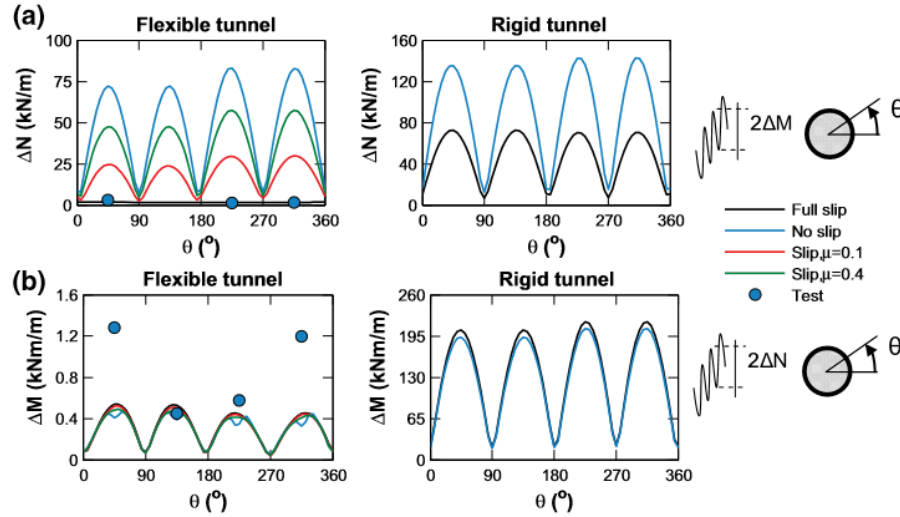


Figure 4.4. Effect of the soil-tunnel interface friction on (a) the axial force and (b) the bending moment for rigid and flexible tunnel (Tsinidis et al. 2016).

These results refer to a plain strain condition occurring when the tunnel is subjected to an uniform seismic shaking (transversal component of seismic shaking).

When such a structure is subjected to seismic waves inclined in any direction respect the tunnel axis indeed, it undergoes to different types of deformations mechanism (Owen & Scholl, 1981) as shown in Figure 4.5.

In the transversal tunnel direction, “ovaling (for circular tunnel) or racking (for rectangular tunnel) deformations” developed when shear waves propagate normally, or nearly, to the tunnel axis, resulting in a distortion of the cross-sectional shape of the tunnel lining.

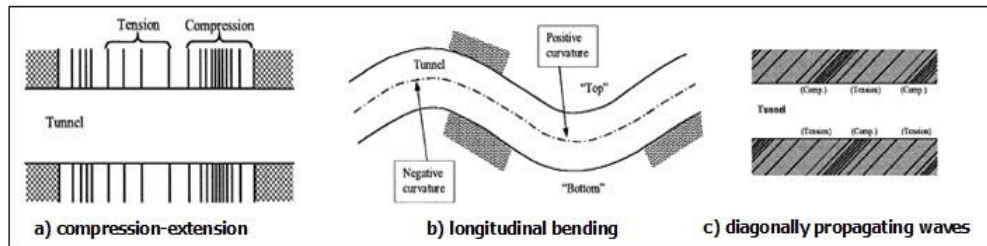
Due to the asynchronous motion along the tunnel axis (not uniform seismic load), a double deformation mechanism involves the tunnel along the longitudinal direction: 1) “axial deformations” generated by the components of seismic waves that produce motions parallel to the axis of the tunnel and cause alternating compression and tension; 2) “bending and shear deformations” in the horizontal tunnel plane, caused by the components of seismic waves producing particle motions perpendicular to the longitudinal axis.

Such deformation mechanisms could induce several damage in a shallow tunnel in soft soil, whose type and size is strictly related to many influencing factors of the soil, the structure and the seismic event, such as:

- type of tunnel (excavated with traditional or mechanized technology);
- the shape, size and depth of the structure;
- the properties of the surrounding ground;
- the properties of the structure;
- relative soil-structure stiffness and interface surface contact behaviour;

- the severity of ground shaking (i.e. peak ground acceleration and magnitude);
- direction of propagation of the earthquake respect the structure.

LONGITUDINAL DIRECTION



TRANSVERSAL DIRECTION

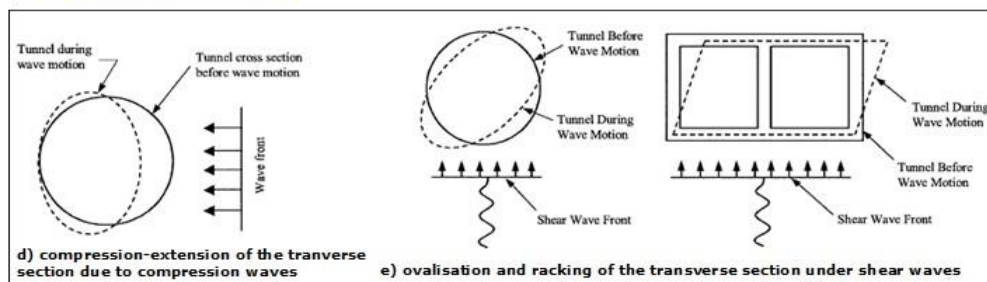


Figure 4.5. Types of tunnel deformations during a seismic event (Owen & Scholl, 1981).

Very few data are available concerning damages to underground structures and tunnels due to earthquakes before 70's. Damages and failures were accurately documented only after this data, when many authors systematically collected data of tunnel damages for different earthquake events. *Dowding & Rozen (1978)* were the first to collect cases of damage to tunnel observed after American and Japanese earthquakes. Such a database was updated by *Owen & Scholl (1981)* after San Francisco (1906) and San Fernando (1971) earthquakes, by *Sharma & Judd (1991)*, *Power et al. (1996)* after Kobe (1995) and Northridge (1995) earthquakes, by *Corigliano (2006)* after Chi-Chi (1999) (Taiwan) and Niigata (2004) (Japan) earthquakes.

Most of all data refer to the tunnels excavated by traditional methods and the most common type of damage are those in Figure 4.6. It can be observed how the different deformation mechanisms introduced before can induce in the tunnel lining cracks in longitudinal, transversal and inclined direction and also shear. This reflects the fact that, as well as the the lining stiffness and the interface behaviour also the seismic event itself, in terms of maximum acceleration and direction of propagation, is a key parameter for the evaluation of the tunnel lining seismic response.

Figure 4.7 shows a case history of tunnel damage after earthquake in Italy. *Monteluco road tunnel*, excavated with traditional method, is located in the center of Italy, three kilometres distant from the epicentre of L'Aquila earthquake event (6 of April 2009, Mw 6.3). After the seismic event, the tunnel has presented a widespread crack pattern, documented by visual survey and by monitoring of a stretch of 450m of the tunnel for about five months after the main event.

The crack pattern involves deformation mechanisms both in transversal that in longitudinal direction and inclined one also, mainly concentrated on the sides of the tunnel, in the order of tenths of a millimetres, and in correspondence of the concrete casting shootings, in the order of centimeters.

The long term monitoring of the crack movements (Figure 4.8) shows an initial tendency to cracks opening, a subsequent tendency to closing, in long term condition instead a tendency to movements

stabilization except for the points located near the concrete casting shootings, the most vulnerable points of the structure in correspondence of which water seepage was been observed.

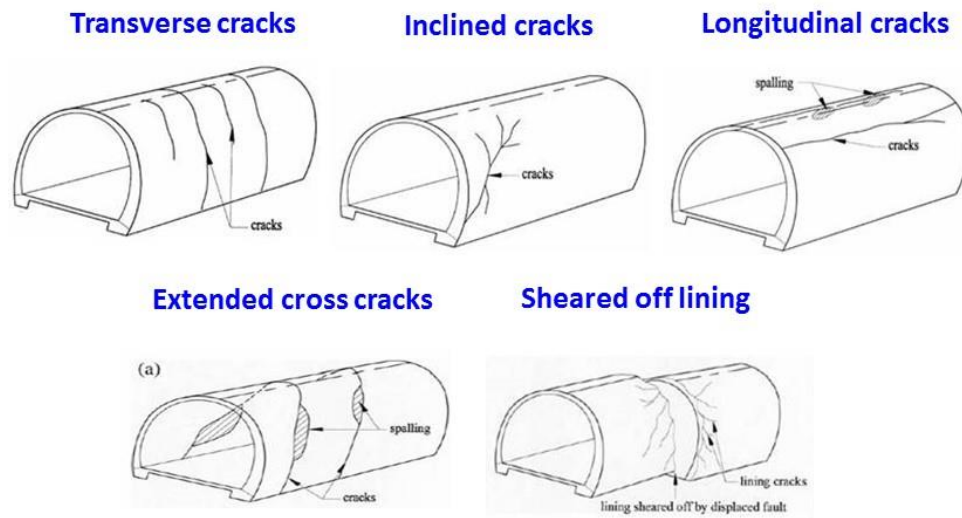


Figure 4.6. Types of tunnel damage (Wang et al. 2001).

It should be noted how in literature there are very few works focusing on the dynamic damages of segmental tunnel lining installed by mechanized excavation, probably due to the fact that this is a quite recent technology that has been experienced not very many observable damages. Dean et al. 2006 conducted an extensive literature search to find tunnel inspection reports from various earthquakes that have occurred in urban areas over the past 25 years and, concerning the segmental lining technology, the authors documented the case history of the *Isobe Dore Shield Tunnel* in Japan. After Kobe Earthquake of January 17, 1995 (Moment magnitude 6.9 and surface horizontal acceleration 0.5g), the damage report of Isobe Dore Tunnel stated the following (JSCE, 1995, p.152): "...there was some spalling in the grooves in the segments between segment rings; otherwise the structure remained undamaged..."

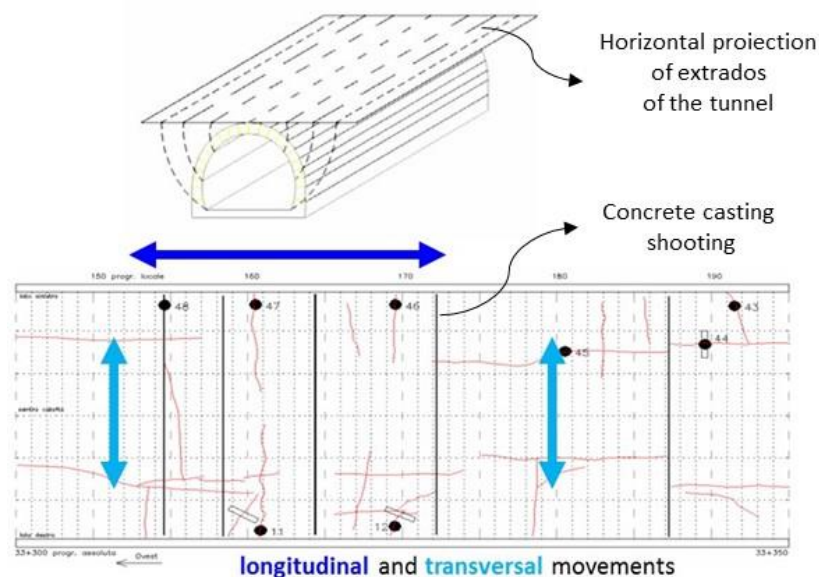


Figure 4.7. Damages after L'Aquila earthquake 2009 observed in Monteluco road tunnel in Italy (Valente et al. 2010).

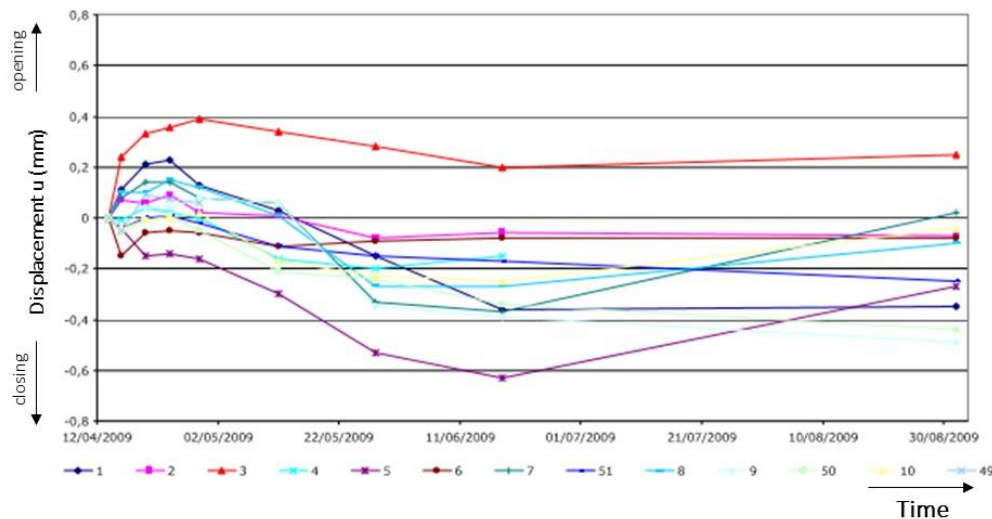


Figure 4.8. Long term monitoring of crack displacements in Monteluco road tunnel in Italy after L'Aquila earthquake (Valente et al. 2010).

This case history shows a different seismic performance of a segmental lining respect the continuous case; the presence of joints makes the lining globally more flexible, with a high demand of rotation in correspondence of the joints that, under high value of acceleration, can experience excessive rotation with a possible lost of watertightness as in the case of Isobe Dore Tunnel.

This issue is not very investigated in the technical literature that is more focused on the case of continuous tunnel lining, approaching the problem with different design methods.

In literature, there are two main approaches of analysis with different complexity and different reliability of the results:

- Uncoupled analysis
- Coupled full dynamic analysis

Uncoupled analysis can be considered a quasi-static approach where the seismic load acting on the structure in a static way is introduced in terms of equivalent forces (Forced-Based-Model, FBM) or equivalent field displacements (Displacement-Based-Method, DBM), assuming that the structure undergoes the free field ground deformation.

Overall the DBM is more appropriate and consistent with the physics of the problem (Pitilakis and Tsiniadis 2010) since the ground distortions generated by the seismic shaking affect the underground structure also that undergoes the soil deformation. The effect of the equivalent seismic load on the structure can be evaluated using analytical formulas (Wang 1993, Penzien & Wu 1998, Penzien 2000) or simplified numerical analysis. The analytical solution are more approximated because refer to a tunnel modelled as an elastic beam, modelling the relative soil-structure relative stiffness in the extreme cases of no slip and full slip interface condition, not considering explicitly the soil-structure interaction. The simplified numerical methods are less approximate approaches allowing an accurate evaluation of the input parameters for the soil-structure interaction analyses.

The full dynamic analysis is the most complete and detailed analysis level solving the motion equations, including the soil-structure interaction, in the analysis domain. Full dynamic analysis allows to investigate the non linear behaviour of the soil and of the structure and the effect of the main influence parameters.

The soil shear modulus G and the damping D for instance, are modified in a multi step procedure at every step of analysis, according with the shear deformation of the soil γ , estimated in the previous time

step for each soil depth. The degradation of the shear soil modulus $G(\gamma)$ and the increase of the damping ratio $D(\gamma)$ with the soil deformation level, are described by the selected $G(\gamma)$ - $D(\gamma)$ curve.

4.2 Approaches of analysis in plane strain

With reference to a real case study (Fabozzi *et al.* 2017) including a large open multi-propped excavation and a circular segmented tunnel in a densely urbanized area of the city centre in Napoli, the section in correspondence of San Pasquale Station (Figure 4.9) has been used to investigate some of the above mentioned aspects.

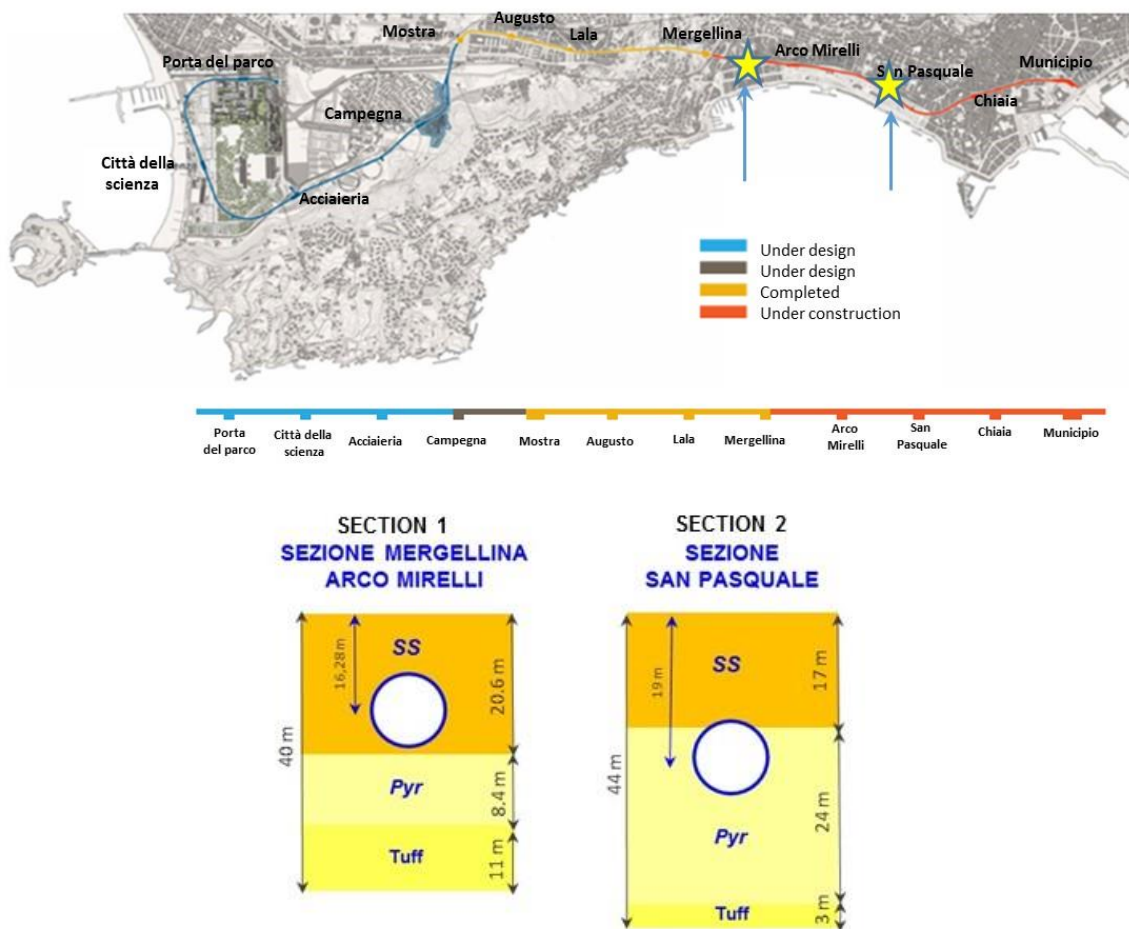


Figure 4.9. Localization of the analysis section and geotechnical model of subsoil of Section 2 - San Pasquale Station of Metro Line 6 of Naples.

The tunnel axis of San Pasquale section is deeper than that of section 1 studied in the Chapter 3 and excavated in between the SS and Pyr layers which have a different thickness respect the previous case.

The physical and mechanical parameters and the calibration of the constitutive model assumed for the three layers are the same of the Section 1 (see Table 3.2 and Table 3.3 respectively).

Pseudo static (DBM) and full dynamic analysis have been compared focusing on the effects of ground shaking on the increment of internal forces in the structure with respect to those acting in static conditions, preliminarily evaluated.

4.2.1 Pseudo-static analysis

Pseudo-static effect of an earthquake has been evaluated through the following steps:

1. numerical modelling of the excavation of the tunnel to calculate the initial state of stress action on the tunnel lining;
2. free-field FF seismic response analyses of the site to calculate the pseudo static load;
3. pseudo-static analyses: the equivalent seismic load calculated with the FF analysis is statically applied to the structure as a distribution of displacements. The quasi-static analysis allows to evaluate the dynamic increment of internal forces in the lining respect the initial static ones.

1. NUMERICAL MODELLING OF THE EXCAVATION OF THE TUNNEL

The segmental section of the tunnel (Figure 4.10a), whose geometry was already described in details in Chapter 3, was modelled for simplicity as an equivalent continuous concrete ring (Figure 4.10b) in the numerical analyses, adopting an equivalent inertia of the lining section, I_{eq} (Table 4.1), defined as proposed by Muir Wood (1975), by the following formula:

$$I_{eq} = I_j + \left(\frac{4}{n}\right)^2 I \quad (4.1)$$

where n is the number of joints, I_j the inertia of a single joint, I that of the continuous lining.

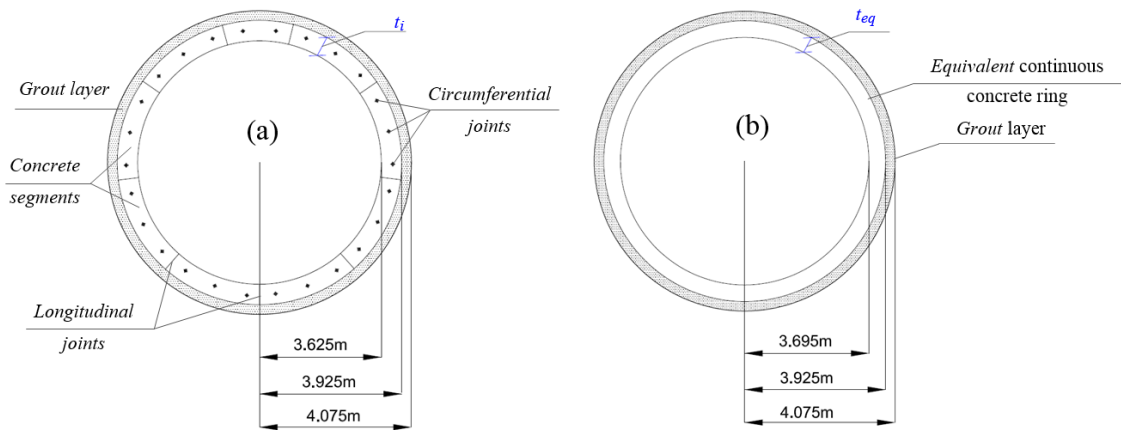


Figure 4.10. (a) Actual vs. (b) simplified geometry of the segmental tunnel lining.

A linear elastic behaviour was assumed for both concrete and grout, with the relevant parameters already summarized in Table 3.3.

The FE mesh of the subsoil and the tunnel developed in Plaxis 2D is shown in Figure 4.11. The lateral boundary conditions during static analysis consisted of fixed displacements in the horizontal direction at the vertical sides of the model and fixed displacements in both directions at the bottom. Displacements along the upper surface were set free.

An interface between the grout and the soil was introduced, with a reducing factor $R = 0.7$ applied to strength and stiffness of the interface material, compared to the surrounding soil.

Material	I m^4/m	t_i m	I_{eq} m^4/m	t_{eq} m
Concrete	0.00225	0.30	0.00101	0.23
Grout	0.00028	0.15	-	-

Table 4.1: Equivalent parameters of the continuous lining.

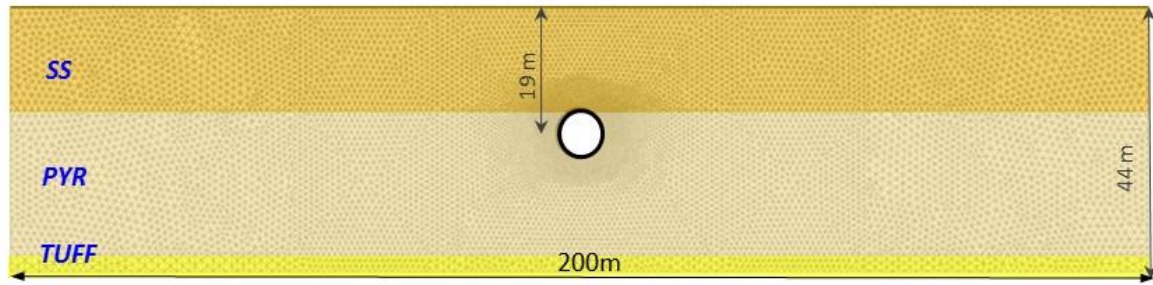


Figure 4.11. 2D FE numerical model.

In order to reproduce the state of stress around the tunnel cavity, taking into account the 3D arching effect that occurs within the soil and the deformations before lining installation, the initial lithostatic stress, σ_0 , was proportionally reduced around the cavity to:

$$\sigma = (1 - \lambda) \sigma_0 \quad (4.2)$$

where the stress relaxation coefficient λ was assumed equal to 0.3. The excavation was then simulated through three phases:

- Phase 1. Generation of the initial lithostatic stress field;
- Phase 2. Stress relaxation;
- Phase 3. Lining installation and grouting, in drained conditions.

Figure 4.12 shows the results of calculations in terms of bending moment M and normal force N induced in the tunnel lining by such a simplified 2D excavation process. Starting from this static state of stress, pseudo-static and full dynamic analyses were performed, as detailed in the following sections.

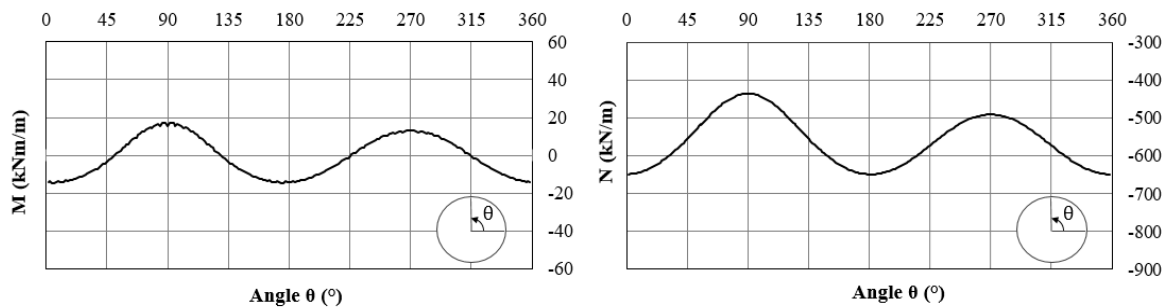


Figure 4.12. Static internal forces in the tunnel lining.

2. FREE-FIELD SEISMIC RESPONSE ANALYSES

According to the Probabilistic Seismic Hazard Analysis (PSHA), adopted by the Italian Building code (NTC, 2008), the reference value of the peak ground acceleration, a_g , for a given design limit state, is related to the probability of exceedance, P_r , of the earthquake along the reference life cycle of the building or infrastructure, VR . For the studied site, the median hazard curve shown in Figure 4.13a provides a value of $a_g=0.168g$, by assuming a 'life safety limit state' (i.e. $P_r=10\%$), and $VR=50y$, which correspond to a return period, TR , of the design earthquake as high as 475y.

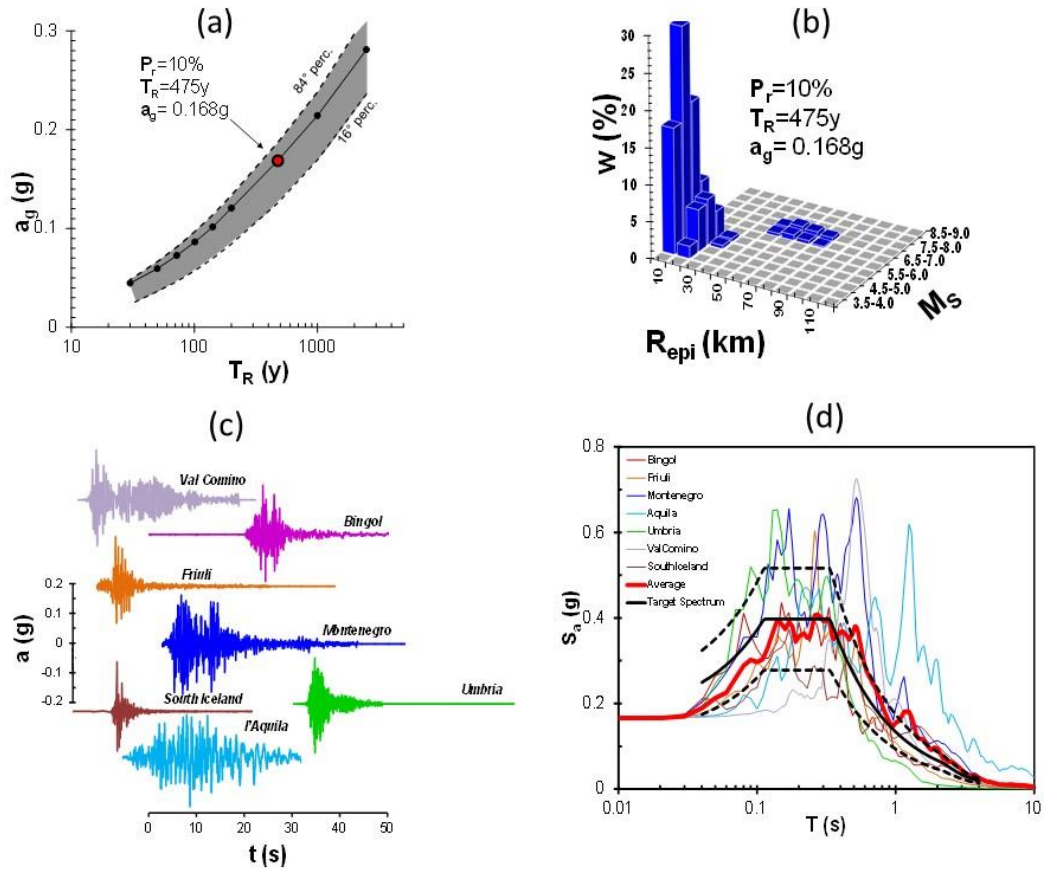


Figure 4.13. (a) Seismic hazard curve for 'Riviera di Chiaia' site; (b) de-aggregation chart; (c) selected accelerograms; input and target spectra (d).

Figure 4.13b reports the corresponding de-aggregation histogram, providing the relative contribution, w (%), to the selected hazard value as a function of the magnitude, M_s , and site-source distance, R_{epi} . The plot reflects the major influence of near-field seismic sources with relatively low potential magnitudes, located in the volcanic areas surrounding the city, compared to the minor dependence of the hazard curve of peak acceleration from far-field high-magnitude sources, pertaining to the Apennine chain fault systems.

The selection of natural seismic input motions used in the dynamic analyses was performed using REXEL code (Iervolino et al., 2009); seven seismic records on rock outcrop belonging to the ranges of $4.5 < M_w < 7$ and $0 < R_{epi} < 100$ km, encompassing the whole de-aggregation histogram (see Figure 4.13b), were selected and scaled to $a_g=0.168g$ in order to result compatible, on the average, with the uniform hazard 'target' spectrum specified by the seismic hazard map for the site, by considering a soil class 'A'

(stiff rock outcrop) according to the NTC (2008). Figures 4.13c-d respectively show the selected time histories and the corresponding elastic response spectra, these latter plotted together with the mean and the target spectrum. Table 4.2 reports the main features of the selected signals, all recorded at European seismic stations, which were subjected to a band-pass filtering in the range of 0.1-25 Hz prior to the seismic response analyses. Given the flatness of the area and the relatively homogeneity of the subsoil, characterized by horizontal soil layering, any topographic effect was excluded and the stratigraphic amplification of the free-field motion was evaluated by means of one-dimensional seismic response analyses. The analyses were carried out using the EERA code (*Bardet et al., 2000*), operating in total stresses and in the frequency domain by a linear equivalent approach. The dependency on shear strain amplitude of the equivalent parameters (shear stiffness and damping ratio) of the materials SS, Pyr and Tuff1 was assumed as described by the curves shown in Figure 4.15.

Earthquake ID	Earthquake name	Date	Mw	Station ID	R_{epi} [km]	Waveform ID
2309	Bingol	01/05/2003	6.3	ST539	14.0	7142
34	Friuli	06/05/1976	6.5	ST20	23.0	55
93	Montenegro	15/04/1979	6.9	ST64	21.0	198
291	Umbria Marche	06/10/1997	5.5	ST236	5.0	651
2142	South Iceland	21/06/2000	6.4	ST2558	5.0	6349
71	Val Comino	11/05/1984	5.5	ATQ	17.4	276
178	l'Aquila	06/04/2009	6.3	FMG	19.3	806

Table 4.2: Main features of the selected seismic signals.

Figure 4.14 shows the results obtained for the seven input motions in terms of vertical profiles of (a) maximum acceleration, a_{max} , (b) maximum shear strain, γ_{max} , and (c) maximum horizontal displacement relative to the bedrock, u_{max} and mobilized value of normalized shear stiffness, G_{mob}/G_0 (d).

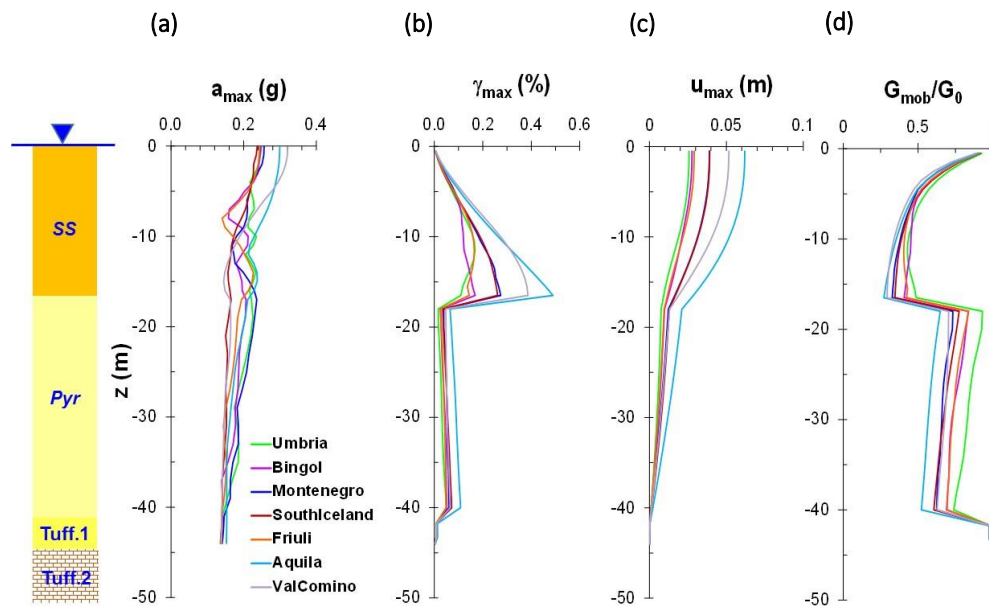


Figure 4.14. Results of 1D linear equivalent response analyses.

It can be observed how highest shear deformations develop within the more deformable SS surface layer and, in particular, L'Aquila earthquake (light blue line) induces the highest, the largest strains throughout the whole soil layering and consequently, the highest horizontal displacements.

This latter input motion was therefore viewed as the most conservative loading condition for predicting the seismic performance of the tunnel with the analyses which will be described in the following sections.

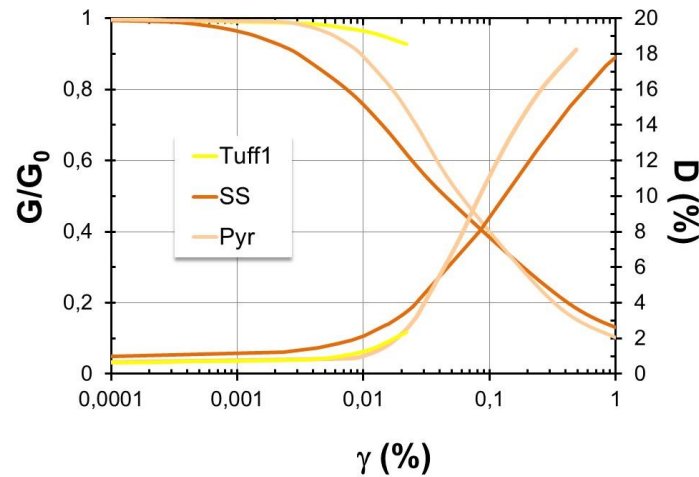


Figure 4.15. Variation with shear strain of normalized stiffness and damping ratio for SS, Pyr and Tuff1.

3. PSEUDO-STATIC ANALYSES

The effect of an earthquake is simulated with an equivalent seismic load, statically applied to the structure generally as a distribution of inertia forces or displacements (e.g. Argyroudis & Pitilakis 2012, Do et al. 2015).

The results of the free-field seismic response analyses described in the previous section were therefore used as pseudo-static loading of the same subsoil-structure models adopted for the static analyses reported in the previous section. The profile of peak horizontal displacements corresponding to the free-field soil response to L'Aquila earthquake (light blue line in Figure 4.14c) was statically applied to the boundaries of the numerical model. The soils were modelled as linearly elastic, by adopting the profile of the equivalent shear modulus, G_{mob} , mobilized in the corresponding free-field analysis (light blue line in Figure 4.14d).

Figure 4.16 shows the FEM mesh adopted in the pseudo-static analysis of the tunnel, with a simplified pattern of the boundary conditions. The distribution of displacements corresponding to the input motion was applied at a distance of three diameters from the tunnel.

The numerical mesh consists of 135.273 elements, with an average size of 0.5m. The lateral boundary conditions during pseudo-static analysis allow for free displacements along the vertical direction; the bottom nodes of the domain are fixed, while those at surface are free to move in vertical direction, and constrained to a constant horizontal displacement equal to the maximum free-field value, as also assumed in previous literature studies (e.g. Do et al., 2015; Tsiniadis et al., 2016).

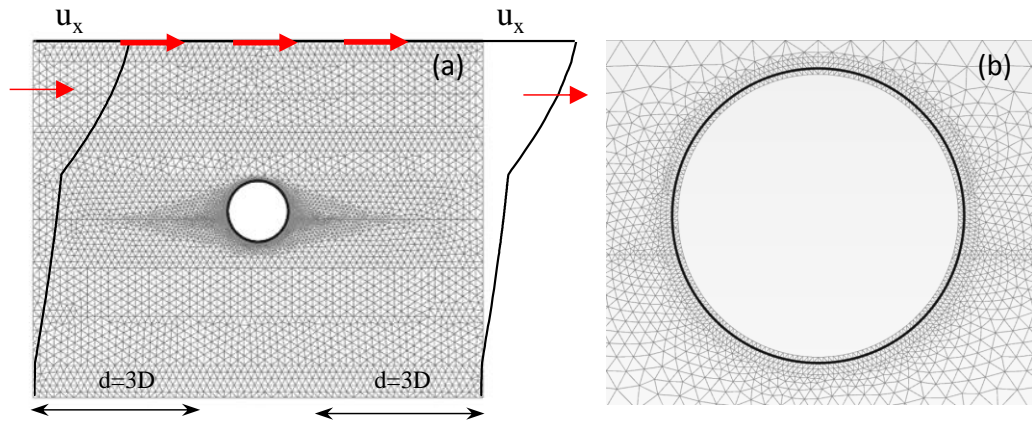


Figure 4.16. (a) Mesh and boundary conditions of the numerical model for pseudo-static analysis of the tunnel, (b) detail of the mesh around the tunnel.

Figure 4.17 shows the contours of horizontal displacements predicted with the above numerical model in free-field conditions (a) and with the presence of the structure (b). The first drawing confirms that the reduced size of the domain was enough to reproduce a homogeneous field of displacements, while the second contour shows the ‘shadowing’ effect induced by the presence of the tunnel on the deformation of the soil around.

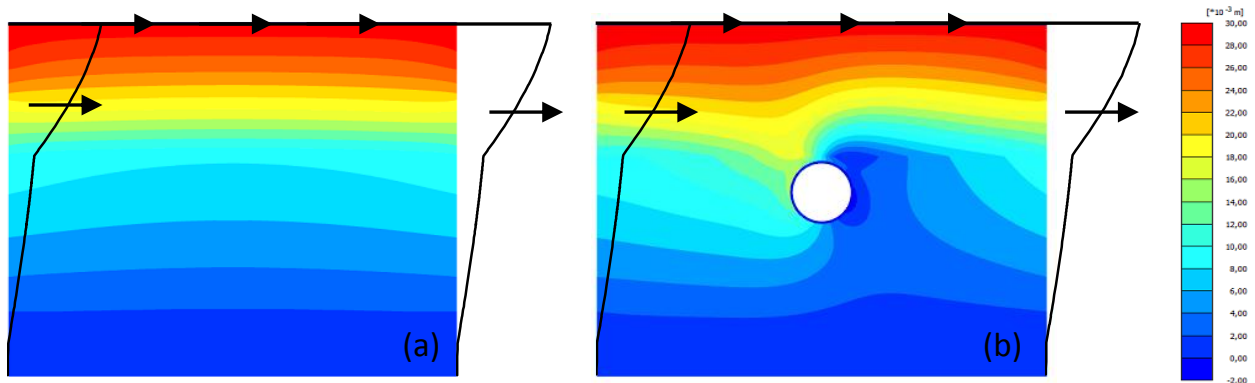


Figure 4.17. Contours of horizontal displacements in free-field conditions (a) and with soil-tunnel interaction (b).

The numerical model used for the pseudo-static analysis (Figure 4.16) has been assumed after a number of sensitivity analysis on the effect of the the distance ‘ d ’ of the boundaries from the tunnel axis and the effect of the presence of the constant horizontal displacement on the top of the model. Figure 4.18a for instance shows as, for a fixed value of boundaries distance (d equal three times the tunnel diameter) the presence of the constant horizontal displacement allows to model an uniform distribution of the imposed horizontal displacements profile to the entire domain. In this case of consequence, the effect of the distance ‘ d ’ (Figure 4.18b) is negligible. On the contrary, in the case of absence of the constant horizontal displacement on the top, the model is not able to induce an uniform deformation mechanism in the entire domain and this effect is amplified increasing the boundaries distance ‘ d ’ (Figure 4.18c).

Note that the displacements profiles shown in Figure 4.18 refer to the middle section of the 2D numerical model.

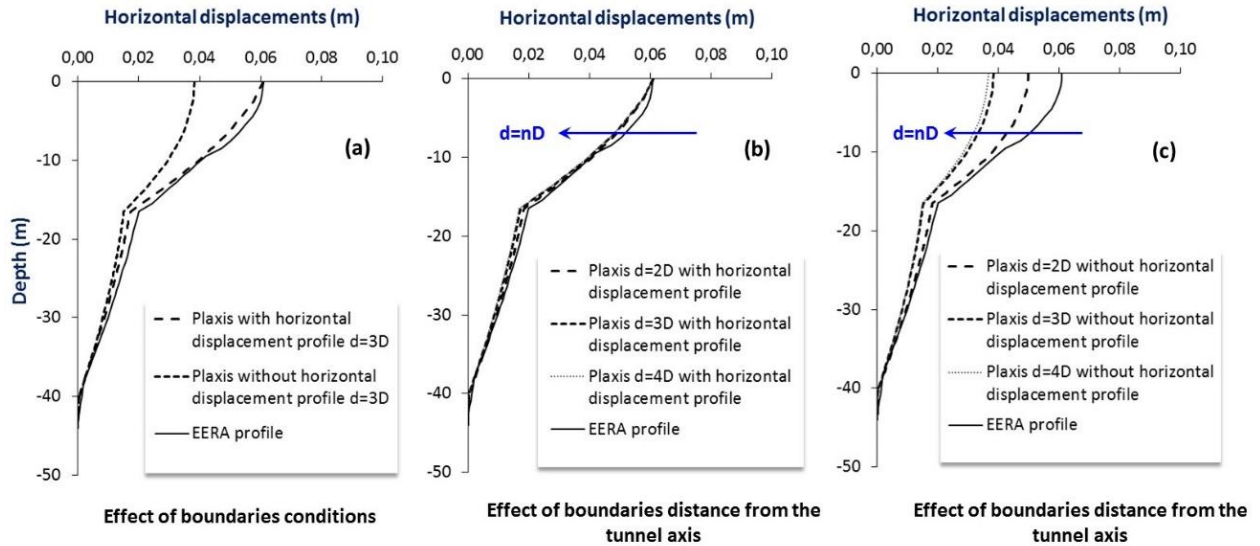


Figure 4.18. Influence of the boundaries condition and the boundaries distance 'd' on the pseudo-static analysis: horizontal displacement profiles in correspondence of the mid section of the 2D model.

The effect of the boundary distance from the structure was investigated also in terms of increments of internal bending moments, ΔM , and hoop forces, ΔN , induced in the transverse tunnel section, only for the case modelling the horizontal displacement constrain.

Figure 4.19 shows the comparison for the cases of boundary distance, d , equal to three, two and one time the tunnel diameter, D . Differences are negligible if not null.

The chosen model good reproduce the homogeneous field of displacements.

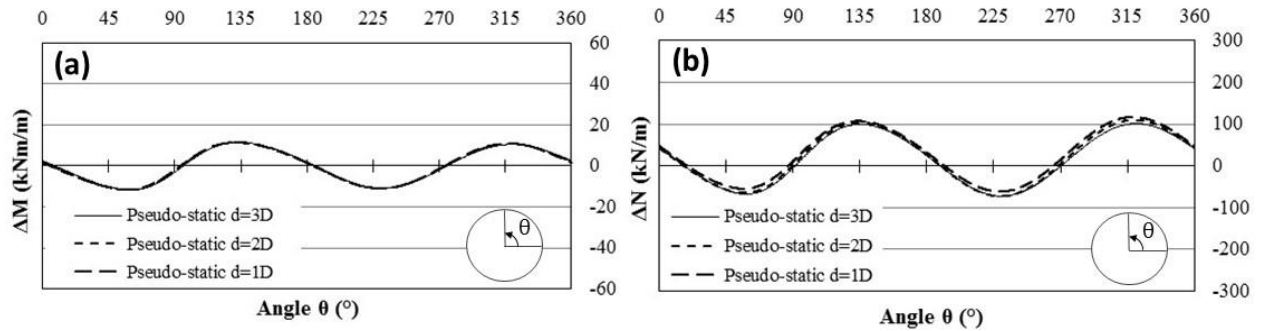


Figure 4.19. Influence of boundaries on the pseudo-static increments of bending moments (a) and hoop forces (b).

4.2.2 Full dynamic analysis

Full dynamic analyses that follow a coupled approach for the soil-structure interaction, provides satisfactory interpretation of non-linear boundary problems during earthquakes.

Mereover, they provide a reliable tool for the seismic design of tunnels, including soil-structure interaction and irreversible soil behaviour (Lanzano G. & Bilotta E. 2014, Lanzano G. et al 2014).

A coupled approach was followed, by including the soil-structure interaction in the step-by-step solution of the equations of motion in the time domain, this time accounting for the pre-failure non-linear behaviour of soil through the 'HSs' constitutive model (Appendix 2).

It is worth mentioning that the same FE mesh used for static analysis (see Figure 4.11) was originally calibrated for the full dynamic analysis. As a matter of fact, the width of such numerical model was originally optimized by a series of sensitivity analyses, in order to reach a true free-field condition at the lateral borders and to minimize the influence of vertical boundaries, modelled with viscous dashpots as suggested by *Lysmer & Kuhlemeyer (1969)*. Also, the mesh was discretized aiming at a reliable propagation of the maximum significant frequency of the input signal (*Kuhlemeyer & Lysmer 1973*), leading to an average size of 0.65m (Figure 4.20).

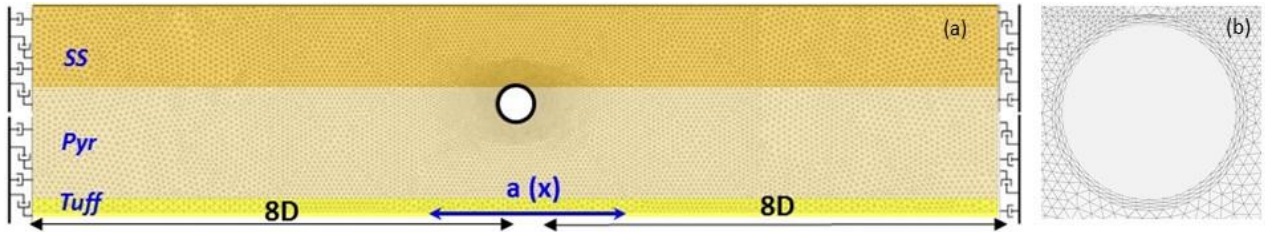


Figure 4.20. (a) Mesh and boundary conditions of the numerical model for full-dynamic analysis of the tunnel; (b) detail of the mesh around the tunnel cavity.

The reference input motion of L'Aquila earthquake was applied at the rigid base of the model (rigid base means fix-end boundary, that is any downward-traveling waves in the soil will be completely reflected back toward the ground surface by the rigid layer) as a time history of acceleration.

An additional small-strain viscous damping was introduced in the dynamic calculation by means of the well-known Rayleigh formulation (*Park & Hashash 2004*), which considers a linear combination of the mass $[M]$ and the stiffness $[K]$ matrices as follows:

$$[C] = \alpha_R[M] + \beta_R[K] \quad (4.3)$$

The damping coefficients, α_R and β_R , were calculated following to the 'double frequency approach', assuming as target values the first natural frequency of the deposit and the main frequency of the input motion. The full dynamic analysis of the tunnel-subsoil system with a non-linear soil constitutive model allowed for predicting the evolution of the internal forces in the lining starting from the excavation stages and until the end of shaking.

Figure 4.21 indeed, shows the time history of the bending moment and the hoop force at the section $\theta=283^\circ$, where the ratio M/N reaches its maximum value over time. The residual bending moment is equal to 8.5 kNm/m, with a peak value of 54 kNm/m, while the residual normal force is equal to 630 kN/m, with a peak value of 692 kN/m.

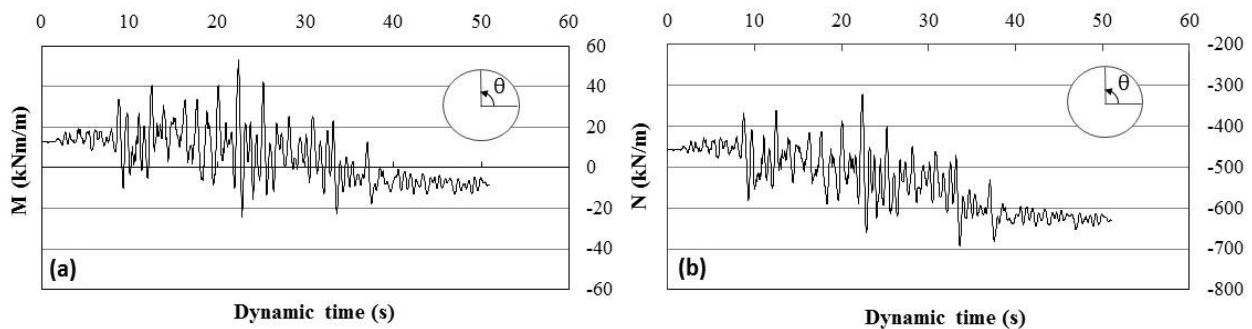


Figure 4.21. Time histories of (a) bending moment, M , and (b) hoop force, N , at the section located at $\vartheta=283^\circ$ in the lining.

Figure 4.22 shows the distribution of the dynamic increment of bending moment ΔM and hoop force ΔN in the transversal tunnel section in correspondence of the peak acceleration of the input signal.

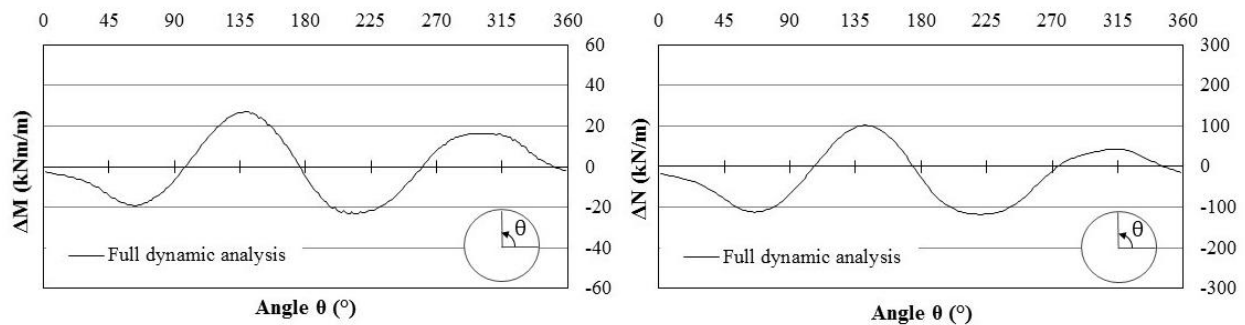


Figure 4.22. Increment of the dynamic increment of bending moment ΔM and hoop force ΔN in the peak acceleration of the full dynamic analysis.

4.2.3 Comparison

Figure 4.23 shows the increments of internal forces around the whole lining resulting from the pseudo-static and full dynamic analyses; in this latter case, the values plotted are those predicted at the time of peak acceleration, for consistency with the assumptions made for applying the pseudo-static approach.

The comparison shows that, at least for this particular case, the pseudo-static analysis underestimates the increment of forces with respect to the full dynamic analysis. This result is in agreement with other previous studies (Bilotta *et al.*, 2007; Argyroudis & Pitilakis, 2012; Tsinidis *et al.*, 2016) showing, in almost all cases of flexible lining, an underestimation of the dynamic increment of the internal forces with the simplified pseudo-static approach as a function of the interface behaviour.

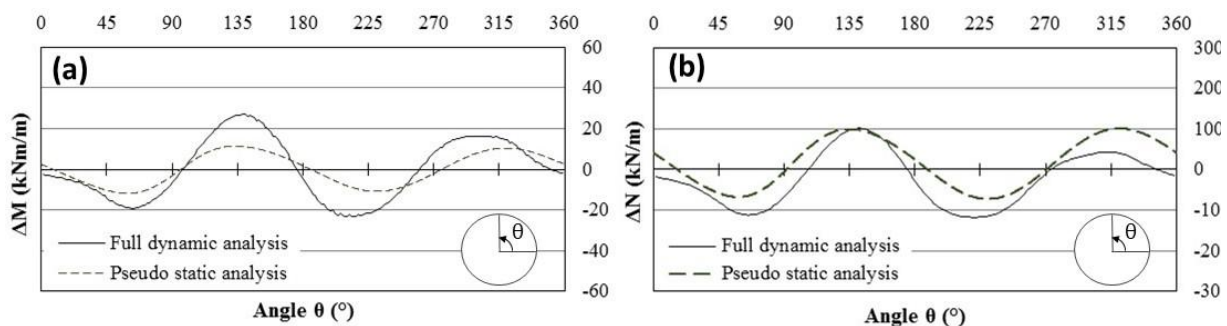


Figure 4.23. Comparison between pseudo-static and full dynamic analyses in terms of seismic increments of (a) bending moment, ΔM , and (b) hoop force, ΔN .

Figure 4.24 for instance shows the effect of the interface friction on the lining internal forces; reducing the friction factor, therefore tending towards a smoother interface, it can be observed a reduction of dynamic increment of normal forces, up to a value about equal to 40%.

The dynamic increment of bending moment is not very influenced by the interface behaviour

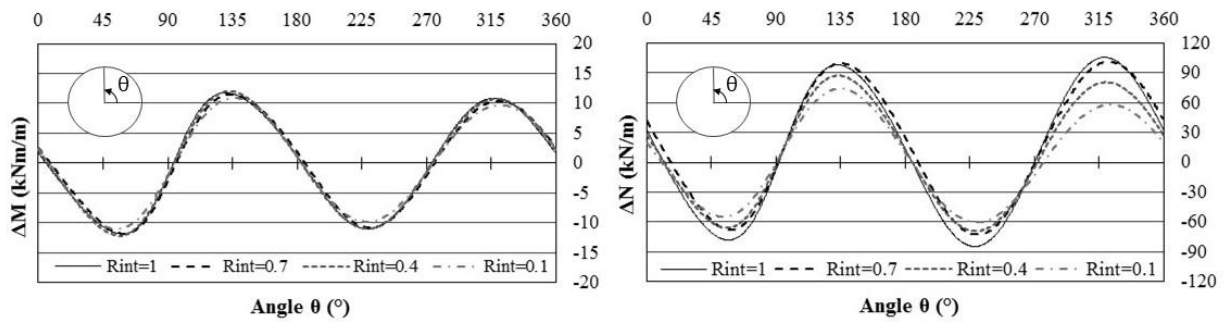


Figure 4.24. Effect of the soil-structure interface behaviour in terms of dynamic increment of internal forces.

4.3 Comparison between dynamic behaviour of segmental and continuous lining

The complex interaction mechanism between the tunnel structure and the surrounding soil during dynamic shaking can be monitored during centrifuge tests on physical models at reduced scale. These tests allow the main mechanisms involved in the evolution of observed phenomena to be identified and provide an extensive base of experimental data to calibrate advanced numerical methods of analysis in ideal situations where soil properties, boundary conditions and dynamic loads are clearly defined.

This paragraph illustrates the results of a numerical study aimed at modelling the performance of continuous and segmental linings of shallow tunnel under seismic loading. A set of 3D finite-element full dynamic analyses have been carried out, calibrated on the experimental results of a centrifuge test on a model tunnel in a dense dry sand layer subjected to transversal dynamic loading (Lanzano G. *et al* 2012). The numerical study was extended to model and compare the seismic demand of a continuous and a segmental reinforced concrete lining, including the effect of the excavation process on the pre-seismic conditions and the influence of different input signals.

The results show that 1) even in rather simple ground conditions, a suitable constitutive model for soil is needed to capture the effect of soil-lining interaction during and after the seismic event; 2) the effect of the construction stage on the seismic demand of the tunnel lining is clearly evidenced, indicating that the pre-seismic ground conditions influences the magnitude of changes of internal force during and after shaking; 3) the significant effect of the jointed pattern of a segmental lining, which implies a larger flexibility and compressibility in the transverse section, compared to a continuous lining, hence lower structural demand.

4.3.1 Experimental benchmark

The centrifuge test model T3, described in details by Lanzano G. 2009, is the experimental benchmark for the validation of the numerical model used for the study, then extended to model a realistic case, more complex in terms of geometry of the lining and considering natural input signals

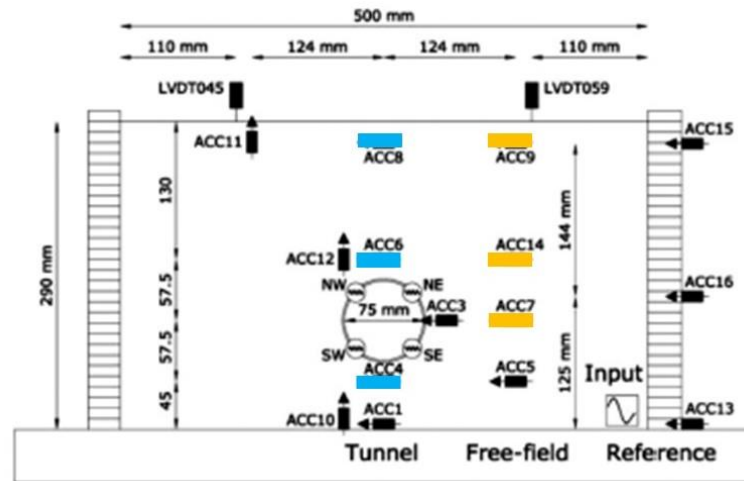
It is the aluminium model of a tunnel (diameter $D=75\text{mm}$, thickness $t=0.5\text{mm}$, cover $C=150\text{mm}$) embedded in a layer of dry Leighton Buzzard sand (fraction E) at relative density of 75% (Figure 4.25). At prototype scale (scaling factor $N=80$), the tunnel diameter is 6 m, the tunnel axis depth is 15 m and the lining thickness is comparable to that of a concrete lining about 0.06 m thick. Figure 4.27 shows for instance, the main scaling laws to compare the model and the prototype.

Vertical and horizontal accelerometers have been used to measure the accelerations of the soil during

the shaking, LVDT in vertical direction for the displacements reading at surface and four strain gauges along the transverse tunnel section for the of lining strains monitoring.

The numerical model has been implemented in the finite element (FE) code Plaxis 3D. Figure 4.26 shows the numerical mesh of model T3 at prototype scale: the vertical depth is 80 times the relevant small scale dimension (23.2 m), the width (200 m) has been established by a series of parametric analyses in order to reach a free-field condition and minimise the influence of boundaries. A longitudinal stretch of the model of 150 m has been considered to guarantee plane strain conditions in the central reference section, to be compared to the experimental results.

(a)



(b)

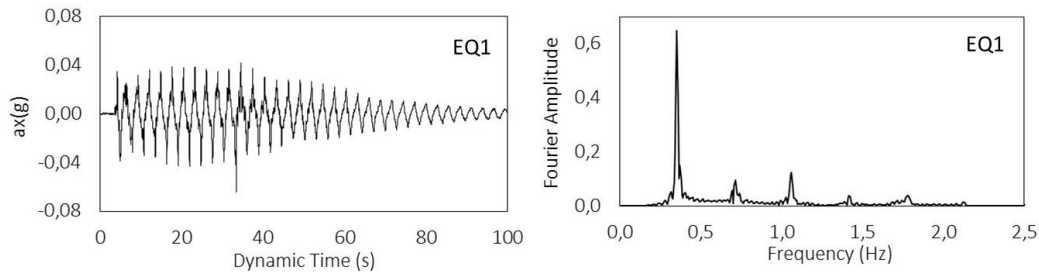


Figure 4.25. (a) Layout of model T3; (b) Input motion EQ1 reference ACC13 (at prototype scale).

The lateral boundary conditions consist on fixed displacements in the horizontal direction perpendicular to the vertical sides of the mesh in static condition; viscous dashpots are applied during dynamic stages of analysis (Lysmer & Kuhlemeyer 1969), the base of the model is fixed both in vertical and in horizontal directions, the nodes at the top surface instead are completely free. The minimum mesh size was set as a function of the maximum investigable frequency of the signal $f_{max} = 0.375$ Hz (Kuhlemeyer & Lysmer 1973).

The pseudo-harmonic input signal, read by the reference accelerometer ACC13 and scaled up to prototype scale (Figure 4.27b), was applied at the base of the numerical model. It was preliminary band-pass filtered in the interval of frequency 15–130 Hz in order to reduce the high-frequency content of the signal.

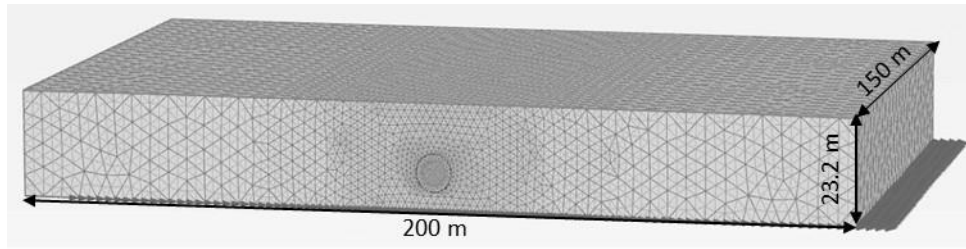


Figure 4.26. Three dimensional numerical mesh.

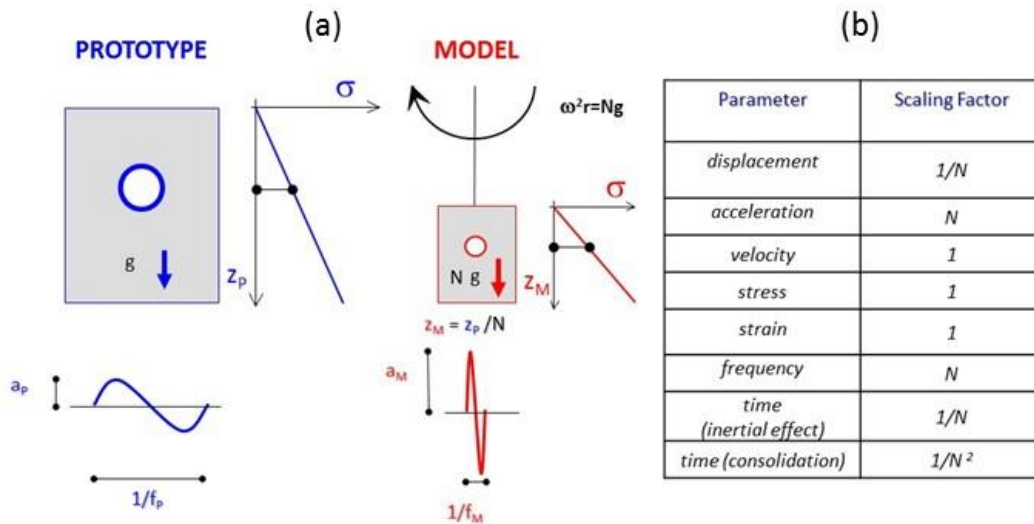


Figure 4.27. (a) Stresses distribution in the prototype and the centrifuge model; (b) Scaling factor prototype model.

The lining is a structural elastic plate ($EI=3.7 \cdot 10^2$ kNm²/m; $EA=2.8 \cdot 10^6$ kN/m) with a very smooth interface; the interface factor $R_{interface}$, available in the code to define the interface conditions, was set equal to 0.05, as calibrated by *Lanzano et al. 2014* matching the best interpretation of experimental dynamic increments of hoop forces, a reasonable value for relative flexible tunnel subjected to a “soft” seismic loading conditions. The dynamic behaviour of the sandy layer has been modelled with the Hardening Soil with small strain overlay constitutive model (*Benz 2007*) using the parameters shown in Table 4.3.

φ °	ψ °	c' kN/m ²	E_{ref}^{50} kN/m ²	E_{ref}^{oed} kN/m ²	E_{ref}^{ur} kN/m ²	$\gamma_{0.7}$ -	G_0^{ref} kN/m ²	p_{ref} kN/m ²	$\alpha_{Rayleigh}$ -	$\beta_{Rayleigh}$ -
38.6	8.2	0.01	18.60E ³	20.50E ³	60.16E ³	0.50E ⁻³	72.70E ³	100	0.0668	0.704 E ⁻³

Table 4.3 Soil properties and constitutive models calibration (*Lanzano G. et al. 2016*).

The mechanical parameters of the soil were derived from *Lanzano et al. 2016*.

Figure 4.28 and Figure 4.29 show the comparison between some experimental and numerical results in terms of accelerations time histories and Fourier spectra along the **tunnel** and the **free field** respectively. The numerical results are in good agreement with the experimental data, both in terms of acceleration and in terms of Fourier amplitude. There is an evidence of over-amplification of the signal at high frequencies, as observed also by *Conti et al. 2014* and *Amorosi et al. 2014*, partially reduced by the additional contribution of the introduced Rayleigh damping (Figure 4.30).

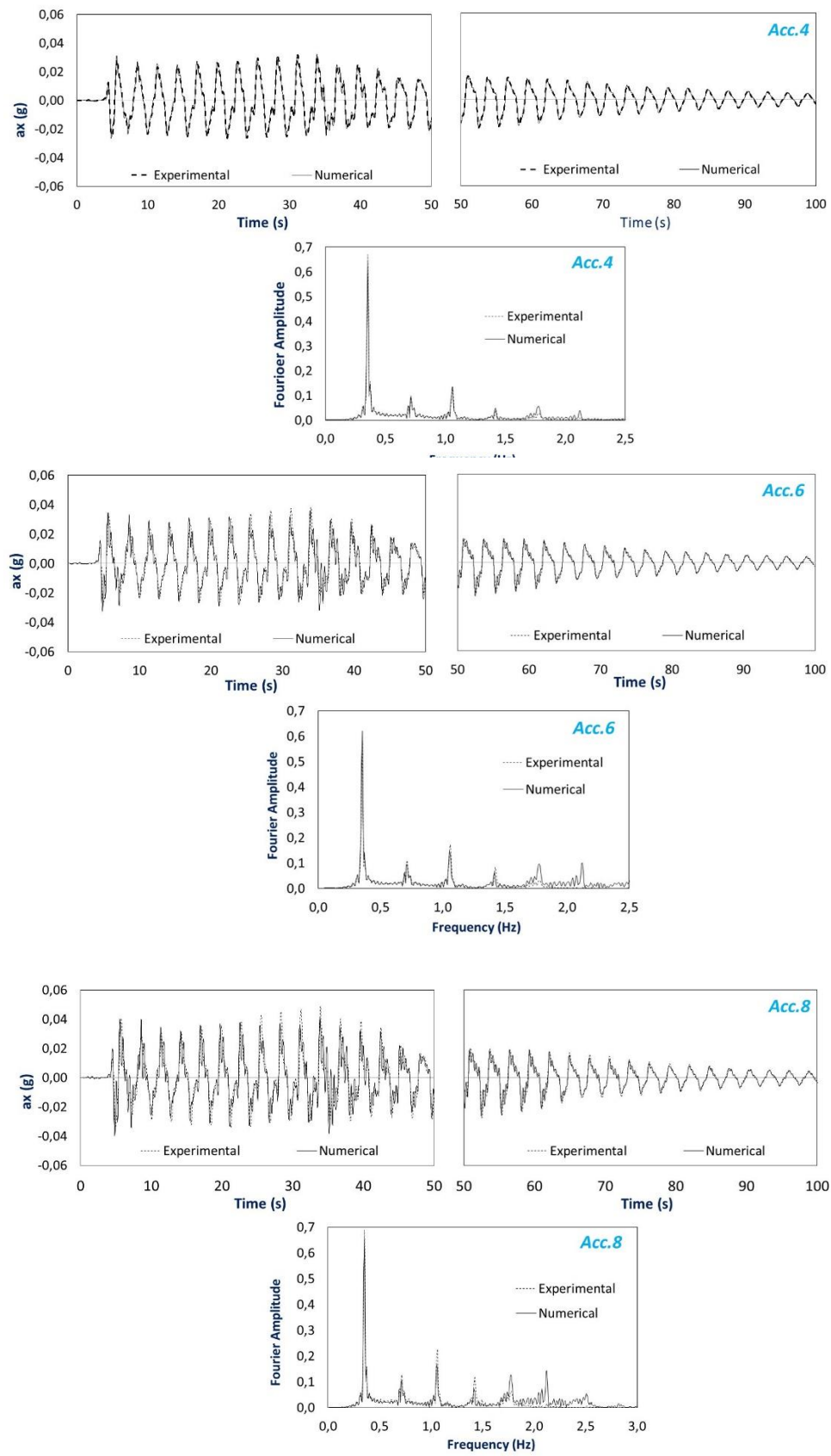


Figure 4.28. Comparison between experimental and numerical results in correspondence of the accelerometers along the tunnel vertical.

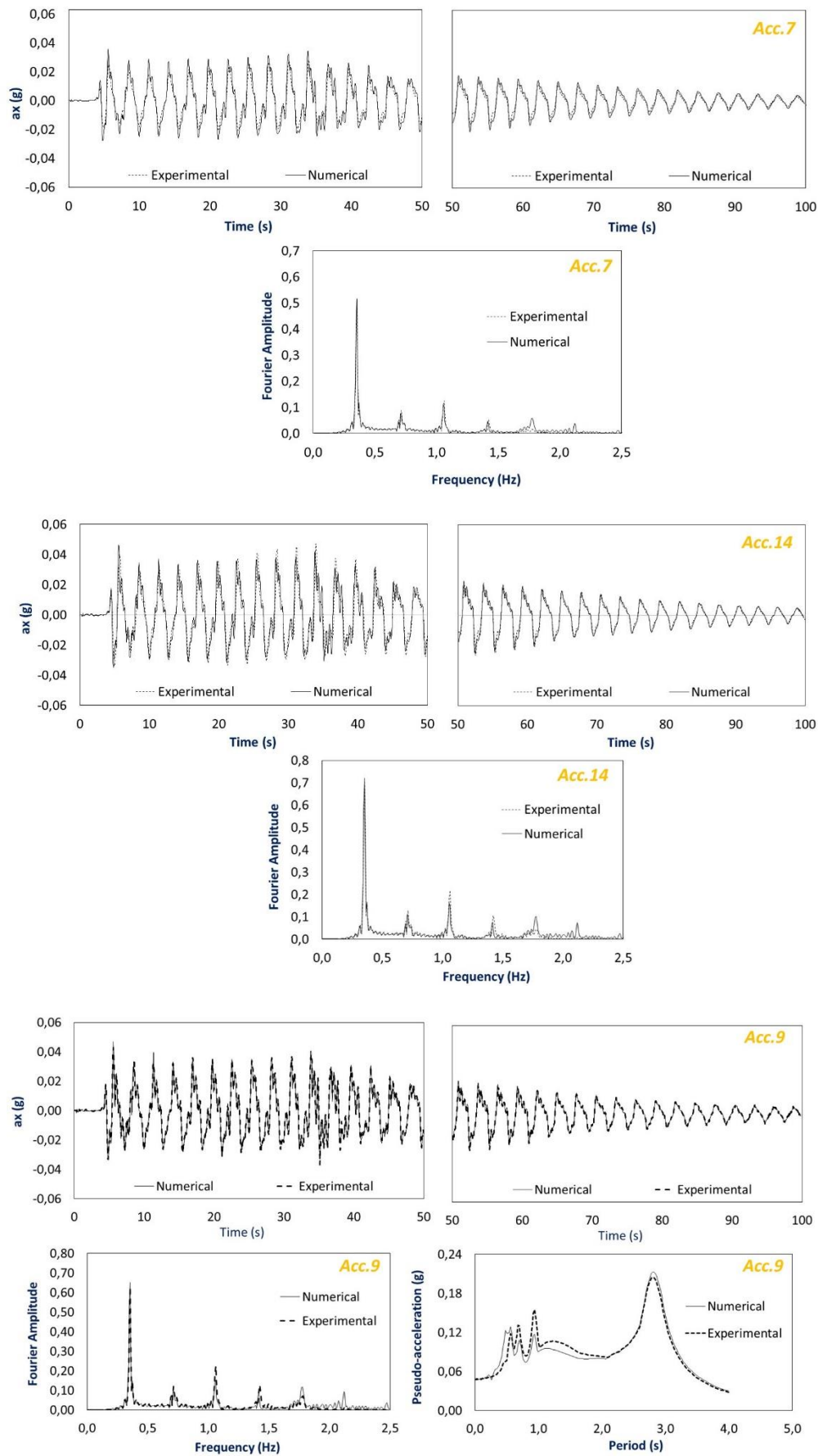


Figure 4.29. Comparison between experimental and numerical results in correspondence of the accelerometers along the free field vertical.

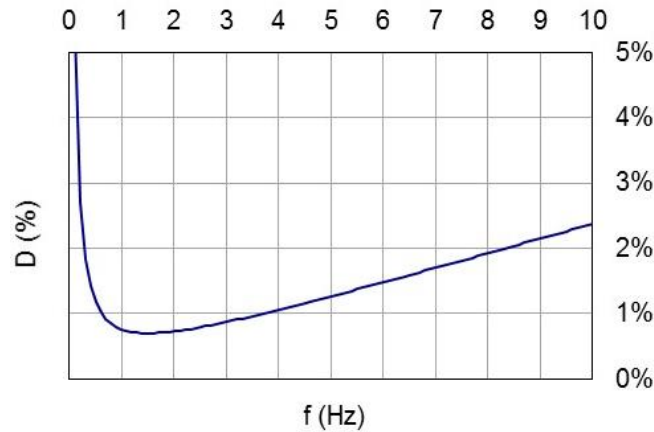


Figure 4.30. Rayleigh damping function adopted in the numerical analysis.

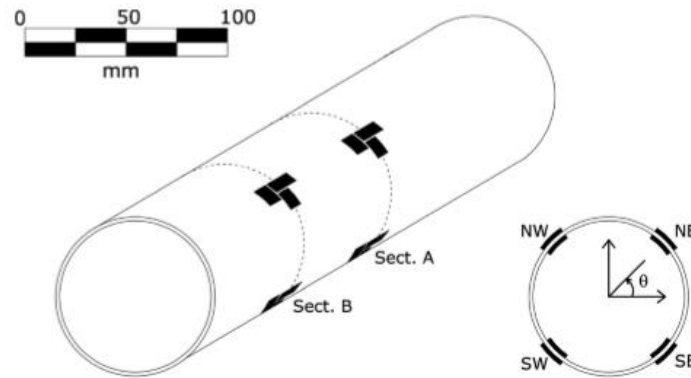


Figure 4.31. Strain gauges location layout (Lanzano et al. 2012).

As introduced above, the strain measurements on the tube were performed in two sections, to check that no boundary effects occurred and the plane-strain conditions were ensured. The main instrumented section (section A in Figure 4.31) was located at the mid-span of the tube and a second section was instrumented at 50 mm aside (section B in Figure 4.31).

Tab 4.4 shows the comparison between the experimental and numerical internal forces (M, N) at the end of the spin up stage.

The time histories of bending moments M and hoop forces N measured during model shaking are shown and compared with the numerical ones in Figure 4.32 and 4.33.

Positive values represent bending moment with tensile stress increments on the internal lining surface and compressive hoop force, respectively. Both values of bending moments (Figure 4.32) and hoop forces (Figure 4.33), experimental and numerical ones, have been carried out in prototype scale and refer those measured along the main section A, that are practically the same of those recorded in the section B.

Experimental data show a trend to increase during shaking, with a reversible change of internal forces due to the cycling loading and an their irreversible increment due to plastic strains arising in the soil during shaking.

Overall, the numerical results of the tunnel lining are less satisfactory than the soil ones, as observed in many other literature works (Bilotta et al. 2014, Lanzano & Bilotta 2014, Conti et al. 2014, Amorosi et

al. 2014, Tsinidis et al. 2016).

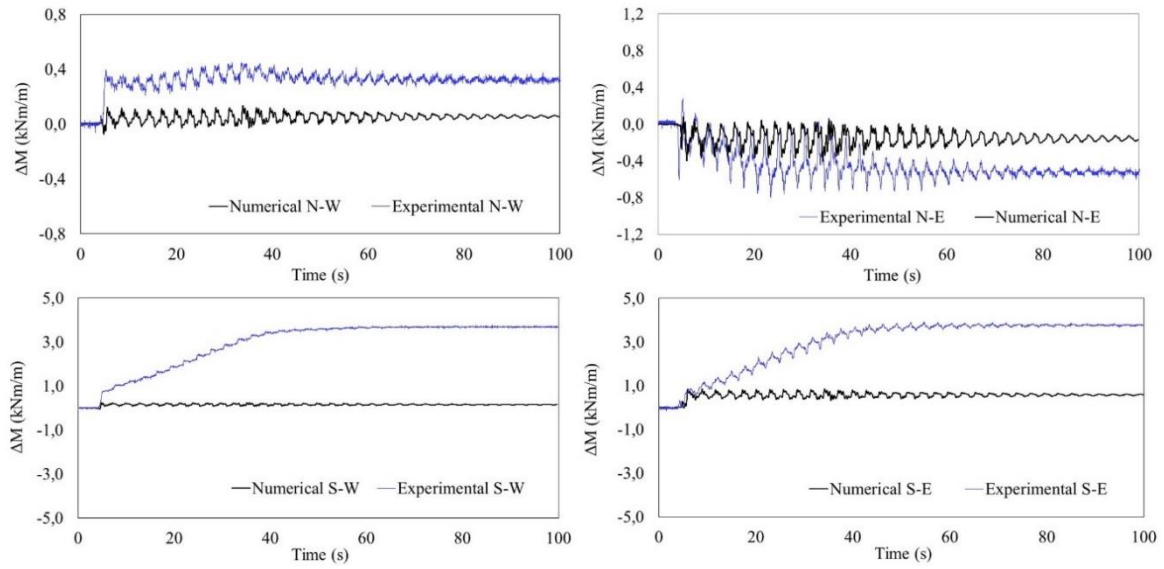


Figure 4.32. Comparison between experimental and numerical dynamic increment of bending moment.

For instance, the transient values of bending moment and hoop force are in reasonable agreement with the experimental ones while the permanent values are rather different, are underestimated in all cases. These latter are due to mainly the densification of the soil around the tunnel, as observed by Lanzano et al. 2012.

The different interpretation carried out by the numerical analysis of the permanent forces in the lining, may be due to a possible non homogeneity of the soil around the tunnel, not included in the numerical model. This possible condition could generate different soil-structure relative stiffness compared with that one computed in the model, and could affect the soil-structure interface behaviour also that is very influencing in term of hoop forces (see §4.2).

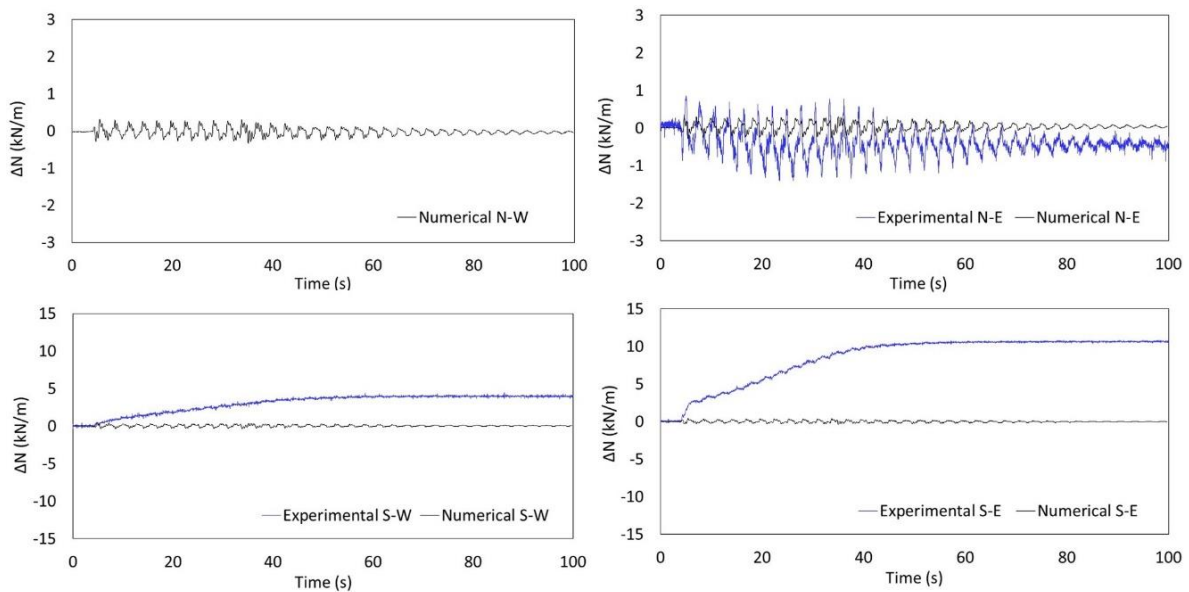


Figure 4.33. Comparison between experimental and numerical dynamic increment of hoop force.

There is also a scale effect on the computational numerical model response for the interpretation of the internal tunnel lining forces, switching from the model to prototype scale.

Lanzano e Bilotta 2014 infact, show how the different scale affects in particular the permanent rate of force rather than the reversible one. The prototype scale for instance, that was adopted in these numerical analysis, provides a closer interpretation of the experimental data respect the model scale in terms of normal forces in particular, less influencing the bending moments.

Once verified the ability of the 3D model to back-calculate the experimental results, the calculations were extended to analyse the behaviour in the same sand layer of different tunnel lining technologies, continuous and segmental one.

Continuous concrete lining has a thickness $t = 0.3\text{m}$ and diameter $D = 6\text{m}$. Axial and flexural stiffness of the ring were set to $EA = 10.5\text{E}^6 \text{ kN/m}$ and $EI = 78.75\text{E}^3 \text{ kNm}^2/\text{m}$, respectively, and a realistic interface was assumed setting $R_{\text{interface}} = 0.7$. With regard of the segmental lining, the joints pattern adopted in the analysis is the same of the static case of metro Line 6 of Naples (see Chapter 3).

A set of 3D full dynamic analysis have been performed using different natural input signals applied as time histories of acceleration at the base of the mesh, starting from different initial conditions, considering and not considering the effect of the tunnel construction. The main results are discussed in the next paragraphs.

4.3.2 Influence of pre-seismic conditions

Despite what was modelled in the centrifuge test, where the tunnel lining was already in place when the ground stresses were applied during spin up, in reality tunnelling involves a rather complex construction process. Such a process modifies the soil stresses around the tunnel and this may influence the dynamic response of the tunnel lining during following shaking. Hence the effects of a full excavation process were taken into account in the analyses.

Typical mechanized tunnelling by an earth pressure balance (EPB) machine was simulated in the analyses by modelling in stages the advancement of lined cavity up to the completion of the full tunnel stretch, as follows. A stiff cylindrical plate modelled the TBM shield. To take into account the shield tapering a linearly varying diameter contraction was applied along the plate, up to a maximum value of 0.2%. The last installed ring of lining, positioned under the TBM tail skin, was modelled with an elastic volume of concrete ($E=36 \text{ GPa}$) and loaded in longitudinal direction by a jack thrust of 30 MN. Just behind the installed ring, the injected grout in its early fresh state was modelled by applying an uniform radial pressure both on the adjacent ring and against the soil; along the rest of the lining the hardened grout was modelled as a layer 0.15 m thick, having an elastic stiffness $E=15 \text{ GPa}$. The effect of grout hardening has been modelled in a more simple way respect that shows in the Chapter 3.

In Figure 4.34 the distribution of bending moment (Figure 4.34a), hoop force (Figure 4.34b) and longitudinal force (Figure 4.34c) in the transverse reference section are shown referring to the static 'pre-shaking' for both cases of simulated excavation (red lines) and wished-in-place tunnel (blue lines). The stress change due to the excavation ensures lower internal loadings in terms of bending moments and normal forces with respect to the case of a wished-in-place tunnel; furthermore, the latter is almost not loaded in longitudinal direction.

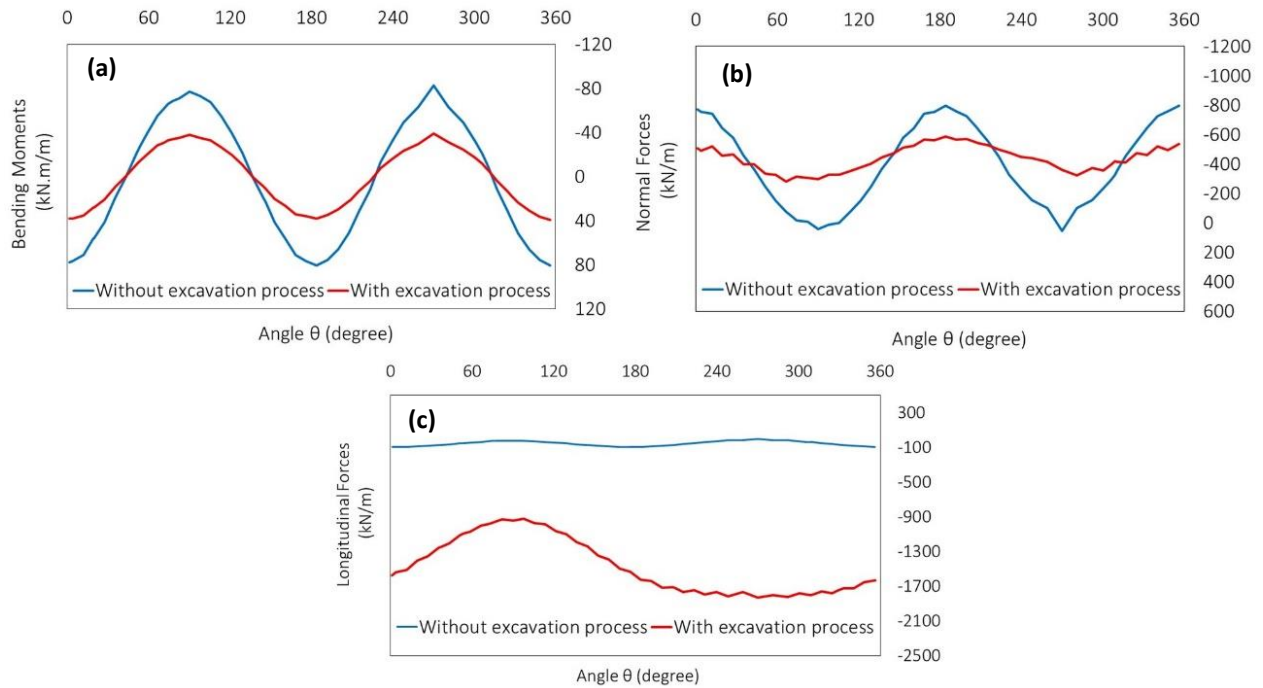


Figure 4.34. Distribution along the transverse reference section of (a) bending moment, (b) hoop force, (c) longitudinal force in static 'pre-shaking'.

Once completed the whole tunnel stretch, the dynamic analysis was carried out similarly to that described in detailed before (§4.3.1). The results were compared with those obtained without simulating the excavation. Figure 4.36 shows, as an example, the case of South Iceland Earthquake ($M_w=6.4$, 2000) extracted from the European Strong Motion database.

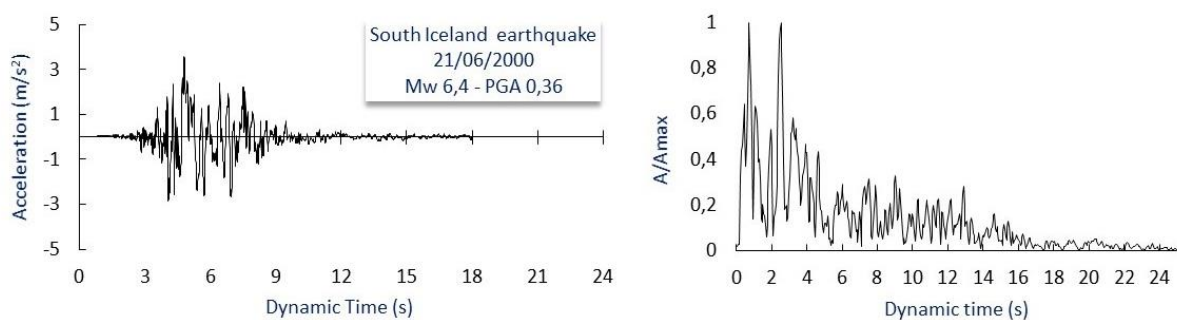


Figure 4.35. South Iceland Earthquake 2000 ($M = 6.4$): (a) time history; (b) Fourier spectrum.

The cycling action of the seismic loading involves a continuous redistribution of stress in the soil and around the tunnel cavity in particular, as it has been emerged from centrifuge test (Lanzano 2009). Figure 4.36 shows the position of such points around the tunnel (O, M, K, P, N, L) for which the stress redistribution during the dynamic seismic shaking has been plotted in terms of deviatoric stress 'q' and mean pressure 'p' in Figure 4.37. The peak and permanent values of q and p time histories of such a points tend to increase as these approach to the gallery. This is the effect of the soil-structure interaction

that affects not only the soil but the lining also; Figure 4.38 for instance, shows the time histories of bending moment (a) and hoop force (b) calculated at the point NE of the reference central section of the continuous tunnel lining.

Note that the results shown in Figure 4.37 and Figure 4.38 have been carried out in the case of simulated excavation.

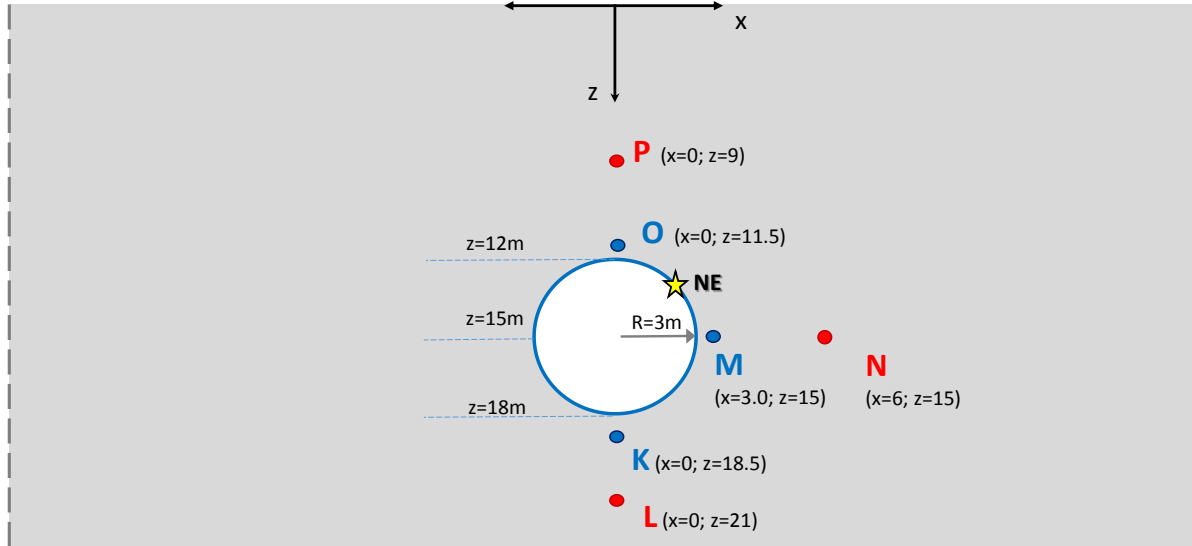


Figure 4.36. Position of the selected points around the tunnel cavity.

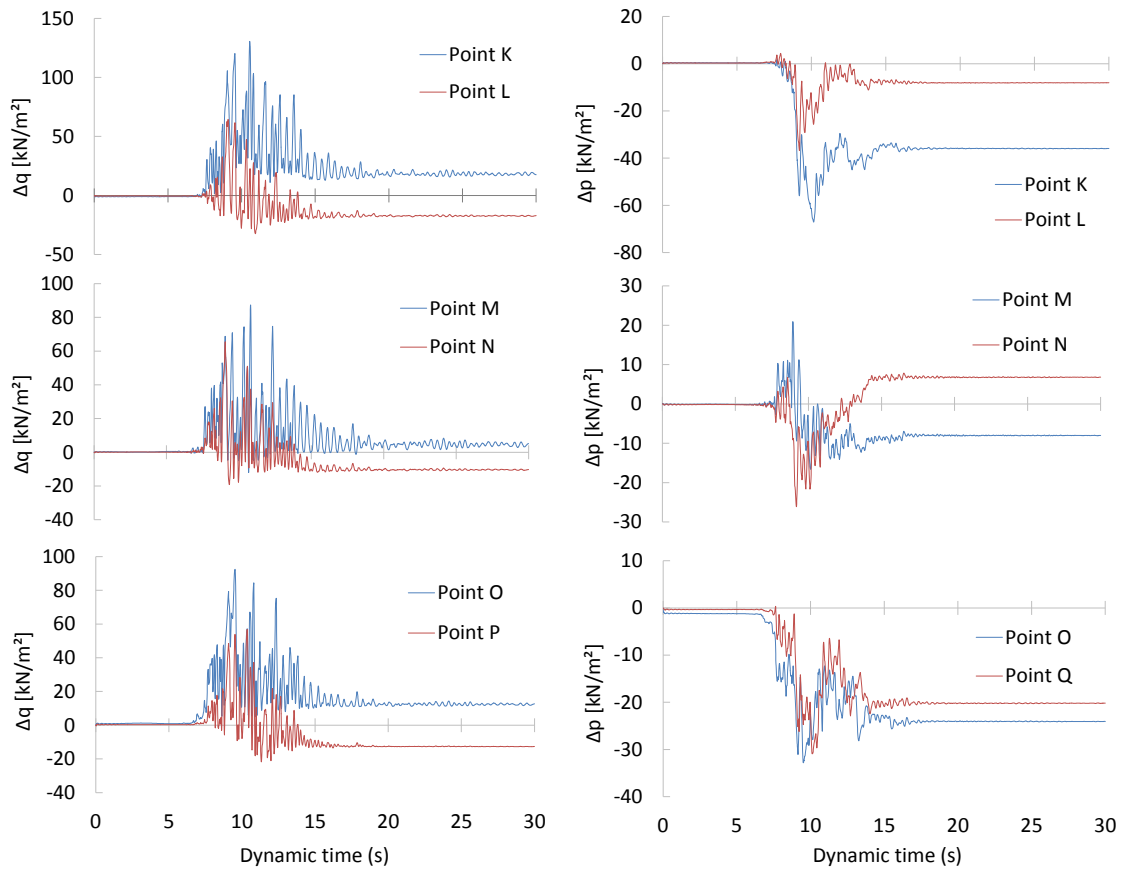


Fig. 4.37. Time histories of the stresses q and p around the tunnel cavity (South Iceland Earthquake $M_w=6.4$, $a=0.36g$).

A permanent accumulation of internal loads in the tunnel at the end of shaking can be observed, about 30% the maximum transient change calculated during shaking. This result confirms the experimental evidences obtained by *Lanzano et al. 2012* and the need to use a suitable elastic-plastic constitutive model for soil to capture such an effect. Figure 4.39 shows the comparison in terms of dynamic permanent distribution of bending moment (Figure 4.39a) and hoop force (Figure 4.39b) in the transverse reference section between the cases of simulated excavation (red lines) and wished-in-place tunnel (blue lines).

Continuous lines correspond to the static 'pre-shaking' while the dashed lines to the 'post-shaking' conditions. Because the effect of stress release around the cavity during the excavation is that of a lower internal loadings in terms of bending moments (Figure 4.34a) and normal forces (Figure 4.34b), with respect to the case of a wished-in-place tunnel, as a consequence this effect involves, in terms of permanent change of internal forces, higher values in the case of simulated excavation. This highlights the effect of construction on the seismic demand of the tunnel lining; the soil stiffness around the tunnel gradually decreases during the excavation, hence the relative stiffness of the tunnel lining during the following shaking is larger, thus increasing the changes of internal forces.

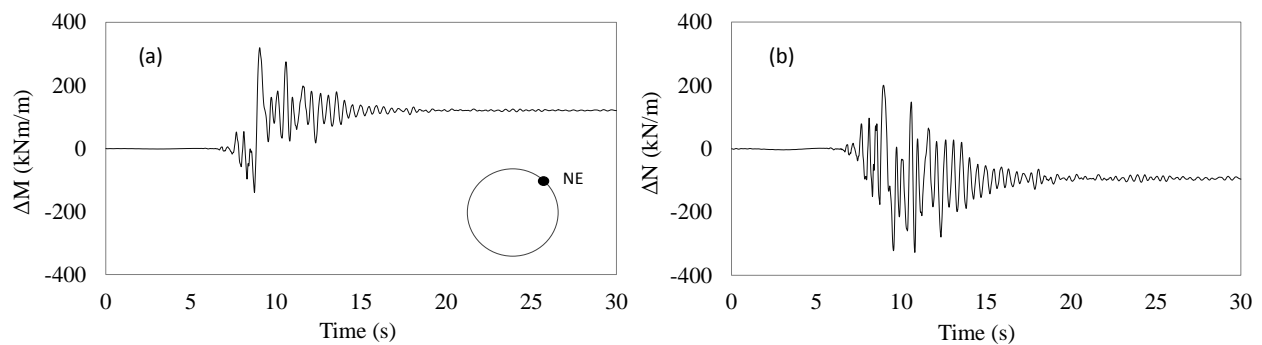


Figure 4.38. Time histories of internal forces in the point NE: (a) bending moment; (b) hoop force (South Iceland Earthquake Mw=6.4, $a=0.36g$).

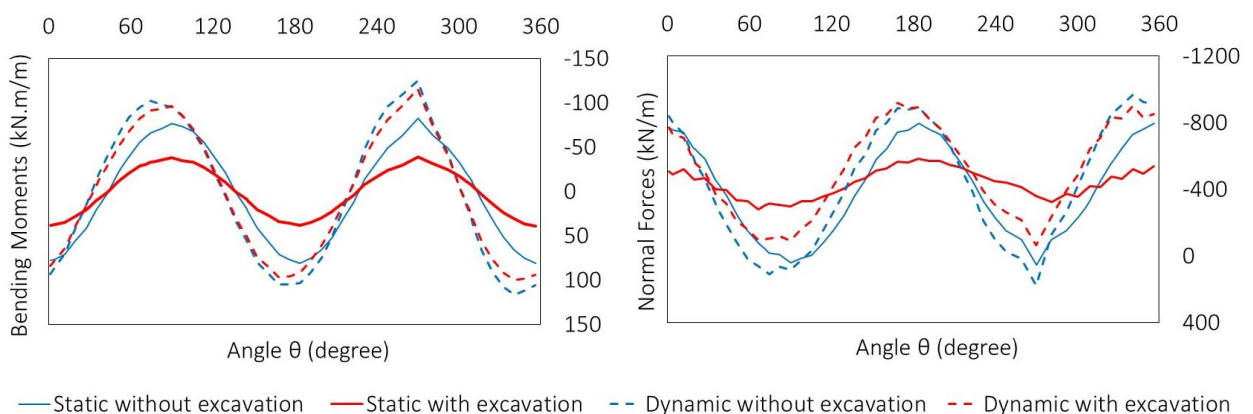


Figure 4.39. Distribution along the transverse reference section of bending moment and hoop force: static 'pre-shaking' -continuous lines- and 'post-shaking' -dashed lines- (South Iceland Earthquake Mw=6.4, $a=0.36g$).

4.3.3 Influence of the segmental layout

The segmental layout of pre-cast concrete lining typically installed with a TBM, affects its structural demand, generally reducing the internal forces that arise in static conditions, compared to a *continuous* lining having the same structural section (see Chapter 1 and Chapter 3).

In order to analyse the effect of the jointed layout of the tunnel lining under shaking, a further set of analysis were carried out. The geometry of the segmental lining is that one of Metro Line 6 of Naples retrieved in Figure 4.40 where the adopted joint moment-rotation relationship is included also.

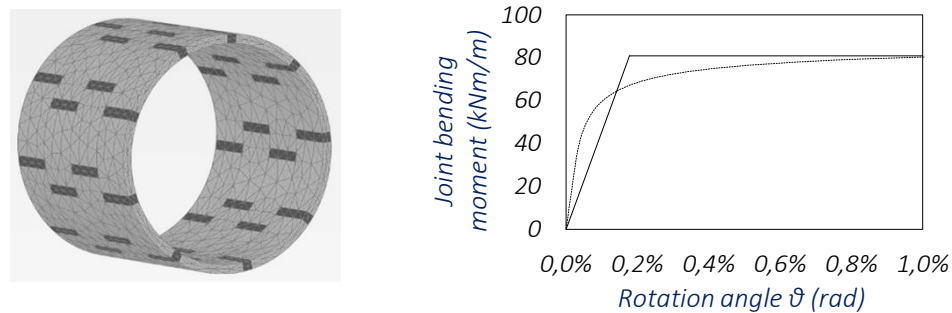


Figure 4.40. 3D numerical model of segmental lining and joint moment-rotation relationship.

In Figure 4.41 the distribution along the transverse reference section of bending moment (Figure 4.41a) and hoop force (Figure 4.41b) calculated at the end of shaking are shown. It is evident the lower structural demand of the segmental lining compared to the continuous lining. In the point NE for example, Figure 4.42 shows the lower seismic demand of the segmental lining, both in terms of bending moment and hoop force, up a value about of 50% lower respect the continuous case.

Despite the fact that the loads acting in the segmental lining at the end the earthquake are lower than in the continuous lining, in the former case a possible fragility may arise due to the relative rotation between segments. This may induce decompression of the joint and consequent dislocation of the rubber gasket that guarantee water-tightness at the contact.

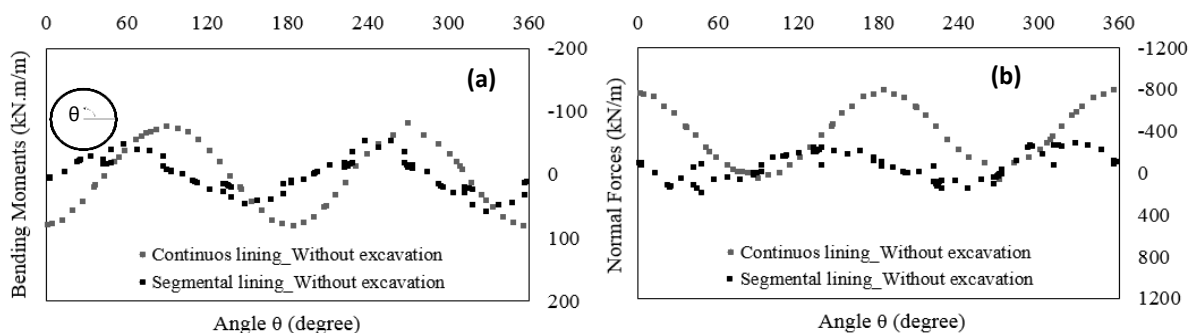


Figure 4.41. Distribution along the transverse reference section of (a) bending moment, (b) hoop force: continuous vs. segmental lining (South Iceland Earthquake $M_w=6.4$, $a=0.36g$).

Figure 4.43 for instance, shows the time histories of relative rotation between segments during shaking, calculated in the joints at 45° , 135° , 225° , and 315° about the horizontal tunnel axis. It is interesting to point out that permanent relative rotations remains in between segments at the end of

shaking. Their magnitude is sometimes rather close to the peak values calculated during shaking, suggesting a potential permanent loss of water-tightness of the lining.

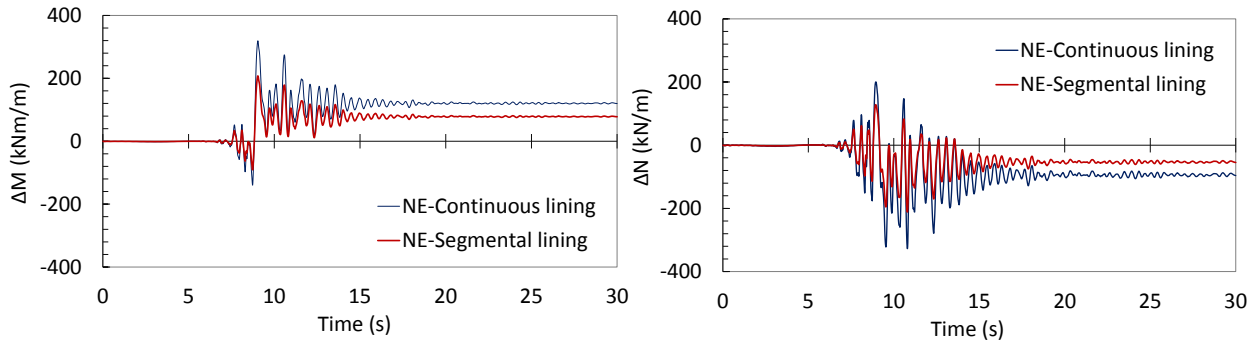


Figure 4.42. Dynamic increment of bending moment and hoop force in NE point: continuous vs. segmental lining (South Iceland Earthquake $M_w=6.4$, $a=0.36g$).

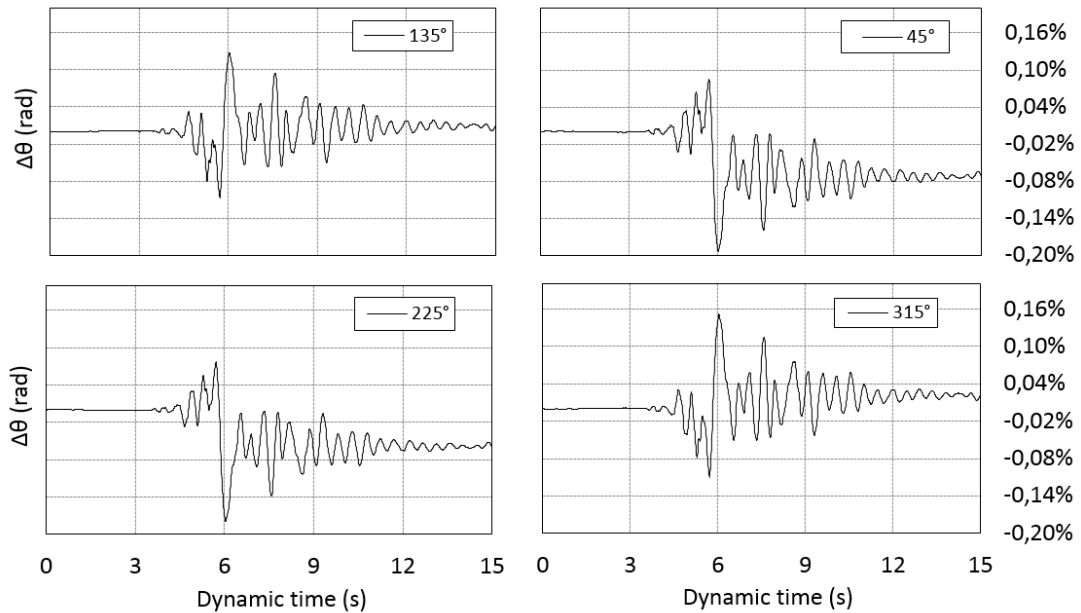


Figure 4.43. Time histories of relative rotation between segments (South Iceland Earthquake $M_w=6.4$, $a=0.36g$).

A set of three dimensional analysis has been performed for different natural earthquake to investigate the effect of the peak ground acceleration and the content of frequency of the signals on the joints rotation.

Figure 4.44 shows the time histories of acceleration and the relative Fourier Spectra of the earthquake signals adopted in the analysis, while Figures 4.45 - 4.46 - 4.47 - 4.48 - 4.49 show the time histories of the rotations of the joints that most suffer the deformation mechanism of the structure during seismic shaking.

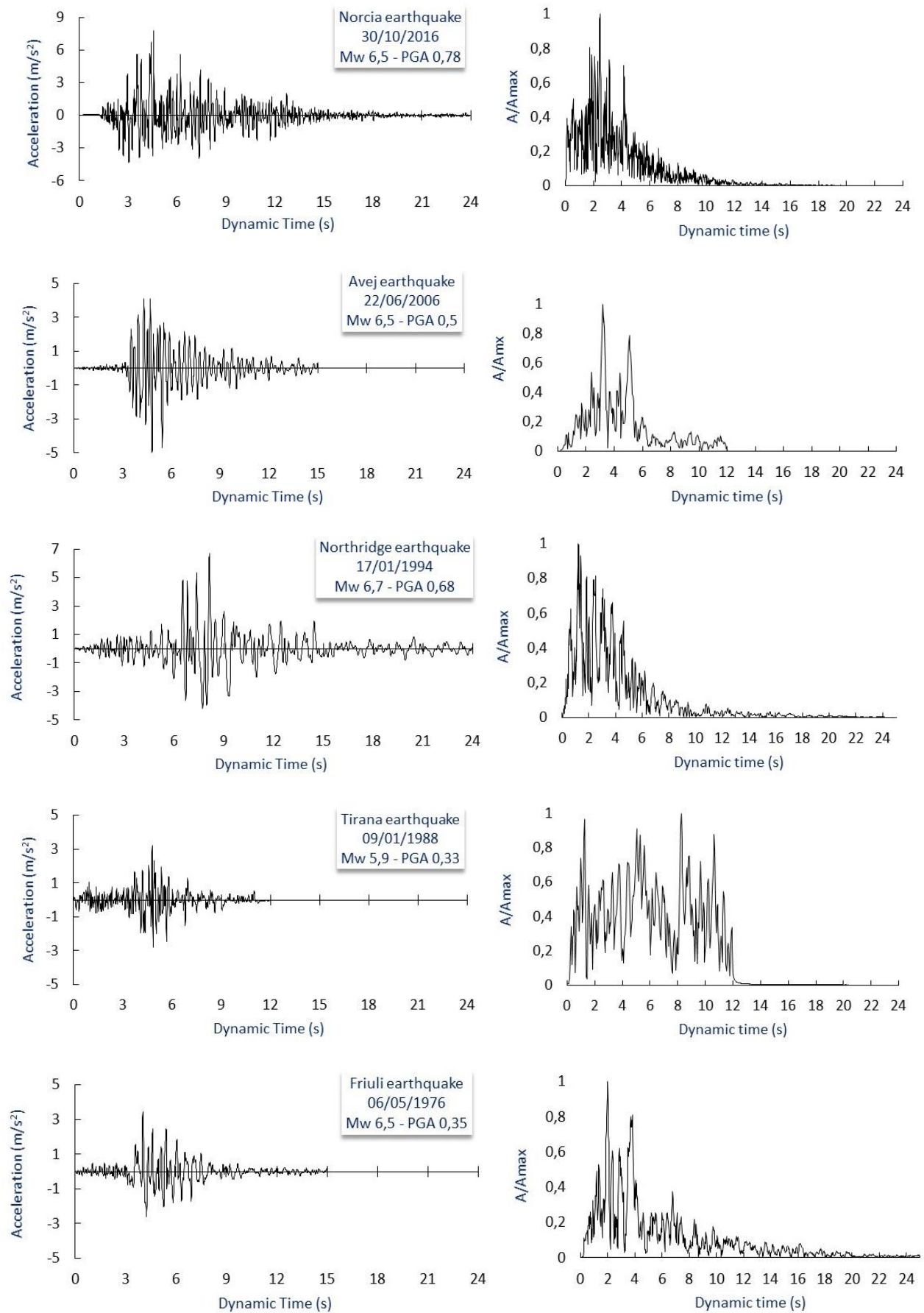


Figure 4.44. Time histories and Fourier Spectra of the recorded earthquake signals adopted for 3D analysis for the evaluation of joints rotation in the segmental tunnel lining.

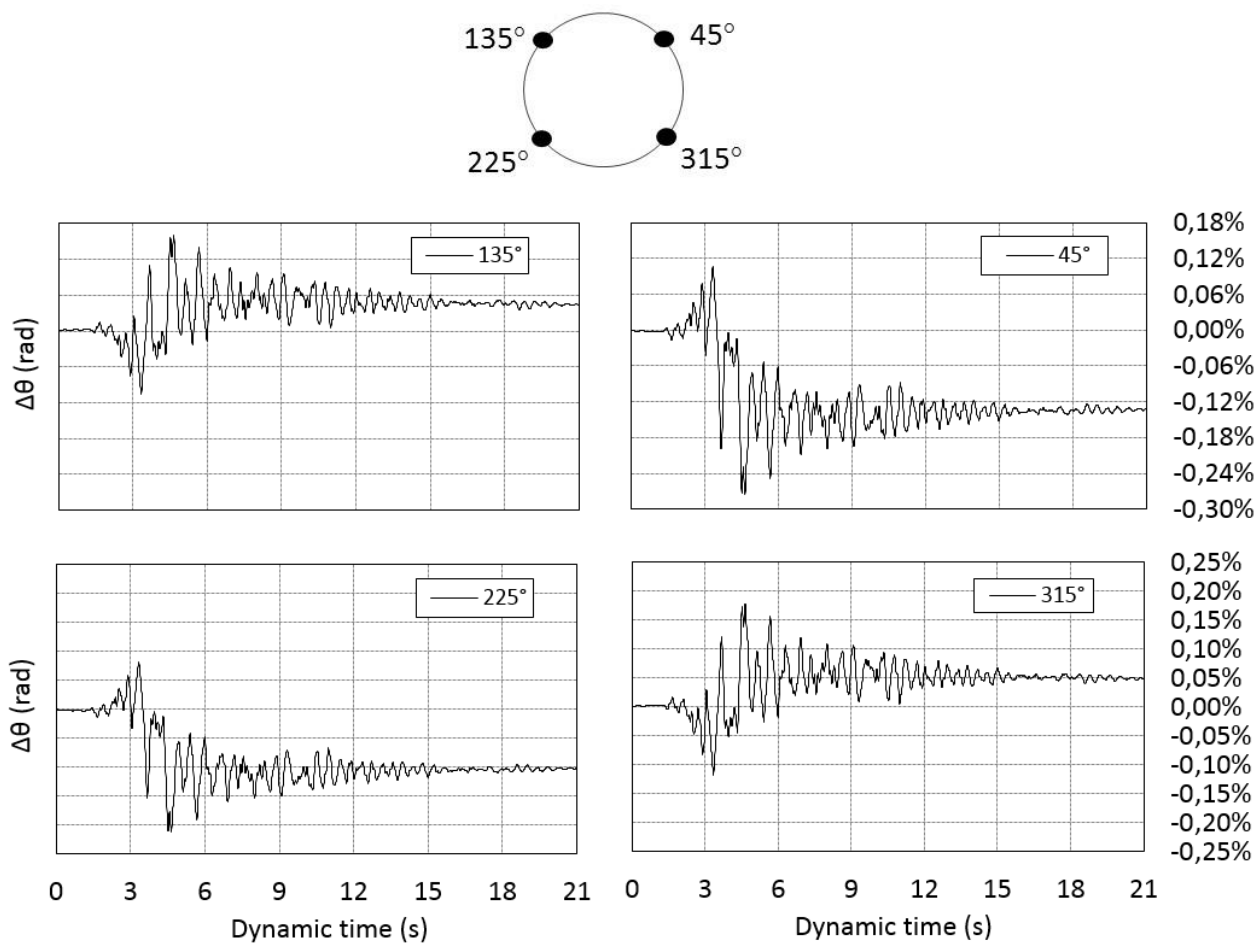


Figure 4.45. Time histories of joints rotation during Norcia earthquake (Italy).

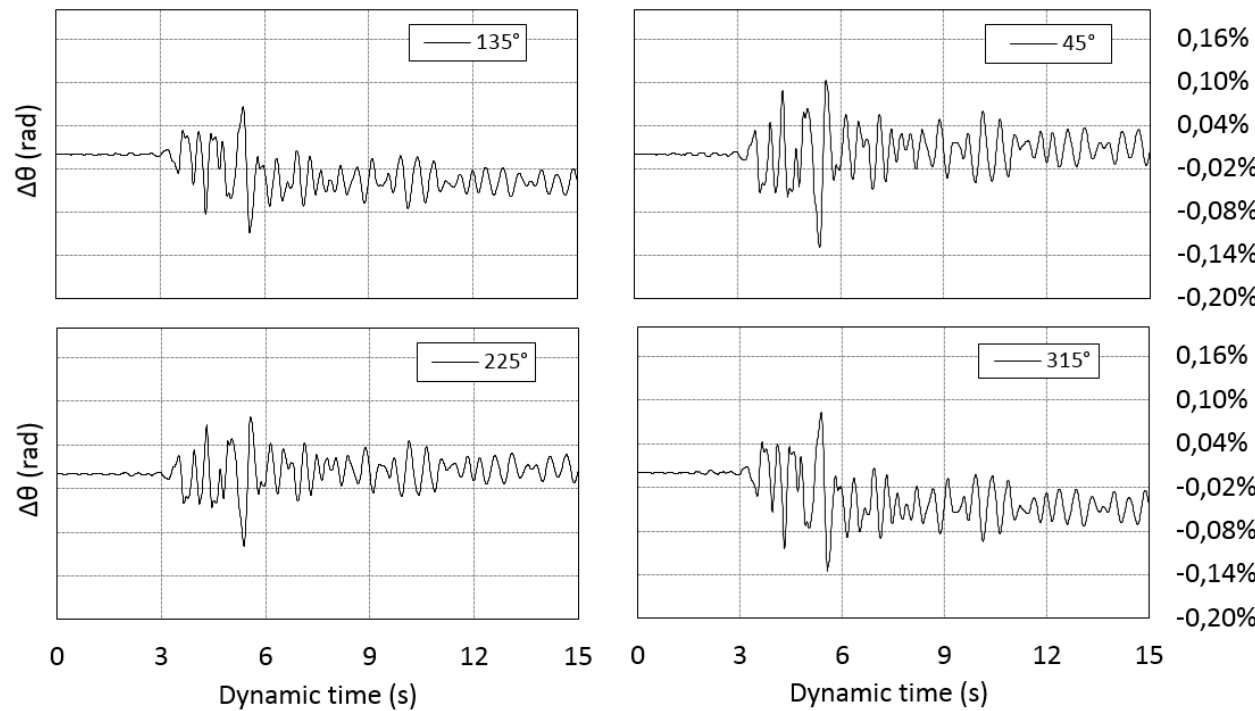


Figure 4.46. Time histories of joints rotation during Avej earthquake.

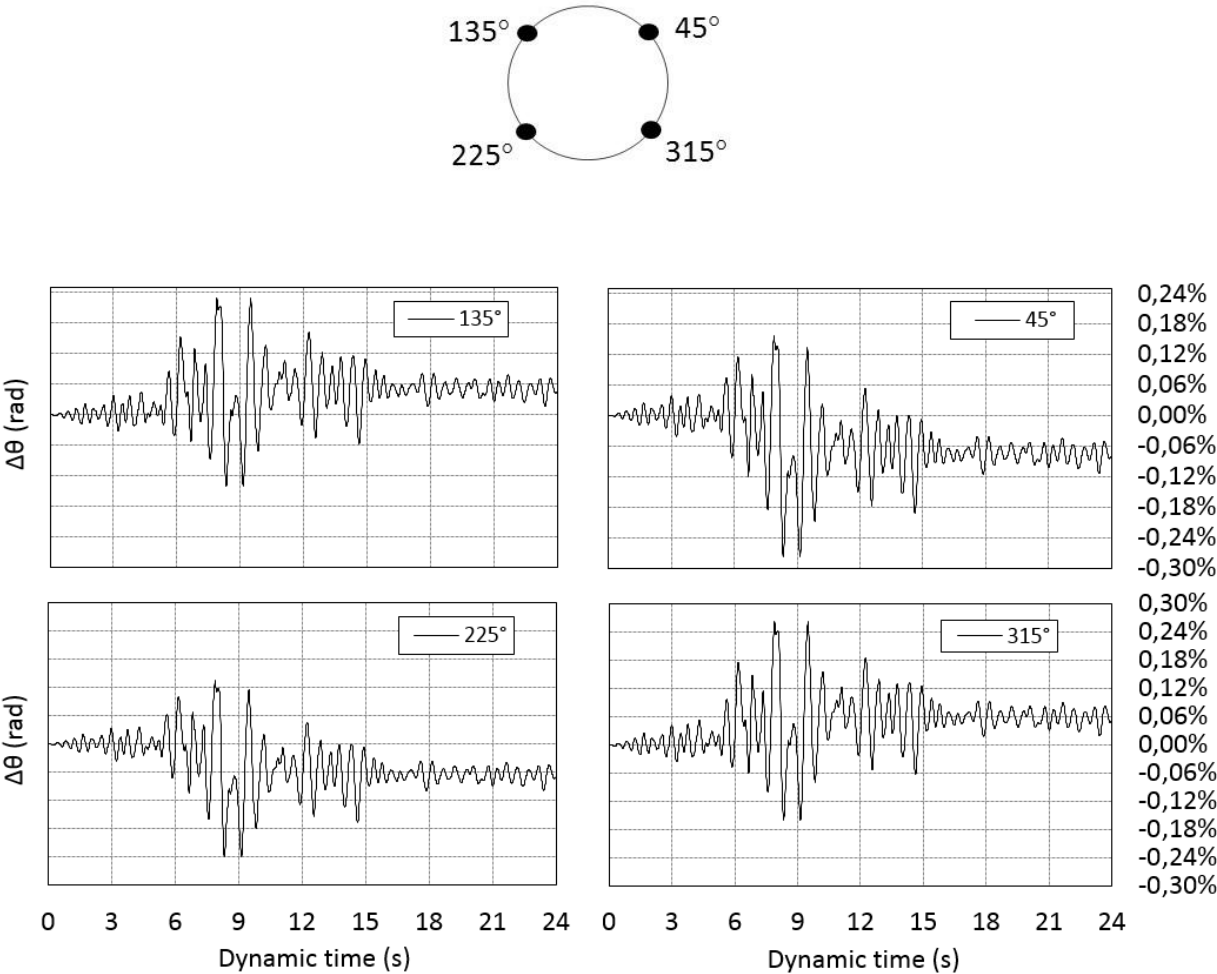


Figure 4.47. Time histories of joints rotation during Northridge earthquake.

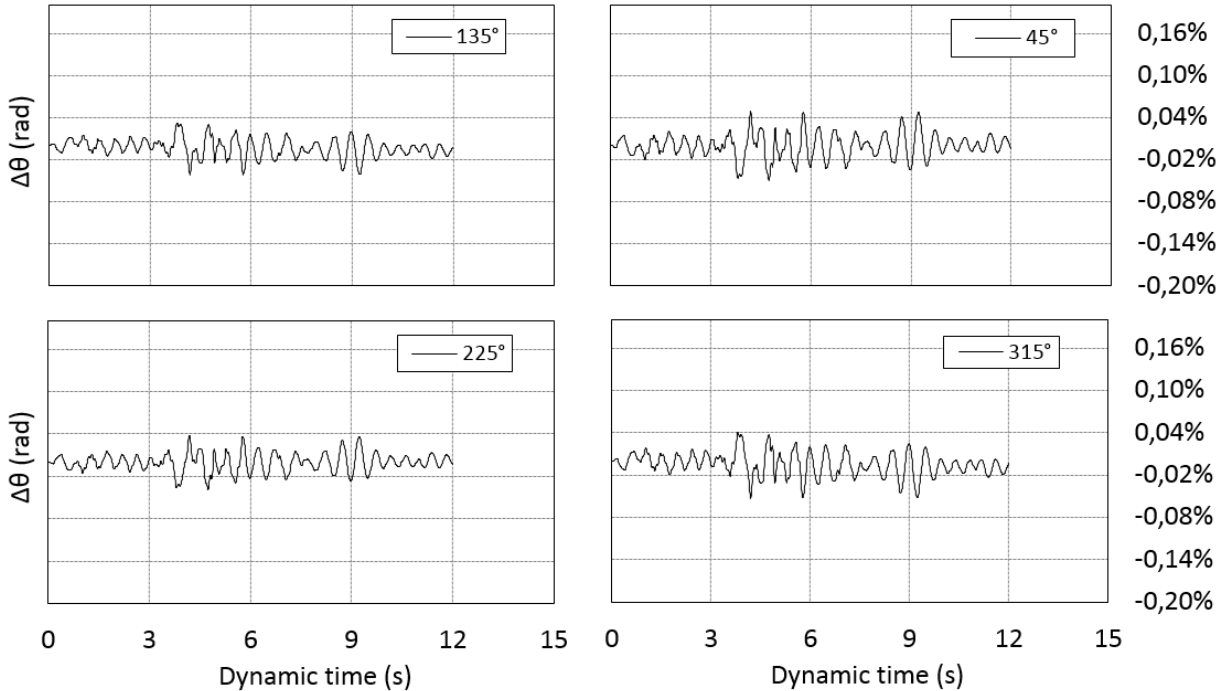


Figure 4.48. Time histories of joints rotation during Tirana earthquake.

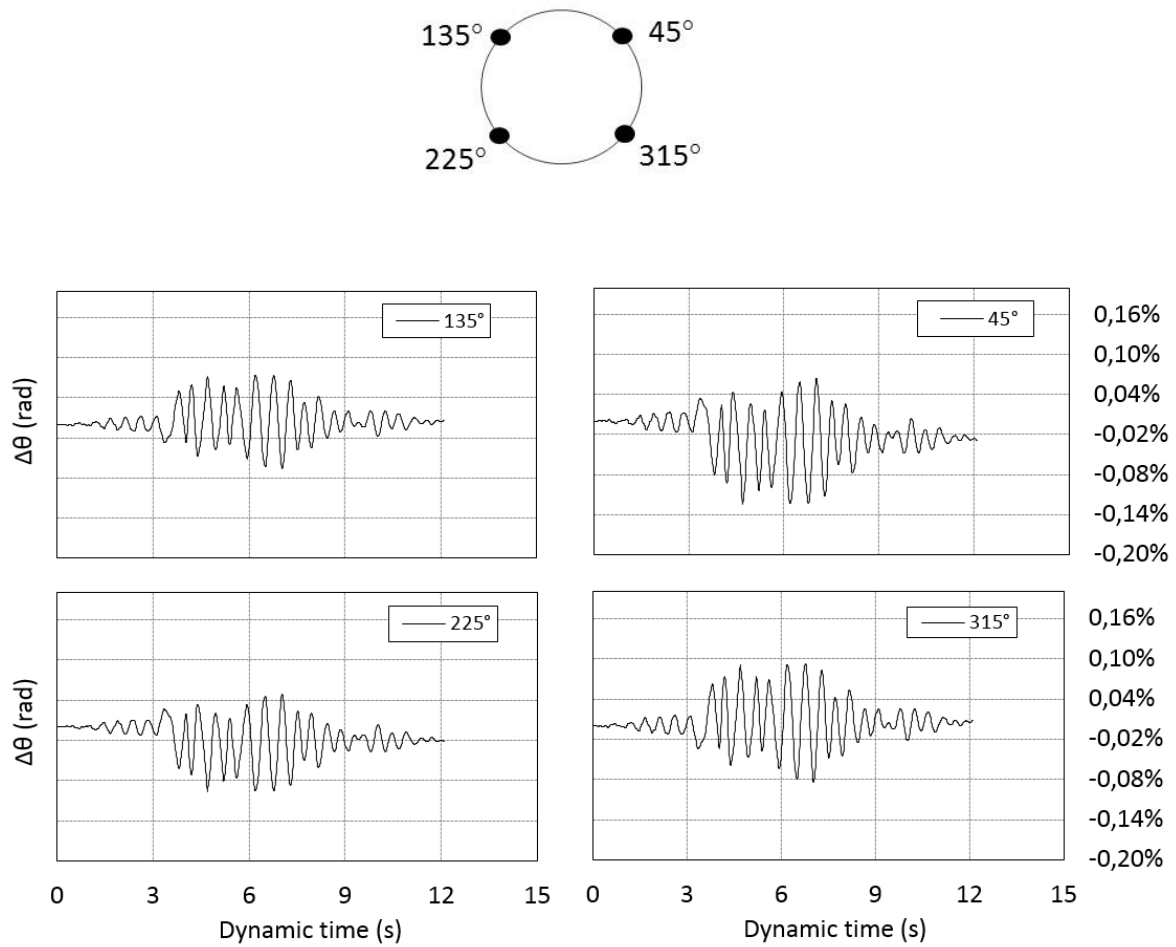


Figure 4.49. Time histories of joints rotation during Friuli earthquake (Italy).

The results in Figures 4.45 - 4.46 - 4.47 - 4.48 - 4.49 show that the peak and permanent values of joints rotation increase with peak ground acceleration increasing. It should be noted that a negative joint rotation corresponds to the opening of the extrados while a negative value corresponds to the opening of the intrados of the joint (Figure 4.50).

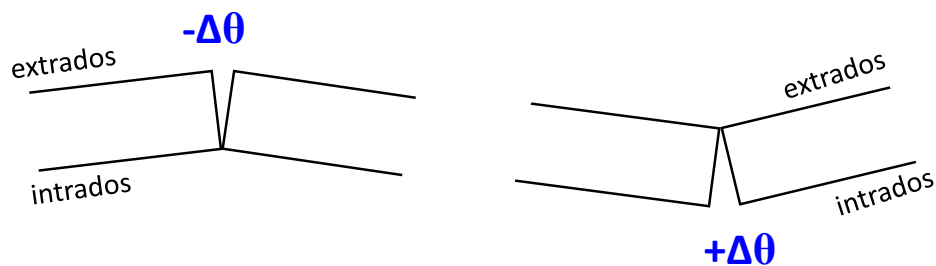


Figure 4.50. Adopted sign convention of joint rotation.

In almost all considered cases, the joint located at $\theta=45^\circ$ is the most stressed, recording the highest value both in terms of peak and permanent rotation.

Table 4.4 resumes all results obtained respect the selected earthquakes, comparing the peak and residue values for each joint.

Earthquake event	Date	Mw	PGA	Joint	$ \Delta\theta_{peak}^{3D} $ rad%	$ \Delta\theta_{peak}^{3D} $ grad	$ \Delta\theta_{residue}^{3D} $ rad%	$ \Delta\theta_{residue}^{3D} $ grad
Norcia (Italy)	30/10/2016	6.5	0.78	45°	0.274	0.157	0.1323	0.0758
				135°	0.161	0.092	0.0437	0.0250
				225°	0.210	0.120	0.1010	0.0579
				315°	0.180	0.103	0.0500	0.0286
Avej	22/06/2006	6.5	0.5	45°	0.130	0.074	0.0056	0.0032
				135°	0.108	0.062	0.0350	0.0200
				225°	0.100	0.057	0.0128	0.0073
				315°	0.140	0.080	0.0543	0.0311
South Iceland (after shock)	21/06/2000	6.4	0.36	45°	0.194	0.111	0.0737	0.0422
				135°	0.128	0.073	0.0104	0.0060
				225°	0.178	0.102	0.0596	0.0341
				315°	0.152	0.087	0.0232	0.0133
Northridge	17/01/1994	6.7	0.68	45°	0.278	0.159	0.0807	0.0462
				135°	0.230	0.132	0.0455	0.0261
				225°	0.240	0.138	0.0697	0.0399
				315°	0.262	0.150	0.0519	0.0297
Tirana	09/01/1988	5.9	0.33	45°	0.050	0.029	0.0040	0.0023
				135°	0.043	0.024	0.0026	0.0015
				225°	0.038	0.022	0.0031	0.0018
				315°	0.053	0.030	0.0033	0.0019
Friuli (Italy)	06/05/1976	6.5	0.35	45°	0.125	0.071	0.0287	0.0164
				135°	0.073	0.042	0.0062	0.0036
				225°	0.110	0.063	0.0220	0.0126
				315°	0.090	0.052	0.0080	0.0046

Table 4.4 Peak and permanent values of joint rotations during a set of natural earthquakes

In Figure 4.51, the rotation demand of the selected points is associated with the capacity $M-\theta$ curve assumed for the joints; the peak rotation values exceed the yielding rotation in almost all joints for the different selected PGAs, the residual rotation values instead exceed the yielding rotation in the joints in the case of higher values of PGA.

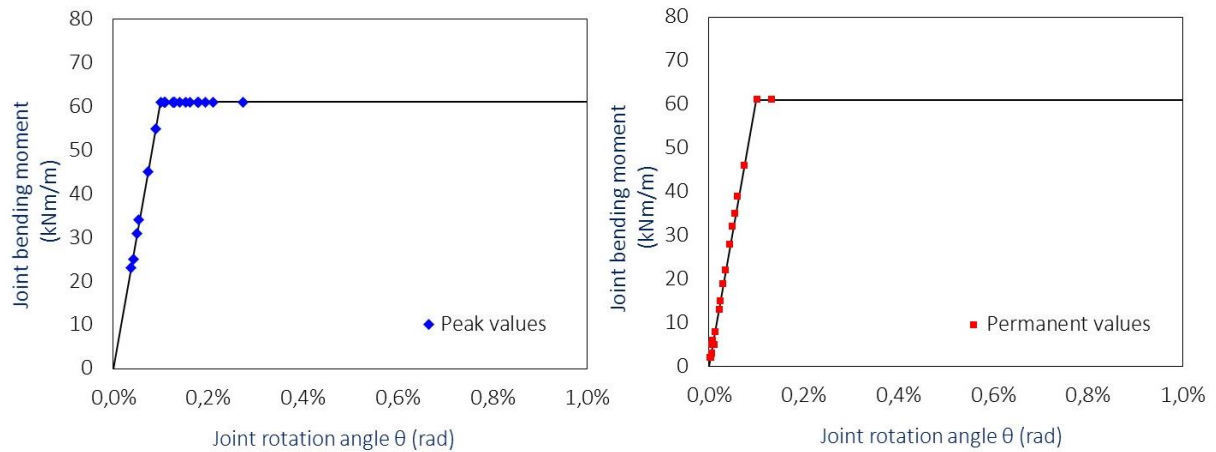


Figure 4.51. Demand rotation points of the joints under different peak ground acceleration values.

Numerical results included in this paragraph show the significant effect of the jointed pattern of a segmental lining, which implies a larger flexibility and compressibility in the transverse section, compared to a continuous lining, hence lower structural demand. On the other hand, permanent rotations of the joints were computed at the end of the dynamic stages, which may represent a further structural fragility of a segmental lining under seismic shaking. This evidence may lead to some concerns in highly permeable soils, where an excessive rotation of joints may produce dislocation of gaskets and cause severe inflow from groundwater.

CHAPTER 5

Seismic vulnerability of segmental tunnel lining

Introduction

The experience from past earthquakes (see Chapter 4) reveals that underground structures are exposed to seismic risk and their seismic vulnerability (or fragility) is strictly related to the tunnel technology, the interaction developing during seismic shaking with the surrounding soil, the intensity of the event. Each of this factors plays an important role in terms of probability of damage and loss of functionality of the underground structure.

For engineering perspective, 'seismic hazard' and 'seismic risk' are different concepts. Seismic hazard describes phenomena generated by earthquakes that have potential to cause harm, seismic risk is the likelihood of experiencing a specified level of seismic hazard in a given time exposure. Seismic hazard occurs naturally and can be evaluated from instrumental, historical, and geological observations, seismic risk is by definition an interdisciplinary topic depending on the hazard itself, the exposure and the structure vulnerability:

$$\text{Risk} = \text{Hazard} \times \text{Vulnerability} \times \text{Exposure}$$

Nowadays the '*seismic risk assessment*', defined as the estimation of the probability of expected damages and losses due to seismic hazards of a structure, is a very common tool in the seismic engineering and generally adopted for the protection of strategic structures.

In this context the '*seismic vulnerability of underground structures*' has been investigated in detail, considering two different possible technologies of tunnel lining, continuous and segmental one.

The fragility curves are usually adopted as forecast method of vulnerability of the structure, constructed for different levels of damage. The seismic vulnerability assessment of tunnels is generally based on empirical fragility curves (e.g. *Hazus 1999; ALA 2001*). They are derived from the statistical analysis of observed damages in past earthquakes. Some authors have calculated fragility curves based on the results of numerical analyses (e.g. *Argyroudis & Pitilakis 2012*), defining the damage index in terms of ratio between the flexural demand and capacity of the structural section of the tunnel lining. All above mentioned works refer to continuous tunnel lining. However, in the case of mechanized tunneling it is made of jointed segments, the results included in the Chapter 4 have shown the significant effect of the jointed pattern of a segmental lining which implies a lower structural demand than a continuous ring and a potential fragility associated to an excessive joint rotation.

Analytical fragility curves for segmental tunnel lining, based on 2D non-linear full dynamic analysis, have been constructed assuming the longitudinal joint rotation as the potential damage parameter. The framework of the problem, procedure of numerical simulations and definition of numerical fragility curves for minor, moderate and extensive damage and for different soil types (B, C and D) are here discussed.

5.1 Fragility curves

The vulnerability assessment of a single structure, or of a class of them, represents one of the most important topic of the seismic engineering. Fragility curves are one of the most used methods for the rapid assessment of the structure performance at different hazard levels. They give the probability of reaching a defined structural damage level with respect to a given level of seismic intensity motion. The latter can be expressed in terms of ground motion intensity measures as Peak Ground Acceleration (PGA) and Velocity (PGV) or Permanent Ground Displacement (PGD).

One procedure to describe the fragility curves, generally adopted in civil engineering (*Shinozuka et al. 2000, Hazus 2004, Moschonas 2009, Argyroudis & Pitilakis 2012*), is based on log-normal probability distribution as follows:

$$P_f(d_s \geq d_{si}|IM) = \phi \left[\frac{1}{\beta_{tot}} \ln \left(\frac{IM}{IM_{mi}} \right) \right] \quad (5.1)$$

With

$$\beta_{tot} = \sqrt{\beta_{ds}^2 + \beta_c^2 + \beta_d^2} \quad (5.2)$$

and:

- $P_f()$ is the probability of exceedance of a particular damage level, d_s , for a given seismic intensity measure IM ;
- IM_{mi} is the median of the intensity motion values IM , for which the tunnel reaches the damage level d_{si} ;
- β_{tot} is the total standard deviation of the natural logarithm;
- ϕ is the standard cumulative probability function.

The log-normal dispersion is estimated by the standard deviation β_{tot} . Generally, three types of uncertainties are taken into account:

- the damage level definition (β_{ds}),
- the structure capacity (β_c),
- the seismic input (β_d).

Based on the log-normal probability distribution function, Figure 5.1 shows the general flowchart of the procedure for deriving numerical fragility curves for ‘*continuous lining*’ of tunnels in alluvial deposits proposed by *Argyroudis & Pitilakis 2012*, the only analytical curves available in literature. The proposed approach is based on pseudo-static analysis following the Displacement-Based-Method, DBM (§4.2.1), performed with Plaxis 2D. The response of the free field soil profile and the induced seismic ground deformations have been calculated through 1D non-linear numerical analysis in EERA code. The profile of displacements of the soil in FF condition and the shear modulus and damping level derived from the 1D analysis have been used to model the 2D soil-tunnel interaction adopting the Mohr-Coulomb criterion.

For a fixed structure technology, the authors consider different typical soil profiles (soil types B, C and D) to investigate the influence of the different soil-structure relative stiffness.

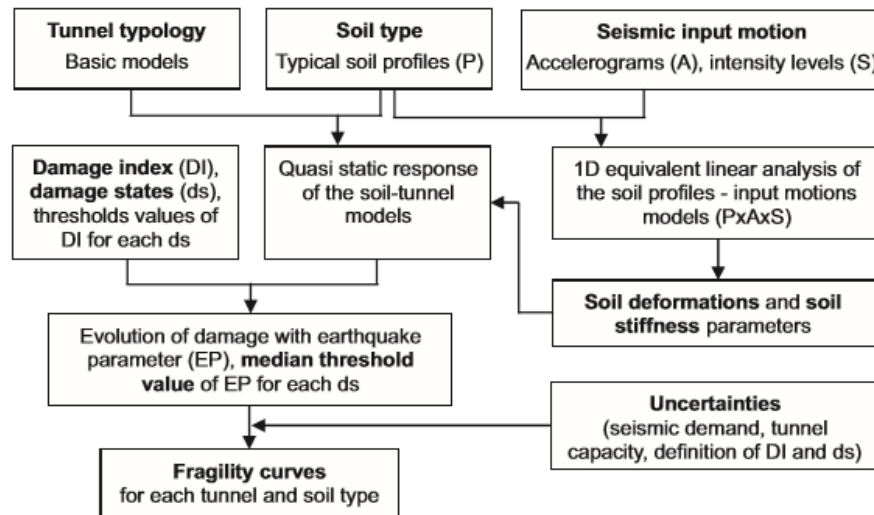


Figure 5.1. General flowchart of the procedure for deriving numerical fragility curves for 'continuous lining' of circular tunnels (Argyroudis & Pitilakis 2012).

Considering the lack of references on the evaluation of the damage index for tunnel, the author proposed as damage index (DI) the ratio between the actual (M) and capacity (M_{Rd}) bending moment of the tunnel cross section, defining the range of damage index for five different damage state (ds_i) as in Table 5.1. The actual bending moment (M) is calculated as the combination of static and seismic loads while the capacity of the tunnel is estimated based on material and geometry properties of the tunnel section considering the induced static and seismic axial forces (N) and bending moments (M).

Damage state (ds_i)	Range of damage index (DI)	Central value of damage index
ds0. None	$M/M_{Rd} \leq 1.0$	–
ds1. Minor/slight	$1.0 < M/M_{Rd} \leq 1.5$	1.25
ds2. Moderate	$1.5 < M/M_{Rd} \leq 2.5$	2.00
ds3. Extensive	$2.5 < M/M_{Rd} \leq 3.5$	3.00
ds4. Collapse	$M/M_{Rd} > 3.5$	–

Table 5.1. Proposed damages states for continuous circular tunnel lining (Argyroudis & Pitilakis 2012).

The effect of seismic structure response has been evaluated for a set of seismic input motions recorded from different real earthquakes (Table 5.2) scaled from 0.1 to 0.7 g in order to calculate the induced stresses in the tunnel for gradually increasing level of seismic intensity.

The work of the author focuses on a structural type of tunnel which is not localized (it is not an existing tunnel), this is the reason why the input signals have been selected looking at the intensity of the event only (peak ground acceleration, magnitude, frequency content), without a site-specific seismic hazard assessment (deterministic DSHA or probabilistic PSHA seismic hazard assessment).

Record station	Earthquake	Magnitude M_w	Epicentral distance (km)	PGA (g)	Predominant period (sec)
1 OTE	Kozani, 1995	6.5	17.0	0.142	0.50
2 Kypseli	Parnitha, 1999	6.0	10.0	0.120	0.43
3 Gebze	Kocaeli, 1999	7.4	41.8	0.218	1.06
4 Cubbio-Piene	Umbria-Marche, 1998	4.8	18.0	0.235	1.08
5 Hercegnovi Novi	Montenegro, 1979	6.9	65.0	0.256	0.74
6 Sturmo	Campano Lucano, 1980	7.0	32.0	0.323	2.30
7 Gilroy1	Loma Prieta, 1989	6.9	28.6	0.440	0.37
8 Griffith Park Observ.	Northridge, 1994	6.7	25.4	0.289	0.10
9 Whitewater Trout Farm	Palm Springs, 1986	6.2	7.3	0.517	0.52

Table 5.2. Selected records applied to the bedrock of the soil profiles. (Argyroudis & Pitilakis 2012).

The definition of the median threshold value of PGA for each damage state (IM_{mi} in the Eq. 5.1) is based on the construction of the diagram of the computed damage indices versus PGA at the ground surface (e.g. Figure 5.2) according to the definitions of Table 5.1.

The diagram is estimated by linear regression analysis, considering the natural logarithm of the damage index (LnDI) as the dependent variable and PGA as the independent variable.

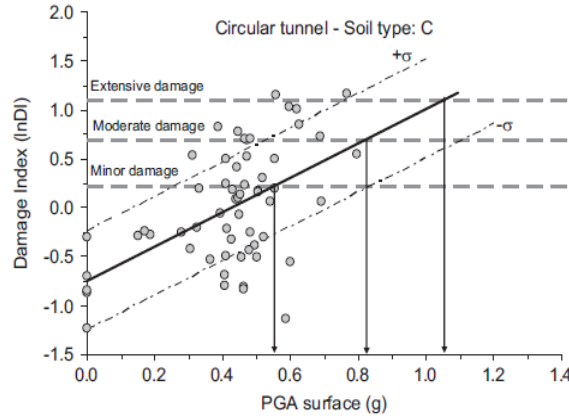


Figure 5.2. Examples of the evolution of damages with PGA at the ground surface (Argyroudis & Pitilakis 2012).

Figure 5.3 shows the fragility curves carried out by the authors for the different soil types, which correlate the probability of damage (%) with the PGA, the earthquake intensity parameter selected by the authors. Comparing the fragility curves derived for the three soil types, it should be noted how, for the same PGA, the vulnerability is gradually increasing from soil type B to D; consistently with what we expected, a more deformable soil undergoes higher deformation affecting the tunnel response in terms of increment of internal forces, exhibiting a higher vulnerability under seismic loads.

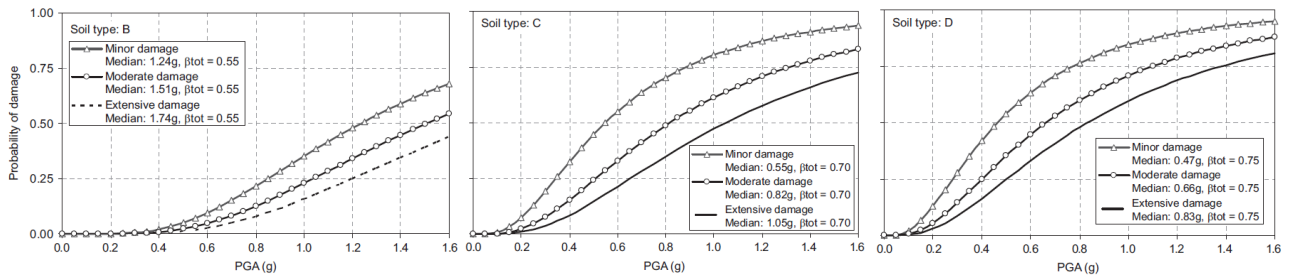


Figure 5.3. Numerical fragility curves for 'continuous lining' of circular tunnels for different soil types (Argyroudis & Pitilakis 2012).

5.1.1 Continuous lining

Based on the approach proposed by Argyroudis & Pitilakis 2012 (§5.1), the effect of coupled full dynamic analysis on the definition of the fragility curves for continuous circular tunnel has been investigated in the construction of the fragility curves. To this end, the flowchart of the procedure introduced before (§5.1) has been modified as in Figure 5.4. The red box for instance, indicates the changes carried out after Argyroudis & Pitilakis 2012.

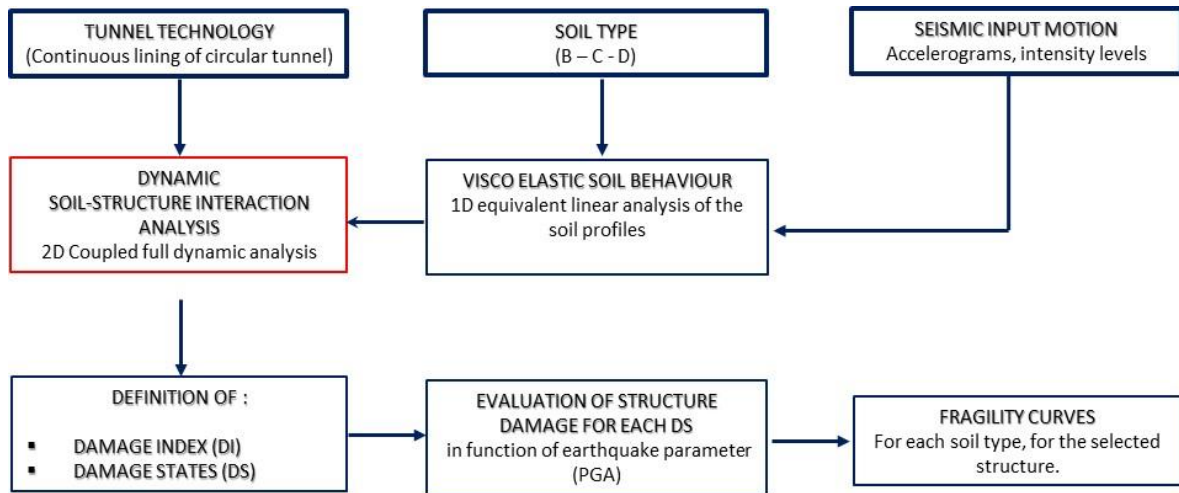


Figure 5.4. Proposed flowchart of the procedure for deriving numerical fragility curves for 'continuous lining' of circular tunnels modified after Argyroudis & Pitilakis 2012.

1D FREE FIELD ANALYSIS

A set of finite element coupled equivalent linear-visco-elastic analysis has been carried out in PLAXIS 2D, taking into account the effect of non-linear soil behaviour in 1D equivalent free field ground response analysis performed in EERA code (this procedure has been already introduced in the Chapter 4, §4.2.1).

The analysis refer to three different ideal soil deposits corresponding to soil type B, C and D according with Eurocode 8 shear velocity values shown in Figure 5.5.

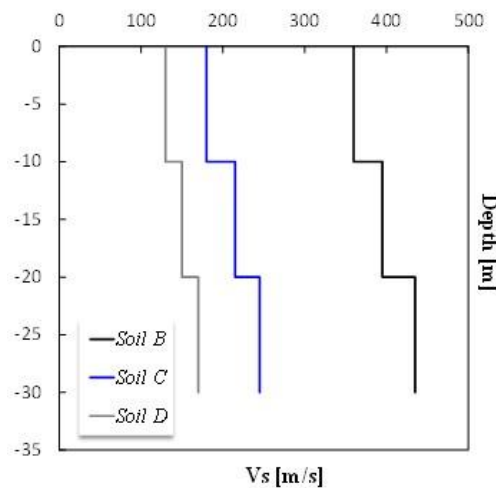
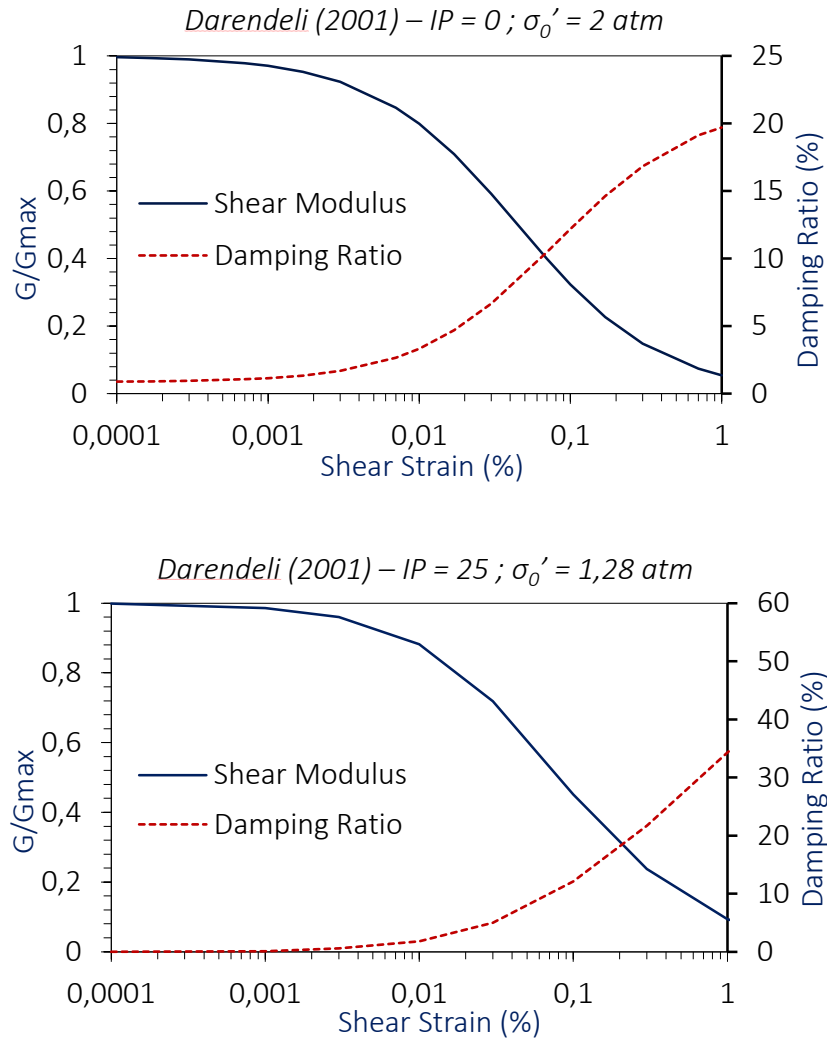


Figure 5.5. Selected velocity profiles according with EC8.

Table 5.3 shows the main parameters assumed for the different soil types. The variation of the shear modulus G/G_{\max} and the damping ratio D with the strain level γ have been selected according with existing literature curves. A curve with a plasticity index $IP=0\%$ was adopted for the soil types B and C, corresponding to sand, while a curve with $IP=25\%$ was selected for the soil type D, corresponding to clay, (Figure 5.6).

Soil Type	Literature Curve	IP	γ (kN/m ³)	$V_{s,30}$ (EC8)
B	Darendeli 2001, Sand	-	20	394.3
C	Darendeli 2001, Sand	-	20	213.3
D	Darendeli 2001, Clay	25	20	150.0

Table 5.3. Properties of different soil types.

Figure 5.6. Adopted literature curves of shear modulus reduction G/G_{max} and variation of damping ratio D with shear strain level γ (Darendeli 2001).

The non-linear equivalent viscous 1D analysis were carried out for a soil layer depth of 30m, discretized in a number of sub layers according with *Kuhlemeyer & Lysmer 1973* criteria, overlaying a relative rigid bedrock ($V_{bedrock}=1200$ m/s; $\gamma_{bedrock}=22$ kN/m³; $D_0=1\%$). Sublayers 1.25m thick have been adopted for the soil type B, sublayers 1m thick for soil types C and D.

The set of input signals used for the construction of the fragility curves is listed in Table 5.4. The input motions were selected so as their mean spectrum to match the Eurocode EC8–1 spectrum ($M>6$) for ground type A (rock). Figure 5.7 for instance, shows the spectral matching. Furthermore, the signals amplitude are to gradually scaled increasing the seismic intensity, as suggested by *Argyroudis & Pitilakis 2012*.

In the iterative procedure, the ratio of the effective and maximum shear strain is assumed equal to 0.65. The computed mobilized shear modulus G and damping ratio D to each subsoil layers, for each

seismic event and for each soil type, have been used in the coupled FE analysis. Figure 5.8 shows, as an example, the output of EERA code in terms of variation of shear modulus and the damping ratio with the soil depth.

<i>Event</i>	<i>Date</i>	<i>M_w</i>	<i>PGA g</i>
Campano Lucano	23/11/1980	6.9	0.10 – 0.20
SE of Tirana	09/01/1988	5.9	0.20 – 0.30
Montenegro	15/04/1979	6.9	0.15 – 0.20
Bingol	01/05/2003	6.3	0.20 – 0.30
Friuli	06-05-0976	6.5	0.25 – 0.30
South Icelend	17/09/2000	6.5	0.35 – 0.4 – 0.45
Tabas	16/09/1978	7.3	0.40 – 0.50
Avej	22/06/2002	6.5	0.25 – 0.35 – 0.5
South Icelend (after shock)	21/06/2000	6.4	0.15 – 0.20

Table 5.4. Selected input signals.

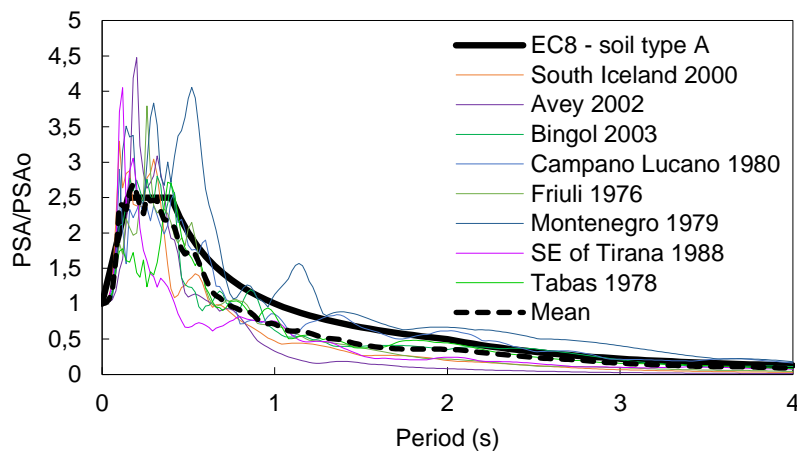


Figure 5.7. Comparison between the mean spectra and EC8-1 spectra (soil type A).

This is the procedure adopted for the 1D FF analysis for the three types of soil B, C and D, for each scaled earthquake.

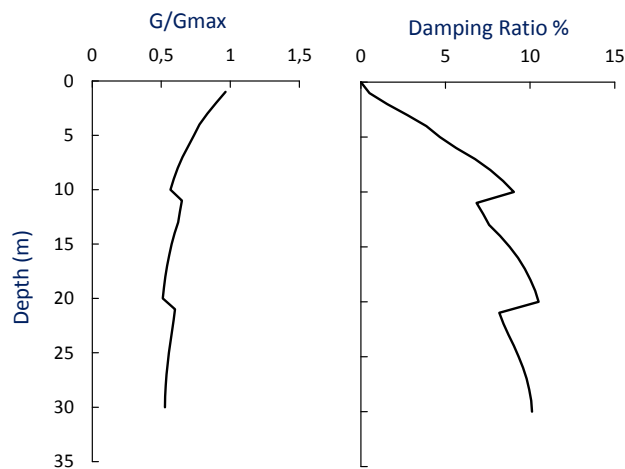


Figure 5.8. Mobilized shear modulus G/G_{max} and damping ratio D output of EERA code (Campano-Lucano Earthquake $a=0.1g$).

FULL DYNAMIC FE ANALYSIS

Once defined the FF ground response with 1D non-linear analysis for all above mentioned cases, EERA output have used to calibrate the 2D numerical model implemented in Plaxis 2D, carrying out viscous linear elastic analysis. The validation of the numerical model has been done comparing the free field response of the 1D and 2D model. The numerical mesh of this latter is shown in Figure 5.9a. The procedure of coupled analysis, the criteria and details adopted in the numerical model have been already introduced in the Chapter 4 (§4.2.2).

Figure 5.10 shows, as example, the free field response of the soil evaluated with EERA and Plaxis 2D for the case of Campano Lucano earthquake in terms of acceleration and pseudo-acceleration of the point on the top of the free field vertical (see Figure 5.9a).

The comparison between EERA code and Plaxis in FF condition has been done for all combinations of analysis, that is for the soil type B, C, D and for all selected signals.

The free field numerical analysis have be followed by the soil-structure interaction analysis and the Figure 5.9b shows the adopted mesh for this analysis.

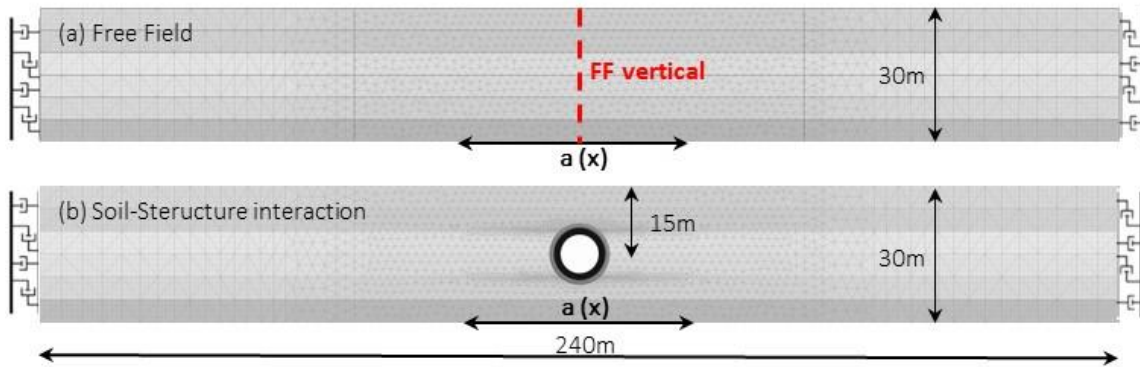


Figure 5.9. Numerical 2D mesh in Plaxis for (a) free field and (b) soil-structure interaction analysis.

The tunnel section has an external diameter of 10m, the tunnel axis is 15m under the ground surface modelled with an elastic plate ($E_{\text{concrete}}=30.5 \cdot 10^6 \text{ kN/m}^2$, $t_{\text{lining}}=0.50\text{m}$, $\nu=0.2$) assuming a damping of the structure equal to 2% for the target frequencies of 1Hz and 10Hz.

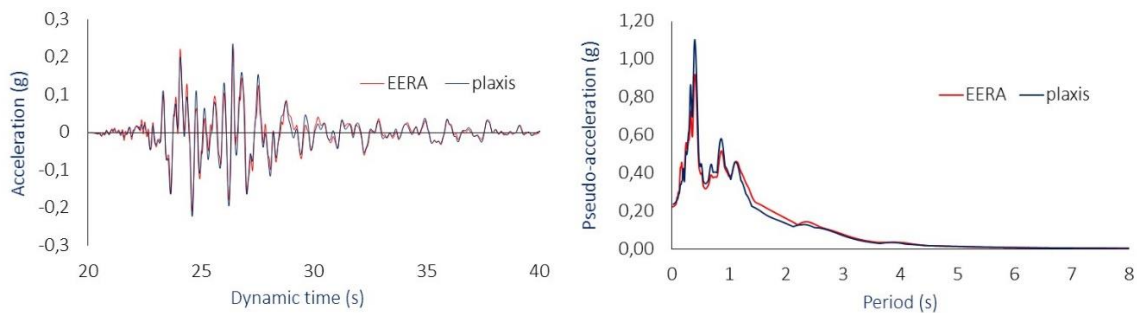


Figure 5.10. Comparison of the FF soil response between EERA and Plaxis 2D (Campano-Lucano Earthquake).

The full dynamic coupled analysis follows an initial static stage where in a simplified way the effect of the tunnel excavation has been taken into account. The convergence-confinement method for instance

has used for this end, assuming a relaxation factor equal to 0.3. The soil structure interaction has been simulated with an interface element reducing of 30% the adjacent soil strength and stiffness ($R_{\text{interface}} 0.7$).

At the end of the dynamic seismic shaking of the maximum values of the internal forces in the lining are computed; Figure 5.11 shows as example the envelope of the maximum bending moment and normal forces evaluated during the Bingol earthquake scaled up to 0.5g. The maximum bending moment reached during the dynamic shaking represent the seismic demand of the structure, as defined by *Argyroudis & Pitilakis 201*.

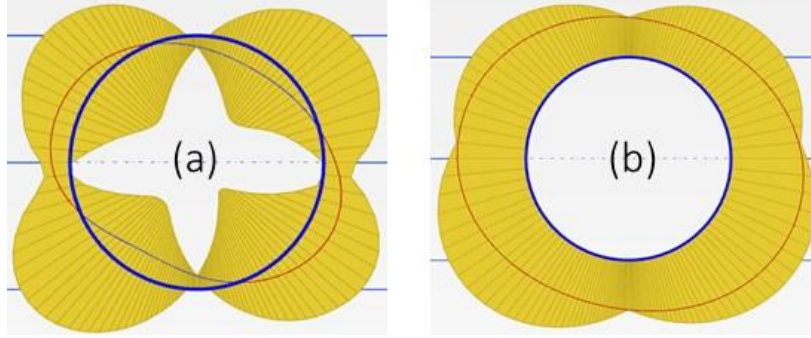


Figure 5.11. Example of envelope of (a) maximum bending moment and (b) normal force in the tunnel section during the dynamic time (Bingol earthquake 0.5g).

CONSTRUCTION OF FRAGILITY CURVES

Following the approach proposed by *Argyroudis & Pitilakis 2012*, the dispersion charts of damage are defined for each soil types assuming the PGA the control parameter while the natural logarithm of the damage index ID the dependent variable. The damage index ID has been calculate as in the following equation:

$$\frac{\text{Structure Demand}(t)}{\text{Structure capacity}(t)} = \max(t) \frac{M}{M_{Rd}(N_{Rd})} \quad (5.3)$$

In the Equation 5.3, 'M' is the maximum bending moment of the tunnel section computed during the dynamic time including the static contribution, 'M_{Rd}' is resistant bending moment evaluated in function of the resistant normal force. Table 5.5 includes the section tunnel properties used for the evaluation of the structure capacity.

Thickness (mm)	Length (mm)	Steel	Concrete	Superior bars	Inferior bars	Concrete cover (mm)
500	1000	B450C	C35/45	8φ12	8φ12	40

Table 5.5. Properties of the tunnel lining section (b=1m)

Figure 5.12 shows the dispersion charts of damage (PGA, LnID) for the soil types B, C and D. A linear regression line fits the data set, bounded by the corresponding standard deviation, allowing to identify the median threshold value of PGA for each damage state (Minor, Moderate and Extensive) in function of the ranges of the DI proposed by *Argyroudis & Pitilakis 2012* for each state of damage.

At this point, the fragility curves can be derived in terms of PGA (Equation 5.4).

$$P_f(d_s \geq d_{si} | PGA) = \phi \left[\frac{1}{\beta_{tot}} \ln \left(\frac{PGA}{PGA_{mi}} \right) \right] \quad (5.4)$$

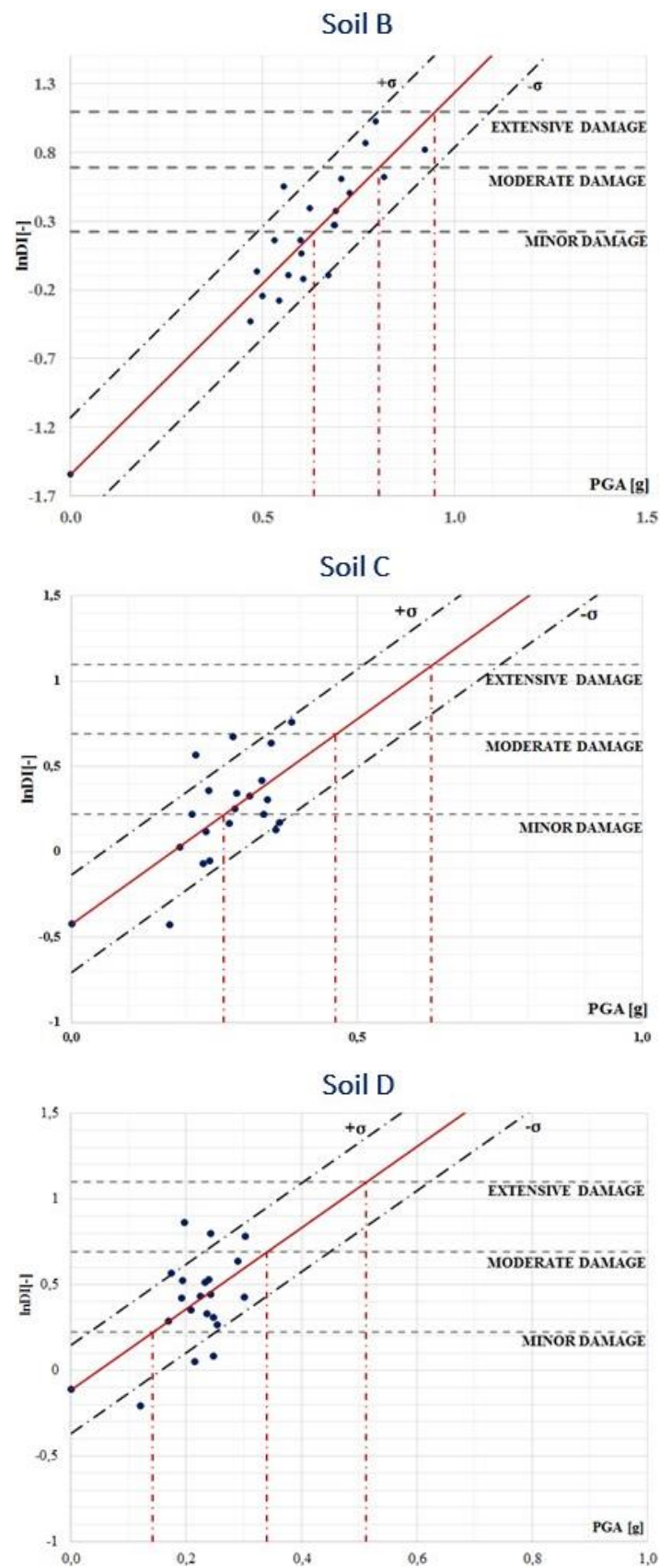


Figure 5.12. Evolution of damages with PGA at the ground surface. Estimation of the median threshold values of PGA for each damage state.

In the Equation 5.4 which represents a log-normal probability distribution, 'PGA' is the actual value, 'PGA_{mi}' is the median of PGA values for which the tunnel reaches the damage level d_{si} , ' β_{tot} ' is the total standard deviation of the natural logarithm including three types of uncertainties: one related to the damage level definition (β_{ds}) assumed equal to 0.4 following the Hazus approach for buildings (NIBS. HAZUS-MH 2004), one related to the structure capacity (β_c) assumed equal to 0.3 following the BART studies (Salmon et al. 2003) and one related to the seismic input (β_d) equal to the standard deviation of the damage index computed from different input accelerograms.

Figure 5.13a shows the fragility curves obtained with this procedure based on 2D visco-elastic full dynamic analysis, including the values of β_{tot} and the median of the acceleration values μ for each level of damage and each soil types. Respect the same damage level, softer soils are characterized by a higher probability of damage than those surrounded by stiffer soils, therefore a soil type D has a higher probability of damage respect a soil type B for an assigned value of PGA. It can be noticed how, for the same value of PGA, the probability of damage decreases with the increasing of the damage level (from Minor to Extensive damage) for every type of soil type. This result lets to observe that the probability of extensive damage is rather low in this type of underground structure, unless rather high value of PGA. This structures are more vulnerable in terms of minor and moderate damage and this result is in good agreement with observed cases history (see Chapter 4).

Further analysis have been carried out adopting a more advanced constitutive model for the soil to investigate its influence. For instance, the dry Leighton Buzzard sand (fraction E) at relative density of 75%, adopted in centrifuge model (Lanzano G. 2009) that has introduced and back-analyzed in the Chapter 4, has been adopted as soil type C ($V_{s,30}=219$ m/s). Non-linear visco-elasto-plastic analysis have been performed based on the calibration parameters of the constitutive model resumed in Table 4.3. This set of analysis does not require the validation of the numerical model in free field condition.

The comparison between the two constitutive model is shown for the soil type C only in Figure 5.13b. The more realistic results obtained with the non-linear visco-elasto-plastic analysis provide a lower values of probability of damage, for every damage level. As it could be expected, the equivalent viscous linear elastic approach overestimate the probability of damage up to a value of 15%-20% in the specific case of soil type C.

A comparison between the analytical curves of Argyroudis & Pitilakis 2012 is proposed in Figure 5.14a. The approach used by the authors based on pseudo-static analysis underestimates the probability of structure damage, in all cases. These results were expected by the authors which compared, for some cases, the results obtained with the uncoupled and coupled approach. Also the results shown in this work (see Chapter 4, §4.2.3) left thinking the same conclusion.

A modified version of the fragility curves obtained by Argyroudis & Pitilakis 2012 is here proposed.

Because in the iteration procedure available in EERA code the maximum shear strains γ_{max} are computed in function of the effective ones γ_{eff} ($\gamma_{eff}=R_\gamma * \gamma_{max}$ with $R_\gamma=0.65$), the displacement profiles applied by the authors on the boundaries of the numerical model to simulate pseudo-static seismic load likely produce a reduction of the real load that should be applied on the tunnel structure.

This effect is not included in the coupled numerical approach therefore, to make consistent the comparison between the two approaches, coupled and uncoupled one, the median of the PGA values obtained by the authors for every fragility curves has been scaled of a coefficient equal to 2 that takes into account the effect of reduction of 0.65 of the maximum shear strains. This value that multiplies the deviation standard, μ , of each curve, has been established dividing by 0.65 the average value of the ratio M/M_{rd} calculated by the authors with the pseudo-static analysis.

Figure 5.14b shows the comparison between the fragility curves based on coupled approach and those modified after Argyroudis & Pitilakis 2012 based on coupled approach.

A set of comparisons has been done with '*empirical fragility curves*' available in the technical literature.

Figure 5.15a and Figure 5.16a for instance, show the comparison with *ALA 2001*, based on *Power et al. 1998* database, while Figure 5.15b and Figure 5.16b refer to *HAZUS 2004*.

Analytical fragility curves, even if less realistic because based on a distribution of damages simulated in an 'artificial' way while the empirical one are based on statistical analysis of observed damages in past earthquakes, are more sensitive to the type of lining, geologic media and then can take into account the relative soil-structure relative stiffness and the interfaces condition. Empirical classifications do not differentiate for soil and structure type associating qualitative and quantitative information to define the damage level.

If for above ground structures the empirical fragility curves can be consider rather reliable, it couldn't be said the same for underground structures which dynamic behaviour is dominated by the soil response, not included in the empirical approach.

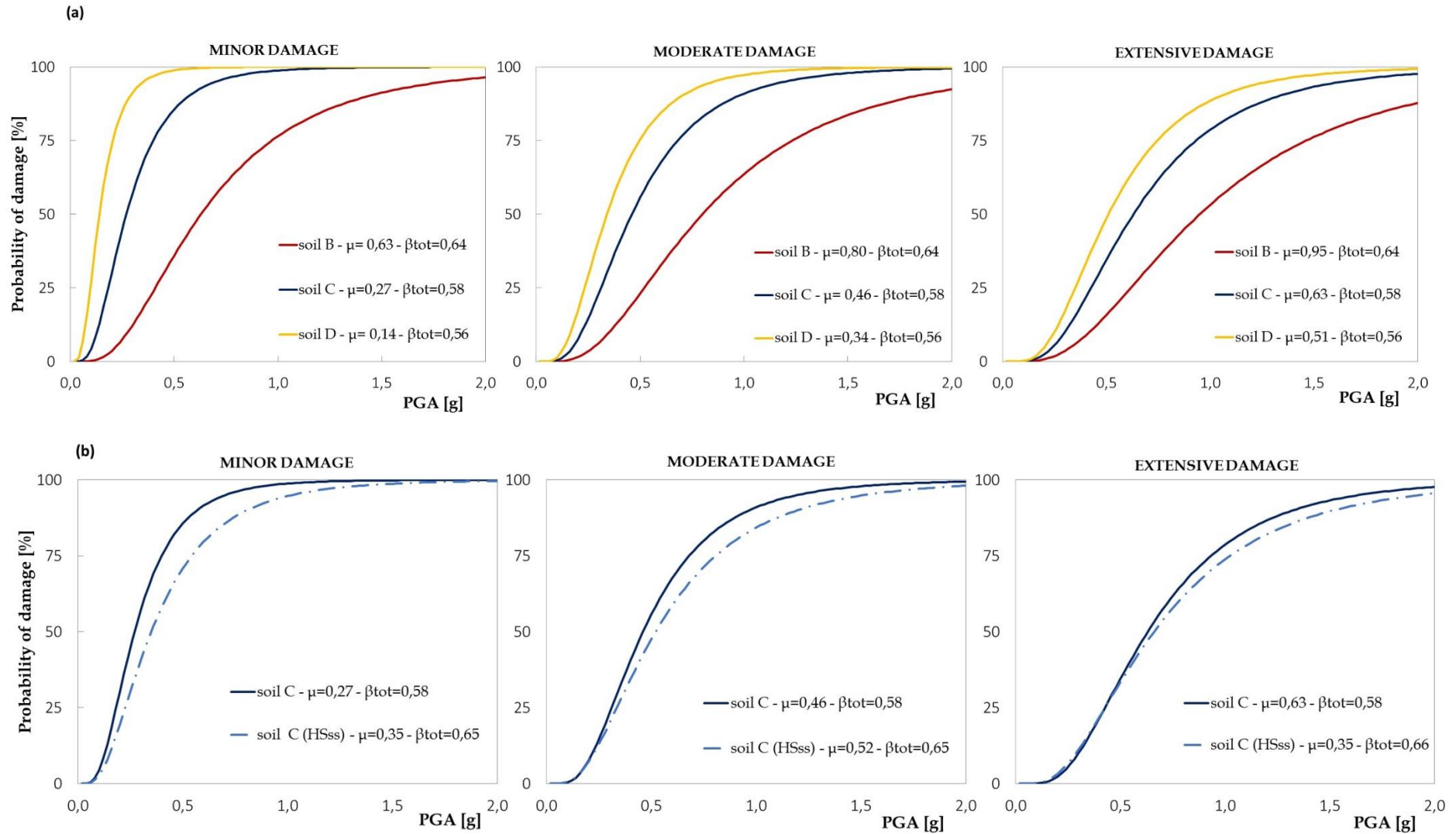


Figure 5.13. (a) Analytical fragility curves for circular continuous tunnel lining based on 2D full dynamic visco-elastic analysis; (b) Comparison with fragility curves based on 2D full dynamic visco-elastic-plastic analysis for soil type C.

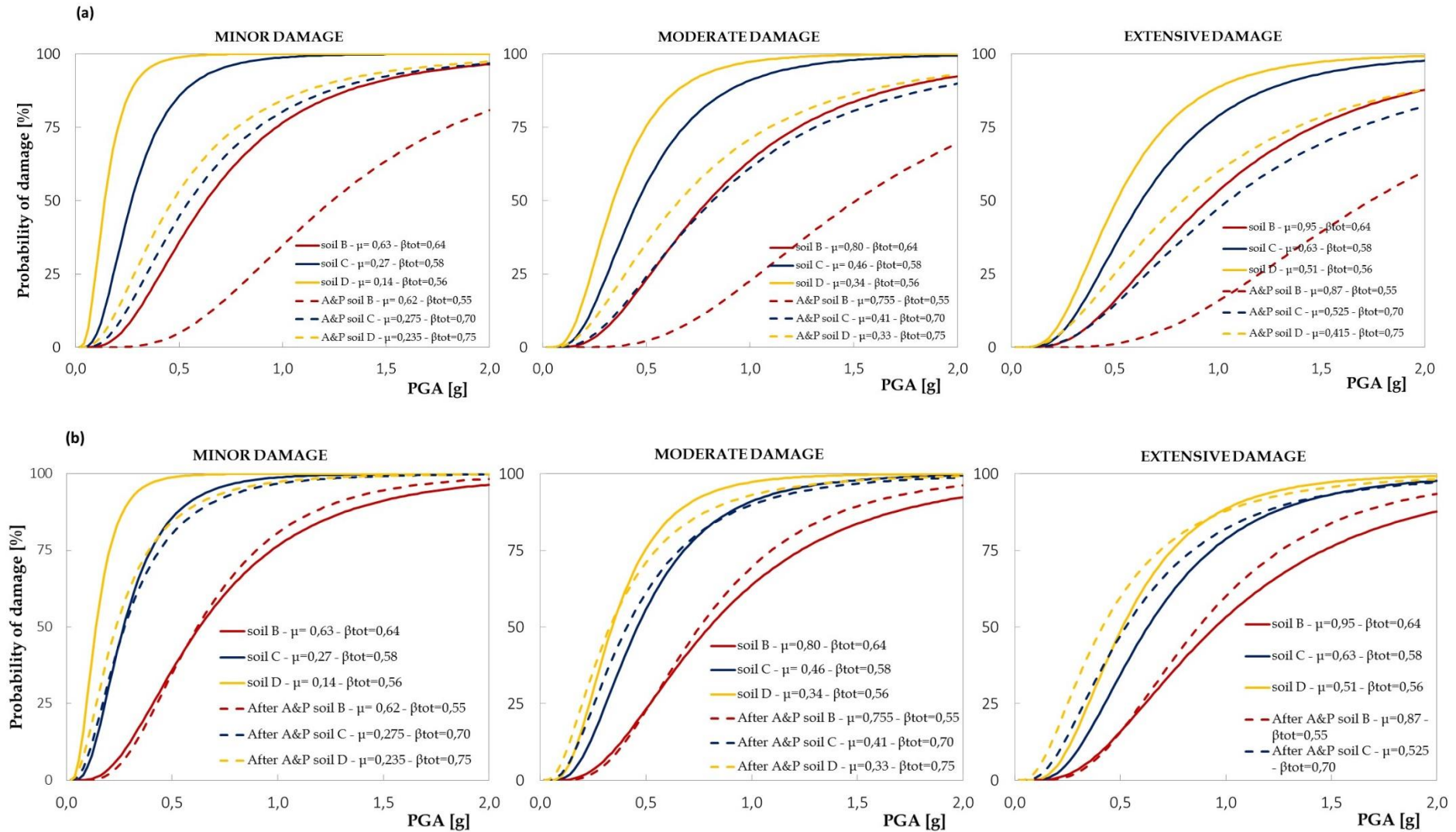


Figure 5.14. Comparison with analytical fragility curves for circular tunnel lining of (a) Argyroudis & Pitilakis 2012 and (b) modified after Argyroudis & Pitilakis 2012.

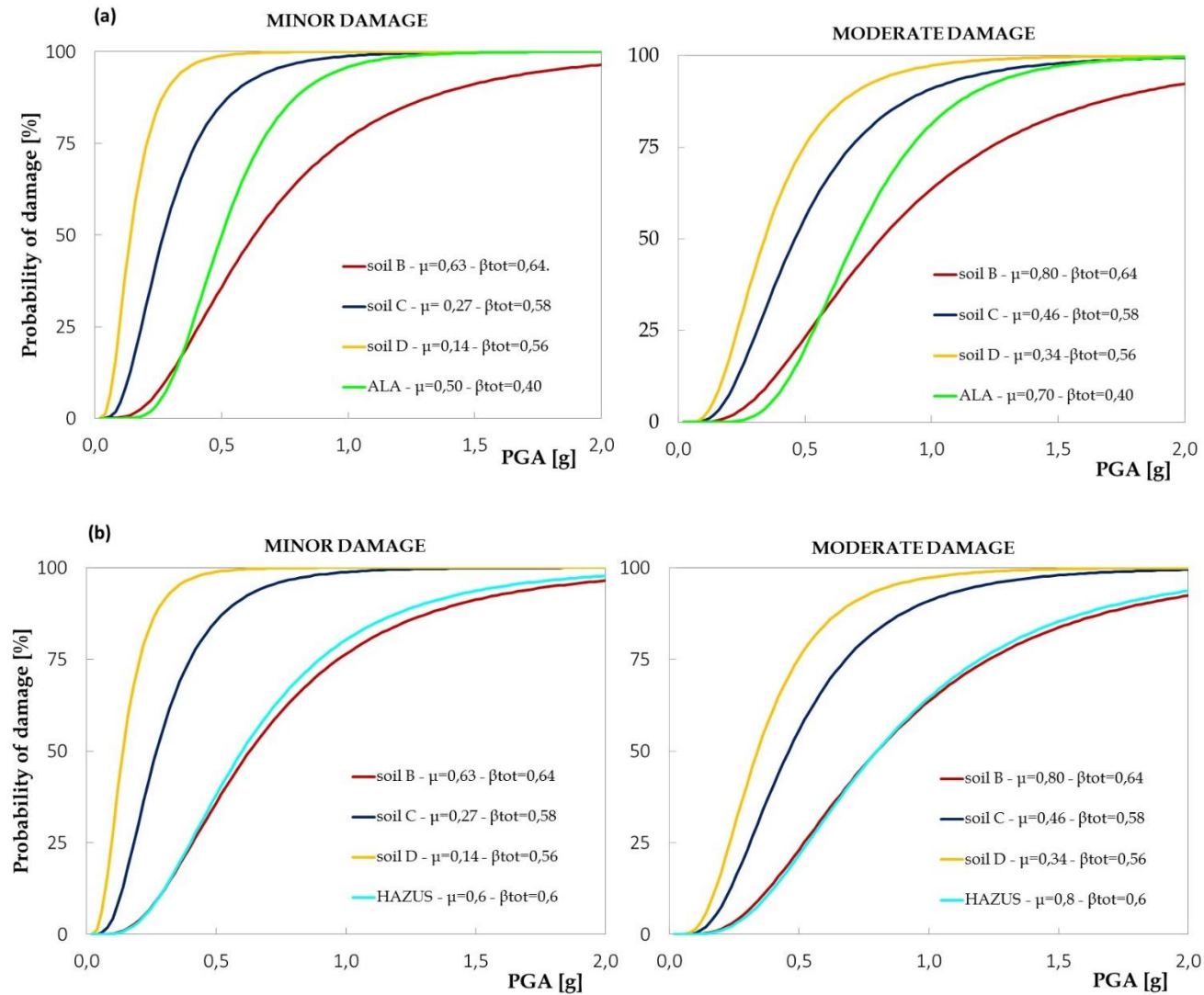


Figure 5.15. Comparison between analytical fragility curves for circular tunnel lining with (a) empirical fragility curves ALA 2001 and (b) empirical fragility curves HAZUS 2004.

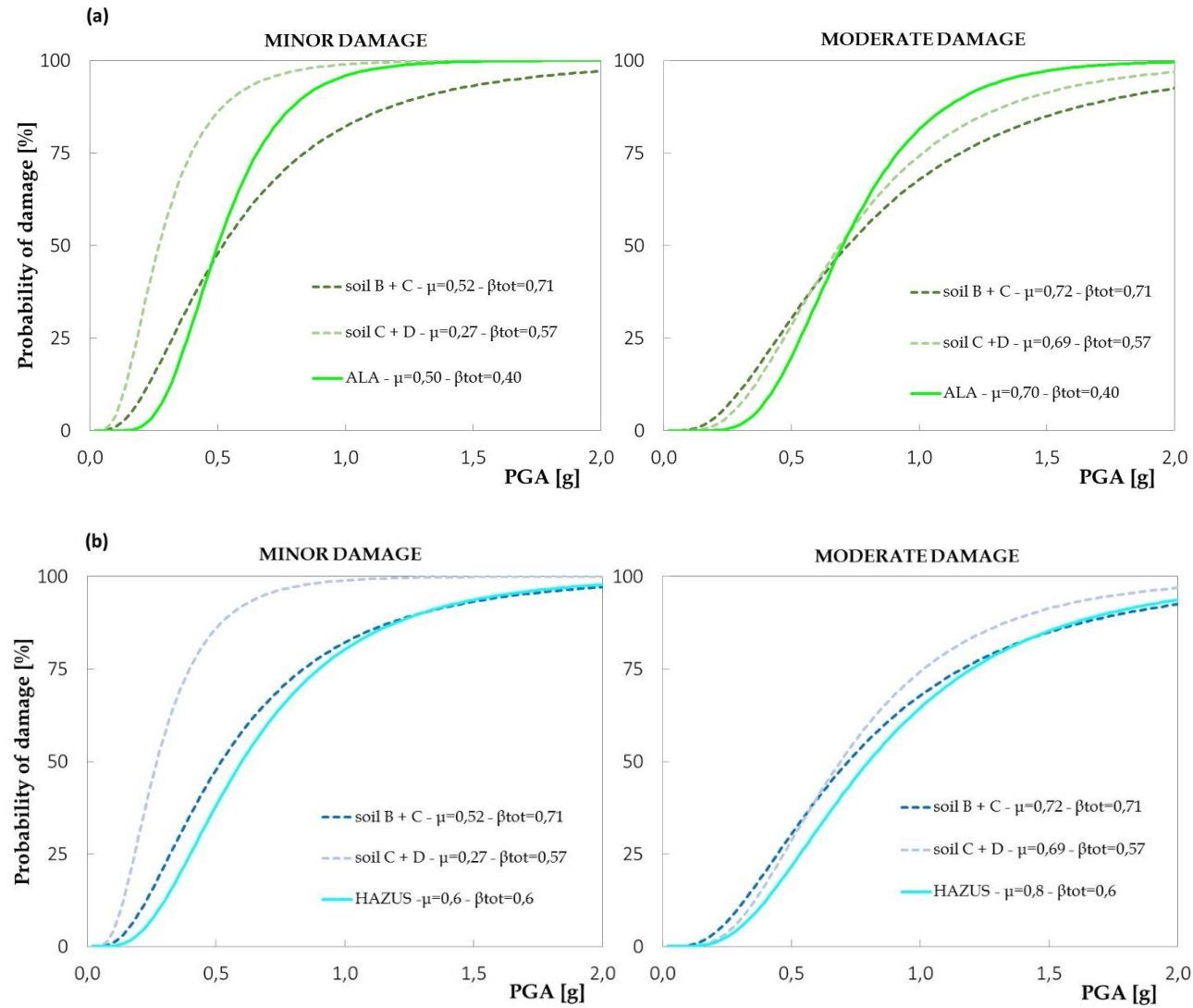


Figure 5.16. Comparison between analytical fragility curves for circular tunnel lining with (a) empirical fragility curves ALA 2001 and (b) empirical fragility curves HAZUS 2004.

5.1.2 Segmental lining

The numerical investigation showed in the Chapter 4 have highlighted the substantially different behaviour of a continuous lining respect the segmental one under seismic loads, commonly adopted in mechanized tunneling. There is a significant effect of the jointed pattern of a segmental lining which implies a lower structural demand than a continuous ring and a potential fragility associated to an excessive joint rotation. Based on these numerical evidences, the analytical fragility curves for segmental tunnel lining have been constructed with a similar approach followed in the case of continuous lining. Figure 5.17 for instance, shows the flowchart adopted in the case of segmental lining that differs from the continuous one in the parts highlighted in red.

Apart from the different technology, the fragility curves carried out in the case of segmental lining are based on visco-elasto-plastic non-linear coupled analysis, refer to a different damage index ID and damage state DS respect the continuous case, both proposed in this work, related to the Peak Ground Acceleration, PGA, and the Permanent Ground Displacement, PGD.

In this section it is discussing only the aspects which differ from the continuous case.

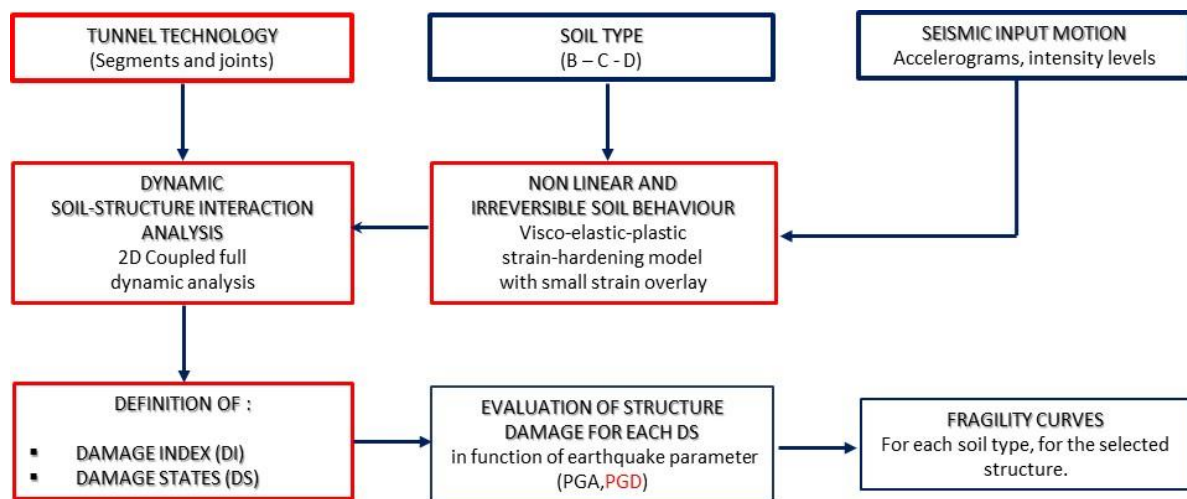


Figure 5.17. Proposed flowchart of the procedure for deriving numerical fragility curves for 'segmental lining' of circular tunnels.

The tunnel section dimension and position (diameter, segments thickness, depth of the tunnel axis) and the soil-structure interface properties are the same of the continuous case. The tunnel lining has been divided in a number of segments equal to ten (Figure 5.18), the longitudinal joints are numerically modelled as elasto-plastic springs with $M-\theta$ relation as in Figure 5.18. The joint type simulates the behaviour of a flat non-bolted longitudinal joint with a height of the contact area between the segments equal to 0.25m.

The numerical study has considered three different ground conditions, corresponding to the soil types B, C and D of Eurocode 8 site classification (EC8, 2004).

Soil type C ($V_{s,30}=219$ m/s) is the same adopted for the visco-elasto-plastic analysis in the case of continuous lining for which experimental tests for the calibration of the constitutive parameters have been performed (Lanzano G. et al. 2016). As soil types B and D, ideal soil layers with equivalent shear wave velocity $V_{s,30}$ equal to 395 m/s and 150 m/s respectively have been assumed.

As just mentioned, the soil type B and D are ideal soils, therefore the corresponding geotechnical parameters (soil weight γ_d , friction angle ϕ_{pk} and the angle of dilatancy ψ_{pk}) have been assigned to the soil types coupling the soil B together with a sand while the soil type D with a clay weakly over-consolidated.

The stiffness soil parameters instead, have been obtained scaling the parameters associated to the soil C proportionally to the corresponding shear velocity $V_{s,30}$. The parameters computed in this way for the soil type B and D are listed in the Table 5.6 together with the soil type C parameters.

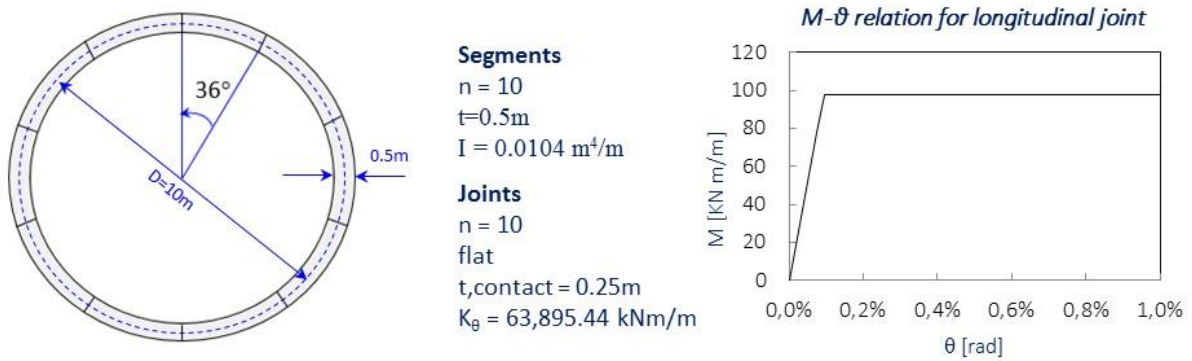


Figure 5.18. Geometry of segmental tunnel section considered for the definition of the relative fragility curves.

To validate the calibration parameters assumed for the soil type B and D in reference to the adopted constitutive model Hardening Soil Small Strain, HSss, the behaviour of a soil element has been modelled in stress paths corresponding to drained and undrained triaxial tests, oedometer tests, simple cyclic shear tests simulated in Plaxis 2D.

	Type B	Type C	Type D
$V_{s,30}$ [m/s]	395	219	150
γ_d [kN/m ³]	20	15.2	18
E_{50}^{ref} [MPa]	80	18.6	10
E_{oed}^{ref} [MPa]	87	20.5	11
E_{ur}^{ref} [MPa]	198	62.2	25
ν_{ur} [-]	0.2	0.2	0.2
m [-]	0.4	0.4	0.8
G_0^{ref} [MPa]	310	72.7	40
$\gamma_{0.7}$ [-]	0.00017	0.00058	0.0003
ϕ_{pk} [-]	40	38.6	25
ψ_{pk} [-]	6	8.2	2
c' [kPa]	0.01	0.01	0.01
α_R [-]	2.09E-01	6.68E-02	1.77E-01
β_R [-]	4.30E-04	7.04E-04	9.55E-04

Table 5.6. Constitutive parameters of HSss for the soil type B, C and D.

Figures 5.19 and 5.20 show for instance the τ - γ cycles corresponding to simple cyclic shear test with increased level of deformation γ for the soil types B and D respectively. Figure 5.21 instead, compares the

different cyclic behaviour of the two soil types. Starting from these results, the degradation curve of the shear modulus G and the damping ratio D have been computed for soil B and D shown in Figure 5.22.

The curves $G(\gamma)/G_0$ and $D(\gamma)$ obtained with numerical shear tests for soil type B and D, have been compared with literature curves. The curves made available by *Darendeli (2001)* for different soil types for instance were taken as targets. In particular, the literature curves used for soil type B refer to a dry sand with an effective stress σ'_0 equal to 2 atm, while for soil type D they refer to a slightly over consolidated clay (OCR=2) with a plasticity index IP equal to 25 and an effective stress σ'_0 equal to 1.28 atm.

Figure 5.22 shows the comparison between the numerical and literature curves for soil B and D while for the soil type C the curves are taken from *Lanzano et al. (2016)*, comparing the experimental laboratory results (resonant column RC and torsional shear TS laboratory tests for instance) with the numerical simulations.

The numerical procedure to perform the coupled dynamic analysis is the same adopted in the Chapters 4 and 5 (§ 4.2.2, 5.1.1), starting from a computed pre-seismic state of stress due to the tunnel excavation.

What should be discussed in more details, is the choice of the damage index ID, the damage states DS and the intensity motion parameter IM for such tunnel lining technology.

Because under seismic uniform load condition the longitudinal joints are the most vulnerable points of the segmental tunnel lining, as observed in the numerical results shown in the Chapter 4, the damage index proposed in this work has been expressed in function of the longitudinal joint rotation. This choice assumes that the failure mechanism of such structure could be more 'prospective' in correspondence of the joint and not in correspondence of the concrete segments, as in the case of continuous lining for which the damage index is suitably related to the maximum resistant moment reached in the lining section.

However, to support and validate this choice, the analytical fragility curves have been defined also assuming as damage index the value of $\max(M/M_{Rd})$, as proposed by *Argyroudis & Pitilakis 2012* in the case of continuous lining, and the comparison between the two approaches shows that in the case of segmental lining the joints are actually more exposed to be damage.

As introduced in the Chapter 1 about the rotational capability of the longitudinal joints, it has been discussed that they are mainly interested to three different working stages depending on the eccentricity $e=N/M$ of the resultant of the normal force in the joint contact section. In the case of eccentricity $e<t/6$, the joint is closed, that is completely under compression, and it behaves as linear-elastic; as soon as eccentricity $e=t/6$ the joint starts to open ($e>t/6$). At high values of rotation, third stage, plastic strains occur in the concrete until the joint fails.

What can be alarming is the rotation threshold for which the joint starts to open. Based on this scenario, the *Janßen's* analytical solution has been adopted to define the threshold values of the damage index in function of the proposed damage states. The damage index and the criteria to estimate the damage states DS are specified in Table 5.7.

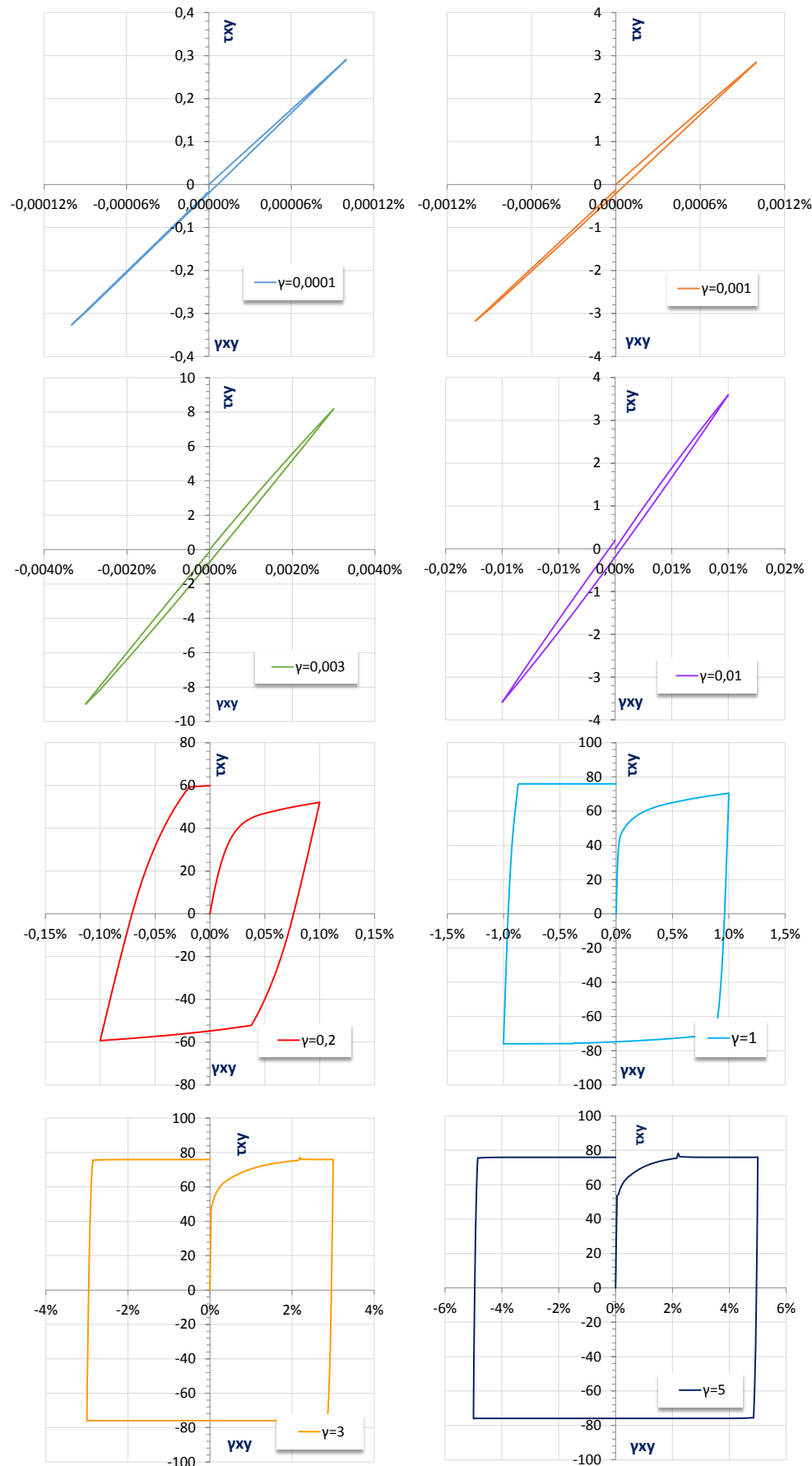


Figure 5.19. Cyclic shear test on soil sample type B in Plaxis 2D.

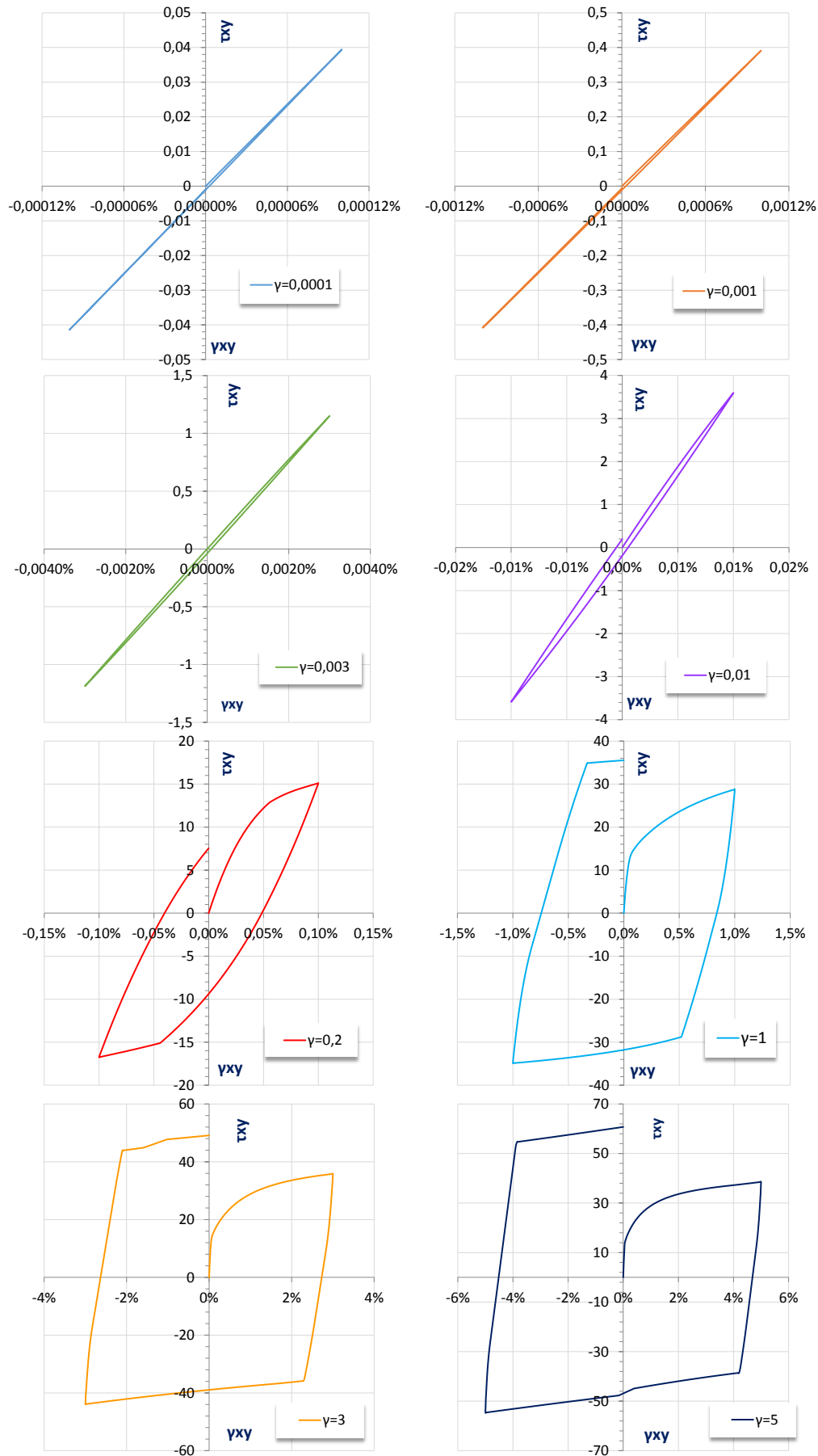


Figure 5.20. Cyclic shear test on soil sample type D in Plaxis 2D.

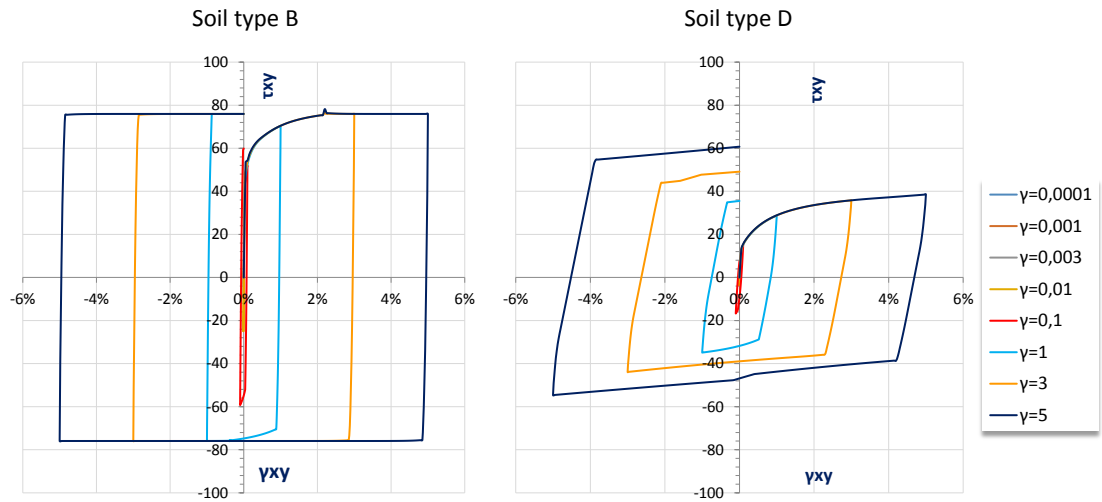


Figure 5.21. Isteretic behaviour of the ideal soil types B and D.

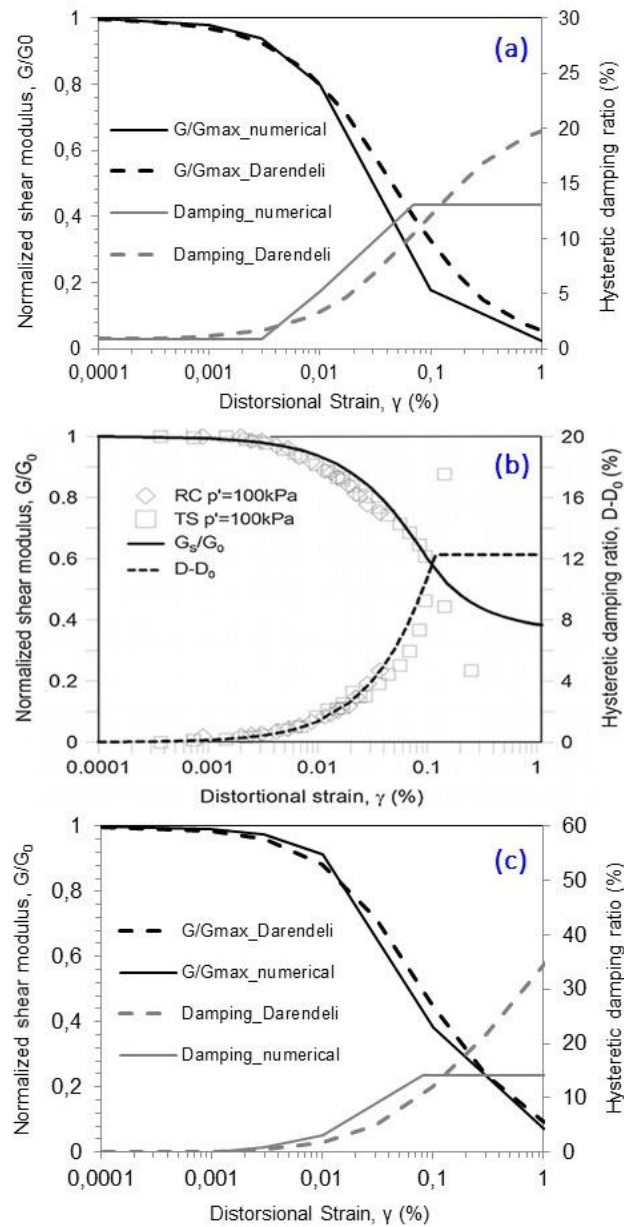


Figure 5.22. Comparison of numerical and literature curves of G/G_0 and D for soil type B, soil type C (after Lanzano et al. 2016) and soil type D.

The performance of the joint is expressed as a ratio between the 'permanent rotation ϕ_r ' of the joint and reference joint rotation threshold (Equation 5.5).

$$DI = \max(t) \frac{\phi_{r,permanent}}{\phi_{threshold}} \quad (5.5)$$

Three values of rotation were set as thresholds for damage state definition (Figure 5.23):

- ϕ_1 is the first critical threshold, in which the joint opening occurred, defined as $\phi_1 = NI^2/6EI = 12M/Ebl^2$ ($b=l$);
- ϕ_y is the yielding rotation;
- ϕ_u is the ultimate rotation.

Damage state (DSi)	Damage Index (DI) Range	Median value
DS1: none	$\phi_r/\phi_1 \leq 1$	-
DS2: minor/slight	$1 \leq \phi_r/\phi_1 \leq 1.5$	$1.25 \phi_1$
DS3: moderate	$1.5 \leq \phi_r/\phi_1 \leq 2\phi_r/\phi_1 - 1.5\phi_y$	ϕ_y
DS4: extensive	$2\phi_r/\phi_1 - 1.5 \leq \phi_r/\phi_1 \leq \phi_u/\phi_1$	$\phi_y - 0.75\phi_y + 0.5\phi_u$

Table 5.7. Damage index definition in terms of relative joint rotations.

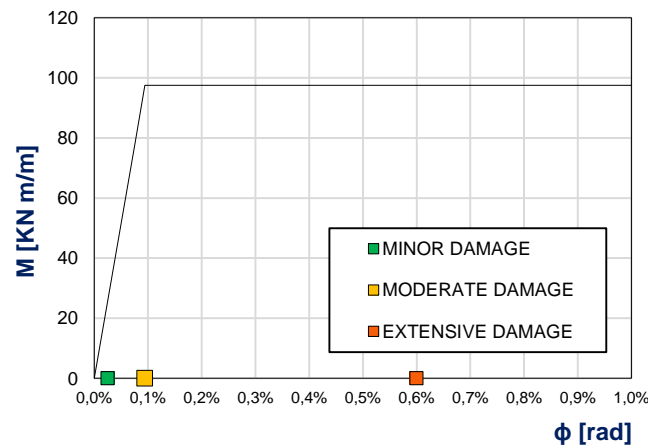


Figure 5.23. Rotation thresholds for damage states definition.

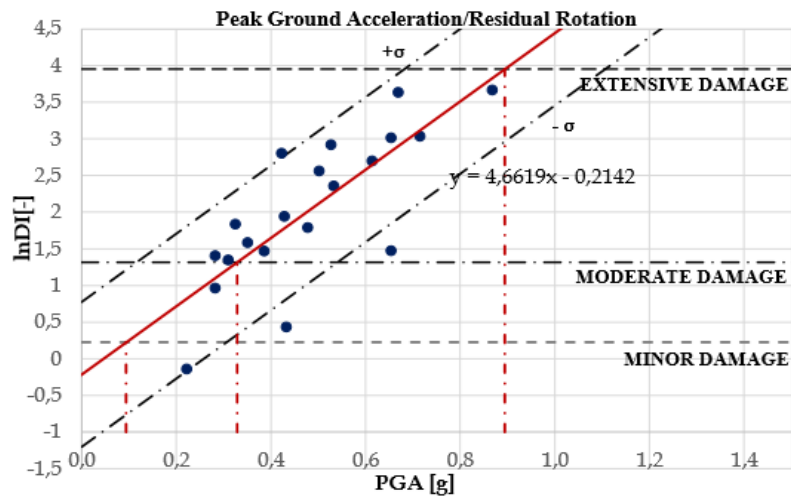
Because the numerical results for segmental lining (see Chapter 4) have shown that for usual PGA values of real earthquakes longitudinal joints undergo to opening but not to a completely collapse, an excessive rotation of joints under high value of PGA may produce dislocation of gaskets and cause severe inflow from groundwater, a probably condition that may occur in the case of moderate damage.

Such a problem has been already highlighted into an interesting work of *Faisal I. Shalabi et al. 2012* based on experimental tests with cyclic loads on a set of longitudinal and circumferential joint types.

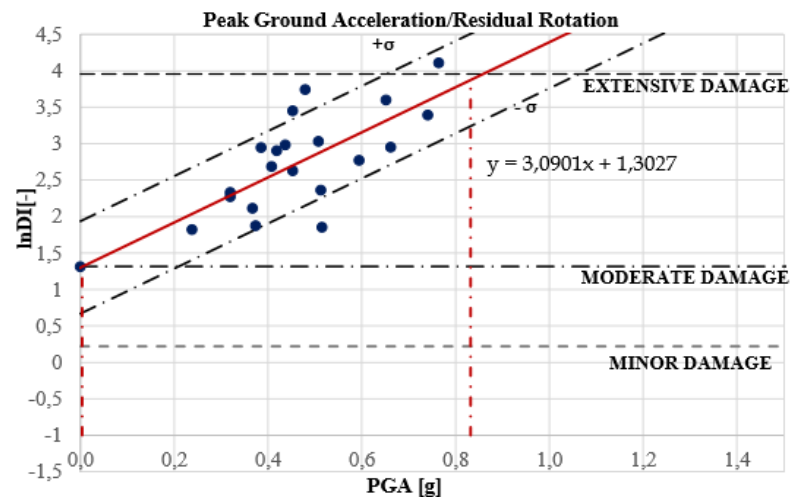
In this scenario, it seems to be more appropriate refer to the permanent value of joint rotation, computed at the end of the seismic shaking, rather than the peak one. In this case PGA and PGD were selected as IMs. The permanent displacement at the ground surface was used since it may be related to permanent rotation at a tunnel joints. PGD is also commonly used as IM for other buried structures as pipelines subjected to ground failure deformations (*O'Rourke and Liu 1999*).

Figures 5.24 and 5.25 show the dispersion charts of damage for the soil types B, C and D in terms of PGA and PGD respectively.

SOIL TYPE B



SOIL TYPE C



SOIL TYPE D

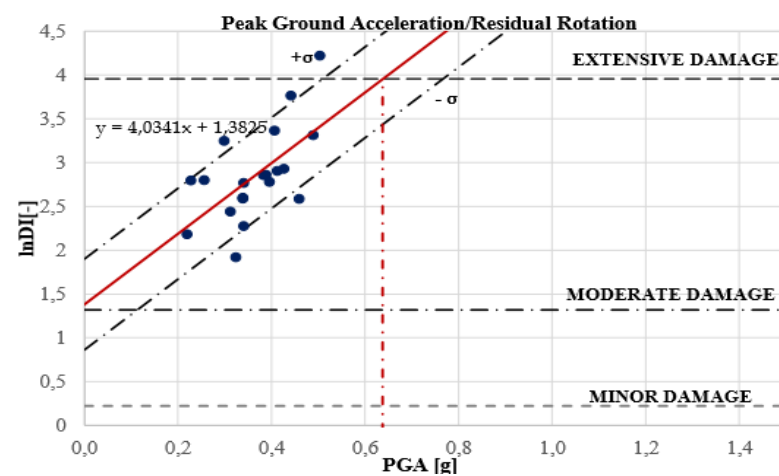
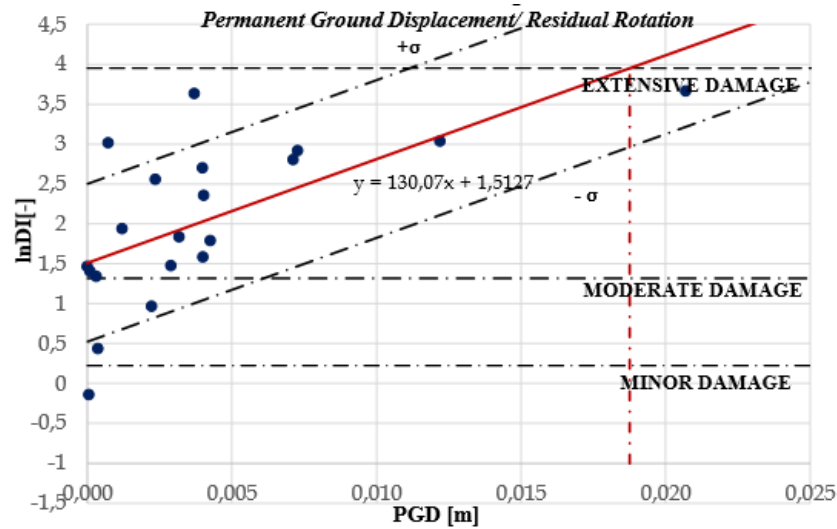
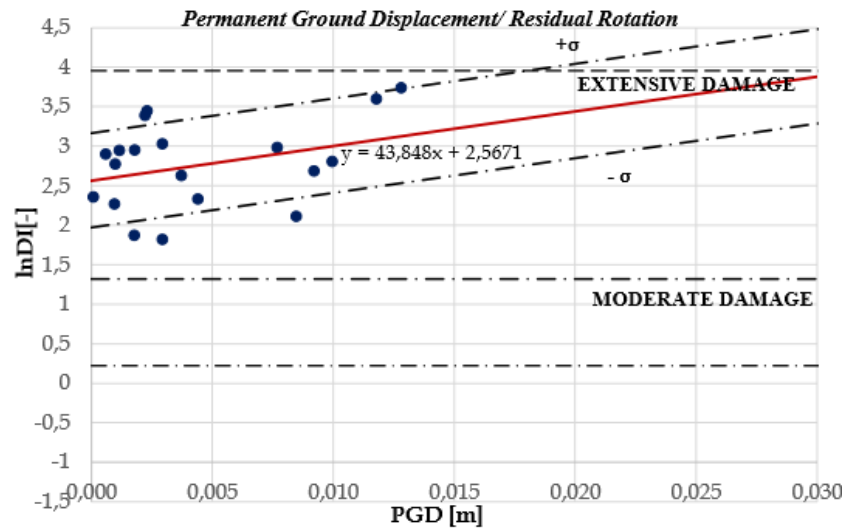


Figure 5.24. Evolution of damages with PGA at the ground surface. Estimation of the median threshold values of PGA for each damage state.

SOIL TYPE B



SOIL TYPE C



SOIL TYPE D

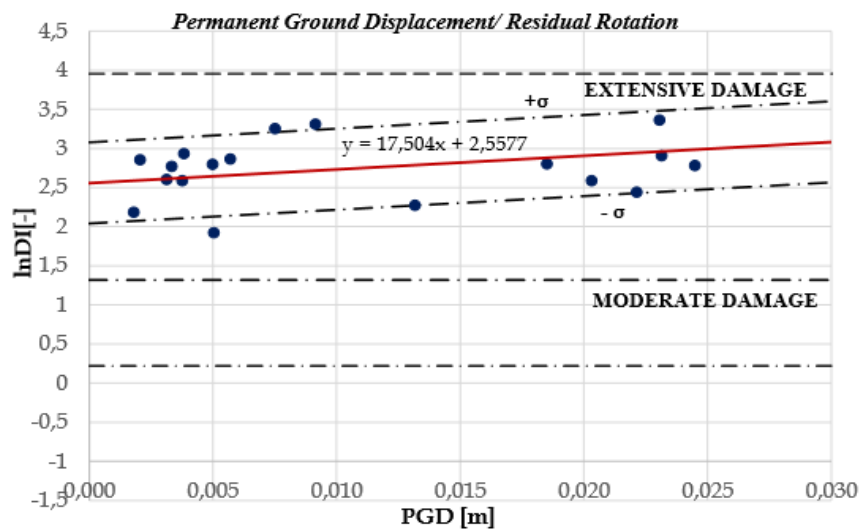


Figure 5.25. Evolution of damages with PGD at the ground surface. Estimation of the median threshold values of PGD for each damage state.

Figure 5.26 shows the fragility curves obtained, when possible, in the case of soil type B, C and D assuming the PGA as IMi. As in the case of continuous lining, the probability of damage increases for more soft soil ($B \rightarrow C \rightarrow D$) and increases with the decreasing of the damage level ($DS4 \rightarrow DS3 \rightarrow DS2$).

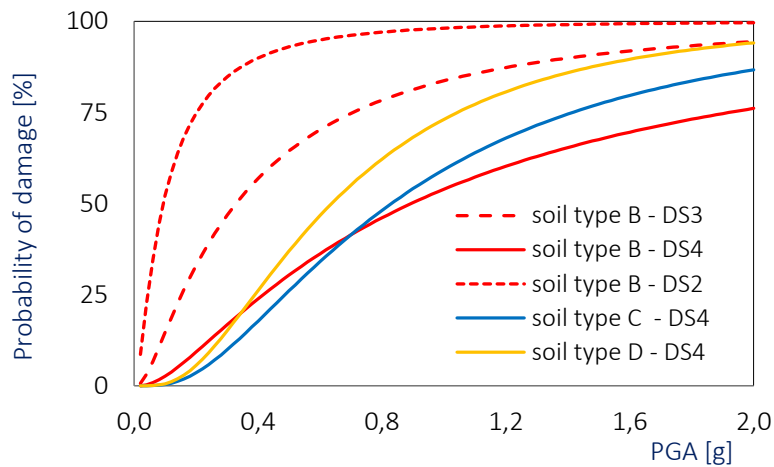


Figure 5.26. Fragility curves for segmental lining based on residual relative joint rotation and peak ground acceleration (PGA).

Comparing the computed rotation fragility curves in terms of Peak Ground Acceleration and Permanent Ground Displacement (Figure 5.27) it can be noticed that, unlike to what happens in terms of PGA, the probability of damage increases with the stiffness of soils in the case of PGD assumed as IMi. This is due to the fact that, to achieve the same PGD, a stiffer soil has to be subjected to larger seismic accelerations than a softer soil.

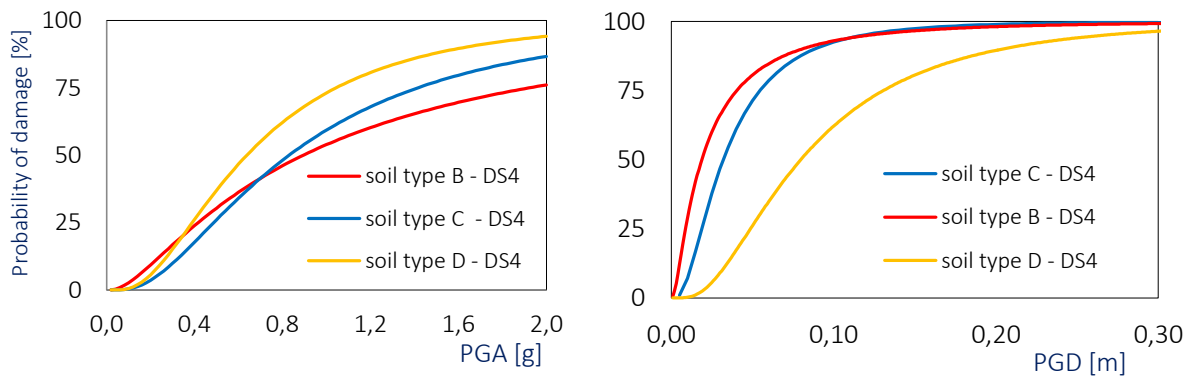


Figure 5.27. Comparison between fragility curves for segmental lining based on residual relative joint rotation and peak ground acceleration (PGA) vs permanent ground displacement (PGD).

Figure 5.28 shows the comparison between the empirical fragility curves proposed by ALA 2001 for the cases of minor and moderate damages and those obtained in this study for all categories of soil type B+C+D. Once again, it should be mentioned that empirical curves don't distinguish the tunnel technologies; overall the numeric curves are less sensible than the empiric ones to little variations of PGA.

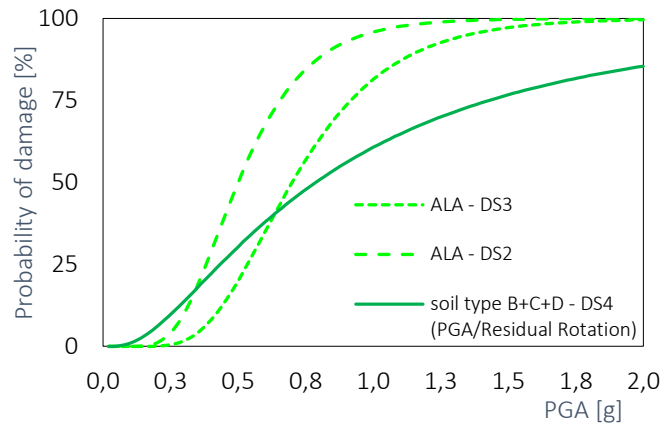


Figure 5.28. Comparison between the empirical fragility curves by ALA (2001) for the cases of minor and moderate damages and those obtained in this study for all category B, C e D.

A further set of fragility curves for segmental tunnel lining has been carried assuming as damage index the value of $\max(M(t)/M_{Rd})$, as proposed by Argyroudis & Pitilakis 2012 in the case of continuous lining.

Figure 5.29 for instance, shows the proposed curves for the soil types B and D in function of the maximum bending moment (curves on the left) and the residual bending moment (curves on the right) computed during the dynamic time in the segments of the tunnel, selecting the PGA as the IMi.

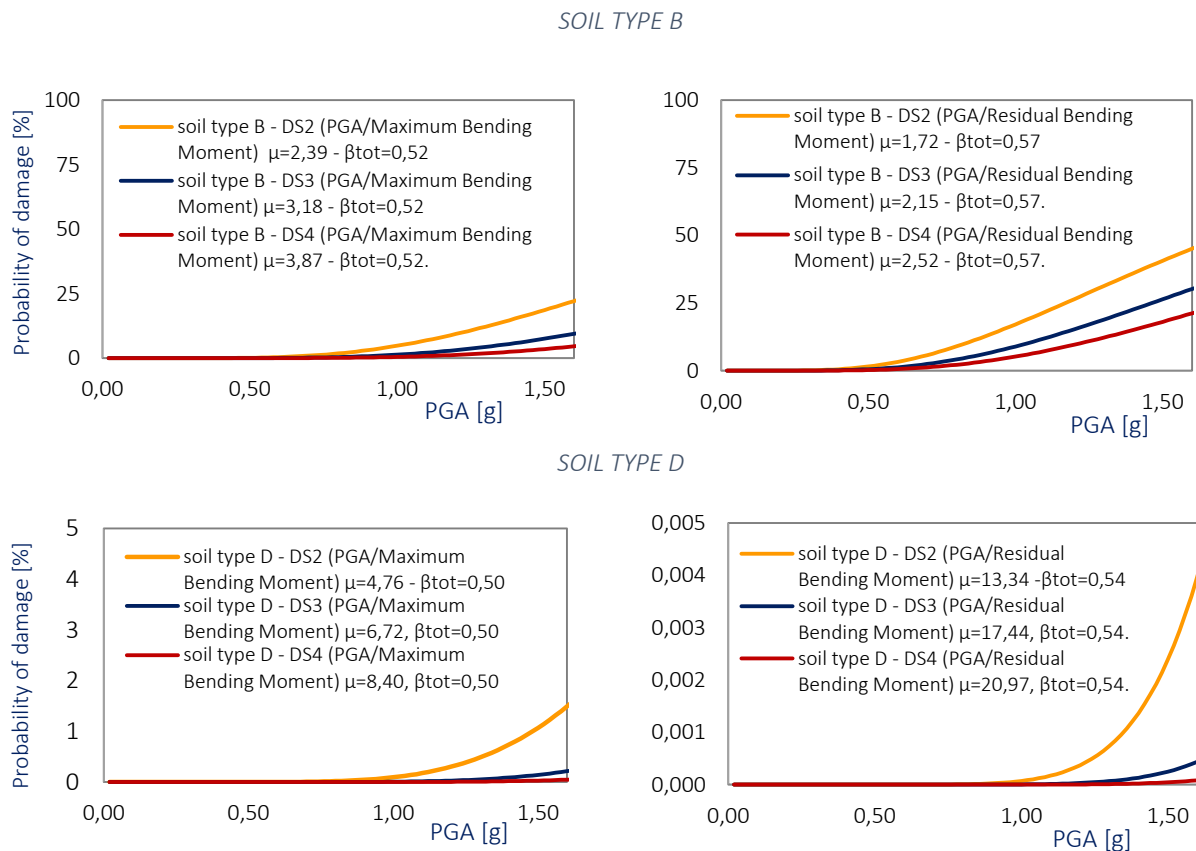


Figure 5.29. Fragility curves for segmental lining assuming $DI = \max(M_{peak}/M_{Rd})$ -curves on the left- and $DI = \max(M_{residual}/M_{Rd})$ -curves on the right- in function of PGA for soil types B and D.

In all cases, the probability of damage is very low because the maximum resistant moment in the section is actually never reached. Figure 5.30 shows the comparison of all the fragility curves shown in Figure 5.29 with the empirical ones proposed by ALA 2001 where is possible to better appreciate the low seismic vulnerability of the concrete segments in the segmental tunnel lining.

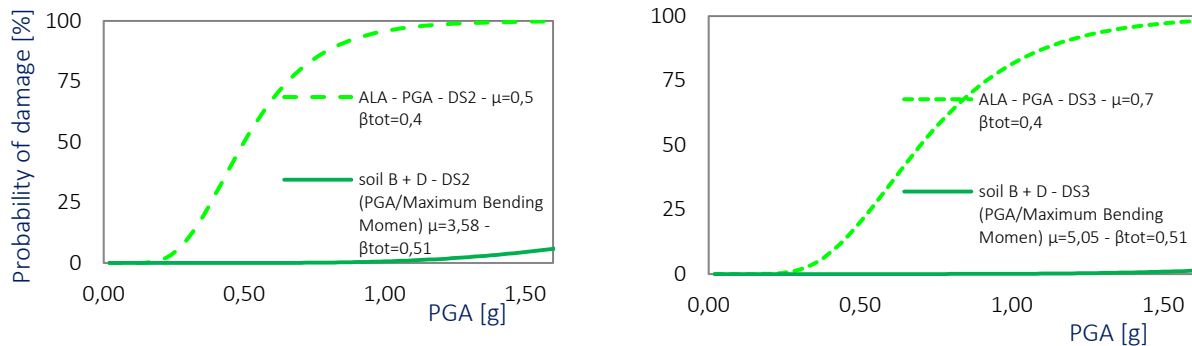


Figure 5.30. Comparison between the fragility curves for segmental lining assuming proposed in function of the maximum bending moment for soil types B+D and the empirical curves proposed by ALA 2001.

To point out the different exposure to be damaged of the segment and longitudinal joint in the segmental tunnel lining, Figure 5.31 shows the comparison between a fragility curve based on the residual bending moment $M_{residual}$ (red curve) and the residual joint rotation $\phi_{residual}$ (black curve) in function of the permanent ground displacement PGD for the soil type B; for the same level of damage, the fragility curve in terms of relative joints rotation is more severe than that in terms of residual bending moment at the same PGD level.

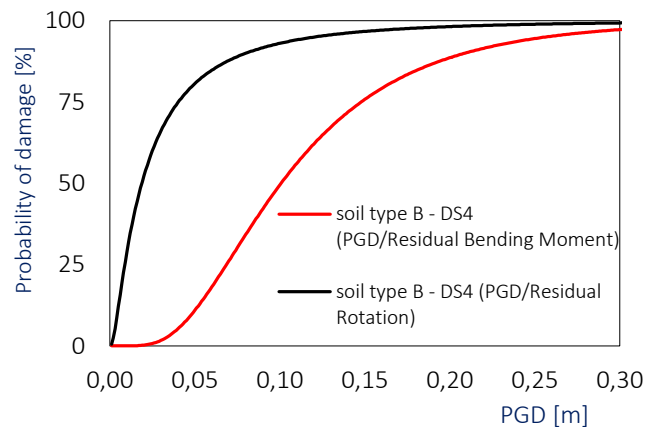
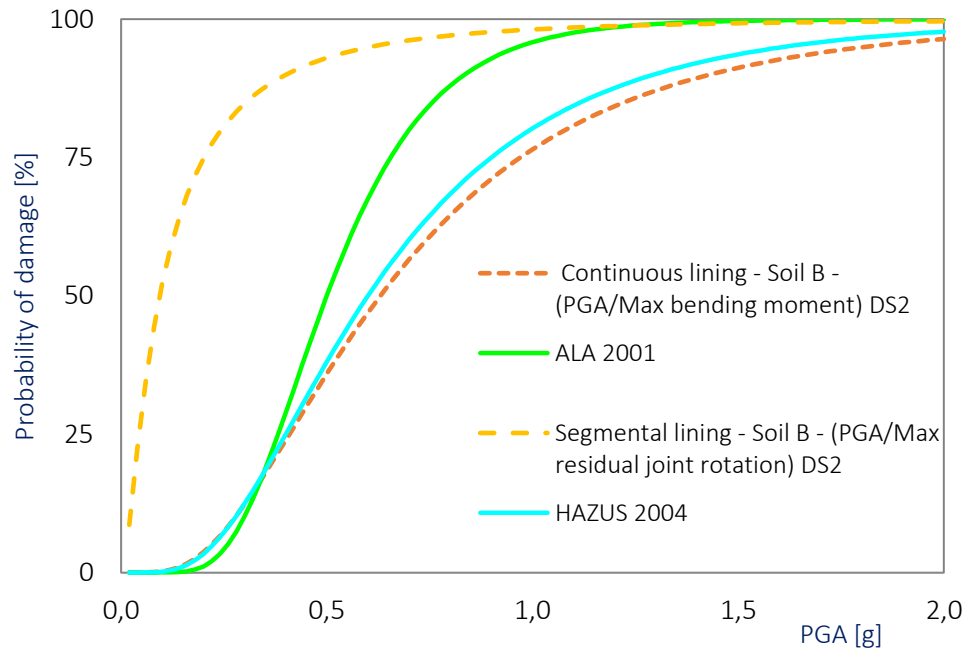


Figure 5.31. Comparison between the fragility curves for segmental lining assuming proposed in function of the maximum bending moment for soil types B+D and the empirical curves proposed by ALA 2001.

Finally, it seems to be interesting comparing the fragility curves obtained in the case of continuous lining, based on the DI proposed by Argyroudis & Pitilakis 2012 and those obtained in the case of segmental lining based on the DI proposed in this work. Figure 5.32 shows this comparison together with the empirical curves available in literature in the case of soil type B for DS2 and DS3. In this conditions, the longitudinal joints of segmental lining seems to be more exposed to seismic damage respect the continuous tunnel lining for a defined value of PGA. Anyway, it should be remember that the segmental lining fragility curves are more reliable, because derived from visco-elasto-plastic analysis using an

advanced constitutive model for the soil (HSss), while the continuous lining fragility ones are based on visco-elastic numerical analysis.

MINOR DAMAGE



MODERATE DAMAGE

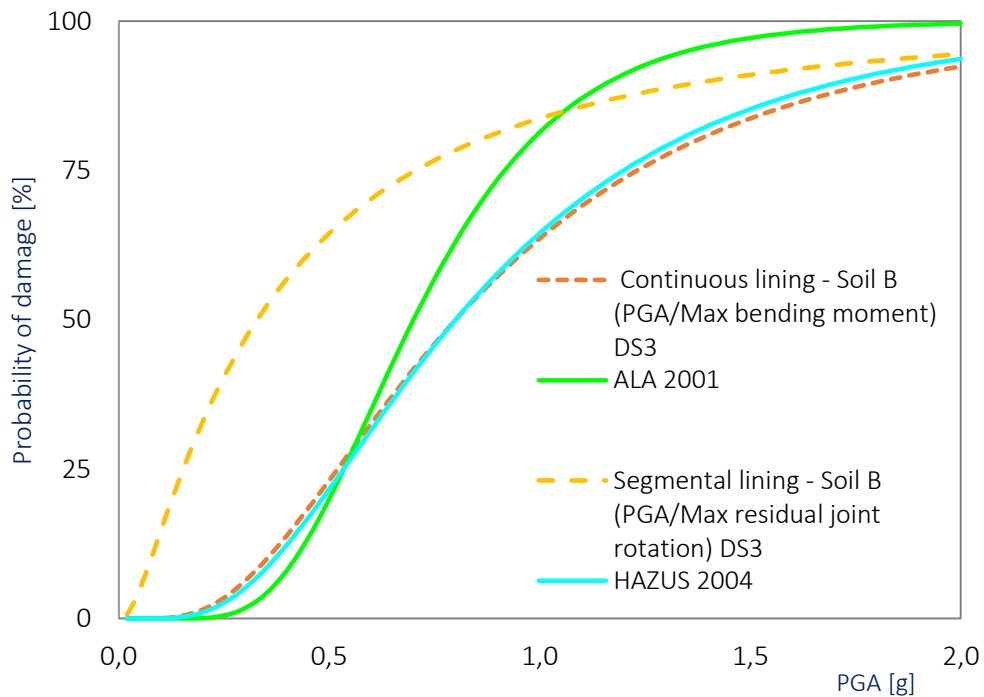


Figure 5.32. Comparison between the fragility curves for continuous lining (PGA vs Max bending moment), segmental lining (PGA vs Max residual joint rotation) and empirical curves proposed by ALA 2001 and HAZUS 2004 for soil type B, for DS2 and DS3.

5.2 Feasibility of early warning system for segmental tunnel lining

In structural engineering, fragility curves are commonly used as a vital component of Earthquake Early Warning Systems (EEWS) based on thresholds, which represents a tool for the implementation of protective measures aiming at reducing the vulnerability of structure to seismic risk.

In many countries particularly exposed to seismic risk, as Japan, California, Mexico, Turkey, EEWS systems are often adopted for the seismic protection of the public structures (e.g. schools, hospitals) and also of the transportation systems (e.g., bridges and railways; Figure 5.33).

Seismic Early Warning systems aims to provide warnings of imminent danger. They can be either based on simple thresholds or on rapid estimates of the earthquake source parameters (i.e., location and magnitude), but in any case, they utilize the capability of modern real-time systems to process and transmit information faster than seismic waves propagate. The maximum achievable warning time of an earthquake early warning system is defined by the difference between the detection of the faster P-wave (5-7 km/s) by a seismic sensor and the arrival of higher amplitude S-waves (3-5 km/s) at the user site, and is defined lead-time. P waves are no destructive waves, they can be analysed to derive important information about the seismic source size, while the S waves are slower but carry much of the energetic content of the seismic event, and hence have a high destructive potential.

The lead-time is the key parameter for implementing preventive 'security' actions, such as: stop surgical operations in hospitals; slow trains to prevent encounter stretches of track with a possible risk of derailment; alert aircraft to postpone take-off or landing; prevent additional cars from entering the freeway; to stop the distribution of flammable substances (such as urban gas) which may cause fire due to damage to the pipes; warn workers in factories because they interrupt dangerous production activities; warn school children to protect themselves under the table before the S-waves reach their school. It should be noted also that, because the available time to take protective measures is function of the lead-time between P and S waves, it increases with the increasing of the seismic source distance, since the time-delay between the P and S waves increases (Figure 5.34).

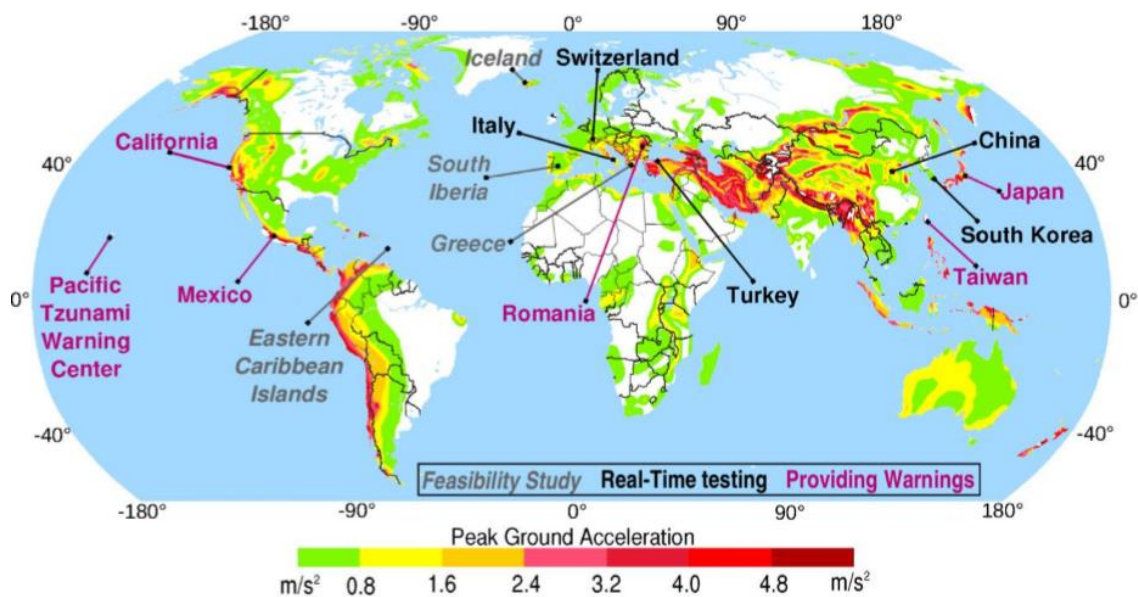


Figure 5.33. Worldwide Early Warning System.

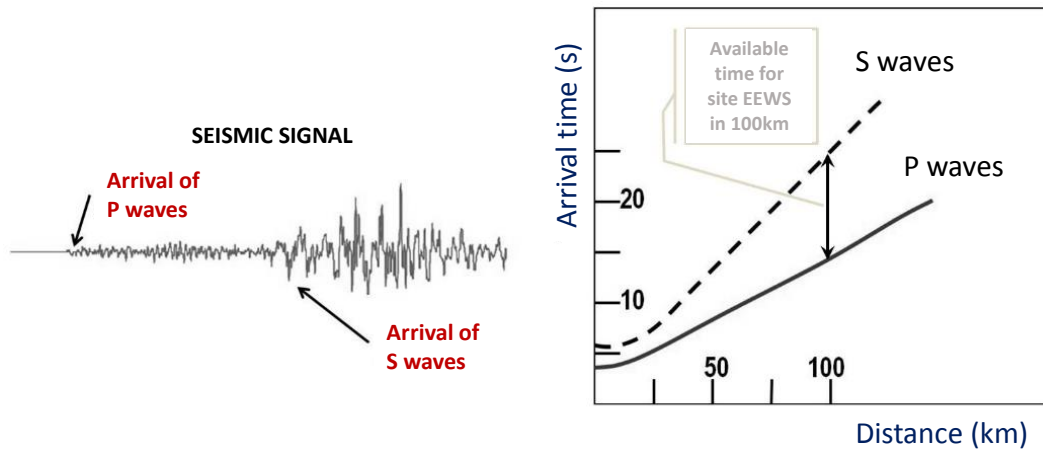


Figure 5.34. Arrival times of S waves and P waves.

Typically, EEWS follows two basic approaches: ‘regional’ (or network based), and single station ‘on-site’ warning. Regional early warning systems are based on the use of a seismic network located near one or more known epicentral areas, for which the aims are to detect and locate an earthquake and to determine its magnitude from the analysis of the first few seconds of the arriving P waves at more stations (Satriano *et al.*, 2011). The lead-time for a regional system is defined as the time difference between the S waves recorded in the source area and the arrival of first P waves at the target site, and the necessary computation and data transmission times. On-site early warning systems, instead, are intended for target sites located too close to a seismogenic area, where the analysis of data recorded at more stations of a regional network determines a lead time too small to warn the target in case of an event. For this reason, on-site systems rely on seismic sensors installed directly at the target site and exploit only the information carried by the faster early P waves. In this case, the lead time is equal to the S-wave minus the P-wave arrival times.

Figure 5.35 shows the warning- and lead-times of the regional and on-site system: the first on-site warning occurs before the first regional warning while the expected lead-time of “Regional system increases with distance and it is about twice than for “On-site” systems.

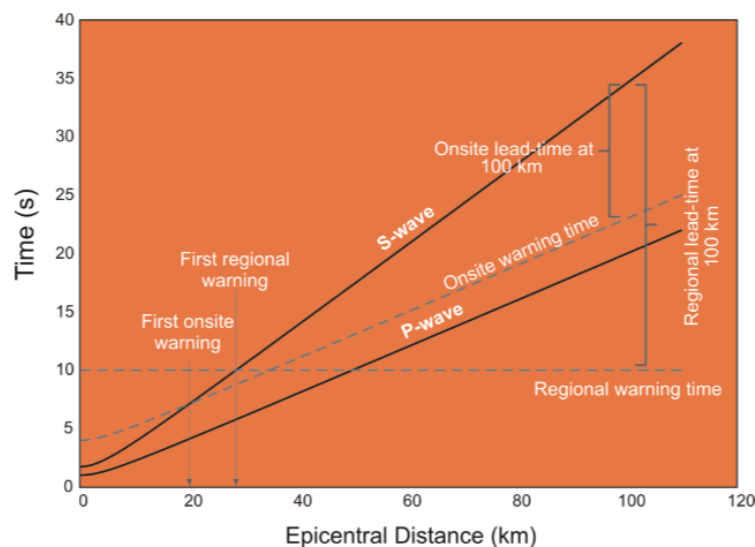


Figure 5.35. Warning- and lead-times for regional and on-site EEWS.

Among the EEWS operating worldwide, Figure 5.36 shows the localization of sites provides warnings and real time testing, distinguishing between regional and real time systems. One of the best-known example of on-site EEWS in the world is the one developed by the Japanese Railway in the 1960s to slow down or stop trains before seismic shaking affected trains running at high speed (Nakamura 1988, 1989; Nakamura & Tucker 1988). Nakamura used a single station approach, where seismic signals are processed locally and an earthquake warning is issued when ground motion exceeds the trigger threshold. This system, called UrEDAS, has been widely used in the Japanese railway system.

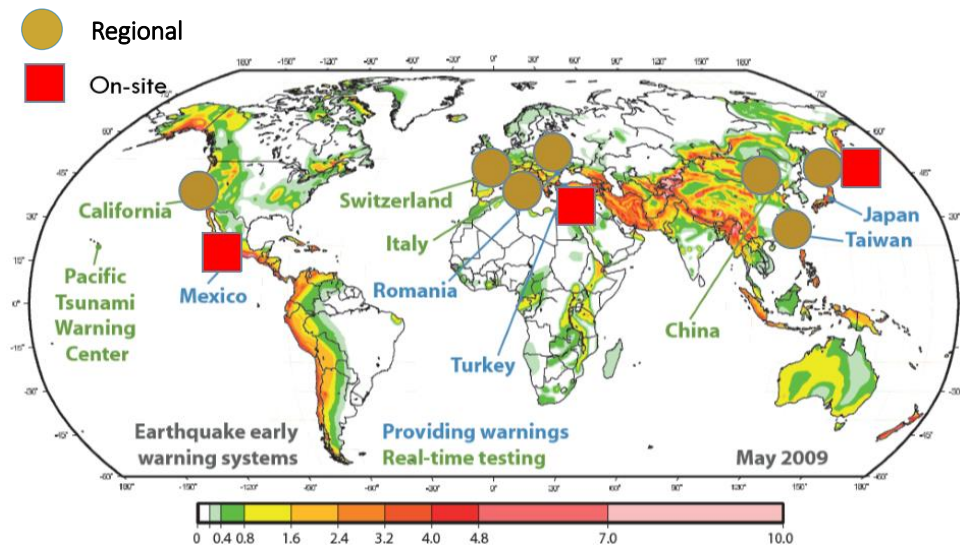


Figure 5.36. Worldwide regional and on-site EEWS.

In this thesis, a preliminary feasibility study concerning the use of a threshold-based EEWS for segmental tunnel lining has been conducted for some Italian target sites. The approach proposed hereinafter combines regional and on-site approaches with the fragility curves described in the previous part of this Chapter. Overall, the basic idea is to derive in real-time the probability of damage for segmental tunnel lining before the arrival of S-waves by intersecting the fragility curves with the PGA predicted by an EEWS at the target site. Figure 5.37 for instance, shows a schematic application of the fragility curves.

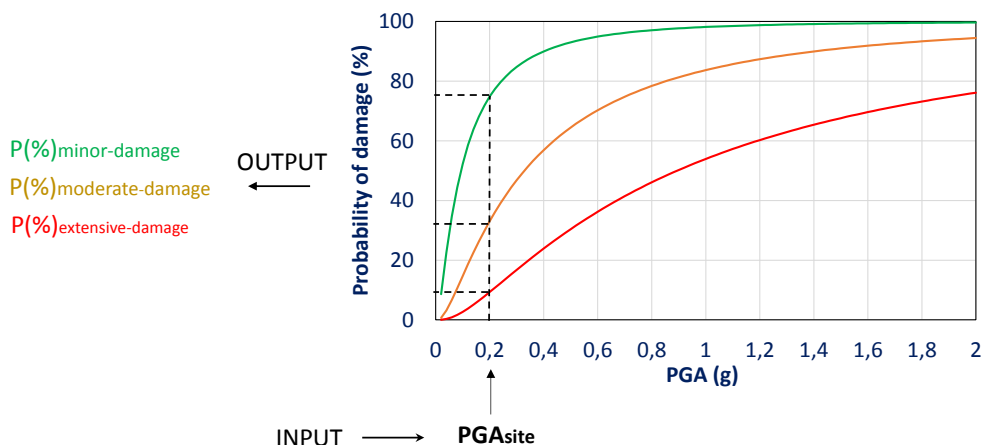


Figure 5.37. Schematic application of the fragility curves.

The PGA value at the target site is the parameter required to evaluate the possible damage level at the structure. The other parameter of interest is the available lead-time, which requires the event location to be determined.

Three approaches have been adopted in this work to provide the PGA and the lead-time for the possible seismic threats expected at a target site, defined as follow:

LEVEL '0' - The PGA at the target site is determined on the basis of the Probabilistic Seismic Hazard Analysis (PSHA, NTC 2008); no information is available on the lead-time. This approach allows to verify the security of the target with respect to the ground motion expected from the Italian code.

LEVEL '1' - The PGA and the lead-time at the target site are derived by a disaggregation of the PSHA, which allows to identify the seismic threats (i.e., combination of magnitude and epicentral distance) hampering a target site. This approach allows to verify the security of the target with respect to a set of virtual seismic source that are derived by PSHA for the specific site.

LEVEL '2' - The PGA at the target site is predicted through a real-time and evolutionary estimation of location, magnitude and using a ground motion prediction equation. This approach is applicable only in the cases where exist a network dedicated to EEW activities (e.g., the ISNet network in the Irpinia region, southern Italy) and an EEW software. In this study, the software *PRESTo* (i.e., *PRobabilistic and Evolutionary early warning SysTem*; Satriano et al. 2011, <http://www.prestoews.org>), a free and open source software platform for EEW developed by the RISSCLab group of the University Federico II in Naples, Italy, has been considered. In this case, the lead time is estimated considering the site-to-epicenter distance and the P- and S-waves velocity.

Three target sites have been chosen (Figure 5.38):

- The high speed railway tunnel Bologna-Firenze (lat: 43.764, lon: 11.2749);
- The San Giovanni railway tunnel (lat: 42.265, lon: 14.482),
- The Metro Line 6 of Naples (lat: 40.832, lon: 14.217).

The cases of high speed railway tunnel Bologna-Firenze and the Metro Line 6 of Naples have been chosen because object of study in the first part of this work, where we have focused on the static aspects of the segmental tunnel lining behaviour (see Chapter 3). The San Giovanni railway tunnel is instead a representative case of a segmental tunnel lining that experienced many of the strong earthquakes that in the last years occurred in Central Italy (i.e., >60 km of distance from the source area).

In the next section the probabilistic seismic hazard and the real-time approaches are described in detail for these Italian target sites.



Figure 5.38. Localization of the target sites in Italy.

5.2.1 Probabilistic seismic hazard approach

The goal of this earthquake engineering analyses is to ensure that the tunnel structure can withstand a given level of ground shaking while maintaining a desired level of performance. Questions of interest are: what level of ground shaking should be used to perform this analysis? Which value of PGA should be used in the fragility curves to define the probability of damage?

The Probabilistic Seismic Hazard Analysis (PSHA), on which is based the Italian seismic code, provides the 'design earthquakes' in terms of magnitude, location and other parameters such as faulting style, computing the average return period of ground motions exceeding a given intensity measure (IM) threshold at the considered site.

At its most basic level, PSHA is composed of five steps:

1. Identification all earthquake sources capable of producing damaging ground motions;
2. Characterization of the earthquake magnitudes distribution (the rates at which earthquakes of various magnitudes are expected to occur);
3. Characterization of the source-to-site distances distribution associated with potential earthquakes;
4. Prediction of the resulting distribution of ground motion intensity as a function of earthquake magnitude, distance, etc., by adopting ground-motion prediction equations;
5. Combination of uncertainties in earthquake size, location and ground motion intensity, using a calculation known as the total probability theorem;

As result, for a given a seismic source model and a ground-motion prediction equation, the PSHA provides the seismic hazard maps correlating the probability of exceedance (Pr) of a ground motion level (IM) in a defined return period (Tr). Figure 5.39, for instance, shows the seismic hazard maps of Italy for four probabilities of exceedance equal to 81%, 63%, 10% and 5%.

In the approach defined before as *LEVEL '0'*, these values of PGA derived from the PSHA are used to preliminarily estimate the probability of the different damage levels (minor, moderate and extensive damage) for different values of Pr (81%, 63%, 10% and 5%).

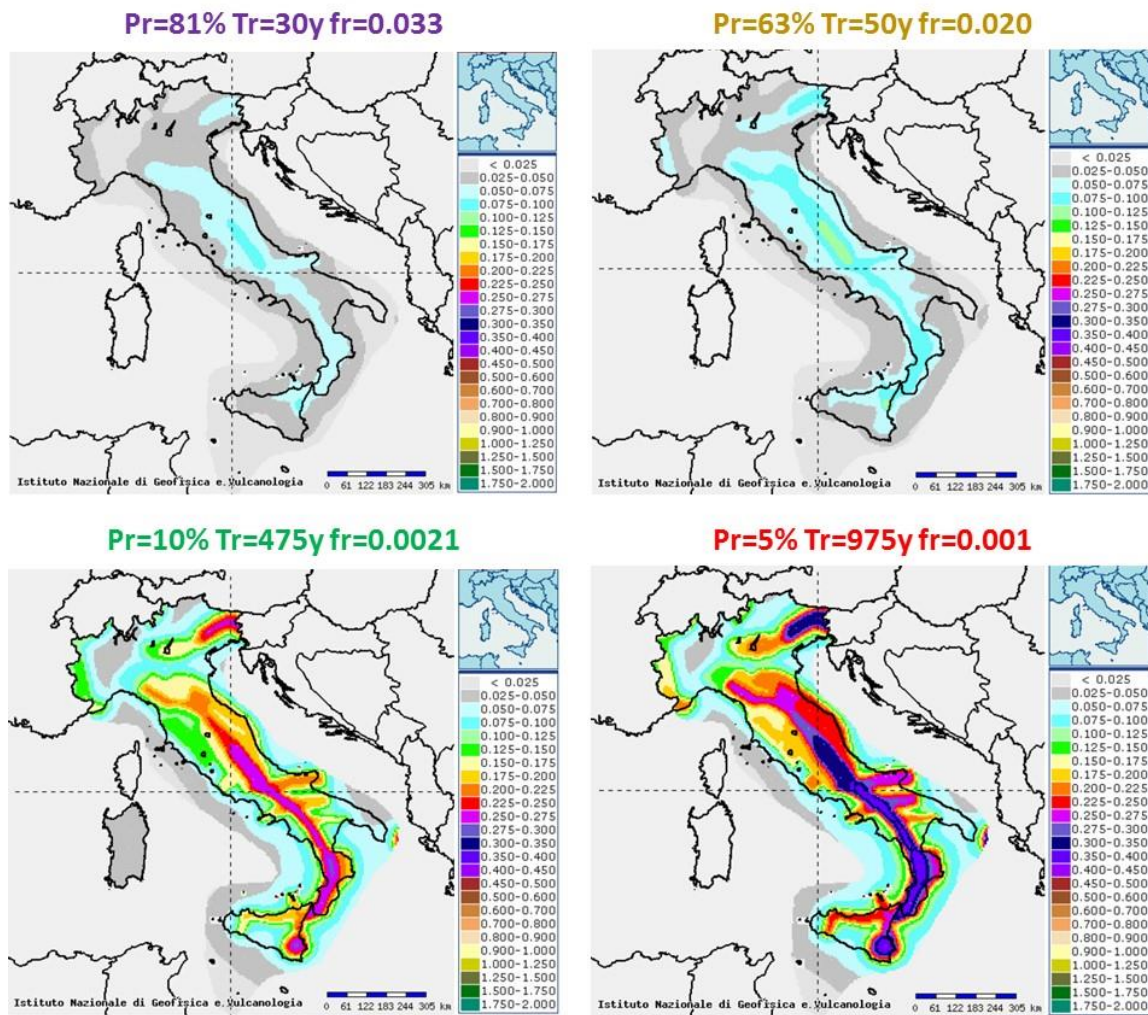


Figure 5.39. Seismic hazard maps of Italy for different return periods (Istituto Nazionale di Geofisica e Vulcanologia).

LEVEL '0'

The procedure followed in the LEVEL '0' starts with the evaluation of the PGA at the target sites in function of the difference exceedance probabilities considered by the Italian code (i.e., $Pr=81\%$, $Pr=63\%$, $Pr=10\%$, $Pr=5\%$) with the help of the data made available by the *Istituto 'Nazionale di Geofisica e Vulcanologia - INGV'*. Figure 5.40 shows, as example, the case of **Napoli**, for which as a function of the coordinates of the target site, the PGA value in correspondence of the 50% percentile is assumed for each probability of exceedance. Table 5.7 summarizes the PGA calculated values for Napoli, Firenze and Rocca San Giovanni as function of Pr .

Once calculated the PGA expected at the site, this is multiplied for the amplification site coefficient ' S_s ' indicated by the Italian code to calculate the corresponding PGA_{site} at the surface.

These amplified values of PGA are shown in Table 5.8 for all sites. The PGA_{site} is the input value with which the fragility curves have been intersected to evaluate the probability of damage to the structure.

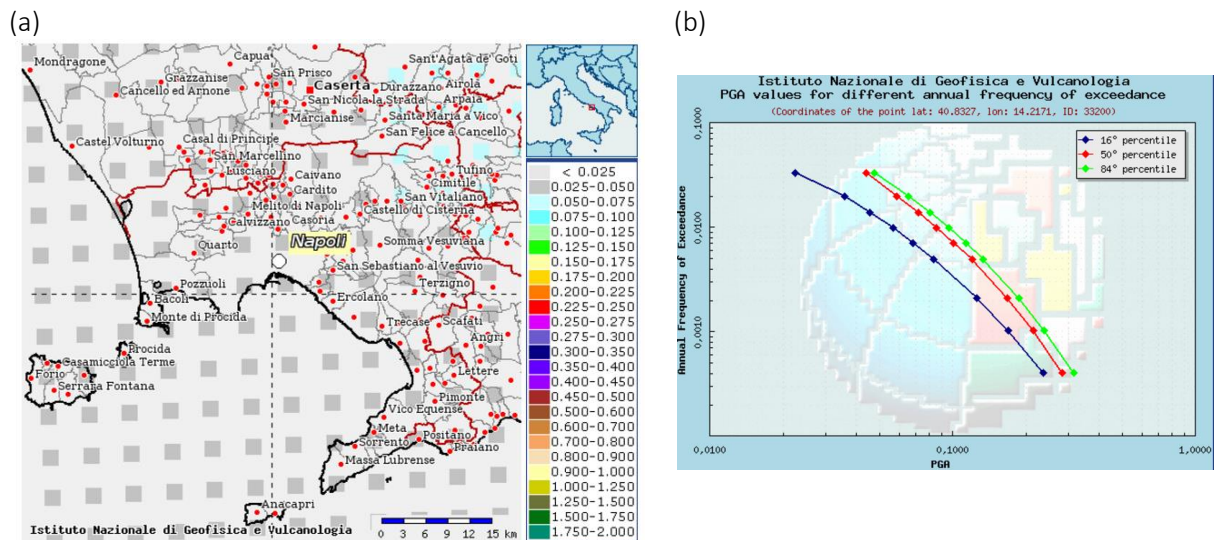


Figure 5.40. (a) Grid map of hazard for $Pr=81\%$ and (b) variation of PGA with the annual frequency of exceedance in the target site of Naples (Istituto Nazionale di Geofisica e Vulcanologia INGV).

fr	a(g)		
	NAPOLI		
	16° percentile	50° percentile	84° percentile
0,000	0,236	0,281	0,316
0,001	0,169	0,214	0,238
0,002	0,125	0,168	0,187
0,005	0,083	0,120	0,133
0,007	0,069	0,101	0,113
0,010	0,057	0,086	0,096
0,014	0,046	0,072	0,080
0,020	0,036	0,059	0,065
0,033	0,022	0,044	0,047

fr	a(g)		
	FIRENZE		
	16° percentile	50° percentile	84° percentile
0,000	0,189	0,218	0,243
0,001	0,145	0,165	0,178
0,002	0,114	0,130	0,137
0,005	0,078	0,093	0,100
0,007	0,066	0,079	0,089
0,010	0,056	0,071	0,079
0,014	0,045	0,063	0,071
0,020	0,037	0,056	0,061
0,033	0,028	0,046	0,051

fr	a(g)		
	ROCCA SAN GIOVANNI		
	16° percentile	50° percentile	84° percentile
0,000	0,118	0,146	0,164
0,001	0,092	0,115	0,126
0,002	0,074	0,094	0,103
0,005	0,055	0,073	0,080
0,007	0,048	0,065	0,071
0,010	0,041	0,058	0,064
0,014	0,036	0,052	0,057
0,020	0,030	0,046	0,050
0,033	0,022	0,038	0,041

Table 5.7 Selected values of PGA with the annual frequency of exceedance ($Pr=81\%$, $Pr=63\%$, $Pr=10\%$, $Pr=5\%$) in the target sites of Napoli, Firenze and Rocca San Giovanni.

Table 5.8 presents the probability of minor, moderate and excessive damage for the Firenze, Rocca San Giovanni and Napoli target sites. The probability increases from extensive to minor damage and with the decreasing of the probability of exceedance Pr . With this approach, the probabilities of extensive damage are very low for all targets, while the probabilities of minor and moderate damage are not negligible. It should be observed that, between the selected target sites, Napoli is the most exposed one, presenting the higher values of PGA_{site} .

This simple approach allows to quickly assess on probabilistically bases what ground motion level could occur at the considered sites, which in turn is used to assess the possible level of damage for such kind of structures. However, since the PSHA does not provide direct indications about the location of the seismic sources that contributed to the hazard, it is not possible to compute the available lead-time. A possible strategy to overcome this issue is to exploit the disaggregation of seismic hazard, the basic idea of LEVEL-1

VN=50y; cu=1; VR=50y			a(g)*Ss	Probability of damage %		
Pr (%)	Tr (y)	fr	FIRENZE	minor	moderate	extensive
81	30	0,033	0,055	34,7	6,7	0,30
63	50	0,020	0,067	44,4	10,6	1,66
10	475	0,002	0,156	68,1	26,3	6,44
5	975	0,001	0,198	74,8	33,1	9,31
Pr (%)	Tr (y)	fr	Rocca San Giovanni	minor	moderate	extensive
81	30	0,033	0,045	22,6	3,2	0,30
63	50	0,020	0,055	34,7	6,7	0,85
10	475	0,002	0,113	58,6	18,7	3,81
5	975	0,001	0,137	63,8	22,6	5,08
Pr (%)	Tr (y)	fr	NAPOLI	minor	moderate	extensive
81	30	0,033	0,053	28,61	4,90	0,04
63	50	0,020	0,070	56,57	8,64	0,15
10	475	0,002	0,202	74,80	33,06	5,81
5	975	0,001	0,257	81,58	41,81	11,38

Table 5.8 Probability of minor, moderate and extensive damage (%) calculated in function of Pr in the target sites of Napoli, Firenze and Rocca San Giovanni.

LEVEL '1'

The LEVEL '1' procedure is again based on the PSHA adopted by the Italian code, but incorporates the disaggregation analysis of the seismic hazard to identify 'virtual sources' (i.e., in terms of epicentral distance and magnitude) that provide the higher contribution to the hazard. Hence, the disaggregation is for us a means to identify scenario (i.e., seismic events) of interest for the structures. Indeed, disaggregation maps are expressed in terms of magnitude (M_s), source to site distance (R_{epi}) and the contribution to the hazard ($w\%$). Figure 5.41a shows as example the disaggregation map for **Napoli** (i.e., considering **Pr=10%**), from which results that the hazard at the considered site is mainly controlled by two near seismic threats (i.e., in the seismogenic map of Italy, they correspond to the zones 927 and 928, Figure 5.41b).

Hence, for each pair of (M_s - R_{epi}) derived from the disaggregation analysis, the lead-time and the PGA at the site have been evaluated. The lead time is function of the epicentral distance (R_{epi}) between the target and the virtual source, where we assume P-waves and S-wave velocities of 5.5km/sec and 3.2 km/s, respectively. The acceleration at the target sites has then been calculated with the ground motion prediction equation, GMPE, *Bindi et al.2011* (Equation 5.6):

$$\log_{10} Y = e_1 + F_D(R, M) + F_M(M) + F_S + F_{sof} \quad (5.6)$$

where: e_1 is a constant term, $F_D(R, M)$ the distance function (Equation 5.7), $F_M(M)$ the magnitude scaling (Equation 5.8), F_S the site amplification, F_{sof} the style of faulting correction, M the moment magnitude, R the epicentral distance (in km), $Y=Y(\text{PGA, in cm/s}^2; \text{PGV, cm/s})$, M_{ref} , R_{ref} and M_h coefficients.

$$F_D(R, M) = [c_1 + c_2(M - M_{ref})] \log_{10} \left(\frac{\sqrt{R_{JB}^2 + h^2}}{R_{ref}} \right) - c_3 \left(\sqrt{R_{JB}^2 + h^2} - R_{ref} \right) \quad (5.7)$$

$$F_M(M) = \begin{cases} b_1(M - M_h) + b_2(M - M_h)^2 & \text{for } M \leq M_h \\ b_3(M - M_h) & \text{for } M > M_h \end{cases} \quad (5.8)$$

In the application F_{sof} and F_S have been not considered.

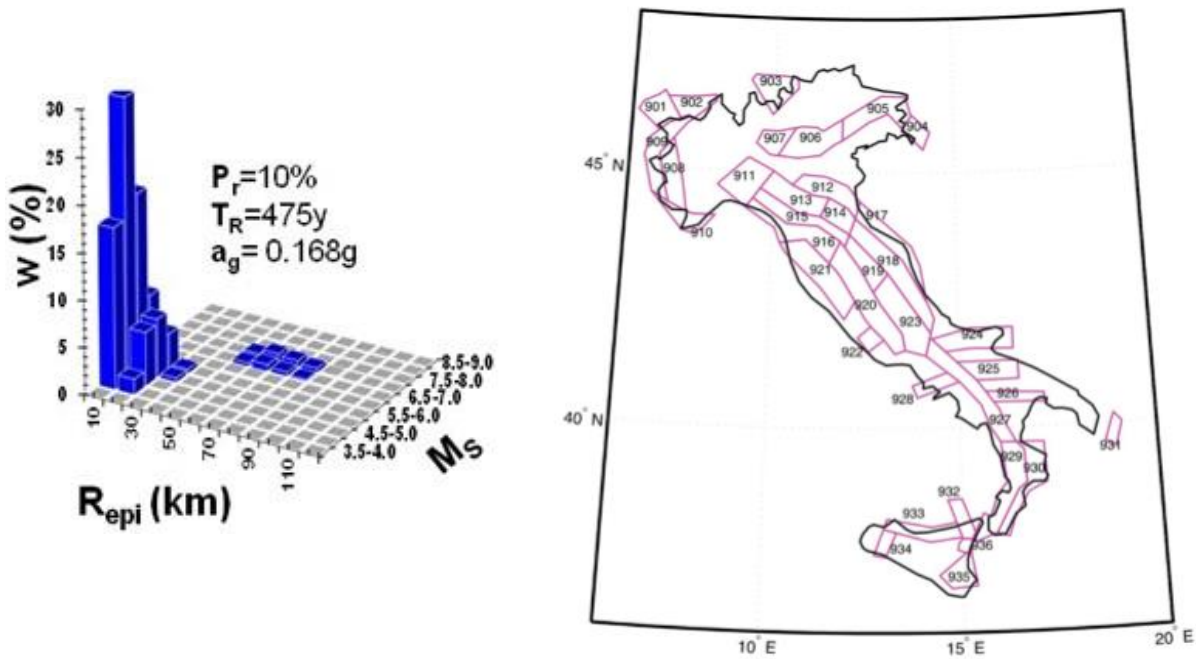


Figure 5.41 (a) Disaggregation map of Napoli and (b) seismogenetic zones for Italy (Meletti et al. 2008).

Following this procedure, a disaggregation map, a lead-time map and an acceleration map are computed for the sites **Napoli**, **Firenze** and **Rocca San Giovanni**, considering different probabilities of exceedance (i.e., $Pr=81\%$, $Pr=63\%$, $Pr=10\%$, $Pr=5\%$, Figures 5.42-5.44-5.46-5.48-5.50-5.52-5.54-5.56-5.58-5.60-5.62-5.64, respectively). The PGA maps have been in turn used in combination with the fragility curves to produce, still considering all M_s - R_{epi} pairs, the final maps with the probability of minor, moderate and extensive damage (-5.43-5.45-5.47-5.49-5.51-5.53-5.55-5.57-5.59-5.61-5.63-5.65).

Taking as example the case of **Napoli** ($Pr=81\%$), the disaggregation map indicates that the seismic threat responsible for the highest contribution to hazard is located at 15km from the target, has magnitude $M=5$. Given this scenario, the surface acceleration expected at the target is $0.03g$, to which corresponds a probability of minor, moderate and extensive damage equal to $< 20\%$, $< 3\%$, $\approx 0\%$, respectively.

The seismic threat showing the highest acceleration at the site is a source located at 5km of distance from the site and magnitude $M=6$. Such kind of source would be associated to the high value of

probability of damage. On the other hand, this virtual source is associated to a very low contribution to the hazard, and therefore is considered unlikely.

NAPOLI - PHSA - Pr=81% in 50y

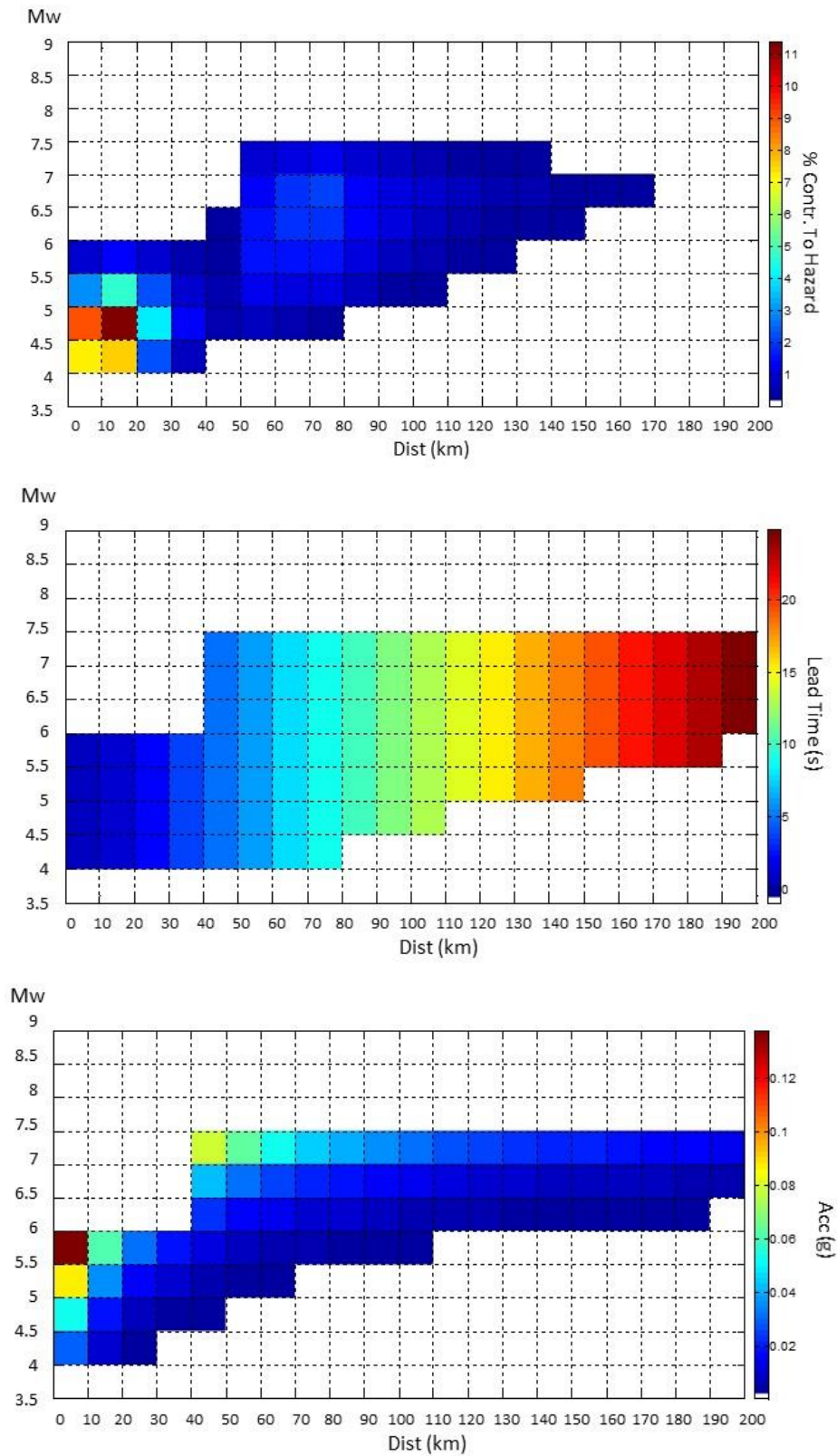


Figure 5.42. Disaggregation, lead-time and acceleration maps of target site of Napoli (Pr=81%).

NAPOLI – Probability of Damage - Pr=81% in 50y

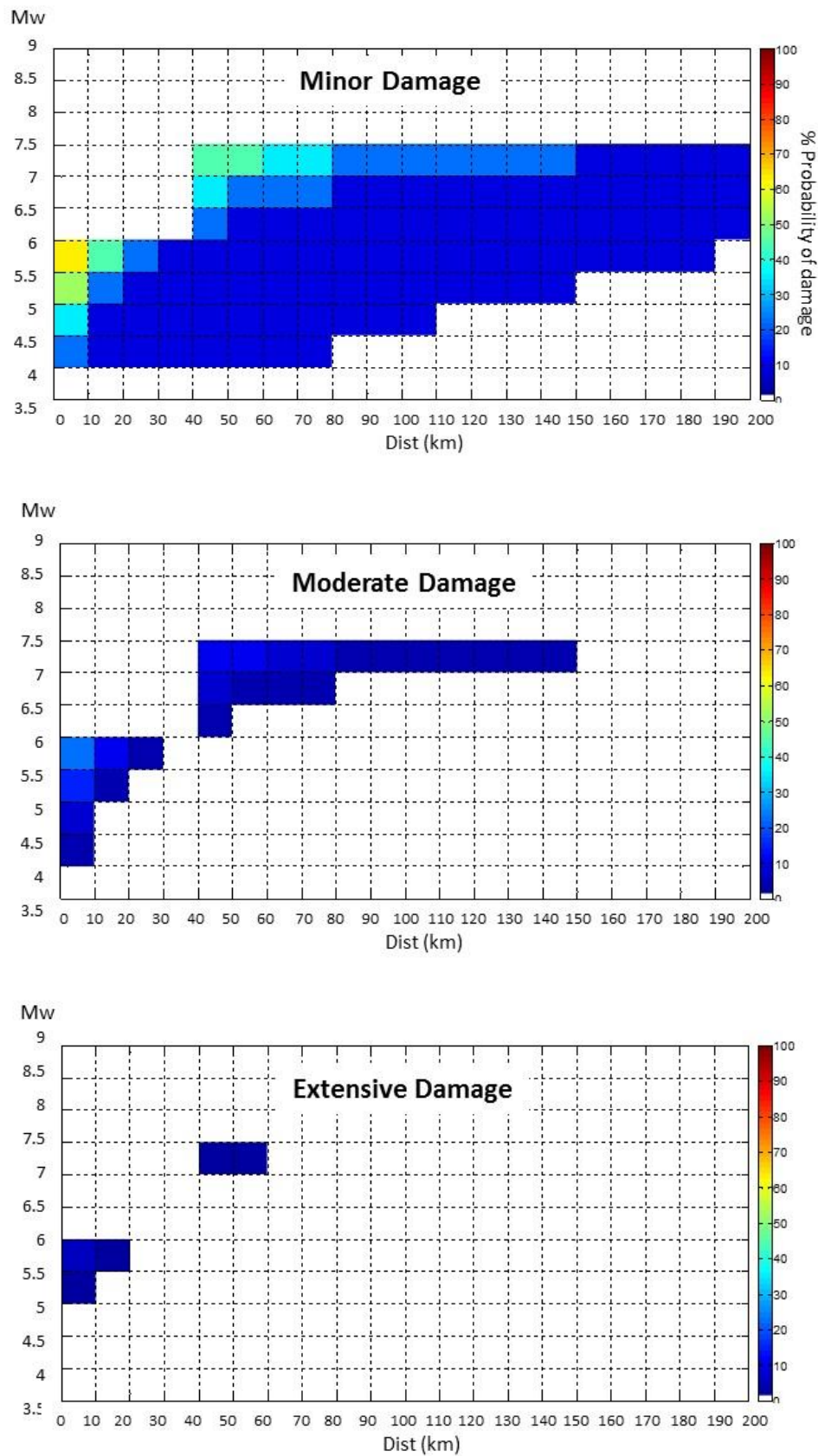


Figure 5.43. Probability of damage maps of target site of Napoli (Pr=81%).

NAPOLI - PHSA - Pr=63% in 50y

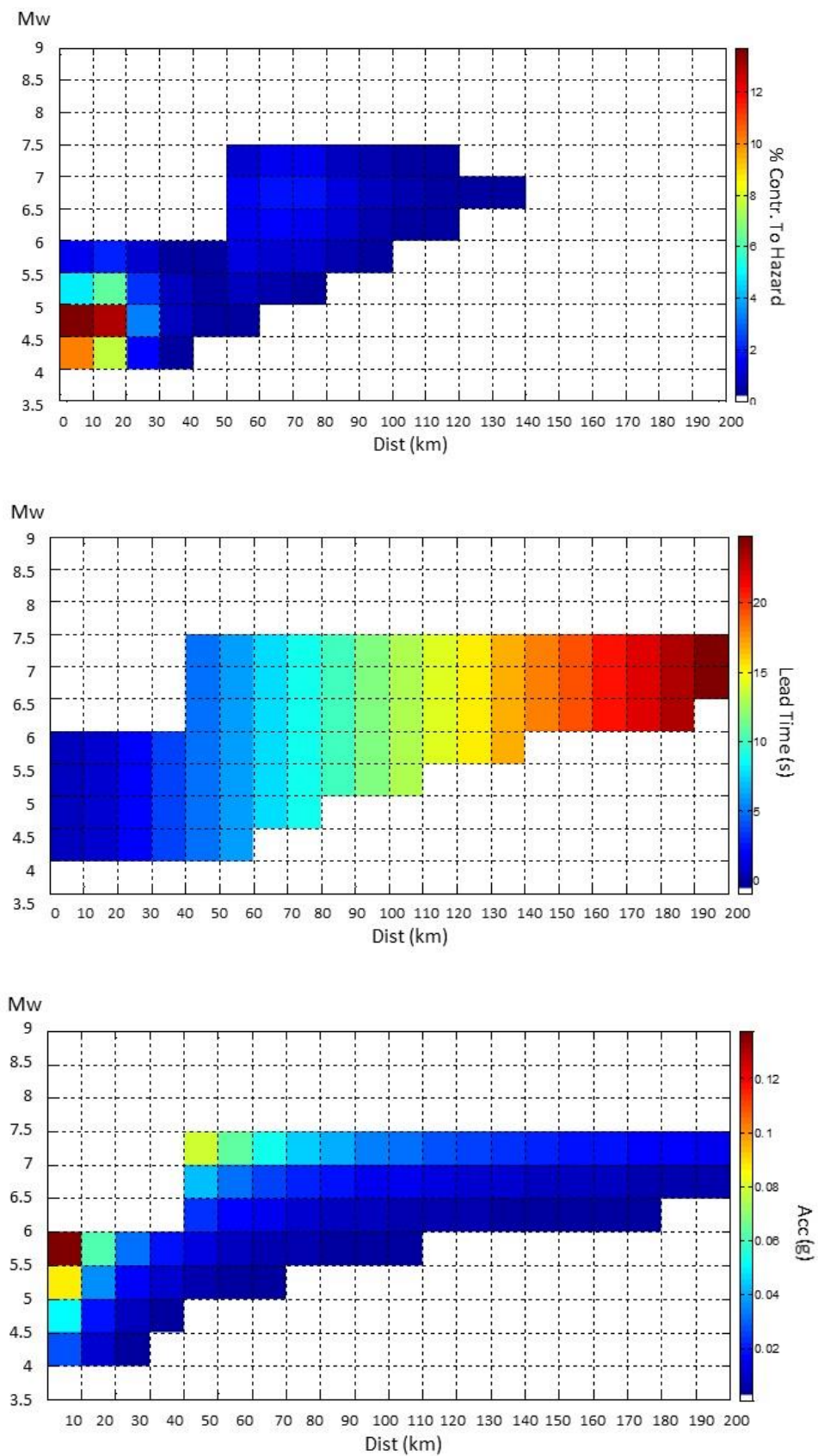


Figure 5.44. Disaggregation, lead-time and acceleration maps of target site of Napoli (Pr=63%).

NAPOLI – Probability of Damage - Pr=63% in 50y

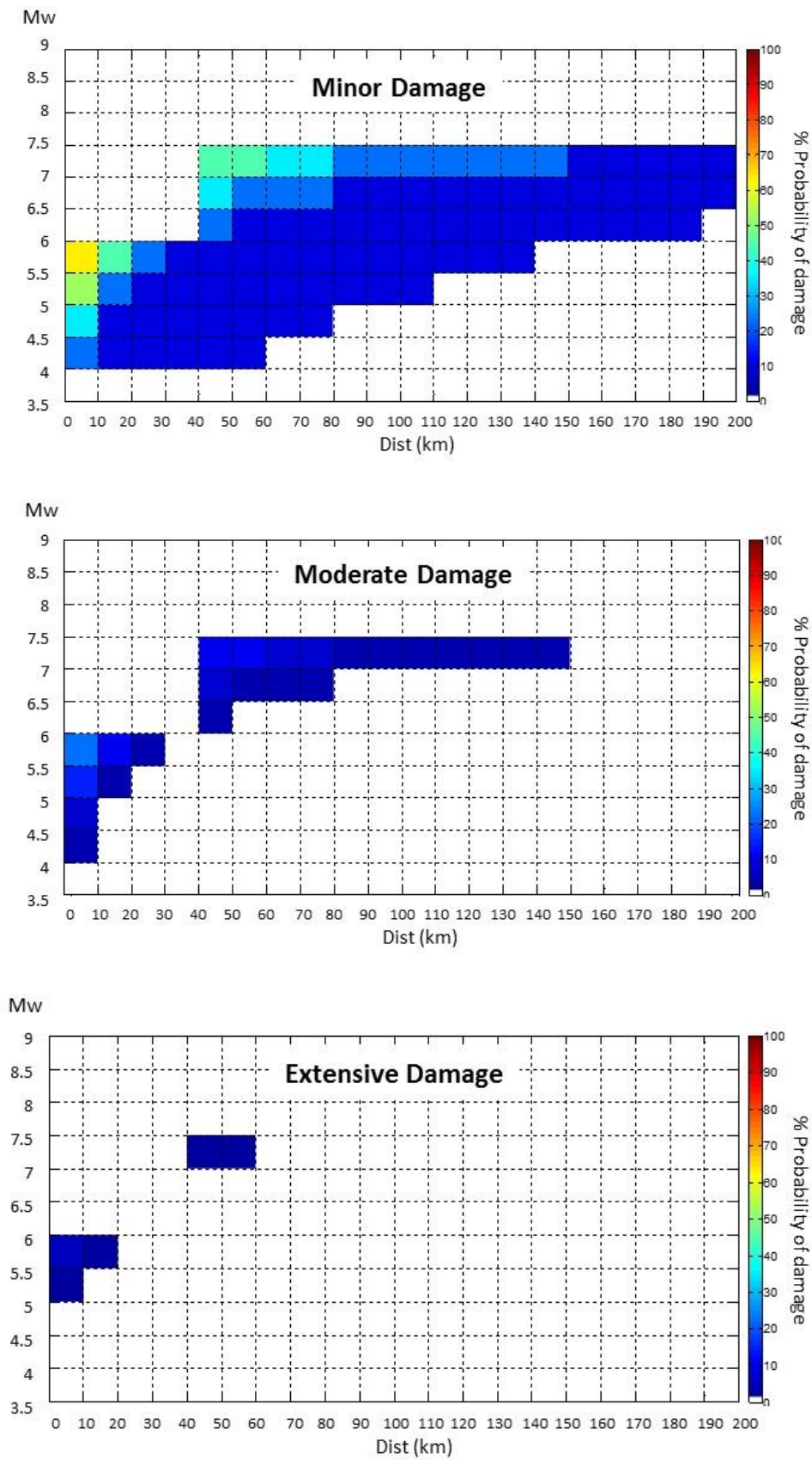


Figure 5.45. Probability of damage maps of target site of Napoli (Pr=63%).

NAPOLI - PHSA - Pr=10% in 50y

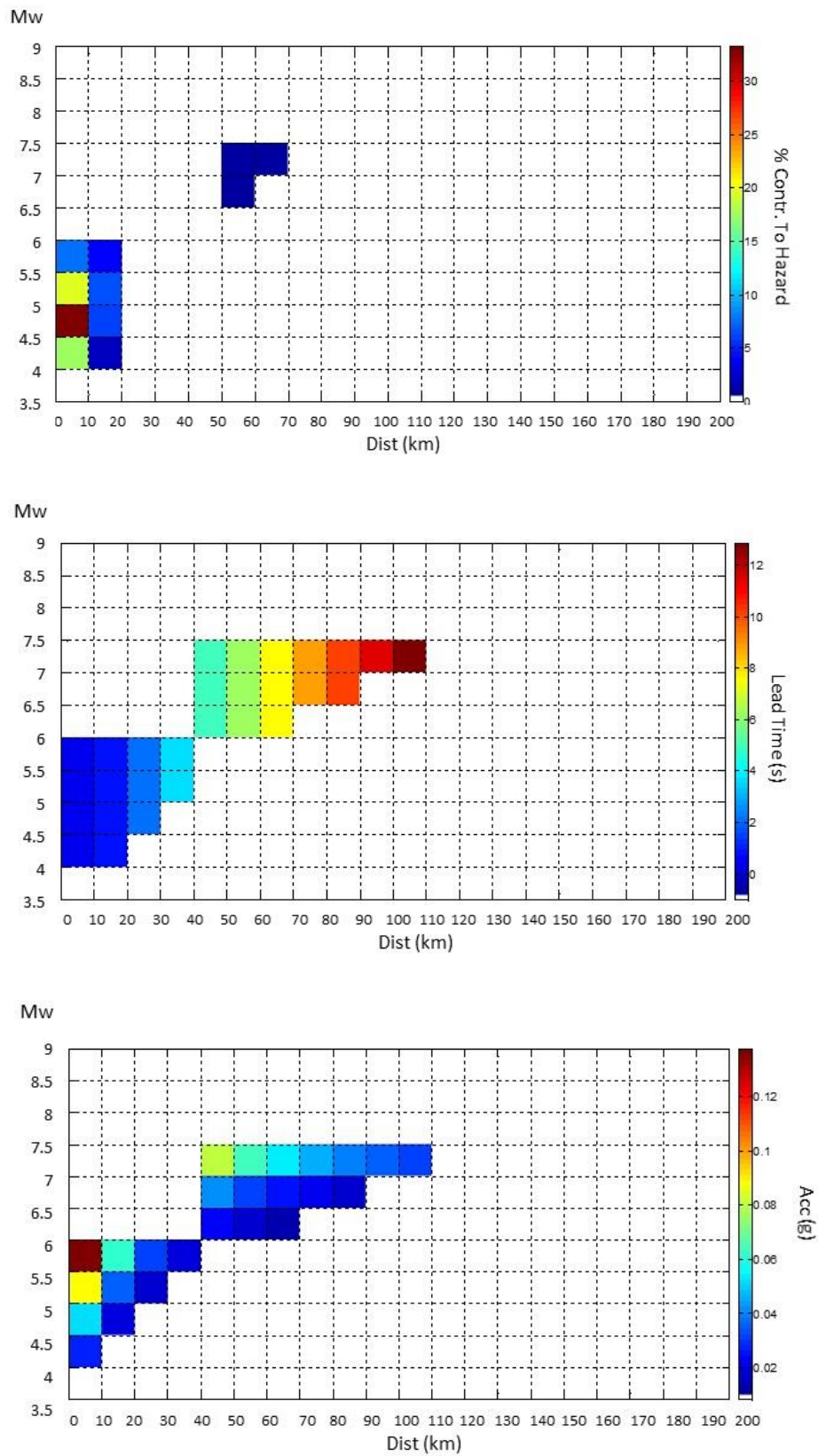


Figure 5.46. Disaggregation, lead-time and acceleration maps of target site of Napoli (Pr=10%).

NAPOLI – Probability of Damage - Pr=10% in 50y

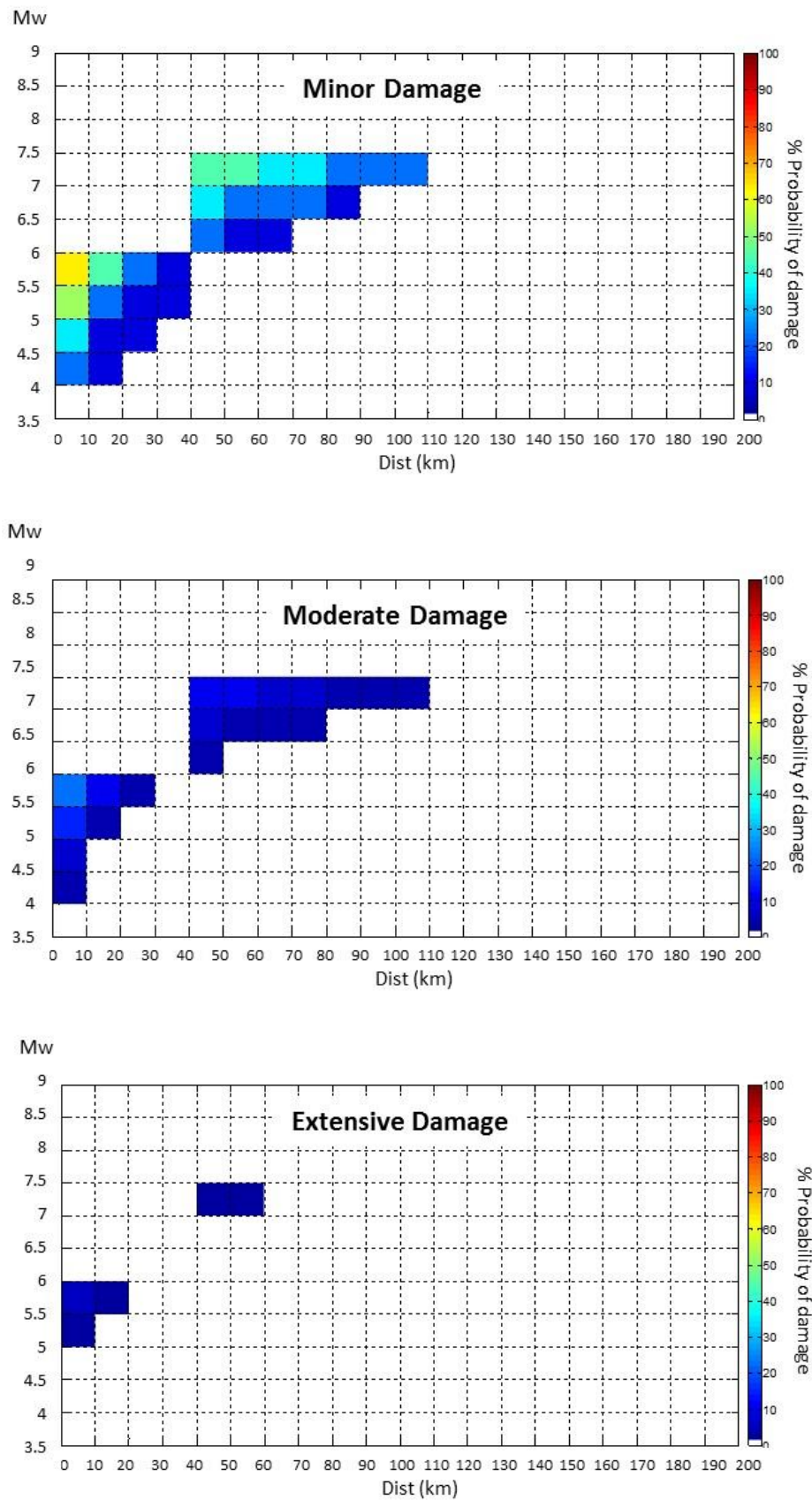


Figure 5.47. Probability of damage maps of target site of Napoli (Pr=10%).

NAPOLI - PHSA - Pr=5% in 50y

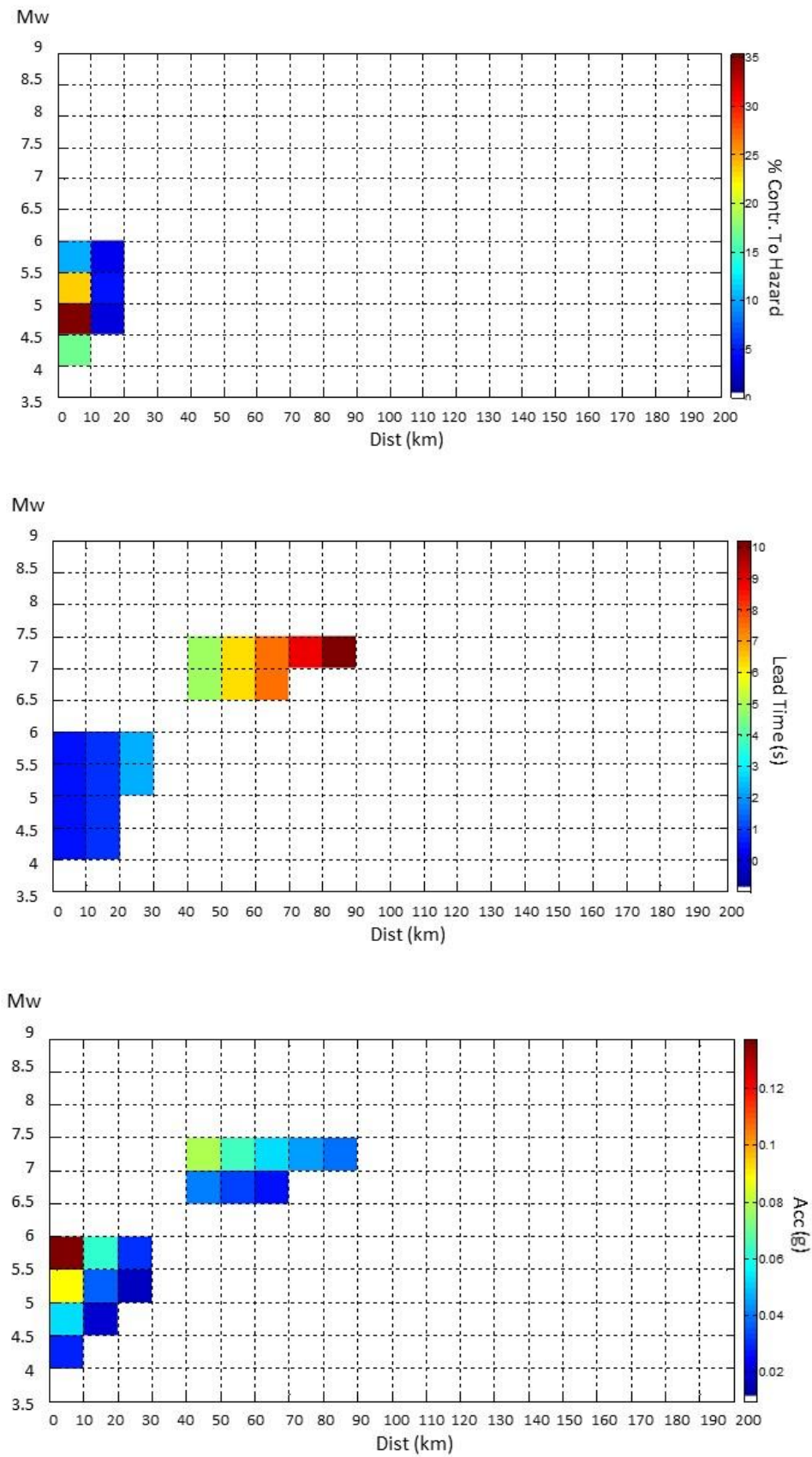


Figure 5.48. Disaggregation, lead-time and acceleration maps of target site of Napoli (Pr=5%).

NAPOLI – Probability of Damage - Pr=5% in 50y

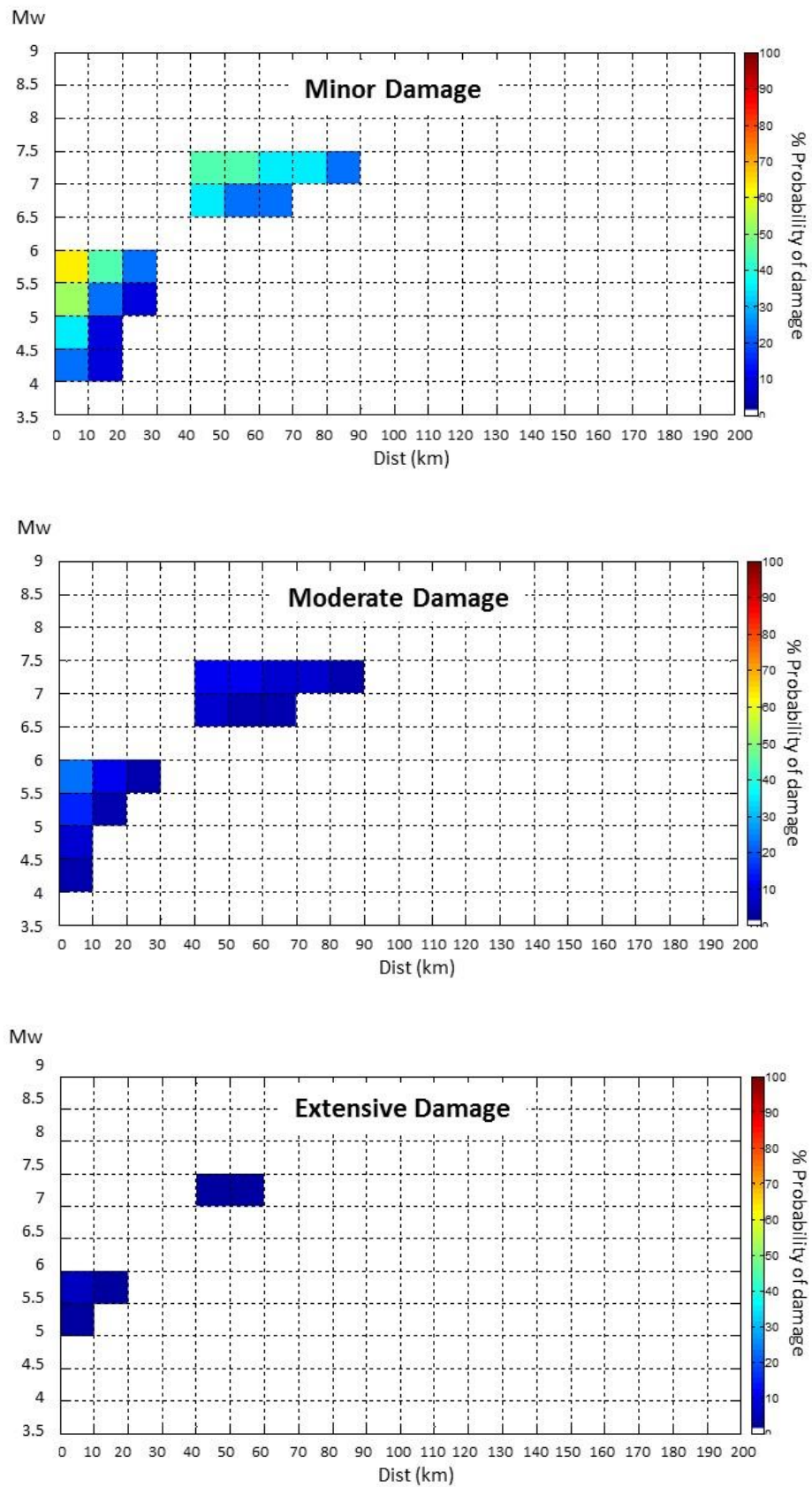


Figure 5.49. Probability of damage maps of target site of Napoli (Pr=5%).

FIRENZE - PHSA - Pr=81% in 50y

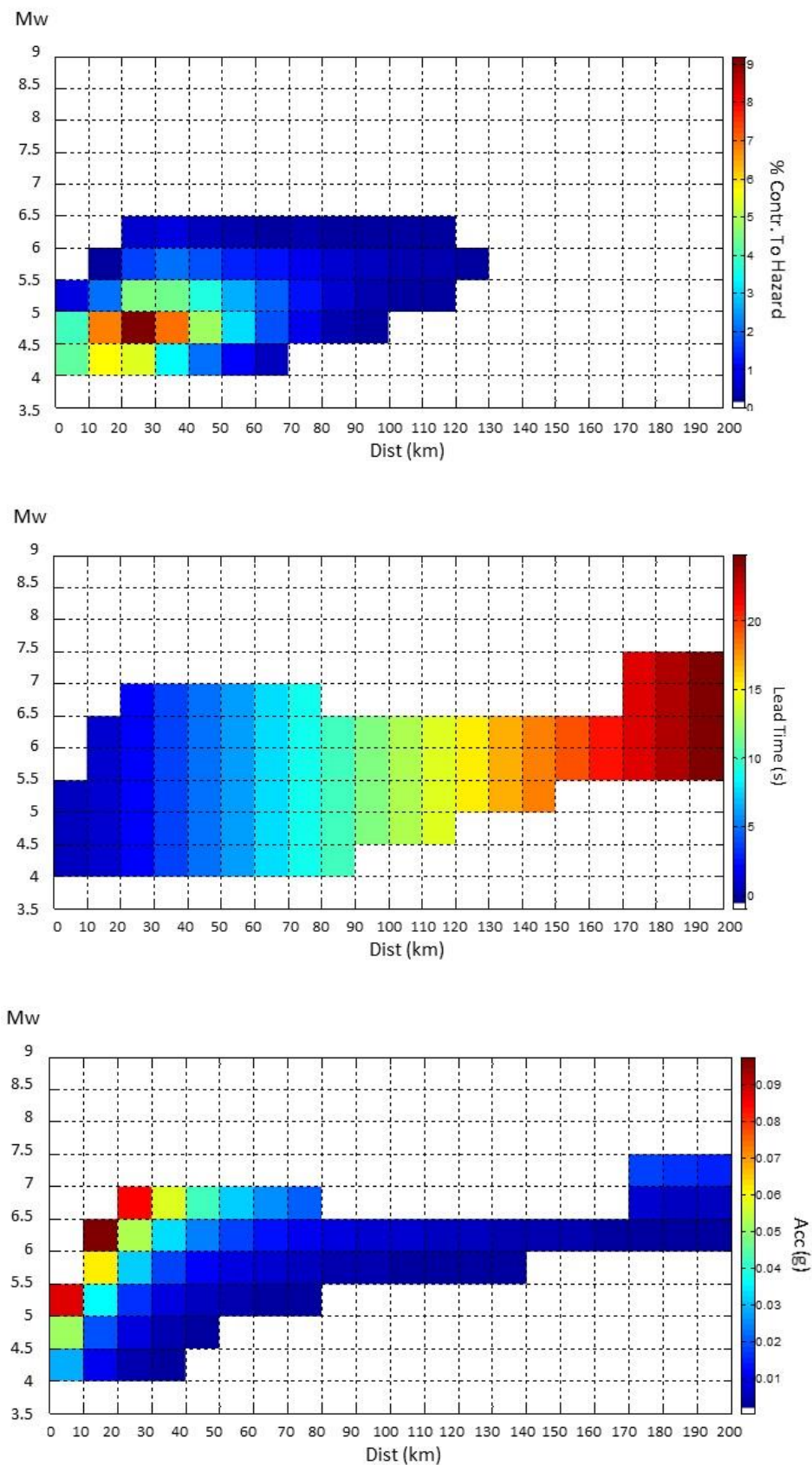


Figure 5.50. Disaggregation, lead-time and acceleration maps of target site of Firenze (Pr=81%).

FIRENZE – Probability of Damage - Pr=81% in 50y

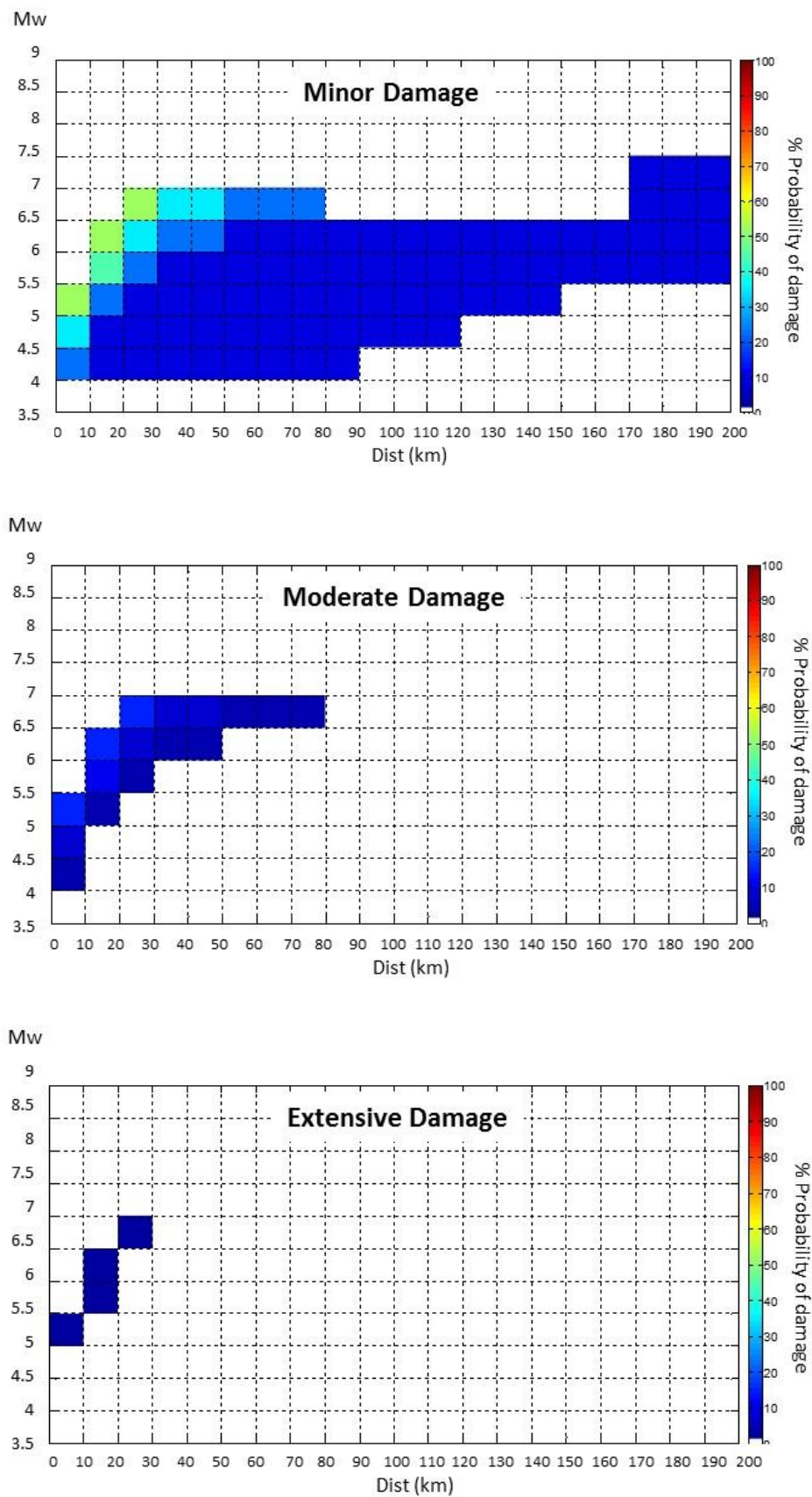


Figure 5.51. Probability of damage maps of target site of Firenze (Pr=81%).

FIRENZE - PHSA - Pr=63% in 50y

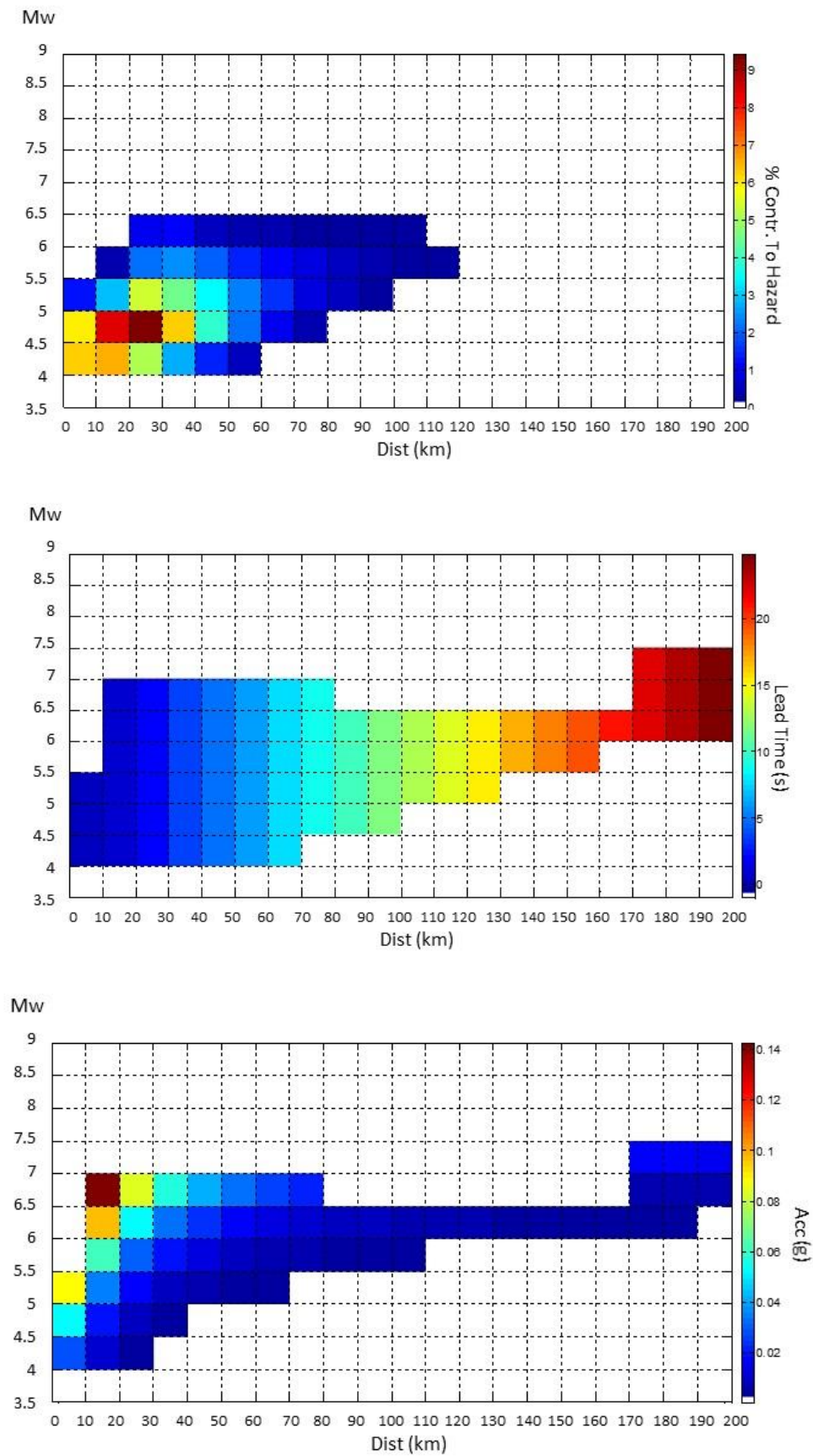


Figure 5.52. Disaggregation, lead-time and acceleration maps of target site of Firenze (Pr=63%).

FIRENZE – Probability of Damage - Pr=63% in 50y

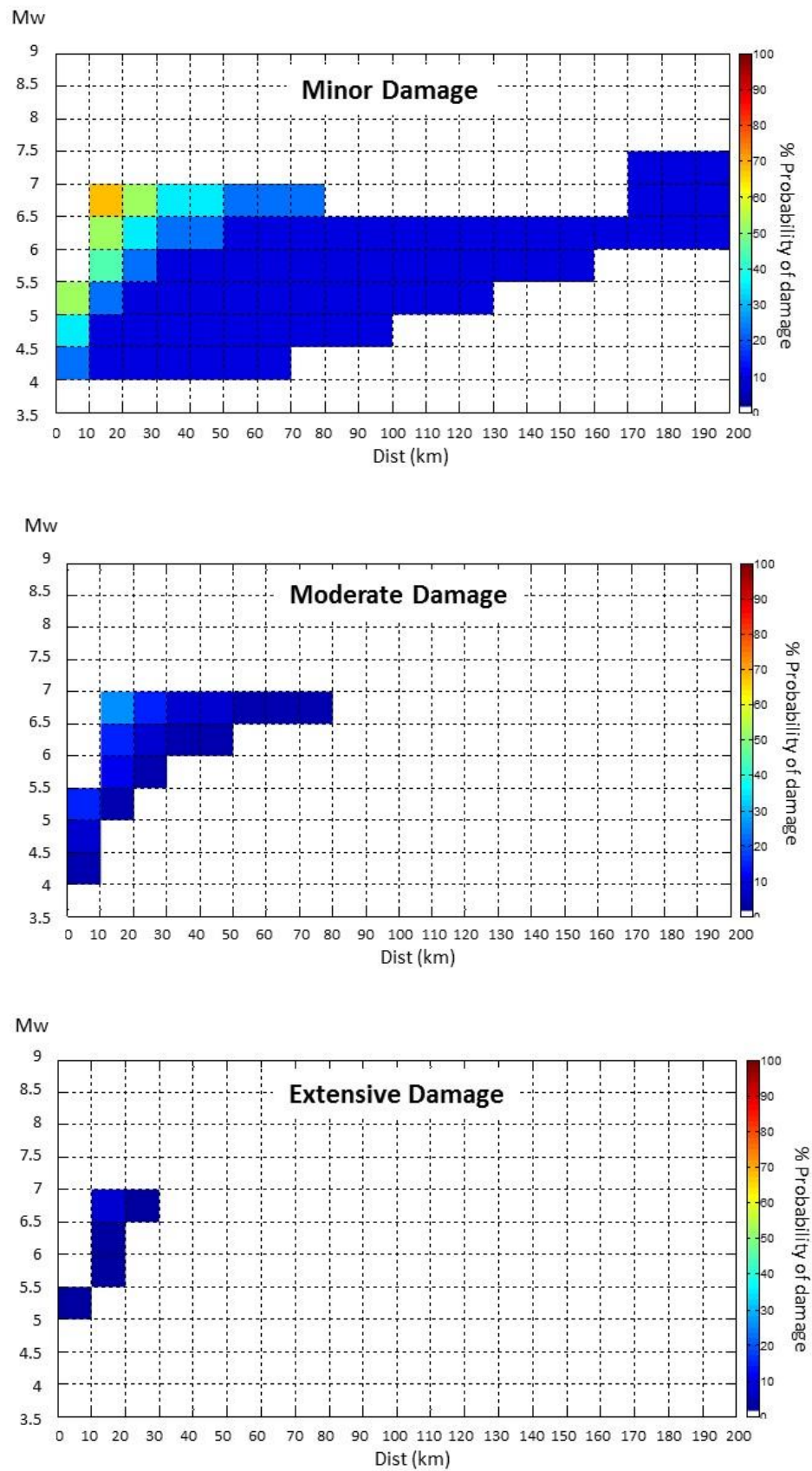


Figure 5.53. Probability of damage maps of target site of Firenze (Pr=63%).

FIRENZE - PHSA - Pr=10% in 50y

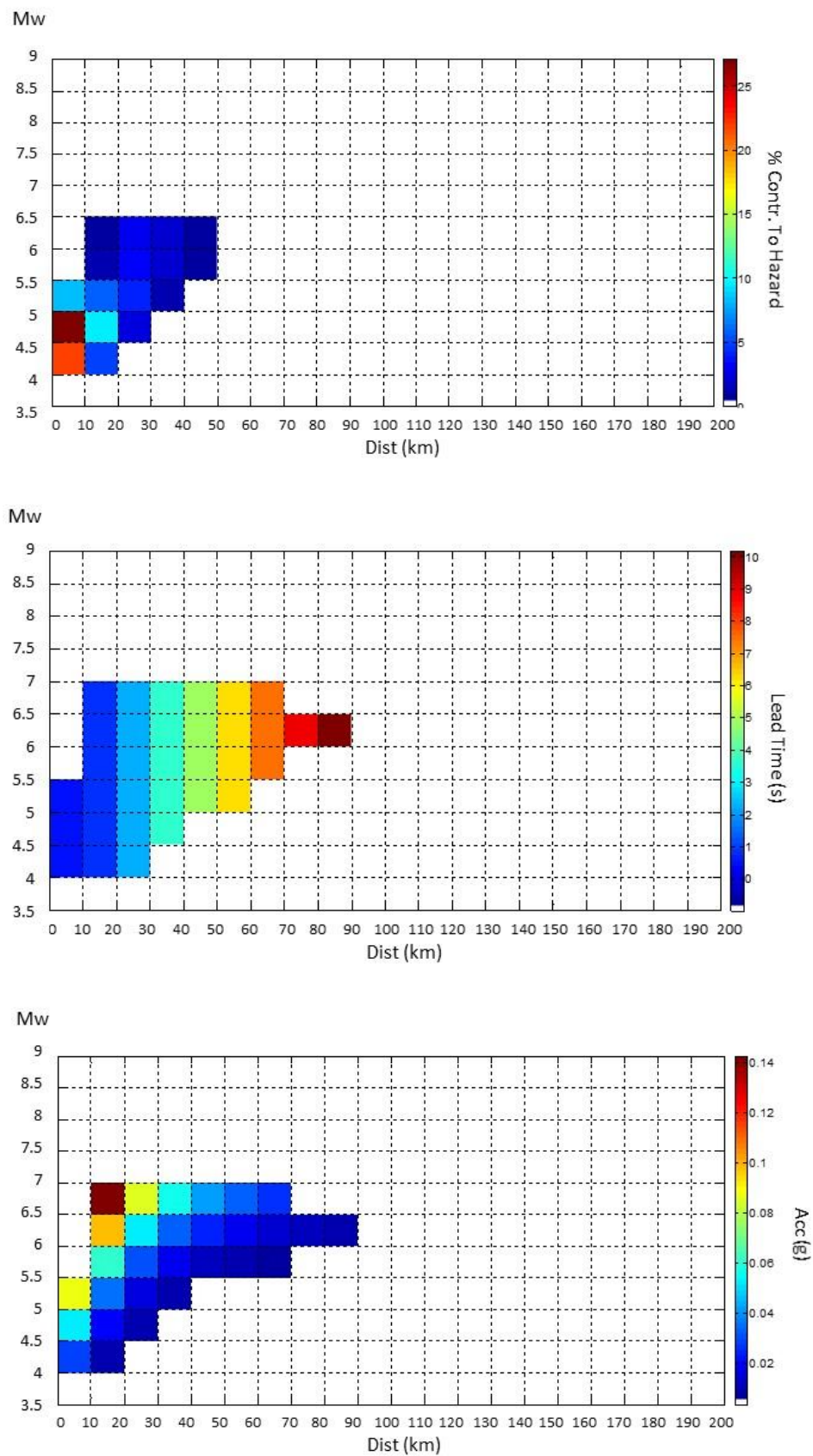


Figure 5.54. Disaggregation, lead-time and acceleration maps of target site of Firenze (Pr=10%).

FIRENZE – Probability of Damage - Pr=10% in 50y

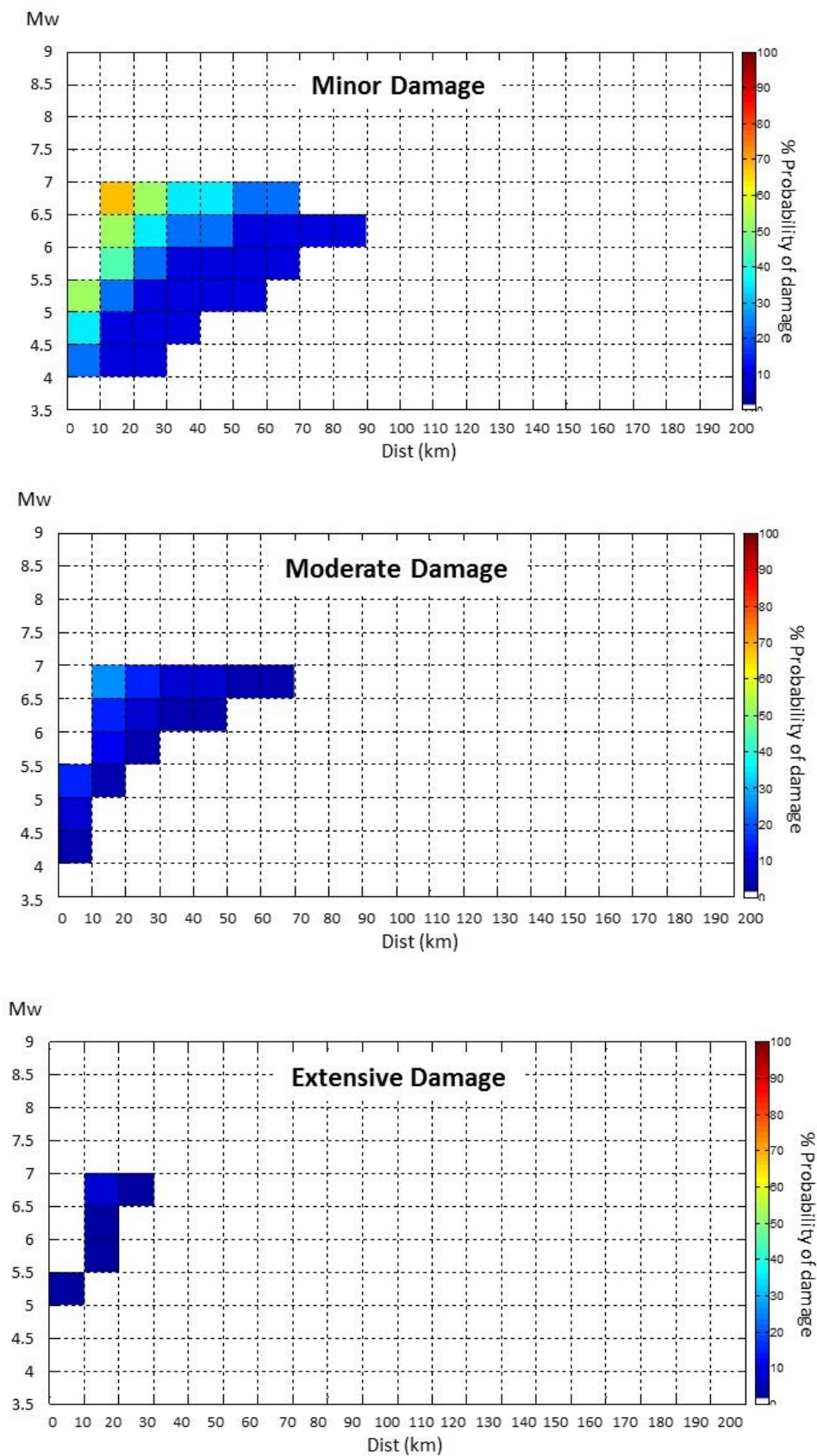


Figure 5.55. Probability of damage maps of target site of Firenze (Pr=10%).

FIRENZE - PHSA - Pr=5% in 50y

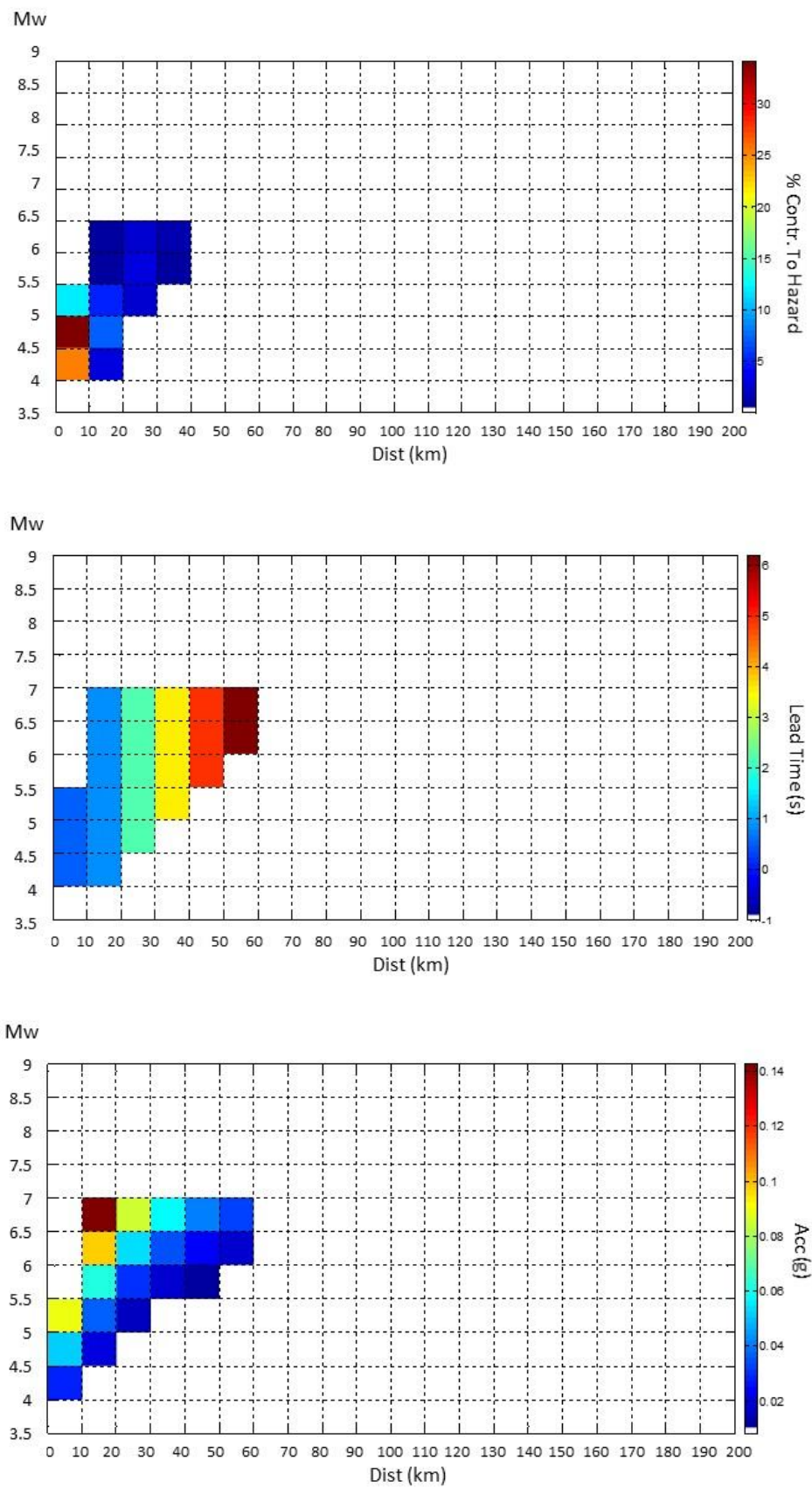


Figure 5.56. Disaggregation, lead-time and acceleration maps of target site of Firenze (Pr=5%).

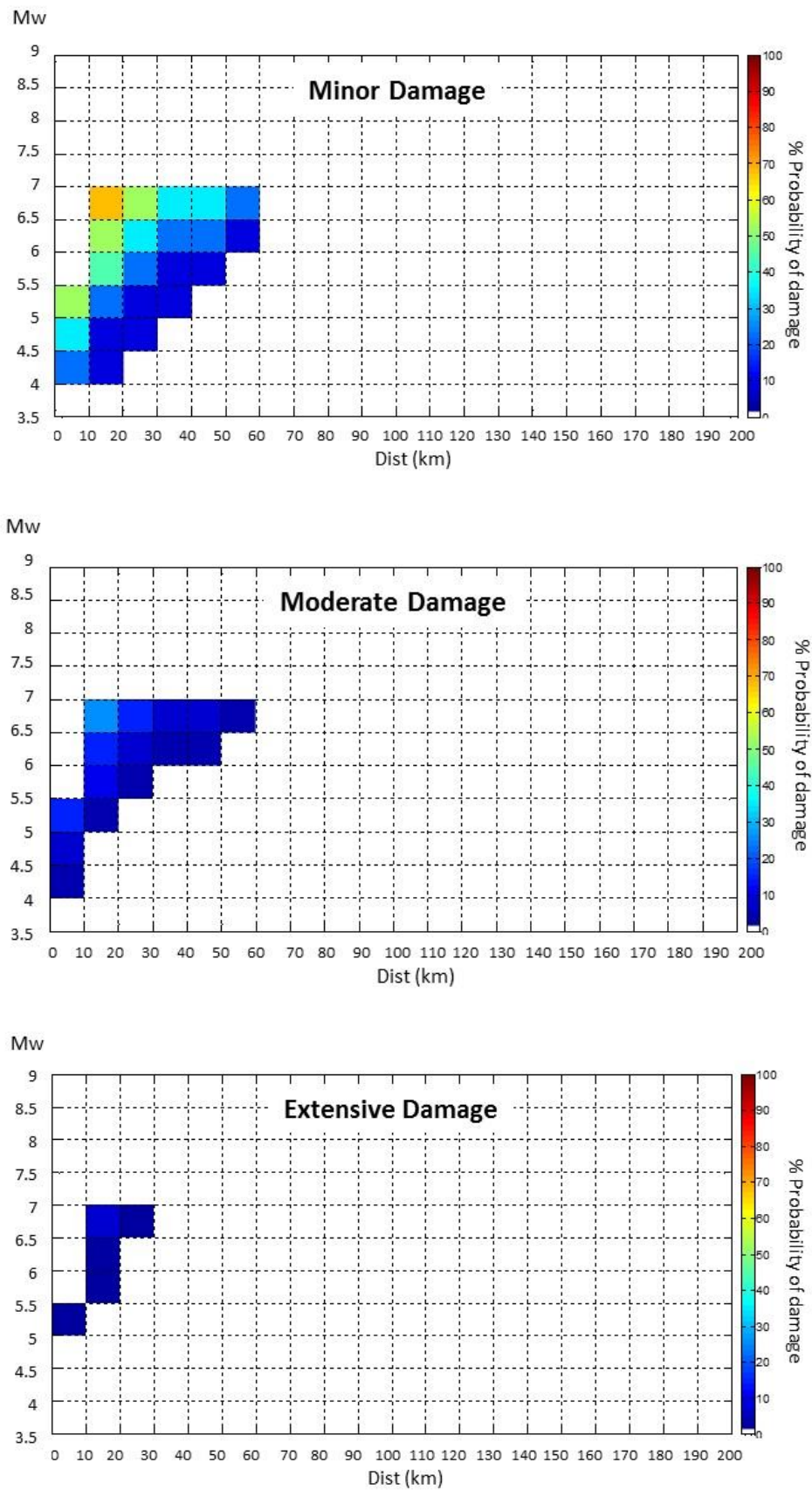
FIRENZE – Probability of Damage - Pr=5% in 50y

Figure 5.57. Probability of damage maps of target site of Firenze (Pr=5%).

ROCCA SAN GIOVANNI - PHSA - Pr=81% in 50y

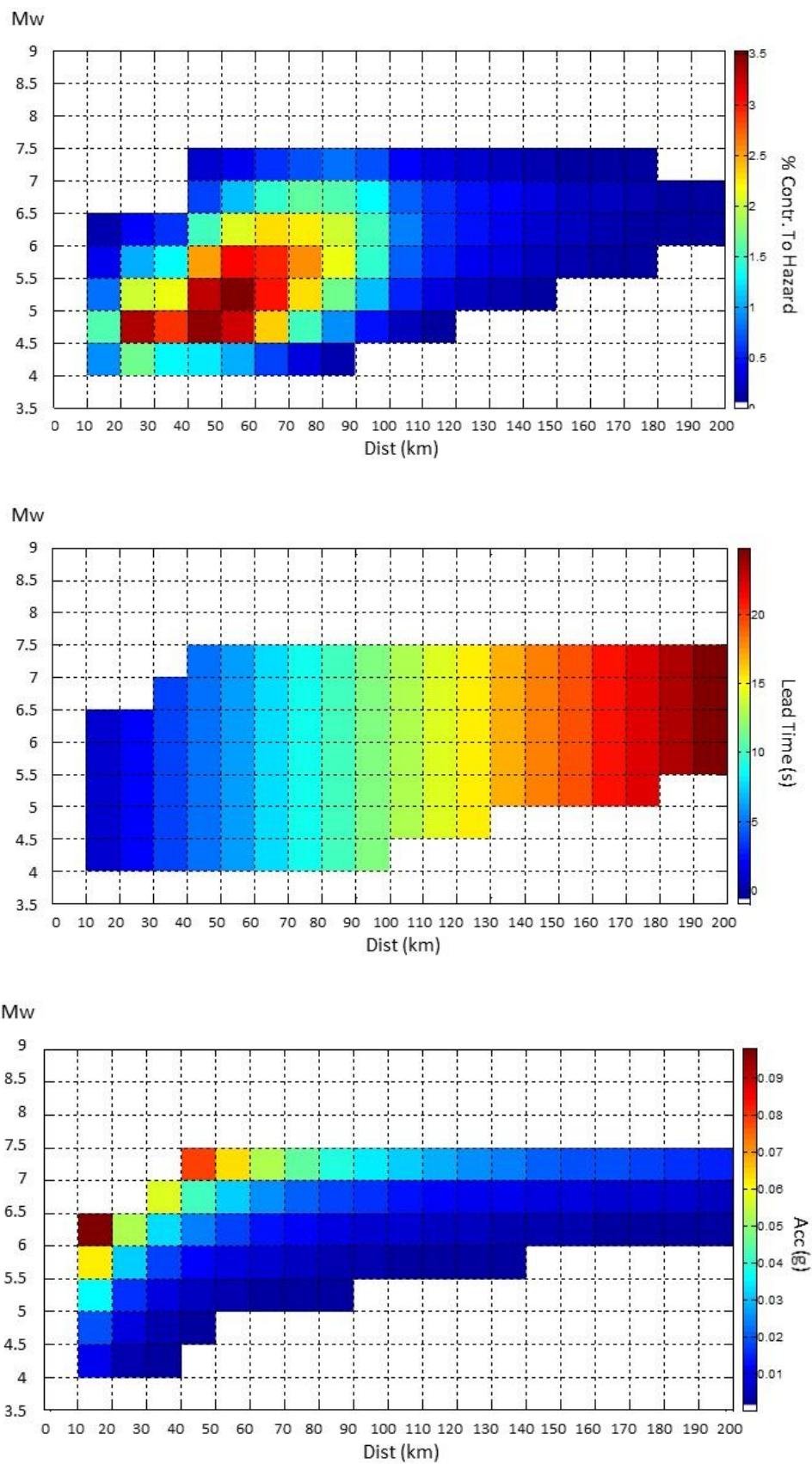


Figure 5.58. Disaggregation, lead-time and acceleration maps of target site of Rocca San Giovanni (Pr=81%).

ROCCA SAN GIOVANNI– Probability of Damage - Pr=5% in 50y

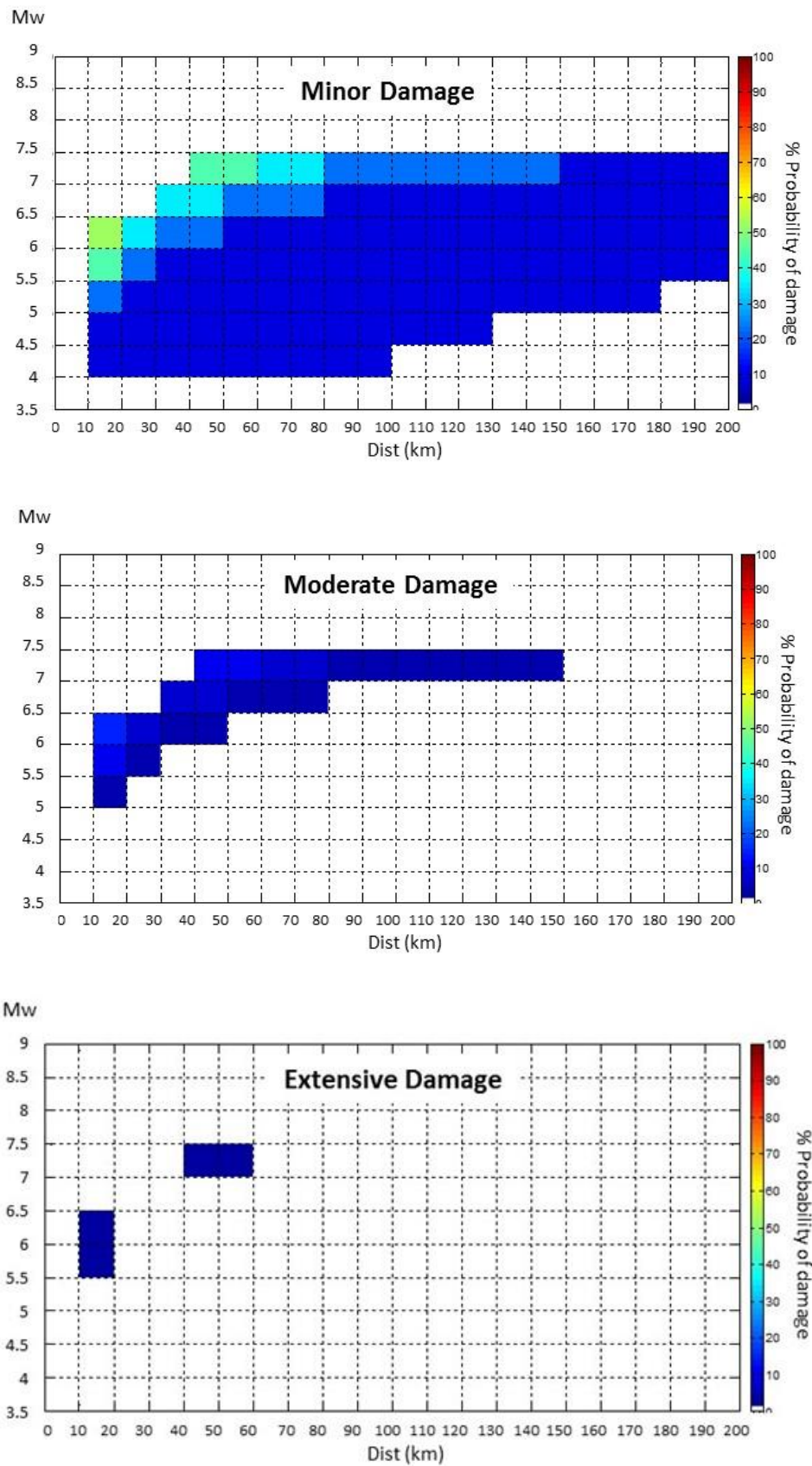


Figure 5.59. Probability of damage maps of target site of Rocca San Giovanni (Pr=81%).

ROCCA SAN GIOVANNI - PHSA - Pr=63% in 50y

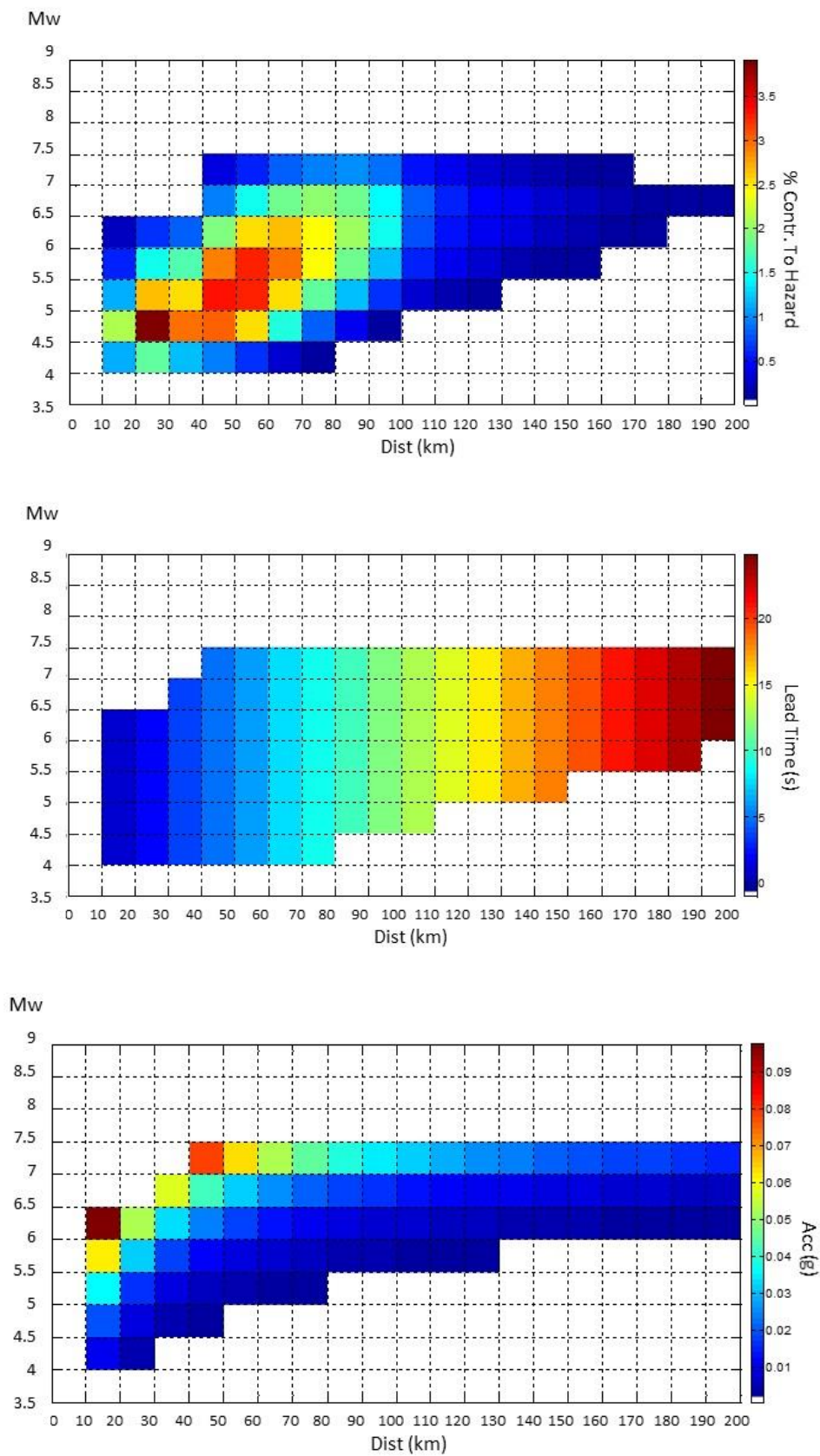


Figure 5.60. Disaggregation, lead-time and acceleration maps of target site of Rocca San Giovanni (Pr=63%).

ROCCA SAN GIOVANNI– Probability of Damage - Pr=63% in 50y

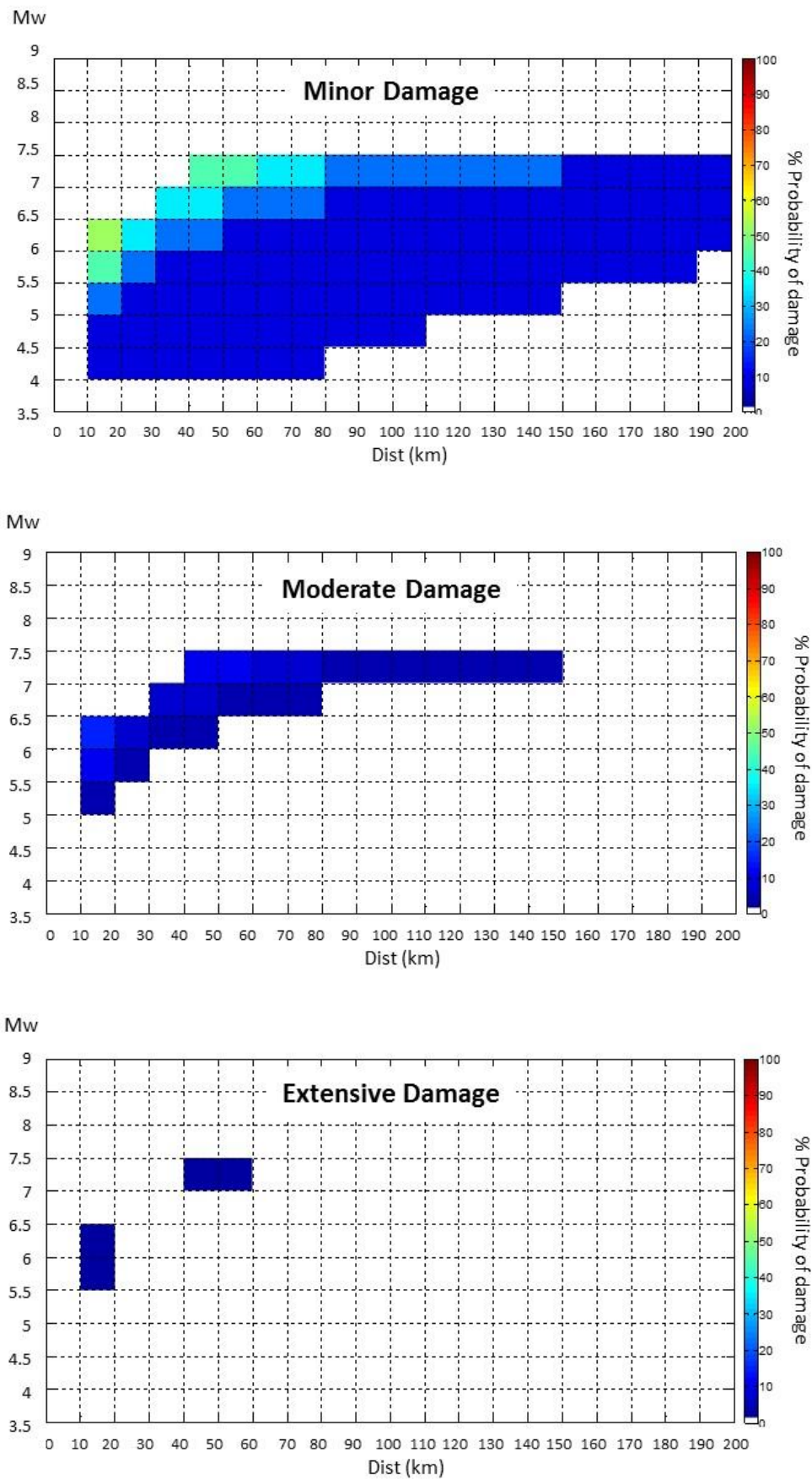


Figure 5.61. Probability of damage maps of target site of Rocca San Giovanni ($\text{Pr}=63\%$).

ROCCA SAN GIOVANNI - PHSA - Pr=10% in 50y

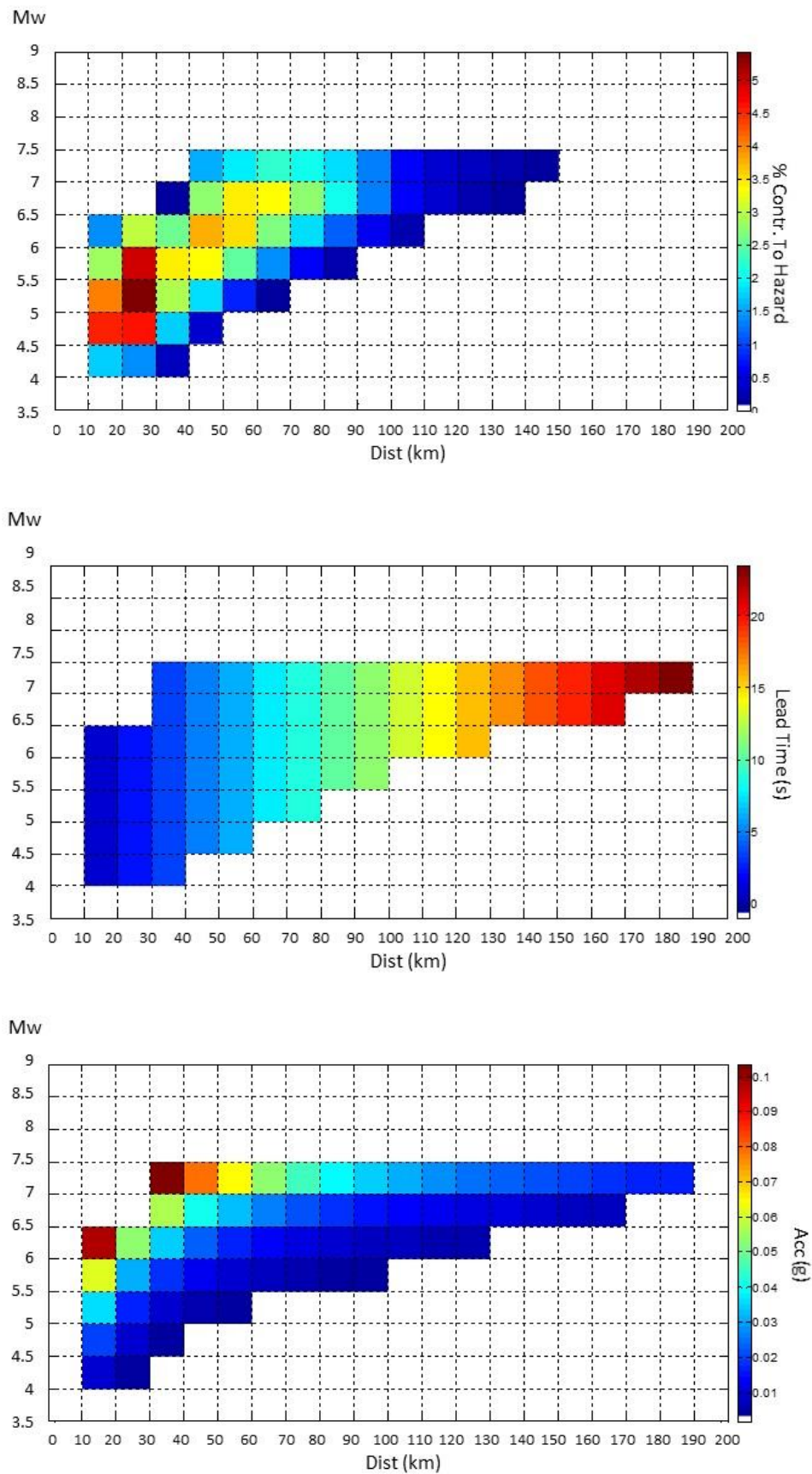


Figure 5.62. Disaggregation, lead-time and acceleration maps of target site of Rocca San Giovanni (Pr=10%).

ROCCA SAN GIOVANNI– Probability of Damage - Pr=10% in 50y

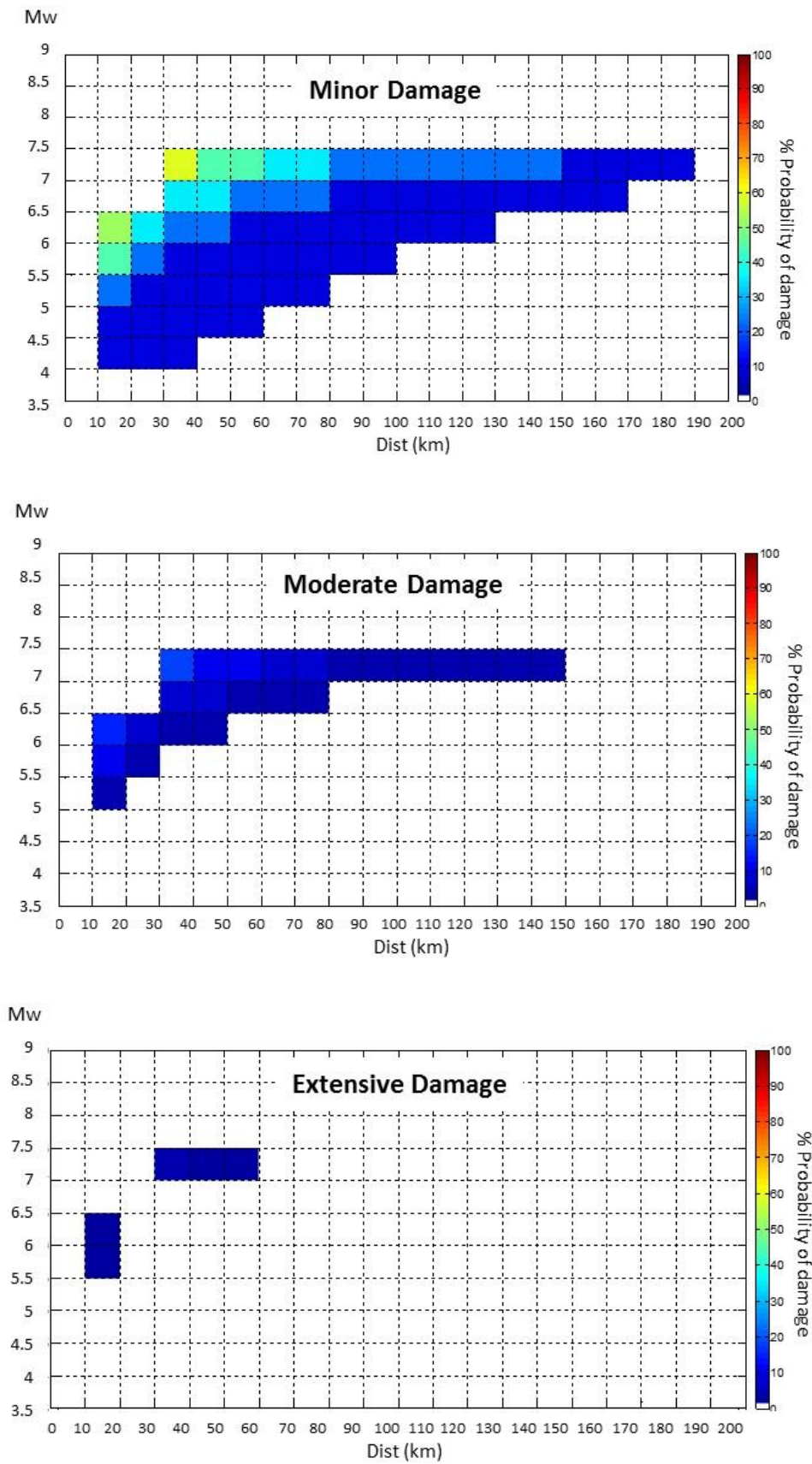


Figure 5.63. Probability of damage maps of target site of Rocca San Giovanni (Pr=10%).

ROCCA SAN GIOVANNI - PHSA - Pr=5% in 50y

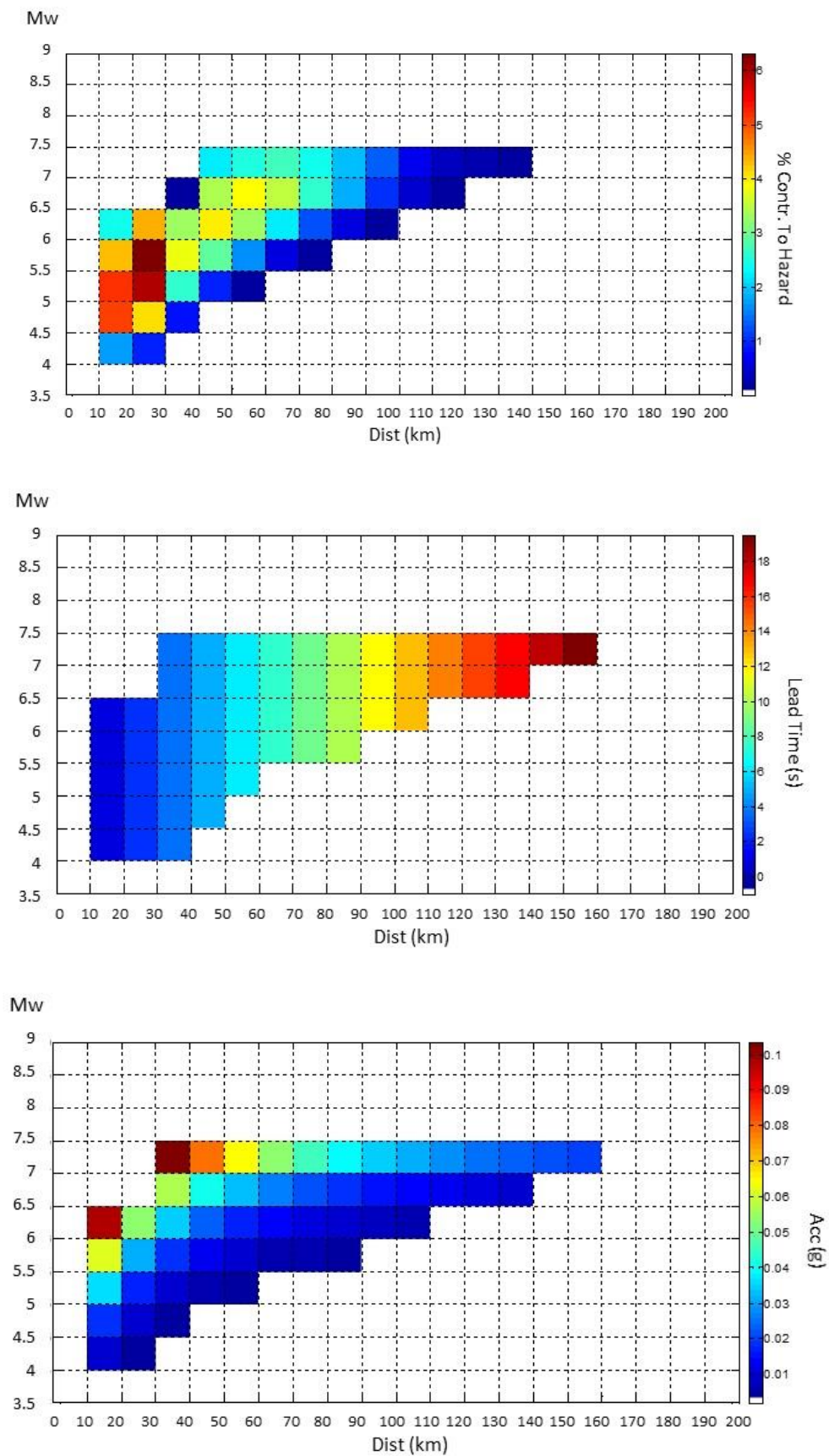


Figure 5.64. Disaggregation, lead-time and acceleration maps of target site of Rocca San Giovanni (Pr=5%).

ROCCA SAN GIOVANNI– Probability of Damage - Pr=5% in 50y

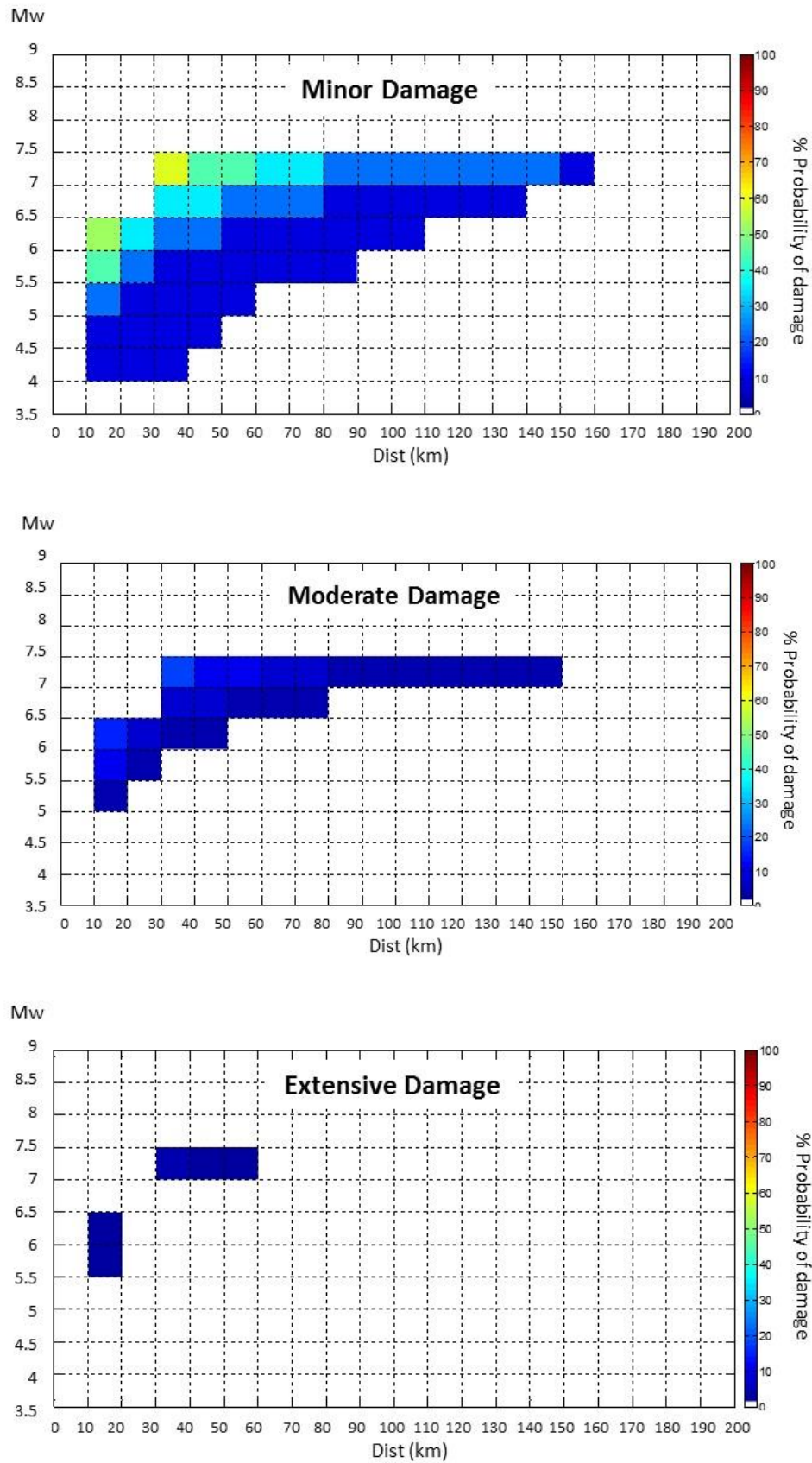


Figure 5.65. Probability of damage maps of target site of Rocca San Giovanni (Pr=5%).

In terms of lead-times, the results of the LEVEL-1 analysis indicates that considering the threats having the major contribution to the hazard the lead-time is in general low and not sufficient for implementing 'Regional Early Warning' approaches. On the contrary, on-site EEWS based on simple thresholds could provide warnings of imminent danger with enough time to protect the considered structure.

A similar situation is observed for the target named **Firenze**, for which the major threat is a 'virtual source' at about 20 km and magnitude $M \sim 5$. Therefore, also in this case the site of interest is too near to the seismic threat to consider feasible to warn the site by regional EEWS. On the contrary, for the case of **Rocca San Giovanni**, where for $Pr=81\%$, to the major threats correspond to seismic sources of moderate magnitude (4.5 – 5.75) at distances between 25 km and 65 km, the estimated lead-times are considered sufficiently large to suggest the use of a regional EEWS.

Currently in Italy there are more than 750 accelerometric stations installed across the whole Country's active seismic zones and a significant number of these stations (about 500) are nodes of the RAN (Italian accelerometric network; <http://www.protezionecivile.gov.it/jcms/it/ran.wp>) managed by the Italian Department of Civil Protection (Dipartimento della Protezione Civile, DPC), whose data are used for emergency response services, as well as being shared with the seismological and engineering communities for technical and scientific applications (Emolo A. et al. 2016). Picozzi et al. 2015 explored the scientific feasibility of a nation-wide EEWS in Italy that exploits the RAN and the regional EEW software PRESTo to provide the Italian DPC with the necessary information for planning the implementation of an operational EEWS in Italy. The software PRESTo is experimented at the ISNet (Irpina Seismic Network, Figure 5.66), a network located in South of Italy (Campania) developed after the Irpinia Earthquake (on 23 of November, 1980, $M=6.9$) to monitor the seismicity of the area.

Therefore, the Metro Line 6 of Napoli could be alerted by the regional EEWS given by ISNet and PRESTo from the Irpinia seismic threat, an area capable of generating events with magnitude larger than $M 7$ and corresponding to the zones 927 in the seismogenic map of Italy (Figure 5.41b).



Figure 5.66. Irpinia Seismic Network

5.2.2 Real time approach

The real-time approach is not bounded to the probabilistic approach proposed by the national code, and consists in the simulation of the effects of a real seismic event on the target site.

To this purpose, we exploit the *PRESTo-PRobabilistic and Evolutionary early warning SysTem* (Satriano et al. 2011, <http://www.prestoews.org>), which has been used to predict the PGA at the target

site through real-time and evolutionary location and magnitude estimates and a ground motion prediction equation. In this case, the application has been carried out only for the site of **Rocca San Giovanni**, simulating the occurrence of the largest seismic events that have recently interested that area.

That is to say, the Mw 6.1 L'Aquila Earthquake (occurred on 6 of April 2009) and the Mw 6.5 Norcia Earthquake (occurred on 30 of November 2016, $M=6.5$).

LEVEL '2'

Norcia earthquake (30 of November 2016, $M=6.5$)



Figure 5.67. Localization of Norcia earthquake and processed accelerometer stations during the seismic event.

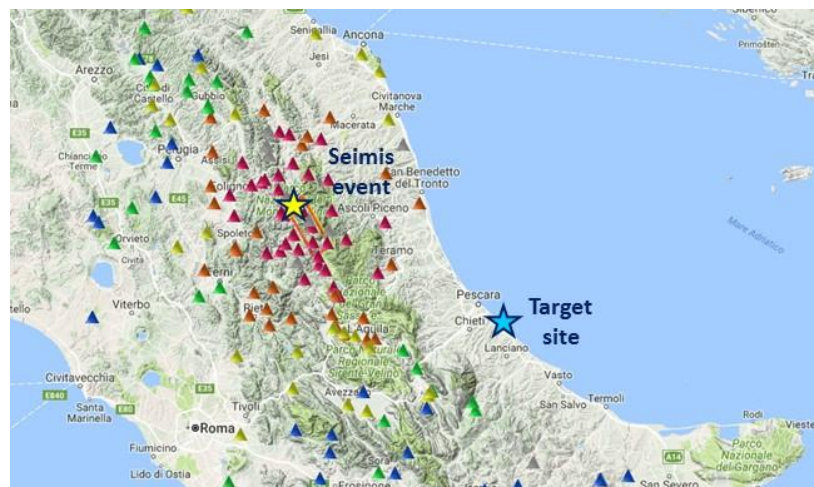


Figure 5.68. Zoom in of the localization of Norcia earthquake and the target site Rocca San Giovanni.

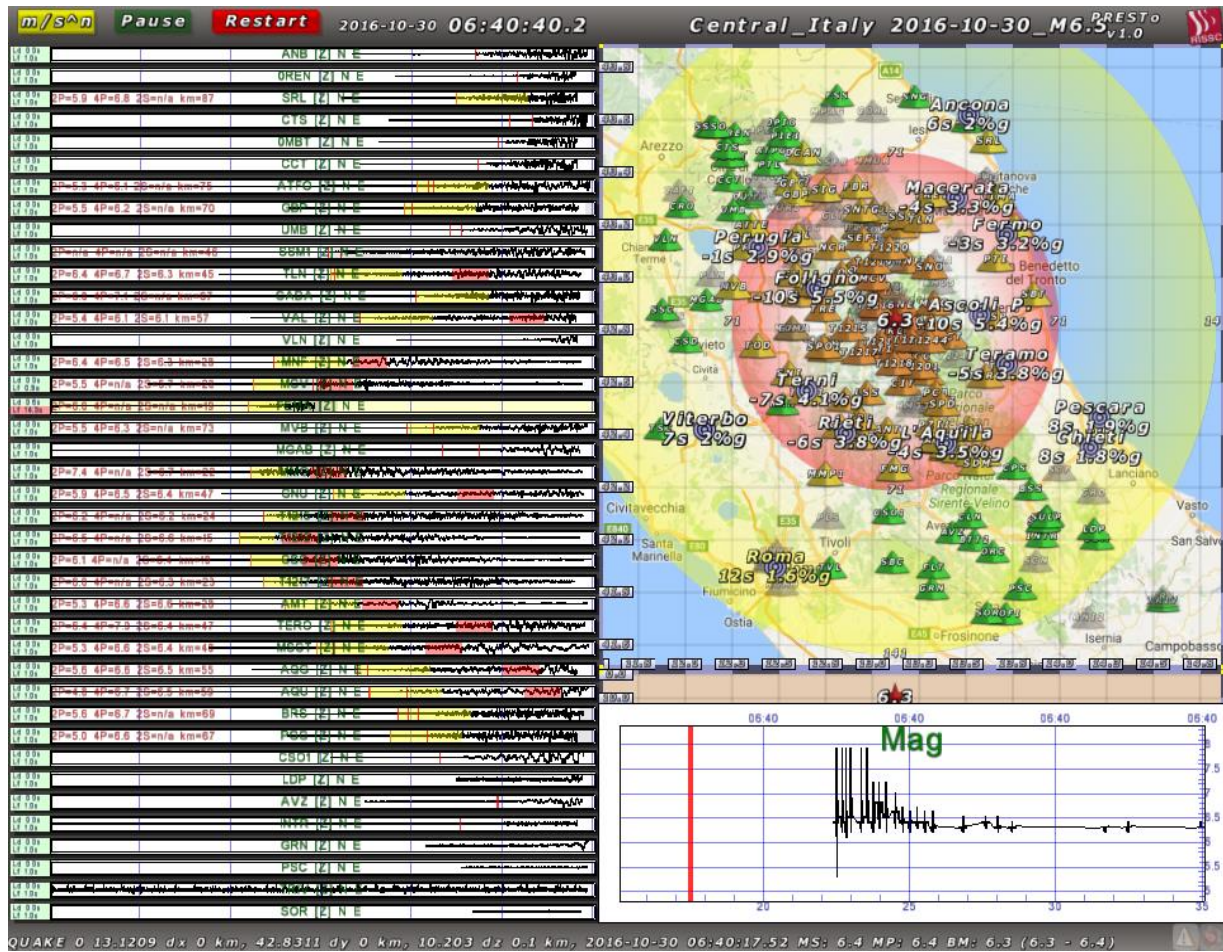


Figure 5.69. Real-time simulation of Norcia earthquake with PRESTo to determine the PGA value at the target site Rocca San Giovanni.

PRESTo has been used to analyse the RAN recordings of these two earthquakes simulating their occurrence and to estimate the PGA values at the target site Rocca San Giovanni as if they were occurring in real time, and thus providing a real-time estimation of the probability of damage. Figures 5.67 and 5.68 and Figures 5.70 and 5.71 show, for instance, the localization of the target site respect Norcia and L'Aquila epicentres, respectively.

As the time passes and more stations are triggered (Figure 5.69), the location and magnitude estimates are updated using all available data, thus providing continuously refined information about the earthquake parameters and ground shaking predictions at target sites.

Figures 5.72 and 5.73 show the results of the simulations in terms of estimated PGA (Figures 5.72a for Norcia earthquake and 5.73a for L'Aquila earthquake, respectively) and the probability of damage (Figures 5.72b for Norcia earthquake and 5.73b for L'Aquila earthquake, respectively) as function of the time from the origin time of the event.

The results show that for both seismic events the estimated PGA at the target site are such to lead us to forecast almost null probability of moderate and minor damage, and a value lower of the 10% of minor damage. Such results agree with the real response of the railway tunnel Rocca San Giovanni during the considered seismic events, during which any kind of damage was reported.

L'Aquila earthquake (6 of April 2009, M=6.1)



Figure 5.70. Localization of L'Aquila earthquake and processed accelerometer stations during the seismic event.

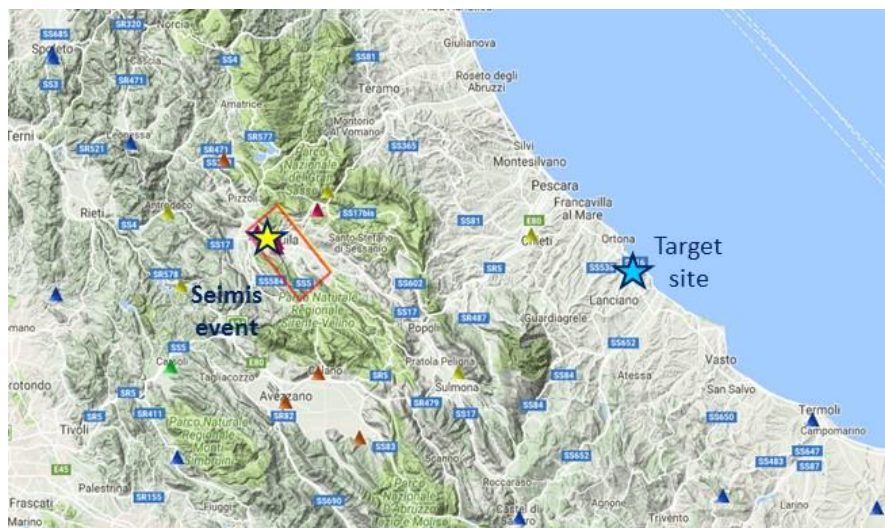


Figure 5.71. Zoom in of the localization of L'Aquila earthquake and the target site Rocca San Giovanni.

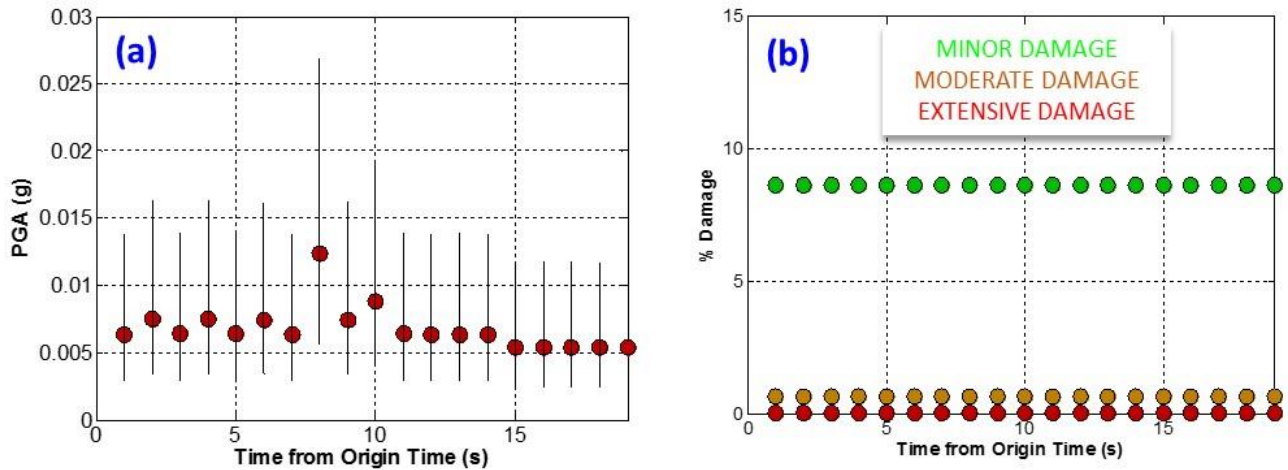


Figure 5.72. Real-time estimation of PGA and (b) probability of damage at the target site Rocca San Giovanni during Norcia earthquake.

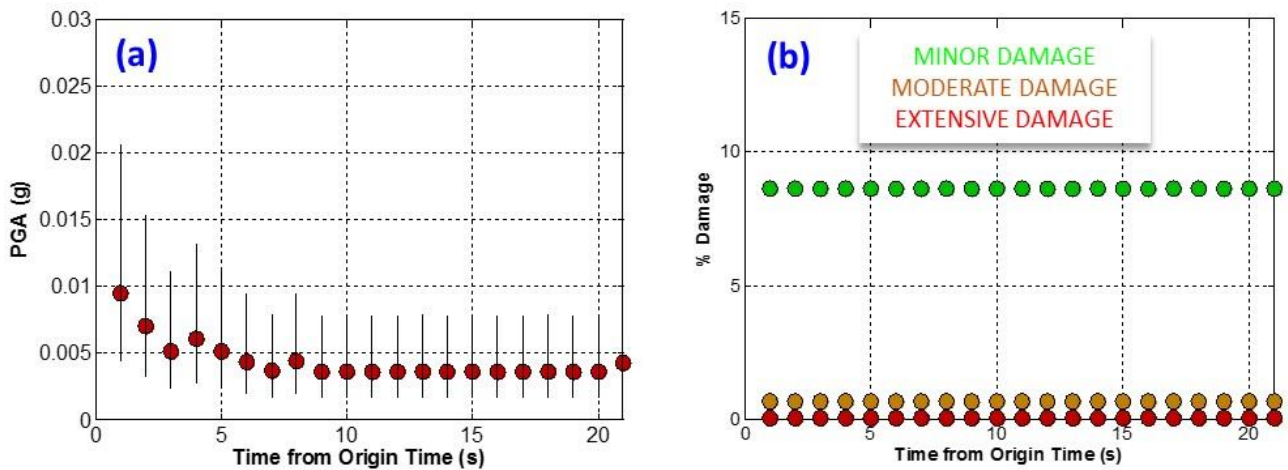


Figure 5.73. Real-time estimation of PGA and (b) probability of damage at the target site Rocca San Giovanni during L'Aquila earthquake.

The probabilistic approach defined with the LEVEL '2', based on the hazard disaggregation, provides a useful tool to study the feasibility of EEWS. These results indicate that two of the selected targets could benefit of an on-site EEWS. Concerning the target in Napoli, we found that a regional EEWS given by the combination of the ISNet network and software PRESTo could be effective to protect the Metro Line 6 of Napoli from the seismic threat represented by the Irpinia area.

THIRD PART: Behaviour of tunnel under non uniform seismic load

CHAPTER 6

Tunnel - ground interaction during non uniform seismic shaking

Introduction

The engineering problem of dynamic soil-underground-structure interaction is commonly studied assuming the structure infinitely long with an uniform cross-section (buried tunnel, immersed tunnel, pipeline) and the incident seismic wave with a direction perpendicular to the axis of the structure which does not vary along this axis, then assuming a plain strain problem.

Actually 'long' underground structure, that is the length of the structure is much longer than the wave length, undergoes to deformation also in longitudinal direction making the problem three dimensional. The longitudinal deformation pattern derives from the spatial incoherence of the seismic motion induced by the horizontal propagation of surface and body waves respect the structure axis.

This spatial variation of the seismic ground motion implies a modification of the free field soil response respect the case in which the spatial incoherence is not considered. As consequence, because the underground structure is governed by the surrounding soil deformation during seismic shaking, the free field soil response under asynchronous seismic motion should be different than the synchronous case.

This chapter focuses on the effect of the travelling wave passage along the tunnel axis on the seismic response of the structure. This loading condition is named in this Chapter '*non-uniform seismic load*' and it is compared with the uniform seismic load in plain strain condition.

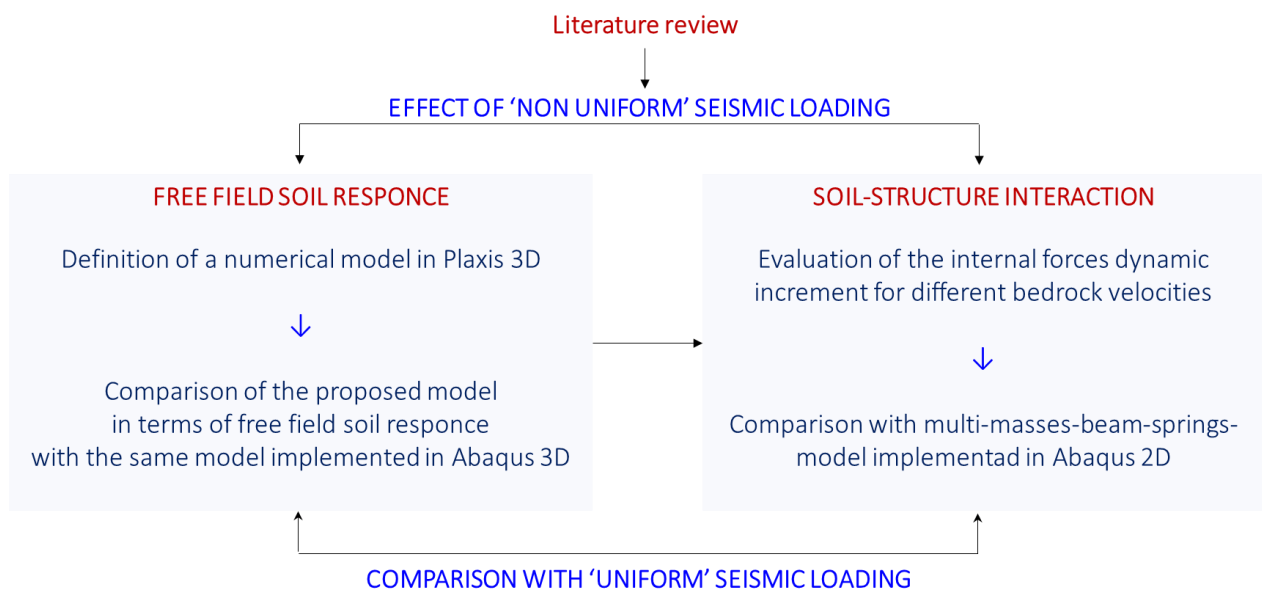


Figure 6.1. Layout of the Chapter 6.

A three dimensional numerical model able to catch the main deformation mechanisms of the soil subjected to multi-directional seismic motion, has been developed in the FE code Plaxis 3D. The free field soil response under travelling waves has been compared with the results obtained on the same model developed in Abaqus 3D.

Once validated the free-field numerical model, the soil structure interaction has been investigated with a set of parametrical analysis varying longitudinal time-lag of the travelling wave in terms of dynamic increment of transversal and longitudinal internal forces arising in the lining. A comparison between uniform and not uniform seismic load is shown for different seismic loading cases.

A simplified 2D multi-masses-beam-springs model developed by *Li Chong 2016* has been implemented in Abaqus 2D in order to compare the longitudinal component of dynamic increment of internal forces evaluated with two and three dimensional numerical method.

Figure 6.1 shows the organization scheme of this Chapter.

6.1 Literature review

As introduced in the Chapter 4, tunnels are subjected to different deformation mechanisms such as shear deformation (\rightarrow ovaling and racking for circular and rectangular shaped tunnel respectively), axial compression and extension and longitudinal bending (\rightarrow deforming the tunnel like a snake). Shear deformation is induced by the vertically propagating shear waves (uniform seismic load), the axial deformations in tunnels are generated by the components of seismic waves that produce motions parallel to the axis of the tunnel (non uniform seismic load), bending deformations are caused by the components of seismic waves producing particle motions perpendicular to the longitudinal axis (non uniform seismic load).

Current research on the topic distinguishes (a) analytical solutions and (b) numerical methods that, in different way and level of detail, solve the problem.

In the next paragraph the following analytical solutions are discussed in detail:

- i. Free field deformation approach - *St. John and Zahrah 1987*
- ii. Seismic deformation method - *Kawashima 1999*
- iii. Beam springs model - *Yu H. et al. 2016*
- iv. Mass-beam-springs model - *Kiyomiya O. 1995*
- v. Multi masses beam springs model - *Li C. et al. 2017.*

Free field and seismic deformation methods for instance, using a pseudo-static approach, evaluate similarly the effect of seismic soil deformation on the tunnel structure without taking explicitly into account its presence and then the soil-structure interaction. Both methods include the effect of the incidence of the seismic wave respect the tunnel axis without simulating the effect of wave travelling.

The beam spring model studies the effect of the travelling wave in a pseudo-static way acting directly on the structure. The soil structure interaction is modelling with springs elements representing the stiffness of the soil which seismic behaviour is not including in the model.

Masses and multi-masses beam-springs models study the soil structure-interaction with SDOF and MDOF equivalent systems respectively, under non uniform seismic loads.

These latter represent the most advanced and sophisticated analytical methods to study the longitudinal behaviour of tunnel under seismic shaking.

Regarding the numerical solutions on the topic, they are less large respect the analytical ones because they are very time consuming and need very large computer memory, respect the case of uniform seismic load too. In particular, the following numerical approaches are discussed in detail:

- I. Pseudo-static 3D numerical analysis, *Park et al. 2009*,
- II. 3D multi-scale method, *Yu H. et al. 2013*,
- III. 3D full dynamic analysis, *Li & Song 2014*.

6.1.1 Analytical solutions

Closed-form expressions existing in literature simply estimate the tunnel strains and stresses arising in the tunnel lining modelling the seismic wave field as a plane wave with the same amplitude in every tunnel segment, differing only in their arrival time (coherence). Wave scattering and three dimensional propagation are neglected, even if these phenomena can determine a variation of stress and strain along the tunnel axis. Figure 6.2 shows schematically the geometry of the problem. Named C the propagation velocity along the tunnel axis of length l , ϕ the incidence angle and L the wavelength of the plane waves, the condition causing the motion phase displacement on the structure is $l > L = C/f$. This condition shows that the effect of longitudinal propagation is remarkable for lower propagation velocity and is not negligible for lower frequencies (*Rampello, 2005*).

Consider a planar wave front advancing with speed C and impinging on the tunnel axis with an angle ϕ . The sinusoidal signal is used to represent an accelerogram with an equivalent energy content. The apparent velocity of the waves on the tunnel axis is $C_x = C/\cos\phi$.

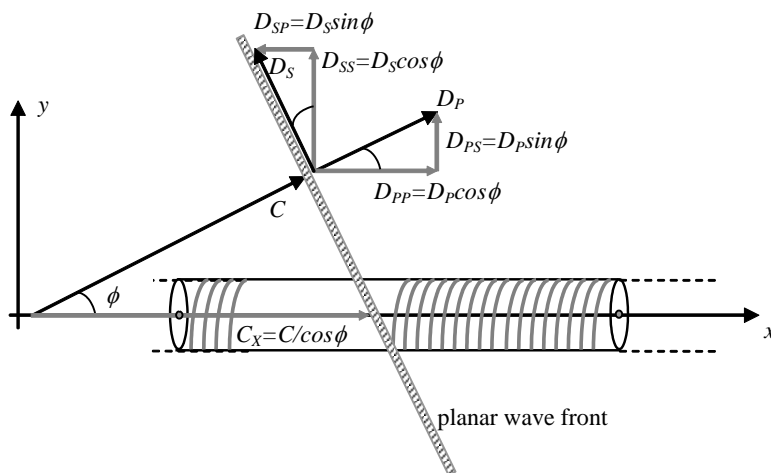


Figure 6.2. Geometry of the problem (*Vanzi, 2000*).

Compression P waves travelling in the ϕ direction with amplitude D_p causes, along the tunnel axis, both a train of compression waves, with amplitude $D_{pp} = D_p \cos\phi$, and a train of shear waves with amplitude $D_{ps} = D_p \sin\phi$. Shear S waves with amplitude D_s can be decomposed similarly: they produce both

compression waves with amplitude $D_{sp}=D_s \sin \phi$, along the tunnel axis, and shear waves with amplitude $D_{ss}=D_s \cos \phi$, acting transversally. Finally the stresses are coupled unless the incidence angle is 0° or 90° (Figure 6.2).

i. Free field deformation approach - St. John and Zahrah 1987

St. John and Zahrah 1987 used the Newmark's approach to develop closed formula for free field axial and curvature strains due to the compression, shear and Rayleigh waves. Based on this, they used pseudo-static approach (free-field deformation method) to estimate the strains and curvature of the tunnel subjected to a harmonic motion propagating at an incident angle respect the tunnel axis. The free field approach does not consider the soil-structure interaction and this may underestimate or overestimate the structure deformation in function mainly of structure stiffness respect the surrounding soil.

The starting point of the analytical procedure is the equation of planar wave propagation in x direction through a homogeneous medium:

$$u(x, t) = f(x - Ct) \quad (6.1)$$

In 6.1, t is the time and C is the wave propagation speed in the medium. In order to calculate the curvature and strain in the wave propagation direction, the $u(x, t)$ is derived to x :

$$\frac{\partial u}{\partial x} = -\frac{1}{C} \frac{\partial u}{\partial t} \quad (6.2)$$

$$\frac{\partial^2 u}{\partial x^2} = -\frac{1}{C^2} \frac{\partial^2 u}{\partial t^2} \quad (6.3)$$

Using the equations 6.2 and 6.3 the strain and curvature in free-field conditions are calculated for the three different types of waves (P, S, and Rayleigh waves). For example, for the compression P wave, the maximum longitudinal strain value is:

$$\varepsilon_{lm} = \frac{V_p}{C_p} \quad (6.4)$$

where V_p is the peak ground velocity of seismic signal (amplitude for sinusoidal waves) and C_p is the propagation velocity for the compression waves. If the maximum curvature for shear waves S is considered, the expression will be:

$$\frac{1}{\rho_m} = \frac{a_s}{C_s^2} \quad (6.5)$$

a_s is the peak ground acceleration of the seismic signal (amplitude for sinusoidal waves) and C_s is the propagation speed for shear waves. In the general case, the P, S and Rayleigh waves propagate in the medium with a generic angle of incidence on the underground structure. In Table 6.1, the components of deformation and curvature relevant to the different wave types, their maximum values and the angles of incidence for which the maximum occurs are shown (the P, S or R notation is relative to compression, shear and Rayleigh waves).

The axial and bending deformations are combined in order to calculate the total longitudinal strain. The values relative to compression waves P and shear waves S are:

$$\varepsilon_{ap} = \frac{V_p}{C_p} \cos^2 \phi + r \frac{a_p}{C_p^2} \sin \phi \cos^2 \phi \quad (6.6)$$

$$\varepsilon_{as} = \frac{V_s}{C_s} \sin \phi \cos \phi + r \frac{a_s}{C_s^2} \cos^3 \phi \quad (6.7)$$

Wave Type	Longitudinal strain	Normal strain	Shear strain	Curvature
<i>P waves</i>	$\varepsilon_l = \frac{V_p}{C_p} \cos^2 \phi$ $\varepsilon_{lm} = \frac{V_p}{C_p}$ (for $\phi = 0^\circ$)	$\varepsilon_n = \frac{V_p}{C_p} \sin^2 \phi$ $\varepsilon_{nm} = \frac{V_p}{C_p}$ (for $\phi = 90^\circ$)	$\gamma = \frac{V_p}{C_p} \sin \phi \cos \phi$ $\gamma_m = \frac{V_p}{2C_p}$ (for $\phi = 45^\circ$)	$\frac{1}{\rho} = \frac{a_p}{C_p^2} \sin \phi \cos^2 \phi$ $\frac{1}{\rho_m} = 0.385 \frac{a_p}{C_p^2}$ (for $\phi \cong 35^\circ$)
<i>S waves</i>	$\varepsilon_l = \frac{V_s}{C_s} \sin \phi \cos \phi$ $\varepsilon_{lm} = \frac{V_s}{2C_s}$ (for $\phi = 45^\circ$)	$\varepsilon_n = \frac{V_s}{C_s} \sin \phi \cos \phi$ $\varepsilon_{nm} = \frac{V_s}{2C_s}$ (for $\phi = 45^\circ$)	$\gamma = \frac{V_s}{C_s} \cos^2 \phi$ $\gamma_m = \frac{V_s}{2C_s}$ (for $\phi = 0^\circ$)	$\frac{1}{\rho} = \frac{a_s}{C_s^2} \cos^3 \phi$ $\frac{1}{\rho_m} = \frac{a_s}{C_s^2}$ (for $\phi = 0^\circ$)
<i>Rayleigh waves (compressional component)</i>	$\varepsilon_l = \frac{V_{RP}}{C_R} \cos^2 \phi$ $\varepsilon_{lm} = \frac{V_{RP}}{C_R}$ (for $\phi = 0^\circ$)	$\varepsilon_n = \frac{V_{RP}}{C_R} \sin^2 \phi$ $\varepsilon_{nm} = \frac{V_{RP}}{C_R}$ (for $\phi = 0^\circ$)	$\gamma = \frac{V_{RP}}{C_R} \sin \phi \cos \phi$ $\gamma_m = \frac{V_{RP}}{2C_R}$ (for $\phi = 45^\circ$)	$\frac{1}{\rho} = \frac{a_{RP}}{C_R^2} \sin \phi \cos^2 \phi$ $\frac{1}{\rho_m} = 0.385 \frac{a_{RP}}{C_R^2}$ (for $\phi \cong 35^\circ$)
<i>Rayleigh waves (shear component)</i>		$\varepsilon_n = \frac{V_{RS}}{C_R} \sin \phi$ $\varepsilon_{nm} = \frac{V_{RS}}{C_R}$ (for $\phi = 90^\circ$)	$\gamma = \frac{V_{RS}}{C_R} \cos \phi$ $\gamma_m = \frac{V_{RS}}{C_R}$ (for $\phi = 0^\circ$)	$\frac{1}{\rho} = \frac{a_{RS}}{C_R^2} \cos^2 \phi$ $\frac{1}{\rho_m} = \frac{a_{RS}}{C_R^2}$ (for $\phi = 0^\circ$)
The Poisson's ratio and dynamic modulus of a deposit can be computed from measured P and S waves propagation velocities in an elastic medium: $v_s = \frac{1}{2} \left(\frac{C_p}{C_s} \right)^2 - 2$ or $C_p = \sqrt{\frac{1}{(1-2v_s)}} C_s$; $E_s = \rho_s C_p^2 \frac{(1+v_s)(1-2v_s)}{(1-v_s)}$				

Table 6.1: strain and curvature due to body and surface waves (St.John & Zahrah 1987)

The analytical solutions are obtained using a quasi-static representation of the seismic actions and neglecting the dynamic effects of the soil/structure interaction.

In the followings, only the shear wave S is considered; the analytical procedures are formally the same also for compression waves P but, as some Authors observed (St.John & Zahrah, 1987, Hashash et al., 2001), the corresponding seismic strains are lower in comparison.

Considering a tunnel subjected to a sinusoidal wave S with wavelength L and amplitude D the displacements values are (Figure 6.3):

$$u_y = D \cos \phi \sin \left(\frac{2\pi x}{L / \cos \phi} \right) \quad (6.8)$$

$$u_x = D \sin \phi \sin \left(\frac{2\pi x}{L / \cos \phi} \right) \quad (6.9)$$

The wavelength parameter L of the ideal sinusoidal signal representing the earthquake action is defined as $L = T_s C_s$ (Wang, 1993), where T_s is the fundamental period of the deposit, which can be calculated for instance according to Idriss and Seed 1968, and C_s is the propagation speed of the shear waves.

The sinusoidal wave amplitude D comes from specific site conditions. Generally the parameter D can be computed according to the following expressions (Hashash et al., 2001), in which it is the only unknown quantity, by equalling the deformations values in free-field conditions (6.10 and 6.11) and the structure strain of an elastic beam:

- for axial free-field deformations: $\frac{2\pi D}{L} = \frac{V_S}{C_S} \sin \phi \cos \phi$ (6.10)

- for bending free-field deformations: $\frac{4\pi^2 D}{L^2} = \frac{a_S}{C_S} \cos^3 \phi$ (6.11)

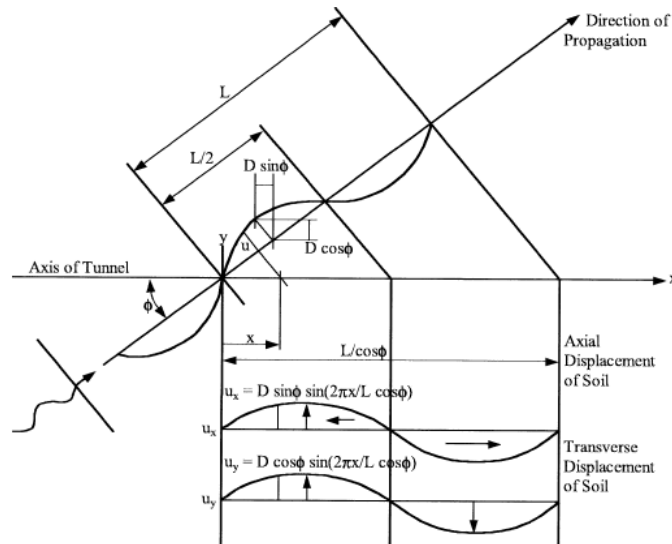


Figure 6.3. Displacements due to a sinusoidal shear wave.

Once obtained all the wave parameters, the following expressions of the seismic internal forces in the tunnel lining can be computed (St.John & Zahrah, 1987):

$$N = \left(\frac{2\pi}{L} \right) \sin \phi \cos \phi E_t A D \cos \left(\frac{2\pi x}{L / \cos \phi} \right) \quad (6.12)$$

$$T = \left(\frac{2\pi}{L} \right)^3 \cos^4 \phi E_t I A \cos \left(\frac{2\pi x}{L / \cos \phi} \right) \quad (6.13)$$

$$M = \left(\frac{2\pi}{L} \right)^2 \cos^3 \phi E_t I A \sin \left(\frac{2\pi x}{L / \cos \phi} \right) \quad (6.14)$$

where E_t is the Young's modulus of the structure, I is the second moment of area, A is the area of the transverse section.

The Equations 6.12, 6.13 and 6.14 were obtained without considering the dynamic soil-structure interaction. Therefore, if the structure is stiffer than the surrounding ground, it distorts less, as a

consequence of the interaction.

If the structure is considered as an elastic beam on an elastic soil, the static interaction is considered and the equation to solve is:

$$E_t I \frac{d^4 u_t}{dx^4} = p \quad (6.15)$$

where u_t is the structure deformation and p is the interface stress. The contact action at the interface between the soil and the structure is modelled through a bed of linearly elastic springs:

$$p = K_t (u_y - u_t) \quad (6.16)$$

Substituting Equation 6.16 in 6.15 the tunnel curvature obtained is lower than the value of the previous calculation. A reduction parameter can be used to take into account this difference:

$$R_1 = \frac{1}{1 + \frac{E_t I}{K_t} \left(\frac{2\pi}{L} \right)^4 \cos^4 \phi} \quad (6.17)$$

Shear forces and bending moments must be reduced using the R factor in order to obtain correct solutions. The same approach is used to find the expression of the axial force from the equation:

$$E_t A \frac{d^2 u_a}{dx^2} = K_a (u_a - u_x) \quad (6.18)$$

A reduction factor is obtained to be multiplied by the previous Equation 6.12 for axial forces:

$$R_2 = \frac{1}{1 + \frac{E_t A}{K_a} \left(\frac{2\pi}{L} \right)^2 \cos^2 \phi} \quad (6.19)$$

According to Eqs 6.12, 6.13, 6.14 and 6.17, the angle that maximizes bending moments and shear forces is $\phi=0^\circ$. On the other hand the condition of maximum axial force does not follow straightforward from Eqs. 6.12, 6.13, 6.14 and 6.19, but it is common assumption in design that the maximum axial force can be computed for $\phi=45^\circ$, which corresponds to the exact maximum condition when the soil-structure interaction is neglected (6.12, 6.13, 6.14)

In soft soil the structure modifies the deformation of the surrounding ground, therefore Eqs 6.17 and 6.19, which accounts for interaction, should be used; on the other hand, in rock and stiff soil the use of the free-field expressions 6.12, 6.13, 6.14 are usually enough accurate due to the high contrast of stiffness between the tunnel and the ground.

According to Eqs. 6.12, 6.13, 6.14, as structural stiffness increases due to tunnel lining reinforcements, this generally determines an increase of the seismic loads in the lining. In order to avoid this, flexible joints can be designed.

When the use of Eqs. 6.17 and 6.19 are needed, the spring constants K_t and K_a shall be determined. They represent the ratios between the interface soil-structure interaction loads and the corresponding displacements. Literature values for this constants (Wang, 1993) are a function of the wavelength of incident wave:

$$K_t = K_a = \frac{16\pi G_s (1-\nu_s)}{(3-4\nu_s)} \frac{d}{L} \quad (6.20)$$

where G_s and ν are the shear stiffness modulus and Poisson ratio for the medium and d is the diameter of the circular tunnel.

This elastic coefficients must be representative of the dynamic behaviour and the cyclic load of the sinusoidal wave.

ii. Seismic deformation method - Kawashima 1999

A new quasi-static method was used in Japan for the design of underground fuel pipelines from the Chiba Port to the International Airport of Marita (JRA, 1976): in this method the seismic deformation of the ground is assumed as the seismic action on the pipelines. In the following years the method was improved until it became the main design method in Japan for all the underground structures under seismic conditions, known as 'Seismic Deformation Method'.

According to the method, a long tunnel is modelled as an elastic beam in elastic soil. The equations of motion in the longitudinal and transverse directions are expressed as:

$$m \frac{\partial^2 u_a(x,t)}{\partial t^2} + E_t A \frac{\partial^2 u_a(x,t)}{\partial x^2} = K_a \{u_x(x,t) - u_a(x,t)\} \quad (6.21)$$

$$m \frac{\partial^2 u_t(x,t)}{\partial t^2} + E_t I \frac{\partial^4 u_t(x,t)}{\partial x^4} = K_t \{u_y(x,t) - u_t(x,t)\} \quad (6.22)$$

where m is the mass of lining for unit length, $E_t A$ and $E_t I$ are the axial and bending stiffness of the tunnel section; u_a and u_t are the longitudinal and transversal displacements of section x at the time t ; u_x and u_y are the displacements at the same instant t of the soil surrounding the same section x , K_a and K_t are the elastic constants of the springs modelling the soil reaction in the longitudinal and transversal direction.

To use the above formulas in design, the soil displacements u_x and u_y are computed in the method by assuming an ideal soil deformation of sinusoidal shape having wavelength L (Figure 6.4).

The *free-field* deformation of the soil surrounding the tunnel is the result of different components due to the non homogeneous subsoil characteristics, the thickness of soft soil layers, and the signal variation compared to the bedrock registration.

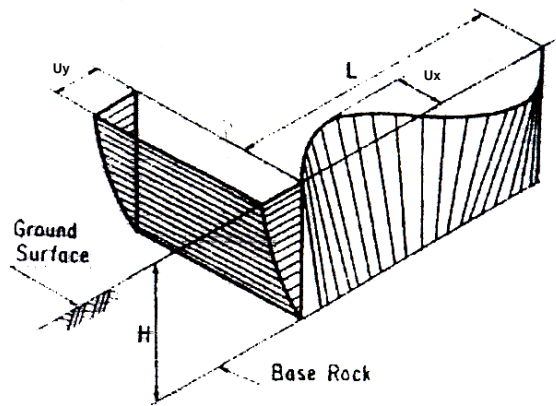


Figure 6.4. Ideal displacements of tunnel axis (Kawashima 1999).

In order to take into account such a variability, the wavelength L of the ideal *free-field* displacement function is not the simple wavelength of the wave passing through the medium but rather an equivalent value that give a good agreement of the six seismic deformation components. The L adopted value is:

$$L = \frac{2L_1L_2}{L_1 + L_2}; L_1 = V_S T_S; L_2 = V_{SB} T_S \quad (6.23)$$

V_S and V_{SB} are the propagation velocity of the shear waves in the soil and in the bedrock respectively. T_S is the fundamental period of soil layer, calculated as:

$$T_S = 1.25 \sum_i \frac{4H_i}{V_{Si}} \quad (6.24)$$

H_i and V_{Si} are the thickness and the shear waves propagation velocity of the i -th sub-layer, that is for each sub-layer in which the soil is divided. Once the wavelength L is defined, the design value of the soil displacement both in longitudinal and transversal direction is given by the following expression:

$$u(x, t) = u_h \cos\left(\frac{\pi z}{2H}\right) \sin\left(\frac{2\pi x}{L}\right) \quad (6.25)$$

where u_h is the horizontal displacement at surface and is obtained, in the hypothesis of homogeneous soil, as:

$$u_h = \frac{2}{\pi^2} S_V T_S \quad (6.26)$$

where S_V is the design peak ground velocity of the bedrock response spectrum.

By substituting Eq. 6.25 in the 6.21 and 6.22, the differential equation can be solved and the axial forces and bending moments on the structure are given as:

$$N_h = c_{ta} c_{ja} \frac{\pi E_t A}{L} \tilde{u}_h \quad (6.27)$$

$$N_v = c_{ta} c_{ja} \frac{\pi E_t A}{L} \frac{\tilde{u}_h + \tilde{u}_v}{2} \quad (6.28)$$

$$M_h = c_{tt} c_{jt} \frac{4\pi^2 E_t I_h}{L^2} \tilde{u}_h \quad (6.29)$$

$$M_v = c_{tv} c_{jv} \frac{4\pi^2 E_t I_v}{L^2} \tilde{u}_v \quad (6.30)$$

In these expressions N_h and N_v represent the axial forces in the horizontal and vertical direction; M_h and M_v are the bending moments in the horizontal and the vertical plane containing the tunnel axis. Other terms appear in the Eqs. (23-26): \tilde{u}_h and \tilde{u}_v are the displacements at the tunnel depth, in the horizontal and vertical direction; c_{ta} , c_{tt} and c_{tv} are the transmission factors of displacements from the soil to the structure, in the axial and transversal components direction; finally c_{ja} , c_{jt} and c_{jv} are the modification factors due to the contours conditions of the longitudinal element.

The transmission factors are:

$$c_{ta} = \frac{1}{1 + \left(\frac{2\pi}{\lambda_a L'}\right)^2}; \lambda_a = \sqrt{\frac{K_a}{EA}}; L' = \sqrt{2}L \quad (6.31)$$

$$c_{tt} = \frac{1}{1 + \left(\frac{2\pi}{\lambda_h L}\right)^4}; \lambda_t = 4\sqrt{\frac{K_t}{EI_h}} \quad (6.32)$$

$$c_{tv} = \frac{1}{1 + \left(\frac{2\pi}{\lambda_v L}\right)^4}; \lambda_v = 4\sqrt{\frac{K_v}{EI_v}} \quad (6.33)$$

where K are the spring stiffness in which the soil is modelled. The axial force (6.27) and the bending moment (6.29) expressions, combined with static loads, are used in the design of the underground Japanese structures.

iii. Beam-springs model - Yu et al. 2016

Yu et al. 2016 proposed a new analytical solution for dynamic response of long lined tunnels subjected to travelling loads taking into account both the inerzia forces and the soil-structure interaction.

Figure 6.5 shows the idealization of the problem: the long lined tunnel is assumed to be infinitely long with a uniform cross-section and to behave as linear elastic. A constant stiffness EI and mass per unit length ρA is considered, where E is the Young's modulus of elasticity, I the moment of inertia of the tunnel cross section, ρ the density of the tunnel liner, A the area of cross section of the tunnel. The tunnel is supported by a viscoelastic foundation with constant spring stiffness K and viscous damping C per unit length.

The surrounding soil medium is assumed to be isotropic and homogeneous and to behave as viscoelastic; the travelling loads are assumed to be plane harmonic loads and propagate parallel to tunnel axis.

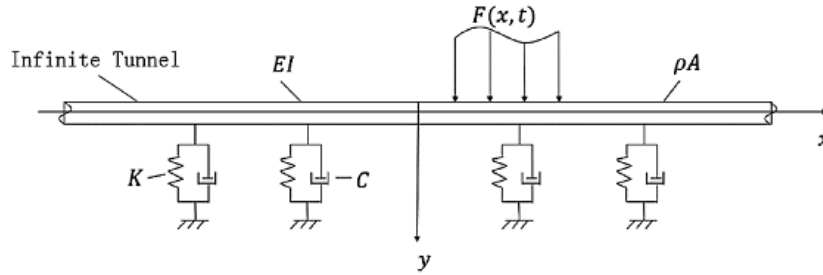


Figure 6.5. Long lined tunnel on a viscoelastic foundation subjected to travelling loads (Yu H. et al. 2016).

Defining $y(x, t)$ as the vertical deflection of the tunnel and $F(x, t)$ as the plane harmonic travelling loads, the wave-passage loads can be expressed as:

$$F(x, t) = \begin{cases} 0 & \text{for } x > Vt \\ P \sin \left[2\pi \Omega \left(t - \frac{x}{V} \right) \right] & \text{for } x \leq Vt \end{cases} \quad (6.34)$$

where V , Ω and P are the wave velocity, the frequency and amplitude of the loads, respectively.

The tunnel structure is assumed to behave linear elastically and deform only due to the normal travelling loadings perpendicular to the tunnel axis (deformations of the tunnel structure due to axial forces are neglected); the tunnel is assumed to behave as an Euler-Bernoulli beam.

The governing equation of the tunnel with constant cross section resting on a viscoelastic foundation subjected to travelling loads is given by the following linear partial differential equation:

$$EI \frac{\partial^4 y(x,t)}{\partial x^4} + \rho A \frac{\partial^2 y(x,t)}{\partial t^2} + C \frac{\partial y(x,t)}{\partial t} + Ky(x,t) = F(x,t) \quad (6.35)$$

assuming as boundary conditions the following ones:

$$\blacksquare \text{ Initial boundary condition : } y(x,t)_{t=0} = 0; \quad \left(\frac{\partial y(x,t)}{\partial t} \right)_{t=0} = 0 \quad (6.36)$$

$$\blacksquare \text{ Infinite boundary condition: } \lim_{x \rightarrow \pm\infty} \frac{\partial^n y(x,t)}{\partial x^n} = 0 \quad (n = 0,1,2,3) \quad (6.37)$$

To obtain the analytical solution of the problem, the Fourier transform is used to simplify the governing equation of the tunnel in space domain, whereas the Laplace transform is employed to reduce the equation in time domain. The governing equation of the tunnel based on the integration transform, therefore, is changed to an algebraic equation so that the solution can be conveniently given in the frequency domain. Finally, the convolution theorem is employed to convert the solution into the time domain.

Equation 6.38 is the integral representation of the displacement response of the long lined tunnel on the viscoelastic foundation subjected to travelling loads.

$$y(x,t) = \frac{P}{\pi \rho A} \int_0^{+\infty} \int_0^t \int_0^{V_s} \left\{ \frac{\cos[u(r-x)]}{\beta(u)} \sin \left[2\pi \Omega \left(s - \frac{r}{V} \right) \right] e^{-\alpha(t-s)} \sin[\beta(u)(t-s)] \right\} dr ds du \quad (6.38)$$

The velocity $v(x,t)$ and acceleration $a(x,t)$ responses of the tunnel structure can be obtained as the first and second derivatives of displacement response with respect to time domain:

$$v(x,t) = \frac{P}{\pi \rho A} \int_0^{+\infty} \int_0^t \int_0^{V_s} \left\{ \frac{\cos[u(r-x)]}{\beta(u)} \sin \left[2\pi \Omega \left(s - \frac{r}{V} \right) \right] e^{-\alpha(t-s)} \{ -\alpha \sin[\beta(u)(t-s)] + \beta(u) \cos[\beta(u)(t-s)] \} \right\} dr ds du \quad (6.39)$$

$$a(x,t) = \frac{P}{\pi \rho A} \left\{ \int_0^{+\infty} \int_0^t \int_0^{V_s} \left\{ \frac{\cos[u(r-x)]}{\beta(u)} \sin \left[2\pi \Omega \left(s - \frac{r}{V} \right) \right] e^{-\alpha(t-s)} \{ [\alpha^2 - \beta^2(u)] \sin[\beta(u)(t-s)] - 2\alpha\beta(u) \cos[\beta(u)(t-s)] \} \right\} dr ds du + \int_0^{+\infty} \int_0^{V_t} \cos \left[u(r-x) \right] \sin \left[2\pi \Omega \left(t - \frac{r}{V} \right) \right] dr du \right\} \quad (6.40)$$

Analytical solutions for the bending moment $M(x,t)$ and shear force $Q(x,t)$ response of the tunnel can be acquired as the second and third derivatives of displacement response with respect to space domain x , and each multiplied by a coefficient $(-EI)$.

$$M(x,t) = \frac{PEI}{\pi \rho A} \int_0^{+\infty} \int_0^t \int_0^{V_s} \left\{ \frac{u^2 \cos[u(r-x)]}{\beta(u)} \sin \left[2\pi \Omega \left(s - \frac{r}{V} \right) \right] e^{-\alpha(t-s)} \sin[\beta(u)(t-s)] \right\} dr ds du \quad (6.41)$$

$$Q(x,t) = \frac{PEI}{\pi \rho A} \int_0^{+\infty} \int_0^t \int_0^{V_s} \left\{ \frac{u^3 \sin[u(r-x)]}{\beta(u)} \sin \left[2\pi \Omega \left(s - \frac{r}{V} \right) \right] e^{-\alpha(t-s)} \sin[\beta(u)(t-s)] \right\} dr ds du \quad (6.42)$$

The equation 6.38 is deduced assuming $C^2 \leq 4K\rho A$. When $C^2 \geq 4K\rho A$, the equation 6.38 becomes as follows (Equation 6.43) and the analytical solution for velocity, bending moment and shear forces derived from this.

$$y(x, t) = \frac{P}{\pi\rho A} \int_0^{u_0} \int_0^t \int_0^{V_s} \left\{ \frac{\cos[u(r-x)]}{\beta_0(u)} \sin \left[2\pi\Omega \left(s - \frac{r}{V} \right) \right] e^{-\alpha(t-s)} \sin[\beta_0(u)(t-s)] \right\} dr ds du + \frac{P}{\pi\rho A} \int_0^{+\infty} \int_0^t \int_0^{V_s} \left\{ \frac{\cos[u(r-x)]}{\beta(u)} \sin \left[2\pi\Omega \left(s - \frac{r}{V} \right) \right] e^{-\alpha(t-s)} \sin[\beta(u)(t-s)] \right\} dr ds du \quad (6.43)$$

where:

$$u_0 = \sqrt[4]{\frac{1}{EI} \left(\frac{C^2}{4\rho A} - K \right)}; \quad \beta_0(u) = \sqrt{-\frac{EI}{\rho A} u^4 - \frac{K}{\rho A} + \frac{C^2}{4(\rho A)^2}} \quad (6.44)$$

iv. Mass beam springs model - Kiyomiya O. 1995

The mass-beam-springs model is the earthquake resistant design method developed in Japan for the immersed tunnel (Kiyomiya O. 1995), based on the modal response of a linear system. One-dimensional seismic response analysis of soil is used to solve the problem of horizontal shear waves (SH waves) vertically propagating through a horizontally layered soil deposit from an underlying bedrock. With respect to linearly viscoelastic problem, the soil of each layer is assumed to behave as a Kelvin-Voigt solid which is represented by a constant elastic spring and a viscous damper in parallel. In this way, the wave equation is formulated to account for the properties of both elasticity and viscosity.

Figure 6.6 shows the scheme of the idealized model. The surface layer is divided into a number of slices, perpendicular to the tunnel axis. Each slice is represented by an equivalent mass-spring system. The SDOF system consists of a mass representing the mass of a slice, a spring and a dashpot connecting the mass to the base rock. The model is on the basis of the assumption that the ground displacement is dominated by the fundamental shearing vibration.

Overall, the modal response of a linear system is essentially dependent on its modal properties, such as natural frequencies, mode shapes, modal participation factors and modal damping ratios etc. In the equivalent SDOF system, three modal properties, i.e. (1) the natural frequency, (2) modal effective mass and (3) modal damping ratio, are used to evaluate the mass, spring and dashpot constants of the system.

Note that the only mass of the equivalent SDOF system is actually located at the first modal effective height of the real system.

The spring constant of K_3 is determined so that the natural period of the system coincides with the natural period of the first mode of shear vibration of the slice. The model does not consider that the natural period of vibration of the ground is influenced by the presence of the tunnel. The neighboring masses are connected to one another along the tunnel axis by springs and dashpots. The spring constant of K_2 is related to the push-pull resistance to the axial relative displacement between adjacent ground slices or the shear resistance to the lateral relative displacement.

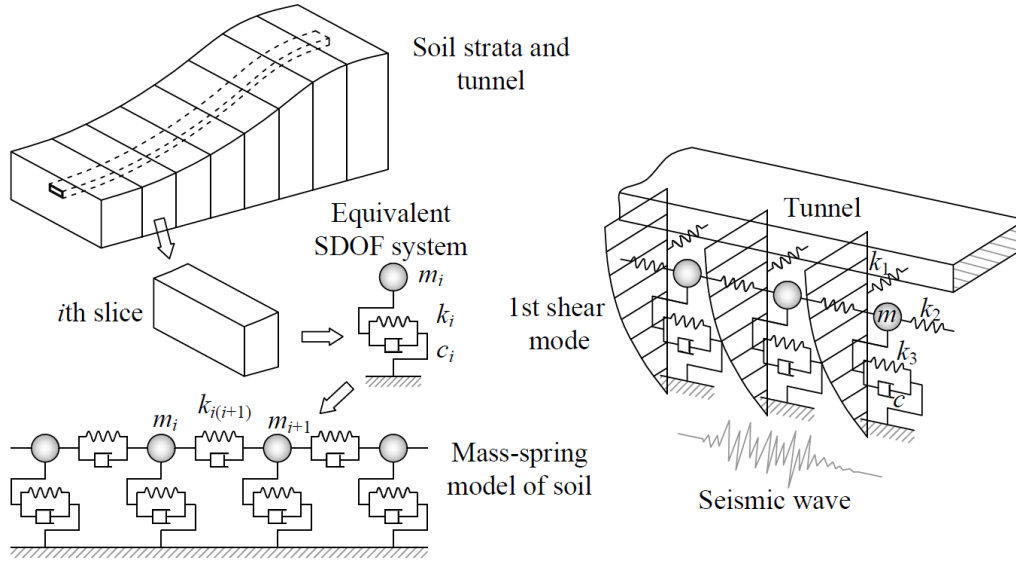


Figure 6.6. Scheme of masses-beam-springs-model (Kiyomiya 1995).

The tunnel is assumed to be an elastic beam supported by elastic or inelastic springs K_1 representing soil rigidity. One end of each spring is considered to displace the same as the displacement of the ground calculated by the total model of the surface layer. In this way, the seismic response of the tunnel can be calculated.

Figure 6.7 shows in more detail the springs K_2 (Figure 6.7a) related the axial deformation between adjacent cross section, and K_1 (Figure 6.7b) related the shear deformation of the ground between adjacent cross section.

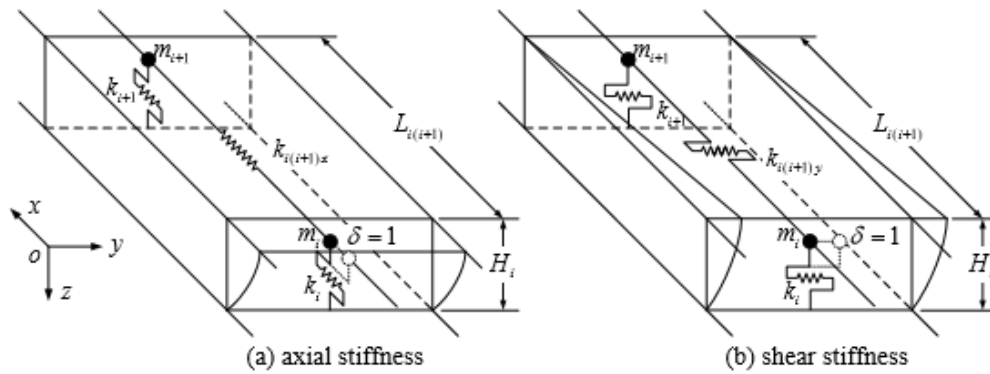


Figure 6.7. Axial and shear springs in masses-beam-springs-model (Li C. 2016).

The response of the surface layer can be calculated by the following equation:

$$[M]\{\ddot{x}\} + [C]\{\dot{x}\} + [K]\{x\} = -[M]\{\ddot{e}\} \quad (6.45)$$

where:

$[M]\{\ddot{x}\}$ is the mass matrix multiplied the accelerations vector;

$[C]\{\dot{x}\}$ is the damping matrix by K_1 and K_2 multiplied the velocities vector;

$[K]\{x\}$ is the rigid matrix multiplied the displacements vector;

$[M]\{\ddot{e}\}$ is the mass matrix multiplied the input acceleration vector.

Seismic waves are applied at the base of the model and the response displacement of each mass is calculated. The displacement of the ground and at the position of the tunnel are obtained multiplying the displacements of the mass for the respective participation factors for the fundamental vibration mode.

v. Multi masses beam springs model - Li C. et al. 2017

The model represents an evolution of the masses-beam-springs model, performing one-dimensional ground seismic analysis with an equivalent MDOF system. Unlike the equivalent SDOF system, the MDOF proposed model is based on four modal properties, i.e. (1) the natural frequency, (2) modal effective mass, (3) modal effective height and (4) modal damping ratio:

- (1) Natural frequency of the equivalent MDOF system for each mode coincides with that of the corresponding vibration mode of the soil deposit.
- (2) Modal effective mass of the equivalent MDOF system for each mode equals to that obtained from corresponding vibration mode of the soil deposit.
- (3) Modal effective heights of the equivalent MDOF system are consistent with the counterparts of the soil deposit.
- (4) The equivalent MDOF system and the actual soil deposit have identical modal damping ratio for each mode.

Figure 6.8 shows the MDOF discretization of a horizontally layered deposit. The configuration of dashpots in Figure 6.8b makes the damping property of the whole system viscous while the configuration in Figure 6.8c, proposed by the authors, is hysteretic.

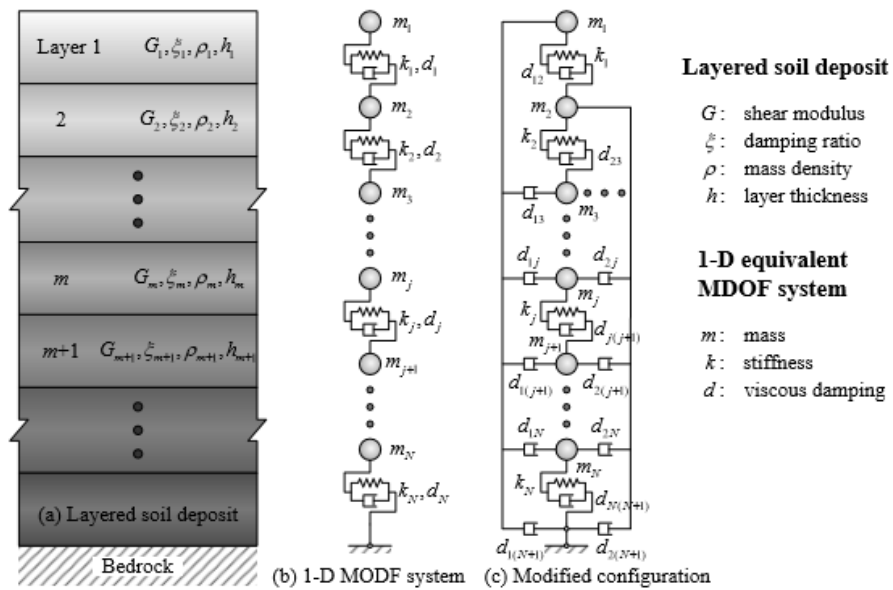


Figure 6.8. Horizontally layered soil deposit on rigid bedrock and the corresponding one-dimensional (1-D) equivalent MDOF system (Li C. et al. 2017).

The physical parameters of the modal problem are represented with the follow constants of the equivalent MDOF system.

The mass and spring constants, for instance, are:

$$m_j = \frac{\Theta_{j-1}^2}{\Psi_{j-1} \Psi_j} \quad k_j = \frac{\Theta_{j-1} \Theta_j}{\Psi_j^2} \quad (6.46)$$

Where:

$$\Theta_j = \sum_{l=1}^{C_{N-j}^{N-j}} \left(\prod_{n \in S_l^{(N-j)}} M_n^e \omega_n^2 \right) \left(\prod_{m < n \in S_l^{(N-j)}} (\omega_m^2 - \omega_n^2)^2 \right) \quad (6.47)$$

$$\Psi_j = \sum_{l=1}^{C_{N-j}^{N-j}} \left(\prod_{n \in S_l^{(N-j)}} M_n^e \omega_n^4 \right) \left(\prod_{m < n \in S_l^{(N-j)}} (\omega_m^2 - \omega_n^2)^2 \right) \quad (6.48)$$

ω_n and M_n are the n -th natural frequency and the n -th modal effective mass of 1-D soil column respectively; $S_l^{(N-j)}$ is the l -th number set formed by arbitrarily selecting $N-j$ numbers from the set of integers from 1 to N , $l=1,2,\dots,C_N^{N-1}$; C_N^{N-1} is the number of combinations of selecting $N-j$ numbers from N numbers; $j=1,2,\dots,N$; $\Theta_j = \Psi_j = 1$.

The dashpot constants of the equivalent MDOF system are determined as:

$$d_{jk} = -m_j m_k \sum_{n=1}^N \frac{2\xi_n \omega_n \Gamma_n^2}{M_n^e} \varphi_{jn} \varphi_{kn} \quad d_{j(N+1)} = \sum_{k=1}^N \left(m_j m_k \sum_{n=1}^N \frac{2\xi_n \omega_n \Gamma_n^2}{M_n^e} \varphi_{jn} \varphi_{kn} \right) \quad (6.49)$$

where d_{jk} represents the dashpot between every two m_j and m_k , and $d_{j(N+1)}$ is the dashpot between each mass m_j and the base.

The height for mode n of one-dimensional MDOF system associated with horizontal shear vibration is defined as:

$$h_j = \sum_{n=1}^N \varphi_{jn} \Gamma_n h_n^e \quad (6.50)$$

Where:

Γ_n is the modal participation factor expressed as

$$\Gamma_n = \prod_{m=1, m \neq n}^N \frac{\omega_m^2}{\omega_m^2 - \omega_n^2} \quad (6.51)$$

φ_{jn} is the n -th mode shape of the j th mass of the equivalent MDOF system and h_n^e is the n -th modal effective height of 1-D soil column expressed as

$$h_n^e = \frac{\sum_{j=1}^N h_j m_j \varphi_{jn}}{\sum_{j=1}^N m_j \varphi_{jn}} \quad (6.51)$$

where h_j is the height of the j -th mass over the base.

Figure 6.9 shows the normalized heights of masses in the equivalent MDOF system for a homogeneous soil layer calibrated by the authors; it should be noted how the height of the mass corresponding to the SDOF system is the is that assumed in the masses-beam-springs-model (Kiyomiya 1995).

By expanding the methodology of mode equivalence from one-dimensional into two-dimensional, a two-dimensional equivalent MDOF system is developed for two-dimensional ground response analysis, schematically represented in Figure 6.10.

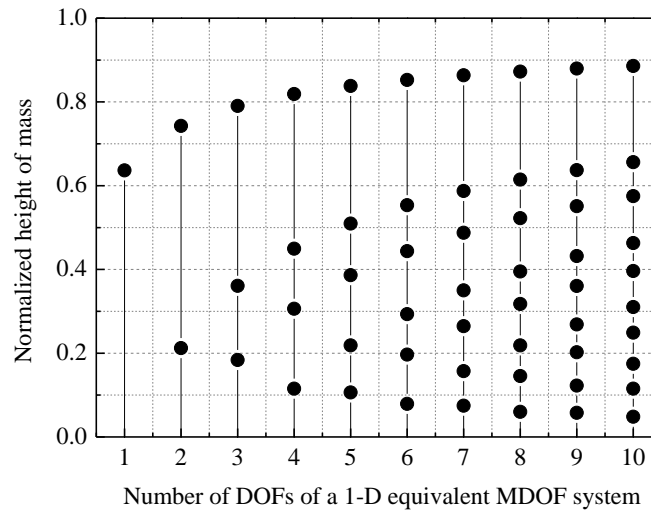


Figure 6.9. Normalized heights of masses in the equivalent MDOF system for a homogeneous soil layer (Li C. et al. 2017).

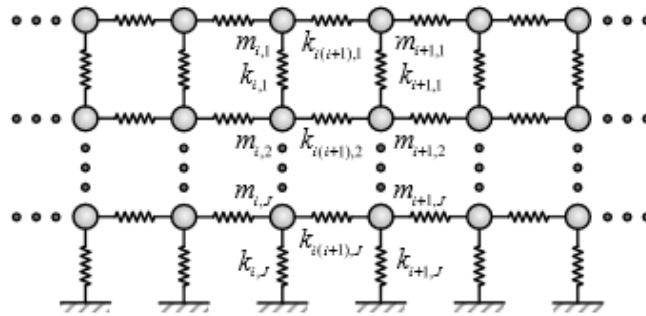


Figure 6.10. Scheme of 2D equivalent MDOF system (Li C. 2016).

6.1.2 Numerical solutions

1. Pseudo-static 3D numerical analysis, Park et al. 2009

Park et al. 2009 proposed a new procedure for simulating the tunnel response under spatial varying ground motion using the longitudinal displacement profile to perform pseudo-static 3D FEM analysis.

Starting from the definition of the coherency function which describes the spatial variability of the ground motion in correlation of the amplitude and the phase angles of two ground motion time histories $u_j(t)$ and $u_k(t)$

$$\gamma_{jk}(\omega) = \frac{S_{jk}(\omega)}{\sqrt{S_{jj}(\omega)S_{kk}(\omega)}} \quad (6.52)$$

where ω is the circular frequency, $S_{jk}(\omega)$ is the cross-power spectrum of the motion $u_j(t)$, $S_{jj}(\omega)$ and $S_{kk}(\omega)$ the auto-power spectrum of the motion $u_j(t)$ and $u_k(t)$ respectively, different empirical and semi-empirical function have been proposed in literature to characterize the spatial variation of the ground motion. Figure 6.11 shows some empirical coherency functions function of the level of frequency and the separation distance.

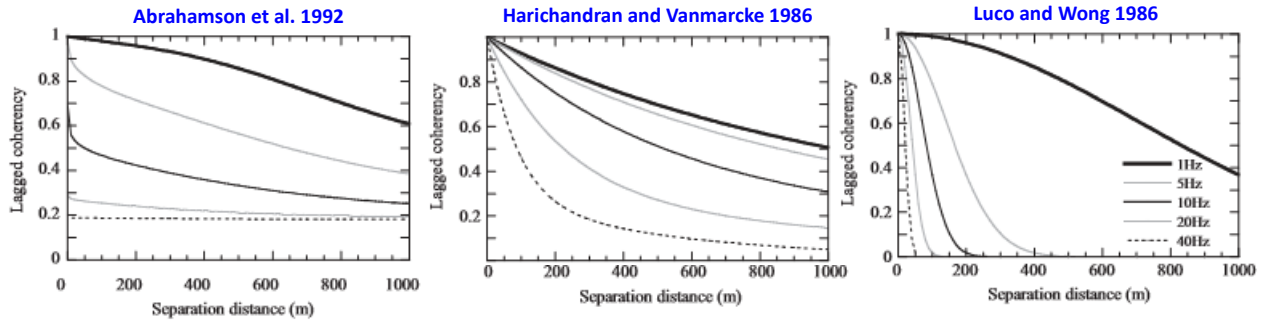


Figure 6.11. Empirical coherency functions (after Park et al. 2009).

The coherency function and the procedure proposed by Abrahamson et al. 1992 has been adopted by the authors to generate the pseudo-static displacement profile. It comes to generate displacements time history of a selected earthquake starting from the acceleration time history, base line corrected before, in such reference point along the tunnel axis. Figure 6.12 shows the geometry of the studied problem, it is a tunnel 1000m long with a diameter of 10m and the reference points are at 300m 600m and 1000m.

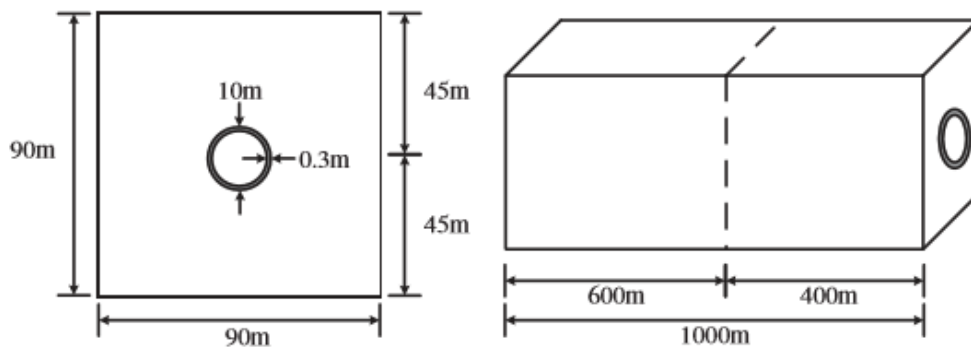


Figure 6.12. Geometry of the problem (Park et al. 2009).

The reference and calculated ground motion displacements time histories in correspondence of the reference points are shown in Figure 6.13a. This displacements times histories are used to characterized the ground deformation shape in longitudinal direction linking the displacements in the reference nodes along the tunnel axis in each time step of the ground motion. Figure 6.13b shows the longitudinal displacements profiles along the structure at different time step.

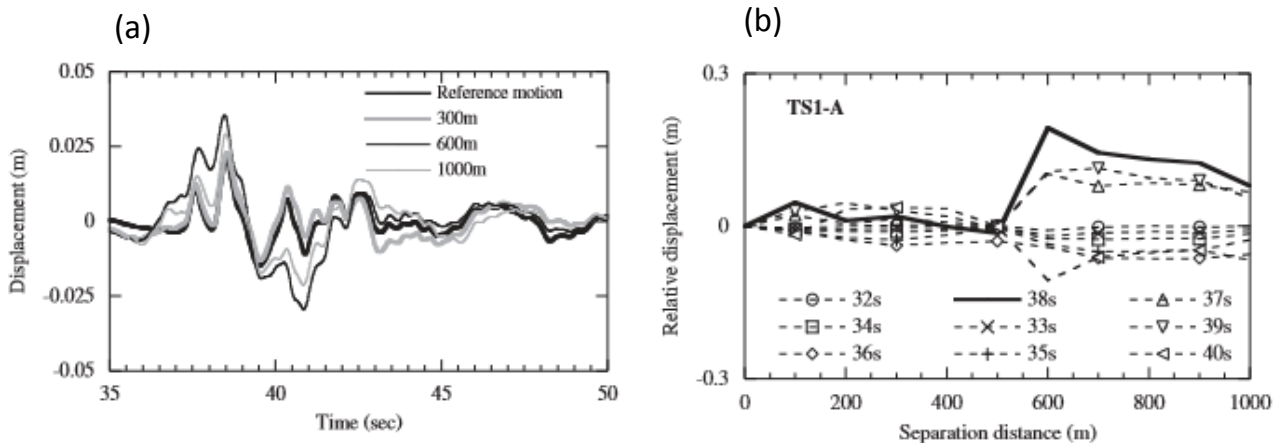


Figure 6.13. (a) Reference and calculated ground motion displacements time histories in correspondence of the reference points 300m, 600 and 1000m; (b) Longitudinal displacements profiles along the structure at different time step (Park et al. 2009).

The selected ground motion is Kobe earthquake 1995. These displacements profiles refer to the ground surface so that, to obtain the same distribution at the tunnel depth, the generated motion need to be deconvolved to the bedrock and then propagated at the tunnel depth.

The ground profiles used in the analysis are shown in Figure 6.14 referring to three different soil types in the instant of time of maximum curvature. The ground is assumed to be both uniform (Figure 6.14a) and non uniform (Figure 6.14b) changing the soil properties from type 1 to 2 and from type 1 to 3, with the boundary between the two soil types as in Figure 6.12.

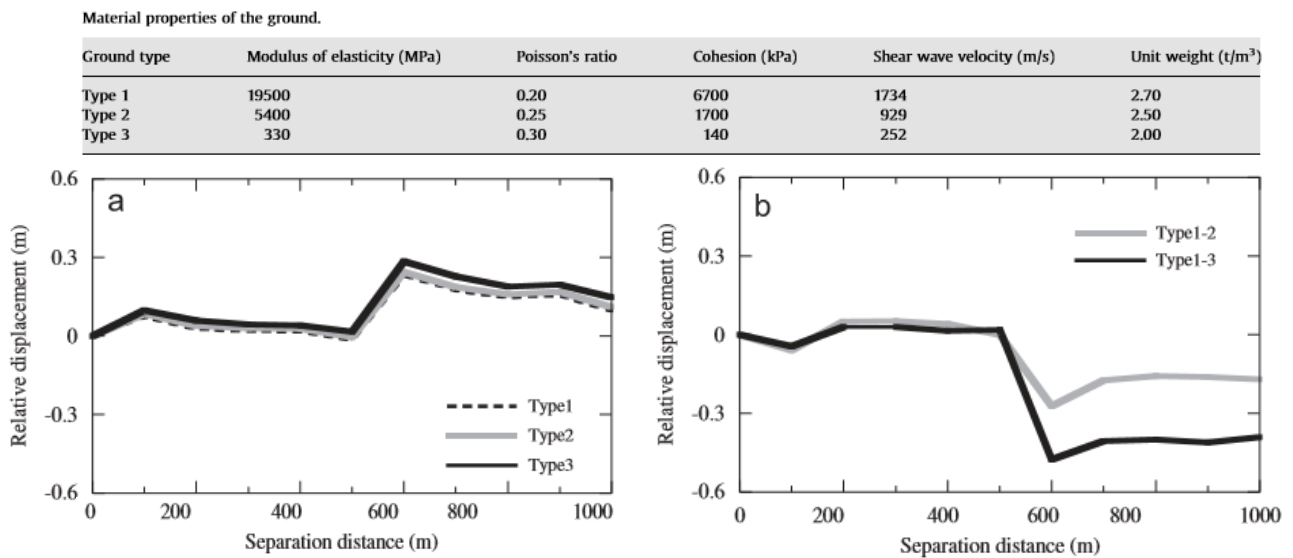


Figure 6.14. (a) Longitudinal displacements profile at the tunnel depth for uniform ground, soil types 1, 2 and 3; (b) longitudinal displacements profile at the tunnel depth for non uniform ground, soil types 1, 2 and 3; (Park et al. 2009).

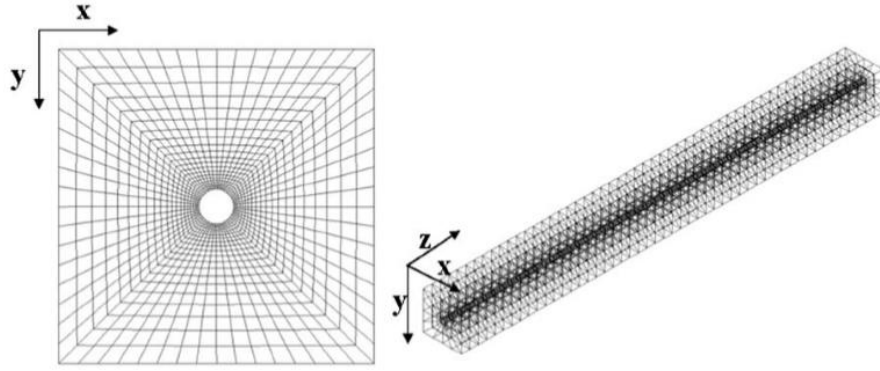


Figure 6.15. 3D numerical mesh for pseudo-static analysis (Park et al. 2009).

Pseudo-static analysis performed on the 3D numerical mesh shown in Figure 6.15 give the results in Figure 6.16 and 6.17 for uniform and non uniform ground profile respectively.

The results are shown in terms of σ_r , axial stress in the radial direction, M_r , bending moment in the radial direction, σ_H , axial stress in longitudinal direction, M_H , bending moment due to the curvature in the horizontal plane. The increment of the longitudinal stress σ_H is significant respect the radial one that is rather negligible; longitudinal and radial increment of bending moments are instead similar and low respect the stress component.

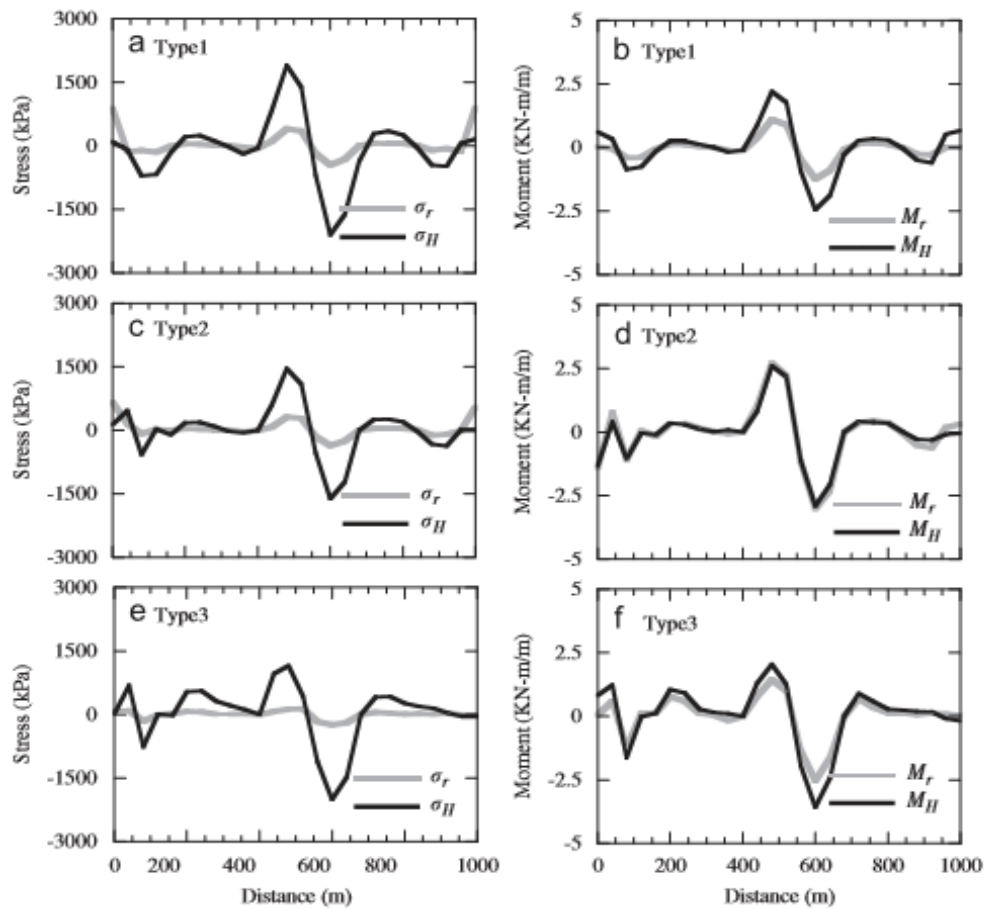


Figure 6.16. Calculated stresses and moments due to the spatially variable ground motion for uniform ground profile (Park et al. 2009).

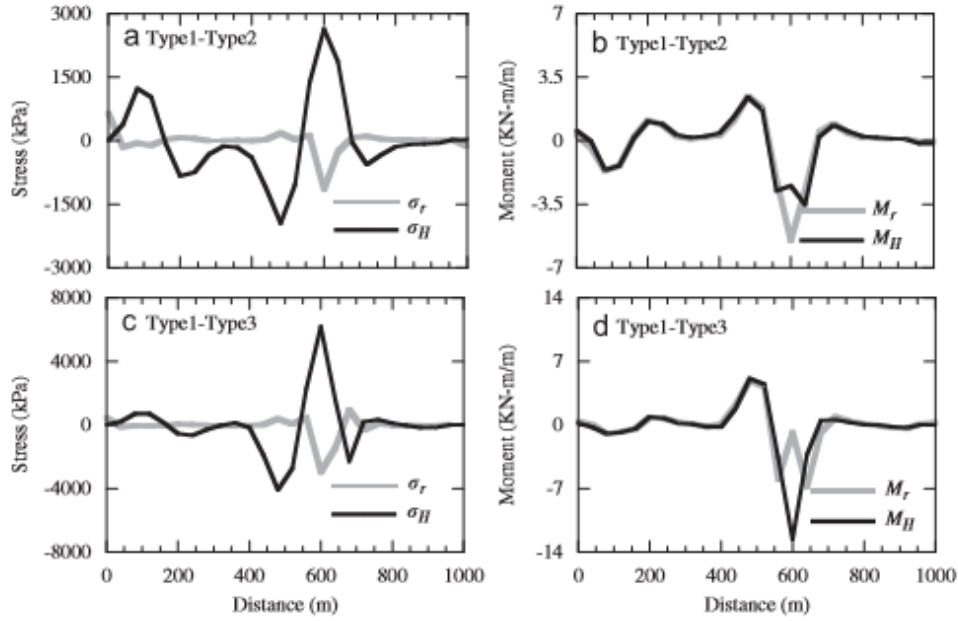


Figure 6.17. Calculated stresses and moments due to the spatially variable ground motion for non uniform ground profile (Park et al. 2009).

II. 3D multi-scale method, Yu H. et al. 2013

Although the current high performance of computers and their large mass storage capability allow to run large 3D FEM full dynamic analysis, the numerical model could be very expensive, if not impossible, to run if including structural details such as segmental lining, bolts, construction process, even with the most advanced supercomputer. Taking in mind this issue, multi-scale method are developed to provide an alternative method to overcome such difficulties. Coarse-scale mesh for instance, is adopted to model the seismic response of the full length of the tunnel subjected to different seismic loading, fine-scale mesh is adopted to include structural details, such as shafts, tunnel segments, joints and bolts, in the model.

The method consists of two steps of analysis: in the first step a regular coarse mesh model all the domain in order to determine the seismic response characteristic of the system and to identify the areas where refine mesh is needed; in the second step these last areas are replaced by a refined mesh and a new simulation with the coupled coarse and refined mesh is carried out. An overlapping domain between the coarse and refined mesh is needed to avoid that high frequency waves may reflected in correspondence of the coarse/refined mesh interface.

Figure 6.19 shows the coupled mesh where Ω_0^C is the coarse sub-domain, Ω_0^R is the refined subdomain and Ω_0^{int} the overlapping domain.

With reference to the studied case of the Qingcaosha water-conveyance double lines shield tunnel (Figure 6.19) in Shanghai, China, Figure 6.20 shows the coarse mesh adopted for the numerical 3D model while 6.21 shows the multi scale mesh adopted for the segmental tunnel lining.

Twenty two control sections were fixed along the tunnel (Figure 6.20a), nine section for the island section (D1→D9), eight for the cross river segment (G1→G8), five for the land segment (L1→L5).

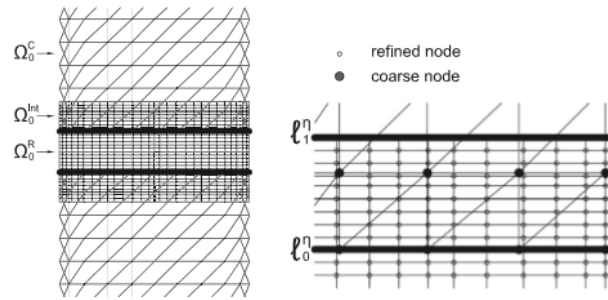


Figure 6.18 Coupled mesh scheme in the 3D multi scale method (Yu H. et al. 2013).

The results of the coarse model carried out for Shanghai earthquake under non uniform loading condition modelled offsetting the arrival time in each point along the longitudinal direction (see scheme in Figure 6.22), show a significant effect if comparing with the non uniform case. The time delay has been obtained assuming a shear wave velocity for the bedrock equal to 500m/s.

Figure 6.23 for instance, shows the time histories of the dynamic increments of transversal (Figure 6.23a) and longitudinal (Figure 6.23b) displacements in the case of uniform and non uniform seismic loading, referring to the G5 reference section. This last condition accounts higher value of displacements in both cases; similar results are shown in terms of maximum ovalization of the tunnel section (Figure 6.24).

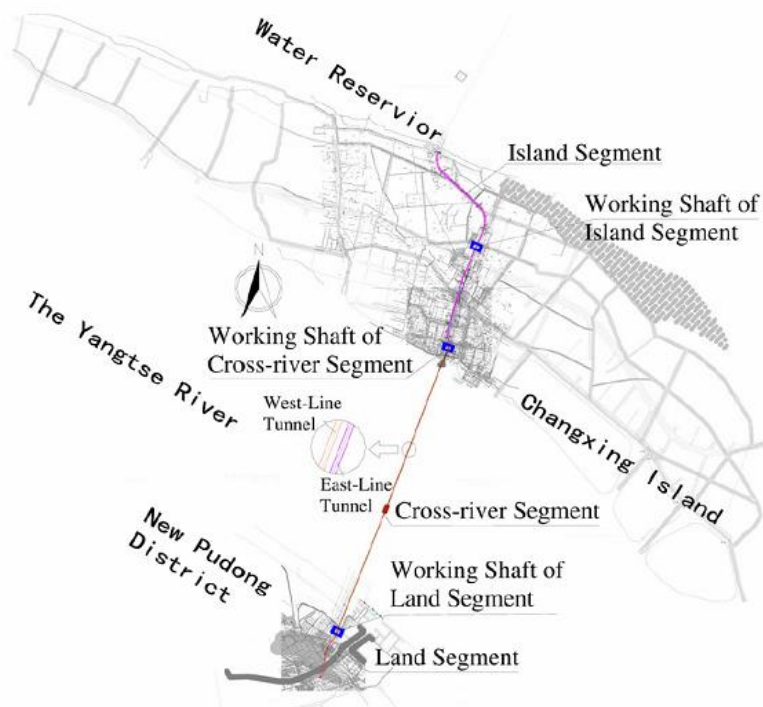


Figure 6.19. Map of Qingcaosha in Shanghai, China (Yu H. et al. 2013).

Very interesting are also the results obtained with the multi-scale coarse-refined mesh (Figure 6.21) to account some details of the structure. The multi scale model for instance, is able to catch for example the main deformation mechanism occurring in correspondence of the circumferential joints, schematically represented in figure 6.25.

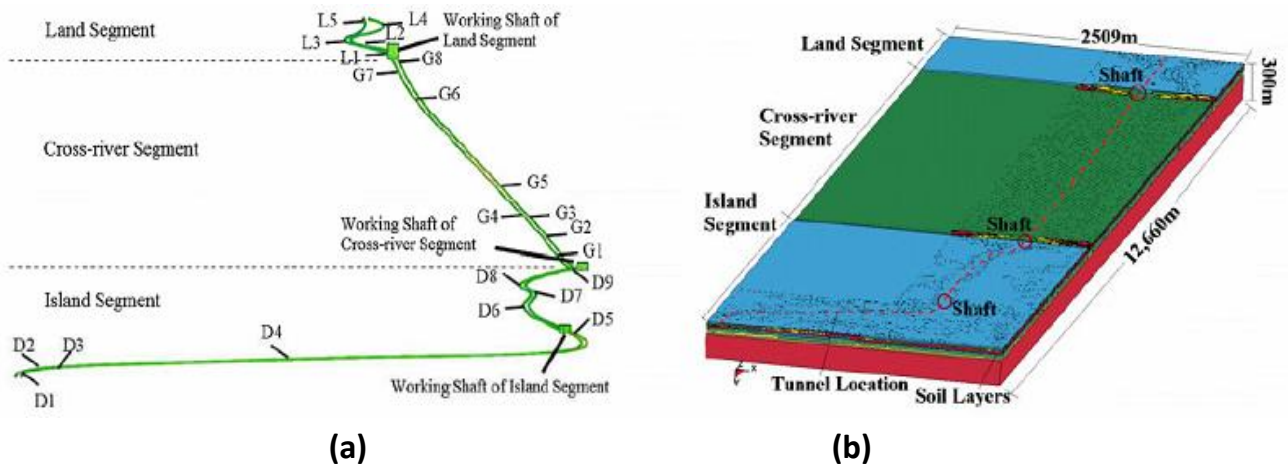


Figure 6.20. (a) Coarse scale tunnel model; (b) Coarse scale soil and tunnel model (Yu H. et al. 2013).

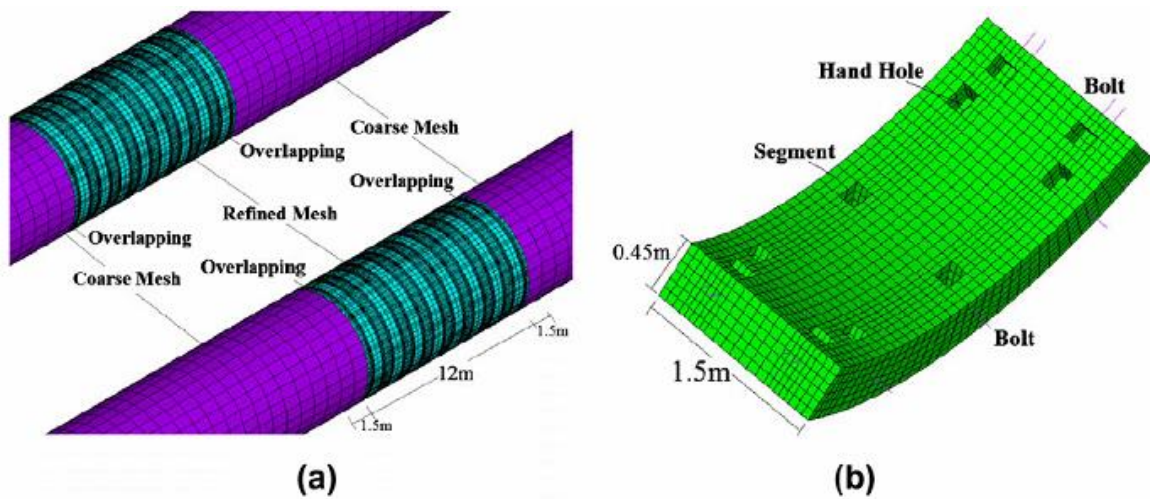


Figure 6.21. Mesh of multi scale tunnel model: coarse-refined mesh location; (b) detail of the segment mesh (Yu H. et al. 2013).

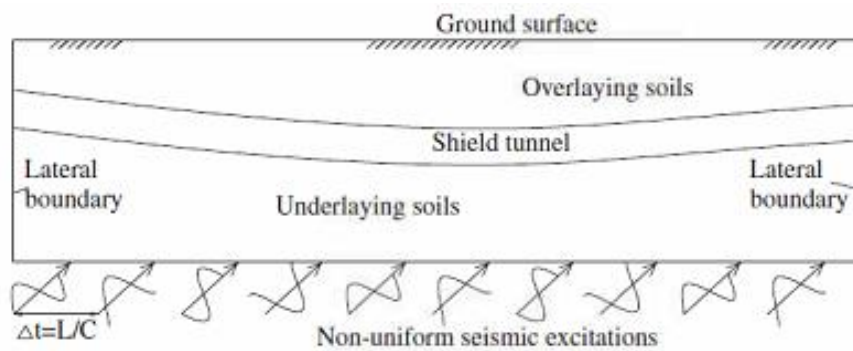


Figure 6.22. Non uniform seismic input mode (Yu H. et al. 2013).

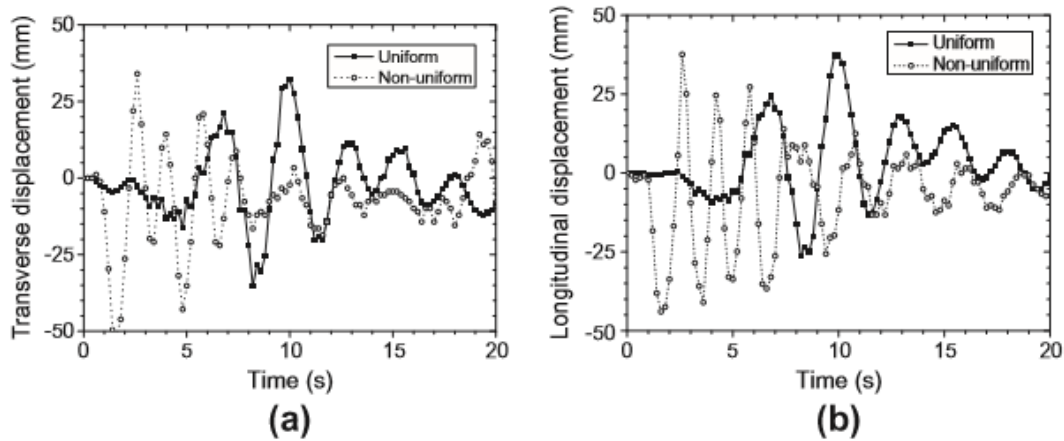


Figure 6.23. Time histories of the dynamic increment of transversal and longitudinal displacements in G5 section under uniform and not uniform shaking of Shanghai earthquake (Yu H. et al. 2013).

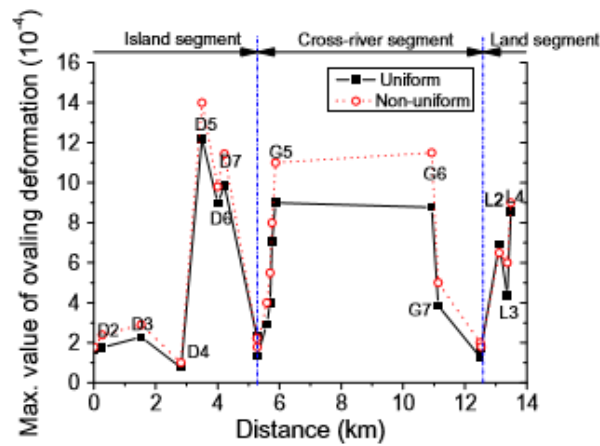


Figure 6.24. Maximum ovalization of tunnel in G5 section under uniform and not uniform shaking of Shanghai earthquake (Yu H. et al. 2013).

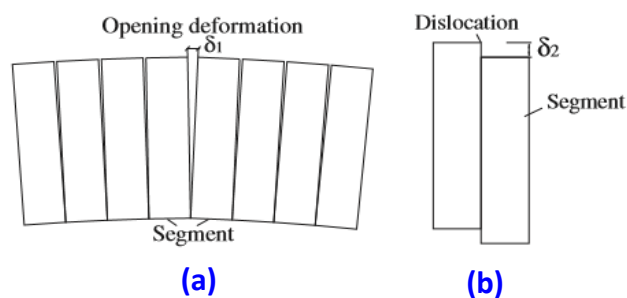


Figure 6.25. Deformation patterns of the circumferential joints: (a) joint opening; (b) joint dislocation (Yu H. et al. 2013).

Time histories of the circumferential joint opening and dislocation are shown in Figure 6.26a and Figure 6.26b respectively. The maximum value of joint opening is equal about to 2mm while the maximum value of joint dislocation is equal about to 2.5mm, with residual values lower than 1mm in both cases.

These values are not very high to think about failure problems of the joints, the authors in fact state that they are lower than allowable upper limits of the Chinese design code.

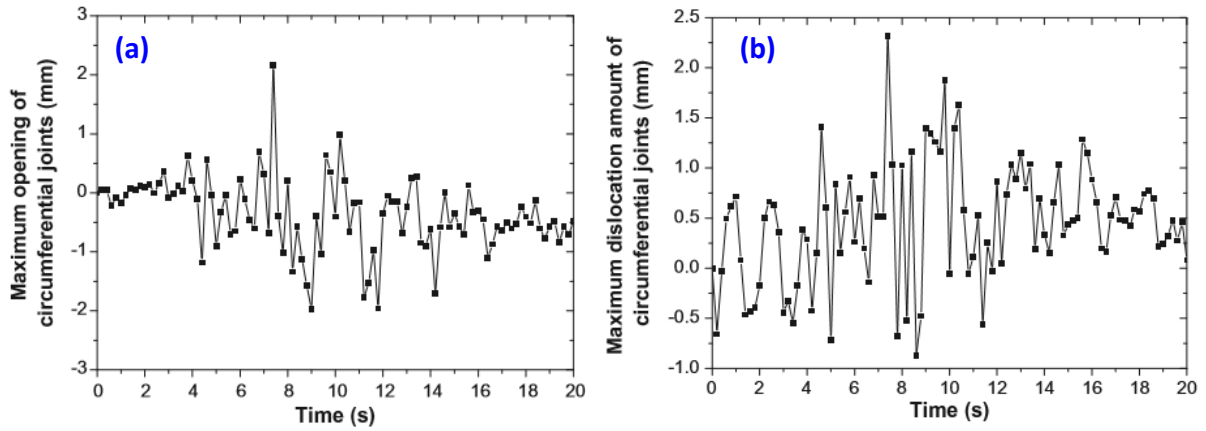


Figure 6.26 Time histories of circumferential joint (a) opening and (b) dislocation in correspondence of the section G5 (Yu H. et al. 2013).

This results refer to a low value of scaled PGA equal to 0.1g. Surely for higher values of PGA, the peak and permanent values of circumferential joints openings and dislocations can achieve values such as to compromise the water sealing in correspondence of the joint. It should be noted, in addition, that this results are relative to a seismic loading condition including a transversal and longitudinal uniform shaking; in a non uniform seismic loading condition in longitudinal direction, these values could undergo to an increasing in terms of peak and permanent values.

III. 3D full dynamic analysis, Li & Song 2014

A 3D numerical procedure has been proposed by Li & Song 2014 to study the problem of the asynchronous seismic motion along the tunnel axis under the hypothesis of rigid bedrock and the oblique seismic incidence of body waves, a likely condition in near field problems where the incident direction is not vertical because the waves don't experience enough refraction during propagation.

Figure 6.27a for instance, shows the scheme of the problem: the waves is oblique respect the vertical direction with the angle θ and has an incident angle φ respect the tunnel axis.

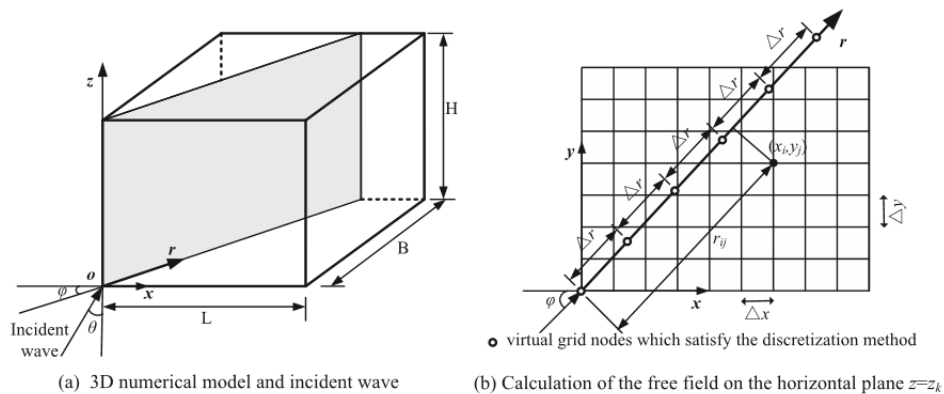


Figure 6.27. Statement of the problem (Li & Song 2014).

The proposed procedure, schematically shown in Figure 6.28, starts with the computation of the free field wave motion by compiling a FORTRAN compiler combined with the finite element software ANSYS 3D. By solving 1D equations obtaining the displacements of the nodes in each vertical, the 1D response analysis is extended to the 3D case. The finite element discretization scheme is shown in Figure 6.27b: the horizontal plane is discretized into a rectangular grid $\Delta y \times \Delta x$ while the grid points along the incidence plane are spaced of $\Delta r = c_r * \Delta t$, where c_r is the horizontal apparent velocity of the incidence wave ($c_r = c/\sin\theta$) and Δt is the time step chosen to satisfy the stability condition of the central difference method and given by

- $\Delta t \leq \Delta z/c_p \rightarrow$ for P and SV oblique incidence problem,
- $\Delta t \leq \Delta z/c_s \rightarrow$ for SH oblique incidence problem.

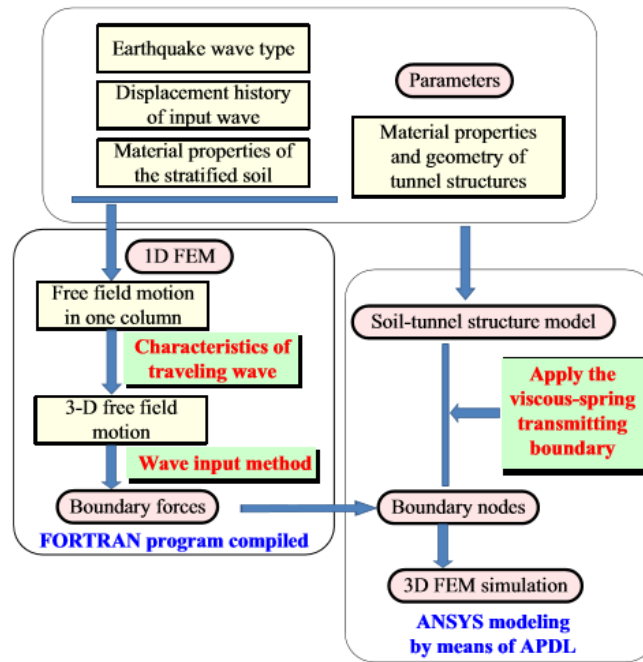


Figure 6.28. Statement of the problem (Li & Song 2014).

A soil-structure interaction analysis has been carried out assuming the 3D mesh in Figure 6.29b and the Dirac impulse with θ angle equal to 45° and ϕ angle equal to 30° (Figure 6.29a).

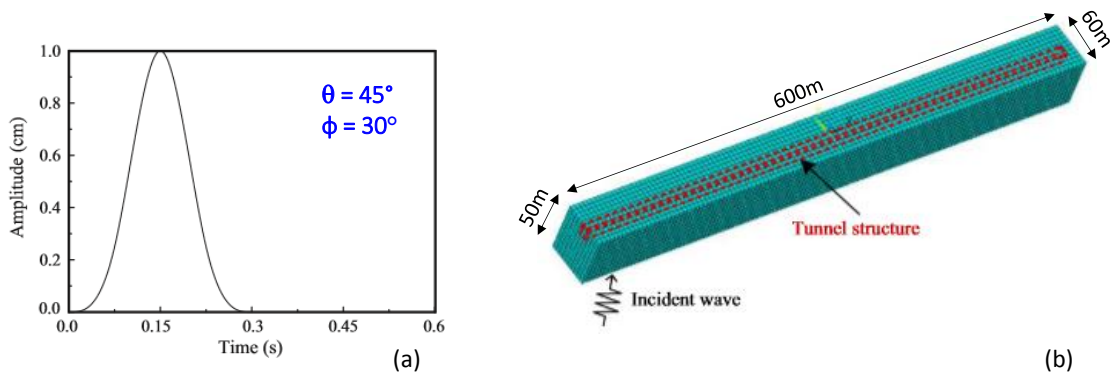


Figure 6.29. (a) Dirac input displacement; (b) stretch of the 3D numerical mesh (Li & Song 2014).

The effect of the Dirac impulse passage along the tunnel is evaluated in terms of soil and structure displacements (Figure 6.30) and induced forces in the structure (Figure 6.31).

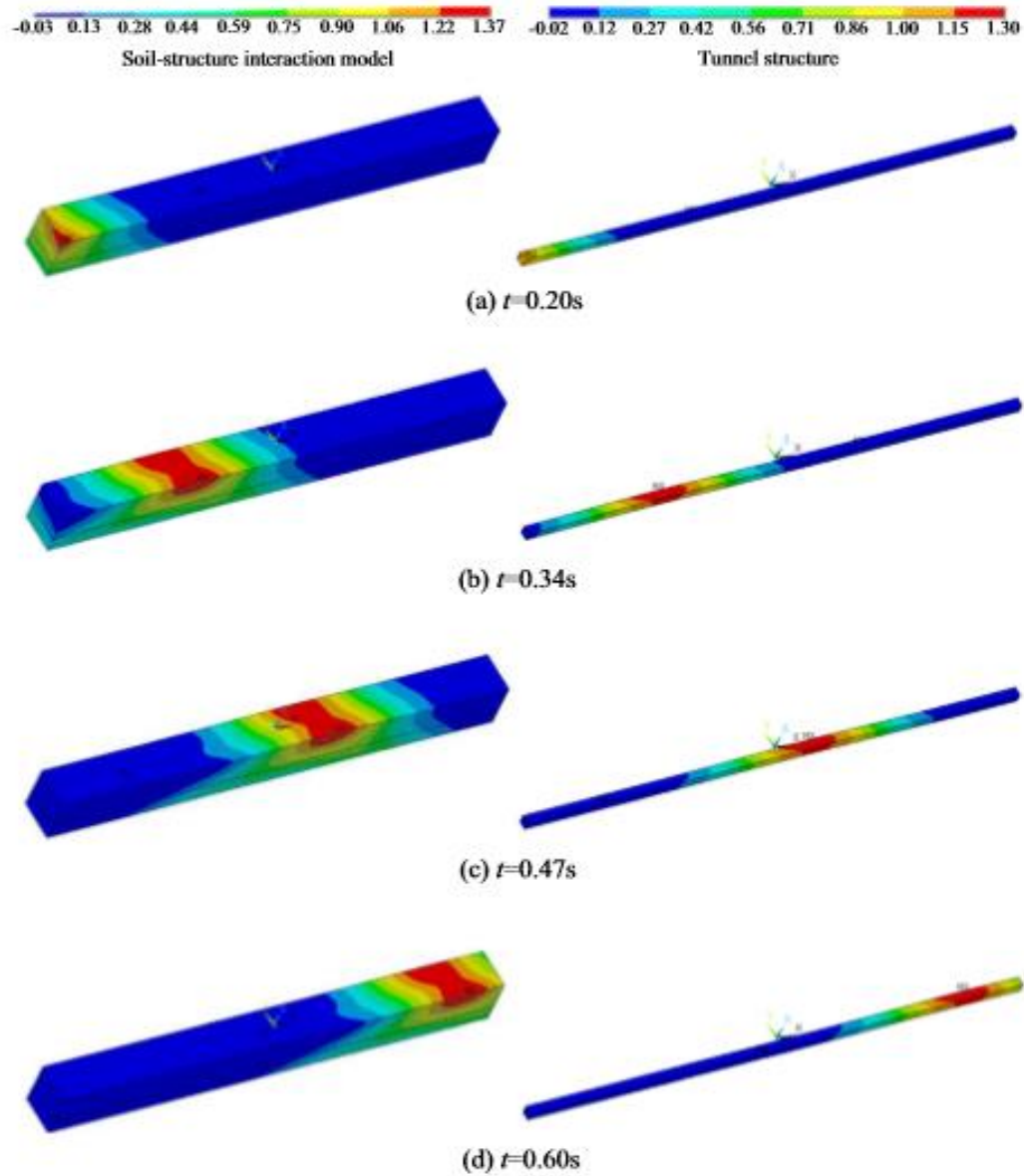


Figure 6.30. Soil and structure displacements during Dirac impulse passage along the tunnel (Li & Song 2014).

In Figure 6.30 the effect of the wave passage is clear: the tunnel is subjected to the same deformation mechanism along the length in different instants of time, the same happens in terms of internal forces.

Figure 6.31 for instance, shows the time history of the longitudinal axial Force F_x , shear force F_z and the bending moment in the horizontal plane M_z , each of which is characterized by the same amplitude in with a time delay along the tunnel axis.

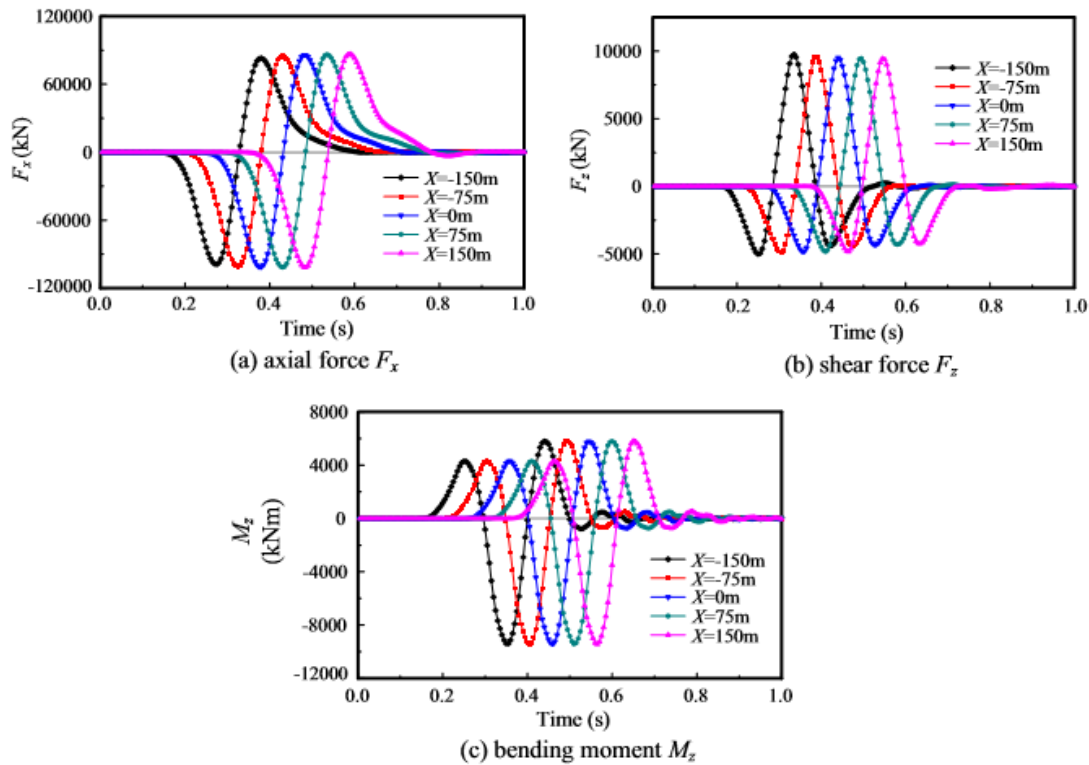


Figure 6.31. Time histories of tunnel lining internal forces at different point along the tunnel axis during Dirac impulse passage (Li & Song 2014).

6.2 Numerical analysis

A three dimensional numerical model able to catch the main deformation mechanisms of the soil subjected to multi-directional seismic motion, has been proposed.

It has been developed in the FE code Plaxis 3D. The free field soil response under travelling waves has been compared with the results obtained on the same model developed in Abaqus 3D.

Once validated the free-field numerical model, the soil structure interaction has been investigated with a set of parametrical analyses varying longitudinal time-lag of the travelling wave in terms of dynamic increment of transversal and longitudinal internal forces arising in the lining. A comparison between uniform and non uniform seismic load is shown for different seismic loading cases.

A simplified 2D multi-masses-beam-springs model developed by Li Chong 2016 has been implemented in Abaqus 2D in order to compare the longitudinal component of dynamic increment of internal forces evaluated with two and three dimensional numerical method.

6.2.1 3D full dynamic analysis: Free-field condition

The effect of travelling waves along the longitudinal direction is here dealt assuming that the input wave propagates vertically from a rigid bedrock to the ground surface. The asynchronous of the seismic motion is induced by a seismic wave shaking perpendicular to the tunnel axis and propagating longitudinally at the same time.

This is an 'ideal' condition that may occur in far field seismic problems when the wave arrives perpendicularly at the ground surface and the wave front is transversal with respect to the tunnel axis.

Under these hypotheses, a three dimensional FE model has been developed in Plaxis 3D to investigate firstly the free field soil response under asynchronous seismic motion and compared with the results obtained on the same model developed in Abaqus 3D

Figure 6.32 for instance, shows the geometric scheme adopted in Plaxis 3D and Abaqus 3D codes. The soil domain has a depth H of 60m, where is located the rigid bedrock, a width B of 200m and a length Y of 400m.

The soil is assumed to behave elastically and Table 6.1 resumes the main soil elastic parameters. The soil and bedrock velocities in particular are assumed equal to 250m/s and 800m/s respectively. The bedrock velocity for instance, has been used to determine the time delay (time lag) of the wave along the longitudinal direction. The selected input motion is a harmonic single-oscillation wave with an amplitude of 0.1g and a frequency equal to 4Hz (Figure 6.33).

The asynchronous of the seismic motion has been simulated assigning to the bedrock the same harmonic input offsetting along the longitudinal direction of the calculated time lag.

In Plaxis code the time history of the input acceleration signal (or velocity or displacement) is usually assigned to a surface displacement that modelled the rigid bedrock while in Abaqus the input is assigned to each node of the surface bedrock.

In Plaxis code, the bedrock surface has been divided into a number of surfaces displacement, 16 surfaces with a depth y_i equal to 25m, and to each displacement surface has been set the harmonic input with a time lag TL_{yi} equal to 0.03s along the longitudinal direction calculated in Equation 6.53.

$$TL_{yi} = \frac{y_i}{v_b} = 0.03s \quad (6.53)$$

$$TL_{tot} = \frac{y}{v_b} = 0.5s \quad (6.54)$$

Likewise, in Abaqus the input at the bedrock base has been assigned directly to the mesh nodes with the same spatial time delay in the longitudinal direction assumed in Plaxis code.

Figure 6.33 shows the first and the last harmonic input signal assigned to both bedrock models; the total time lag TL_{tot} between the first and the last signal is equal to 0.5s (Equation 6.54).

$\gamma_{soil} (kN/m^3)$	$V_{soil} (m/s)$	v_{soil}	$f_{soil} (Hz)$	$V_{bedrock} (m/s)$
20	250	0.3	1.04	800

Table 6.1 Soil elastic parameters.

The mesh size was set as a function of the maximum investigable frequency of the signal $f_{max} = 4Hz$ (Kuhlemeyer & Lysmer 1973) and equal to $h_{max} = V_s / (4 * f_{max}) = 7.8m$. Figure 6.34 and Figure 6.35 shows the numerical mesh implemented in Plaxis 3D and Abaqus 3D respectively.

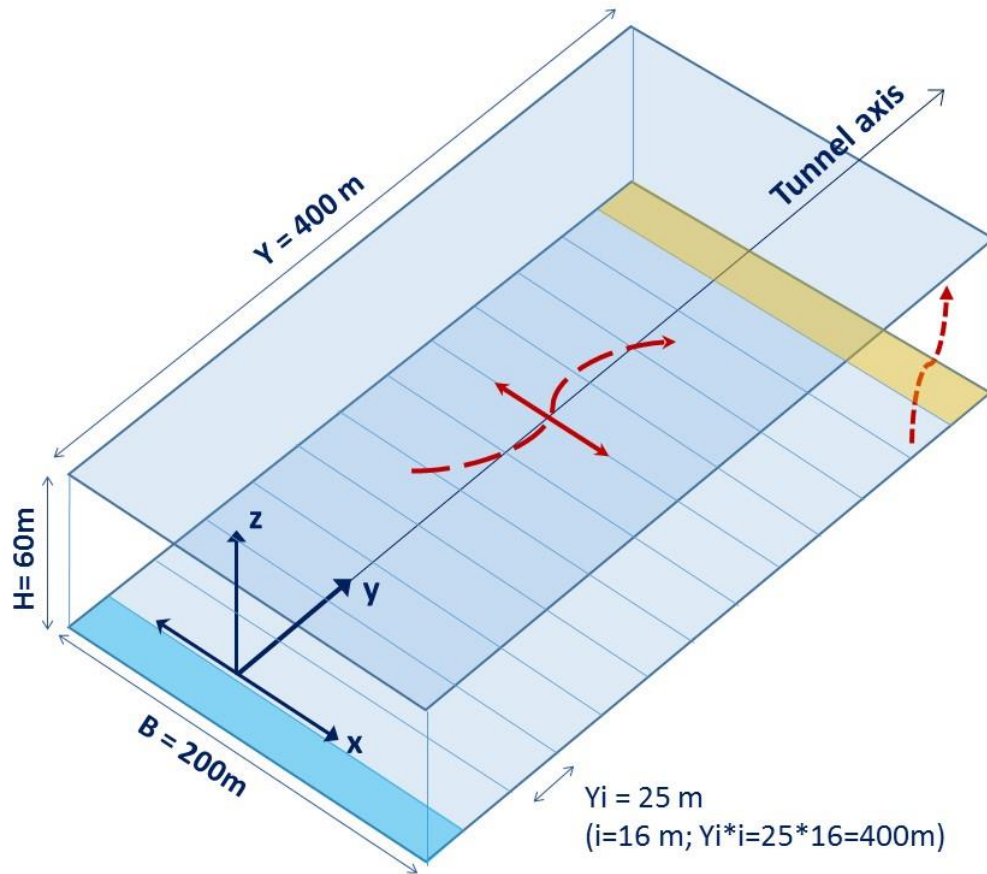


Figure 6.32. Geometric scheme adopted in Plaxis 3D and Abaqus 3D to simulate the asynchronous of the seismic motion in longitudinal direction y .

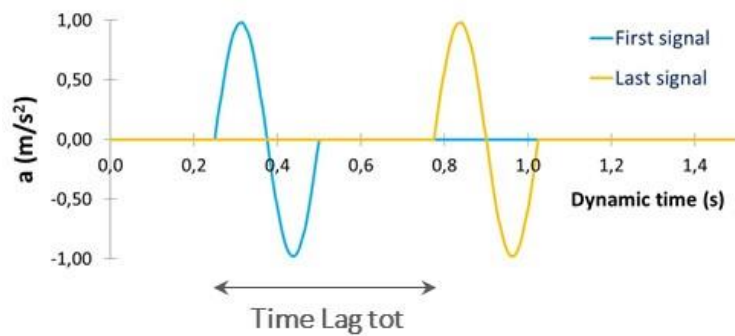


Figure 6.33. Harmonic input signals along the longitudinal direction.

The average size of finite elements in Plaxis code is set equal to 2.9m, modelled with 3D triangular elements (Figure 6.34). The mesh is regular both in transversal and then in longitudinal direction to avoid any effect of the different element dimension in any direction. The zoom in on the transversal section of the mesh is shown in Figure 6.34, this elements distribution is the same in longitudinal direction.

The mesh implemented in Abaqus 3D instead, is made by quadrangular elements with the dimensions equal to 2.5m (Figure 6.35), in order to satisfy the above mentioned criteria of *Kuhlemeyer & Lysmer 1973*.

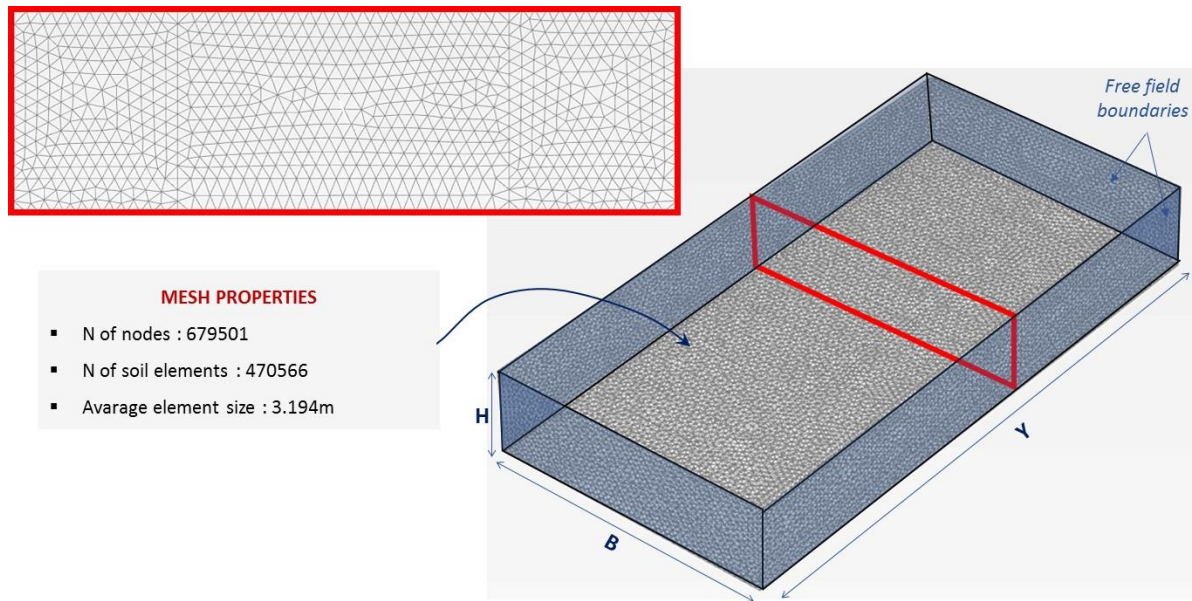


Figure 6.34. Numerical mesh in Plaxis 3D.

'Free field boundaries' have been applied in Plaxis on each vertical boundary of the model, both in transversal and longitudinal direction, as highlighted in grey in Figure 6.34. In Abaqus code 'continuum infinite 3D elements (CIN3D8)' have been applied only on the transversal vertical boundaries while longitudinal vertical boundaries are not absorbent and then, the free field condition in the transversal direction has been achieved moving away the longitudinal vertical boundaries from the tunnel axis up to a distance of 200m (vs 100m in Plaxis code), thus reaching a width B of the model equal to 400m (vs 200m in Plaxis code) as in Figure 6.35.

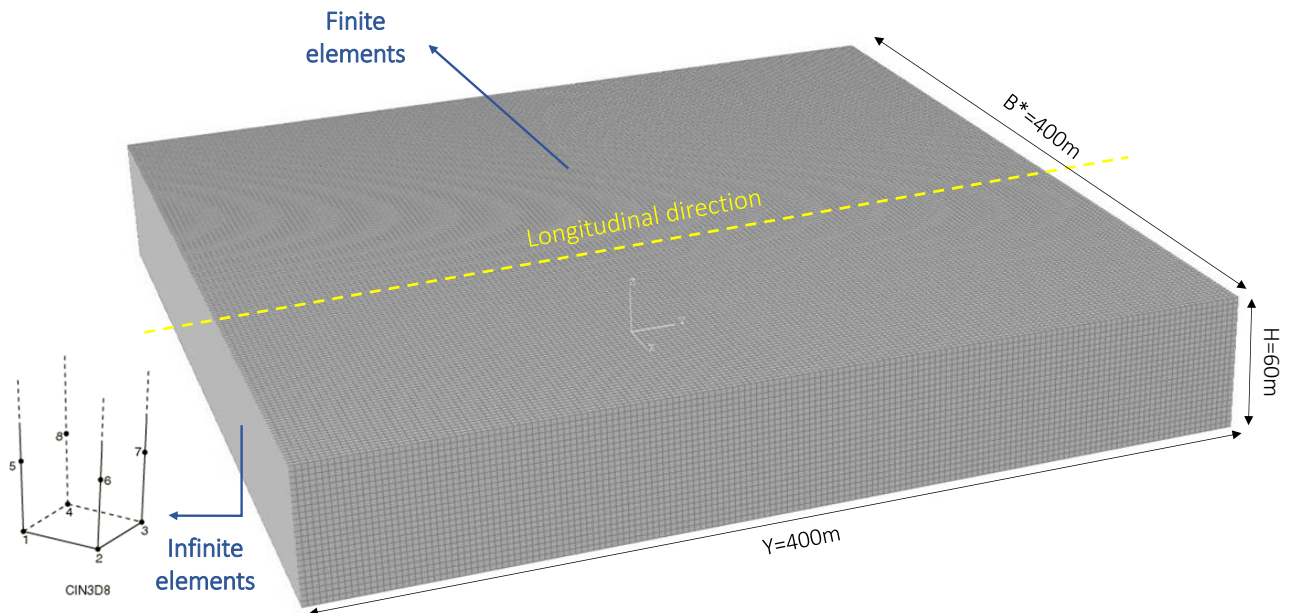


Figure 6.35. Numerical mesh in Abaqus 3D.

Elastic full dynamic analysis have been carried out in Plaxis and Abaqus codes. Some control points have been chosen to compare the free field soil response between the two analysis. Figure 6.36 for

instance, shows the selected control points along the ground surface of the longitudinal vertical section in the middle of the model.

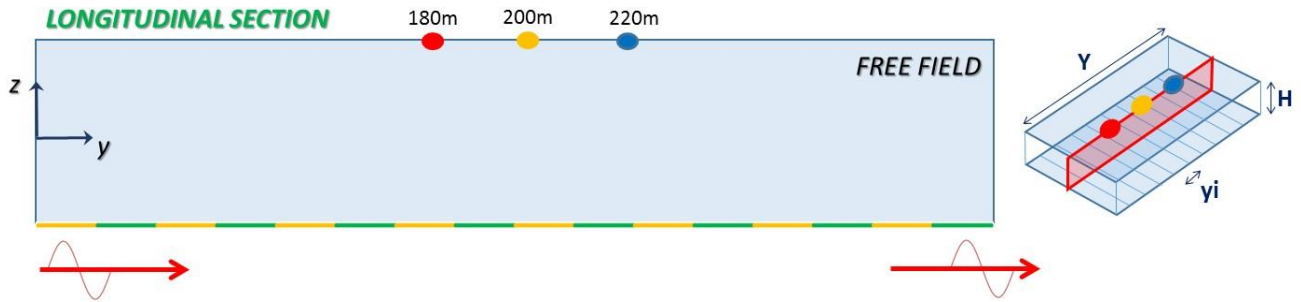


Figure 6.36. Control points along the ground surface of the longitudinal vertical section in the middle of the model for the free field asynchronous analysis.

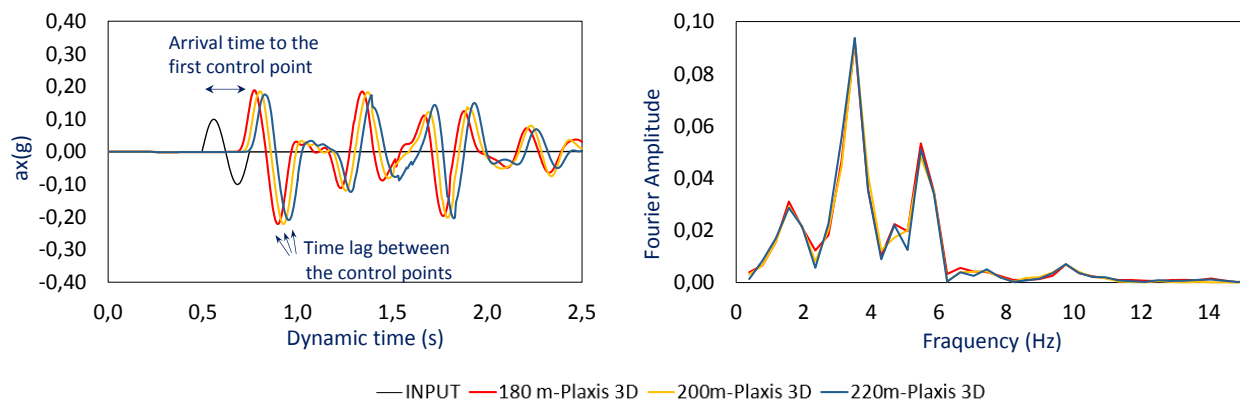


Figure 6.37. Time histories of acceleration and Fourier spectra of the control points in the free field asynchronous analysis in Plaxis 3D.

Figure 6.37 shows the free field soil response in correspondence of the selected control points located at 180m, 200m and 220m respect the origin of the y axis. It can be observe that there is a time delay between the input wave (black line in Figure 6.37) and the first point at $y=180\text{m}$. This is the time that the input needs to arrive at the selected point, proportional to the travelled distance and the wave velocity.

Likewise, there is time delay (time lag) between the arrival times in the three selected points. These are shifted of a time-lag proportionally to their distance (equal to 20m). The free field response of the control points is thus the same in terms of acceleration, just shifted in the time domain, and accordingly the points exhibit the same Fourier spectra. This last has a content of frequencies, is not a single-frequency spectra like that of the input signal, because the total dynamic time Δt_{dyn} of the analysis is equal to 2.5s while the harmonic signal is 0.25s in duration, so that there is an overlap between the travelling waves inducing the generation of other frequencies.

In Figure 6.38 there is the comparison in terms of time histories of acceleration and Fourier spectra in the control points calculated with Plaxis and Abaqus models. Both models behave similarly and the comparison is considered to be good enough to validate the proposed model in free field condition.

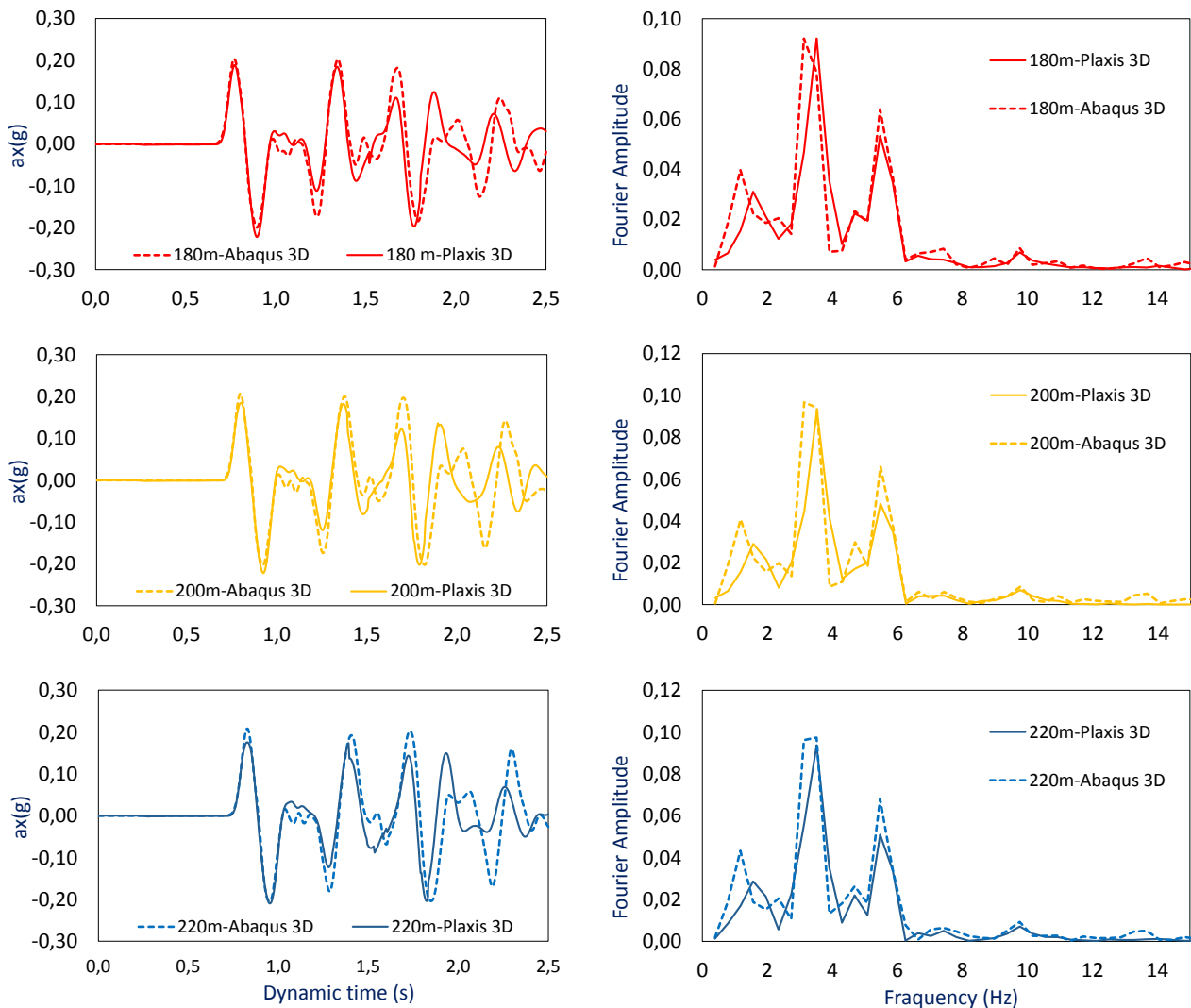


Figure 6.38. Comparison between the time histories of acceleration and Fourier spectra of the control points in the free field asynchronous analysis in Plaxis and Abaqus 3D.

6.2.2 3D full dynamic analysis: Soil-structure interaction

Once validated the free-field numerical model, the soil structure interaction has been investigated considering in the analysis a tunnel with a constant diameter equal to 6m and the axis depth equal to 30m (Figure 6.39).

Table 6.2 resumes the main elastic parameters of the lining. The tunnel lining is continuous, modelled with an elastic structural plate working under 'no slip' interaction condition at the soil-structure interface. The input signal considered in the analysis is the same adopted in the free field analysis, a harmonic wave with an amplitude of 0.1g and a frequency of 4Hz, with a number of oscillations equal to five.

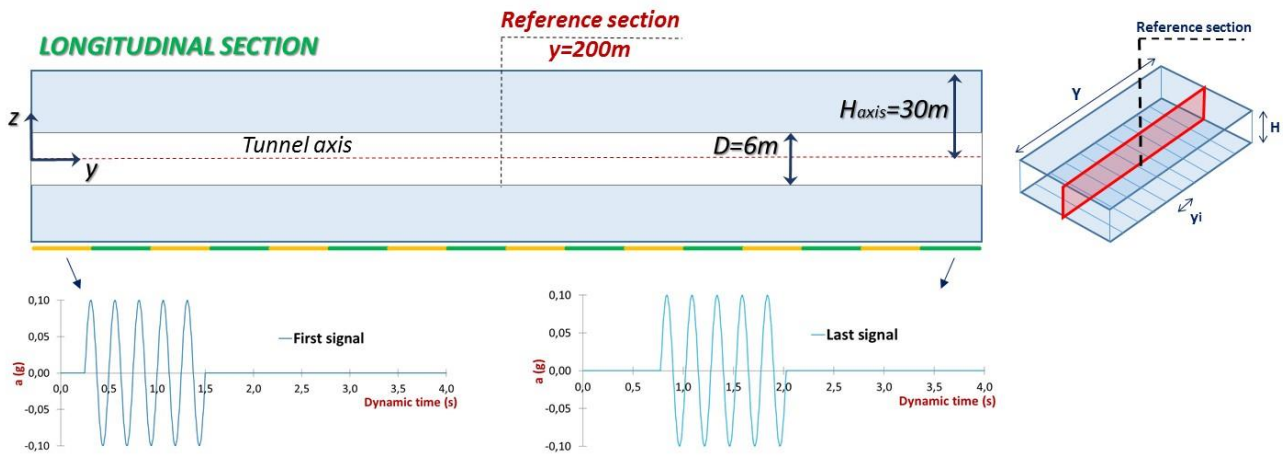


Figure 6.39. Control points along the ground surface of the longitudinal vertical section in the middle of the model for the free field asynchronous analysis.

$\gamma_{concrete} (kN/m^3)$	$E_{concrete} (MPa)$	$t_{lining} (m)$	ν
25	35	0.3	0.15

Table 6.2 Tunnel lining elastic parameters.

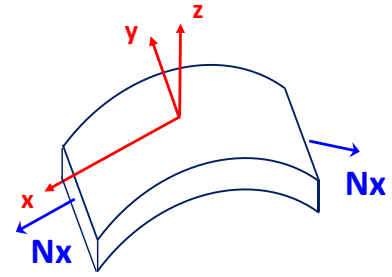
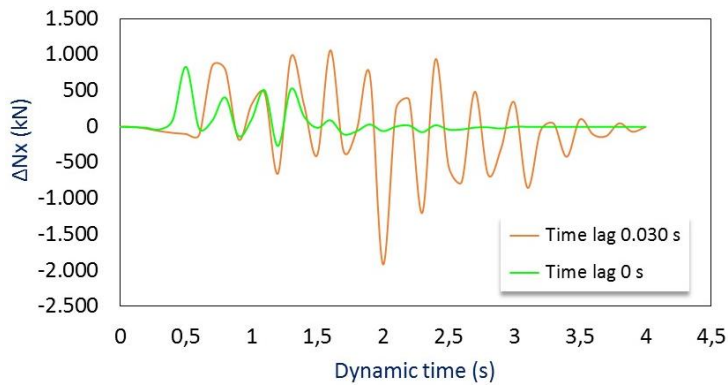
The objective of this analysis is to investigate the effect of the asynchronous ground motion respect the synchronous case. To this end, the same analysis has been carried out under the uniform seismic load condition too, and a comparison between the two models has been proposed.

The comparison has been established in terms of dynamic increment of internal forces in a reference tunnel section located at $y=200m$, in the middle of the model (Figure 6.39).

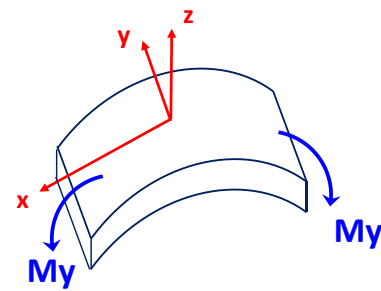
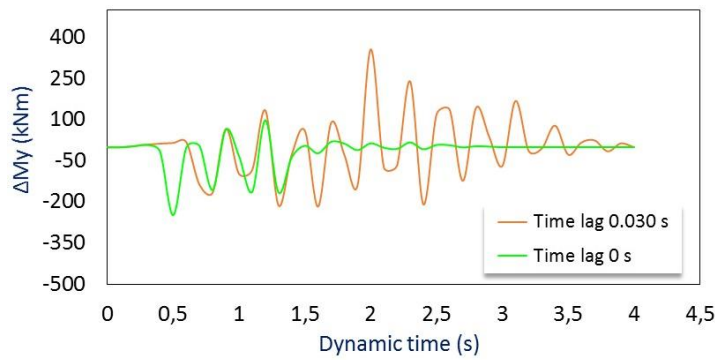
Looking at the Figure 6.40, it is possible appreciate a double effect of the asynchronous ground motion on the tunnel lining response:

- 1) Non uniform seismic load increases the dynamic increment of internal forces in the lining in its transversal plane (N_x and M_y in Figure 6.41 a, b) respect the case of uniform seismic load (Time Lag = 0s);
- 2) Non uniform seismic load induces axial forces along the tunnel axis, N_y , bending in the horizontal plane, M_z , and shear force perpendicular to the tunnel axis, Q_x (Figure 6.41 c, d, e). These components of forces are null in the case of uniform seismic load.

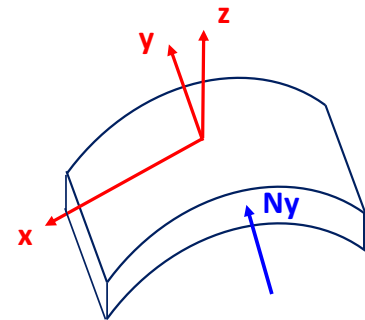
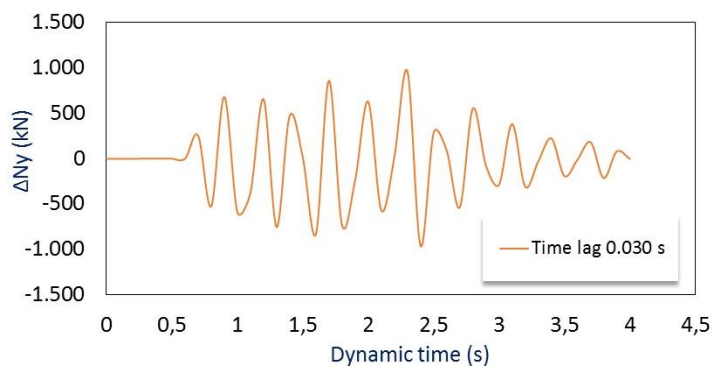
Figure 6.40 shows the time histories of the tunnel lining internal forces referring to the resultant of the transversal tunnel reference section. The shear force in particular has been calculated as the sum of the resultants of the horizontal components of the shear, $Q_x(\theta)$ and $Q_z(\theta)$, acting on the transversal tunnel section (Figure 6.40e). The resultant of the horizontal components of the shear acting vertically on the tunnel section, $\Sigma Q_z(x)$, is negligible respect the resultant of the horizontal components of the shear acting along the local x axis direction, $\Sigma Q_x(x)$.



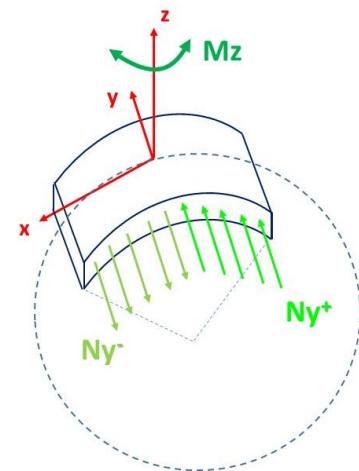
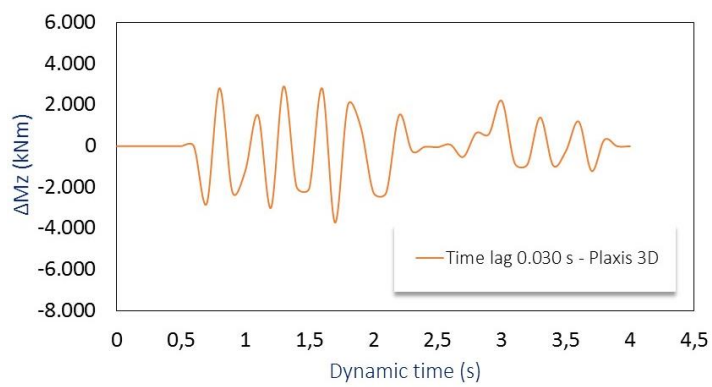
(a)



(b)



(c)



(d)

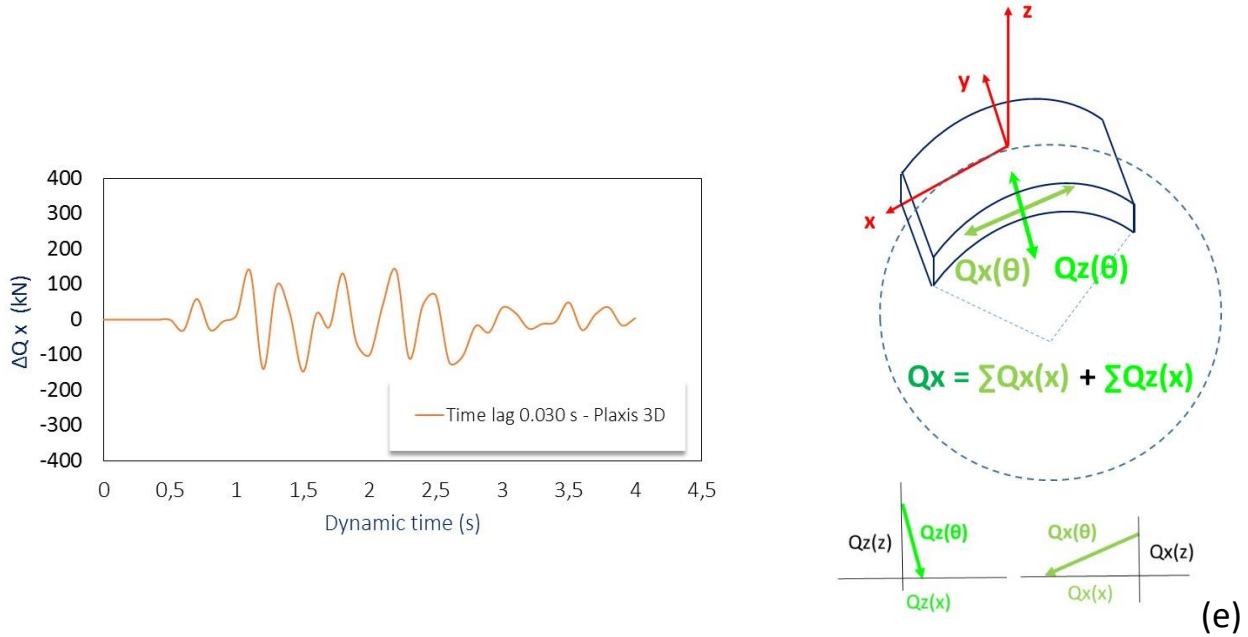


Figure 6.40. Time histories of tunnel lining internal forces induced by non uniform seismic loading for a time lag equal to 0.03s ($\rightarrow V_{bedrock}=800\text{m/s}$) and comparison with the uniform seismic load case.

Another interesting issue on the topic is the effect of the bedrock velocity, thus the time lag, on the asynchronous ground motion. A set of parametrical analysis, for instance, has been carried out varying longitudinal time-lag of the travelling wave to investigate its effect in terms of dynamic increment of transversal and longitudinal internal forces arising in the lining. The following velocities have been considered in the analysis:

- $V_{bedrock} = 800 \text{ m/s} \rightarrow \text{Time Lag} = 0.030 \text{ s}$
- $V_{bedrock} = 1000 \text{ m/s} \rightarrow \text{Time Lag} = 0.025 \text{ s}$
- $V_{bedrock} = 1250 \text{ m/s} \rightarrow \text{Time Lag} = 0.020 \text{ s}$

The results shown in Figure 6.41 stress the effect of the time-lag and/or bedrock velocity: increasing the bedrock velocity, thus decreasing the time-lag along the tunnel axis, there is a decreasing of the dynamic increment of the internal forces in the tunnel lining and viceversa.

Going towards infinity the bedrock velocity, it returns the uniform seismic loading condition.

The numerical results obtained in the proposed 3D model, although under simplified assumptions (elastic soil behaviour, elastic lining behaviour, no-slip soil-structure condition, no structural details such as grout and segmental lining), show a significant effect of the asynchronous ground motion respect the synchronous case. For the investigated bedrock velocities in fact, the difference between the uniform and non uniform seismic loading can achieve up to a maximum value of 50% in terms of N_x and M_y . This seems to be interesting thinking about the likely longitudinal joint performance under non uniform seismic loading which could reach higher values of rotations than those obtained in this work under uniform seismic loading (see Chapter 4). The asynchronous ground motion produces also longitudinal forces, horizontal bending and transversal shear respect the tunnel axis and their magnitude is not negligible in particular thinking about the circumferential joints performance during the dynamic shaking and their possible opening.

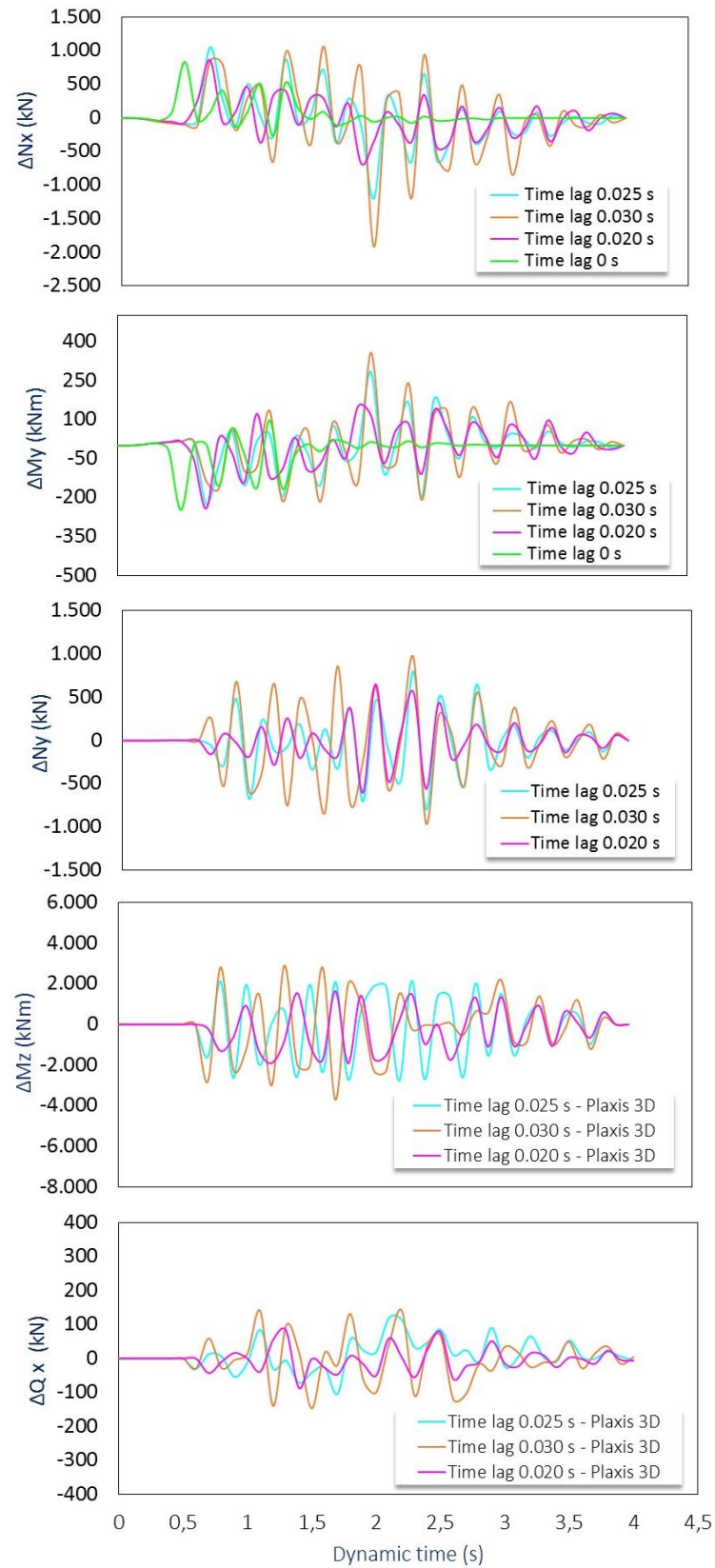


Figure 6.41. Time histories of tunnel lining internal forces induced by non uniform seismic loading for different values of the time-lag ($TL_1=0.03s$, $TL_2=0.025s$, $TL_3=0.02s$).

6.2.3 2D multi-masses-beam-springs model: Soil-structure interaction

A further validation of the proposed numerical model in terms of soil-structure interaction, has been performed comparing the response of the 3D model with that one of the simplified 2D multi-masses-beam-springs model developed by *Li Chong 2016* in his doctoral thesis (introduced in detail before, §6.1.1) and implemented in Abaqus 2D.

The comparison is proposed in terms of dynamic increment of the longitudinal components of the internal forces evaluated with both methods.

The first step is to define the 1D equivalent MDOF system. The 2nd mass of the equivalent 5-DOF system (Figure 6.42) is nearly located at the half height of the homogeneous layer at which is the tunnel axis, so that the equivalent 5-DOF system is selected to represent the homogeneous soil layer.

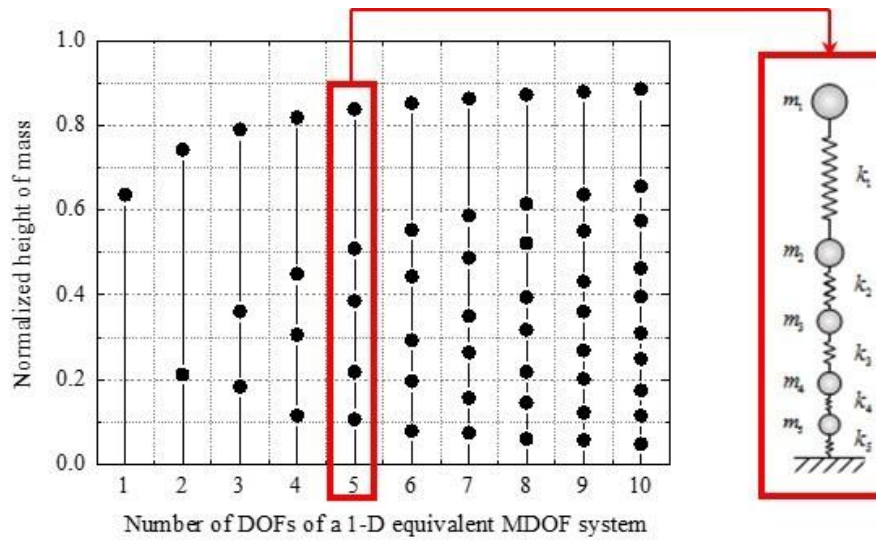


Figure 6.42 Choice of the 1D equivalent MDOF system.

The homogeneous soil layer is firstly to be discretized into a series of 1D equivalent 5-DOF systems in the vertical direction. These 1D equivalent systems are then spring-connected consecutively at corresponding masses to form a 2D equivalent MDOF system, assembled by eighty 5-DOF systems in longitudinal direction spaced of 5m each other.

The longitudinal springs that connect adjacent 1D equivalent systems are determined as in Equation 6.55:

$$k_{jj} = \frac{m_j v_s^2}{l_{jj}^2} \quad (6.55)$$

where m_j is the mass constant of the mass 'j', V_s^2 is the shear velocity of the soil layer and l_{jj}^2 is the length of the longitudinal spring.

The tunnel beam is lastly connected to the 2nd masses with SSI springs determined as in Equation 6.56 (*St.John & Zahrah 1987, §6.1.1*):

$$k_{SSI} = \frac{16\pi G(1-\nu)}{3-4\nu} \frac{D}{\lambda} \quad (6.56)$$

where G is the shear modulus, ν the Poisson's ratio, D the diameter of the circular tunnel and λ the incident wave length.

As such, the simplified model for soil-structure system is built. Figure 6.43 shows the simplified scheme of the multi-masses-beam-springs model implemented in Abaqus 2D. The properties of the soil, the structure and the input signal are the same adopted in the 3D model.

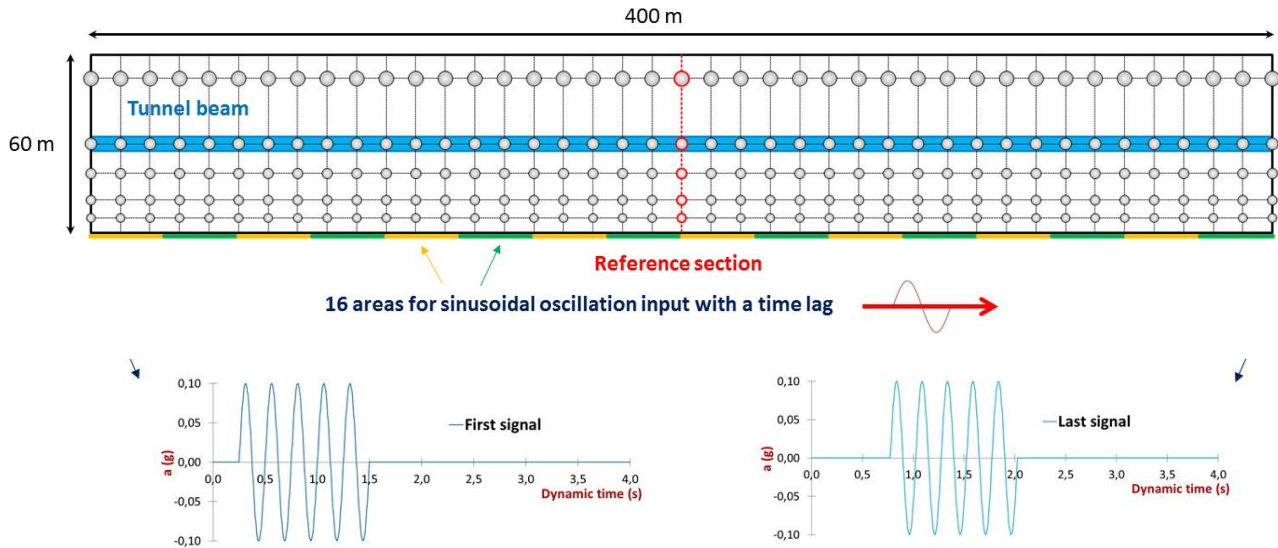


Figure 6.43. Scheme of the 2D equivalent 5-DOF system implemented in Abaqus 2D.

The central section of the model, highlighted in red in Figure 6.43, has been selected to make the comparison between the 3D and 2D models in terms of horizontal bending moment M_z and transversal shear Q_x as established in Figure 6.44.

Figure 6.45 shows the results of the comparison in terms of time histories of the dynamic increment of the resultant of M_z and Q_x in the reference tunnel section for the 3D and 2D model, for different values of time-lag (0.02s, 0.025s, 0.03s). The results of the two models are in a good agreement. Overall, in each case, the 3D model calculates higher values of the the dynamic increment of the internal forces respect the simplified 2D model.

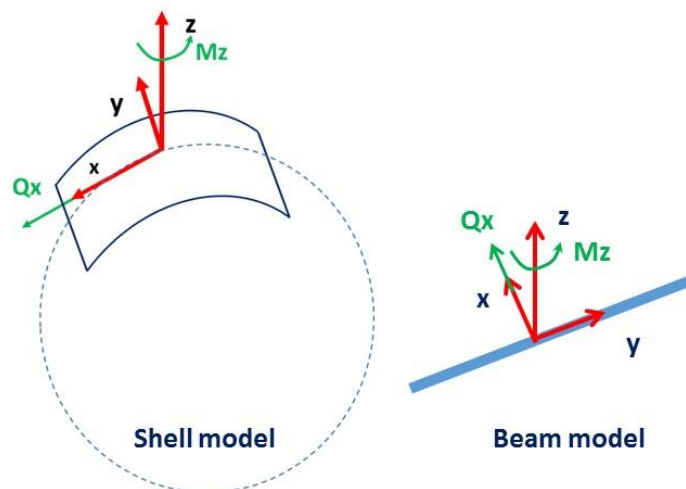


Figure 6.44. Equivalence between 3D and 2D model.

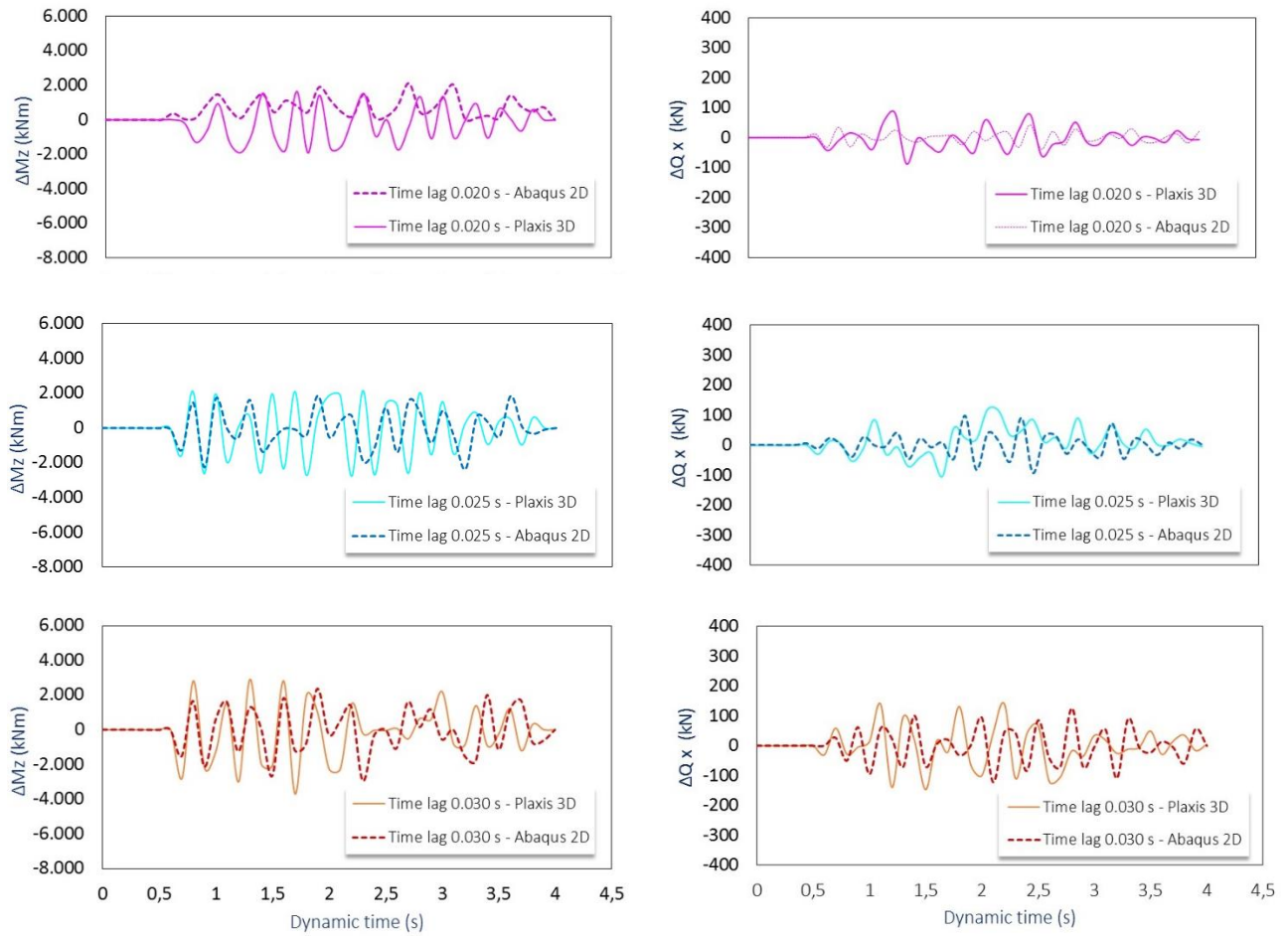


Figure 6.45 Comparison between 3D and 2D model in terms of time histories of dynamic increment of M_z and Q_x in the reference tunnel section under asynchronous ground motion.

CHAPTER 7

Conclusions

The aim of the present dissertation is to investigate the dynamic behaviour of a segmental tunnel lining in soft soil.

A preliminary study of the static performance of the lining structure has been conducted in order to define and calibrate a 3D numerical model of the segmental tunnel lining adopted for the dynamic analysis. The latter were performed both under synchronous and asynchronous seismic motion.

In the case of synchronous seismic motion, a study of the seismic vulnerability of such structures has been also carried out based on the definition of analytical fragility curves, for different levels of damage. A procedure for the risk assessment has been proposed, for the case of segmental tunnel lining, assuming as critical damage parameter the longitudinal joint rotation.

Furthermore, a study of feasibility of Earthquake Early Warning System (EEWS) based on thresholds has been conducted through a probabilistic and a real-time approach for such tunnel structure.

In the first part of the Thesis, the behaviour of segmental tunnel lining under static loads has been investigated and the following conclusions can be drawn.

- The available monitoring data of the case study of Metro Line 6 in Naples have been used to calibrate the proposed model of a segmental lining. The long-term monitoring of the strains in an instrumented segmental ring provided a complete knowledge of the behaviour of the reference section under time-dependent loads, giving a 3D picture of the state of strains in each segment of the ring.
- A 3D numerical model is necessary to model the spatial layout of the segmental lining and the effect of the tunnel excavation in terms of both soil-structure interaction and induced mechanized tunneling loads. The latter seem to have high influence on the lining deformation, thus the soil-structure interaction is only in part responsible of the internal forces arising in the tunnel lining.
- A detailed numerical model of the structure, of the soil and the mechanized excavation allows to take into account the key-parameters affecting the lining deformation.

Concerning the soil-structure interaction, the main role is played by the soil and the contact element between the grout layer, elastic, and the surrounding soil, assumed with a non-linear elastoplastic behaviour.

The mechanized tunneling, on the other hand, affects the lining through the shield conicity, inducing a redistribution of the stresses around the tunnel, the hydraulic jack thrust, that is the first external load applied on the lining ring after its installation, the grout pressure, that induces a rather uniform compressive load to the lining before it is exposed to the radial load of the surrounding soil, the grout hardening that, in function of the permeability of the soil at contact and its mixture, controls the mechanism of loading transfer from the soil to lining.

Finally, the presence of longitudinal and circumferential joints influences the 3D transfer of loads in the radial direction (surrounding soil and grout pressure) and longitudinal direction (hydraulic jack thrust).

In the second part of the Thesis, the behaviour of segmental tunnel lining under uniform seismic loads has been investigated, leading to the following conclusions.

- The influence of the key parameters of the kinematic tunnel-ground interaction, i.e. the relative soil-structure stiffness and the interface properties, have been investigated through different design approaches, based on pseudo-static and full dynamic analysis. The former simplified uncoupled approach simulating the effect of the earthquake with an equivalent seismic load, statically applied to the structure as a distribution of displacements, allows the increment of dynamic internal forces in the lining to be evaluated only in correspondence of the maximum acceleration of the input signal. It does not include the evolution of soil-structure interaction during the earthquake, as in the latter case of full dynamic analysis.

In correspondence of the peak of acceleration, both approaches show that significant seismic increments of internal forces arise in the lining compared to the static values and this result highlights that seismic effects on underground structures should not be overlooked, even in low to moderate seismicity areas. The comparison between the selected design approaches shows that, at least for the studied case, the pseudo-static analysis underestimates the increment of forces with respect to the full dynamic analysis. This difference is strictly related to the lining and soil relative stiffness and interface properties.

- The effect of the segmental lining technology on the tunnel seismic behaviour is such that the segmental lining exhibits a more suitable behaviour compared to a continuous ring for the higher structural flexibility, producing a decrease of stresses in the lining and an increase of the whole structural aseismic capability.

The seismic response of the segmental tunnel lining has been investigated in detail under synchronous seismic motion. Under high levels of ground shaking, longitudinal joints seem to be the most vulnerable points of tunnel structure leading to joints opening.

The magnitude of the possible joints opening depends mainly on the joints technology itself and their spatial pattern, as well as on the seismic event.

Non-linear full dynamic analysis performed for a selected longitudinal joint technology, that is a non-bolted flat joint, show the achievement of peak and permanent values of joints rotations in correspondence of the peak of the dynamic time history and at the end of the dynamic stages respectively. The latter evidence may lead to some concerns in highly permeable soils, since a large rotation at the joints producing dislocation of gaskets may cause groundwater inflow.

- Analytical fragility curves for segmental tunnel lining, based on 2D non-linear full dynamic analysis, have been constructed assuming the permanent rotation of longitudinal joint as the potential damage index, ID. The proposed procedure includes the definition of the damage states, DS, based on three different thresholds of permanent joint rotation, selected in function of the work stages as defined as the analytical solution of *Janßen's* joint.

Assuming as earthquake parameter, IMi, the Peak Ground Acceleration, PGA, the probability of damage increases for softer soil (soil type B → soil type C → soil type D) and increases with the decreasing of the damage level (DS4 → DS3 → DS2).

In terms of Permanent Ground Displacement, PGD, instead, it can be notice that, unlike to what happens in terms of PGA, the probability of damage increases with the stiffness of soils (soil type D

→ soil type C → soil type B). This is due to the fact that, to achieve the same PGD, a stiffer soil has to be subjected to larger seismic accelerations than a softer soil.

- An application of the proposed fragility curves has been done for a preliminary feasibility study concerning the use of a threshold-based Earthquake Early Warning System, EEWS, for segmental tunnel lining conducted for some Italian target sites. The approach proposed combines regional and on-site approaches with the proposed fragility curves. Three approaches have been adopted in this work to provide the PGA and the lead-time for the possible seismic threats expected at a target site; one is based on the Probabilistic Seismic Hazard Analysis (PSHA, NTC 2008) -LEVEL '0'-, one based on the disaggregation of the PSHA -LEVEL '1'- and one on a real-time and evolutionary estimation of location, magnitude and using a ground motion prediction equation -LEVEL '2'-.

The approach followed in the LEVEL '0' allows to quickly assess on probabilistically bases what ground motion level could occur at the considered sites, which in turn is used to assess the possible level of damage for such kind of structures. However, since the PSHA does not provide direct indications about the location of the seismic sources that contributed to the hazard, it is not possible to compute the available lead-time.

The LEVEL '1' procedure is again based on the PSHA adopted by the Italian code, but incorporates the disaggregation analysis of the seismic hazard to identify 'virtual sources' (i.e., in terms of epicentral distance and magnitude) that provide the higher contribution to the hazard. Following this procedure, a disaggregation map, a lead-time map and an acceleration map are computed for the target sites, considering different probabilities of exceedance. In terms of lead-times, the results of the LEVEL-1 analysis indicates for each selected site that, considering the threats having the major contribution to the hazard, the lead-time is in general low and not sufficient for implementing 'Regional Early Warning' approaches.

The real-time approach followed in the LEVEL '2' is not bounded to the probabilistic approach proposed by the national code, and consists in the simulation of the effects of a real seismic event on the target site, thus providing a real-time estimation of the probability of damage. *PRESTo-Probabilistic and Evolutionary early warning SysTem* has been used to predict the PGA at the target site through real-time and evolutionary location and magnitude estimates and a ground motion prediction equation.

Overall, the probabilistic approach defined with the LEVEL '2', based on the hazard disaggregation, provides a useful tool to study the feasibility of EEWS. The results indicate that the selected targets could benefit of an on-site EEWS. Concerning the target in Naples, is shown that a regional EEWS given by the combination of the ISNet network and software PRESTo could be effective to protect the Metro Line 6 of Napoli from the seismic threat represented by the Irpinia area.

Finally, in the third part of the Thesis, the behaviour of segmental tunnel lining under non-uniform seismic loads was also considered. This allowed further conclusions to be drawn.

- The effect of multi-directional seismic motion travelling along the tunnel has been investigated in the case of continuous tunnel lining, including the effect of time lag. The numerical results show that the asynchronous ground motion has a double effect on the tunnel lining response:
 - i. Non uniform seismic load (Time Lag $\neq 0$) increases the dynamic increment of internal forces in the lining in its transversal plane (N_x and M_y) respect the case of uniform seismic load (Time Lag = 0s);

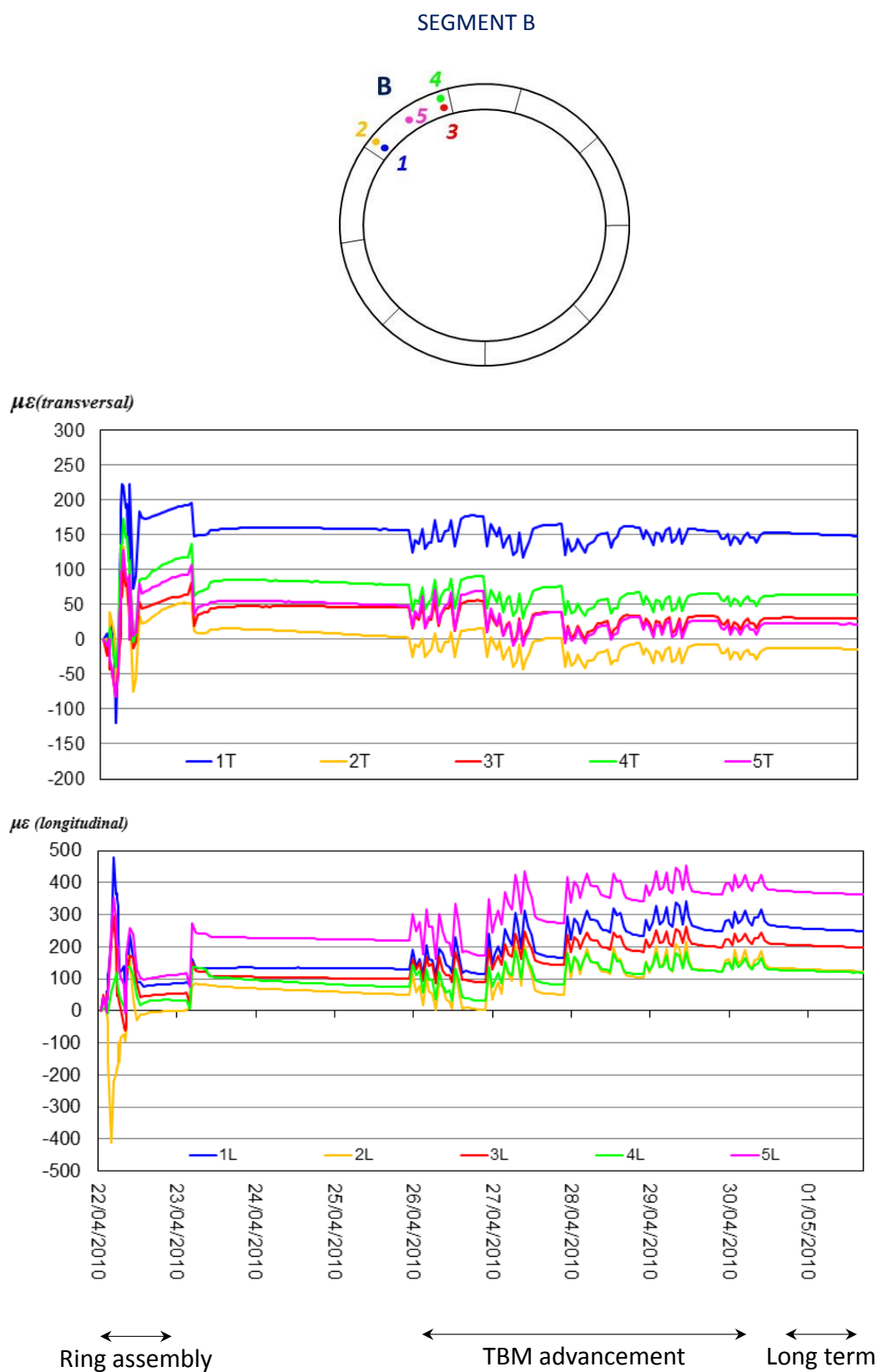
- ii. Non uniform seismic load induces additional axial forces along the tunnel axis, N_y , bending in the horizontal plane, M_z , and shear force perpendicular to the tunnel axis, Q_x . These components of forces are null in the case of uniform seismic load.

The numerical results shows also the effect of the bedrock velocity, hence of the time lag in longitudinal direction, on the asynchronous ground motion: increasing the bedrock velocity, thus decreasing the time-lag along the tunnel axis, a decrease of the dynamic increment of the internal forces in the tunnel lining is observed and viceversa. Going ideally towards infinity the bedrock velocity, the uniform seismic loading condition occurs.

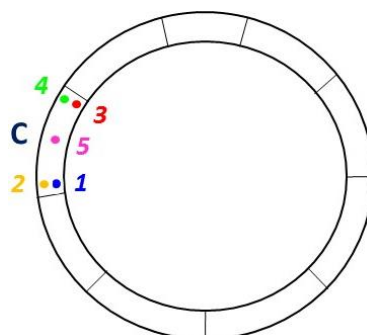
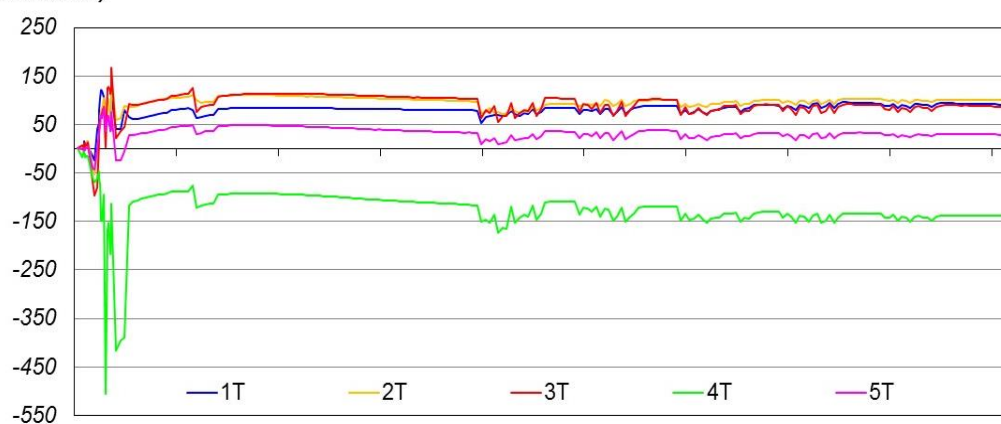
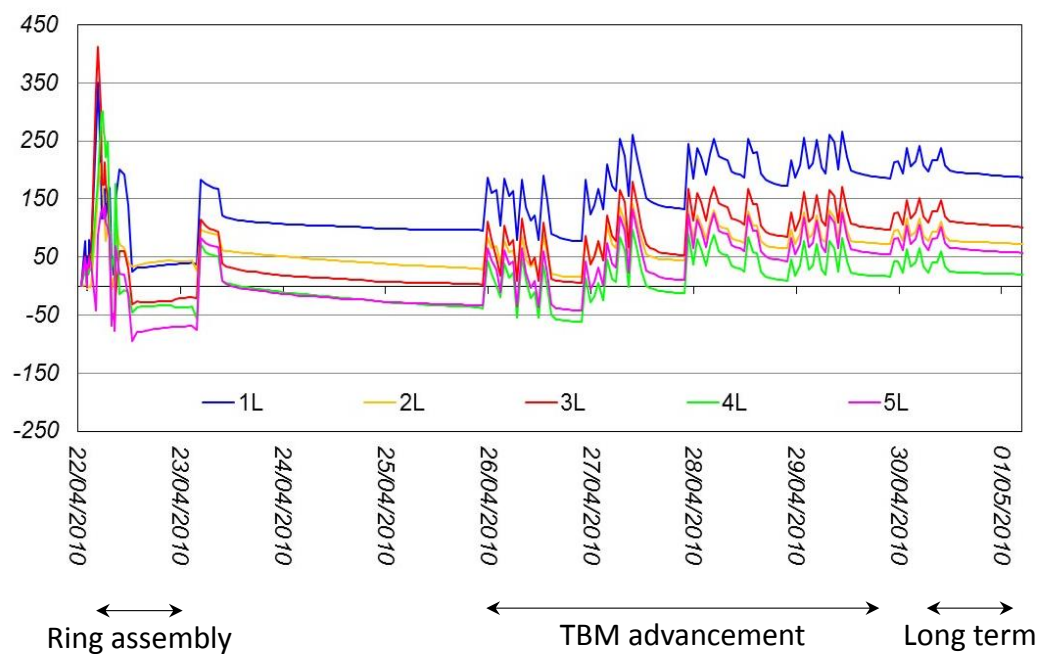
- Overall, the numerical results obtained in the proposed 3D model to simulate the effect of travelling waves along the tunnel axis, although under simplified assumptions (elastic soil behaviour, elastic lining behaviour, no-slip soil-structure conditions, no structural details such as grout and segmental lining), show a significant effect of the asynchronous ground motion respect the synchronous case. For the investigated bedrock velocities, the difference between the uniform and non-uniform seismic loading can achieve a value of 50% in terms of N_x and M_y . This seems to be interesting if one thinks about the longitudinal joint performance under non uniform seismic loading, which could likely reach higher values of rotations than those obtained in this work under uniform seismic loading. The asynchronous ground motion produces also longitudinal forces, horizontal bending and transversal shear with respect to the tunnel axis and their magnitude is not negligible, in particular thinking about the circumferential joints performance during the dynamic shaking and their possible opening.

Appendix 1

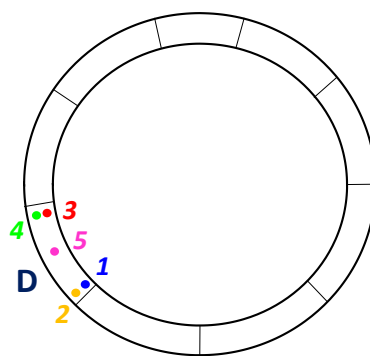
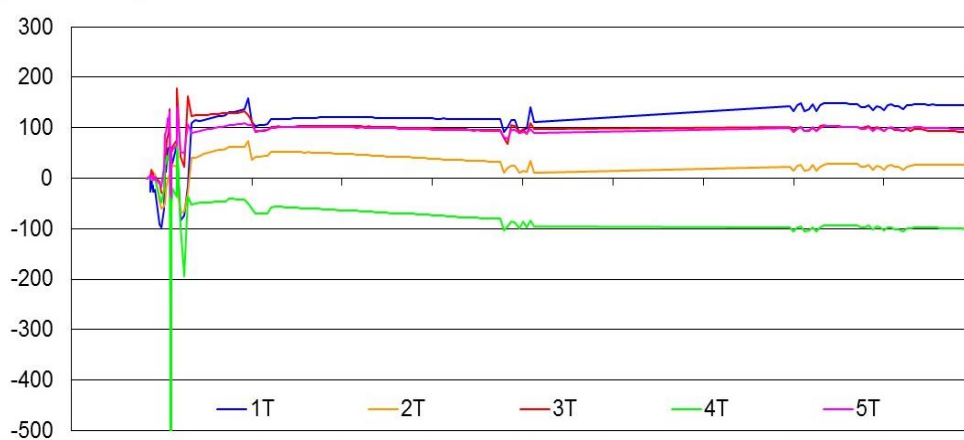
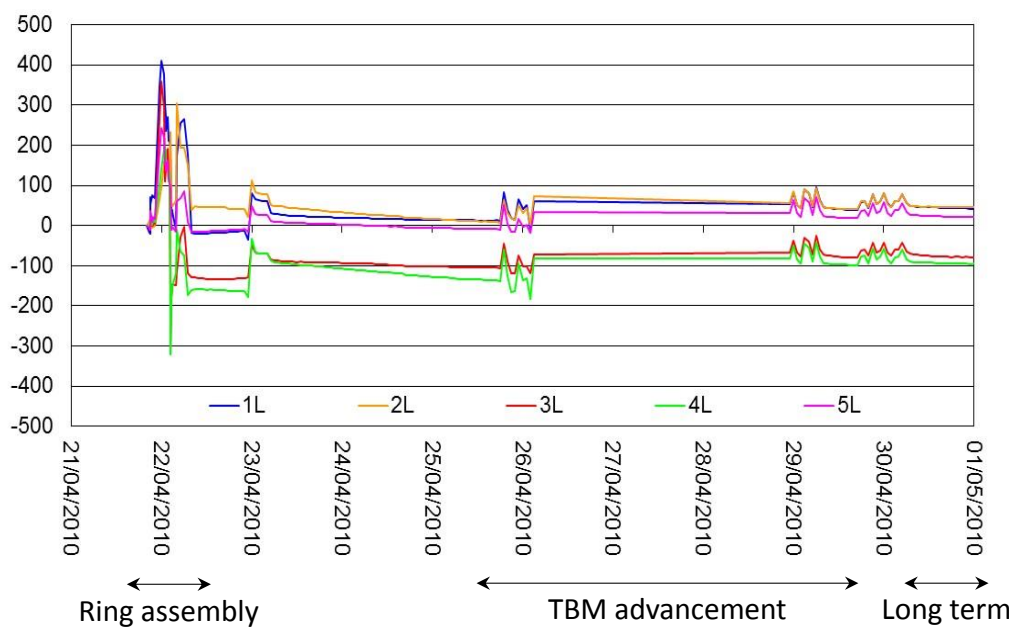
Long term monitoring of the strains in the instrumented segmental section of Metro Line 6 of Naples (after Marino R. 2010)



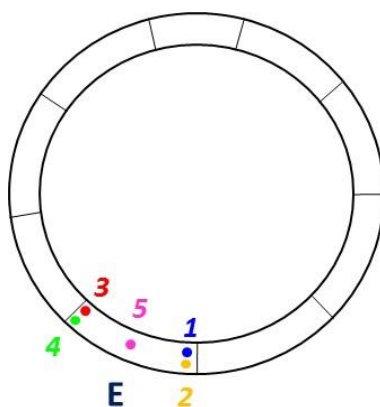
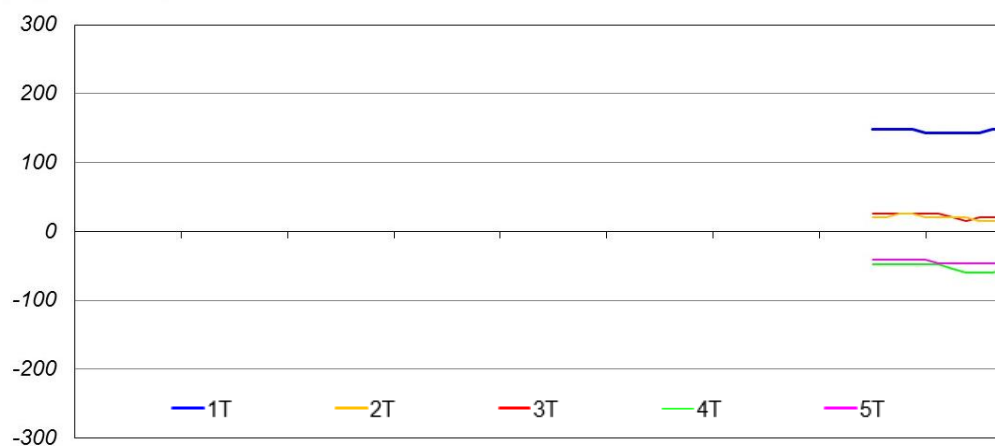
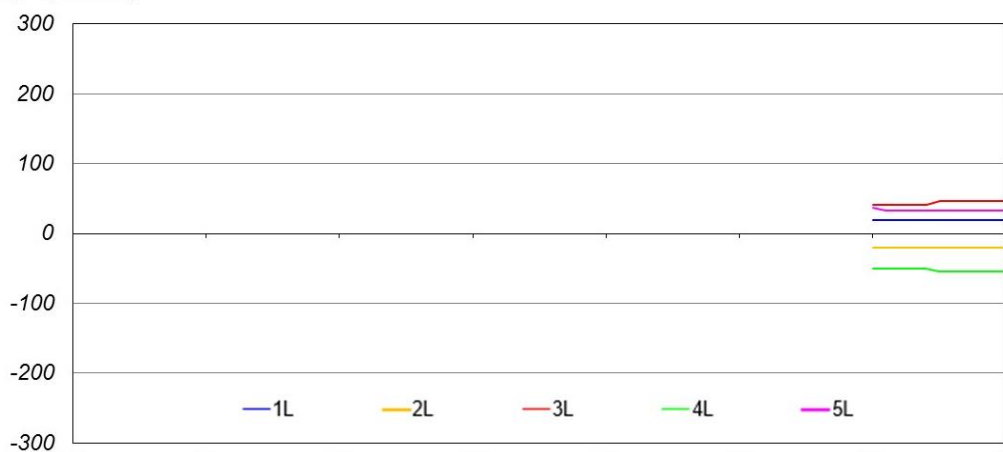
SEGMENT C

 $\mu\epsilon$ (transversal) $\mu\epsilon$ (longitudinal)

SEGMENT D

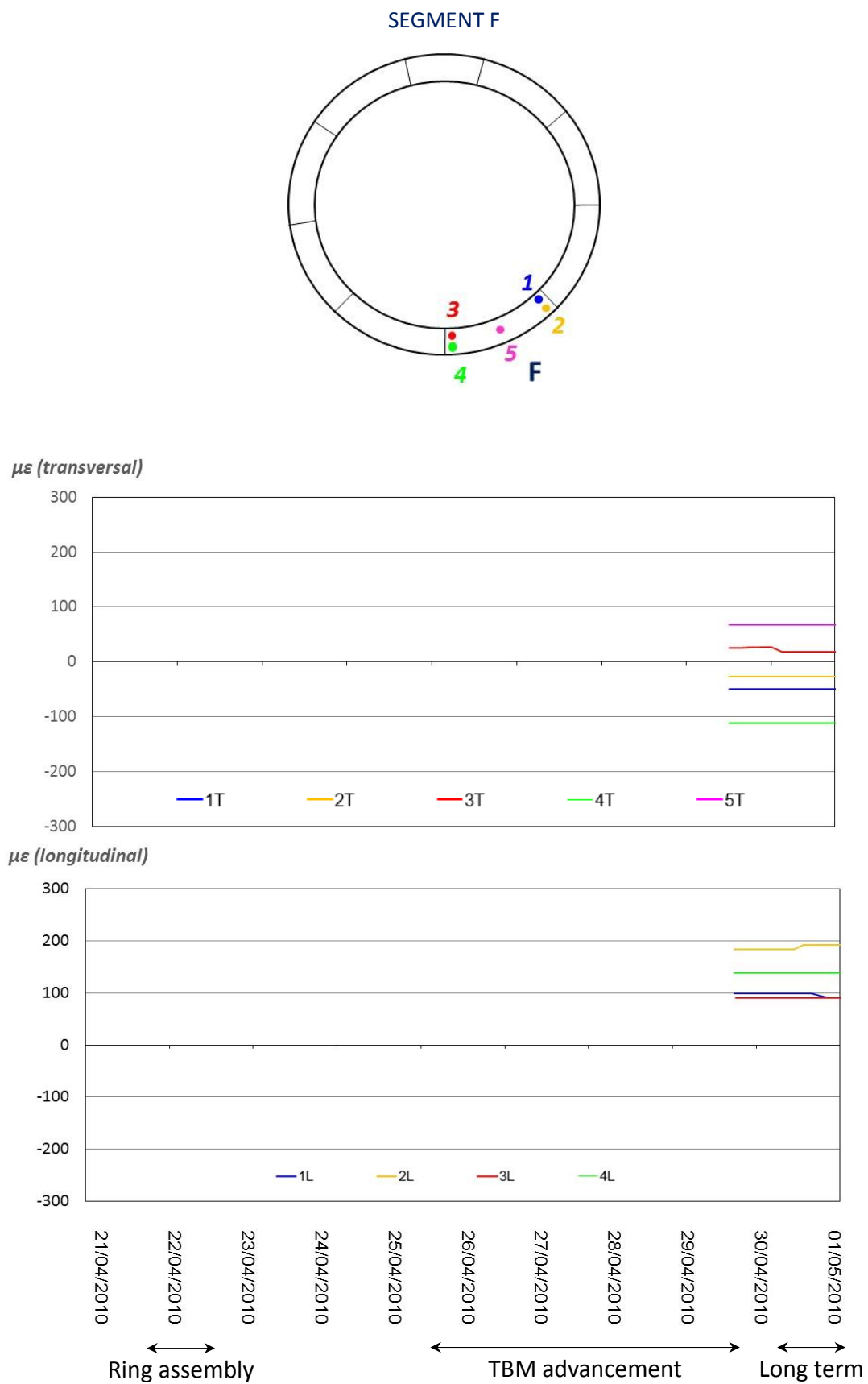
 $\mu\epsilon$ (transversal) $\mu\epsilon$ (longitudinal)

SEGMENT E

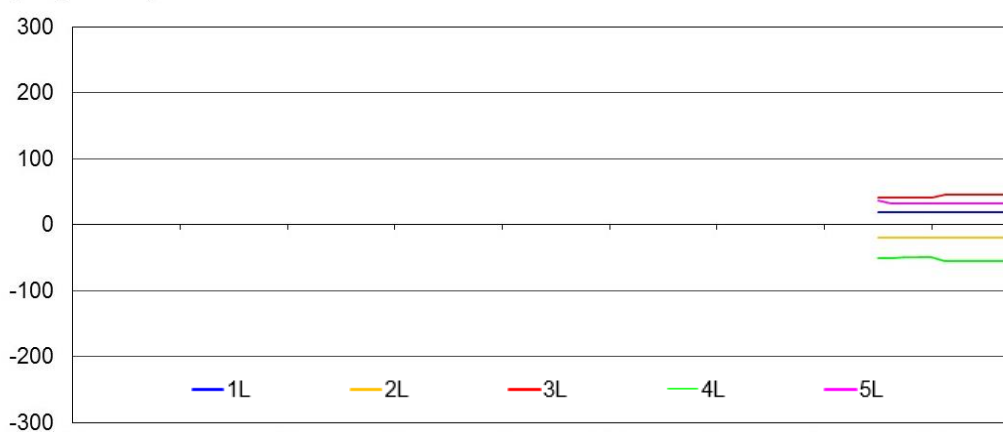
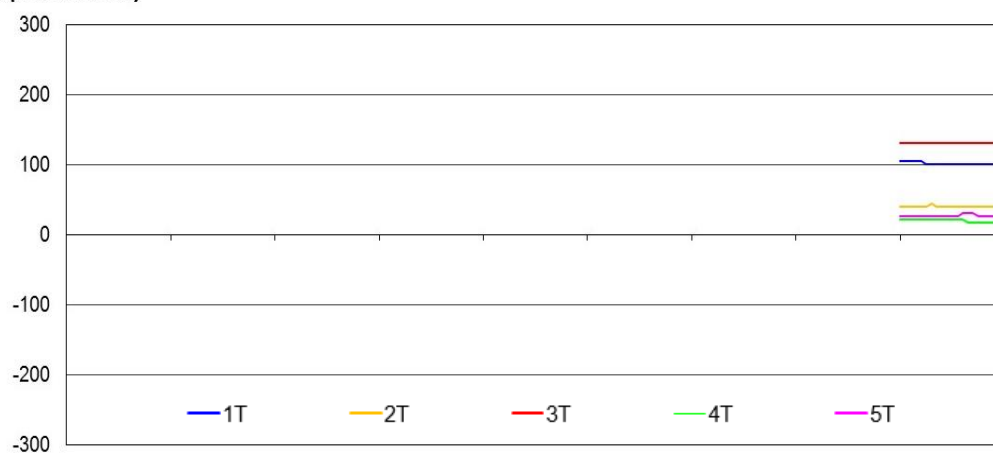
 $\mu\epsilon$ (transversal) $\mu\epsilon$ (longitudinal)

21/04/2010 22/04/2010 23/04/2010 24/04/2010 25/04/2010 26/04/2010 27/04/2010 28/04/2010 29/04/2010 30/04/2010 01/05/2010

Ring assembly TBM advancement Long term



A circular diagram representing a reference genome. The circle is divided into segments by radial lines. Five specific regions are highlighted with colored dots and numbers: 1 (blue), 2 (yellow), 3 (red), 4 (green), and 5 (pink). A large blue 'G' is positioned to the right of the circle, indicating a specific genomic location or feature.



21/04/2010

22/04/2010

23/04/2010

24/04/2010

25/04/2010

26/04/2010

27/04/2010

28/04/2010

29/04/2010

30/04/2010

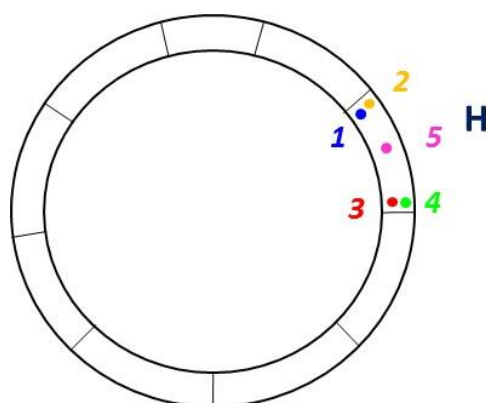
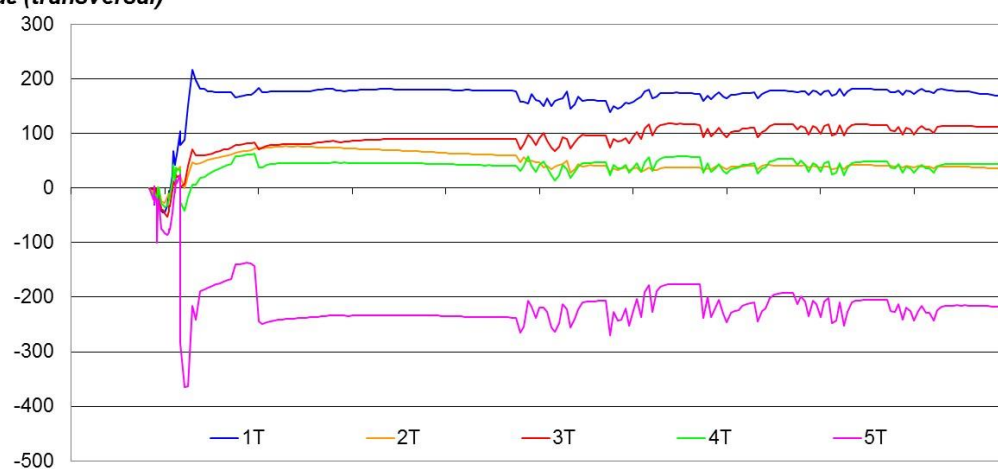
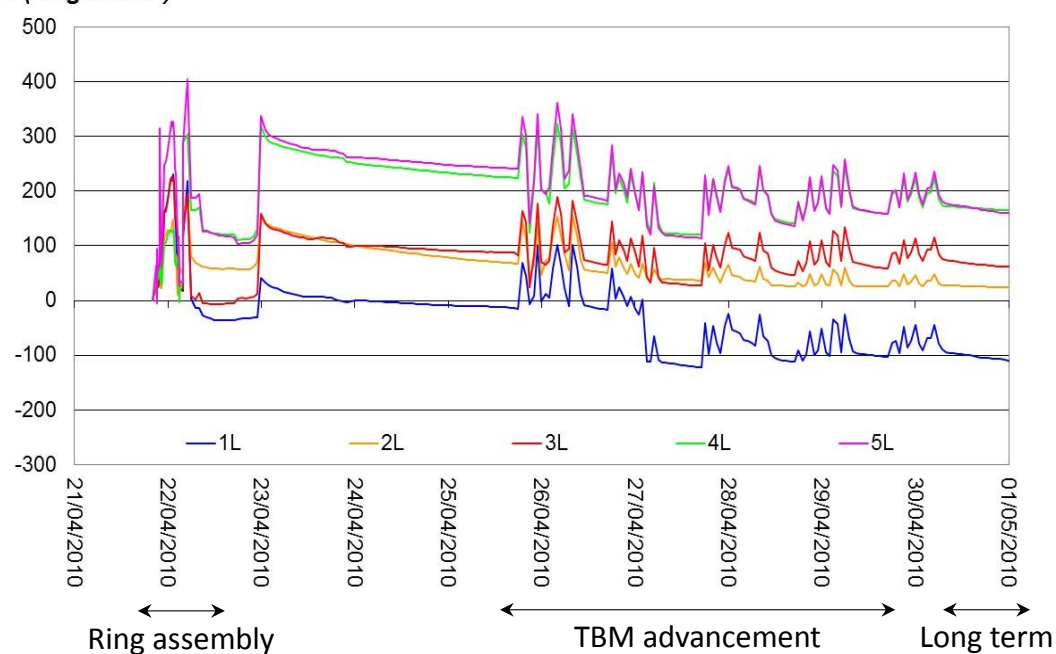
01/05/2010

↔
Ring assembly

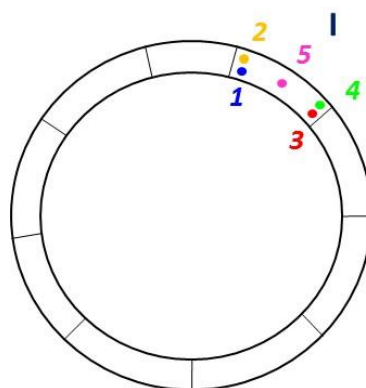
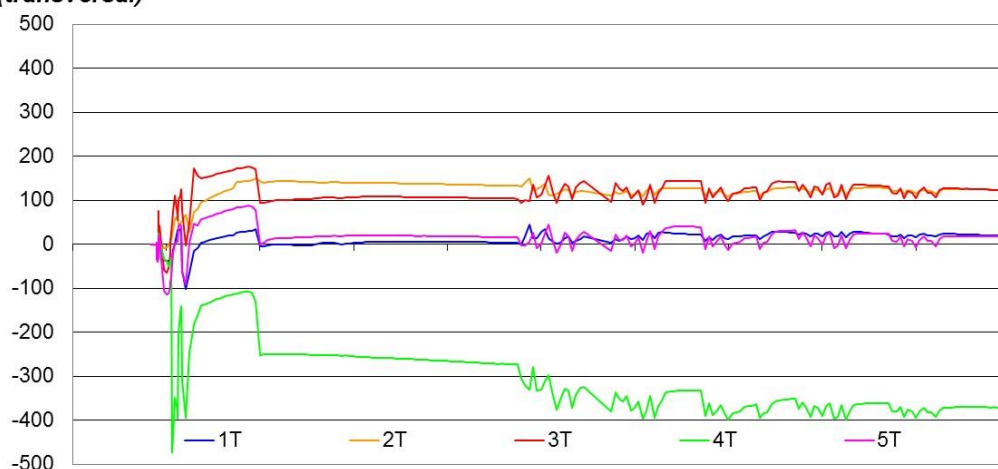
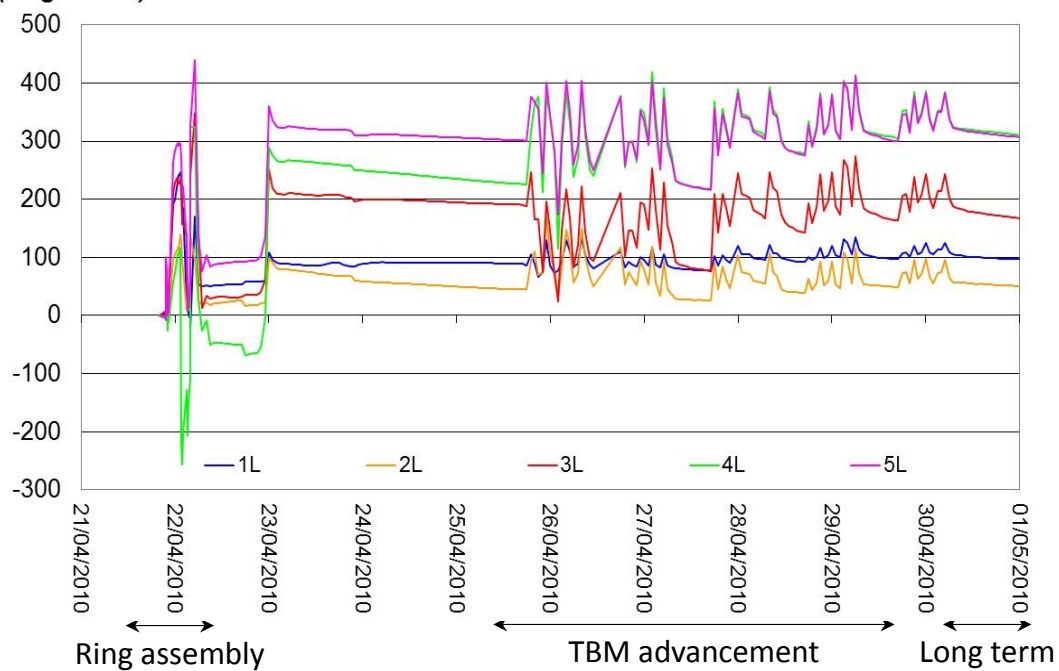
← TBM advancement

Long term

SEGMENT H

 $\mu\epsilon$ (transversal) $\mu\epsilon$ (longitudinal)

SEGMENT I

 $\mu\epsilon$ (transversal) $\mu\epsilon$ (longitudinal)

Appendix 2

Hardening soil 'HS' (Schanz et al. 1999) and Hardening Soil small strain 'HSss' (Benz 2007)

The Hardening Soil model, HS model, is an advanced constitutive model for the simulation of the soil behaviour. As for the Mohr Coulomb model, limiting states of stress are described by means of friction angle, ϕ , cohesion, c , and dilatancy angle ψ . Soil stiffness is described much more accurately by using three different stiffness (Figure A2.1): (1) triaxial loading stiffness E_{50} , (2) triaxial unloading stiffness E_{ur} , (3) oedometer loading stiffness E_{oed} . In contrast to the MC model, the HS model accounts for stress-dependency of the stiffness moduli; this means that all stiffness increase with the pressure, usually referring to the reference pressure p_{ref} .

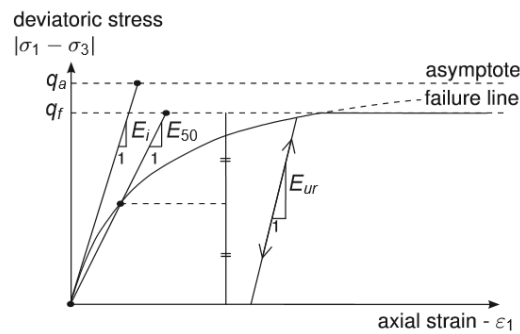


Figure A2.1 Hyperbolic stress-strain relation in primary loading for a standard drained triaxial test
(Plaxis Manual Models)

The basic idea for the Hardening Soil Model is the hyperbolic relationship between the vertical strain ϵ_1 and the deviatoric stress q observed in the primary triaxial loading tests (Figure A1.1, Equation A2.1):

$$-\epsilon_1 = \frac{1}{E_i} \frac{q}{1 - q/q_a} \quad \text{for } q < q_{failure} \quad (A2.1)$$

where q_a is the asymptotic value of the shear strength and E_i the initial stiffness related to the E_{50} with the Equation A2.2:

$$E_i = \frac{2E_{50}}{2 - R_f} \quad (A2.2)$$

As soon as $q = q_{failure}$, the failure criterion is satisfied and perfectly plastic yield occurs. The relation between q_f , given by Equation A2.3, and q_a , is expressed by the failure ratio $R_f < 1$, representing the percentage of failure deviatoric stress q_f reached, usually automatically set equal to 0.9.

$$q_f = \frac{6 \sin \phi_{pk}}{3 - \sin \phi_{pk}} (p + c \cot \phi_{pk}) \quad (A2.3)$$

$$q_a = \frac{q_f}{R_f} \quad (A2.4)$$

The stress strain behaviour for primary loading is highly non linear. Instead of using the tangent stiffness modulus for primary loading E_i , difficult to determine, the secant Young's modulus E_{50} is defined. It is expressed by Equation A2.5:

$$E_{50} = E_{50}^{ref} \left(\frac{\sigma_3 + c \cot \phi_{pk}}{p^{ref} + c \cot \phi_{pk}} \right)^m \quad (A2.5)$$

where E_{50}^{ref} is the reference stiffness modulus corresponding to a reference stress p^{ref} , and m represents the amount of stress dependency of the actual stiffness on the minor principal stress σ'_3 (the effective confining pressure in a triaxial test). E_{50}^{ref} is determined from triaxial stress-strain-curve for a 50% mobilization of the maximum shear strength q_f .

For un-reloading stress paths, the stress-dependent E_{ur}^{ref} stiffness modulus is used. It is expressed by equation A2.6 and defined as the unloading-reloading Young's modulus in a wide unloading-reloading cycle corresponding to the reference pressure $\sigma^{ref}=100\text{KPa}$

$$E_{ur} = E_{ur}^{ref} \left(\frac{\sigma_3 + c \cot \varphi_{pk}}{p^{ref} + c \cot \varphi_{pk}} \right)^m \quad (\text{A2.6})$$

Differently from elastic models, elasto plastic hardening soil model does not imply a fixed relationship between the triaxial stiffness E_{50} and the stiffness obtained by an oedometer test E_{oed} . These two stiffness are two different inputs, E_{oed} is defined as in Equation A2.7:

$$E_{oed} = E_{oed}^{ref} \left(\frac{c \cos \varphi - \frac{\sigma'_3}{K_0} \sin \varphi}{c \cos \varphi + p^{ref} \sin \varphi} \right)^m \quad (\text{A2.7})$$

The Hardening Soil small strain model (Benz 2007), HSss model, is a modification of the HS model capable of taking into account the very high soil stiffness observed at very low strain levels, its reduction with the strain level (Figure A2.2) and the early accumulation of plastic deformation.

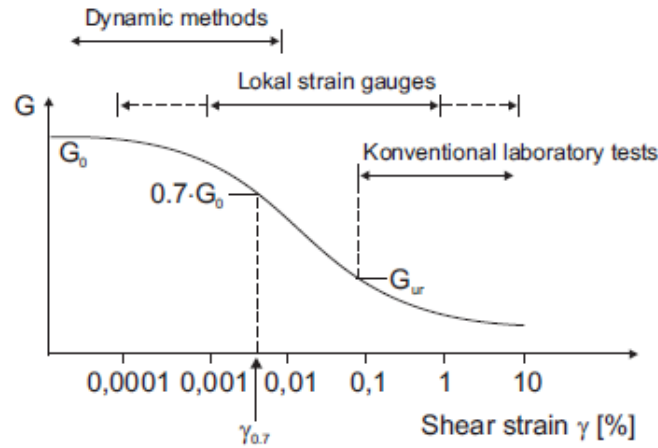


Figure A2.2 Characteristic stiffness-strain behaviour of soil with typical strain ranges for laboratory tests.

As shown in Figure A2.2, for deformation γ exceeding the value of 10^{-5} , there is a rapid decrease of the stiffness of the soil, in terms of the shear modulus G . These aspects are taken into account through two additional parameters to the original model HS: the initial shear stiffness G_0 , and the shear strain $\gamma_{0.7}$, defined as the strain at of which the secant modulus G_s is reduced to about 70% from the G_0 value. The analytical expressions are given below (Equation A2.8 and Equation A2.9).

$$G_0 = G_0^{ref} \left(\frac{c \cos \varphi - \sigma'_3 \sin \varphi}{c \cos \varphi + p^{ref} \sin \varphi} \right)^m \quad (\text{A2.8})$$

$$G = \frac{G_0}{1 + 0.43 \frac{\gamma}{\gamma_{0.7}}} \quad (\text{A2.9})$$

Where G_0^{ref} is the small strain shear modulus at the reference pressure $p_{\text{ref}} = 100$ kPa, σ'_3 is the minimum principal effective stress, m is a constant, c' is the effective cohesion and ϕ is the angle of shear resistance.

The evolution of the shear modulus with the increase in the shear strain is included in the constitutive formulation by the expression of the stiffness reduction curve proposed by *Hardin and Drnevich 1972*, successively modified by *Santos and Correia 2001* in Equation A2.10:

$$\frac{G_s}{G_0} = \frac{1}{1 + a \left| \frac{\gamma}{\gamma_{0.7}} \right|} \quad (\text{A2.10})$$

where G_s is the secant shear modulus, ' a ' is a constant equal to 0.385 and $\gamma_{0.7}$ is the shear strain at which the shear modulus is reduced to about 70% of its initial value.

The derivative of Equation A2.10, with respect to the shear strain, provides the tangent shear modulus, G_t , expressed by the Equation A2.11:

$$\frac{G_t}{G_0} = \frac{1}{\left(1 + a \left| \frac{\gamma}{\gamma_{0.7}} \right| \right)^2} \quad (\text{A2.11})$$

The tangent shear modulus is bounded by a lower limit corresponding to the shear modulus G_{ur} (Equation A2.12):

$$G_t > G_{ur} = \frac{E_{ur}}{2(1 + \nu_{ur})} \quad (\text{A2.12})$$

This latter is selected by the user, referring to a medium value of the shear strain level, $\gamma_{\text{cut-off}}$, after which the reversible response is characterised by a constant value of the tangent stiffness with the strain (Figure A2.3). The expression of $\gamma_{\text{cut-off}}$ is provided in the equation A2.13:

$$\gamma_{\text{cut-off}} = \frac{1}{0.385} \left(\sqrt{\frac{G_0^{\text{ref}}}{G_{ur}^{\text{ref}}} - 1} \right) \gamma_{0.7} \quad (\text{A2.13})$$

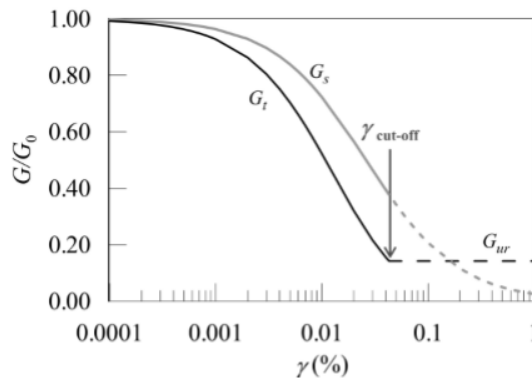


Figure A2.3 Decay curves of the tangent and secant shear stiffness moduli of the HSss model.

Appendix 3

Expression of the cohesion adopted for the calibration of the elasto-plastic joint model.

The Mohr Coulomb constitutive model has been adopted to describe the elasto-plastic joint behaviour. The expression of the cohesion, c , (Equation A3.1) adopted for the calibration of the joint MC model, has been obtained under the hypothesis of uniaxial compression of the material ($\sigma'_1 = \sigma'_{cy}$ and $\sigma'_3 = 0$).

$$c = \left(-\frac{\sigma_{cy}}{2\sqrt{k_p}} \right) \quad (\text{A3.1})$$

In the σ_3 - σ_1 stress plane, the shear failure locus is expressed by the Equation A3.2:

$$\frac{1}{2}(\sigma'_3 - \sigma'_1) + \frac{1}{2}(\sigma'_3 + \sigma'_1)\sin\varphi - c \cos\varphi = 0 \quad (\text{A3.2})$$

In uniaxial compression, equation A3.2 can be written as follows:

$$-\frac{1}{2}\sigma'_1 + \frac{1}{2}\sigma'_1\sin\varphi - c \cos\varphi = 0 \quad (\text{A3.3})$$

$$\sigma'_1 - \sigma'_1\sin\varphi + 2c \cos\varphi = 0 \quad (\text{A3.4})$$

$$\sigma'_1(1 - \sin\varphi) = -2c \cos\varphi \quad (\text{A3.5})$$

$$\sigma'_1 = \frac{-2c\sqrt{(1-\sin\varphi)^2}}{1-\sin\varphi} \quad (\text{A3.6})$$

$$\sigma'_1 = -2c \sqrt{\frac{(1+\sin\varphi)(1-\sin\varphi)}{(1-\sin\varphi)^2}} \quad (\text{A3.7})$$

$$\sigma'_1 = -2c \sqrt{\frac{(1+\sin\varphi)}{(1-\sin\varphi)}} \quad (\text{A3.8})$$

$$\sigma'_1 = -2c\sqrt{k_p} \quad (\text{A3.9})$$

The cohesion, c , can be derived as follows:

$$c = \left(-\frac{\sigma_{cy}}{2\sqrt{k_p}} \right) \quad (\text{A3.10})$$

where σ_{cy} is the compressive yielding strength of the concrete.

References

- Abrahamson NA, Schneider JF, Stepp JC. Empirical spatial coherency functions for applications to soil-structure interaction. *earthquake Spectra* 1992; 7:1-27.
- Afifipour M, Sharifzadeh M, Shahriar K, Jamshidi H (2011) Interaction of twin tunnels and shallow foundation at Zand underpass, Shiraz metro, Iran. *Tunnelling and Underground Space Technology* 26:356–363.
- AFTES, 1999. The Design, sizing and construction of precast concrete segments installed at the rear of a TBM. AFTES recommendations 1999.
- American Lifelines Alliance (ALA) 2001. Seismic Fragility Formulation for Water Systems, part 1, Guideline, ASCE-FEMA, Reston, VA 2001.
- Amorosi, A., Boldini, D., Falcone, G. (2014). Numerical prediction of tunnel performance during centrifuge dynamic tests. *Acta Geotechnica*, 9 (4), pp. 581-596.
- Argyroudis A., Pitilakis K. 2012. Seismic fragility curves of shallow tunnels in alluvional deposits. *Soil Dynamics and Earthquake Engineering* 35 - 1-12.
- Arnau & Molins 2011a. Experimental and analytical study of the structural response of the segmental tunnel lining based on an in situ loading test. Part 1: Test configuration and execution. *Tunnelling and Underground Space Technology* 26(2011) 764-777.
- Arnau O, Molins C 2011b Experimental and analytical study of the structural response of segmental tunnel linings based on an in situ loading test. Part 2: numerical simulation. *Tunn Undergr Space Technol* 26:778–788.
- Arnau et al 2012. Longitudinal time-dependent response of segmental tunnel lining. *Tunnelling and Underground Space Technology* 28(2012) 98-108.
- Arnau O., Molins C. 2012. Three dimensional structural response of segmental tunnel linings. *Engineering Structures* 44:210-221.
- ASTM C939-10 Standard Test Method for Flow of Grout for Preplaced-Aggregate Concrete (Flow Cone Method).
- ASTM C942-10 Test Method for Compressive Strength of Grouts for Preplaced-Aggregate Concrete in the Laboratory.
- Aversa S., Bilotta E., Russo G., di Luccio A. (2015). Ground movements induced by TBM excavation under an historic church in Napoli. *Proc. XVI ECSMGE*. Edinburgh, 13-17 September 2015.
- Bardet J., Ichii K., & Lin C. (2000). EERA a Computer Program for Equivalent-linear Earthquake site 624 Response Analyses of Layered Soil Deposits. Univ. of Southern California, Dep. of Civil Eng.
- Barla G, Barla M, Bonini M, Gamba F et al (2005) Two and three dimensional modelling and monitoring of the Metro Torino. 11th International conference of Iacmag, Turin (Italy).
- Benz T. Small-strain stiffness of soils and its numerical consequences. PhD thesis, Univ. Stuttgart (2007).
- Bezuijen et al. 2004. Field measurements of grout pressure during tunnelling of Sophia rail tunnel. *Soil and foundation*. Vol.44, No.1, 38-48.
- Bezuijen & Talmon 2009. Special lecture: Processes around a TBM. *Geotechnical Aspects of Underground Construction in Soft Ground* – Taylor & Francis Group, London, ISBN 978-0-415-48475-6.

- Bilotta E., Lanzano G., Russo G., Santucci de Magistris F., Silvestri F. (2007). Methods for the seismic analysis of transverse section of circular tunnels in soft ground. ISSMGE-ERTC12 Workshop at XIV ECSMGE "Geotechnical Aspects of EC8", Chapter 22, Patron Editore.
- Bilotta E., Lanzano G., Madabhushi G., Silvestri F. (2014). A numerical Round Robin on tunnels under seismic actions. *Acta Geotechnica* DOI 10.1007/s11440-014-0330-3.
- Bilotta E., Paolillo A., Russo G., Aversa S., 2017. Displacements induced by tunnelling under historical building. *Tunnelling and underground Space technology*. 61 (2017) 221-232.
- Bindi D. et al. 2011. Ground motion prediction equation derived from the Italian strong motion database. *Bull Earthquake Eng* DOI.10.1007/s10518-011-9313-z.
- Bitetti B., "Effects of tunnelling in urban areas". Ph.D. dissertation, (2010), Second University of Naples.
- Blom C. et al. 1999. Three-dimensional structural analyses of the shield-driven "Green Heart" tunnel of the high-speed line South. *TunnUndergrSpaceTechnol*. 14 (2):217-22.
- Bloom, C.B.M. 2001. Design philosophy of concrete linings for tunnel in soft soil. PhD thesis. Technische Universiteit Delft.
- Brinkgreve, R.B.J., Swolfs, W.M. & Engine, E. 2013. PLAXIS 3D user's manual, PLAXIS bv, the Netherlands.
- Caratelli et al. 2016. Precast tunnel segments with GFRP reinforcement. *Tunneling and Underground Space Technology*. 60 (2016) 10-20.
- Cavalaro S. 2009. Aspectos tecnologicos de tuneles construidos con tuneladore y dovelas prefabricadas de hormigon. PhF thesis. Universitat Politecnica de Catalunya.
- Cavalaro S.H.P. et al. 2011. Structural analysis of contact deficiencies in segmented lining. *Tunnelling and Underground Space Technology* 26(2011) 734-749.
- Cavalaro S., Aguado A. 2013. Packer behaviour under simple and coupled stresses. *Tunn Undergr Space Technol* 28:159-173 Do N.-A., Dias D., Oreste P., Djeran-Maigre I., 2D numerical investigation of segmental tunnel lining behaviour. *Tunnel and Undergroun Space Technology* 37-115-127.
- Cavallaro A. 2011. Structural behaviour of reinforced concrete lining segments during TBM operation. Master thesis in Emerging Technologies for Construction. University of Naples Federico II.
- Clough G.W. & Schmidt B. (1981). Design and performance of excavation and tunnel in soft clay. *Soft Clay Engineering*, Elsevier, 569-634.
- Conti R., G. Viggiani G., Perugini F., Numerical modelling of centrifuge dynamic test of circular tunnel in dry sand. *Acta Geotechnica* (2014) 9:597-612 DOI 10.1007/s11440-013-0286-8.
- Corigliano M., (2006), Seismic response of deep tunnel in near-fault conditions, Tesi di Dottorato in Ingegneria Geotecnica, Politecnico di Torino.
- Dean A., Young D., Kramer G.J.E. (2006) Use & Performance of Precast concrete tunnel Linings in Seismic Areas; IAEG 2006. The geological Society of London.
- Dias D, Kastner R. (2000)a. Slurry shield tunnelling: comparison between in situ data and three dimensional numerical simulations. *Geotech-Year* 27-30 Nov. 2000, Bangkok, Thailand 23.
- Dias D, Kastner R., Maghazi M. (2000)b. Three dimensional simulation of slurry shield tunnelling. *Proc. of the International Symposium on Geotechnical aspects of underground construction in soft ground*. Balkema, Rotterdam, pp 351-356.

- Ding et al. 2004. Analysis of shield tunnel. *International Journal for Numerical and Analytical Methods in Geomechanics*. 28:57-91.
- Do et al. (a) 2013. Three-dimensional numerical simulation for mechanized tunneling in soft ground: the influence of the joint pattern. *Acta Geotechnica* DOI 10.1007/s11440-013-0279-7.
- Do et al. (b) 2013. 2D numerical investigation of segmental tunnel lining behaviour. *Tunnel and Underground Space Technology* 37(2013) 115-127.
- Do et al. 2014. A new numerical approach to the hyperstatic reaction method for segmental tunnel linings. *International journal for numerical and analytical methods in geomechanics*.
- Do N.A., Dias D., Oreste P., Maigre I. D. (2015). 2D Numerical investigation of segmental tunnel lining 639 under seismic loading. *Soil Dynamics and Earthquake Engineering* 72 (2015) 66-76.
- Dowding C.H., Rozen A., (1978), Damage to rock tunnels from earthquake shaking, American Society of Civil Engineers, *Journal of Geotechnical Engineering Division*, Vol.104, p. 175-191.
- El Naggar H, Hinchberger S, Lo KY. A closed-form solution for composite tunnel linings in a homogenous infinite isotropic elastic medium. *Can Geotech J* 2008; 45:266–87.
- Emolo A. et al. 2016. Earthquake early warning feasibility in the Campania region (southern Italy) and demonstration system for public school buildings. *Bull Earthquake Eng* (2016) 14:2513–2529 DOI 10.1007/s10518-016-9865-z.
- EC8. Eurocode 8. Design of structures for Earthquake Resistance. Brussels, Belgium: European Committee for standardization; 2004. The European Standard EN 1998-1.
- Evangelista A., Pellegrino A. (1990). Caratteristiche geotecniche di alcune rocce tenere italiane. III ciclo di Conferenze di Meccanica e Ingegneria delle Rocce, MIR90, Torino.
- Fabozzi S., Licata V., Autuori S., Bilotta E., Russo G., Silvestri F., Prediction of the seismic behaviour of an underground railway station and a tunnel in Napoli (Italy). *Underground Space* 2017 (In press).
- Faisal I. Shalabi et al. 2012. Concrete segment tunnel lining sealant performance under earthquake loading. *Tunnelling and underground Space Technology* 31(2012) 51-60.
- Fargnoli, V., 2015. Soil-structure interaction during tunnelling in urban area: observation and 3D numerical modelling. Ph.D. thesis, University of Bologna.
- Feddema, A, Mller, M, Zon, W.H., Hashimoto, T, 2001. ETAC two-component grout field test at Botlek rail tunnel. *Modern Tunneling Science and Technology*, Swets & Zeitlinger, p.809-815.
- Fei et al. 2014. Model test study on effective ratio of segment transverse bending rigidity of shield tunnel. *Tunnelling and Underground Space Technology* 41:193– 205.
- Feng et al. 2011. Prototype tests on effective bending rigidity ratios of segmental lining structure for shield tunnel with large cross-section. *Chinese Journal of Geotechnical Engineering*. Volume 33, Issue 11, November 2011, Pages 1750-1758.
- Groeneweg T.W. 2007. Shield driven tunnels in ultrahigh strength concrete. Reduction of the tunnel lining thickness. PhD thesis. Delft University of Technology.
- Guan et al. 2015. Studies on the key parameters in segmental lining design. *Journal of Rock Mechanics and Geotechnical Engineering* 7:674-683.
- Guglielmetti, V., Grasso, P., Mahtab, A., Xu, S., 2008. *Mechanized Tunnelling in Urban Areas: Design methodology and construction control*. CRC Press.

- Gunn, M. J., 1993. The prediction of surface settlement profiles due to tunnelling. In: Houlsby, G. T., Schofield, A. N. (Eds.), *Predictive soil mechanics*. Proceedings of the Wroth memorial symposium, 27-29 July 1992, St. Catherine's College, Oxford. Thomas Telford, pp. 304–316.
- Hardin B.O. and Drnevich V. (1972). Shear modulus and damping in soils: design equations and curves. *Journal of Soil Mechanics and Foundations Division, ASCE* 98(7): 667-692.
- Harding and Chappell 2014. State of the art precast linings. *North American Tunneling Journal*, Oct/Nov issue, TGS Media, Tunbridge Wells, UK.
- Harichandran RS, Vanmarcke EH. Stochastic variation of earthquake ground motion in space and time. *Journal of Engineering Mechanics* 1986; 112(2):154-74.
- Hashash Y.M.A., Hook J.J., Schmidt B., Yao J.I.-C. (2001). Seismic design and analysis of underground structures. *Tunnelling and Underground Space Technology* 16, 247–293.
- Hashash Y.M.A., Park D., Yao J.I.-C. (2005). Ovaling de-formations of circular tunnels under seismic loading, an up-date on seismic design and analyses of underground structures, *Tunnelling and Underground Space Technology*, 20, 435-441.
- Hashimoto T., Brinkman J., Konda T., Kano Y., Feddema. Simultaneous Backfill Grouting, Pressure Development in Construction Phase and in the Long-Term.
- HAZUS 1999. Earthquake loss estimation methodology—technical and user manual. Federal Emergency Management Agency, Washington.
- Hefny AM, Tan FC, Macalevery NF. Numerical study on the behavior of jointed tunnel lining. *J Inst Civ Eng* 2004; 44:108–18.
- Hefny AM, Chua HC. An investigation into the behavior of jointed tunnel lining. *Tunnel Underground Space Technology* 2006; 21:428.
- Hirata, T, 1989. Study on behavior of cohesive soil in type shield tunneling work and on construction technique. Doctoral Thesis, Kyoto University, p.45.
- Hoefsloot, F.J.M. 2008. Analytical solution longitudinal behaviour Tunnel lining. Proceeding 6th Int. Symposium on Underground Construction in soft Ground, Shanghai Hordijk, D.A. Gijsbers F.B.J.: Laboratorium proeven tunnel segmenten, CUR/COB, Projectbureau boortunnels, June 199.
- Huang et al. 2006. Study on transverse effective rigidity ratio of shield tunnel. *Chin. J. Geotech. Eng.* 28(1), 11-18.
- Huo H, Bobet A, Fernandez G, Ramirez J (2005) Load transfer mechanisms between underground structure and surrounding ground: evaluation of the failure of the Daikai station. *J Geotech Geoenviron Eng* 131(12):1522–1533.
- Janssen P. Tragverhalten von tunnelausbauten mit gelenktubbing, Ph.D. Thesis Technischen Universitat Carolo-Wilhelmina, Braunschweig, December 1983.
- Japanese Society of Civil Engineers (JSCE). Japanese standard for shield tunnelling, 1996.
- Kartal M.E., Basaga H.B., Bayraktar A. Muvafik M., “Effects of semi-rigid connection on structural responses”. *Electronic journal of structural engineering*. (2010) 10:22-35.
- Kawashima K. (1999). Seismic design of underground structures in soft ground: a review, *Geotechnical Aspects of Underground Construction in Soft Ground*, Kusakabe, Fujita & Miyazaki (eds). Balkema, Rotterdam, ISBN 90 5809 1 066.
- Klappers C. et al. 2006. Structural analyses of segmental lining—coupled beam and spring analyses versus 3DFEM calculations with shell elements. *Tunn Undergr Space Technol* 21:254–25.

- Koiama Y. 2003. Present status and technology of shield tunnelling method in Japan. *Tunnelling and Underground Space Technology* (18):145-59.
- KIYOMIYA Osamu (1995) Earthquake-resistant Design Features of Immersed Tunnels in Japan, *Tunneling and Underground Space Technology* 465, Vol. 10, No. 4, pp. 463–475
- Kojizumi J. 2006. Segment design from allowable stress method to limit state method. Tokyo: Japan Society of Civil Engineering (in Japanese).
- Kouretzis G, Sloan S, Carter J (2013) Effect of interface friction on tunnel liner internal forces due to seismic S- and P-wave propagation. *Soil Dyn Earthq Eng* 46:41–51.
- Koyama and Nishimura 1998. Design of lining segment of shield tunnel using a beam-spring model. Quarterly Report of RTRI (Railway Technical Research Institute) (Japan). Volume 39, Issue 1, February 1998, Pages 23-27.
- Kuhlemeyer R.L and Lysmer J. (1973) Finite Element Method Accuracy for Wave Propagation Problems. *Journal of the Soil Mechanics and Foundation Division*, 99(5), 421- 427.
- Lambrugh A, Rodriguez LM, Castellanza R (2012) Development and validation of a 3D numerical model for TBM–EPB mechanised excavations. *Comput Geotech* 40:97–113.
- Lanzano Giovanni. Physical and analytical modelling of tunnels under dynamic loadings. Ph.D. dissertation (2009) University of Naples, Federico II.
- Lanzano G, Bilotta E, Russo G, Silvestri F, Madabhushi PG (2012) Centrifuge modelling of seismic loading on tunnels in sand. *Geotech Test J* 35(6):1–16.
- Lanzano G., Bilotta E., Russo G., Silvestri F. 2014a. Experimental and numerical study on circular tunnels under seismic loading. *Eur J of Environm and Civil Eng* doi:10.1080/19648189.2014.893211.
- Lanzano G., Bilotta E. (2014). Permanent increments of internal forces on a tunnel lining due to dynamic loadings. *Proc. 8th Int Symp on Geotech Aspects of Underground Construction in Soft Ground*, 203-208.
- Lanzano G., Visone C., Bilotta E., F.S. De Magistris (2016) Experimental assessment of the stress-strain behaviour of Leighton Buzzard Sand for the calibration of a constitutive model.
- Lee et al. 2001. An analytical solution for a jointed shield-driven tunnel lining. *International journal for numerical and analytical methods in geomechanics*. *Int. J. Numer. Anal. Meth. Geomech.*, 2001; 25:365; 390.
- Lee KM, Ge XW. 2001. The equivalence of a jointed shield-driven tunnel lining to a continuous ring structure. *Can Geotech J* 2001; 38:461–83.
- Li C. 2016. Seismic Response Analysis and Test of Long Segmental Immersed Tunnel. PhD dissertation. Tongji University, Shanghai, China.
- Li C., Yuan J.Y., Yu H.T., Yuan Y. Mode-based equivalent multi-degree-of-freedom system for one-dimensional viscoelastic response analysis of layered soil deposit. *Earthquake Engineering and Engineering Vibration*, 2017. (In press)
- Li et al. 2015. A progressive model to simulate the full mechanical behaviour of concrete segmental lining longitudinal joint. *Engineering Structures*. 93:97-113.
- Li P. & Song 2014. Three-dimensional numerical analysis for the longitudinal seismic response of tunnels under an asynchronous wave input. *Computers and Geotechnics*. 63 (2015) 229-243.
- Liu JH, Hou XY. Shield-driven tunnels. Beijing: China Railway Press; 1991. p. 152–303.

- Liu et al. 2015. Experimental investigation of the ultimate bearing capacity of continuously-jointed segmental tunnel linings. *Structure & Infrastructure Engineering*. 2015: 1-16.
- Liu et al. 2017a. Ultimate Load-carrying Capacity of the Longitudinal Joints in Segmental Tunnel Linings. *Structural Concrete*.
- Liu et al. 2017b. Investigation of the structural effect induced by stagger joints in segmental tunnel linings: direct insight from mechanical behaviours of longitudinal and circumferential joints. *Tunnelling and underground Space technology* (In press).
- Luco JE, Wong HL. Response of a rigid foundation to a spatially random ground motion. *Earthquake Engineering and Structural Dynamics* 1986:14891-908.
- Lysmer & Kuhlemeyer (1969). Finite dynamic model for infinite media", *J. of Eng. Mech. Div., ASCE*: 859-877, 1969.
- Maidl B., Herrenknecht M., Maidl U., Wehrmeyer G. *Mechanised Shield Tunnelling*, 2nd Edition. 2011 Ernst & Sohn, Berlin.
- Marino R., "Misura di deformazione nei rivestimenti di gallerie metropolitane". Ph.D. dissertation, (2010), University of Naples, Federico II.
- Meletti C, Galadini F, Valensise G, Stucchi M, Basili R, Barba S, et al. A seismic source zone model for the seismic hazard assessment of the Italian territory. *Tectonophysics* 2008; 450:85–108.
- Migliazza M, Chiorboli M, Giani G (2009) Comparison of analytical method, 3D finite element model with experimental subsidence measurements resulting from the extension of the Milan underground. *Comput Geotech* 36:113–124.
- Mo H.H. and Chen J.S. 2008 Study of inner force and dislocation of segments caused by shield machine attitude. *Tunnelling and Underground Space technology*. 23 (2008) 281-291.
- Mollon G (2010) Etude de 'terministe et probabiliste du comportement des tunnels. Ph.D. dissertation, INSA de Lyon. N.d'ordre 2010ISAL0110 58.
- Mollon G, Dias D, Soubra A (2013) Probabilistic analyses of tunnelling-induced ground movements. *Acta Geotech* 8:181–199.
- Moschonas I, Kappos A, Panetsos P, Papadopoulos V, Makarios T, Thanopoulou P. Seismic fragility curves for Greek bridges: methodology and case studies. *Bulletin of Earthquake Engineering* 2009; 7:439–68.
- Muir Wood, A. M. 1975. The circular tunnel in elastic ground. *Géotechnique* 25, No.1, 115-117.
- Nakamura Y. 1988. On the urgent earthquake detection and alarm system (UrEDAS). Presented at Ninth World Conf. Earthq. Eng., Tokyo.
- Nakamura Y. 1989. Earthquake alarm system for Japan Railways. *Reproduction* 109:1–7.
- Nakamura Y, Tucker BE. 1988. Japan's earthquake warning system: should it be imported to California? *Calif. Geol.* 41(2):33–40.
- Ng C, Lee K, Tang D (2004) Three-dimensional numerical investigations of new Austrian tunnelling method (NATM) twin tunnel interactions. *Can Geotech J* 41:523–539.
- NIBS. HAZUS-MH: Technical Manuals. Washington, DC: Federal Emergency Management Agency and National Institute of Building Science; 2004.
- Ochmanski m. 2016. Numerical analyses of the effect of tunnel construction. Doctoral Thesis. University of Cassino and Southern Lazio, Italy. Silesian University of Technology, Poland.
- O'Rourke, M. J., and Liu, X. (1999). Response of buried pipelines subject to earthquake effects.

- Owen G.N., Scholl R.E., (1981), Earthquake engineering of large underground structures, Report no. FHWA/RD-80/195. Federal Highway Administration and National Science Foundation.
- Park, D. and Hashash, Y. M. A., "Soil damping formulation in nonlinear time domain site response analysis," *Journal of Earthquake Engineering* 8(2), 2004, pp. 249-274.
- Park D. et al. 2009. Simulation of tunnel response under spatially varying ground motion. *Soil Dynamics and Earthquakes Engineering*. 29(2009) 1417-1424.
- Peila, Daniele; Borio, Luca; Pelizza, Sebastiano. The Behaviour of a Two-Component Back-Filling Grout used in a Tunnel-Boring Machine. *ACTA Geotechnica Slovenia*. 2011.
- Penzien J., (2000). Seismically induced racking of tunnel linings, *International Journal of Earthquake Engineering and Structural Dynamics*, 29, 683-691.
- Penzien J., Wu C., Stresses in the lining of bored tunnels. *Earthq Eng Struct Dyn* 27:283-300.
- Pepe G., "Rivestimenti di gallerie in conci prefabbricati: sperimentazione e analisi". Ph.D. dissertation, (2008), University of Naples, Federico II.
- Picozzi M, Zollo A, Brondi P, Colombelli S, Elia L, Martino C (2015) Exploring the feasibility of a nationwide earthquake early warning system in Italy. *J Geophys Res Solid Earth* 120:2446–2465. doi: 10.1002/2014JB011669.
- Pitilakis K, Tsinidis G. (2010). Seismic design of large, long underground structures: metro and parking stations, highway tunnels. In: *Proceedings of international geotechnical conference "Geotechnical Challenges in Megacities" (GEOMOS2010)*, Moscow, Russia, 7-10 June 2010.
- Pitilakis K., Tsinidis G. (2014). Performance and seismic design of underground structures, State-of-Art, In *Earthquake geotechnical engineering design* (eds M. Maugeri and C. Soccodato), *Geotechnical Geological and Earthquake Engineering*, 28, 279-340. http://dx.doi.org/10.1007/978-3-319-03182-684_8_11. Geneva, Switzerland: Springer.
- Power M.S., Rosidi D., Kaneshiro J.Y., (1998), Seismic vulnerability of tunnels and underground structures revisited, *Proceedings of North American Tunneling '98*, Newport Beach, CA, Balkema Rotterdam, p. 243250.
- Putke D I T, Bohun R, Mark D I H P. Experimental analyses of an optimized shear load transfer in the circumferential joints of concrete segmental linings. *Structural Concrete*, 2015, 16(4):572–582.
- Rampello S. (2005), *Costruzioni in sotterraneo e scavi a cielo aperto*. Linee guida AGI: Aspetti geotecnici della progettazione sismica, Parte III: Opere geotecniche, Capitolo 15, pag. 213-225 (in Italian)
- Reference Manual Plaxis 3D.
- Salmon m., Wang J., Jones D., Wu Ch., fragility formulation for the BART system, in: *proceedings of the 6th U.S. Conference on Lifeline Earthquake Engineering*. TCLEE, Long Beach, 2003.
- Santos J.A. and Correia A.G. (2001). Reference threshold shear strain of soil. Its application to obtain a unique strain dependent shear modulus curve for soil. *15th Int. Conf. on Soil Mechanics and Geotechnical Engineering*, Istanbul, vol. 1, pp. 267-270.
- Satriano C, Elia L, Martino C, Lancieri M, Zollo A, Iannaccone G (2011) PRESTo, the earthquake early warning system for southern Italy: concepts, capabilities and future perspectives. *Soil Dynamic Earthquake Engineering* 31:137–153. doi:10.1016/j.soildyn.2010.06.008.
- Schanz T., Vermeer P.A. and Bonnier P.G. (1999). The Hardening Soil Model: formulation and verification. *Plaxis symposium on beyond 2000 in computational geotechnics*, Amsterdam, pp. 281–296.
- Scientific Manual Plaxis 3D.
- Sedarat H, Kozak A, Hashash YMA, Shamsabadi A, Krimotat A (2009) Contact interface in seismic analysis of circular tunnels. *Tunn Undergr Space Technol* 24(4):482–490.

- Sharma S.W.R., Judd, (1991), Underground opening damage from earthquakes, *Engineering Geology*, vol.30, p. 263-276.
- Shinozuka M, Feng MQ, Kim H-K, Kim S-H. Nonlinear static procedure for fragility curve development. *Journal of Engineering Mechanics* 2000; 126: 1287–96.
- St.John C.M., Zahrah T.F. (1987). Aseismic design of underground structures, *Tunnelling and Underground Space Technology*, 2 (2), 165-19.
- Sugimoto M. (2006) Causes of shield segment damage during construction. *International Symposium on Underground Excavation and Tunnelling*. Bangkok, Thailand.
- Sugimoto M. and Sramoon A. 2002. Theoretical model of shield behaviour during excavation. *Journal of Geotechnical and Geoenvironmental Engineering* 128(2), 138-165.
- Teachavorasinskun S. et al. 2010. Influence of segmental joints on tunnel lining. *Tunnelling and Underground Space Technology* 25:490-494.
- Thewes and Budach 2009. Grouting of the annular gap in shield tunnelling – an important factor for minimisation of settlements and production performance. In: *ITA AITES word Tunnel Congress 2009 “safe Tunnelling for the City and Environment”* Budapest.
- Thinert C., Pulsfort M. 2011. Segment design under consideration of the material used to fill the annular gap. *Geomechanics and Tunneling* 4, 665-679.
- Toutlemonde et al. 2000. Tunnel precast segments: an SFRC alternative? In: *Proceedings of the Fifth RILEM Symposium on Fibre-reinforced Concrete (FRC)*, pp 171-180. ISBN: 2-912143-18-7.
- Tsinidis G., Pitilakis K., Anagnostopoulou C. (2016). Circular tunnels in sand: dynamic response and efficiency of seismic analysis methods at extreme lining flexibilities. *Bull Earthquake Eng*, 14:2903–2929 DOI 10.1007/s10518-016-9928-1.
- Valente A., Micheli A., Cedrone L., Bardani C., 2010. La galleria Monteluco (L'Aquila): un caso di galleria soggetta a sisma. *ANAS report*.
- Van Oorsouw R.S. 2010. Behaviour of segment joints in immersed tunnel under seismic loading. Master Thesis. Delft University of Technology.
- Vanzi I., (2000), Elastic and inelastic response of tunnels under longitudinal earthquake excitation, *Journal of Earthquake Engineering*, Imperial College Press, United Kingdom, vol.4(2), Aprile 2000.
- Vinale F. (1988). Caratterizzazione del sottosuolo di un'area campione di Napoli ai fini di una microzonazione sismica. *Rivista Italiana di Geotecnica*, 2(1988), 77-100.
- Wang J., (1993), *Seismic Design of Tunnels: A Simple State-of-the-art Design Approach*, Monograph 7, Parsons, Brinckerhoff, Quade and Douglas Inc, New York.
- Wood, A. M., The circular tunnel in elastic ground. *Geotechnique*, 25(1), 115-127 (1975).
- Wood, D. M., 2004. *Geotechnical Modelling (Applied Geotechnics)*. CRC Press.
- Wood M. Muir Wood Lecture 2012. Segmental ring design. *New Challenges with High Tunnel Diameter*.
- Zhao C., Lavasan A.A., Barciaga t., Zarev V., Datcheva M., 2015. Model Validation and calibration via back analysis for mechanized tunnel simulation – The Western Scheldt tunnel case. *Computers and geotechnics* 69(2015) 601-614.
- Yu H. et al 2013. Seismic analysis of a long tunnel based on multi scale method. *Engineering Structures*. 49 (2013) 572-587.
- Yu H.T., Cai C., Guan X.F., Yuan Y. Analytical solution for long lined tunnels subjected to travelling loads. *Tunnelling and Underground Space Technology*, 2016, 58: 209-215.

- Yu H.T. et al. 2016a. Multi point shaking table test for lung tunnels subjected to non uniform seismic loadings – Part II: Application to the HZM immersed tunnel. *Soil Dynamics and Earthquake Engineering* (In press).
- Yuan Yong et al. 2016. Multi point shaking table test for lung tunnels subjected to non uniform seismic loadings – Part I: Theory and validation. *Soil dynamics and earthquake Engineering* (In press).
- Zhong, and Huang. et al. 2003. The method to confirm the effective bending stiffness of shield-driven tunnel lining. *Geology and Prospecting*. Volume 39, Pages 185-189.
- Zhong X., Zhu W., Huang Z., Han Y. 2006. Effect of joint structure on the joint stiffness for shield tunnel lining. *Tunnelling and Underground Space technology*. 21, 406-407.